# The Propagation of Strike-Slip Faults

# Using 3D Seismic Data

## Chris Wild

**Submitted in partial fulfilment of the requirements for the degree of Ph.D.**

**School of Earth and Ocean Sciences**

**Cardiff University**

**January 2015**

# **Summary**

The application of 3D seismic data to the study of fault evolution has greatly increased our understanding of how normal and thrust faults propagate. Specifically, by combining displacement distribution plots and a thorough analysis of the fault geometry, we can determine: linkage history, restrictions to fault growth, and blind versus emergent propagation. However, these methods have never been applied to strike-slip faults in seismic data due to the difficulty in imaging kinematic indicators or piercing points that quantify displacement.

This thesis presents a novel technique that allows for the rapid identification of kinematic indicators in two 3D seismic datasets from the Levant Basin, Eastern Mediterranean, which enables the displacement distribution of strike-slip faults to be analysed beyond what has been accomplished by traditional field-based studies. The high quality of the data also enables the detailed investigation into the 3D geometry of strike-slip faults to be used in conjunction with the displacement data to better understand the upward vertical propagation history. Results indicate that high displacement faults show distinctly different geometries from low displacement faults, and that strain rate and propagation mode may be integral in controlling geometry type. Furthermore, the geometry of the naturally occurring examples presented here, shows distinct differences from analogue studies, and suggests future work should be applied to understanding what controls these discrepancies.

The displacement distribution also allowed insight into fault network relationships at the regional scale, in addition to individual faults. In particular, the 3D geometry of conjugate intersections, branching intersections, and tip structures was explored. The results yielded very complex and confounding structural relationships, which suggest that deformation is rarely as simple as 2D interpretations show, and thus may have significant consequences to precious resource extraction.

# **<u>Acknowledgements</u>**

# **Table of Contents**

# 5    A PRELIMINARY ANALYSIS OF STRIKE-SLIP FAULT PROPAGATION AT FAULT INTERSECTIONS AND FAULT TIPS IN 3D  264

# <u>Table of Figures</u>

**Chapter 1-**

## Chapter 2-

## Chapter 3-

## Chapter 4-

## Chapter 5-

## Chapter 6-

# Table of Table(s)

# Chapter 1

# Introduction

# 1  Introduction

## 1.1  Rationale

Studies conducted on normal faults using three-dimensional (3D) seismic reflection data (e.g. Childs et al., 1995; 1996; Kattenhorn and Pollard, 2001; Marchal et al., 2003; Lohr et al., 2008) have greatly enhanced our understanding of fault propagation and evolution both kinematically and geometrically.  Principally, 3D studies have furthered the work of field-based and 2D seismic studies that established how an isolated fault nucleates, propagates radially, and accrues displacement to a maximum at the fault centre, and decreases to zero at the tip-line loop (Figure 1.1) (Rippon, 1984; Watterson, 1986; Barnett, 1987).  The displacement distribution of a fault can thus provide insight into fault growth, including whether the fault was isolated or restricted (either by proximity to another fault or mechanical stratigraphy), its linkage history, and propagation condition (i.e. blind or syn-kinematic) (Walsh and Watterson, 1988; Cartwright et al., 1995; Nicol et al., 1996; Baudon and Cartwright, 2008a).

This technique has also been applied to thrust systems (e.g. Briggs et al., 2006; 2009; Higgins et al., 2007; 2009; Morley et al., 2011); however, strike-slip faults remain relatively understudied, especially in seismic data, with displacement quantification limited to one stratigraphic horizon in field studies (e.g. Peacock, 1991; Nixon et al., 2011). This is primarily due to three reasons:

1. The horizontal displacement of strike-slip faults makes bedding planes very difficult to correlate across faults and thus piercing points must be identified using other features (this is especially true in seismic data, Figure 1.2, which illustrates that traditional cross-sections cannot determine fault slip in and out of the page).

2. Complex structures are often associated with strike-slip faulting (including folds, fractures, and normal and thrust faults) combined with sub-vertical fault strands, means strike-slip faults are both confusing and often poorly imaged in seismic data.

3. Most studies using 3D seismic data tend to focus on faulted regions where greater hydrocarbon accumulations are located, such as extensional basins and thrust

tectonics, and thus seismic data is more rarely shot in regions exclusively deformed by strike-slip faults.

This latter point is evidenced in the literature as many authors have conducted studies of strike-slip faults using field studies, sandbox modelling, mechanical analysis, and seismotectonics. However, a deeper investigation into strike-slip fault propagation and evolution has yet to be conducted using 3D seismic data, with most studies instead focussing on basin evolution (e.g. Hsiao, 2004; 2010; Jiang et al., 2011; Ghalayini et al., 2014) or on constraining strike-slip fault restoration (Durand-Riard et al., 2013; Benesh et al., 2013).

However, strike-slip faults remain fundamentally important as major earthquakes are caused by strike-slip movement, including the San Andreas Fault, California; the Dead Sea Fault, traversing through Israel, Lebanon, and Syria; and the Eastern and Northern Anatolian faults around Turkey. Furthermore, as hydrocarbon prices continue to increase, smaller hydrocarbon accumulations found in strike-slip systems will become increasingly important. Finally many faults exhibit oblique slip, and therefore an improved understanding of the strike-slip component will have significance in settings dominated by extension and compression.

Thus 3D seismic data provides an excellent opportunity to explore strike-slip fault propagation by fully visualising the fault plane in 3D geometry and observing the fault deforming several key stratigraphic horizons in plan view. This extends beyond what can be observed in the field, whilst also exhibiting features of naturally occurring examples instead of relying on predicted outcomes from analogue modelling (e.g. Tchalenko, 1970; Wilcox et al., 1973; Naylor et al., 1986).
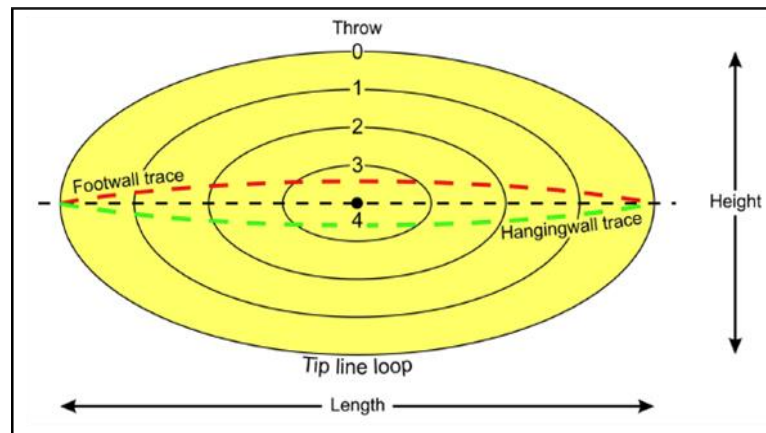
Figure 1.1 - Cartoon of the idealistic fault displacement distribution for an isolated fault. The fault plane is contoured so that displacement decreases in equal increments with distance from the centre, each following the elliptical shape of the fault plane.  Adapted from (Needham et al., 1996).
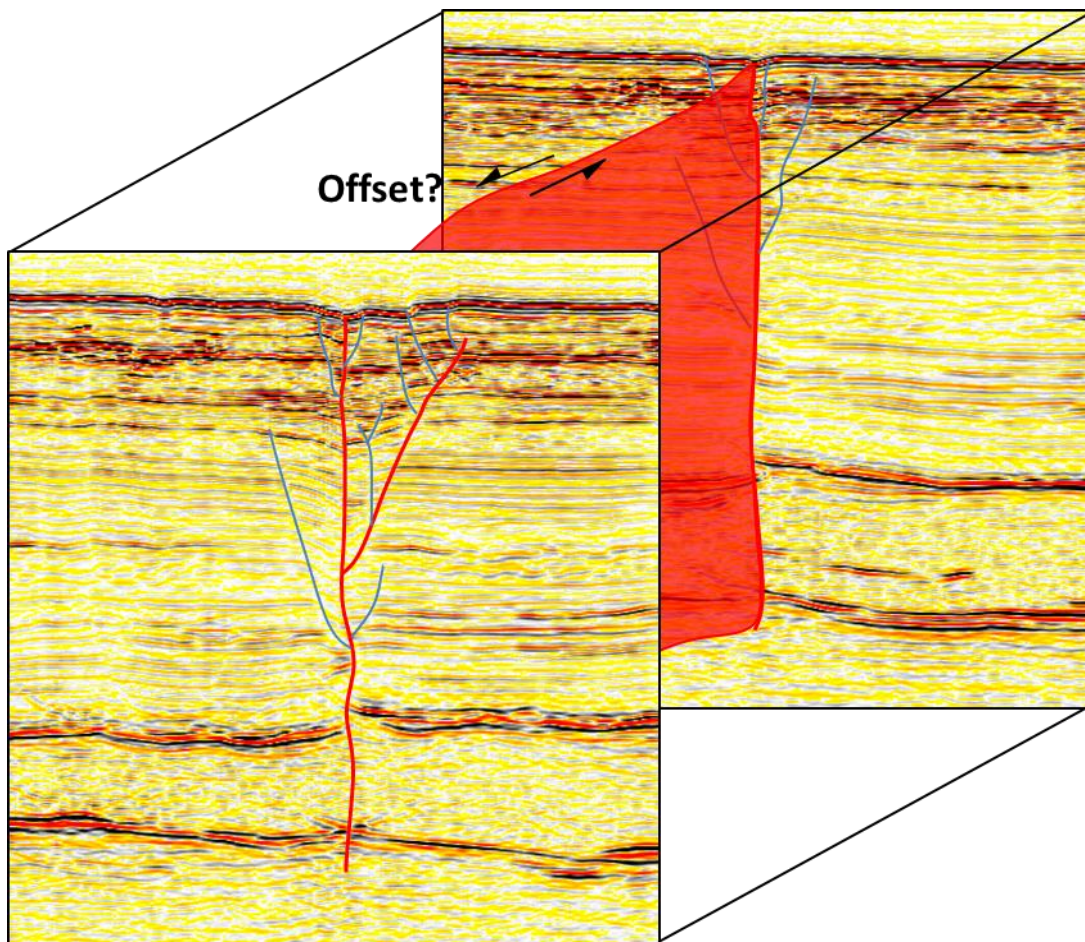


Figure 1.2 - Diagram illustrating how two seismic profile lines can be used to interpret the fault presence and structure; however, there is no way of correlating how much lateral offset or displacement has occurred across a strike-slip fault.

## 1.2   Aims

The primary aim of this thesis is to conduct an investigation of how strike-slip faults propagate using 3D seismic data using examples from two high resolution 3D seismic datasets from the Levant Basin, in the Eastern Mediterranean Sea (Figure 1.3).  This will be accomplished in four major stages:

1.  Establishing a methodology that allows for the quantification of strike-slip fault offset in seismic data using kinematic indicators.

2.  Applying this quantification to create the first 3D displacement distribution contoured plot for a strike-slip fault.

3.  Conducting a thorough analysis of strike-slip fault geometry in conjunction with stage 2, and use the results from both to develop new insights into lateral and vertical fault propagation.

4.  Exploring how strike-slip faults interact and propagate at fault intersections in 3D.

The remainder of this chapter serves to provide a review of some of the most relevant prior works conducted on strike-slip faults, in order to show what has already been completed, and illustrate how the results of this thesis are relevant to furthering the work completed in this field.  This will begin with a summary of strike-slip fault terms and basic attributes before focussing on the two major areas of strike-slip fault research: field based studies and analogue modelling.  The final sections will describe how 3D seismic data has furthered our knowledge of normal faults and summarise the prior work of strike-slip faults in seismic data. The chapter will conclude with a synopsis of the subsequent chapters to show how the four aims will inspect strike-slip fault propagation.
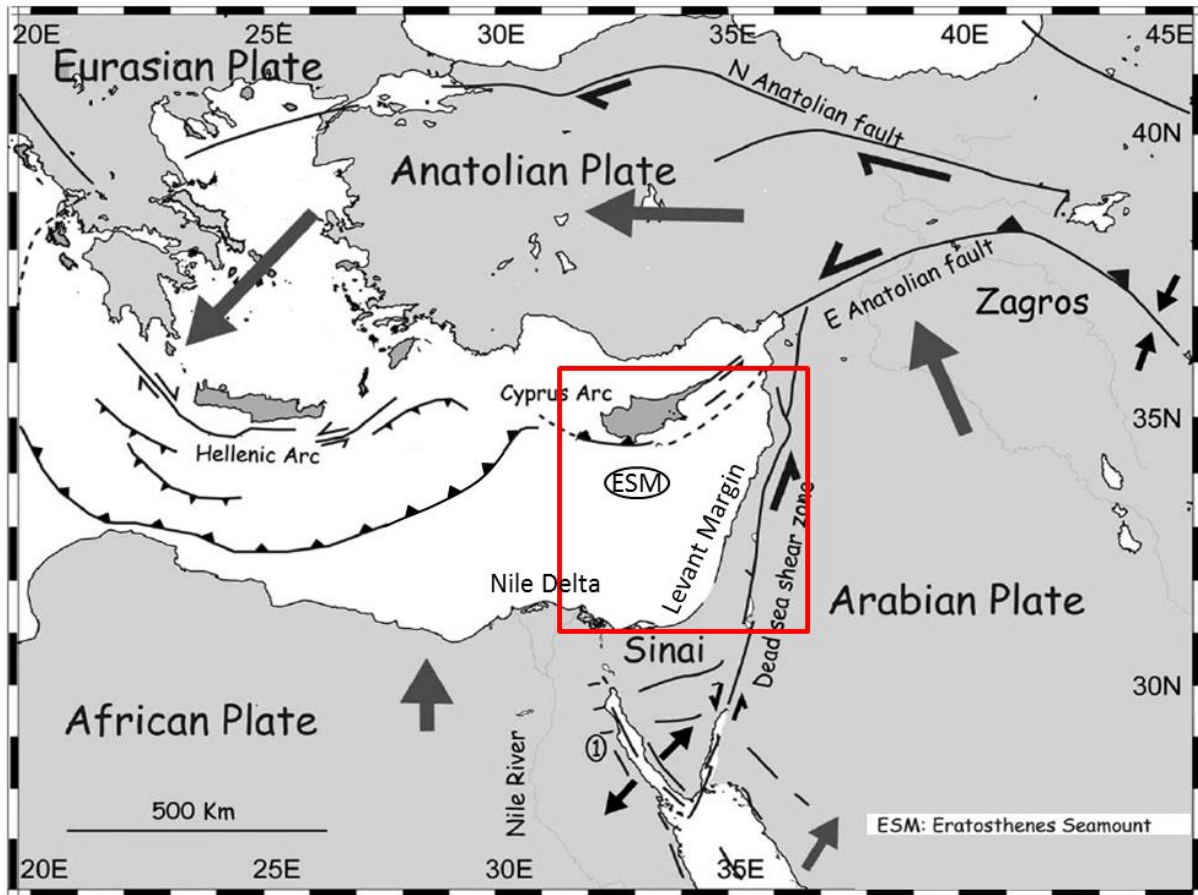
Figure 1.3a – Tectonic setting of the study area.  ESM = Eratosthenes Seamount.  Region in red depicted in 1.3b (next page).  Adapted from Loncke et al., (2006).
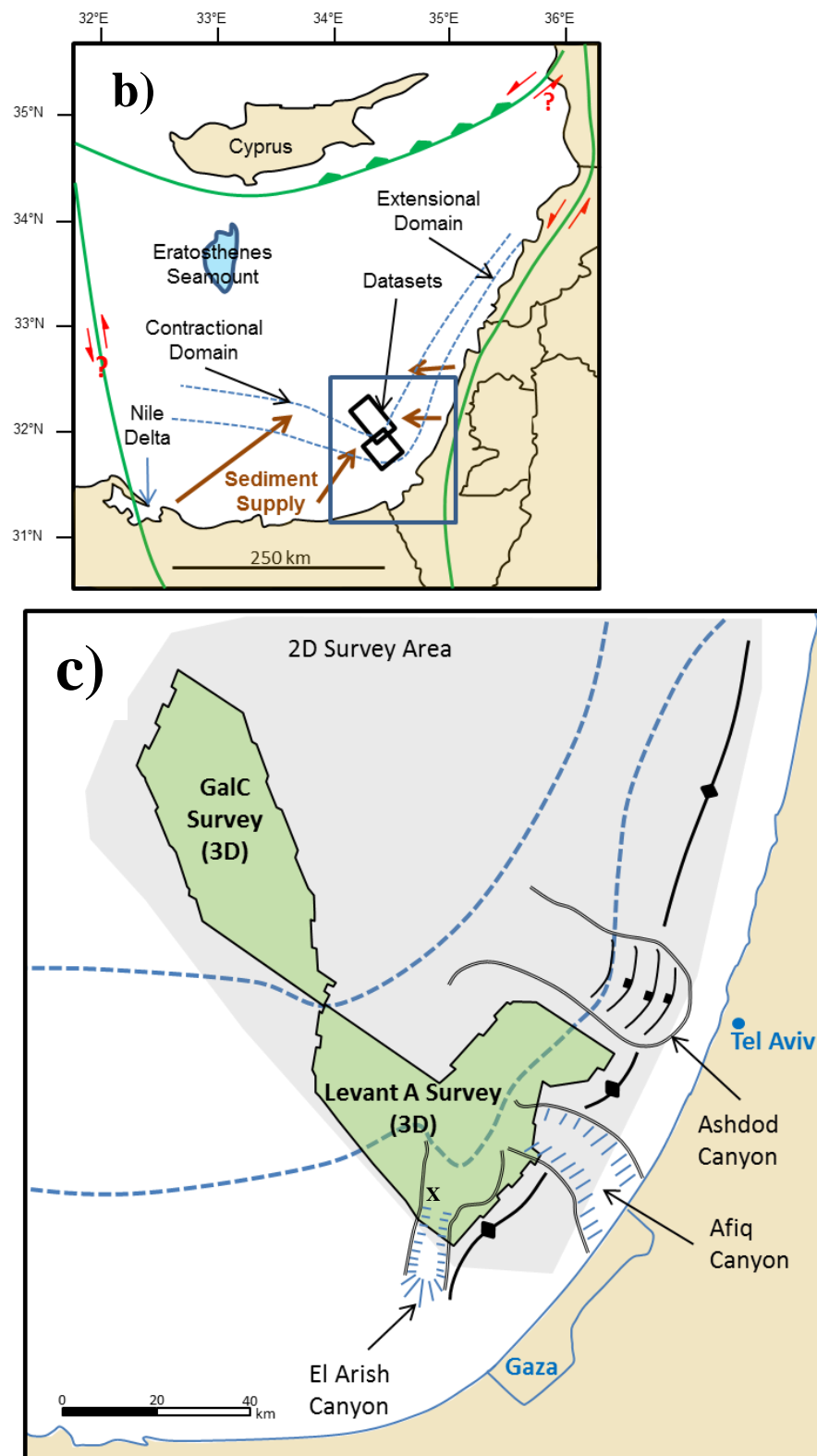
Figure 1.3 - Location map of the datasets in the Levant Basin, Eastern Mediterranean Sea. b) Shows the boundaries of the Sinai micro-plate, relative domains of the deformation, and sediment supply by salt flow down-slope.  c) Shows the outlines of the two 3D seismic datasets used in this thesis.  Also included are canyons mentioned in prior works and the Syrian Arc folds.  X denotes location of the well Gaza Marine-1 (GM-1), which was used to tie lithology to regional works and derive the velocity used for depth conversions.

## 1.3   Strike-Slip Fault Basics:   Terminology, Structural Characteristics, and Mechanics

Before describing much of the work completed on strike-slip faults, this section summarises the basic terminology, structure, and mechanics in order to provide context for the subsequent sections.

### 1.3.1   Terminology:

Several terms surrounding strike-slip faults can be used synonymously; however, it is not always clear why different terms exist.  Therefore this section provides a list of terms and brief definitions to help avoid confusion with prior studies:

*Strike-Slip fault*:  A strike-slip fault is defined as a vertical fault on which movement is caused by a horizontal shear parallel to the fault's strike (Bates, 1987; Twiss, 1992).

*Wrench fault*:  Term initially used to define a deep-seated, regional, nearly vertical strike-slip fault which involves igneous and metamorphic basement rocks as well as supracrustal sedimentary rocks by Moody & Hill (Moody), but has been adapted by many authors as a term referring to any type of strike-slip fault.  Although the name implies some form of rotational torque applied, this is not always the case (Sylvester, 1988) and will therefore be avoided for the remainder of this thesis.

*Transform fault*:  Plate-bounding strike-slip fault of regional scale that cuts through the lithosphere and fully accommodates motion between plates (e.g. San Andreas Fault).  These generally comprise zones of many associated smaller faults with displacements extending for hundreds of kilometres (Sylvester, 1988; Twiss, 1992).

*Transcurrent fault*:  A regional-scale strike-slip fault on continental crust that can have displacements of hundreds of kilometres but is not part of a plate boundary (similar to the initial usage of the term wrench fault) and does not cut the lithosphere (Sylvester, 1988; Twiss, 1992).

8

*Tear fault*:  Relatively small-scale, local strike-slip faults and are often secondary features in relation to other structures such as folds, thrust faults, and normal faults and as such can strike transverse to the strike of the zone of deformed rocks in a region (Sylvester, 1988; Twiss, 1992).

*Transfer fault*:  A fault in a region where multiple faults interact and "overstep" or "link", connecting and transferring displacement between faults, which can either be parallel or in an en echelon arrangement (Sylvester, 1988; Twiss, 1992).

The faults studied in this thesis are thin-skinned (due to detaching into a salt layer) and do not reach the size of transform or transcurrent faults, and are not secondary features like tear faults, and are therefore referred to as strike-slip faults herein.  Although the faults do form linkages and transfer displacement, the term transfer fault is avoided in favour of transfer zone, jog, step-over, and bend which are described below.

### 1.3.2   Structural Characteristics:

Displacement on a strike-slip fault occurs horizontally and is parallel to fault strike (Bates, 1987; Twiss, 1992).  Due to this horizontal nature, fault traces often create straight lines that cut through topography, with no uplifting or downthrown movement occurring on each side of the fault.  However along the fault, one side will tend to be topographically higher than other, and this will alternate along the fault trace due to oblique-slip movement, causing both strike-slip and dip-slip components (either reverse or normal movement) to occur (Sylvester, 1988; Twiss, 1992).  Displacement occurs as a left or right-lateral motion, more commonly referred to as sinistral or dextral (Figure 1.4) (Twiss, 1992).

Strike-slip faults often comprise segments, which curve and bend towards each other, causing local compressional areas known as restraining bends or extensional areas known as releasing bends (Twiss, 1992).  These bends can also be referred to as step-overs or jogs, with extensional jogs subsiding to form depressions comprising extensional duplexes, normal faults, and fractures.  Large scale extensional jogs form pull-apart basins, which can be associated with hydrocarbons (Sylvester, 1988).  In contrast, compressional jogs form "pop up" structures (e.g. contractional duplexes and thrust faults or folds), see Figure 1.5 (Woodcock and Fischer, 1986; Woodcock and Daly, 1986; Sylvester, 1988).

9

Extensional and compressional jogs observed in cross-section form flower structures, with a tulip shape indicating a negative flower structure (extensional) and a palm tree indicating a positive flower structure (compressional, Figure 1.6) (Sylvester, 1988). Flower structures are also identified along fault segments, and can show localised transtensional and transpressional elements, described later (Naylor et al., 1986). However, it is important to note that the term flower structure in textbooks more often relates to the large scale pop-up and pull-apart structures observed in jogs of major faults, which is created through a series of fault reactivations, linkages, and growth (described later, Section 1.4); whilst the flower structures from the analogue sandbox models form from en echelon arrays of faults at the surface (Section 1.5).

In order to establish a fault geometry that shows notable differences to published examples in the literature, the flower structure term will be avoided for the majority of this thesis. However, the discussion chapter will address this discrepancy and link the findings.
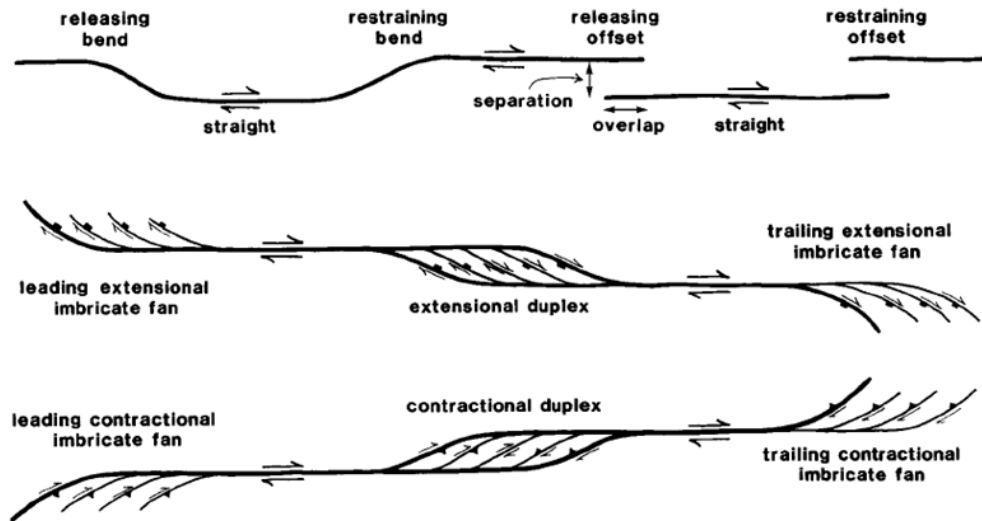
Figure 1.4 ‑ Cartoon morphology of strike-slip faults at bends, note that releasing bends cause extensional duplexes, whilst restraining bends cause contractional duplexes.  If a fault terminates it often ends in a "horsetail splay", which creates imbricate fans of normal or thrust faults depending on the tectonic setting. Adapted from Woodock & Fischer (1986).



Figure 1.5 ‑ a) and b) are examples of thrust fault duplexes, and normal fault duplexes, respectively.  c), d), and e) show duplexes resulting from both restraining and releasing bends, causing pop-up structures and subsiding basins, respectively.  Note that the faults bounding the sides of the structures changes from dominantly strike-slip movement to normal or reverse movement. Adapted from Woodock & Fischer (1986).

Figure 1.6 ‑ Cartoon examples of flowers structures.  a)  a negative (tulip) structure and b) a positive (palm tree) structure. Adapted from Woodcock & Fisher (1986).

### 1.3.3  Basic Mechanics:

The basic mechanics of strike-slip fault formation are derived from two theories: pure shear and simple shear (Sylvester, 1988).

*Pure shear:* First proposed by Anderson (1905) to explain fault orientations in a homogeneous medium relative to a tri-axial stress, it is also known as the Coulomb-Anderson model of shear. Pure shear predicts a conjugate set of complementary sinistral and dextral strike-slip faults will form (known as conjugate faults) at an angle of $\varphi$ and $-\varphi$, with $\varphi$ = internal friction angle (Figure 1.7). Furthermore, it predicts that extension fractures or normal faults will form perpendicular to the elongation axis, whilst folds and thrust faults will form parallel to the shortening axis. Conjugate faults can only accommodate bulk strain as long as propagation occurs contemporaneously between them; otherwise accommodation space problems occur, which can only be compensated by rotation (Horsfield, 1980; Sylvester, 1988). According to Sylvester (1988), pure shear examples are rarely seen in nature and the concept has led many researchers from the 1950's and 1960's to produce incorrect interpretations. Furthermore, if formation occurs from pure shear, then they tend to be relegated to fold-thrust belts, where the conjugate faults transect fold trends (Sylvester, 1988). However, more recent field based studies show that conjugate faults can exist at smaller scales and in regions not dominated by fold-and-thrusting (e.g. Freund, 1970; Zhao and Johnson, 1991; Kelly et al., 1998). These studies further suggest that the conjugate faults do not occur synchronously and are actually progressively offset by alternating dominance of a fault set (Zhao and Johnson, 1991; Kelly et al., 1998). Nixon et al., (2011) demonstrated that conjugate faulting occurred in regions with minimal extension and undergoes little rotation. In summary, conjugate faulting is characteristic of bulk pure shear, but there appears to be discrepancies with the timing of slip on these faults.

*Simple shear:* Early experiments showed that simple shear incorporates a monoclinic symmetry of strain as it accounts for rotation and produces a greater variety of structures than pure shear, Figure 1.7 (Cloos, 1928; Riedel, 1929; Tchalenko, 1970). Along with the through-going fault zone, simple shear produces the following set of structures, with their genesis noted in Figure 1.8:

*Riedel (R) shears* - these form en echelon patterns of the earth's surface, usually at an angle of φ/2 with the through going fault and show synthetic displacement.

*Conjugate Riedel (R') shears* - occurring at 90° - φ/2 to the through-going fault or the principal displacement zone (PDZ). These demonstrate antithetic slip to the PDZ (Tchalenko, 1970).

*P shears* – secondary synthetic faults at an angle of - φ/2 to the PDZ (Tchalenko, 1970).

*T fractures* – also known as extension fractures, these can also develop into normal faults at around 45° to the PDZ (Sylvester, 1988).

*Folds* – these can also form thrust faults at restraining bends and initially form at 45° to the PDZ, but rotate with continued deformation (Sylvester, 1988).

*Y shears* – shears that form parallel to the PDZ (at a low angle between both R and P shears). These generally form later in a strike-slip fault evolution, producing the anatomising fault zones seen in nature (Naylor et al., 1986; Sylvester, 1988; Tchalenko, 1970).

*Other Shears* – these are characterised by short-lived splay faults *(S)* that develop near the tips of R shears, and strike more than 17° to the PDZ; and lower angle shears *(L)* that strike at less than 17° and also develop at R shear tips or between R shears.

Together, these structures normally form en echelon patterns (Figure 1.9), in long, relatively narrow damage zones (Kim et al., 2004) and have been studied in detail by several authors (Tchalenko, 1970; Wilcox et al., 1973; Naylor et al., 1986). Simple shear describes much of the deformation found in field examples, including extensional fractures in the Valley of Fire (Flodin and Aydin, 2004a; 2004b), folds and thrust faults in transpressional events (Sylvester and Smith, 1976) and en echelon surficial patterns (Kim et al., 2004).

Ultimately, faulting under these two mechanisms occurs in nature, but why faults show evidence of each mechanism and when, remains a source of confusion. Faults in this thesis show evidence of both mechanisms and will be addressed in Chapter 6.
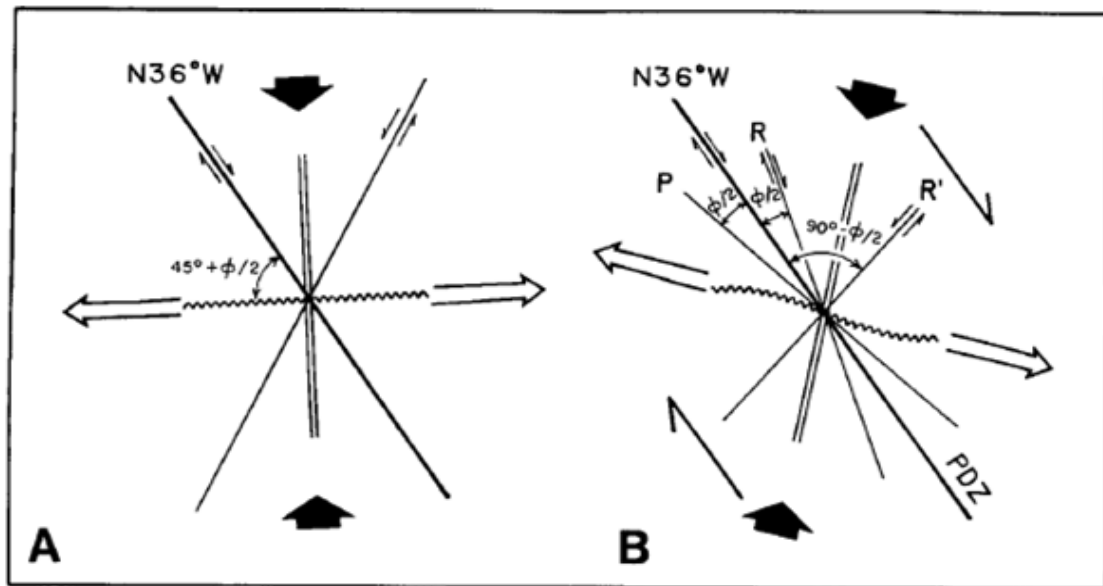
Figure 1.7 ‑ a) An example of the structures produced by pure shear, and b) and examples of structures produced by simple shear.  Black arrows indicate maximum stress directions ($\sigma_1$), whilst clear arrows indicate minimum stress ($\sigma_3$) or tension.  Note PDZ can be referred to as the through-going fault zone. Adapted from Sylvester (1988).
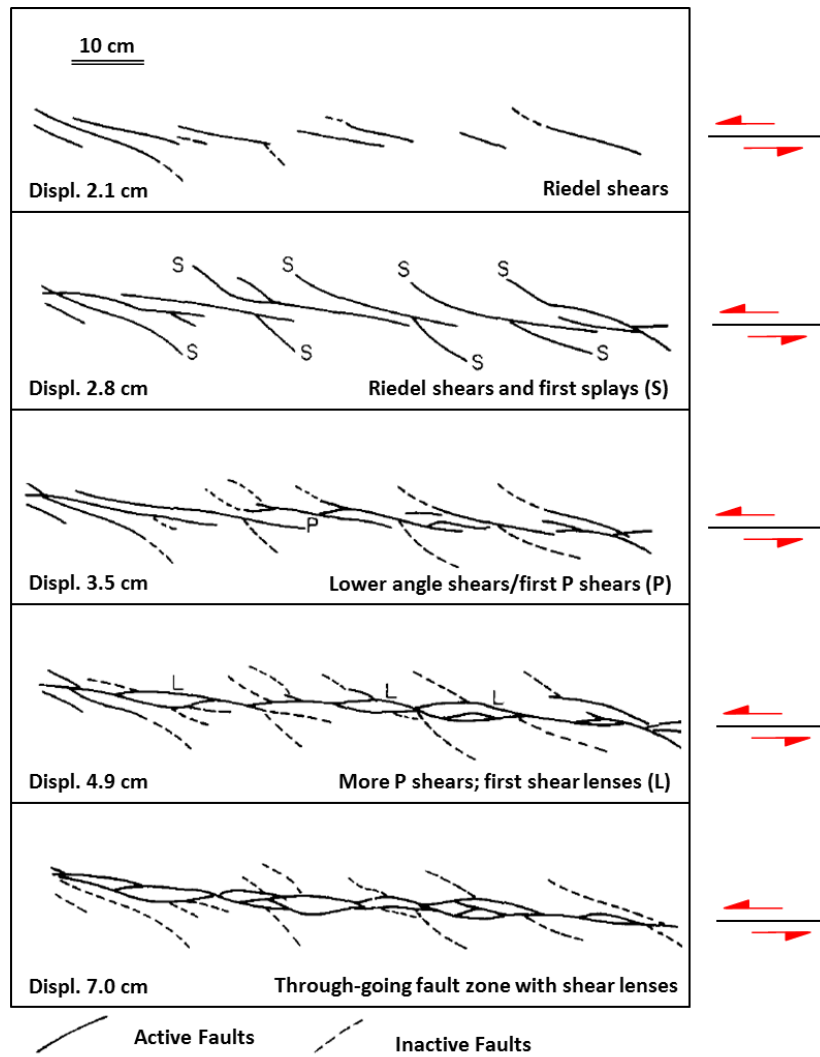
Figure 1.8 – Example genesis of structures created by experiments undergoing simple shear deformation with increasing displacement.  Note that the structure form en echelon arrangements. Adapted from Naylor et al (1986).
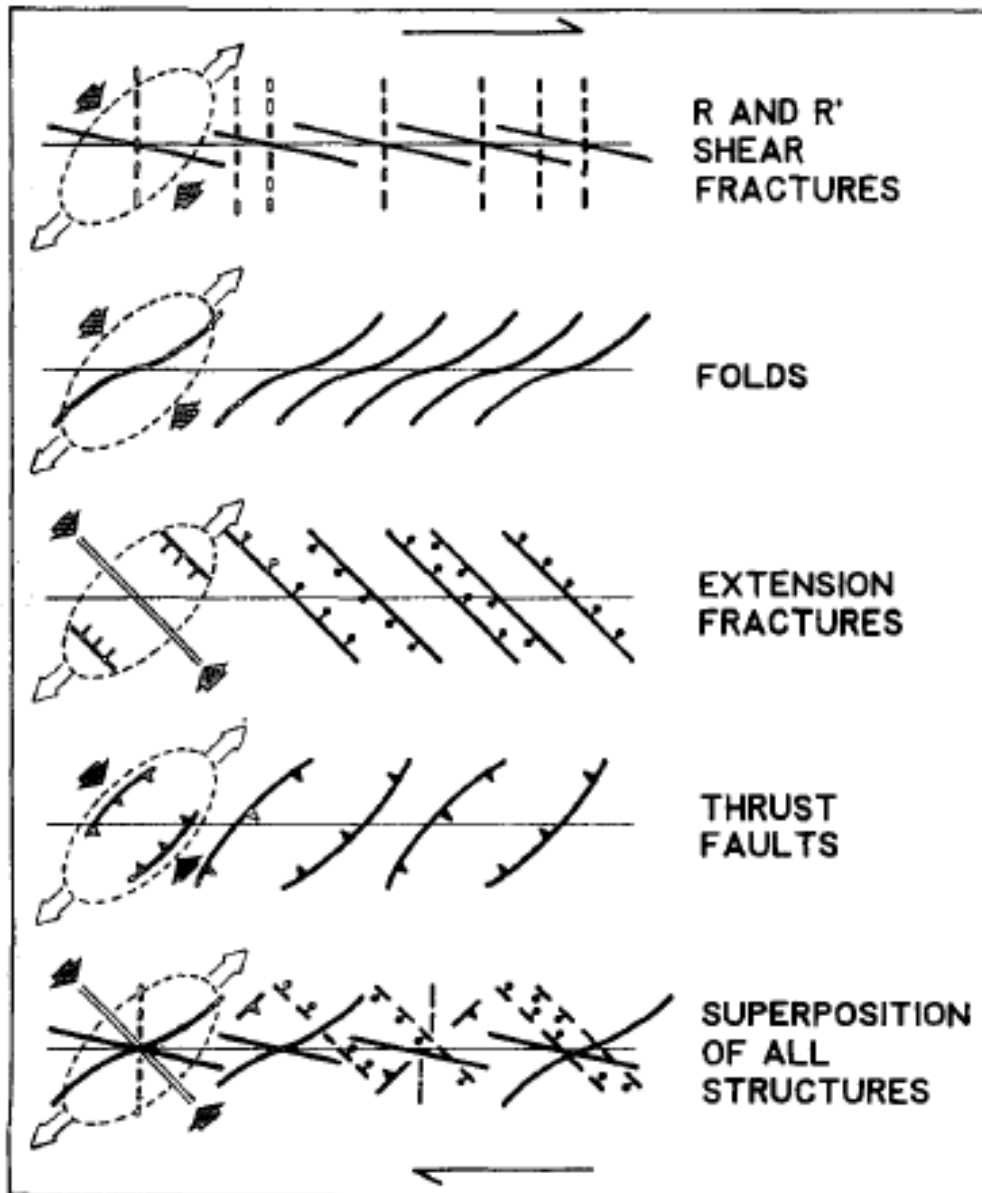
Figure 1.9 - Examples of structure orientations as seen in nature, generally forming en echelon patterns along the underlying through-going fault. Adapted from Sylvester (1988).

## 1.4   Strike-Slip Fault Propagation in Field Studies

The study of strike-slip fault propagation using field studies have been conducted by a variety of authors, generally focussing on three areas: 1) nucleation at pore/crack openings and growth by shear, 2) linkage of major faults, and 3) propagation inferences via fault damage zones (e.g. Segall and Pollard, 1983; Martel et al., 1988; Martel and Pollard, 1989; Martel, 1990; Peacock and Sanderson, 1995; Willemse et al., 1997; Kim et al., 2004; Flodin and Aydin, 2004b).  The following sections explore how these processes impact our understanding of strike-slip fault evolution.

### 1.4.1   Fault Nucleation:

According to fault mechanics, there are three types of fracture propagation models: mode I, mode II, and mode III (Figure 1.10) (Bombolakis and Brace, 1963; Engelder and Price, 1993).  Traditionally, mode I fractures open under tensile stress, whilst mode II and mode III fractures open under a shear stress.  Mode II further applies to normal and reverse faults with a sliding motion, whilst mode III occurs at strike-slip faults with a tearing motion (Engelder and Price, 1993).  Detailed field studies of strike-slip faults suggest that fault nucleation and evolution, however, are not this simple.

An early field study of granodiorite in the Sierra Nevada mountain range of California, concluded that the strike-slip fault network had nucleated from a set of joints that had opened as mode I dilational fractures.  These joints were subsequently sheared due to a change in either direction of $\sigma_1$ or a second deformation event (Segall and Pollard, 1983).  Deformed mineral fillings of these joints show that shearing converted the joints into small faults. A set of secondary fractures then occurs at the fault tips, which contain no shear, but their opening is kinematically consistent with the altered stress state, thus allowing faults to propagate towards other larger faults creating a "linkage" (Segall and Pollard, 1983).

Fault nucleation by the later shearing of fractures is not limited to studies on igneous rocks, and has been documented in both limestones and sandstones (Kelly et al., 1998; Flodin and Aydin, 2004b).  Another study conducted in limestones at Somerset, UK by Willemse et al., (1997) concluded that faults did not originate as slipping-planes (as in mode II or mode III) in shear, but as pressure-solution seams or anti-cracks (anti-mode I).  These were probably

mechanically weaker than the calcite filled mode I veins, thus providing the weakness needed for faults to nucleate. (Willemse et al., 1997).

Despite the slightly different medium for fault initiation, evidence from field studies suggests Modes II and III do not operate as primary fracture mechanisms, but as a secondary deformation features on macroscopic faults following the initiation by a mode I or anti-Mode I crack (Willemse et al., 1997; Flodin and Aydin, 2004b). Kelly et al., (1998) corroborated this by suggesting that fault growth created "damage zones", which consist of smaller faults and veins (subsidiary fractures) in the vicinity of the master fault.  As the fault propagates, a "process zone" moves with the fault-tip leaving the former damaged zone behind, creating an asymmetric damage around the tip, indicative of Mode II deformation (Kelly et al., 1998). These are described in greater detail in Section 1.4.3.
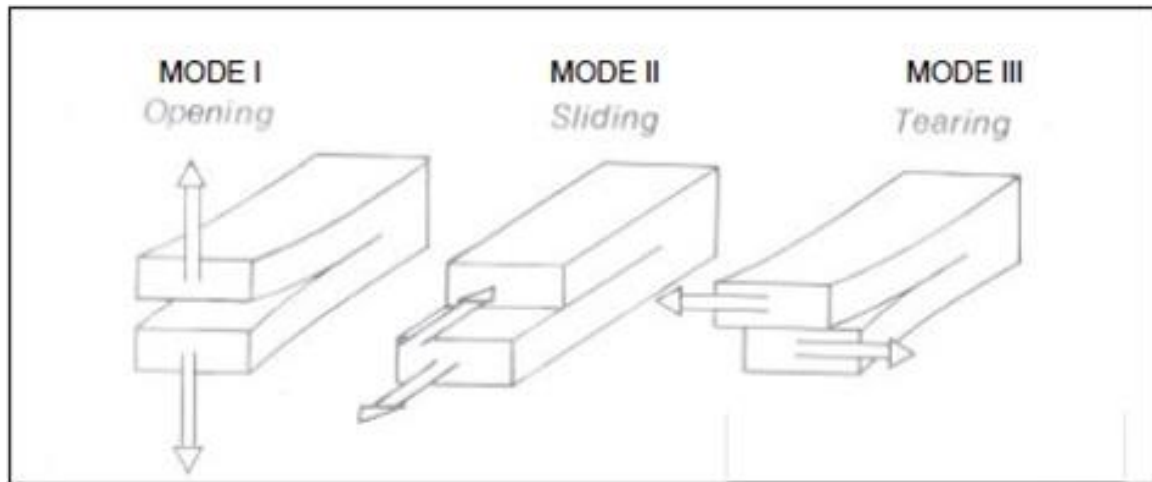
Figure 1.10 ‑ Cartoon depicting the three modes of fracture propagation.  Mode I: opens under tensile stress and produces joints.  Mode II: opens with a sliding motion under a shear stress perpendicular to fracture front. Mode III: opens under a sliding motion under a shear stress parallel to facture front. Adapted from Engelder (1992).
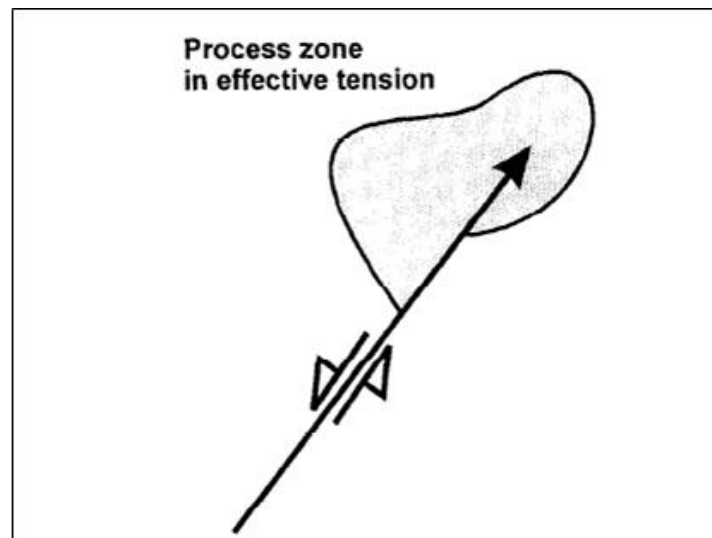


Figure 1.11 ‑ Cartoon of the "Process Zone" in effective tension.  The shaded area at the fault-tip contains micro-cracks or new damage created by the stress field surrounding the fault.  Its asymmetric nature is caused by a Mode II shearing, causing extension on one side and contraction on the other.  Adapted from Kelly et al (1998).

### 1.4.2   Fault Linkage:

Faults observed in the field appear to grow towards each other, and interact, eventually causing a "linkage" between the faults, creating a master through-going fault (Segall and Pollard, 1983; Peacock, 1991; Flodin and Aydin, 2004b).  Evidence of linkage as a significant form of fault propagation was recognised in works on normal faults by Cartwright et al., (1995) using fault displacement/trace-length (D/L) scatter plots to show that the "scatter" was caused by fault interaction rather than mechanical changes in joint strength or error.  They showed that faults grow radially, with fault length growing by the same proportion as displacement increases (Figure 1.12).  When linkage occurs, the individual fault will experience an increase in displacement without the proportionate growth in length; however, overall displacement becomes significantly lower relative to fault length.  Following linkage, displacement will accrue without further propagation until the D/L ratio stabilises to the standard curve (Cartwright et al., 1995).

Fault linkage has also been recognised in strike-slip systems by several authors (e.g. Segall and Pollard, 1983; Peacock, 1991; Willemse et al., 1997; Flodin and Aydin, 2004b). Peacock (1991) first applied d-x profile data from normal faults to strike-slip faults in order to understand their evolution.  Linkage of segments as well as conjugate relationships produced "E" type d-x profiles, displaying high displacement gradients at their tips (Figure 1.13).  These profiles changed to "D" types at contractional bends, signifying a decrease in total displacement due to the two faults interacting and sharing displacement (Peacock, 1991; Peacock and Sanderson, 1995).  Using the d-x profiles, they developed a four-stage evolution of segment linkage: 1) isolated faults propagate towards each other, 2) interaction occurs, 3) a connecting fault or faults link the two segments, and 4) a through-going fault is produced leaving either a contractional or extensional bend (Peacock, 1991).  Peacock & Sanderson (1995) later honed this evolution with stage 2) using a relay ramp to transfer displacement as the faults began to interact and stage 3) increasing rotation and deformation in the transfer zone. Willemse et al., (1997) also supported this observation, noting that 4th and 5th generation solution seams formed in fault zones, creating potential slip planes and providing a mechanism for a future fault to cut through the fault zone.

Other studies have developed analogous models to the transfer zones or relay ramps described by Peacock & Sanderson (1995). For instance, Martel et al., (1988) suggested that linking faults can form simple 'fault zones' which describes fractures or smaller faults that bridge between two faults (Figure 1.14). Whilst the fault network mapped in the Valley of Fire showed that master, 1st order faults formed first, with antithetic faults of progressively smaller orders forming later (Figure 1.15) (Flodin and Aydin, 2004a; Flodin and Aydin, 2004b; Myers and Aydin, 2004).

*d-x Profiles-*

It is worth mentioning that the studies by Cartwright et al (1995), Peacock (1991), Peacock and Sanderson (1995), and numerous other studies all used the d-x profiles as part of their analysis to show that faults grow by linkage. These plots act as 2D displacement distribution analysis that were first described Muraoka and Kamata (1983). It was found that fault profiles in a d-x plot showed two styles of fault displacement reduction towards the tips, which were linked to lithologic control. These were termed Cone shaped or C-type and Mesa shaped or M-type profiles (Figure 1.13), with the C-type profile indicative of a fault cutting through homogeneous incompetent materials, and an M-type profile indicative of a fault cutting through a rigid unit (Muraoka and Kamata, 1983). These naming conventions were thus adopted by Peacock (1991) for the D and E type profiles described above (Figure 1.13), and are referred to in Chapter 4 when d-x profiles are presented.
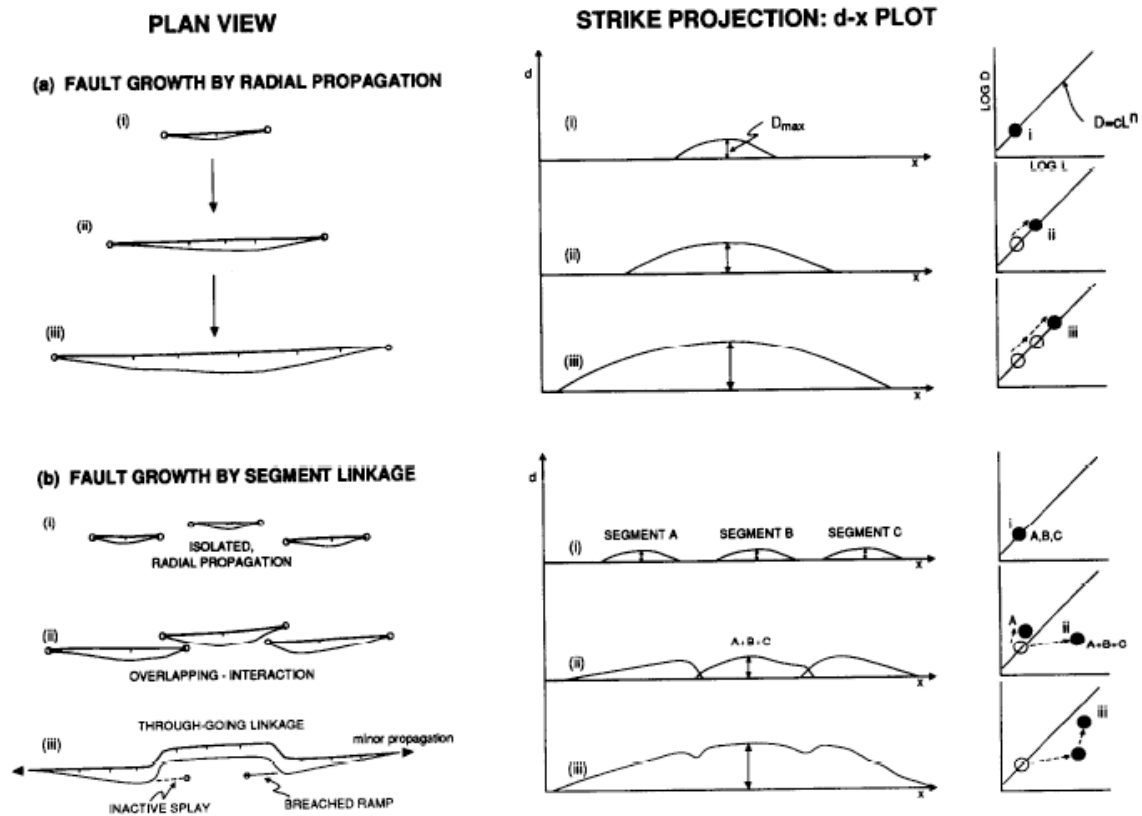
Figure 1.12 - Fault growth models by a) radial propagation and b) segment linkage of normal faults.  The left column shows the cartoon plan version of faults whilst the middle column shows the corresponding d-x (displacement versus distance) plot.  The column to the right is the D/L plot, which is a log maximum of the d-x plot.  From the D/L plots in a) the fault follows a predictable growth pattern along the standard curve, maintaining the same ratio of displacement and trace length growth.  In b), the interaction of multiple segments causes the fault to first accrue more displacement relative to length (b, ii) and falling above the standard curve. Once the linkages occur the overall length becomes very large relative to displacement and thus falls below the standard curve.  Further growth occurs by displacement as the fault zone stabilises back to the standard curve. Adapted from Cartwright et al (1995).
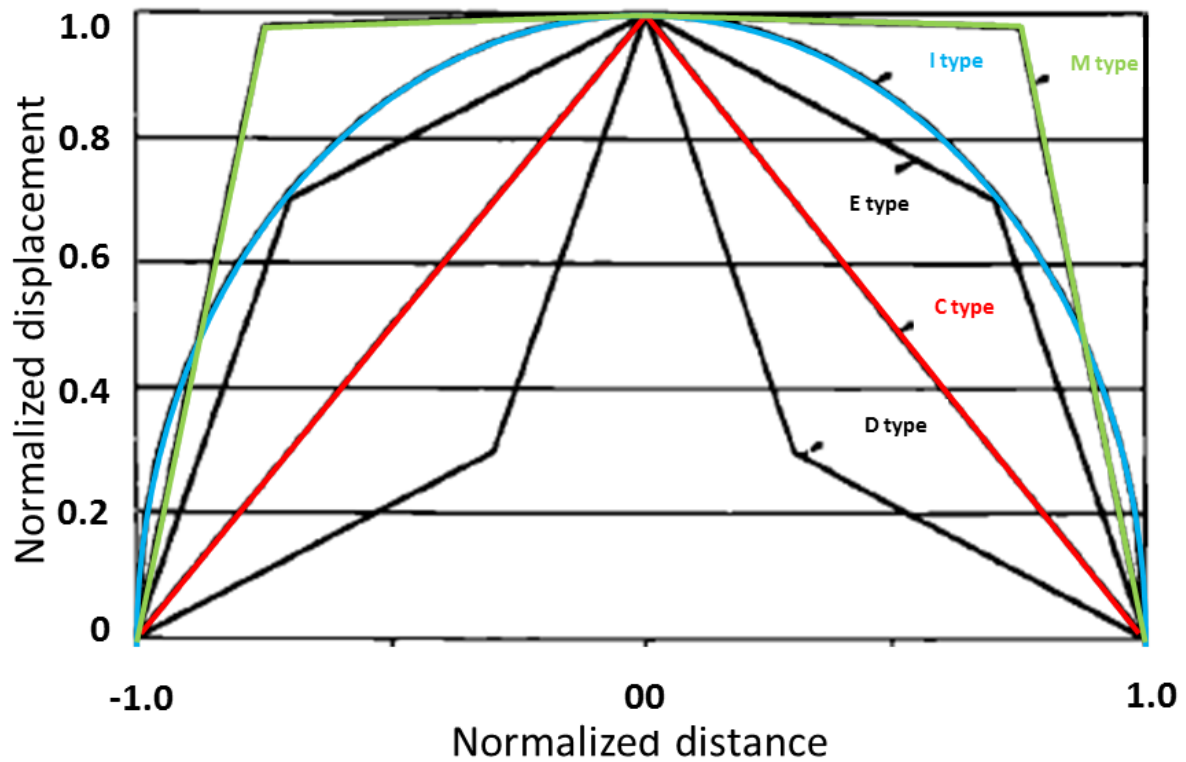
Figure 1.13 – Idealised displacement-distance (d-x) graph, showing a classification of d-x profiles. The graph is normalized, with the point of maximum displacement at distance zero and the tips at -1 and 1. I type = Ideal elastic profile, C type = Cone shaped, M type = Mesa shaped, E type = *elevated* above the C profile, D type = *depressed* below the C type profile. Note C and M type profiles were first described by Muraoka & Kamata (1983). Figure adapted from Peacock (1991).
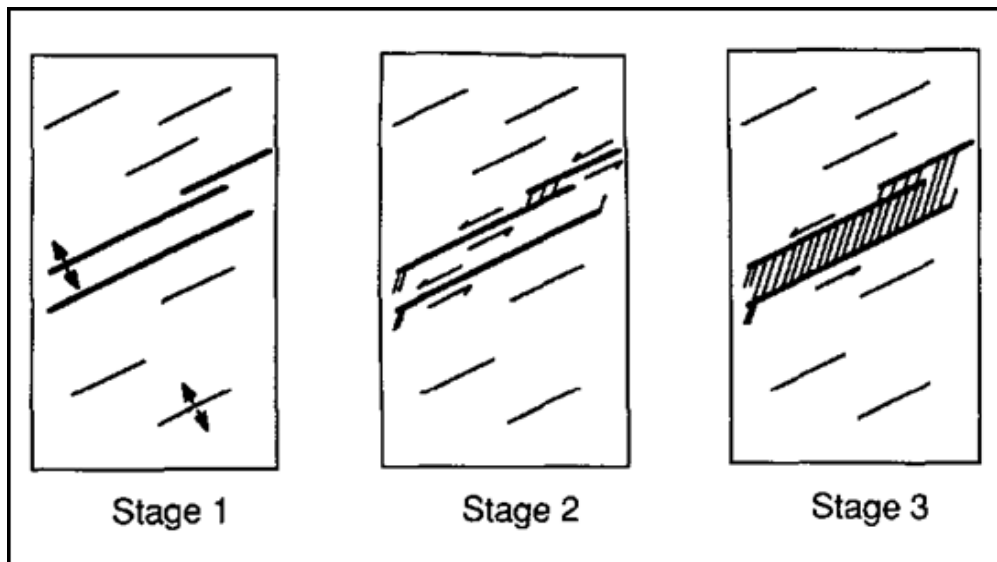
Figure 1.14 ‑ Cartoon summarising the development of simple faults zones.  In stage 1, a zone of echelon fractures/joints form due to mode I opening.  Slip occurs at stage II, creating faults with splay fractures.  In stage III, a simple fault zone has developed with increased fractures occurring, and bounded by the strike-slip faults. Adapted from Martel et al (1998).
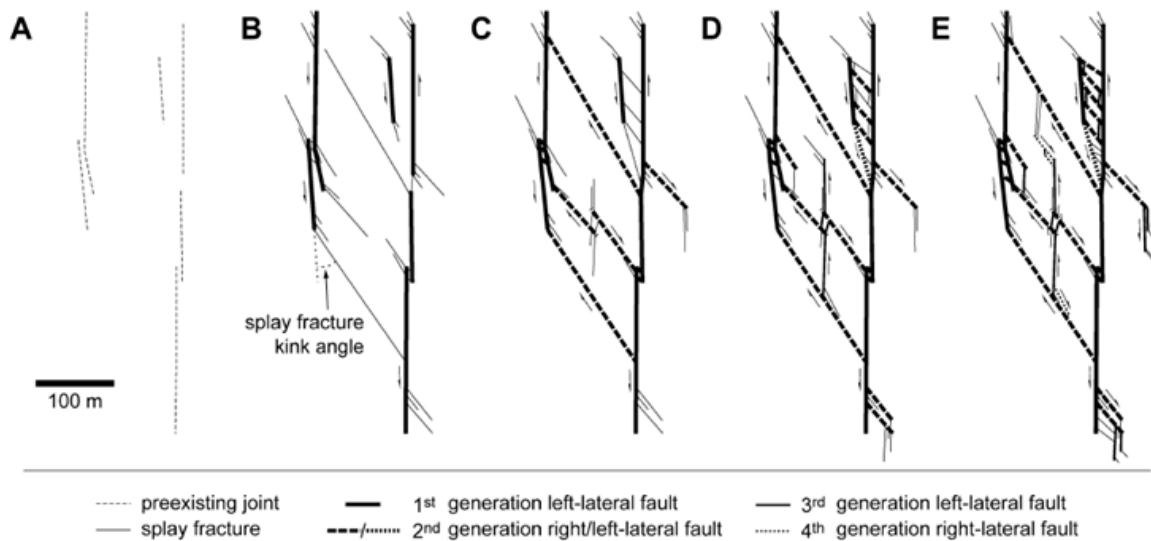


Figure 1.15 - Fault zone evolution proposed by Flodin & Aydin (2004).  A) Pre-existing joints occur due to opening mode I processes.  B) Slip on pre-existing joints follows, creating left-lateral parent faults with splay fractures (usually at fault tips).  C)  Slip occurs on splay fractures, forming 2nd generation right-lateral faults (an antithetic sense of slip), which abut the parent faults.  New splay fractures propagate from the tips of the 2nd generation faults.  D) Slip occurs on the latest set of splay fractures, forming 3rd generation left-lateral faults, with another set of splay fractures forming at their tips. E) A fourth generation of right-lateral faults propagate from the 3rd order splay fractures, creating a fault network.  Note the 2nd generation left lateral faults in D), occurs from a splay fracture that splayed in a different orientation than the network norm, and due to orientation, it was favourable to generate an antithetic sense to the other 2nd generation faults which were right-lateral. Adapted from Flodin & Aydin (2004).

25

### 1.4.3   Damage Zone:

Damage zones, refer to a volume of deformed wall rock around a fault surface that resulted from the propagation, interaction, and build-up of slip along faults (Kim et al., 2004). McGrath & Davison (1995) completed an intensive study of damage zones in all three fault types as an alternative way to analyse how faults propagate, and in which direction.  Studies have grouped damage zones into three types (Kim et al., 2003; 2004; Kim and Sanderson, 2006) (Figure 1.16):

*Tip damage zones* – damage developed in response to stress concentration at or ahead of fault tips,

*Linking damage zones* – damage occurring between fault segments and oversteps, caused by their interaction and linkage, and

*Wall damage zones* – damage initially created by the fault tip, but later abandoned as the fault radially propagates through, occurring along the trace of the fault segment.
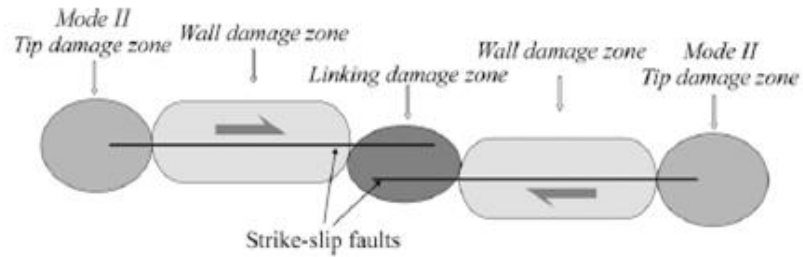
Figure 1.16 ‑ Cartoon depicting where the different damage zones occur along a fault trace. Adapted from Kim et al (2004).
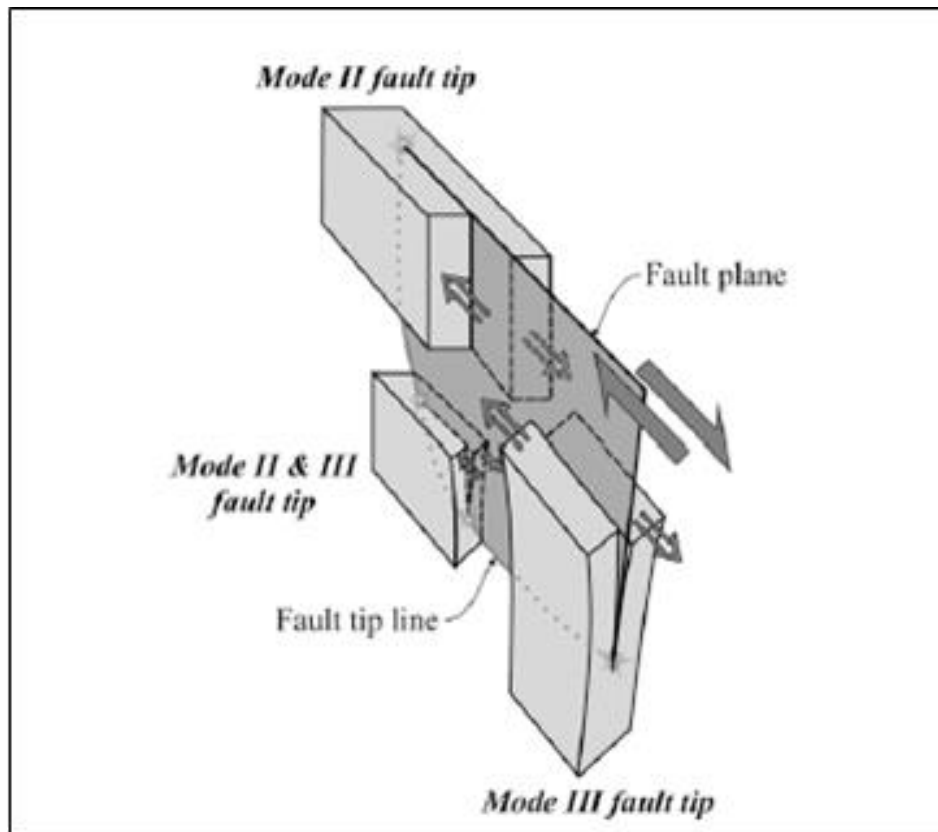


Figure 1.17 ‑ Diagram showing how modes II, III, or both can shear to enable a fault to propagate. Note that mode II slips along the horizontal, whilst mode III affects the top and bottom of fault tip propagation. Adapted from Kim et al (2004).

### *1.4.3.1    Tip Damage Zones:*

Tip damage can be caused by either mode II, mode III, or a combination of both, see Figure 1.17 (Kim et al., 2004).  Mode II damage occurs at the lateral tip of a fault where the tip line is normal to slip direction, whilst mode III slip occurs at up- and down-dip tips of a strike-slip fault.   Mode II tip damage generally produces four types of tip structure (Figure 1.18) (Kim et al., 2003; 2004):

*wing cracks* – occur with a rapid decrease in slip at fault tip and under low confining pressures or low effective stress and tend to be sub-parallel to $\sigma_1$.

*horsetail fractures* – kinematically similar to wing cracks, but finer and more closely spaced with a relatively low angle to the master fault.  They form where slip dies out more gradually and propagate as mode I cracks.

*synthetic branch faults* – similar to splay faults and can link to other fault segments.  They can combine with other damage structures to produce complicated damage zones

*antithetic faults* – faults of opposite sense to master fault, that splay with increasing length away from the master fault tip, and tend to be 30° to $\sigma_1$.

### *1.4.3.2    Linkage Damage Zones:*

Linked damage zones builds upon the structures described in the characteristics section, and is separated into in extensional jogs and contractional jogs.  Assuming that these occur in the horizontal plane, these examples are restricted to mode II linkage, Figure 1.19 (Kim et al., 2004).

*Extensional-*

- *extension fractures* – joints or veins controlled by extension perpendicular to $\sigma_1$.
- *pull-aparts* – type of extension fracture which opens up between two fault segments due to increasing slip.
- *rotated blocks* – blocks rotate as slip builds up along boundary faults, creating antithetic faults (see also, Flodin and Aydin, 2004a).

- *strike-slip duplexes* – also known as isolated lenses as a single fault-bound block, form at a step between two master faults and surround fault-blocks. These are later breached by through-going fault (see also, Woodcock and Daly, 1986).

*Contractional-*

- *relay ramp* – linkage of two segments via a contractional overstep, these contain veins, pressure solution seams, and antithetic faults. These are later breached by through-going faults.
- *rotated blocks* – same as above, but creating synthetic faults.
- *strike-slip duplexes* – similar to above but tend to be rare due to the difficult mechanics required to create these.

### 1.4.3.3    Wall Damage Zones:

Wall damage zones can be classified by 3 end-member geometries in Figure 1.20 (Kim et al., 2004):

*wedge-shaped* – repeated damage zones occurring along a fault trace, with size of wedge increasing away from fault centre (reflecting fault growth through time). These occur from mode II tip propagation and are rarely seen in nature, as majority of fault growth occurs via linkage (Cartwright et al., 1995).

*long and relatively narrow damage zones* – damage developed from mode III tip propagation, caused by extension fractures, which are later reactivated as antithetic faults, and on occasion, synthetic faults. The morphology is likely controlled by the angle between extension fracture and master fault and tend to be symmetrical (Kim et al., 2004).

*asymmetric damage zones* – intensive damage concentrated in one wall of fault due to frictional attrition caused by slip build-up. Block rotation and joint drag are common structures produced. Damage asymmetry has been recognised in other studies (e.g. Faulkner et al., 2008; Mitchell and Faulkner, 2009).

### *1.4.3.4    Damage Zone Evolution:*

McGrath & Davison (1995) suggest that strike-slip faults create the largest variation of damage zone geometries, likely due to differing stress regimes in simple shear, transpression, and transtension scenarios. Furthermore, modes II and III were witnessed in accordance with Kim et al (2004). Debate still exists regarding if true mode II and III fracturing actually occurs as these have not been reproduced in experimental analogue studies (McGrath and Davison, 1995). However, they believe that given enough confining pressure, these modes will fracture, as each mode possesses a different level of fracture toughness (with mode I possessing the least), accounting for the different damage morphologies created by each mode. Regardless, these modes can still be used to identify different styles even if modes II and III simply deform an already opened mode I fracture (McGrath and Davison, 1995).

Kim et al (2003) proposed that modes II and III fractures could affect different areas of the fault in 3D space. If mode II propagates along strike, and mode III fractures up- and down-dip, then together different damage geometries are produced in outcrop based on where on the outcrop dissects the fault ellipse (Figure 1.21). The model elegantly demonstrates how such variation can be found in strike-slip faults. It explains Riedel shears as damage produced by mode III cracks as well as controlling the synthetic and antithetic wall damage.

This theory suggests that viewing faults in the correct plane for mode II damage would be rare, and the majority of examples in nature produce hybrid examples. Mode III damage is also attributed to create antithetic faults early in evolution whilst synthetic faults become prominent later (Kim et al., 2003). Although this may be true, it does not account for the opposite order of shear formation in the Riedel model (described in the next section), suggesting further attention needs to be placed on how damage zones of strike-slip faults propagate upwards and downwards and what geometries are produced. Dominantly lateral tip structures are identified in this study as well as features that may represent the mode II and mode III hybrid structures, and thus these models provide a base for comparison.
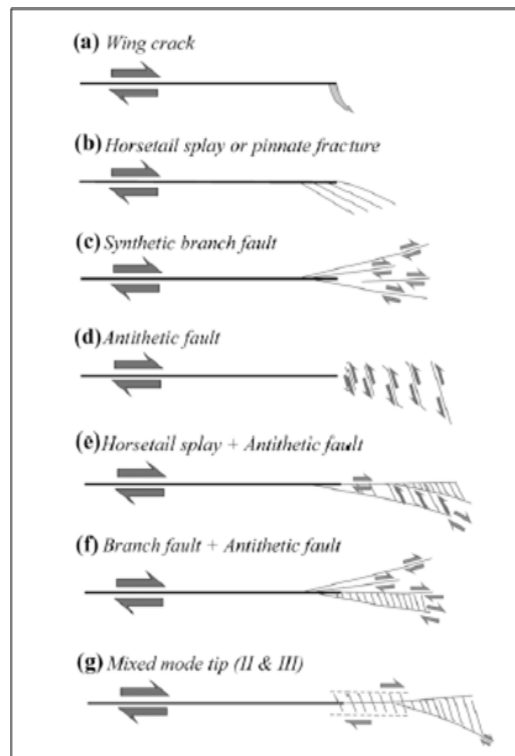
Figure 1.18 ‑ Schematic showing the various morphologies of tip damage zones. Adapted from Kim et al (2004).
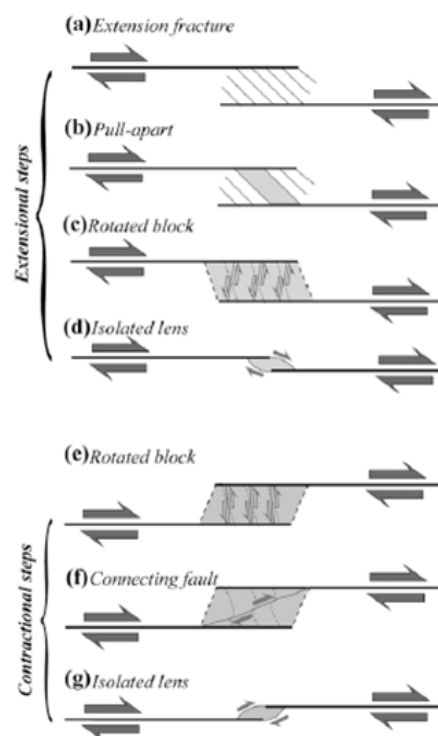


Figure 1.19 ‑ Schematic displaying various morphologies of linkage damage zones. Adapted from Kim et al (2004).

31
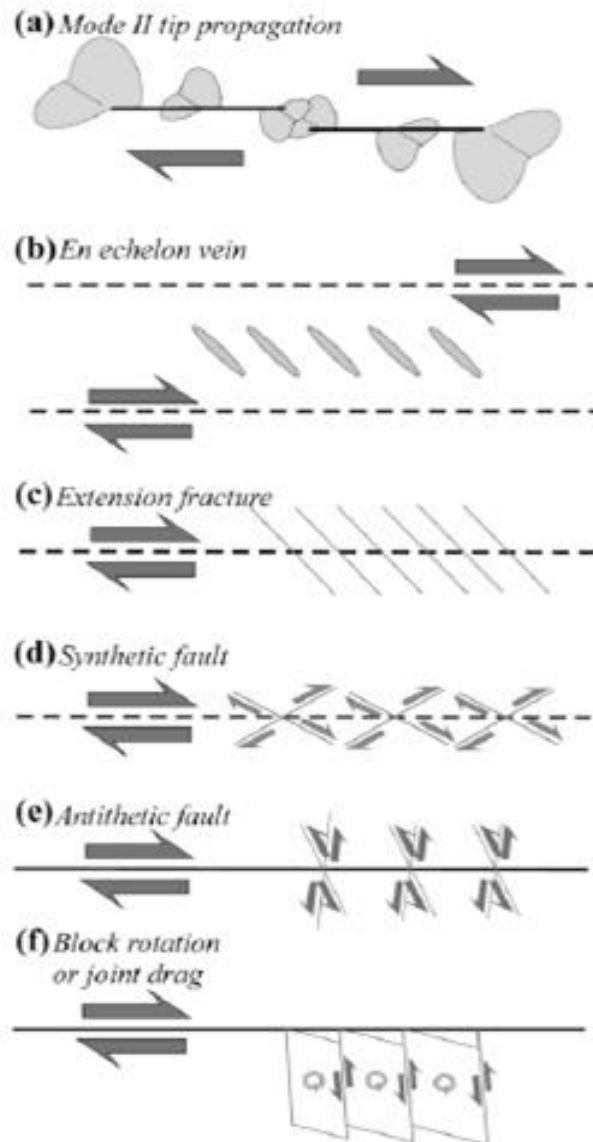
Figure 1.20 ‑ Cartoon of wall damage zone diagrams. a) Is an example of mode II propagation of wedge shaped damage zones whilst the rest are examples of long and narrow damage zones.  Adapted from Kim et al, 2004.
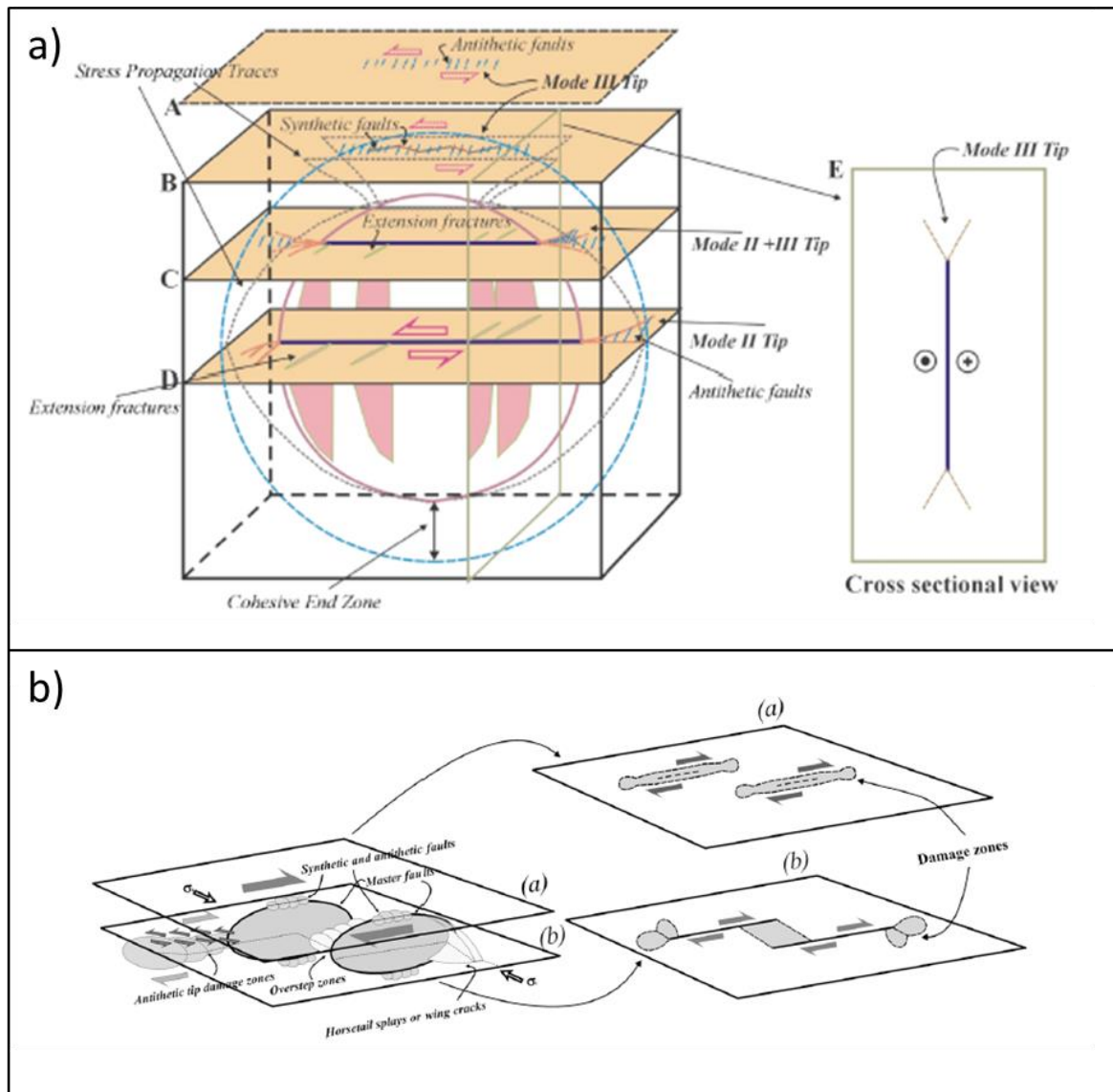
Figure 1.21 ‑ a) and b) show a conceputalised model of the damage zone deformation associated with the depth of the fault observed.  If the fault was viewed through the centre of the master fault, a mode II damage zone would be observed.  A view near the top or base of the fault shows mode III tip damage, and a slice in between would produce damage a hybrid damage zone (mode II + III).  Adapted from Kim et al (2003; 2004).

## 1.5   Strike-Slip Fault Propagation in Analogue Studies

Several studies have investigated strike-slip fault evolution and propagation using experimental models to test a variety of methods. The majority of authors favour methods following a traditional "Riedel experiment" whereby clay or sand is emplaced on two equal sized boards that are sheared past each other (e.g. Tchalenko, 1970; Wilcox et al., 1973) to test the deformation incurred in a sediment overburden by a basement fault. However, some studies (e.g. An and Sammis, 1996) have argued that sliding two boards past each other only produces deformation as a secondary feature, and have therefore inspected how strike-slip faults propagate from inception. The studies using Riedel based experiments have also investigated the effects of transpression (e.g. Naylor et al., 1986; Keller et al., 1997; Ghosh and Chattopadhyay), different lithologies (e.g. Bartlett et al., 1981), folding (e.g. Richard et al., 1991), sedimentation and erosion (e.g. Richard et al., 1995; Le Guerroué and Cobbold, 2006), compaction control (e.g. Schrank and Cruden, 2010); tip structures (e.g. Nurit Hildebrand, 1979; Hempton and Neher, 1986), pre-existing fractures (e.g. An, 1998; Curren and Bird, 2014), releasing bends (e.g. McClay and Dooley, 1995; Atmaoui, 2006; Atmaoui et al., 2006; Smit et al., 2008; Wu et al., 2009), restraining bends (e.g. Dooley and McClay, 1997; Dooley et al., 1999; Mitra and Paul, 2011).

The studies listed above have investigated a wide range of situational deformation, and it is beyond the scope of this introduction to summarise them all. Thus this section will focus the effects of lithology on the Riedel model, as well as the results from the non-Riedel experiments, to illustrate the basic structures expected, their orientations, and order of formation. A short section detailing the effects of transtension and transpression is also presented. For a comprehensive review of analogue studies, see Dooley and Schreurs (2012).

### 1.5.1   Riedel Models:

The earlier works on experimental strike-slip fault models follow similar experiments to the Riedel experiment using different mediums, including: clay, limestone, and sand.

### 1.5.1.1    Clay Experiments

Tchalenko (1970) recreated early studies conducted by Riedel, by placing a thin layer (on order of a few centimetres) of clay on top of 2 equal-sized boards.  As the boards were sheared past each other, the following structural evolution was characterised (Figure 1.22).

*Pre-peak strength deformation* – initial movement of boards where circles marked in the clay were strained to form ellipses (corroborating simple shear movement was occurring), but no shears formed during this stage.

*Peak structure (a)* – Resistance to shear is at a maximum.  R and R' shears form just before peak strength occurs.  Depending on clay water contents these are either formed contemporaneously or the R' slightly precede the R shears.

*Post-peak structure (b)* – Resistance to shear decreases.  R shears extend and angle away from PDZ; however, they are unfavourably oriented to accommodate further displacement. R' in particularly are mechanically unsuited, and are rotated and distorted.  Some low angle (in relation to PDZ) also form.

*Post-peak structure (c)* – Resistance to shear continues to decrease.  P shears form in approximate same angle as R shear on opposite side of PDZ as principal stress direction may have shifted.  They serve to connect individual R shears.  Most of board movement is accommodated by shear displacement.

*Pre-residual structure (d)* – Shears become continuous forming the first visible shears along the PDZ (Y shears).

*Residual structure (e)* – Resistance to shear stabilises.  Further displacement occurs along the PDZ

Interestingly, R' shears do not play a large role in that they form early and are subsequently distorted by the R shears (Tchalenko, 1970).  Further studies have shown that folds and fractures will also form in clay experiments (Wilcox et al., 1973), with fractures only forming early on before being destroyed by later R shears.  However, if the cohesion of the clay is reduced by placing water on it, then tension fractures open and dominate the deformation to the exclusion of other structures (Wilcox et al., 1973).
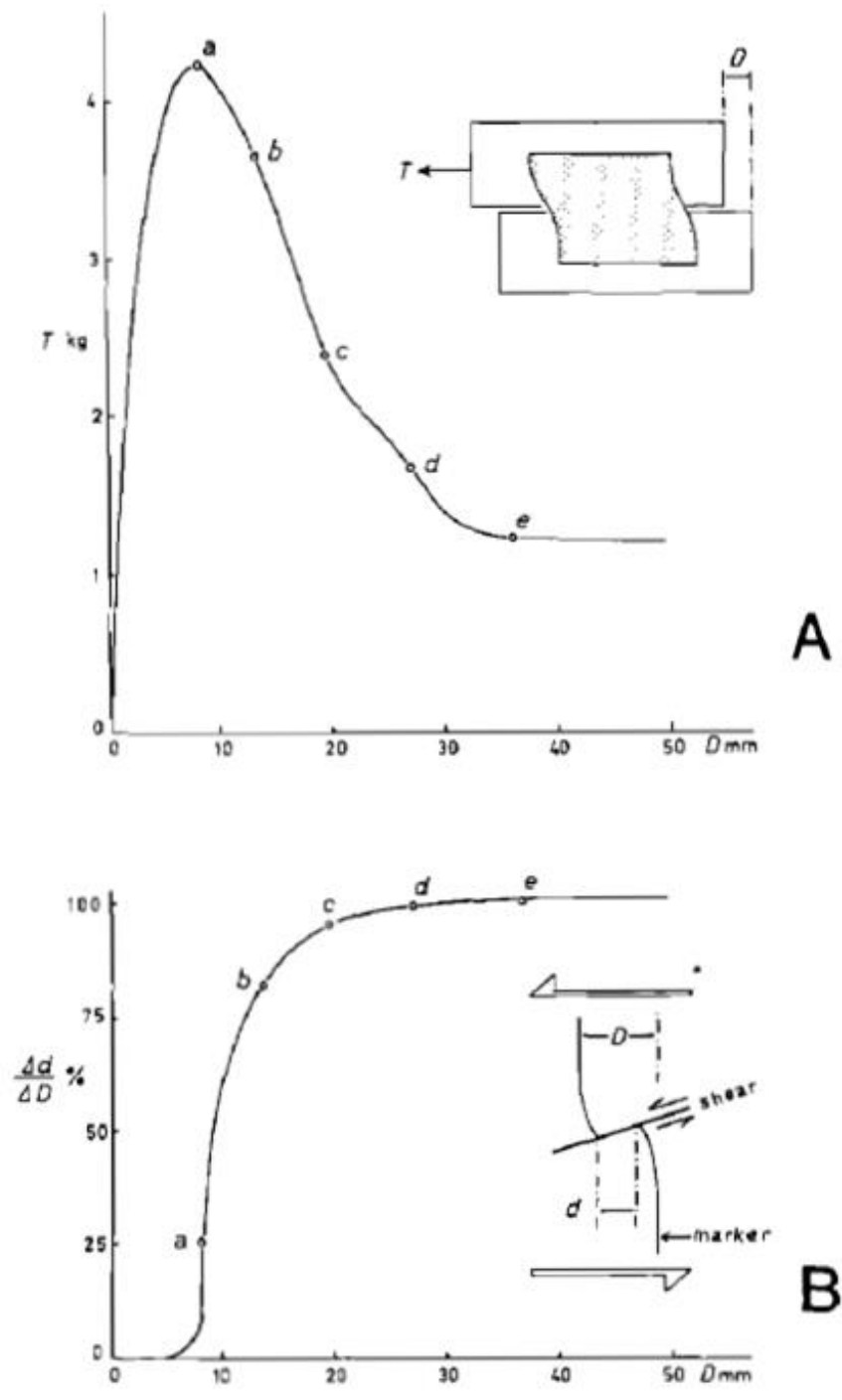
Figure 1.22 - a) Shows the force-displacement curve from the Riedel experiment. As displacement increases, the shear force $T$ greatly increases to approach the peak stage. Further displacement sees a general decrease in shear force until it stabilised in the residual stage. b) Graph showing the proportion of total movement taken up by shears. Note, most of the movement occurs in the first two stages. Adapted from Tchalenko, 1970.

36

### 1.5.1.2    Limestone Experiments

Bartlett et al (1981) conducted later tests using limestones under confining pressures, which showed some contrasting results to the clay models by Tchalenko (1970) and Wilcox et al (1973).  R and P shears formed simultaneously during the peak stage, and were initially short. With increasing displacement during the post-peak stage, the R shears propagated whilst R' shears were relatively rare.  A new P' shear occurs with a similar, but opposite angle to the R' shear (Bartlett et al., 1981). By the pre-residual stage, Y shears dominate the deformation through the PDZ and accommodate most of the displacement.  Extension micro-fractures were also documented parallel with $\sigma_1$.  Increasing confining pressure resulted in increasing the peak shear stress whilst an increase in limestone thickness had no effect on the shear strength.  Furthermore, fault gouge was more developed in experiments with higher confining pressures and shear strain was found to increase with depth (Bartlett et al., 1981).

### 1.5.1.3    Loose Sand Experiments

Naylor et al (1986) used sandbox analogue models to predict strike-slip fault evolution in sand to produce a different order of structural evolution:

1. *En echelon R shears* – formed at around 17° to the PDZ with regions of overlap. Each shear is a "scissor fault" where vertical displacement reverses at the midpoint (where it crosses the basement fault).
2. *Short-lived splay faults* – occur at the tips of the R shears with an angle > 17°.
3. *Low-angle shears* – develop when the splays become inactive either at the tips of the splay or the R shears and strike < 17° to the PDZ.  R' shears also form occasionally, but only when substantial overlap of juxtaposed R shears occur.
4. *P shears* – form at opposite angle to the R shears and serve to connect the R shears along with the low-angle shears.
5. *Final fault formation* – produces an anastomising fault zone with shear lenses and displacement concentrated on through-going faults.

Shears were found to form at angles in accordance with Coulomb-Mohr failure criterion. However, at R shear tips, $\sigma_1$ reorients on both compressional and extensional sides allowing for the secondary splay faults to form.  Likewise, the P shears are attributed to be essentially

subsequent R shears, which form under a maximally reoriented stress field so that no stress affects the original R shears (Naylor et al., 1986).

*R Shear Shape and 3D visualisation-*

Cross-sections through the sandbox produced a 3D visualisation of R shears.  They form helicoidal shapes, which are concave-up and attached to the basement fault at depth (Figure 1.23) (Naylor et al, 1986).  The R shear terminations were not vertical and die out both upwards and downwards.  Horizontal displacement decreases toward the tips whilst adjacent, whilst overlapping shears show displacement transfer.  P shears also form helicoidal shapes but are less pronounced as they join unconnected R shears (Naylor et al., 1986).

Future experiments used computerised X-ray tomography to provide improved 3D visualisation of the structural evolution in loose sand (Mandl, 1988).  Ueta et al (2000) conducted further investigations using different densities and compactions of sand in order to determine their effect on shear shape.  They deduced that each shear developed on either side of the fault with a "cirque" or "shell" shape, creating a tulip structure in cross-section. Further displacement joined the shears together to form the helicoidal shape described by Naylor et al (1986) above the basement fault, reaching up to the surface (Ueta et al., 2000). Under low densities, simulating loose sands, the R shears possess less pronounced helicoidal shapes whilst attaining steeper dips > 75° and striking at a smaller angle with the PDZ.

a.

Overburden

Basement

b.

Sand surface

Basement surface
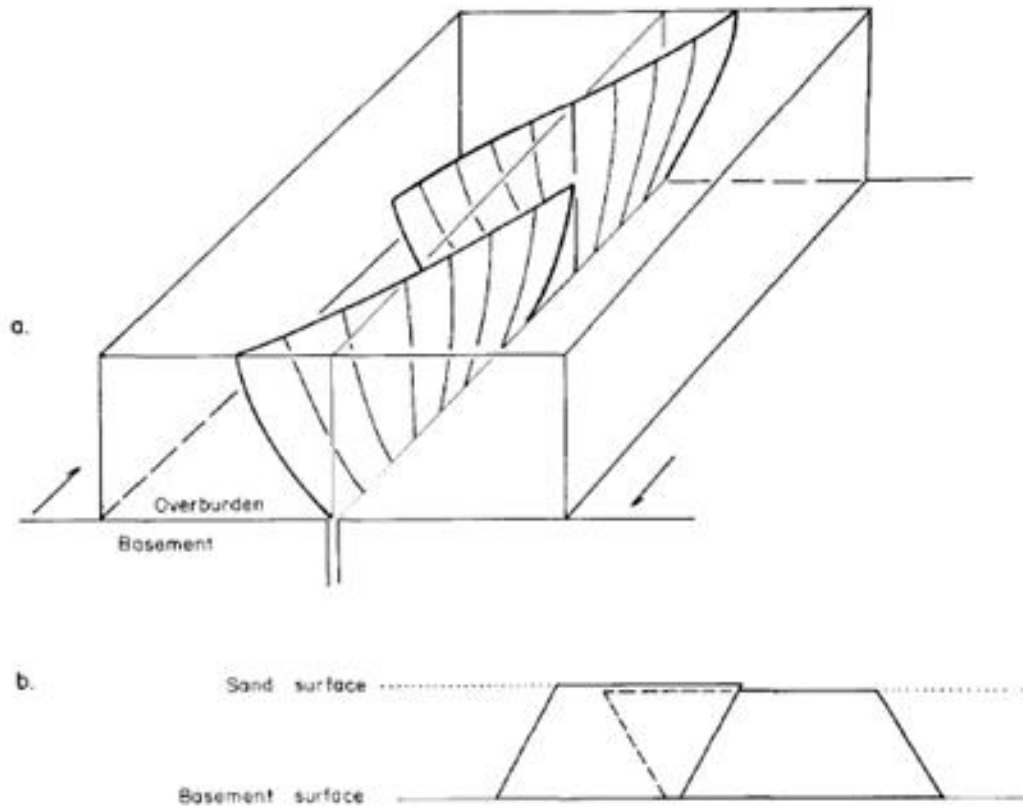
Figure 1.23 ‑ a) 3D view of helicoidal geometry of R shears.  Note the concave-upwards geometry which attaches to the basement fault at depth.  As they cross the basement fault, the vertical sense changes, displaying "scissor faulting".  b) Lateral view of the R shears shows a parallelogram geometry.  Adapted from Naylor et al, 1986.

### *1.5.1.4    Riedel Model Comparison*

The various studies based on analogue modelling have produced relatively similar results, such as the development of R and P shears, however, the timing of their evolution varies with the lithology used.  The same remains true with R' shears and low angle shears.  The tests on limestone conducted by Bartlett et al (1981) produced significantly different results from the other mediums.  This could be attributed to the higher elastic stiffness of limestones (Naylor et al., 1986).  Thus, lithology appears to be a major factor in geometric structure as well as confining pressure.  Initial stress and density of the medium also plays a role, but seem to alter the angles at which these structures form rather than their order of formation.  Finally, the cohesive properties of the overburden are important as it may determine whether tensional fractures form (Wilcox et al., 1973).

### 1.5.2   Absence of Through-going Fault

An & Sammis (1996) proposed an alternative method to test how strike-slip faults nucleate and evolve using a rotating board with a fixed end to induce shear strain.  This board was tilted to allow fault gouge and clay to slide by gravity with one side of the clay fixed to the board (Figure 1.24).  The combined effect created a shear strain in the clay without sliding two boards past each other.  The zone closest to the fixed edge experienced the highest shear strain at the beginning, followed by dilation and hardening.  Strain moved to the next zone away from the fixed edge and follows the same process before transferring strain to the next zone, until eventually spreading to the rest of the sample and achieving a uniform shear deformation (An and Sammis, 1996).  They maintained the same strain rate during the experiment to create the following evolution:

*Protofault Stage* – faults formed with no measurable offset from pores opening generally in defect-free areas.  If protofaults formed in an area with defects, then faults nucleated directly on the defects.  Most formed in conjugate set, denoted as shear 1 ($S_1$) and $S'_1$.

*Simple Fault Stage* – shear displacement occurs upon a small percentage of protofaults, becoming simple faults.  Protofaults that do not experience shear growth are abandoned as all displacement is accommodated by the simple faults. At later stages, small simple fault tips

also terminated with a single fracture or en echelon fracture arrays whilst large simple faults produced horsetail damage geometries.  During propagation, small fractures developed intensively in front of fault tips, producing the "process zone" described in field studies.  A second set of conjugate shears, $S_2$ and $S'_2$, developed as simple faults grew towards each other as well as tensile and compressional linear structures.

*Compound Fault Stage* – formed as the product of end-to-end linkage of simple faults.  Linkage between the $S_1$ conjugate set often occurred with the $S_2$ fault sets and fractures (Figure 1.25).  This linkage made faulting a more chaotic process, as some small faults would link with longer ones whilst a longer faults growth would remain slow if it never linked.

*Through-going fault zone* – eventually linkage between faults occurs to the extent that one fault became larger than the others, creating a through-going fault zone, and forming an angle of 15° clockwise with the simple shear direction.  Deformation became non-uniform at this point with majority of displacement accommodated by the through-going fault.

The most intriguing aspect of this model is the formation of a through-going fault oriented 15° to the theoretical PDZ of the Riedel model (Figure 1.26).  Furthermore, none of the $S_1$ or $S_2$ sets formed in agreement with P shears, with the possible exception of rotated $S'_1$ shears.  The $S_1$ conjugate set, however, could be an equivalent of the R and R' sets, whilst $S_2$ follows a similar angle of the PDZ (An and Sammis, 1996).  They further conclude that as the Riedel experiments use a pre-existing fault as a boundary condition, all subsequent deformation are therefore secondary structures.  Thus, these Riedel models may better represent examples where faults reach the surface and lack confining pressure; whilst, their results represent fault nucleation at depth (An and Sammis, 1996).  However, this leads to further problems, such as when do smaller faults at depth change from a through-going fault at an angle to the PDZ become aligned with the PDZ, and if this happens do the S shears convert to R shears?  Also, as the clay sample slides by gravity, it may be expected that transtension may apply to the top of the sample whilst transpression may apply the bottom (following traditional gravity slope tectonics, e.g. Morley and Guerin, 1996; Rowan et al., 2004), and would likely result in different structures than a scenario under simple shear only.

### 1.5.3   Transtension and Transpression

The study by Naylor et al (1986) also tested how an initial stress state affects fault geometry, with an initial $\sigma_1$ oriented parallel to the basement fault to represent transtension, and an intial $\sigma_1$ perpendicular to the basement fault, representing transpression (Naylor et al., 1986). Under transtension, R shears form almost parallel to the PDZ and were rare, whilst the through-going fault is created early on in evolution. Under transpression, the R shears formed at a greater angle to the PDZ but as displacement continued, these angles decreased. Both conditions were attributed to the way $\sigma_1$ rotated with evolution (Figure 1.27) (Naylor et al., 1986).

Another paper modelling oblique rifting also inspected how transtension affects deformation and they showed that with more extension (relative to strike-slip movement), faults became more dominated by normal faults at the surface (Tron and Brun, 1991). It should be noted the faults modelled in this study were never purely normal faults or purely strike-slip but oblique faults with a dominance of dip-slip or strike-slip motion. This reflects many faults in nature, which will be demonstrated by the faults examined in Chapter 4.

By contrast, Keller et al (1997) used clay-box modelling to investigate the role of transpression at a strike-slip restraining bend between two basement faults. They concluded that the role of P and R shears essentially switched, so that the P shears formed initially under low displacements at the restraining step, whilst R shears dominated the basement faults away from the step-over. With increased displacement, Y shears (parallel to the PDZ) formed as well as R shears. The R shears mostly served to link unconnected P shears, and all shears terminated at the basement fault (Keller et al., 1997).

Thus transtension and transpression clearly affect the geometry of strike-slip faults; however, it remains questionable over how these changes will occur given that three experiments produce significantly different results. For instance was the level of extension in the transtension experiment by the Naylor et al (1986) experiment significantly lower than those applied by Tron and Brun (1991)? Chapter 6 will inspect the effects of transtension in greater detail.
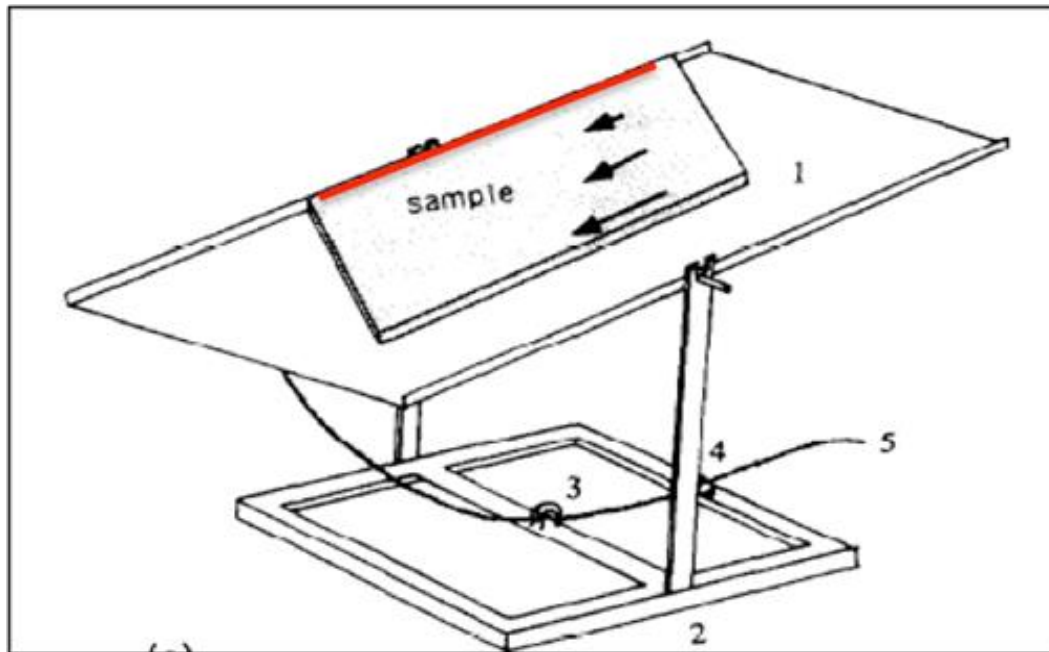
Figure 1.24 – View of the contraption used to produce first order structures without the presence of a through-going fault. The plate (1) was tilted so that the sample could slide down under the force of gravity. However, at the red line, the sample was fixed so that it could not slide, whilst the opposite side would start sliding first, causing the highest shear strain to be experienced in the zone closest to the fixed edge. However, this high strain shifts across the whole sample with continued sliding until the entire sample experiences uniform shear strain. Adapted from An & Sammis, 1996.
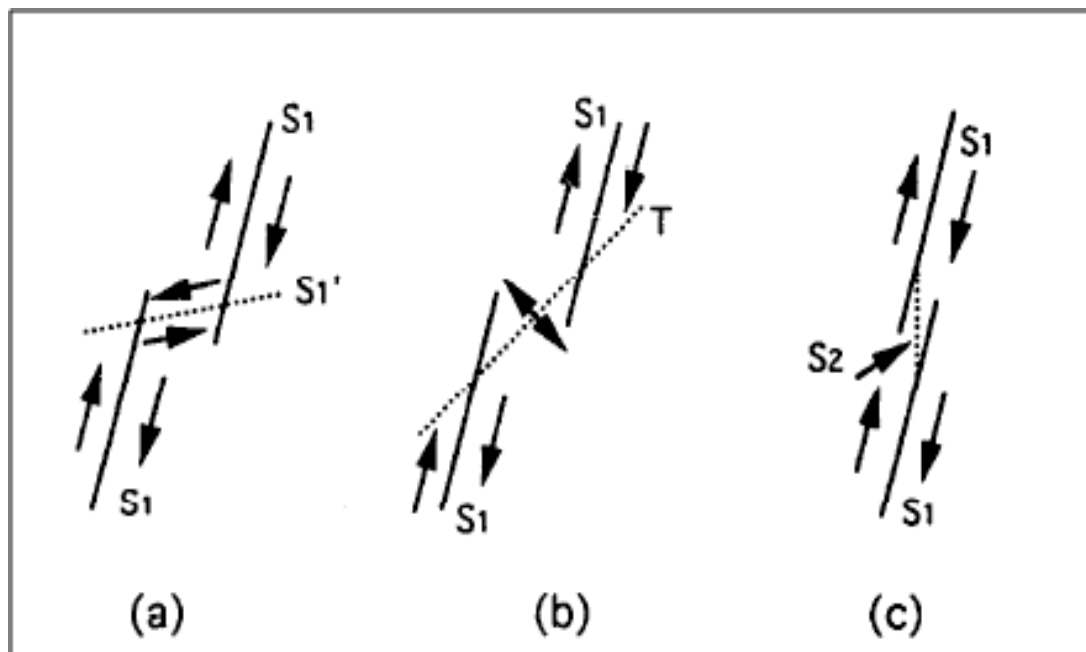


Figure 1.25 – Figure showing the various ways step-overs between simple faults were created. In a), $S'_1$ shears cut between two $S_1$ shears, whilst in b) tensile shears cut the $S_1$ shears. In c) $S_2$ shears cut between the $S_1$ shears. Note that a) and b) produce releasing bends, whilst c) produces a restraining bend. Adapted from An & Sammis, 1996.

(a)

(b)
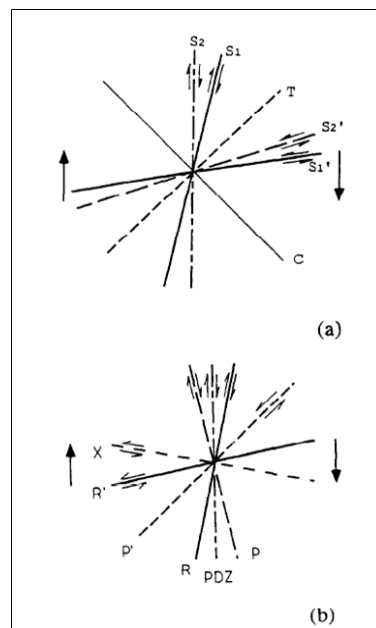
Figure 1.26 - a) shows the new model developed by An & Sammis (1996), whilst b) shows the traditional Riedel model for comparison. Note that the new model does not have the traditional shears but two conjugate sets: $S_1$ & $S'_1$, and $S_2$ & $S'_2$. The $S_2$ conjugate set could be a rotated version of the first set and the $S_1$ set could mimic the R and R' from the Riedel model. There is no PDZ in this alternate model and they also have tensile structures (T) and compressional linear features (C). Adapted from An & Sammis (1996).
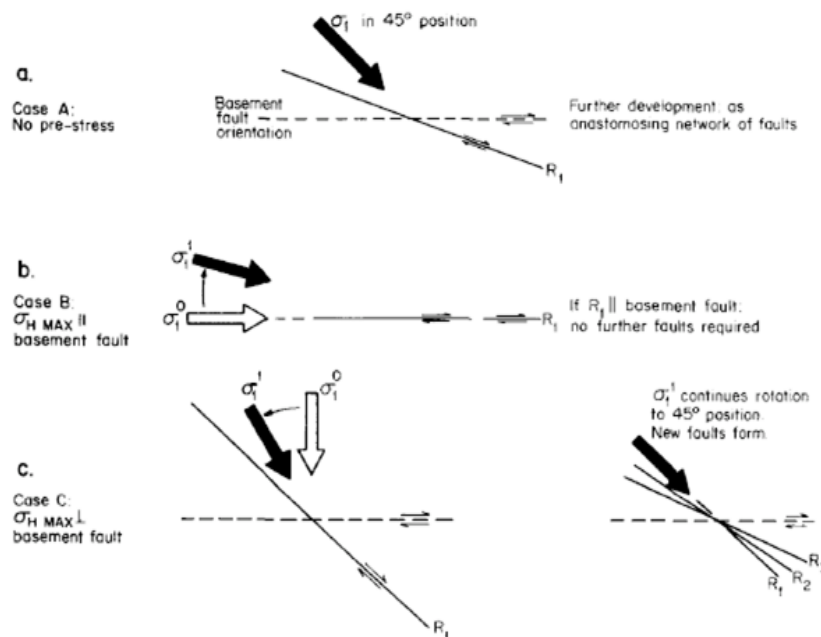


Figure 1.27 - Figure showing how the direction of maximum stress is oriented with a predisposed initial stress. a) Initial test with no pre-stress added and thus $\sigma_1$ is oriented at 45°. b) $\sigma_1$ initially aligned parallel to the PDZ to simulate transtension. When the test begins, the stress field rotates from parallel, so that it becomes mechanically advantageous for the R shears to propagate along the PDZ. c) $\sigma_1$ is oriented perpendicular to the PDZ to simulate transpression, producing R shears at a wider angle than case a). With increasing displacement, the stress field rotates more and R shears at increasing acute angles to the PDZ. Adapted by Naylor et al, 1986.

## 1.6   Normal Fault Studies and Implications for the Study of Strike-Slip Fault Propagation Using 3D Seismic Data

The previous two sections focussed on the nucleation, growth, and propagation of strike-slip faults using field studies and experiments conducted by analogue modelling.  The field-based studies cannot quantify displacement in 3D, and thus determining the propagation history on naturally occurring examples has never been recorded.  This section illustrates how the application of 3D seismic data can be used to study displacement distribution and 3D fault geometry on normal faults.  Specifically, this will focus on how these two methods can determine a faults linkage history, mode of propagation, and whether propagation has been restricted.

*Displacement Distribution-*

Displacement distribution was shown in an idealised case in Figure 1.1, where an isolated fault shows a concentric fault plane with the maximum displacement occurring in the centre of the fault and reducing towards the tips, often forming an elliptical shape (e.g. Watterson, 1986; Barnett, 1987; Walsh and Watterson).  However, kinematic factors such as linkage history and mode of propagation can alter how the displacement is distributed.  For instance early 3D surveys showed that normal faults can not only link laterally (Cartwright et al., 1995; 1996; Cartwright and Mansfield, 1998), but also link vertically, which is often referred to as dip linkage (Mansfield and Cartwright, 1996).  This is shown by displacement minima separating displacement maxima in both cases and is integral to determining whether a fault has propagated principally by radial growth, or has propagated principally by the linkage of fault segments (Figure 1.28).

Furthermore, the application of 3D seismic data has enabled the mode of propagation to be determined.  For instance, a fault can propagate blindly (where a fault deforms through previously deposited units) (e.g. Watterson, 1986; Barnett, 1987; Walsh and Watterson, 1987) or has the fault propagated under syn-kinematic conditions (where a fault becomes emergent with the free surface and grows concurrently with sedimentation) (e.g. Childs et al., 1993; Childs et al., 2003; Baudon and Cartwright, 2008a; 2008b).  This can be determined both by displacement distribution and by the fault geometry and evidence of the surrounding strata.  In the case of the former, if a fault shows an abrupt change from vertical to horizontal

45

contours [also shown by an M-type profile classification (Muraoka and Kamata, 1983) in a D/L plot] and an asymmetric distribution of displacement, then it is indicative of an emergent fault propagating under a syn-sedimentary condition (Childs et al., 2003; Baudon and Cartwright, 2008a).  A blind fault by contrast shows a C-type profile of the vertical D/L plot, and the displacement is distributed evenly with displacement maxima in the centre (Muraoka and Kamata, 1983; Baudon and Cartwright, 2008a).

*3D Fault Geometry -*

The 3D fault geometry can also provide insights into growth history by showing 1) differences in the tip line to indicate blind or emergent propagation, 2) changes in shape, indicating restrictions inhibiting propagation, and 3) undulations, indicating regions of fault linkage.

Baudon and Cartwight (2008b) defined three criteria to recognise if a fault has propagated blindly: a) plunging of the tip-line, b) folding in the strata ahead the upper tip, and c) absence of growth strata in the hanging wall.  Specifically, a) shows that the upper tip was not restricted at any point during upward propagation, and therefore the fault was never emergent at the free surface.  Thus visualisation of the 3D geometry of the fault plane, which includes the tip-line loop allows for insight into the mode of propagation.

It follows that if the tip line loop is not elliptical, it can indicate that propagation was restricted (Benedicto et al., 2003).  Restrictions to propagation can occur at any side of the fault and thus changes in shape from the idealized ellipse can be used to infer the cause of restriction (Figure 1.29, Figure 1.30).  These can be attributed to mechanical stratigraphy i.e. the fault is limited by the layer thickness, a change in lithology, emergence at the free surface (Childs et al., 1993; 1995; 1996), or from other structures such as faults (Nicol et al., 1996).  Changes in the fault shape can result in a fault growing longer laterally rather than vertically, forming larger than average aspect ratios, or vice versa (Nicol et al., 1996).  Restrictions on all sides have led to the identification of many larger faults forming rectangular shapes (Figure 1.30) (Benedicto et al., 2003; Lohr et al., 2008).  For example these can form from larger, parent faults linking with smaller, secondary faults (Figure 1.31, Figure 1.32) (Marchal et al., 2003).

Linkage processes cause undulations in the plane of the fault plane, for example a vertical undulation (Figure 1.33) is a likely artifact of parent-to-tip lateral linkage whilst a horizontal undulation is a product of tip-to-tip vertical linkage. Furthermore, when linkage occurs vertically, "lobate" geometries are formed whilst lateral linkage causes upward and downward bifurcations (Figure 1.32) (Marchal et al., 2003). Another term for the undulations identified in a fault plane are fault corrugations, which are defined as sinuous profiles of ridges and grooves that form parallel to slip direction at a range of scales from several metres to kilometres (Hancock and Barka, 1987; Ferrill et al., 1999). These have been attributed to form from the overlapping of en echelon fault arrays by two breakthrough mechanisms: lateral propagation of curved fault tips and linkage of connecting faults (Ferrill et al., 1999). Thus the presence of undulations or corrugations can indicate fault linkage, which may in turn affect the overall fault shape (Ferrill et al., 1999; Benedicto et al., 2003; Marchal et al., 2003).
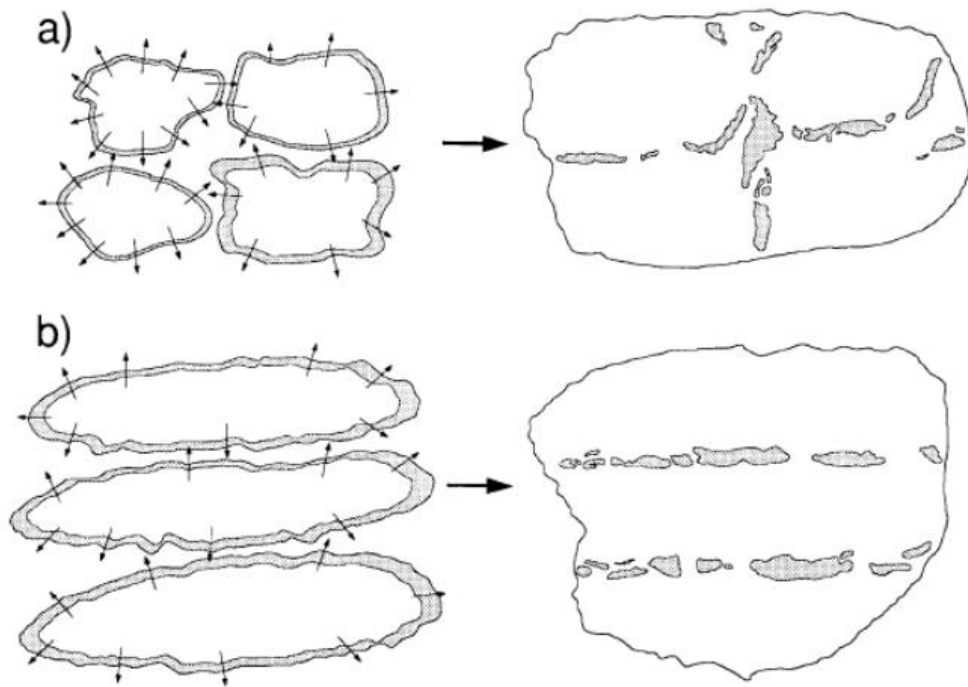
Figure 1.28 - Illustration showing how linking faults will leave patterns or zones of displacement minima, indicating the linkage history and location (these can occur both vertically and laterally as shown in a). Adapted from Mansfield and Cartwright (1996).
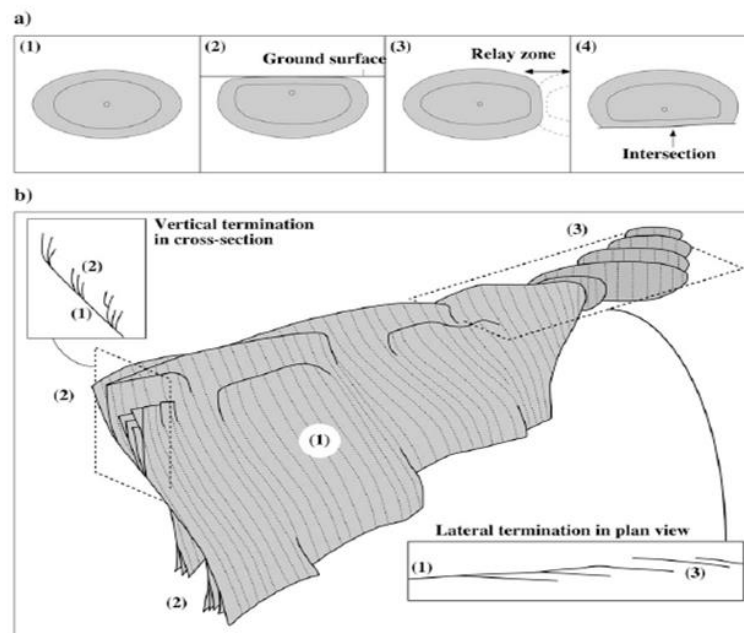


Figure 1.29 - a) Shows how the fault geometry of the ellipse changes with interactions with 2) ground surface, 3) linkage/transfer zone, and 4) vertical linkage. b) Shows normal fault geometries, note how the fault in cross-section resembles a strike-slip fault in cross-section. Adapted from Marchal et al, 2003.
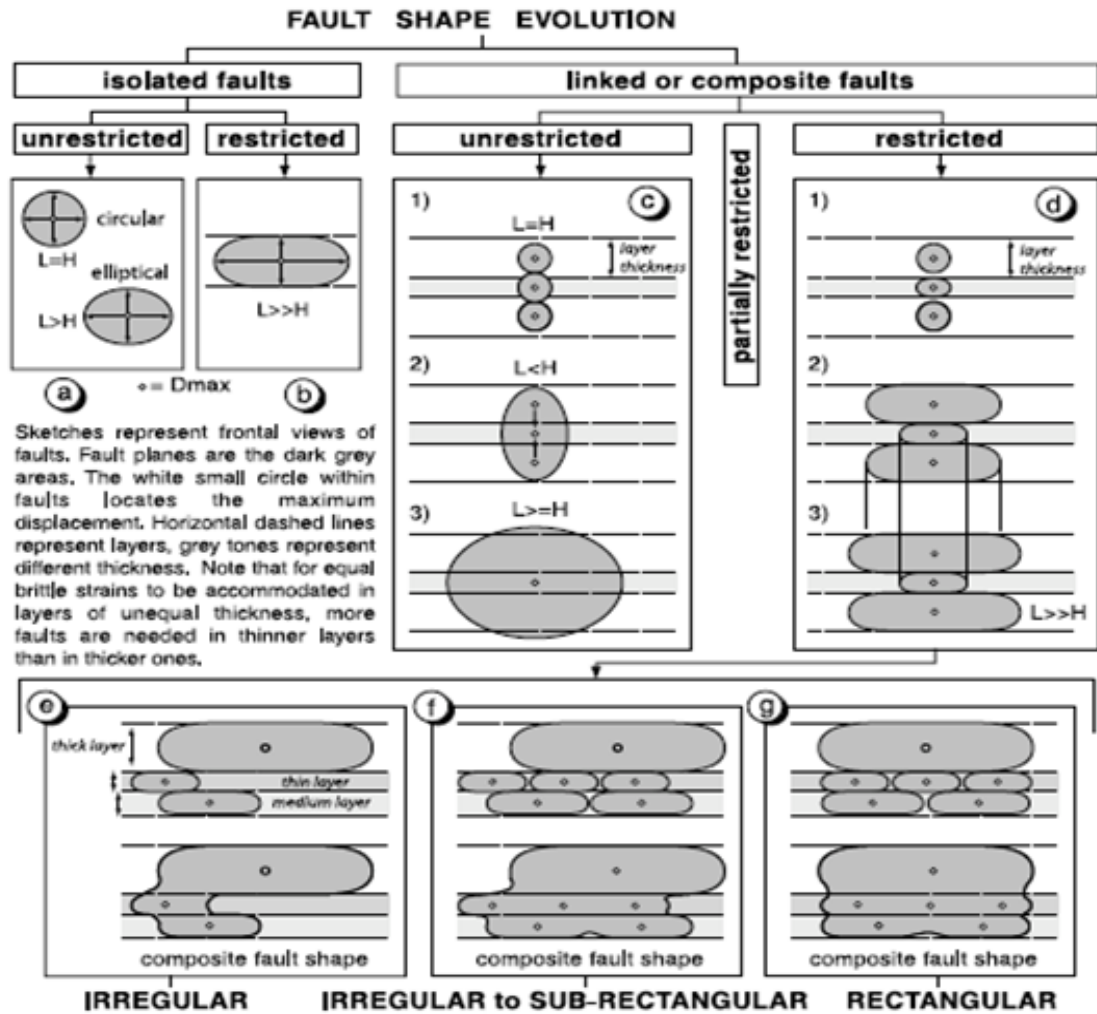
Figure 1.30 – A proposed model of fault evolution when restricted by layers in the stratigraphy.  If a fault is vertically restricted, they become more elliptical and if these elliptical faults link vertically, a rectangular shape evolves to span the fault plane.  Adapted from Benedicto et al, 2003.
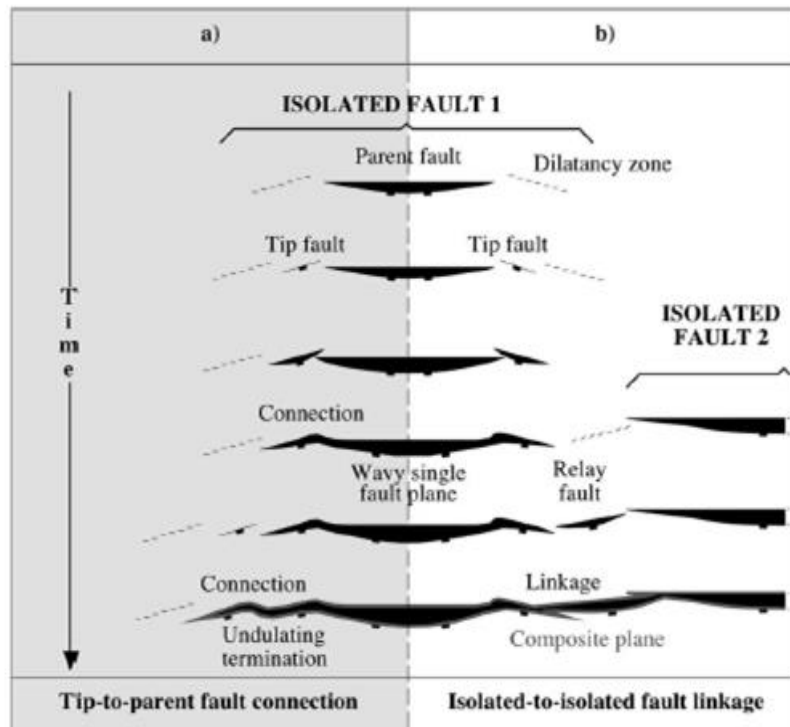
Figure 1.31 - Plan view of the Marchal et al (1998) theory that faults grow by 1) radial propagation, 2) parent-to-tip linkage, 3) tip-to-tip linkage, and 4) isolated-to-isolated linkage. The tip faults are secondary faults that grow later than the parent but then link to form larger faults. Adapted from Marchal et al, 2003.
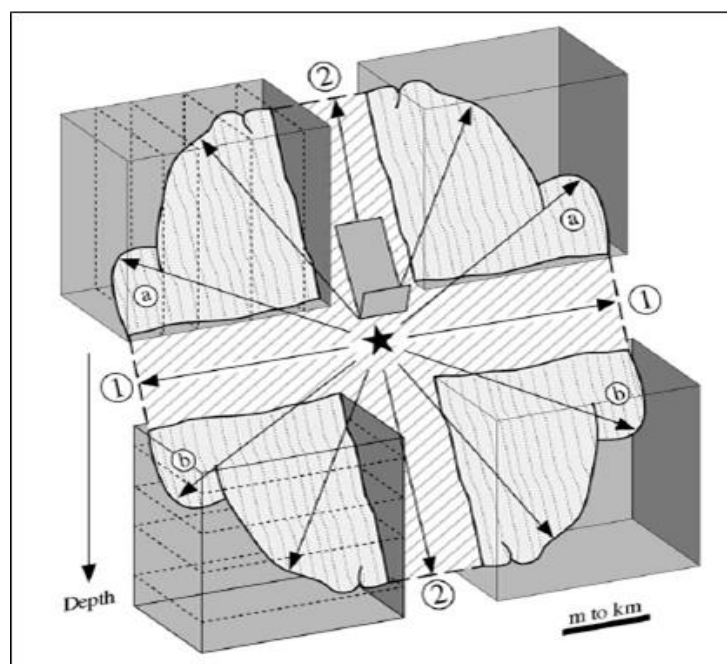


Figure 1.32 - Schematic model showing the geometries of linkage on the fault plane. 1) Represents lateral linkage which can have either a) upward bifurcations or b) downward bifurcations, whilst 2) represents vertical bifurcations which form a "lobate" geometry. Black arrows show propagation directions, large arrow shows sense of slip, and star marks the fault initiation point. Adapted from Marchal et al, 2003.
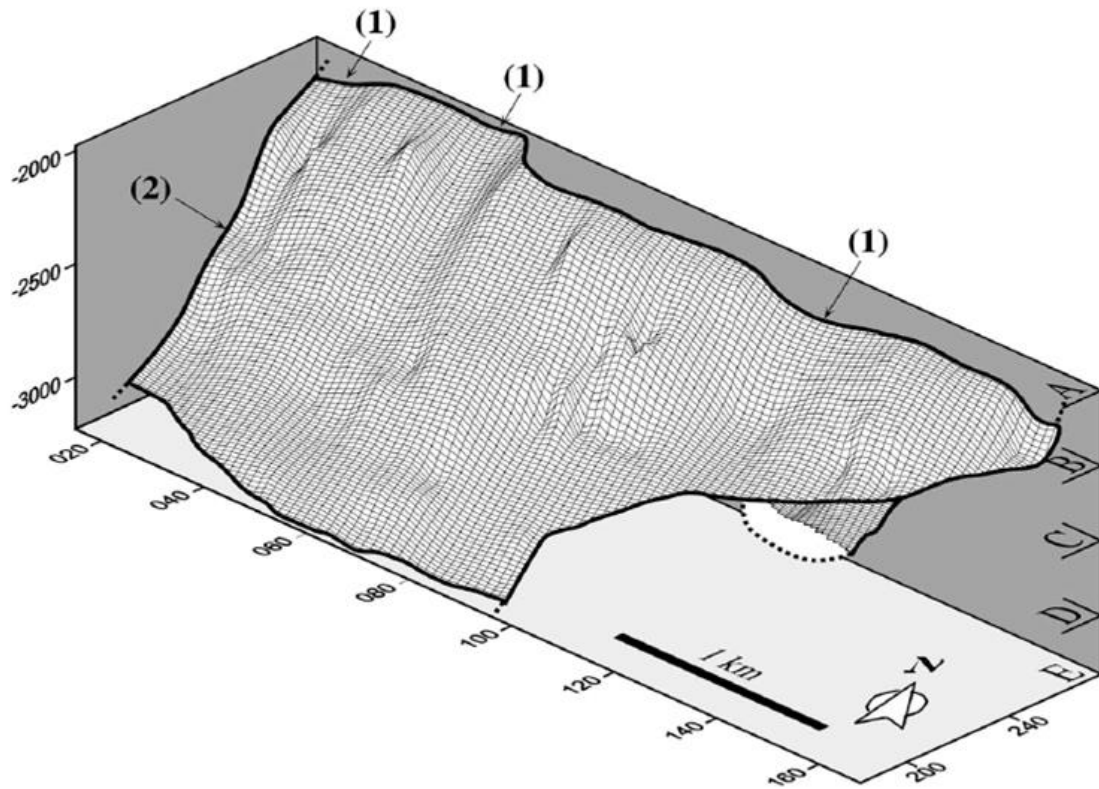
Figure 1.33 - 3D view of a normal fault plane showing undulations. 1) are examples of vertical undulations, marking parent-to-tip lateral linkages, and 2) is an example of horizontal undulations formed from tip-to-tip vertical linkage. Adapted from Marchal et al, 2003.

## 1.7    Strike-Slip Faults in Seismic Studies

Seismic studies of strike-slip faults have not progressed significantly beyond the pioneering studies using 2D lines by Harding (1985).  This work characterised flower structures, and showed that a strike-slip fault can show differing slip-sense (i.e. normal or reverse separation) across the same profile, leading to chaotic interpretations and understanding of the evolution. Most studies of strike-slip faults using 3D seismic data have focussed on the basin evolution of a strike-slip system or hydrocarbon prospectivity, rather than how faults propagate and grow (e.g. Hsiao, 2004; Hsiao et al., 2010; Jiang et al., 2011).

A recent study in the Levant Basin detailed strike-slip faults with secondary structures defining the upper tips; however, little work was conducted to inspect their 3D nature (Ghalayini et al, 2014).  Two studies have shown that strike-slip fault offset can be quantified using 3D seismic data using a similar method; however, the focus of these studies was to restore strike-slip deformation between thrust sheets and did not inspect strike-slip fault evolution (Durand-Riard et al., 2013; Benesh et al., 2013).  Furthermore, these studies were published subsequent to the majority of this thesis being completed, and therefore their methodologies were unknown when the work began.  A prior study using one of the datasets used in this thesis attempted a preliminary inspection of strike-slip fault propagation; however, this focussed on quantifying the displacements of horsetail damage faults to understand fault tip evolution (Nelson, 2007), and this thesis builds upon her work and solidifies her methodologies to better understand strike-slip fault displacement distribution, 3D geometry, and propagation.

## 1.8    Literature Review Summary and Chapter Synopsis

After summarising strike-slip fault studies in both field studies and analogue studies, it is clear that the central aims of this thesis have not been explored in strike-slip faults in the same manner as normal faults, and thus our knowledge of strike-slip fault propagation is comparatively lacking.  This thesis will therefore attempt to bridge the gaps between strike-slip faults and normal faults by providing a framework for measuring strike-slip fault displacement, thereby allowing an analysis of the propagation history.

From analogue studies, there are clearly differences to fault geometry depending on lithology, sedimentation, stress states, and more; thus an analysis of the 3D geometry in a natural setting will help constrain these discrepancies. Furthermore field studies have shown how faults nucleate, link, and grow using displacement-length gradients; however, they are limited to one stratigraphic level and cannot quantify how displacement changes towards the vertical tips. With the exception of the 3D model presented by Kim et al (2003), no studies have focussed on the 3D geometry of basal tips, and therefore this thesis also presents a novel opportunity to explore this aspect. Finally, although several studies have inspected how faults have evolved at intersections, these studies have not be been extrapolated into 3D, and therefore this thesis will attempt a preliminary analysis into fault propagation at conjugate intersections, branching intersections, and tip structures of intersecting faults.

### 1.8.1   Chapter Summaries

*Chapter 2- Geology, Data, and Methodology*

This is a short chapter that will describe the tectonic setting and regional geologic history of the Levant Basin. This will set the context for both datasets by outlining the datasets and methodology that is employed in the subsequent chapters. Furthermore, an overview of the basic geophysical principles behind seismic data, the basics of seismic interpretation, and will be provided.

*Chapter 3- Kinematic Indicators of Strike-Slip Faults in 3D Seismic Data: Implications for Fault Propagation*

This chapter presents a variety of examples from the GalC dataset (Figure 1.3) to clearly illustrate the methodology of quantifying strike-slip fault offset in 3D seismic data. This includes showing the range of features that can be used, the limits and pitfalls of this methodology, and the implications of this methodology to understanding strike-slip fault displacement distribution and timing of the deformation. This chapter thus serves as stage 1 from the central aims (Section 1.2).

*Chapter 4- The Displacement Distribution and Geometric Descriptions of Two Gravity Driven Strike-Slip Faults in 3D Seismic Data*

This chapter uses the Levant A dataset to explore the displacement distribution and 3D geometry of two large strike-slip faults in great detail to determine how the faults propagated and grew. This is the first study to explore how strike-slip faults propagate upwards and downwards using naturally occurring examples, and is therefore the heart of the thesis, inspecting stages 2 and 3 of the central aims. A detailed methodology for mapping rotational faults is also included. This is the only chapter using the Levant A dataset and is very long, thus each fault is considered as a sub-chapter with specific discussions. The final sections of this chapter discuss some of the themes that relate the two faults and in turn, how geometry and displacement used in conjunction allow for insights into fault propagation.

*Chapter 5- A Preliminary Analysis of Strike-Slip Fault Propagation at Fault Intersections and Fault Tips in 3D*

Chapter 5 builds upon the examples of 0Chapter 3 using the GalC dataset to present a regional inspection of strike-slip fault characteristics, such as displacement and length. This information is then applied to inspect: 1) conjugate intersections, 2) branching fault intersections, and 3) lateral and vertical fault tip structures in 3D. This chapter represents stage 4 of the central aims.

*Chapter 6- Discussion*

This chapter compares themes between the two datasets, such as fault geometry controls, faulting in evaporites, and basal tip structure. This chapter also relates the structures and deformation observed in this thesis to the prior work summarised in this chapter. The chapter concludes with ideas for future work, with a focus on uniting analogue studies and field studies, as well as presenting the implications of this study.

*Chapter 7- Conclusion*

A brief conclusion is presented summing up the results and implications of this study.

# Chapter 2

# Geology, Data, and Methodology

# 2   Geology, Data, and Methodology

## 2.1   Regional Geology

The following is divided into the tectonic setting and geologic history.

### 2.1.1   Tectonic Setting

The eastern Mediterranean Region consists of major plate boundaries between three larger plates: the African (Nubian), the Eurasian, and the Arabian, Figure 1.3 (Wdowinski et al., 2006).  The Eurasian plate moves east due to the Mid-Atlantic rift push, whilst the African plate moves slowly to the northeast, and the Arabian plate moves rapidly north (Mascle et al., 2000; Mahmoud et al., 2005).  Together, these form the intervening Anatolian and Sinai microplates.  The Sinai plate is located to the northeast of the African plate and west of the Arabian plate (Taymaz et al., 2007).  GPS and seismotectonic data (e.g. Mascle et al., 2000; Mahmoud et al., 2005; Salamon et al., 2003) show the Sinai plate is bounded to the east by the major sinistral transform fault, the Dead Sea Fault (DSF), which formed from the large velocity difference between the Arabian and African plates.  To the west, the Sinai is likely bounded by another major dextral transform fault, but evidence of this has yet to be corroborated by seismic data (Mascle et al., 2000).  It is also bounded in the west by a feature known as the Eratosthenes Seamount, which is suggested to be a fragment of continental crust (Robertson, 1998b).  To the north of the Sinai plate lies the Anatolian plate which experiences anti-clockwise motion due to the conflicting motion of the Eurasian and Arabian plates.  This creates a thrust-tectonic plate boundary at the Cyprian Arc as well as more recent strike-slip motion (Wdowinski et al., 2006; Taymaz et al., 2007).

The Levant basin is located in the southern portion of the Eastern Mediterranean Sea on the Sinai micro-plate (Figure 2.1).  It is a deepwater basin dominated by thin-skinned gravity slides from the East (the passive continental margin of Israel, Lebanon, and Syria) and the southwest (the Nile Delta) (Cartwright and Jackson, 2008; Bertoni and Cartwright, 2007b). The Levant A survey is located in the extensional and translational domain of the gravity slide, and is reflected by the structures (described in Chapter 4).  The GalC dataset is located

56

in the contractional domain of the slide, and the deformation is dominated by segmented thrust faults, folds, and conjugate strike-slip faults (described in Chapters 3, 5).

## 2.1.2  Geologic History

The Levant initially opened during rifting events beginning in the Early Permian and spanning to the Middle Jurassic, coinciding with the opening of the Neo-Tethys (Gardosh and Druckman, 2006; Garfunkel, 1998).  Increased continental break-up further developed the basin around the end of the Mid-Jurassic (Robertson, 1998a; Garfunkel, 1998).  A regional compression began during the Late Cretaceous, resulting in major plate-boundary deformation and forming the Cyprian Arc to the north as well as initiating the closing of the Neo-Tethys Ocean (Garfunkel, 1998).  The compression similarly initiated a series of NE-SW trending folds along the Levant Margin, known as the Syrian Arc fold belt, which extends from Western Egypt into the Palmyra fold belt in Syria (Eyal and Reches, 1983; Druckman et al., 1995).  Growth packages present on faults from the extensional part of the margin suggest that the compression continued until the late Miocene, (Cartwright and Jackson, 2008).  The Oligocene was dominated by a siliclastic depositional environment (Figure 2.2), whereby significant submarine erosion ensued due to an increase in sedimentation from the intermittent uplift and exposure of the Arabian-African Craton (Druckman et al., 1995).  Slope instabilities and mass transport processes on the continental margin resulted in the incision of large submarine canyons (e.g. El Arish, Afiq, and Ashod, see Figure 1.3) during a Late Miocene capture of the shelf (Druckman et al., 1995).

The Messinian represents an influential part of the eastern Mediterranean stratigraphy, and is characterized by a thick evaporite accumulation of up to 2km thick (Druckman et al., 1995). They are likely comprised of gypsum, anhydrite, halite, and some shaly layers, which can be correlated with the Mavqiim Formation on the Israeli mainland (Hsu et al., 1977; Mart and Ben-Gai, 1982; Bertoni and Cartwright, 2006).  The evaporites formed due to a narrowing connection between Europe and Africa, causing the Mediterranean to be separated from the Atlantic Ocean, and resulting in large sea level fall in an event known as the Messinian Salinity Crisis (Hsu et al., 1977; Cartwright and Jackson, 2008).  The evaporites wedge out landward on the Levant margin, which can be seen in the seismic surveys used in many of the

2D studies (e.g. Cartwright and Jackson, 2008; Gardosh and Druckman, 2006) and 3D studies of the margin (e.g. Bertoni and Cartwright, 2006; Bertoni and Cartwright, 2007b) . The wedging is attributed to erosional truncation, onlap, and truncation (Bertoni and Cartwright, 2006; Gradmann et al., 2005). An important feature of the evaporites is that they are linked to a basinward creeping, forming a thin-skinned detachment that caused much of the post-Messinian deformation in the Levant Basin (Figure 2.1, Figure 2.2) (Cartwright and Jackson, 2008; Gardosh and Druckman, 2006).

The Salinity Crisis ended with the reopening of the Africa and Europe, allowing for marine transgression in the early Pliocene (Cita, 1973). The Levant Basin underwent increased sedimentation during the Pliocene, which included the deposition of the Yafo Sand Member above the Oligocene canyons (Frey-Martinez et al, 2005); although, these appear to pinch out seaward. Basinward, sedimentation was largely sourced by channels (Clark and Cartwright, 2009); however, it appears these were sourced from the Nile Delta to the south (Mart and Ben-Gai, 1982).

The Plio-Pleistocene saw clay-rich, siliclastic detrital sediments prograde over both the Yafo sands and the Messinian evaporites (Mart and Ben-Gai, 1982; Tibor et al., 1992). This progradation of sediments from the Nile coupled with the Messinian salts likely caused subsidence via loading in the southern part of the Levant Margin, accounting for increased sedimentation rates (Tibor et al., 1992). Cartwright & Jackson (2008) suggest that two crustal 'hinges' existed during this time (and likely still exist today) which caused the gravity driven tectonics in the region. To the east (landward) lies an inner hinge separating the uplifted Judean hills from the Syrian folds. These likely produced submarine slope failures, resulting in mass transport deposits. To the west (basinward), the inner hinge separates the Syrian folds from the shallower dipping Syrian Arc. In conjunction, both hinges exert a control on the salt movement resulting from the gravitational slide (Cartwright and Jackson, 2008).
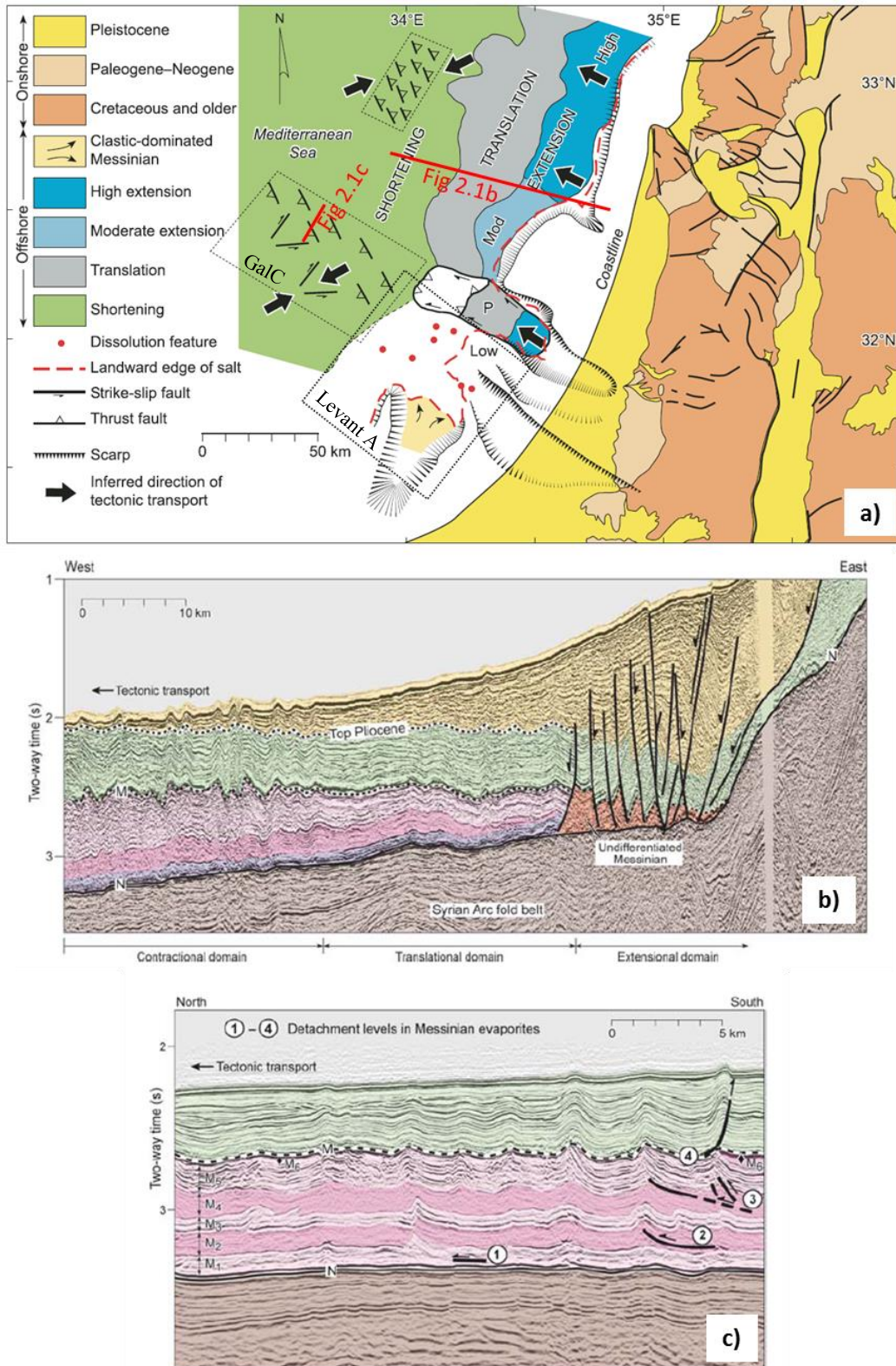
Figure 2.1 – Regional structural map of the Levant Basin (a) illustrating where the deformation occurs, which is driven by gravity tectonics. b) Cross-section highlighting the extensional, translational, and contractional domains. c) Figure highlighting multiple detachment levels within the Messinian evaporites (pink), the movement of which downslope, drives the deformation in the basin.  Adapted from Cartwright et al., 2012.
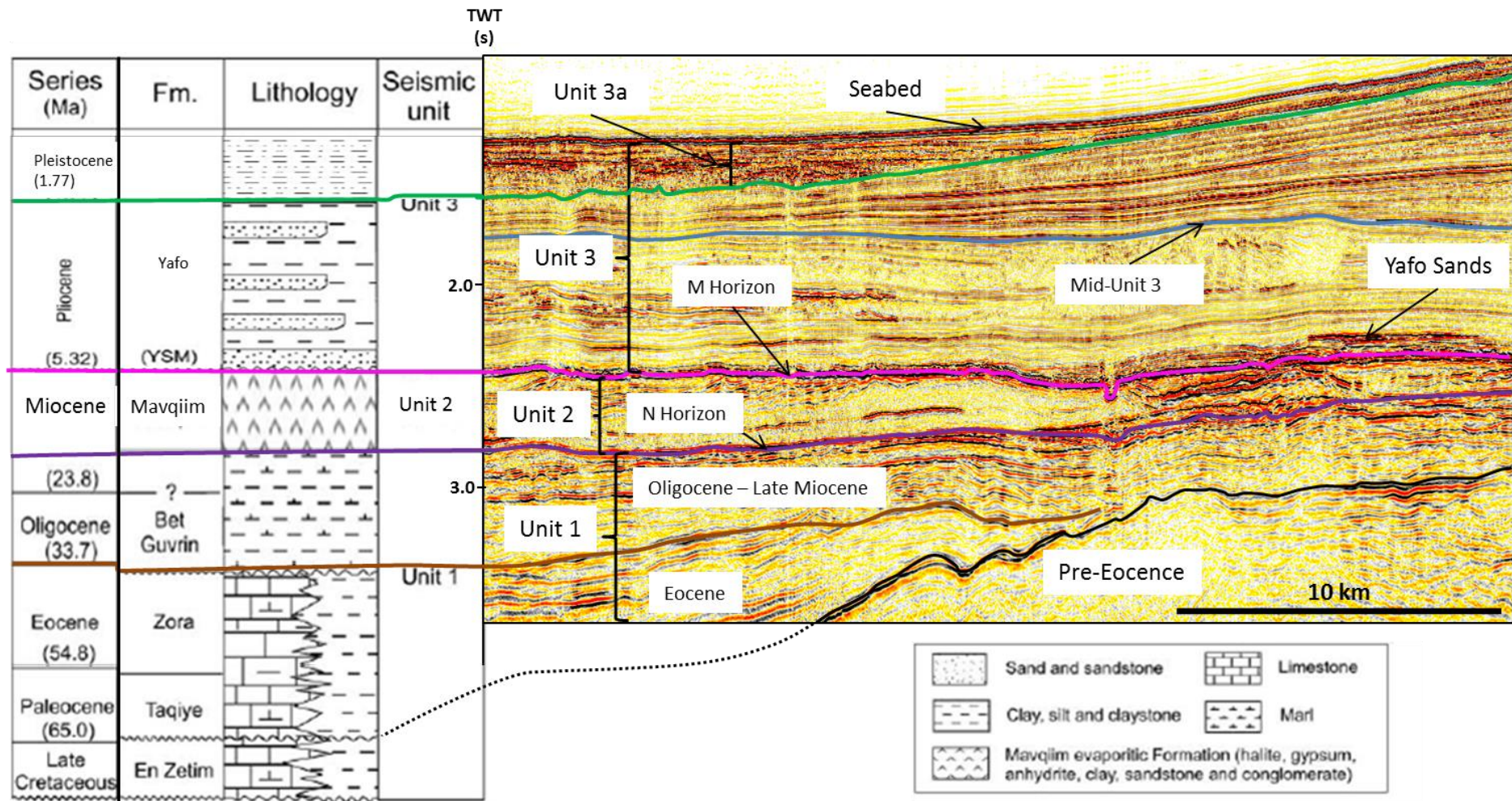
Figure 2.2 – Stratigraphic column juxtaposed with seismic section to show what the seismic expression of the sediments in the Levant Basin.

## 2.2   Data and the Basics of Seismic Data

The data used in this thesis comprise two high resolution 3D seismic data sets from the Levant Margin, Eastern Mediterranean (Figure 1.3).  High resolution 2D seismic lines were also available; however, these were only used to track faults and canyon margins beyond the limits of the 3D datasets, and will therefore not be described further.  Both datasets share similar attributes and are described in more detail Chapters 3 (GalC) and 4 (Levant A).

It should be noted that the only well for these surveys was located in the Levant A dataset in the El Arish Canyon.  This was used to derive the geophysical properties required for this study e.g. velocity, frequency, and resolution limits.  It was also used to derive the lithology of the strata, which is described in detail in Chapter 4.  It is believed that the strata in GalC is the downslope continuation of the Levant A, and thus the lithology of the overburden (Pliocene – recent sediments) are the same (Clark and Cartwright, 2009).  The following summarises the geophysics basics that enable this study to be conducted.

### 2.2.1   Seismic Data Basics

The marine 3D seismic data volumes used in this thesis are typically acquired using an airgun seismic energy source, a series of geophones then detect the reflected energy of compressive (P) waves from physical boundaries within the earth (see also Kearey and Brooks, 2002; Hart, 1999).  The strength of the seismic reflection from an interface is dependent on the acoustic impedance, z, where $z = \rho v$, where $\rho$ is the density of the rock unit and v is the p-wave velocity.  At geological boundaries between rocks of different lithologies – for example a shale layer above a sandstone layer, the contrast in physical properties (namely density) of the two rock units results in a strong acoustic impedance contrast giving a strong reflection.  Seismic surveys also record the time taken for the p-wave to travel to and from the acoustic impedance contrast and as such the vertical scale in many seismic sections is given in two-way travel time (TWT).

Seismic data is displayed in such a way that an increase in acoustic impedance corresponds with a peak in a seismic wavelet (Figure 2.3).  This is termed the 'SEG (Society of Exploration Geophysicists) normal polarity'; this convention also applies to all of the data used in this thesis.  The data used here is zero-phase (Figure 2.3), so called because the

displayed wavelet is symmetrical with the peak corresponding to the zone of maximum energy (e.g. Brown, 1999). There are several advantages to using zero-phase data, namely that the wavelet shape produced reduces uncertainty when associating waveforms with subsurface interfaces and also that a horizon tracked along the centre of the wavelet coincides with the subsurface boundary causing the reflection.

The resolution of 3D seismic data varies with depth both vertically and horizontally, both of which generally decrease with depth. Despite the excellent three dimensional coverage that this data utilises, it should be noted that the smallest geological feature which can be imaged on will typically be an order of magnitude larger than any observations at outcrop scale, and thus the faults studied here represent regional scale deformation.

Vertical resolution defines the potential to separate individual layers and is typically ¼ of the dominant wavelength of the seismic pulse. Above this limit (the tuning thickness), the waveforms interfere constructively and will only enhance the amplitude of the tuned reflection, whose thickness cannot be determined (Brown, 1999). It is possible however, to detect beds with a thickness of $\lambda/30$ where $\lambda$ is the dominant wavelength, but impossible to determine their true thickness (Brown, 1999). Two primary controls affect the horizontal resolution. The first the spacing of the recording hydrophones; this determines the spacing of the depth estimates from which the subsurface interface is reconstructed. The horizontal sampling of a flay lying seismic reflection is typically half of the detector spacing (Fig. 2.3 Kearey and Brooks, 2002). The second factor is the width of the Fresnel zone, which is defined by the energy returned to the detector within half a wavelength of the initial reflected arrival. Within this zone the reflected waves interfere constructively to give the reflected signal (Kearey and Brooks, 2002). Both vertical and horizontal resolution decreases with depth due to loss of higher frequencies via elastic absorption, and due to increasing compaction of sediments. This increases the velocity further, thus lowering the dominant frequency.

Before seismic data can be interpreted, it is filtered to increase the signal to noise ratio and remove unwanted frequencies to improve the vertical and horizontal resolution (Kearey and Brooks, 2002). Data migration is then improved involving a number of processes including correcting the positions of reflections from dipping surfaces and focussing the energy spread over the Fresnel zone (Figure 2.4) to improve resolution (e.g. Brown, 1999; Kearey and

Brooks, 2002). Another purpose of migration is to collapse diffraction patterns caused by discontinuities whose radius of curvature is shorter than the wavelength of the incident rays. Offsets of strata boundaries at faults can commonly cause diffraction patterns which unless removed can make fault interpretation difficult (Brown, 1999).

## 2.2.2  Interpretation Basics

Orthodox interpretation is carried out by mapping. Mapping is the basic process by which three-dimensional surfaces of both structural and stratigraphic features are created. These surfaces can be used to derive additional seismic attributes, further aiding interpretation. Mapping is carried out by tracking the horizon of interest by hand on a series of lines orientated perpendicular to one another typically in the original survey in-line and cross-line directions. In some complex areas, arbitrary lines are also picked, but this is generally rare as these lines are difficult to subsequently correct. Spacing of the initial grid is of the same order of magnitude as the scale of the geological features of interest. The resulting grid then forms the seed points for automated tracking algorithms which interpolate the remaining data. The autotracking process can be controlled via a series of parameters to optimise the final map, for example the time search window can be narrowed in areas where reflections have similar amplitudes to avoid the autracked horizon jumping up or down to another horizon.

Once mapping is complete, a number of horizon based attributes can be derived, adding further interpretation in the form of plan view maps. The three primary ones used in this study are listed below:

- *Time-Dip:* Dip attributes show the derivative of the surface which reveals changes in gradient. Dip attribute maps are excellent indicators of surface morphology and variation in slope, thus clearly delineating folds and channels. Faults are also noticeable where the reflections are disrupted and acoustic impedance reduced.

- *Amplitude:* Seismic amplitude is measured at the crest of the reflection and when displayed in map form enables facies variations to be observed. An example includes where bright, high amplitude reflections in a channel are juxtaposed to finer grained surrounding sediments. Thus channel scarps are imaged well and can be tracked on either side of a fault.

- *RMS Amplitude:* RMS (root mean square) amplitude squares amplitude values over a specific time window and then averages results. As RMS involves the squaring of amplitude values, high amplitudes will tend to become more noticeable on the final map (Brown, 1999). These were of particular interest as channels above and below the interpreted horizon could be captured without mapping additional surfaces and thus saving time in locating kinematic indicators.

The coherence attribute (Brown, 1996) was used heavily in this thesis in conjunction with the above attributes, and is described below (its application will be described in Chapter 3):

- 3-D seismic data are generally binned into a regular grid. By calculating localized waveform similarity in both in-line and cross-line directions, estimates of 3-D dimensional seismic coherence are obtained. Small regions of seismic traces cut by a fault surface generally have a different seismic character than the corresponding regions of neighbouring traces. This results in a sharp discontinuity in local trace-to-trace coherence. Calculating coherence for each grid point along a time slice results in lineaments of low coherence along faults. When this process is repeated for a series of time slices, these lineaments become fault surfaces, even though fault plane reflections have not been recorded. Stratigraphic boundaries generate similar discontinuities. The technique may be employed to produce coherence horizon slice maps, or to transform a reflection amplitude 3-D data volume into an entirely new volume or "cube" of coherence coefficients. Map views of coherence data afford the opportunity to see stratigraphic changes more clearly. For example, a channel is often more apparent in a coherence time slice than a traditional amplitude time slice. (Bahorich and Farmer, 1995).

In addition to the attributes listed above, isochron maps were also utilised. These are maps that show the relative time thickness between two arbitrary horizons, and can delineate large scale canyons, stratigraphic, pinch-outs, and regions that have been uplifted.

*Limitations and sources of error-*

Features with a size that nears the limits of seismic resolution are often sources of error as they may only be partially imaged. In addition, velocity effects can cause artefacts in the seismic data. For instance velocity pull-ups and push-downs result from localised increases

and decreases in the interval velocities of lithological units and can be caused by lateral facies variations. This can affect the measurements of channel depth; however, this effect is minimised due to the measurements focussing on horizontal separation rather than vertical separation.

Lateral velocity contrasts due to the increase in vertical thickness across faults can also result in pull-up and distortions of reflections and can lead to the misinterpretation of how deep a fault may extend. This is elaborated further in Chapter 4.

The vertical and horizontal resolutions, frequency, and other details about the 3D seismic datasets will be described in Chapters 3 (the GalC dataset) and Chapter 4 (the Levant A dataset).

## 2.3  Methodology

Chapter 3 serves as both a methodology and a core chapter to enable the quantification of strike-slip fault offset in seismic data, and is thus not described further here. Chapter 4 applies the methodology established in Chapter 3 and also describes how faults that grow upwards in a rotational manner (i.e. grow upwards following a direction that is not consistent with the 'inferred' stress field) can be mapped as well as the methodology for creating 3D displacement distribution diagrams.
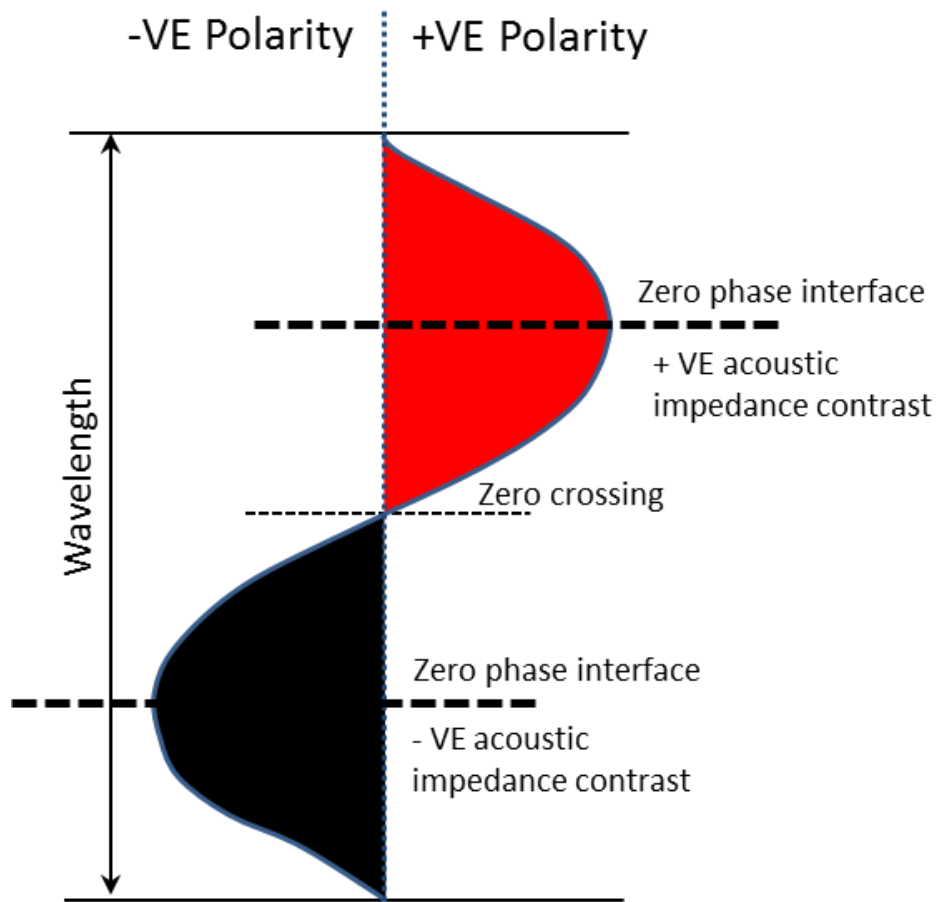
Figure 2.3 – Seismic wave illustrating the conventions of polarity and phase used in this thesis. (adapted from Hart 1999).
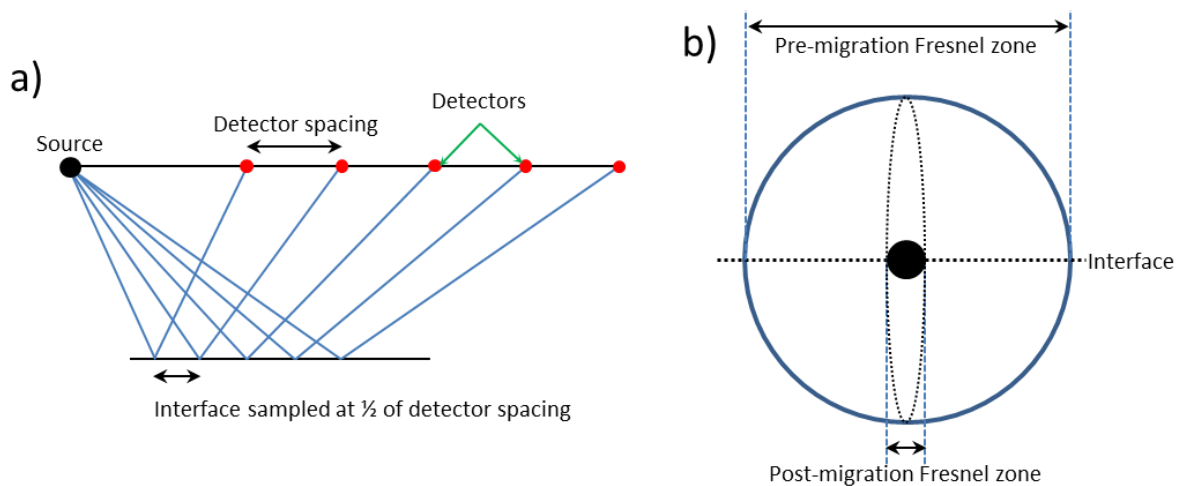


Figure 2.4 – Horizontal resolution and definition of the Fresnel zone. Horizontal resolution in seismic surveys is determined in part by the detector spacing which affects the sampling interval (a). The width of the Fresnel zone (b) also controls the resolution, and 3D migration reduces the size of the Fresnel zone to a small sphere. (adapted from Brown 1999)

# Chapter 3

# Kinematic Indicators of Strike-Slip Faults in 3D Seismic Data: Implications for Fault Propagation

# 3  Kinematic indicators of Strike-Slip Faults in 3D Seismic Data:  Implications for Fault Propagation

## 3.1  Introduction:

The application of three-dimensional (3D) seismic reflection data coupled with increasingly complicated hydrocarbon extraction techniques have seen strike-slip fault related plays to become increasingly important in hydrocarbon exploration across the globe (Hsiao, 2004; Zhu et al., 2009; Jiang et al., 2011).  However, strike-slip faults are relatively under-researched in comparison to normal and thrust faults, particularly regarding their propagation and growth.  Most previous studies of strike-slip faults evolution can be grouped into two categories: (1) field-based (e.g. Segall and Pollard, 1983; Martel et al., 1988; Kim et al., 2003; Flodin and Aydin, 2004b) and (2) experimentally-based using analogue physical models (e.g. Tchalenko, 1970; Bartlett et al., 1981; Naylor et al., 1986; An and Sammis, 1996).  Together, these studies have greatly advanced our understanding of strike-slip faults, but each has a weakness: field-based studies are generally limited to two-dimensional views and experimental models lack the typical material heterogeneities found in nature.  3D seismic data has the advantage of complete imaging of natural strike-slip faults in three dimensions, so that relationships between subsidiary faults in the fault zone can be investigated in detail.  Surprisingly though, strike-slip faults have barely been analysed in detail by seismically-based studies since the pioneering descriptions from 2D seismic data of (e.g. Harding, 1985).  More recent studies on 3D seismic data tend to focus on contextual descriptions of strike-slip faults and their role in regional tectonic evolution (e.g. Hsiao, 2004; Zhu et al., 2009) or on the potential prospectivity of a strike-slip basin (e.g. Jiang et al., 2011), rather than how these faults evolve and propagate.  A major omission in all these studies, however, is the basic measurement of displacement, which as shown by extensive research into normal and thrust faults, is a critical step in reconstructing fault growth histories (Walsh and Watterson, 1988).

This chapter aims to present a simple methodology for kinematic analysis of strike-slip faults in order to facilitate further research into their propagation and growth. 3D seismic data allows the rapid identification of many palaeo-geomorphological features in addition to the standard approaches of structural interpretation (Posamentier and Kolla, 2003). The use of geomorphic markers as piercing points to measure strike-slip displacement is well established in seismological and field based studies of strike-slip faulting (Burbank and Anderson, 2001). Here, the same approach is adopted and applied to the subsurface realm. An interpretational approach for identifying useful palaeo-geomorphological markers that are offset by strike-slip faults is presented. This extends the more established use of offset structural features to measure strike-slip displacement which has been employed for nearly a century (Jones and Pugh, 1915).

Two classes of kinematic indicators are presented in this thesis: 1) stratigraphic and 2) structural that are interpreted from 3D seismic data and associated with a suite of conjugate strike-slip faults from the Levant Basin (Eastern Mediterranean Sea). The stratigraphic class include uniquely recognizable sedimentary    features such as meandering deepwater channels, and grooves left by large intact blocks within internally disaggregated mass transport deposits (MTDs). The structural class includes the systematic offset of older intersecting faults, including strike-slip and normal faults. A secondary aim of this chapter is to discuss the best interpretational methods, using a combination of profile interpretation, orthodox horizon mapping, and attribute analysis, and to identify possible pitfalls in the methodology. In addition to describing a series of illustrative examples, as a guide to applying this methodology elsewhere, we also discuss the potential for identifying systematic displacement variations in three dimensions on a single strike-slip fault as a precursor to analysis of its growth history.

## 3.2   Geological Setting:

The Levant Basin is one of many basins found in the Eastern Mediterranean, and comprises much of the northern, oceanic extent of the Sinai microplate (Figure 3.1). It is bounded to the East by the passive continental margin spanning over Israel, Lebanon, and Syria and to the West by the Eratosthenes Seamount as well as the disputed plate boundary between the Sinai

and African plates (Mascle et al., 2000; Mahmoud et al., 2005; Gardosh and Druckman, 2006). The northern sector of the basin is bounded by the convergent remains of the Cyprian Arc whilst the southern sector is bounded by the north-eastern extent of the deepwater Nile Delta (Mart and Ben-Gai, 1982; Salamon et al., 2003; Wdowinski et al., 2006).

It is believed that the Levant Basin first opened as a product of the rifting sequences during the Early Permian – Middle Jurassic, coinciding with the opening of the Neo-Tethys Ocean (Garfunkel, 1998; Gardosh and Druckman, 2006). Convergence from the Late Cretaceous (Senonian) signalled the closing of the Neo-Tethys as well as the formation of the NE-SW trending Syrian Arc folds, which span much of the Levant Margin as well as onto onshore Syria and Western Egypt (Eyal and Reches, 1983; Druckman et al., 1995). During the Oligocene, siliclastics dominated the depositional environment, with large submarine canyons (e.g. Afiq, El Arish, and Ashod) incising due to intermittent uplift and exposure of the margin (Druckman et al., 1995; Bertoni and Cartwright, 2006).

The depositional environment in the early Miocene changed from clastic to carbonate-dominated, with accumulation of large carbonate platforms (Buchbinder and Zilberman, 1997). By the end Miocene (Messinian), a narrowing of the connection between the Mediterranean Sea and the Atlantic Ocean resulted in dessication of the Mediterranean Sea and deposition of an up-to-2000m thick sequence of evaporites during the 'Messinian Salinity Crisis' (Hsu et al., 1977; Ryan and Cita, 1978; Druckman et al., 1995). The evaporites in the Levant Basin have been correlated to the Mavqiim Formation, which consists of gypsum, anhydrite, and halite (Mart and Ben-Gai, 1982; Bertoni and Cartwright, 2006).

Major re-flooding occurred at the start of the Pliocene (c. 5.5Ma BP) (Buchbinder and Zilberman, 1997) as a consequence of the reopening of the gateway between the Atlantic and the Mediterranean (Cita, 1973). Clastic sediment supply increased dramatically during this time and transport into the basin was largely from the Nile Delta by a combination of deepwater channel systems and along-strike currents (Mart and Ben-Gai, 1982). Major progradation of the shelf-slope system occurred and shorelines advanced into the basin, with a resultant subsidence in part due to the increased load (Tibor et al., 1992), and in part due to regional tilting and uplift of the hinterland. This combination of tectonic uplift of the hinterland and basinal subsidence triggered the onset of gravity tectonics in the late Pliocene, and this regime continued to the present day (Cartwright and Jackson, 2008). This gravity-

driven regime resulted in a typical succession of deformation from up-dip extension domain, to a down-dip contraction with all the component structures detaching on or within the Messinian salt (Gradmann et al., 2005; Cartwright and Jackson, 2008).

The study area is located in the contractional toe domain of this gravity-driven system, and is characterised by thrust faults and associated folding that is commonly associated with deepwater fold and thrust belts (Briggs et al., 2006; Higgins et al., 2007; Morley et al., 2011). However, this dataset is unusual for a deepwater fold and thrust belt in that most of the deformation appears to be accommodated and controlled by a complex, conjugate set of strike-slip faults that detach in the Messinian Evaporites (Mart and Ryan, 2007; Cartwright and Jackson, 2008; Clark and Cartwright, 2009; Cartwright et al., 2012).  The thrust and fold structures are strongly segmented by the conjugate strike-slip faults (Figure 3.1, 3.2), with many thrusts and folds terminating against strike-slip faults.  The onset of thrusting and folding is broadly synchronous in the study area and is dated approximately as late Pliocene by correlation of the growth packages developed on the fold limbs to exploration wells closer to the shelf (Clark and Cartwright, 2011). The deformation persisted from the late Pliocene to the present day, and many of the major structures have a strong bathymetric expression (Figure 3.2).

The stratigraphy of the study area was described in detail by Clark and Cartwright (2009; 2011), and a similar subdivision is followed here, with the main post-Messinian interval (the main interval of interest for this paper) being divided into three units, PM1, and PM2, and PM3 (Figure 3.3).  PM1 is characterised by planar, parallel seismic facies with high lateral continuity, with occasional development of locally incised features interpreted as deepwater channels and their associated levees (Mart and Ryan, 2007; Clark and Cartwright, 2009). PM2 consists of laterally continuous reflections that are characterised by low to medium amplitudes.  Some regions show evidence of onlap and thin onto the thrust related folds in the classical manner of fold-related growth packages (Morley et al., 2011); however, most syn-kinematic thickening is restricted to PM3 (Figure 3.3). PM2 also contains a number of deepwater channel/levees, and locally, a thick mass transport deposit (MTD).  PM3 is characterised by high amplitude, discontinuous reflections and is bounded by the seabed. Several channel complexes are also included in this unit.
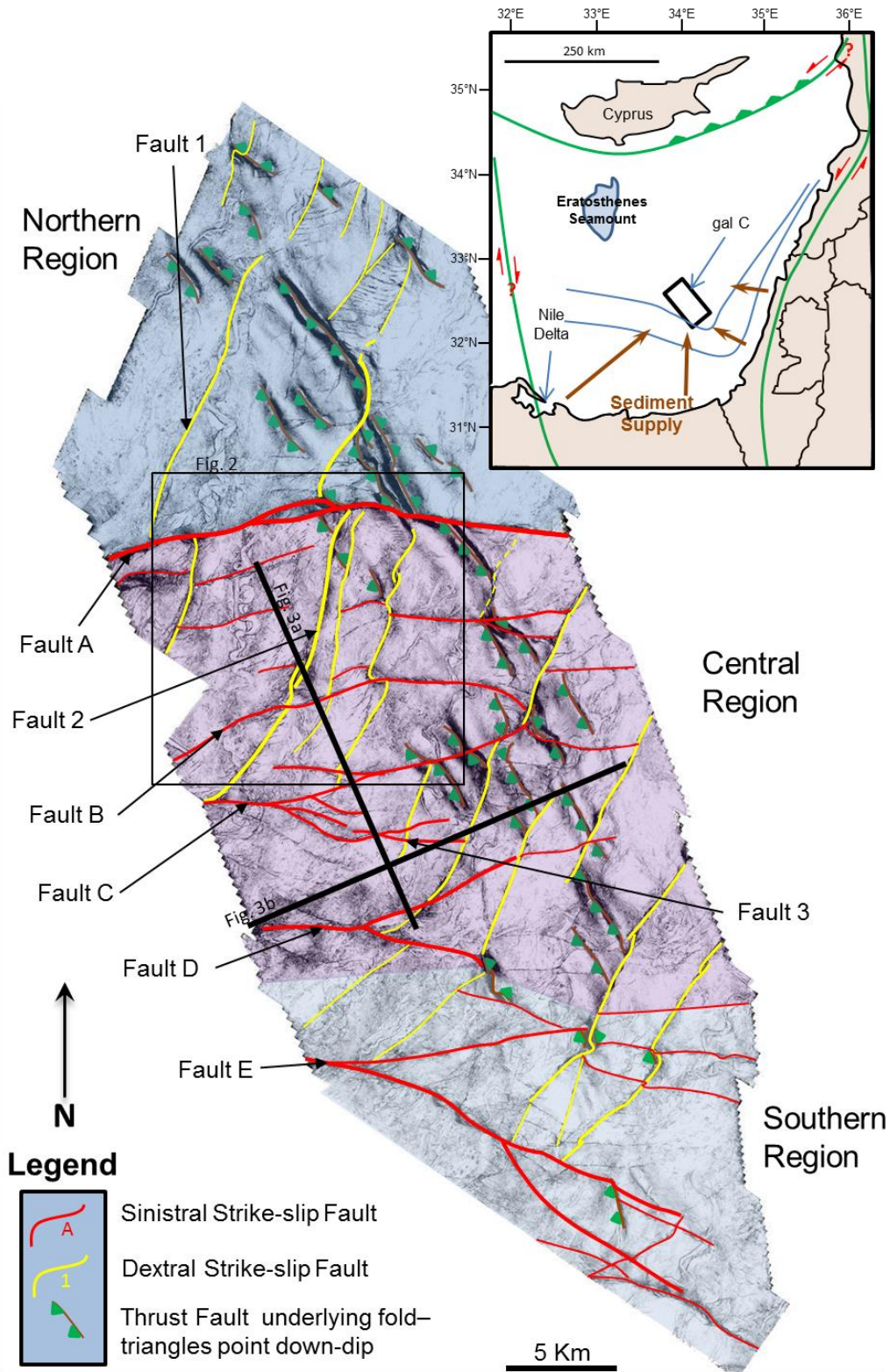
Figure 3.1 - Regional map of the data showing sediment input direction and Sinai microplate boundaries. The close-up of the galC dataset shows a complicated ensemble of structures, with the largest sinistral faults labelled A, B, C, D, and E, and each show offsets greater than 1km. The larger dextral faults are labelled 1 and 2 and show offsets over 1km. Smaller faults of both senses show offsets as low as 50m.
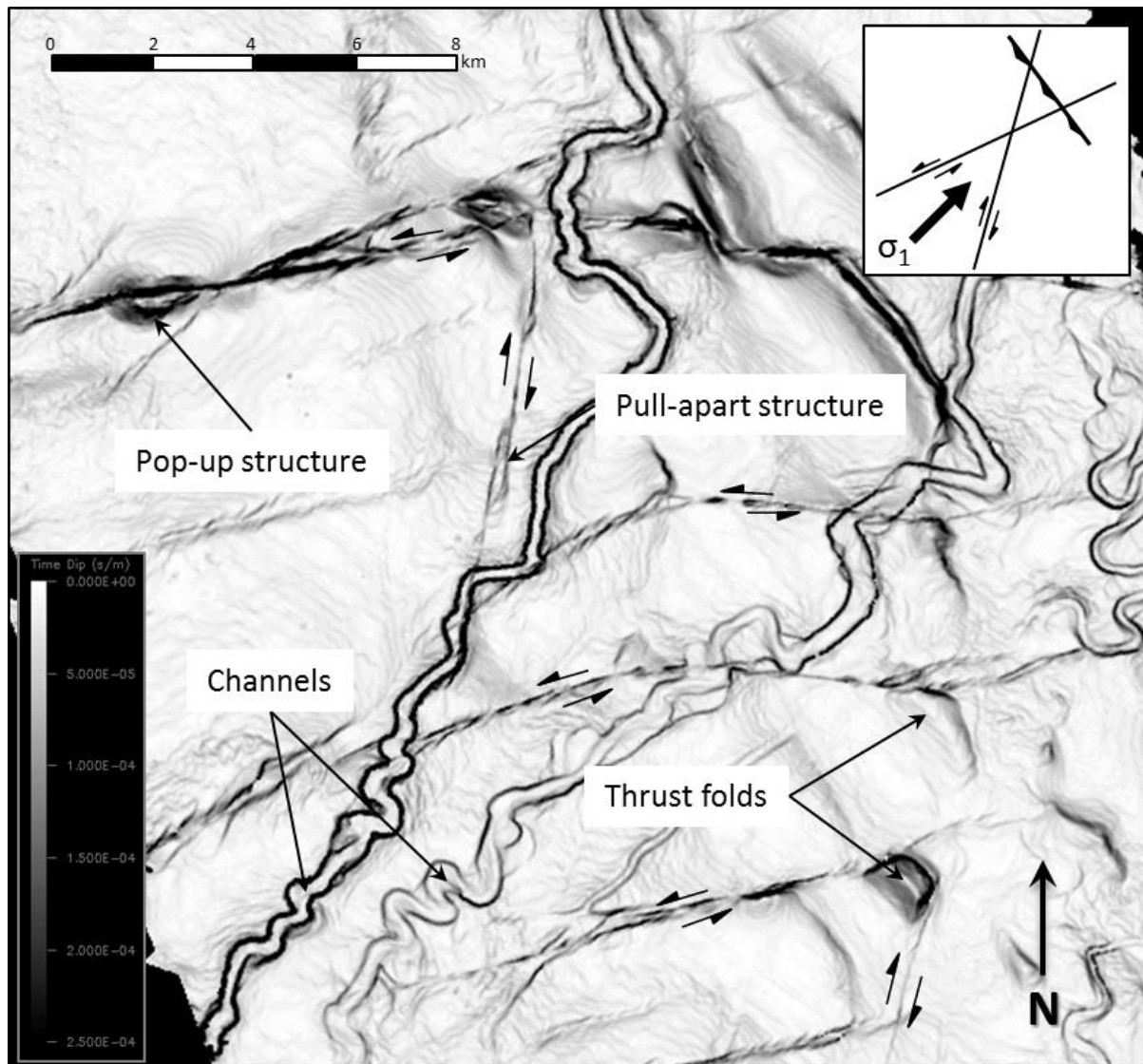
Figure 3.2 - Time-dip map of the seabed showing prominent pop-up and pull-apart structures, which allowed for determination of the slip sense along strike-slip faults, before applying the methodology presented here. The orientation of two conjugate sets of strike-slip faults and thrust folds allowed for an approximation of the $\sigma_1$ direction.
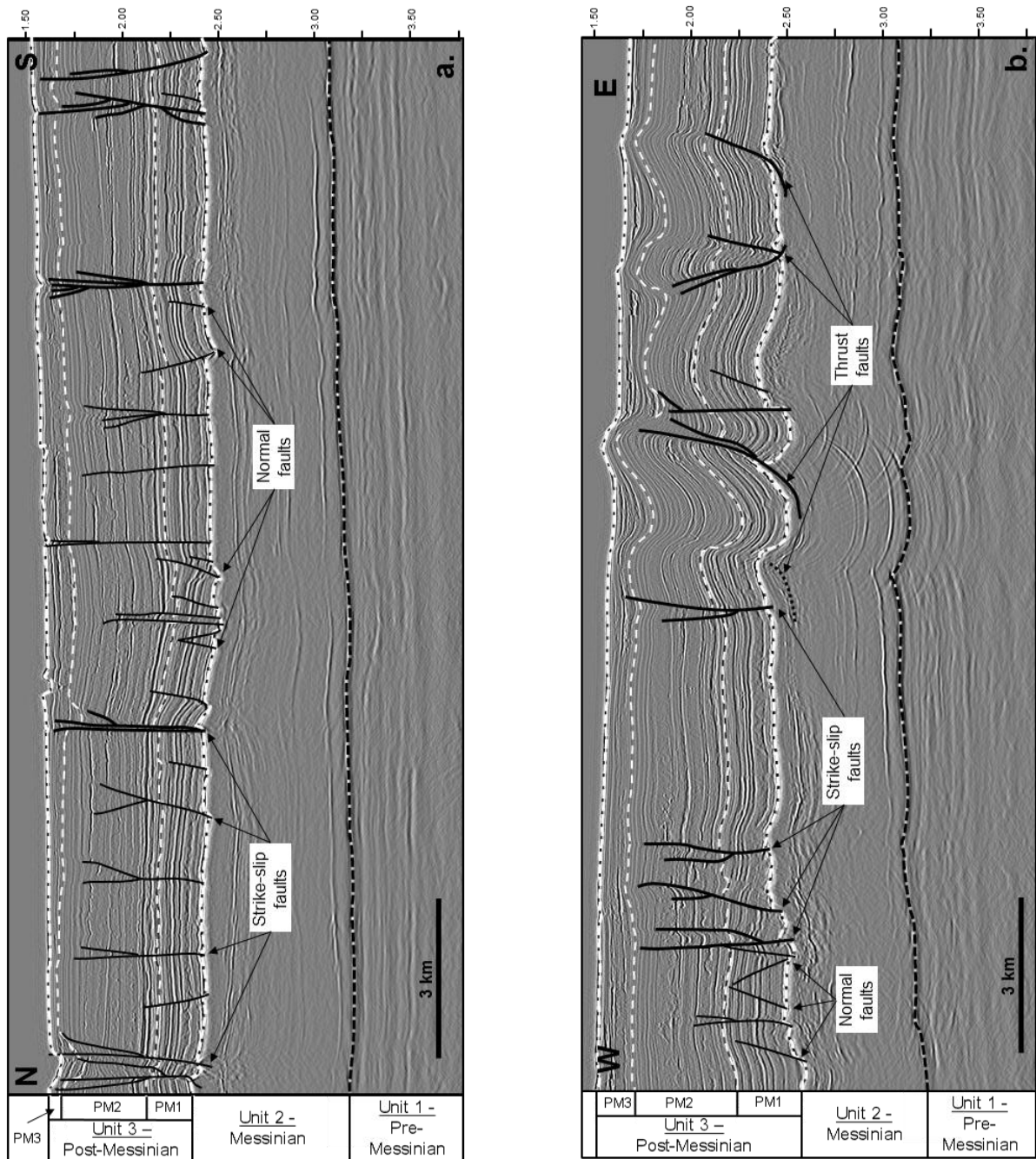
Figure 3.3 - Representative sections.  a) A N-S trending section which is relatively orthogonal to the strike of sinistral strike-slip faults and along strike of the thrust faults.  b) A section along dip of the thrust faults.  The post-Messinian sediments are divided into three units: PM1, PM2, and PM3.  PM1 and PM2 are largely pre-kinematic, whilst PM3 is largely syn-kinematic.  See Figure 3.1 for location.

## 3.3   Data and Methodology

### 3.3.1   Data

The 3D seismic reflection data used in this study was shot by BG Group and partners in 2000 and covers an area of approximately 1400km$^2$. The data was processed using a single pass post-stack time migration to generate a 12.5m by 12.5m grid and a 1ms sampling interval. The data was processed to near zero-phase and is displayed using SEGY normal polarity (with red corresponding to positive amplitudes on seismic sections). Dominant frequencies vary with the stratigraphy, specifically, around 30Hz for the Messinian Evaporites and 50Hz for the sediment overburden. It should be noted that the 30Hz value stated for the evaporites is holistic, and coupled with variable velocities among this unit, produces variable vertical and lateral resolutions (Bertoni and Cartwright, 2006). The interval velocity of the post-Messinian succession of 2000m/s was determined by well checkshot data from equivalent sedimentary units in the exploration wells drilled some 20km to the southeast and (Frey Martinez et al., 2005). Combined with the 50Hz frequency, this results in a vertical resolution of 10m. Lateral resolution is taken as twice the bin size (25m).

### 3.3.2   Methodology

Seismic data were interpreted using Schlumberger's GeoFrame 4.2 software on a UNIX workstation. Standard interpretation methodologies were applied for horizon correlation, and structural interpretation of 3D seismic data (Brown, 1996). Up to 12 horizons were picked throughout the study area in all three PM units, and additional markers were mapped on important features. Seismic attributes such as dip and RMS amplitude were computed and used to identify potential features for use as kinematic indicators (Figure 3.2). The attribute maps highlight both the strike-slip faults and channels that are offset by the faults. The coherency attribute (Bahorich and Farmer, 1995; Brown, 1996) is perhaps the best attribute for rapid detection of often subtle geomorphological features that have potential as kinematic indicators, since it is designed to detect lateral changes in reflection continuity.

Measurement of strike-slip displacement was divided into two parts: first, the sense of fault offset was determined using the geometry of both releasing and restraining bends located between segments and stepping direction in simple en echelon arrangements (Figure 3.2).

75

Second, measurement was made directly from attribute maps once specific 'candidate' offset features were categorised and correlated (see sections 4 and 5). Measurement accuracy for displacement of offset markers is equivalent to the lateral resolution of 25m, but measurement errors may in practice may be much less than this figure, since the overburden is relatively uniformly stratified, and lateral velocity variations are expected to be very small.

## 3.4  Kinematic Indicators – Stratigraphic Class

Numerous geomorphic studies conducted on the San Andreas Fault in the western USA, (Wallace, 1968; Keller et al., 1982; Gaudemer et al., 1989), and several other major strike-slip faults across the world, (e.g. Lensen, 1968; Huang, 1993; e.g. Zhang et al., 2004; Fu et al., 2005) have measured the offset of landforms including beheaded, deflected, and offset channels; pressure ridges; alluvial fans; and even tyre tracks to constrain the offset and growth history of faults (Burbank and Anderson, 2001). Stratigraphic class indicators found in seismic data will not resolve all the landforms listed above, but ample examples of submarine channels and basal grooves associated with the basal surface of a large mass transport deposit (MTD) are found in the dataset. Representative examples of each of these stratigraphic indicators are presented in detail below.

### 3.4.1  Submarine Channels

Channels provide the most diverse and useful examples of kinematic indicator both due to their variety of dimensions and planform geometry as well as their frequency of occurrence within the post-Messinian intervals. Individual channels have their own unique sinuosity, meander wavelength, and dimensions (Wynn et al., 2007; Clark and Cartwright, 2009; Wood and Mize-Spansky, 2009), and these geomorphic parameters allow for accurate correlation of offset channels across a given strike-slip fault. This characteristic makes them ideal candidates as kinematic indicators in many deepwater environments where strike-slip faults may occur. Four examples are presented below to illustrate fault displacement variation within a network, attribute comparisons, variations with depth, and potential pitfalls of the technique.

### 3.4.1.1    Example 1- Fault Offset Variation within a Network

Channel offsets across several closely spaced strike-slip faults reveal a wide variation in offsets in a coherency slice from 1880ms TWT (Figure 3.4).  Fault E, is interpreted as a large sinistral fault, based on the recognition of a number of systematically offset channels. Fault E branches into multiple splays whilst a set of smaller antithetic dextral faults intersect the splays.  One of these dextral faults has a set of smaller antithetic sinistral faults developing lesser offsets (Figure 3.4d).  Figure 3.4b focuses on the southern major sinistral splay where a highly sinuous channel is offset by a distance of 1.04km.  Correlation of this offset channel was established by the strong similarity in planform characteristics of sinuosity, channel width and meander wavelength (Figure 3.5).  Measurements were made on both channel margins and found to be identical.

In some cases only a single channel margin is sufficiently well resolved in the attribute map to allow an accurate measurement to be made.  Figure 3.4c, for example, shows a relatively poorly defined scarp of a strongly meandering channel along the north splay of the sinistral fault and only the eastern margin is well resolved, and can be used to measure an offset of 760m.  Figure 3.4d features the northward continuation of the same channel as Figure 3.4b, where it is offset by multiple sinistral faults.  The offsets at III and IV are lower (70m and 100m), than those at offsets VI and VII. The former are located near the fault tips of smaller faults splaying from a medium sized dextral fault.  The offset channels at VI and VII are located more centrally along the faults as well as being major fault splays of fault E, indicative of the larger displacements (450m and 300m, respectively).  An area of uncertainty exists, located at offsets VI and VII where a smaller channel scarp seems to be present (seen in darker grey) and is used to constrain the offset where the larger channel scarp is more faded.

### 3.4.1.2    Example 2- Comparison Between Seismic Attributes

This example shows offset channels that occur at the top-Messinian unconformity and thus can be imaged by both dip-map and coherency attributes (Figure 3.6).  There are a wide variety of observations here as two channels are offset by strike-slip faults of varying sense and magnitudes of offset, eventually coalescing into one major channel around 850m wide.  However in both attributes, some channels are difficult to correlate across faults, creating

areas of uncertainty where the channel margins are obscured (noted by dashed lines on Figure 3.6). Similarly, fault interpretation, especially on the coherency slice is difficult due to distortion created by the evaporite sequence. To overcome this obstacle, both attributes were compared, enabling offsets to be constrained more accurately as the areas of uncertainty were different in each attribute. Ultimately, the dip-map was the more useful attribute (more measurements were successfully completed) in this example due to its insensitivity to the salt presence.

### 3.4.1.3    *Example 3- Fault Offset Variation with Depth*

The unique ability 3D seismic data to investigate offset variation at different stratigraphic levels is revealed across the eastern segment of fault A. The top slice (Figure 3.7a), taken at 1760ms TWT, is located approximately at the seabed and shows three channels offset by the fault. The eastern two channels (I, II) show offsets of 150m whilst the western channel shows a lower offset of 50m (close-up in Figure 3.8). The reason for this discrepancy is described later.

A second slice at 2060ms TWT (Figure 3.7b, located about 300m below the seabed), shows two more channels offset by fault A, that have greatly increased magnitudes to 2600m at III and 2650m at IV. This is interpreted as indicating a location nearer to the centre of the fault at depth (Barnett, 1987). The slice at 2240ms TWT (Figure 3.7c, located about 180m below the middle slice), still displays a large offset of 2650m at V, indicating that the maximum offset region of the fault is quite large in depth. The presence of a second channel with a faded scarp is located about 3km to the East at VI and provides further offset constraint on the fault; however, the confidence of this correlation is poor and can only be estimated at 1900m. The critical insight from these observations; however, is a sudden change in offset amount occurs in a  relatively short vertical distance between the seabed and the 2060ms TWT slice (c. 300m), whilst offset maxima is maintained vertically for at least c. 200m between 2060ms and 2240ms TWT.

In addition to showing displacement variation with depth, this example also highlights how a kinematic indicator can be used to constrain the timing of deformation. A syn-kinematic channel from the 1760ms TWT slice shows significantly reduced offsets from the eastern channels measured in pre-kinematic conditions (Figure 3.7, 3.8). To elucidate this point, the

large offsets from the 2060ms and 2240ms slices show offsets of around 2.6km (Figure 3.7), whilst the indicators at 1760ms (within syn-kinematic unit PM3), show offsets of 150m. This significant offset reduction can be attributed to the fact that the seabed represents a fault tip i.e. the top extent of a fault (Barnett, 1987), but cannot necessarily be classified as syn-kinematic. However, the western channel (Figure 3.8) is likely syn-kinematic, because 1) it expresses less displacement (50m) from the eastern channels, probably due to erosion of the lateral extents of a channel-scarp to an original position (Gaudemer et al., 1989) and 2) considerable thickening of the channel occurring across the fault, producing a noticeable change in morphology. This ability to determine if a stratigraphic class indicator is syn-kinematic versus pre-kinematic, suggests that the timing of faulting can be constrained by inspecting the nature of the kinematic indicator and comparing it with the surrounding stratigraphy and could be a powerful tool when trying to determine deformation history of strike-slip faults in various basins.

### 3.4.1.4   *Channel measurement accuracy and pitfalls*

Channel margins provide the most obvious 'piercing point' from which we can make displacement measurements, since they are relatively steep features compared to the generally low stratal dips of the slope succession. They are thus usually sharply defined on dip and coherence attribute maps. Care must be taken when channels are associated with one or more levels of terrace, or with cut-off meander loops (Wynn et al., 2007), to ensure that strictly correlative channel features are identified either side of the fault whose displacement is being measured. Observing the channel from Figure 3.4b in profile section (Figure 3.5) allows for features of the channel to be correlated across the fault to 1) verify it is the correct channel seen across a fault (if multiple channels are present), and 2) use the levee crests of the channel to determine which scarp it creates in the dip map or coherency slice. In this example, there is no other channel to obscure the results, but is used to clearly illustrate how the seismic data corroborates the images seen in a seismic attribute.

A common attribute of the channels in this survey is a tendency to travel along the depression caused by a strike-slip fault. In most cases this occurs along dextral faults (Figure 3.9) as they are oriented along the flow direction (down slope) and because most of the dextral faults are buried at the seabed, and their only representation on the surface is a depression from normal slip between splay faults. However, there are cases where this phenomenon occurs

along sinistral faults (Figure 3.10) and as a result it produces a false sense of offset, which at first resembles a dextral fault. Upon further inspection, it can be seen that the channel is actually offset by smaller sinistral splays before bending around and travelling along the fault trace, before abandoning the scarp and continuing down slope.

### 3.4.2   Mass transport deposits (MTDs)

Mass transport deposits (MTDs) exhibit a rich textural variation on many slice-based attributes because of their mode of formation as remobilised sedimentary deposits (Posamentier and Martinsen, 2011). Their internal deformation during downslope transport results in many textural features within the MTD that are linear or curvilinear, and laterally extensive, such as retrogressive extensional fault blocks, basal grooves, internal thrusts or longitudinal slots (Bull et al., 2009). If an MTD is cut by a strike slip fault, as is the case in the study area, it may be possible to identify one or more textural features that can be correlated with high confidence across the fault, and thus provide a kinematic indicator.

An example of the methodology employed to identify potential kinematic indicators in an MTD is given in Figure 3.11. This 1900ms TWT attribute slice through a c. 100m thick MTD found in the southeast of the study area shows a striking pattern of linear features radiating away from a rounded central area (Figure 3.11), and represent the down-slope extension of the MTD. By analogy with similar features interpreted on other MTDs (Gee et al., 2005; Bull et al., 2009), the linear features are interpreted as basal grooves, created by the erosional action of intact blocks traversing down-slope that have propagated ahead of the main mass of the MTD. On seismic profiles, the grooves are visible as v-shape incisions into the basal shear surface of the MTD, supporting their interpretation as being due to basal erosion. At point I on Figure 3.11, these radiating lines are offset by a small splay of fault D, which can be seen dying out just east of the MTD into a horsetail geometry. The offset of all the grooves across this fault is measured at 80m, which is taken as the strike-slip component of the displacement of this fault in this area.

Selected grooves from a coherency slice 40ms below the slice in Figure 3.11a are presented for clearer identification of individual kinematic indicators (Figure 3.11b, c). Here, the individual grooves show offset by small sinistral strike-slip faults, and range 40-80m. The example in Figure 3.11c is offset by multiple faults (shown at III, IV, and V) and has a

distinctly different geometry in the coherency slice than the example in Figure 3.11b.  Here, the groove contains three lines that extend down-slope, with a noticeably thicker line running between the two thinner ones.  This represents a point where a translated block has created a groove that actually pierced the basal shear surface and can be seen in profile-section (Figure 3.12).  It is the only example where the basal shear surface has been pierced, whilst most examples in this dataset appear in sets of two (Figure 3.11), distinguishing the crests of the 'v-shape' caused by the groove.
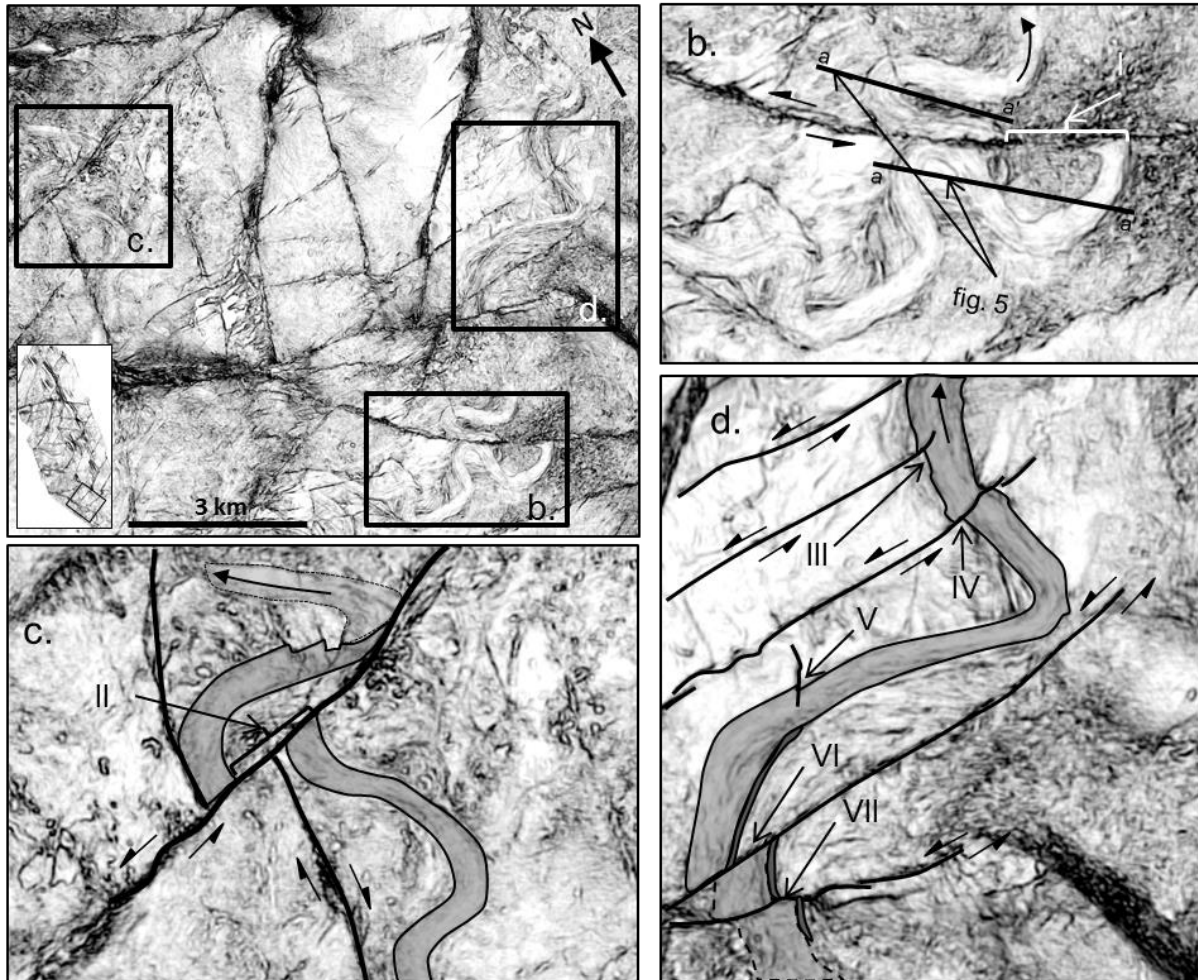
Figure 3.4 - View of a channel offset by multiple faults of varying scales on a coherency slice at 1880ms TWT. In this case all examples are sinistral faults (with the exception of V) and each Roman numeral corresponds to an offset. Note that arrows at end of channels indicate flow direction. b) Close-up of a major fault from the southern region of the dataset with a channel offset at I = 1040m. c) Close-up of a channel that shows one correlatable margin at II = 760m. d) Shows a continuation of the same channel from (b) but is offset by smaller faults splaying off of a larger dextral fault. Measurements correspond to: III = 70m, IV = 100m, V = 60m, VI = 450m, and VII = 300m. Note that the offsets of (VI) and (VII) are from a small channel scarp that may represent an earlier size of the channel, but at this slice provides a more accurate measurement than the main channel.
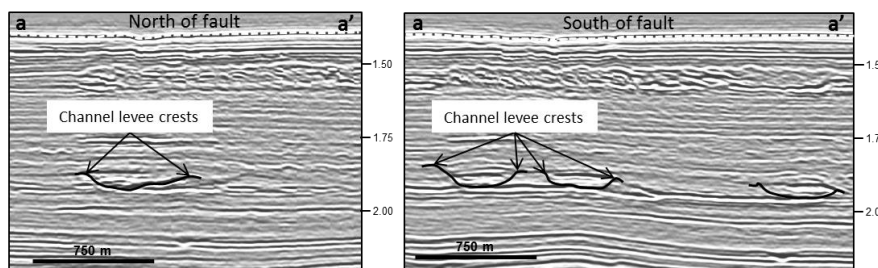


Figure 3.5 - Cross-sections of the major channel on both sides of Fault E. The channel section to the north shows an asymmetrical pattern coinciding with the meander it cuts through. South of the fault, the channel is crossed three times with a more symmetrical shape. The levee crests delineate the lines used to measure offset channel margins.

82
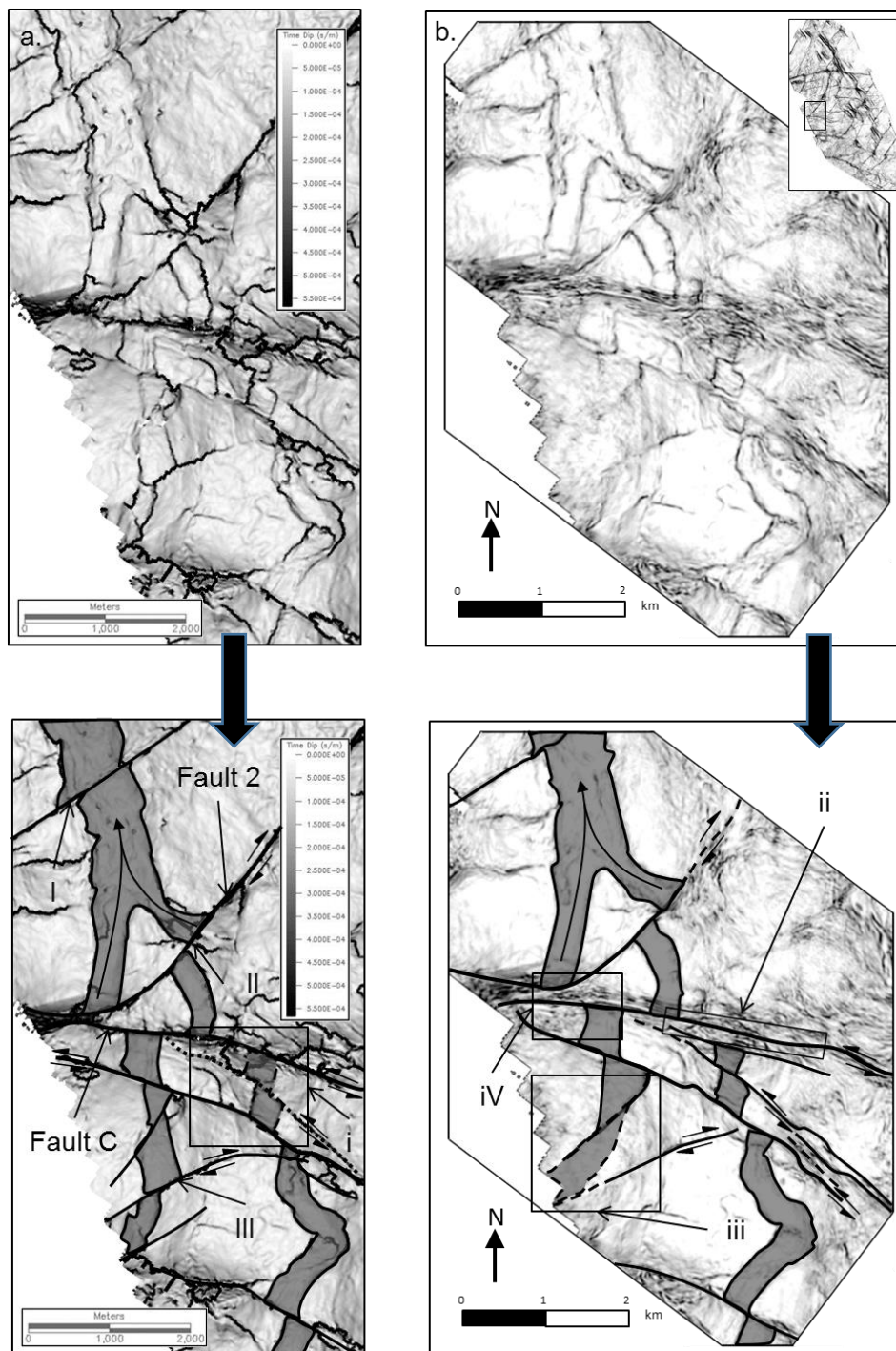
Figure 3.6 - Comparison between seismic attributes, note the bottom image shows the interpretation for both cases.  a) An image of a dip-map from the top-Messinian Unconformity, with one area of uncertainty at i.  Here, a large area of the interpretation is estimation, but with comparison to the coherency slice both the channel and the faults can be constrained.  The fault offset III can be seen curving around and offsetting the second channel, however, in the coherency it appears to die out and is not offset. b) A coherency slice of the same faulted channel with three areas of uncertainty at ii, iii, and iv.  ii is a narrow area of uncertainty, which is likely undergone heavy faulting, distorting the image.  iii is a large area of uncertainty where the dip-map is needed to constrain the channel presence.  iv is a final area of uncertainty that cannot be constrained by either attribute as a section of channel is missing.  Note that the interpretation of faults varies with each attribute, but still enables constraints on channel offset.  Representative offsets: I = 120m, II = 560m, III = 370m.
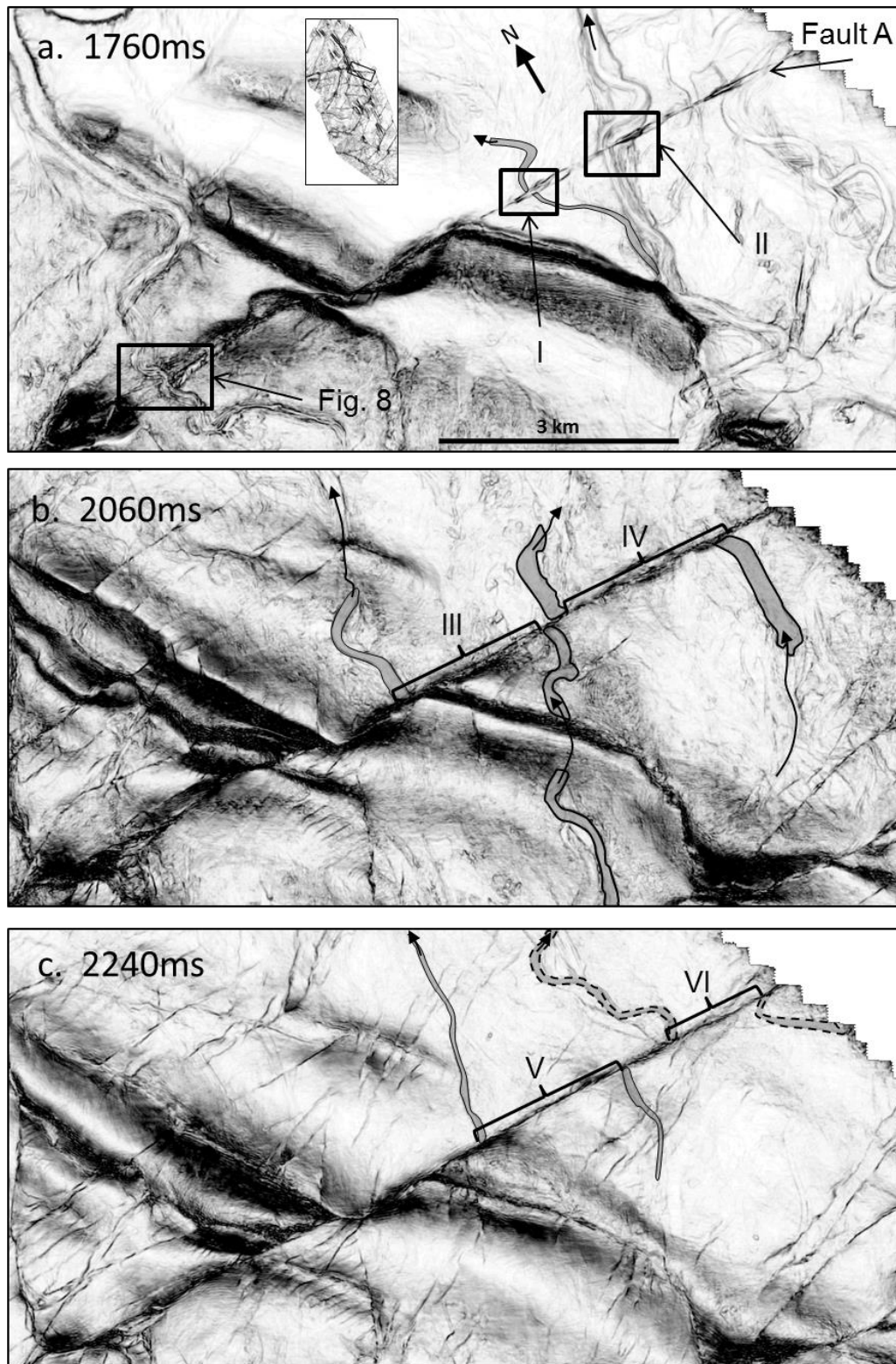
Figure 3.7 - View of eastern segment of fault A, from three levels.  a)  The shallowest slice taken at 1760ms TWT, and shows three channels offset at I = 150m and II = 150m, with the third seen as a close-up in Figure 3.8.  b) The slice at 2060ms TWT is about 300m below the slice from (a) with offsets at III = 2600m and IV = 2650m.  c)  The slice at 2240ms TWT is about 200m below the slice at (b) with offsets at V = 2650m and VI = 1900m.  Note: the channel at VI is difficult to correlate across fault due to its faint appearance.
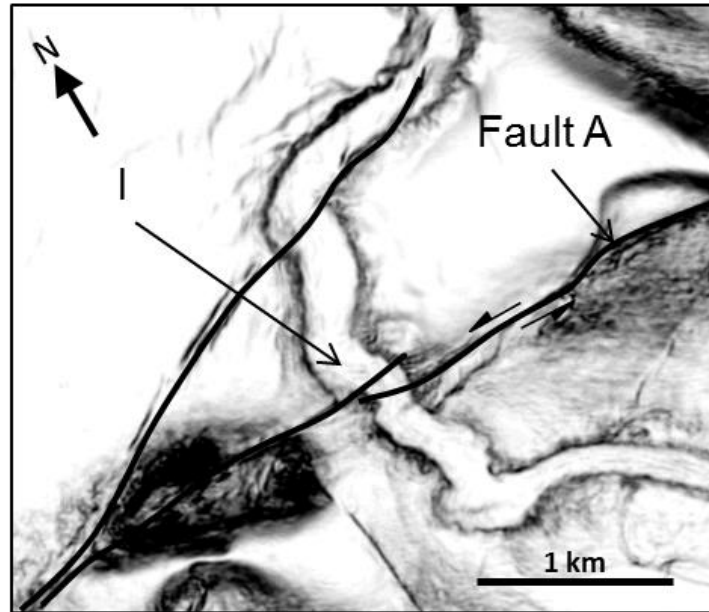
Figure 3.8 - Close-up of a channel crossing fault A, and showing considerable change in width across the fault at I, suggesting a contemporaneous flow of the channel and fault activity.  Measured offset = 50m.
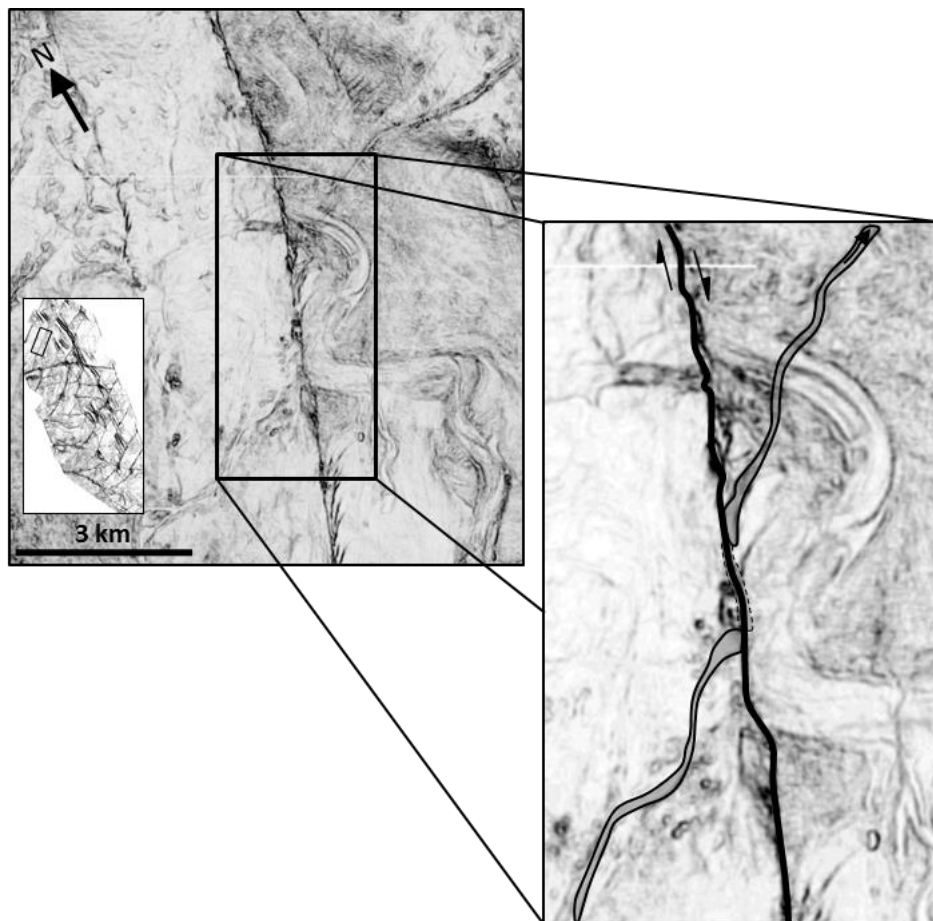


Figure 3.9 - Example of a channel flowing along dextral fault 1, and producing an apparent sinistral offset as a result.

85
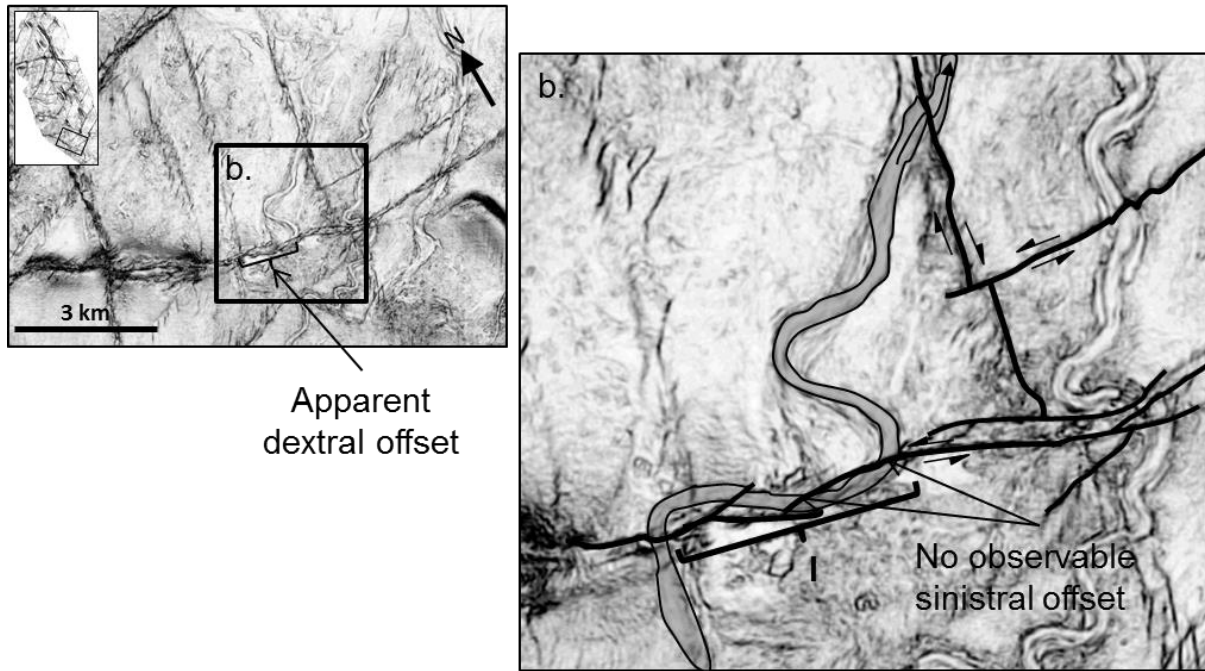
Figure 3.10 - Example of a channel flowing along a splay of fault E from a coherency slice at 1880ms TWT.  A quick interpretation may suggest dextral slip; however, closer inspection reveals the channel travelling along the fault tracing, and showing an apparent dextral offset at I.
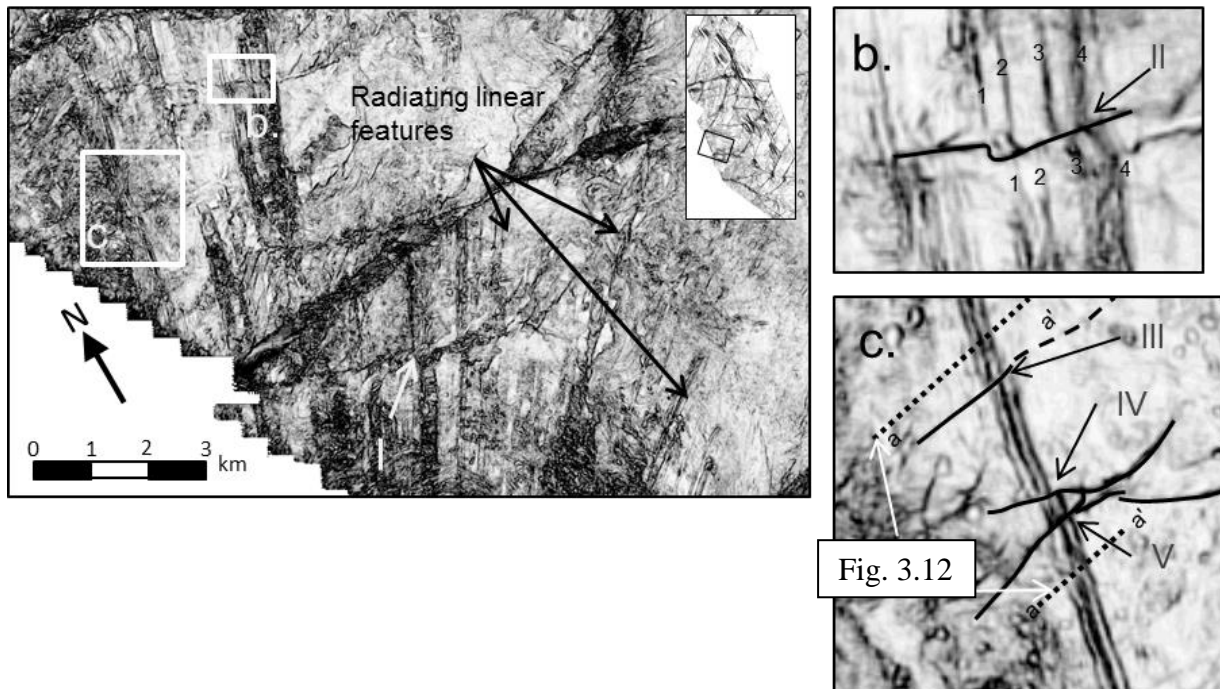


Figure 3.11 - View of an MTD on a coherency slice at 1900ms TWT.  The straight lines radiating out in a divergent pattern are grooves of the MTD and are offset by numerous strike-slip faults.  In this case all examples are sinistral faults and each numeral corresponds to an offset.  Note that zoomed in shots are from a coherency slice 40ms below, to increase the clarity of individual kinematic indicators.  Offsets: I = 80, II = 80m, III = 60m, IV = 50m, and V = 40m.
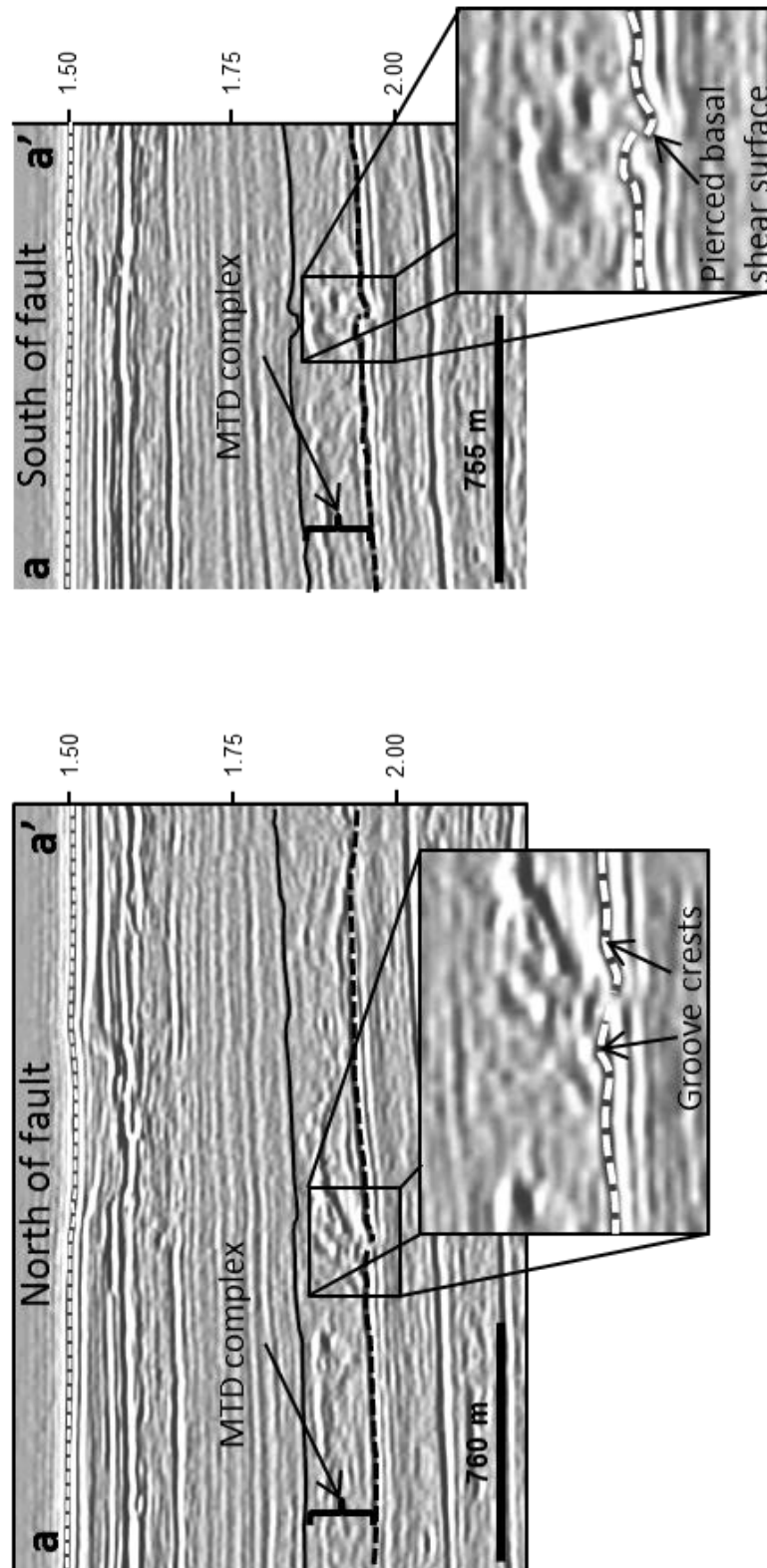
Figure 3.12 - Cross-sections of the MTD from Figure 3.11c both north and south of the fault. Despite having the normal 'v-shape' pattern expected with grooves left by an MTD, its basal shear surface (dotted white line) is pierced, delineating the centre line on the coherency slice.

## 3.5    Kinematic Indicators – Structural Class

Field studies have encompassed the systematic offset of pre-existing structures by younger faults since a pioneering study by (Jones and Pugh, 1915) in west Wales. Here, structural indicators encompass the offset of pre-existing structures including some of the earliest strike-slip faults and blind normal faults.

### 3.5.1    Strike-slip faults

As the strike-slip faults are conjugate, it is expected that the faults would form in a broadly synchronous manner. However, interactions between some of the smaller individual structures may occur at different times, especially nearer to a fault tip. An example of this occurs in Figure 3.13 where Fault 3, a mid-sized dextral fault, has been clearly offset along with its splay near the tip by the southernmost splay of younger sinistral fault C. Offsets measured at I and II are 130 and 120m, respectively, which are close enough within the error of lateral resolution to be considered identical. This value of sinistral displacement is within the range of values of sinistral displacement on Fault C that can be measured about 1km to the east, where a complicated meandering channel with multiple channel margins is offset by values ranging from 110-150m, depending on which groups of channel margins are correlated. In this case, therefore, two classes of kinematic indicator (offset channel and offset conjugate strike-slip fault) are mutually supportive of a sinistral displacement value of just over 100m.

### 3.5.2    Normal faults

A set of pre-existing, blind normal faults (defined using the criteria set forth by Baudon and Cartwright (2008b)- plunging upper tip region and absence of syn-kinematic growth strata), which are located throughout the dataset and are restricted to the stratigraphic unit PM1, are clearly shown to be offset by strike-slip faults. Displacement measurements can only be made on the smaller strike-slip faults because there is a high density of normal faulting and for larger strike-slip faults, it is very difficult to correlate the specific normal faults from one side to the other.

Two representative examples of normal faults being offset by small strike-slips faults are presented in Figure 3.14.  The first example (Figure 3.14b) shows a sinistral fault offsetting a conjugate pair of normal faults with a measured offset of the normal fault pair being 290 and 310m, suggesting an average of 300m for the displacement.  The second example (Figure 3.14c) encompasses a dextral fault with a smaller measured displacement. The two normal faults are offset by 70 and 50m at points III and IV, respectively.  Given the proximity to the tip of the dextral strike slip fault, the variation in offset values is taken as significant, and suggests that there is a reduction of displacement by about 20m between the two piercing points, and this reduction is as would be expected, i.e. in the direction of the tip.
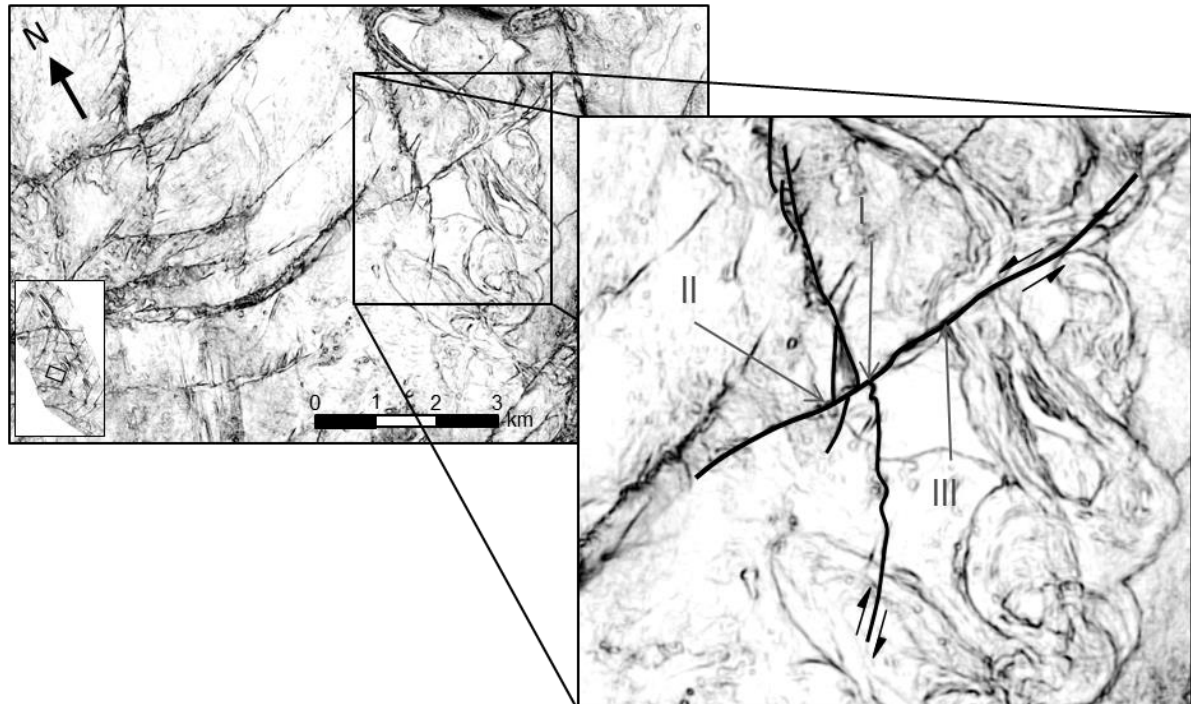
Figure 3.13 - A dextral strike-slip fault (and its splay) is offset by a sinistral strike-slip fault on a coherency slice at 1960ms TWT.   Offset values correspond to: I = 130m (main fault) and II = 120m (splay fault).  Note that a channel is also offset by the C fault splay at III = 110-150m.
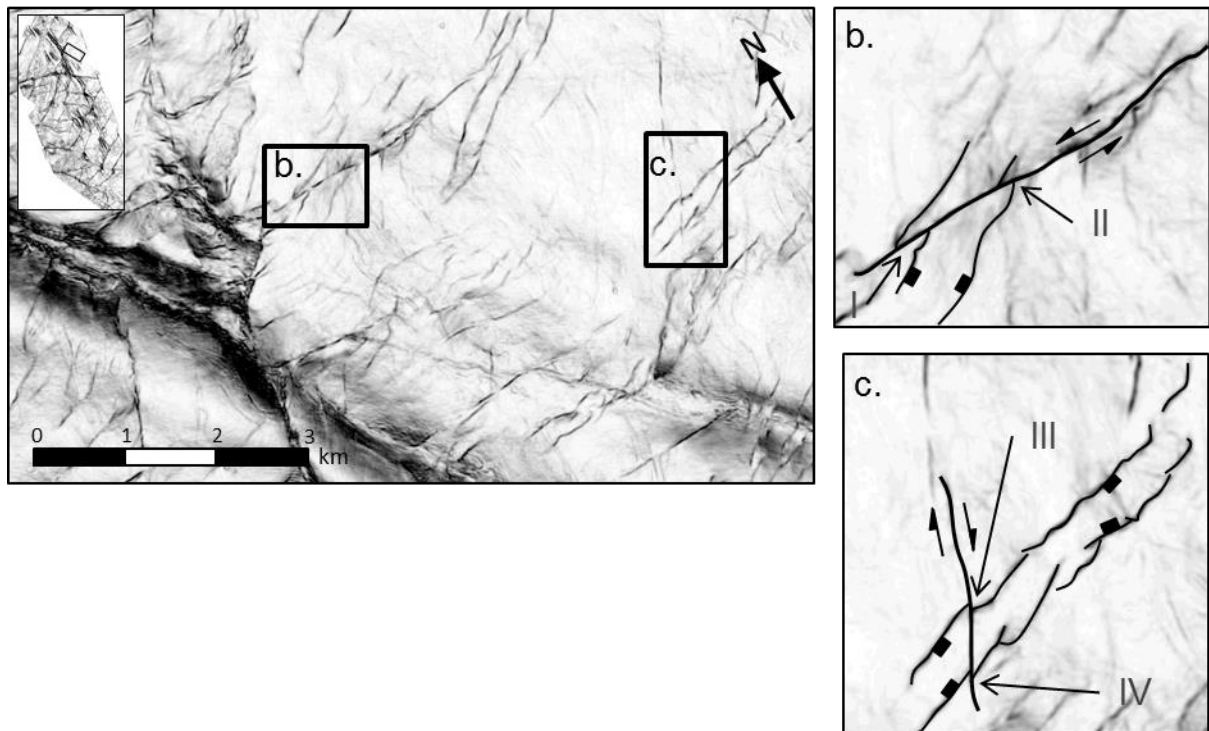


Figure 3.14 - View of conjugate blind normal faults that are offset by strike-slip faults on a coherency slice at 2260ms TWT.  b) Close-up of a sinistral fault offsetting two normal faults with values of I = 310m, and II = 290m.  C) Close-up of a dextral fault offseting two normal faults with values of III =70m and IV = 60m.

## 3.6  Discussion- Implications for fault propagation

The preceding examples demonstrate the utility of 3D seismic data in recognising different types of kinematic indicator associated with strike slip faulting, and using these to measure sense and magnitude of horizontal displacement.  By applying the techniques outlined above, it is possible to analyse the evolution of strike-slip faults in a similar way to the analysis of other types of faults i.e. through a combination of geometrical description linked to displacement measurements (Barnett, 1987). Further implications of this technique are considered below, particularly with respect to unravelling relationships between component faults in a strike-slip system, and relative timing between structures.

### 3.6.1  Variation in a Fault Network

Excellent examples of the potential for using kinematic indicators to resolve relationships between closely spaced and splaying strike-slip faults were presented in Figure 3.4 and Figure 3.6, where offset channels provide multiple kinematic indicators within a small area of splays and intersections of groups of strike-slip faults.  By understanding the changes in displacement between major faults and splays, the connectivity of a region can be better understood as well as providing insights into the evolution of the region, which could both impact hydrocarbon exploration and hazardous earthquake prediction.

### 3.6.2  Variation in displacement on a fault surface

It was demonstrated in Example 3 (Figure 3.7) of the submarine channels that a number of kinematic indicators may be interpreted along a single strike-slip fault.  If these indicators sample different portions of the fault trace, it may then be possible to examine how displacement varies along the fault trace (Figure 3.15), and displacement gradients can be calculated in a directly analogous way to those obtained for strike-slip-faults in the field (e.g. Peacock, 1991; Nixon et al., 2011). Variations in displacement gradient may then be compared to the fault geometry, to investigate whether there is any obvious link between marked or abrupt lateral variations in displacement with secondary or intersecting structures (e.g. splays) or with lithological changes in the deformed sequence.

91

### 3.6.3   Variation in displacement in three dimensions (multiple fault surfaces)

3D seismic data has great potential to impact our understanding of strike-slip fault evolution, simply because it provides a fully three dimensional approach through the interpretation of kinematic indicators on a potentially large number of mapped horizons or attribute slices through the deformed volume. Clearly there is an upper limit of kinematic indicators that will generally be interpretable for any given fault, and this will depend on the environments of deposition, and the distribution of pre-existing structures. Stratigraphic indicators like channels, or textural features associated with MTDs as shown in this paper, exhibit a spatial distribution related to their mode of deposition and preservation (Posamentier and Kolla, 2003), and their length scales of distribution relative to fault dimensions will determine their utility for mapping spatial variation in displacement. In the examples presented here, the deformed interval is quite highly channelized, so it is possible to demonstrate vertical as well as lateral variations in the strike-slip component of displacement (Figure 3.16).  In other strike slip faults in other depositional contexts, it may be possible that even higher spatial resolution of displacement measurements will be possible, for example, where bed forms with 100s of metres wavelength are used as indicators, or where subtle and closely spaced palaeo-geomorphic features associated with unconformities are offset.

The potential then, to measure strike-slip displacement in three dimensions presents an opportunity to examine the factors influencing displacement variation, and also to identify local maxima and minima in horizontal displacement. This could be invaluable, for example, in understanding the relationships between the array of individual fault segments (e.g. R, R', or P shears) that generally comprise a strike-slip fault zone (Tchalenko, 1970; Kim et al., 2003).

### 3.6.4   Timing of Deformation

Timing of deformation can be established in a number of ways using kinematic indicators. Use of structural kinematic indicators is based on a clear temporal relationship of cross-cutting i.e. the offset structure pre-dates the strike-slip fault.  In the study area, the two groups of strike slip faults comprise a conjugate set with a consistent ENE-WSW trending bisectrix, suggesting that they were broadly coeval (Cartwright et al., 2012). However, in detail, we find that some dextral faults offset some sinistral faults, and vice-versa (Figure 3.17a), and

there are also a number of conjugate intersections where no clear offset occurs (Figure 3.17b).

Stratigraphic kinematic indicators can potentially be useful when dating strike-slip faulting, but only if they are embedded within syn-kinematic sedimentary units (e.g. Example 3, Figure 3.8).  The rest of the examples of offset channels and basal grooves presented above all occur within the pre-kinematic interval in the study area, so their offsets simply represent the total horizontal displacement accrued.  For stratigraphic class indicators deposited within a syn-kinematic interval, however, it is possible that the measured offsets correspond to a reduced amount of displacement because of erosional effects and deposition occurring subsequent to fault initiation.  Thus, if centre to upper tip gradients appear higher than expected, it may indicate the presence of a syn-kinematic indicator.  Although not observed here, it may be that future identification of kinematic indicators will be recognised by several geometries outlined in Figure 3.18b-e, which have been identified in field-based studies (e.g. Sieh and Jahns, 1984; Gaudemer et al., 1989; Huang; Fu et al., 2005), and may aid future interpreters working with strike-slip faults.

## 3.7    Conclusion

This study has shown that the application of 3D seismic data can effectively constrain the offset of strike-slip faults using a variety of kinematic indicators.  This allows future studies in 3D seismic data to actively use strike-slip faults as a tool to develop a structural model rather than an unknown factor that may impact hydrocarbon seals.  Furthermore, 3D seismic creates a bridge between studies in the field and sandbox modelling that can be used to improve propagation kinematics and fault evolution understanding in the same way as recent studies conducted on normal and thrust faults.  Finally, these results can be applied to other basins and quantify how fluid flows in a hydrocarbon system dominated by strike-slip fault deformation.
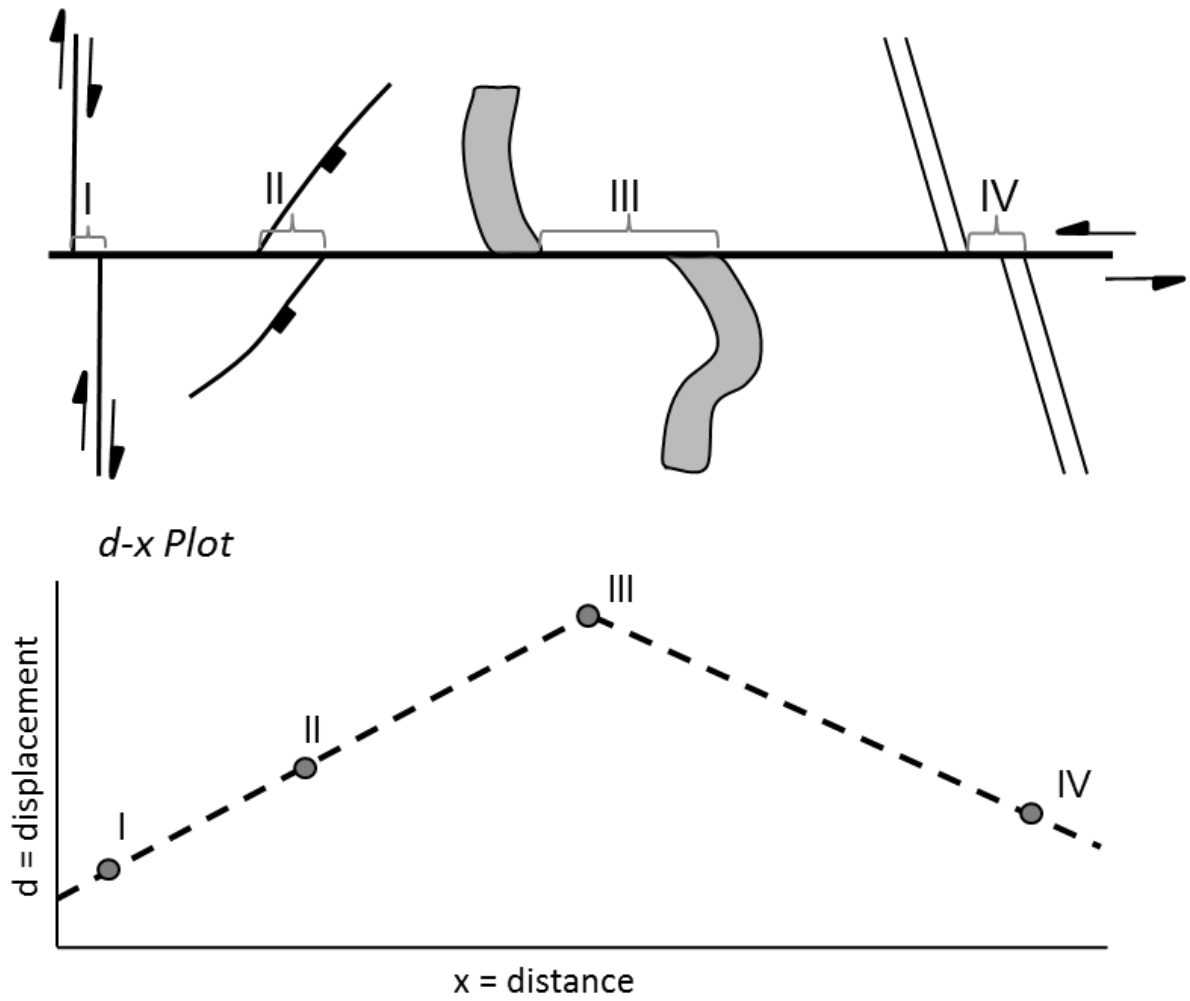
Figure 3.15 - Plan view schematic of a sinistral fault which has offset multiple indicators (a dextral strike-slip fault at I, a normal fault at II, a channel at III, and an MTD at IV) and demonstrate the typical offset changes associated with a single, isolated fault with maximum displacement at the centre, and minimum offset at the tips (Barnett et al., 1987). Quantification of the plot shown here will be presented in Chapter 4.
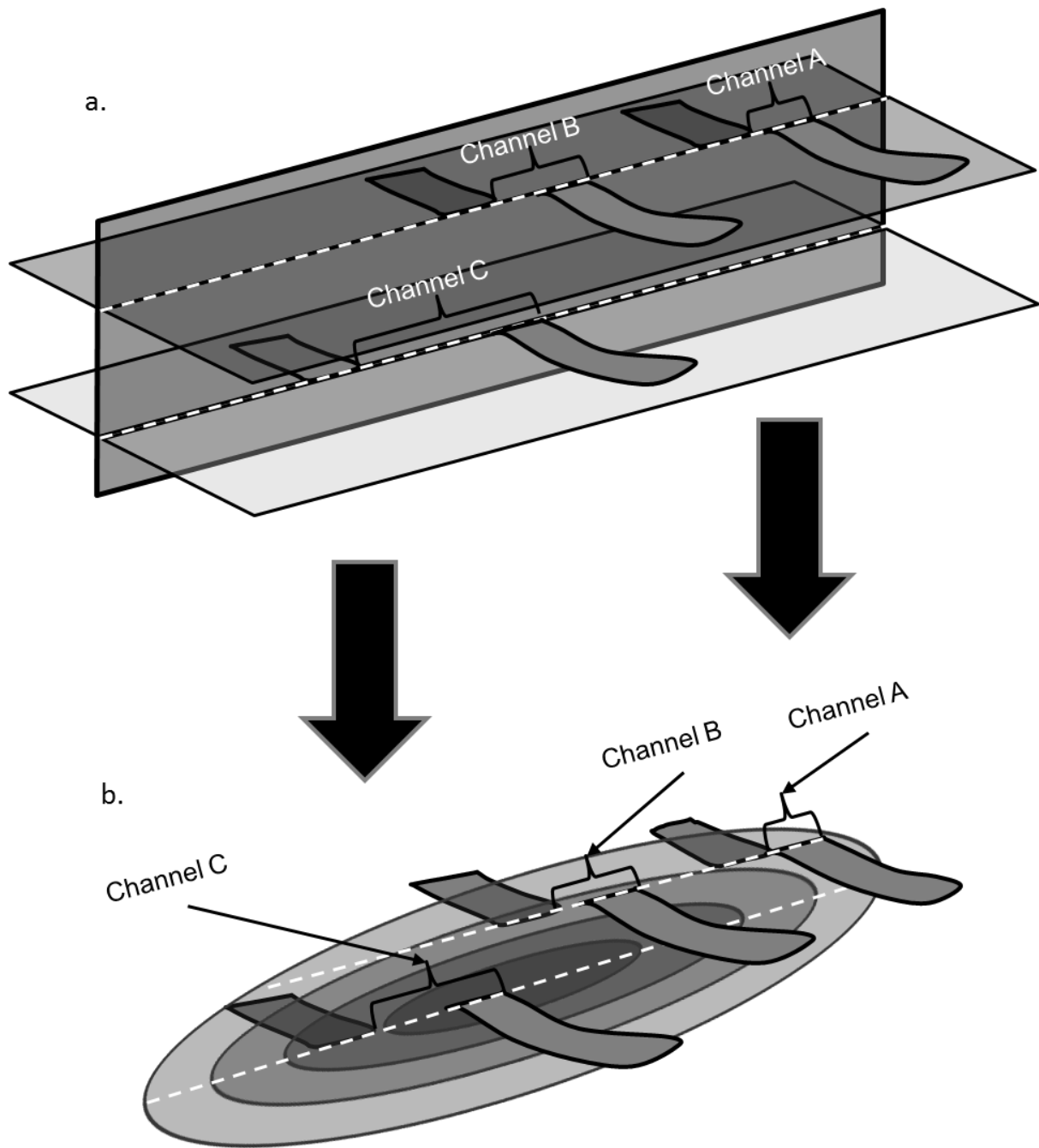
Figure 3.16 - Cartoon showing how kinematic indicators can show offset variation laterally and with depth, which can be organised into a 3D displacement distribution plot. The top horizon has two offset channels (A and B), with B showing an increased offset due to proximity to the fault centre. The lower horizon shows a larger offset of Channel C than channel B due to its proximity to the fault centre vertically.
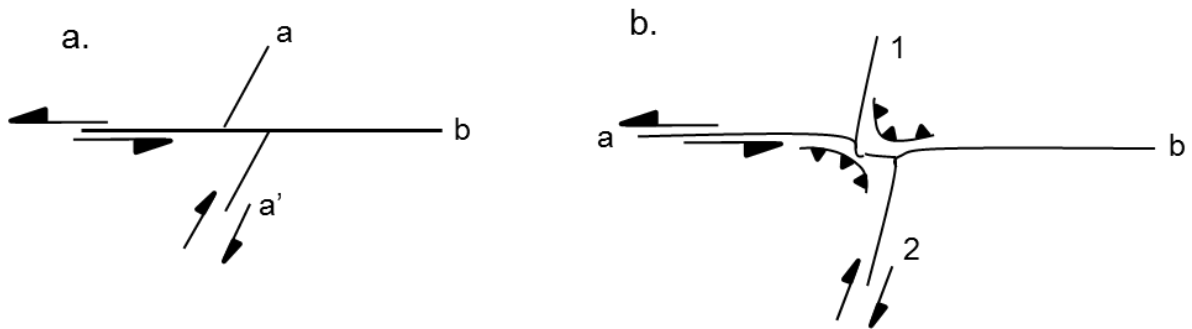
Figure 3.17 - Sketches of the two types of strike-slip fault intersections. a) Shows fault b offsetting the older fault a (as observed in Figure 3.13). This tends to occur in smaller faults or near the tips of the larger faults. b) A more complicated conjugate fault intersection seen occurring between major fault segments, suggesting elements of coeval propagation.
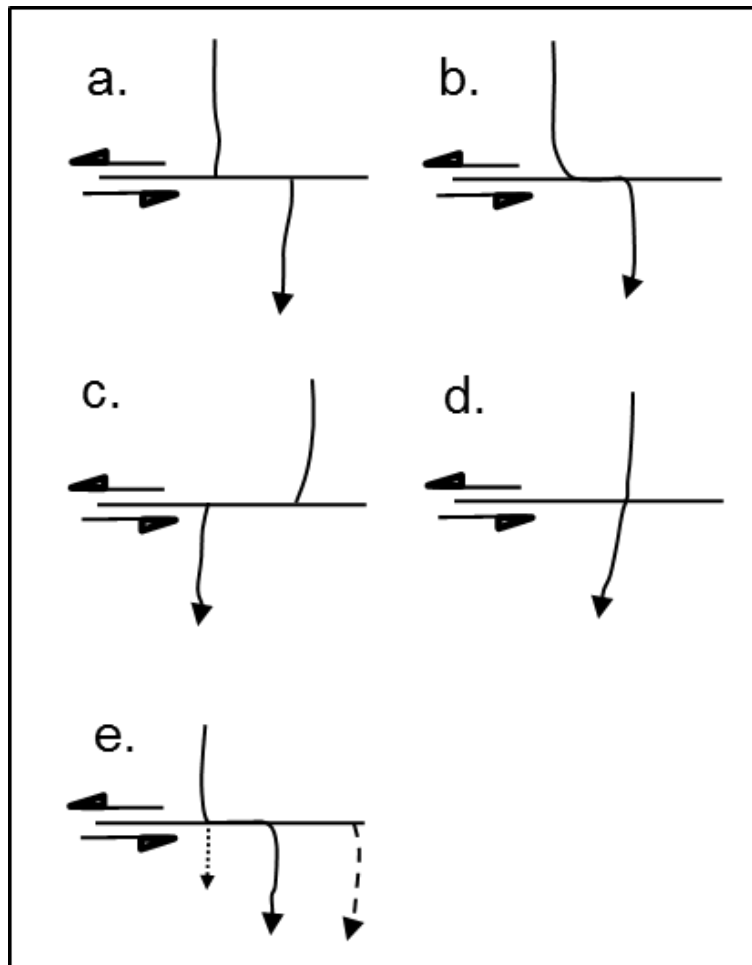


Figure 3.18 - Examples of channel morphologies across a fault that are observed in the field and may apply to seismic data. Note cases b - e are active channels crossing an active fault i.e. syn-kinematic. Case a) by contrast is a paleo-channel crossing an active fault, and shows a clearly cut scarp. b) Channel is offset left-laterally by flowing along the fault. Note that overtime erosion of the lateral extents can make the apparent offset smaller, and this is especially likely in larger channels such as the ones in seismic scale. c) Channel is offset right-laterally down a sinistral fault. d) Channel is not offset across the fault. e) Beheaded channel geometries – dashed line indicates an abandoned/beheaded channel, solid line is present geometry, and dotted line is where a future channel will evolve. Beheaded geometries may be unlikely occurrences due to the considerable size of the channels seen in seismic data (Gaudemer et al., 1989). Adapted from Sieh & Jahhns, 1984; Gaudemer et al, 1989; Huang, 1993; and Fu et al, 2005.

# Chapter 4

# The Displacement Distribution and Geometric Descriptions of Two Gravity Driven Strike-Slip Faults Using 3D Seismic Data

# 4   The Displacement Distribution and Geometric Descriptions of Two Gravity Driven Strike-Slip Faults Using 3D Seismic Data

## 4.1     Introduction:

The geometry and propagation of strike-slip faults have been explored extensively in field studies by several authors (Segall and Pollard, 1983; Martel et al., 1988; Kim et al., 2001; 2003; 2004).  However, these are mostly limited to a 2D perspective along strike of the faults and cannot provide a detailed view in full three-dimensional geometry.  Kim et al. (2003) presented a model of 3D evolution using different 2D perspectives of outcrops (see Figure 1.21). However this model has never been substantially tested by concrete observations.  In seismic data studies have been limited to the pioneering works using 2D profiles by Harding (1985).  Most of our 3D understanding of strike-slip fault propagation is derived from analogue modelling (e.g. Tchalenko, 1970; Naylor et al., 1986; Ueta et al., 2000), but these assume that strike-slip faults originated as sub-vertical, discrete strands and only model the resulting deformation in an overburden, i.e. secondary structures such as Riedel (R) shears. 3D seismic data therefore presents an opportunity to overcome these limitations to not only visualise the geometry of strike-slip faults in greater detail, but strike-slip fault propagation using available kinematic indicators (see Chapter 3 for definition).

The El Arish and Afiq Faults are two exceptionally well imaged strike-slip faults in the Levant A dataset (Figure 4.1) whose displacements are recorded by kinematic indicators (See Chapter 3 for definition), allowing for a novel 3D analysis of the distribution.  Nelson (2007) attempted a preliminary analysis of the displacement distribution on these strike-slip faults and this chapter furthers the approach with analysis between displacement distribution gradients and changes in fault geometry.  The central aim of this chapter is to therefore collate kinematic indicators into contoured displacement distribution plots and juxtapose these results with detailed geometric descriptions to derive insights into strike-slip fault evolution. In particular, these focus on:

- Modes of upward and downward fault propagation

- Lateral fault propagation models

- Influence of strain rate, lithology, and sedimentation on fault geometry

The chapter begins with a description of the data and methodology, followed by descriptions of the stratigraphy and regional structures to provide context for strike-slip fault evolution.

## 4.2    Data

The Levant A dataset is a high resolution 3D seismic survey covering c. 2250km$^2$ and acquired in 2000.  The data was processed to near single phase and uses a single pass 3D post-stack time migration to create a seismic grid of 12.5 x 12.5m$^2$, and sampling interval of 4ms.  The data is SEG normal polarity, meaning a positive amplitude response corresponds to an acoustic impedance increase (seen as red in seismic sections presented in this chapter).

Most of the deformed strata occur in the uppermost unit (Unit 3; see Stratigraphic Description- Section 4.4 for detail) and have a dominant frequency of about 50Hz, with a vertical resolution of 10m and horizontal resolution of 40m.  From a well located in the El Arish Canyon, checkshot data have been used to derive an average velocity of 2000m/s in this unit (Frey Martinez et al., 2005; Bertoni and Cartwright, 2006).  The other major unit, the Messinian Evaporites, have an interval velocity of 4000m/s $\pm$ 500m/s (high variance due to lithological changes within the evaporites). The dominant frequency of the seismic data is 30Hz, providing a vertical resolution of between 22.5 and 50m.  As mentioned in Chapter 3, although the lateral resolution is 40m, this value may in practice may be less where the overburden is relatively uniformly stratified and lateral velocity variations are expected to be very small.
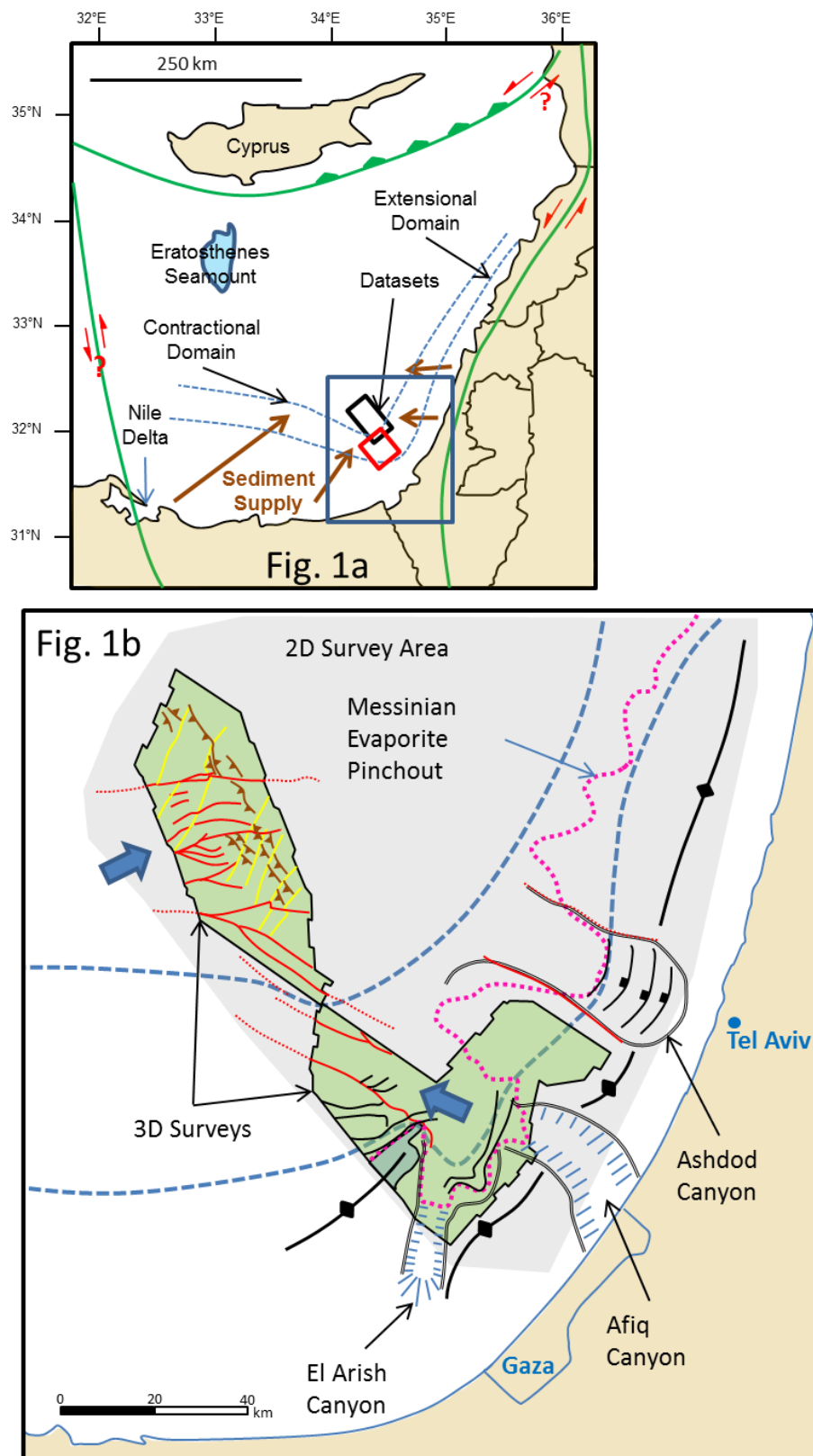
Figure 4.1 - Tectonic setting of the Levant A dataset.  a) Location of the datasets used in this thesis.  Levant A (this chapter) in red and GalC (Chapters 3 and 5) in black.  b) Close-up of the datasets as well region covered by the 2D lines.  Blue arrows denote sediment transport direction driven by gravity downslope.

## 4.3     Methodology

The methodology behind the results in this chapter can be grouped into three parts: 1) orthodox horizon mapping, 2) fault mapping, and 3) displacement distribution. The former two were used to inspect and analyse the fault geometry whilst the latter was used to quantify displacement along the plane of a strike-slip fault. Information derived from 1) and 2) was also used in conjunction with the displacement distribution to build a more complete picture of the distribution plot where kinematic indicators were sparsely positioned, such as locating the fault tips to complete the tip-line and location of branch lines to splay faults.

*Horizon Mapping-*

Orthodox seismic mapping techniques were used with interpretation grids of typically 100m by 100m. Several horizons were mapped regionally over the entire dataset: including the seabed, and the N & M reflections bounding the Messinian Evaporites. A number of additional surfaces were locally mapped and limited to specific regions of deformation. These localised surfaces were not possible to be tracked over larger regions and thus isopach maps are limited to the regional maps horizons defined by the seabed and M and N horizons. Without many isopach maps available, the majority of the analysis of this thesis is therefore carried out on coherency slices and individual profile sections.

*Fault Mapping-*

The quality afforded by 3D seismic data allows strike-slip faults to be mapped in far greater detail and accuracy than prior seismic studies (Harding, 1985). For example, considerable distortion occurs around the fault zone in the examples presented by Harding (1985), whilst the faults in this dataset are clearly delineated within a c. 40m (Figure 4.2) zone of spatial positioning, less than half of the apparent fault zone width of older surveys. The faults are observed as discrete and identifiable by a single fault strand rather than zones comprised of several faults. Importantly, this does not necessarily preclude the fault zone being comprised of several smaller faults which are not observed due to the limits of seismic resolution; however for simplicity in this thesis, the faults are interpreted as discrete fault zones. This point will be explored further in the discussion (Chapter 6).

Mapping the primary structures (e.g. the master through-going faults) was conducted using either seismic profiles or plan view images, such as coherency volumes. However, secondary structures (e.g. faults that splay from the master through-going fault) are very complex due to rotational growth and require simultaneous use of both cross-sectional and plan view images (Figure 4.3). For instance, when mapping a set of en echelon faults, profile sections alone will not differentiate one fault from another and two faults could therefore be misinterpreted as a single fault (Figure 4.3). Therefore, integration of the coherency slices and seismic section was required to correctly map fault geometry in 3D.

Mapping the strike-slip faults in the evaporites proved a very difficult task as the resolution decreases and most of the acoustic response produces a transparent facies. However, there are more brittle layers within the salt that show evidence of faulting (Figure 4.3b) and were used to form an interpretation of the structure within the evaporites (defined later in as Tier C, Section 4.6). Given the poor constraints of the seismic data, these interpretations are made tentatively, and as explained later in both this Chapter and Chapter 6, likely form ductile shear zones rather than discrete fault planes.

*Displacement Distribution-*

Displacement distribution was calculated using the identification of kinematic indicators methodology as described in chapter 3. The magnitude of each measured horizontal (i.e. strike-slip) offset measured was then inputted into a scatter graph using Excel. Contouring was conducted by hand and then digitised. All horizontal components from multiple fault strands are projected orthogonally onto a single fault plane for simplicity.

Dip-slip displacement components occurred on both faults and could be calculated by measuring the difference in kinematic indicator depths on either side of the fault (Figure 4.4). However, as the measured horizontal offset of far exceeds the dip-slip component, dip-slip components were considered negligible for populating the displacement distribution plots. For example, the maximum dip-slip displacement component across the Afiq Fault was 140m (140ms); however, the strike-slip displacement component was 2900m for the same kinematic indicator. The computed net slip therefore equates to 2903m (Figure 4.4) and when accounting for error from seismic resolution limits, the net-slip magnitude is equal to the magnitude of strike-slip offset. Notably, when horizontal slip decreases, the

102

corresponding dip-slip component decreases in a similar fashion so that the ratio of dip-slip to strike-slip movement remains relatively constant across the faults (with the notable exception of the upper tip regions of certain faults, which will be described in detail in the rest of this thesis).

Correlation of kinematic indicators across the fault where larger dip-slip components occurred was difficult on horizontal slicing attributes such as coherency and variance. To overcome this problem, traditional horizon mapping was used to generate attribute maps such as RMS amplitude, maximum positive and negative amplitude, acoustic amplitude, and time-dip. Iso-proportional slicing was created for Unit 3 with an average spacing of 50ms with coherence amplitude extraction used to identify indicators more rapidly. Finally, a flattened variance cube was also utilised. Often, a combination of horizon based attributes and coherency was used to constrain the offset amount as well as using the seismic sections to ensure that kinematic indicators were correctly correlated across the fault.
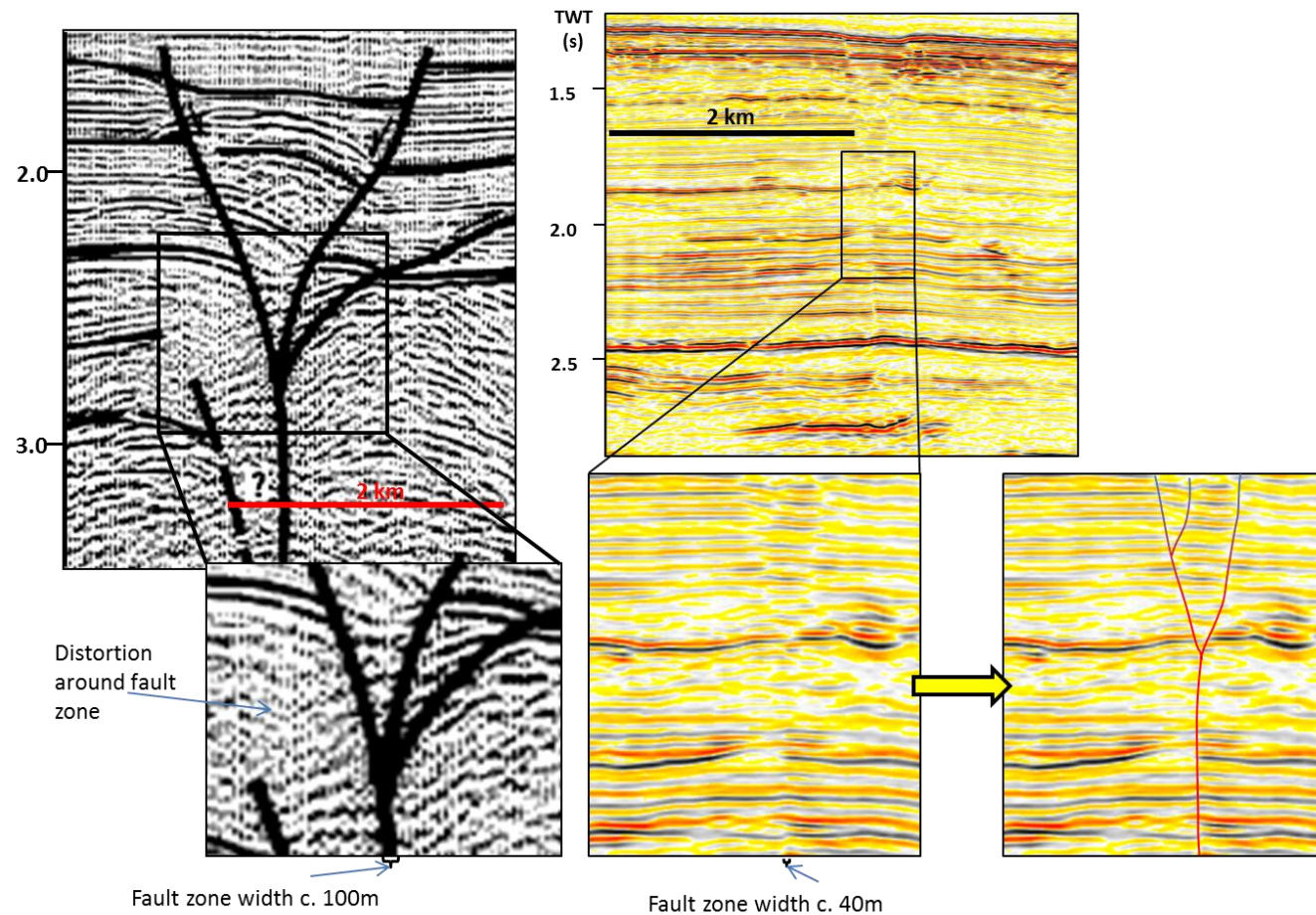
Figure 4.2 - Comparison between the quality of data used by Harding (1985) in 2D lines and 3D lines from this dataset.  This allows faults to be mapped in far greater detail and therefore tease out the 3D nature of strike-slip faults.  Principally the faults shown here show a discrete fault rather than a zone of faulting at this scale.  Note that as a lot of the overburden is comprised of relatively uniform sediments, the lateral resolution may actually be higher than quoted.
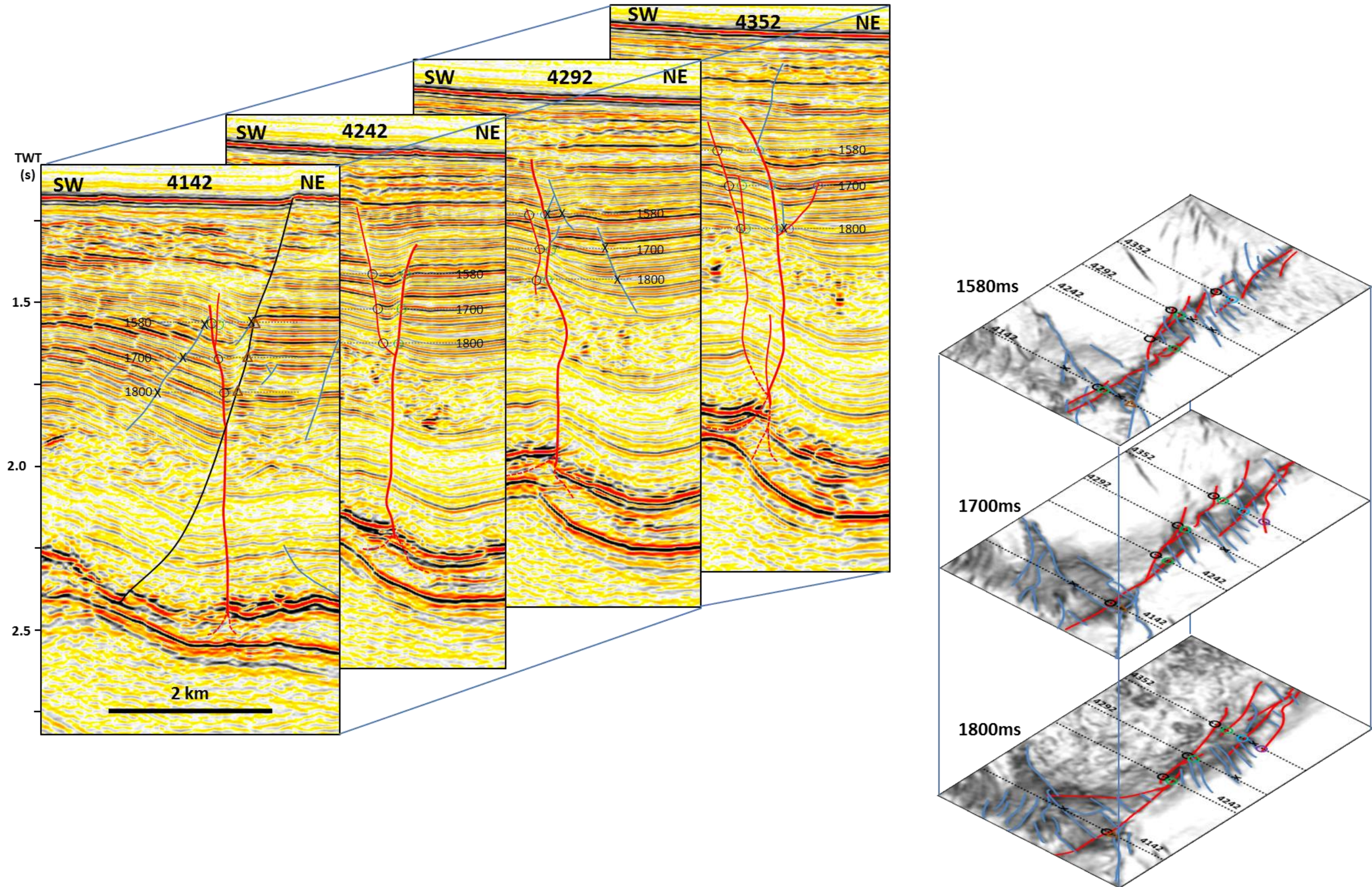
Figure 4.3a - In order to understand the 3D rotational nature of the structures, mapping was conducted using both seismic profiles and coherency slices concurrently.  This enabled a tracking of the structures using either medium, and enabled the 3D mapping shown in GeoViz (Figure 4.26).
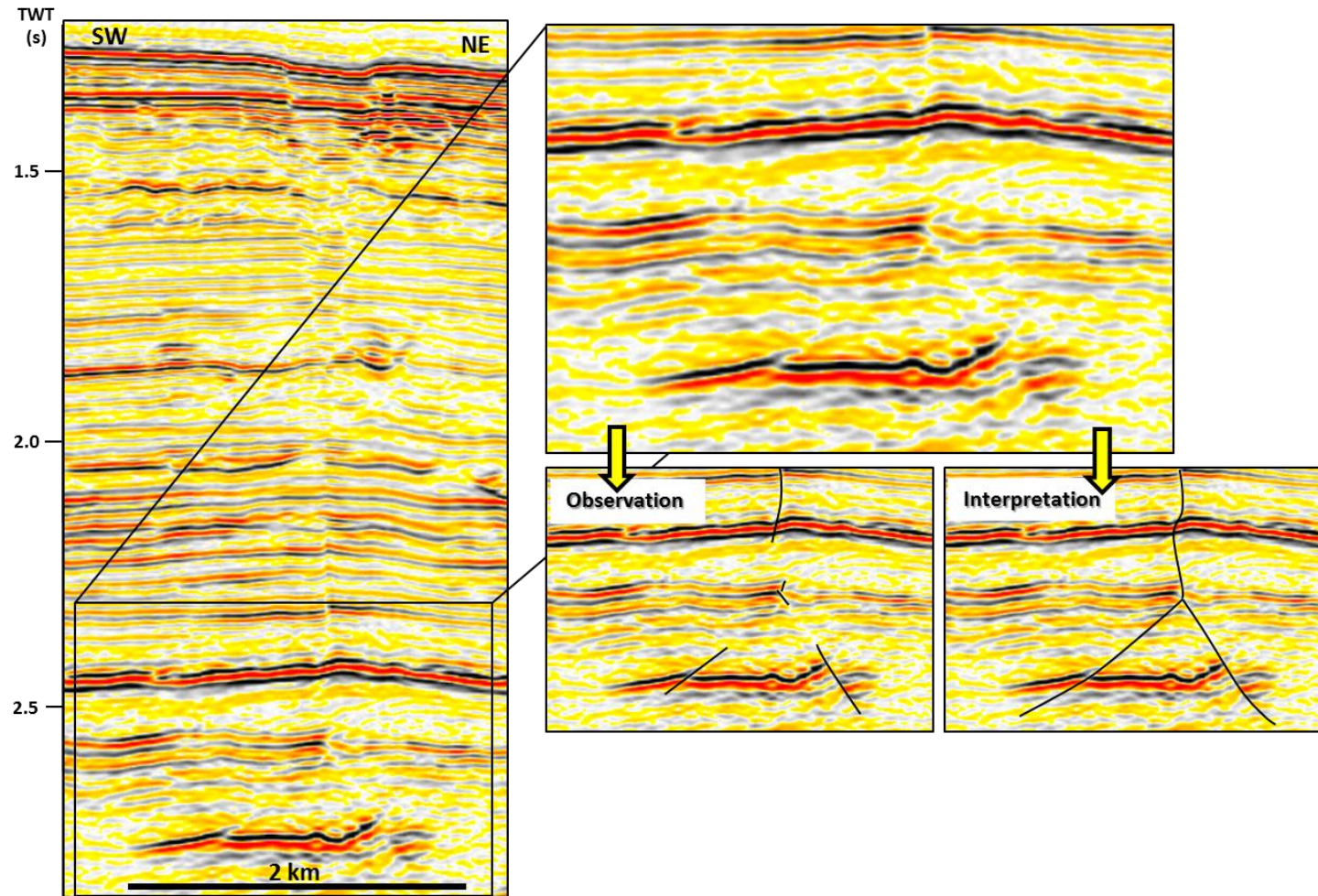
Figure 4.3b – Figure showing the limits of the observations made in the evaporites and how the interpretation is used in this thesis.  Here the interpretation links several strands that likely comprise diffuse shear zones that may link through soft linkage to form an upside down 'Y' shape.
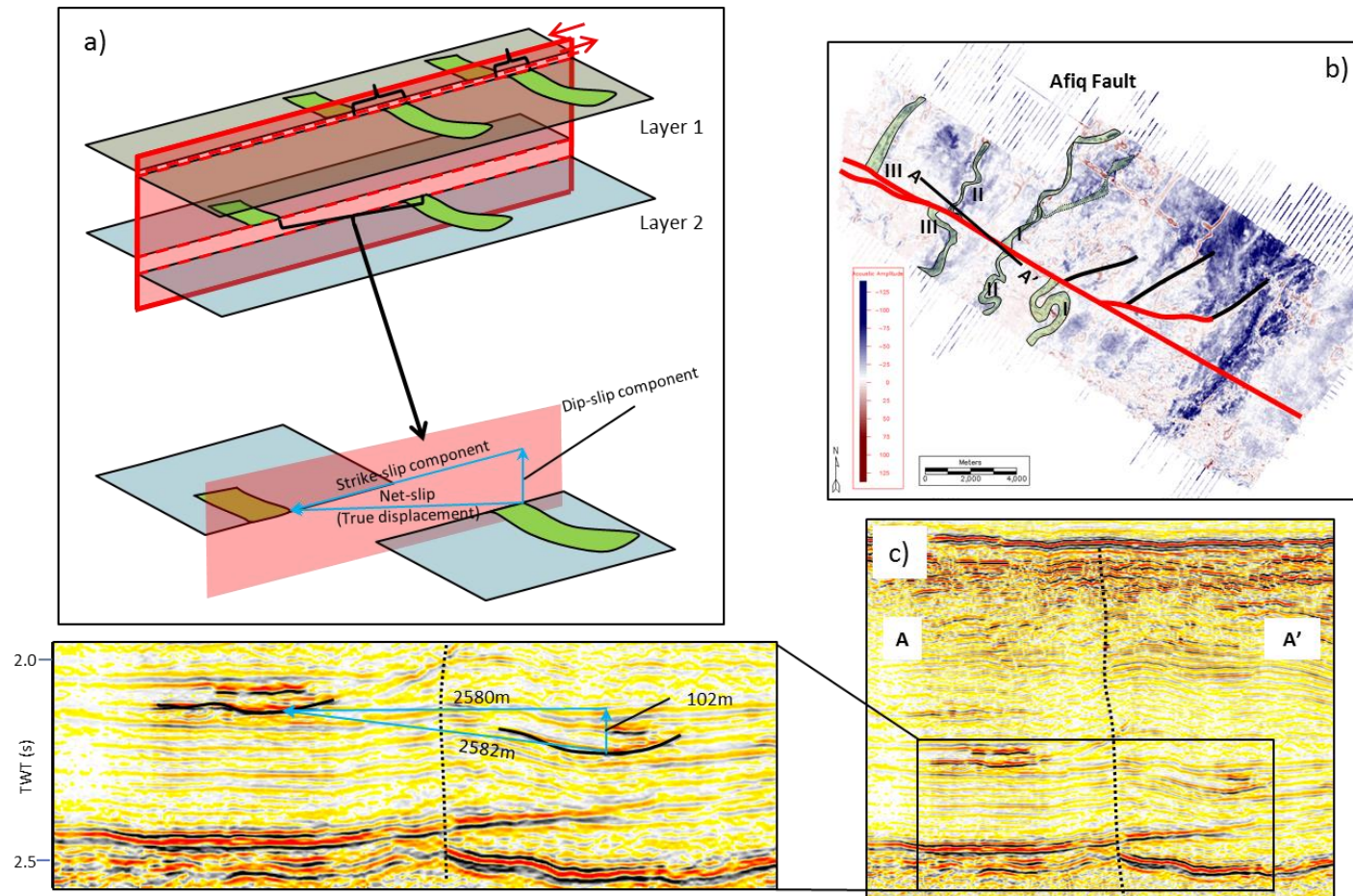
Figure 4.4 - Most kinematic indicators show a component of dip-slip displacement across the fault as shown in the schematic (a). However, the dip-slip component is practically negligible with respect to the large strike-slip component. In the example shown in (b) and (c), the horizontal displacement is 2580m, and the dip-slip component 102m. The resulting net-slip is 2582m and not significantly different from the strike-slip component, given the margin of error of seismic resolution, and therefore a strike-slip measurement can be considered representative of the true displacement vector.

## 4.4      Stratigraphic Description

The seismic stratigraphy in this study comprises sediment packages from the Upper
Cretaceous to Recent and is divided into three major units (Unit 1, Unit 2, and Unit 3) in
accordance with prior studies by Bertoni and Cartwright (2005; 2006) described below.

*Unit 1- (Upper Cretaceous – Upper Miocene)*

Unit 1 comprises mainly units from the Middle Jurassic to Base Messinian and features
mainly deep-water clastic sediments (Figure 4.5).  The ealier Zora, Taqiye, and En Zetim
formations comprise limestones and clay/siltstones (Late Cretaceous to Lower Oligocene),
whilst the later Bet Gurvin and Ziqim formations are dominantly marls and shales (Oligocene
to Late Miocene) (Figure 4.6) (Druckman et al, 1995; Bertoni and Cartwright, 2005).

Two prominent features are exhibited in Unit 1: compressional folds related to the Syrian Arc
Foldbelt and incisional features related to a system of submarine canyons.  The
compressional folds are especially notable in the southwest region of the Levant A dataset
where Unit 1 reflections are deformed by a large Syrian Arc related anticlinal fold (termed
the SAF) causing a regional high that has been interpreted as a palaeo-shelf margin
(described in greater detail in section 4.2.1.3, see Figure 4.7, Figure 4.8).  The folds
incorporate sediments mainly ranging from Bajocian to Turonian in age; however, sediments
dating back to the Permian are present at deeper intervals (Gardosh & Druckman, 2006).  The
submarine canyons likely exerted a significant control on the distribution and architecture of
the overlying Messinian Evaporites (Bertoni and Cartwright, 2006) and thus played an
important role in the basin evolution.  They can be identified where older reflections are
erosionally truncated by a U-shape caused by the fill of higher amplitude reflection sediments
within the canyon (Figure 4.9) that date from the Oligocene to Late Miocene.  The El Arish
and Afiq Canyons are both located in the Levant A dataset where they combine to form a
single canyon confluence.  This confluence incises between plunging folds of the Syrian Arc
where the shelf break is less topographically pronounced (Figure 4.7b).

The seismic stratigraphy changes considerably basinward (towards the west) of the Syrian
Arc shelf as the depositional environment changes from shallow to deep-marine.  Senonian to
lower Oligocene sediments comprise continuous, low amplitude reflections that onlap onto

the SAF and thicken basinwards.  Oligocene to Late Miocene sediments are the youngest

succession in Unit 1 and are composed of very low amplitude, discontinuous reflectors.  They

display variable thicknesses with a dome structure forming above the Syrian Arc anticline

and have been interpreted as overpressured muds (discussed in section 4.2.1.3).

*Unit 2- (Messinian Evaporites)*

Unit 2 comprises evaporites that are bounded at the base of the Messinian by the N reflection

and the top Messinian by the M reflection (Hsu et al, 1973).  The N reflection is a strong

negative reflection, produced from a highly negative impedance response.  This horizon is

generally conformable with the underlying reflectors of Unit 1, with the exception of

localised truncations along the margins of a canyon that can be traced from the extensional

domain to the compressional domain in the GalC dataset (Bertoni and Cartwright, 2005).

Horizon M is a strong, continuous, positive reflection corresponding to an increase in

acoustic impedance from the Unit 3 sediments to the evaporites.  The evaporites pinch-out

marginward towards the east (Figure 4.5, Figure 4.10), whereby the N and M horizons merge

into a single positive reflection, which continues landward and is interpreted to represent the

composite Messinian erosional surface (Ryan, 1978; Bertoni and Cartwright, 2006).

Basinward, the M and N horizons diverge, with a maximum thickness of the Messinian

reaching over 1700m in the GalC dataset.  Internal reflections can be discerned within Unit 2

as a chaotic, transparent facies that alternate with localised medium-high continuous

reflections (Figure 4.5).  These changes in seismic expression have been attributed to changes

in lithology either between evaporite units or siliclastic interbeds (Bertoni and Cartwright,

2006).

The distribution of the evaporites can be traced with a pinch-out line (Figure 4.7, Figure

4.10), and where the submarine canyons are present from Unit 1, the pinch-out location shifts

noticeably  landward [up to 35 km; shown in figure 9 of Bertoni and Cartwright (2006)].  The

preferential Messinian erosion and salt deposition in the axes of these canyons and their

tributaries was suggested by Bertoni & Cartwright (2006), and demonstrates the importance

of basement structure affecting later sediment architecture.

*Unit 3- (Pliocene – Recent)*

109

The sediments comprising Unit 3 are bounded by the M horizon at the base and the top by the seabed.  The Yafo Formation lies at the base of Unit 3 and is composed of two parts that form a prograding and aggrading slope wedge deposit: 1) turbiditic sands and 2) hemipelagic turbiditic claystones. The 50m thick Yafo Sands are interbedded with claystones and marls and are Pliocene in age.  They are restricted to regions where the underlying El Arish and Afiq canyons are present, and delineated by high amplitude and frequency reflections (Figure 4.5) (Frey-Martinez et al, 2005).  The reflections at the base of Unit 3 onlap and downlap against the top Messinian unconformity in the proximal part of the Levant Margin, and become steadily concordant with distance at the GalC dataset.  The remaining Yafo Formation (which overlies the Yafo Sands) is a c. 1700m thick accumulation of Plio-Pleistocene sediments with continuous, moderate to high amplitude reflections.  Numerous slump complexes also comprise the unit (Frey-Martinez et al, 2005).

Two sediment groups comprise Unit 3A [termed Unit T10 in Frey-Martinez et al (2005)], which overly the Yafo formation and range between late Plio-Pleistocene to present age.  The first group consists of several small slump complexes and are characterised by discontinuous, high amplitude reflections that are very difficult to correlate across faults and thus can only be locally tracked.  They are highly channelized and display erosive relationships within the deeper reflections.  The second group consists of a thin layer (c. 20m) of continuous, low amplitude reflections and overlie the first group.
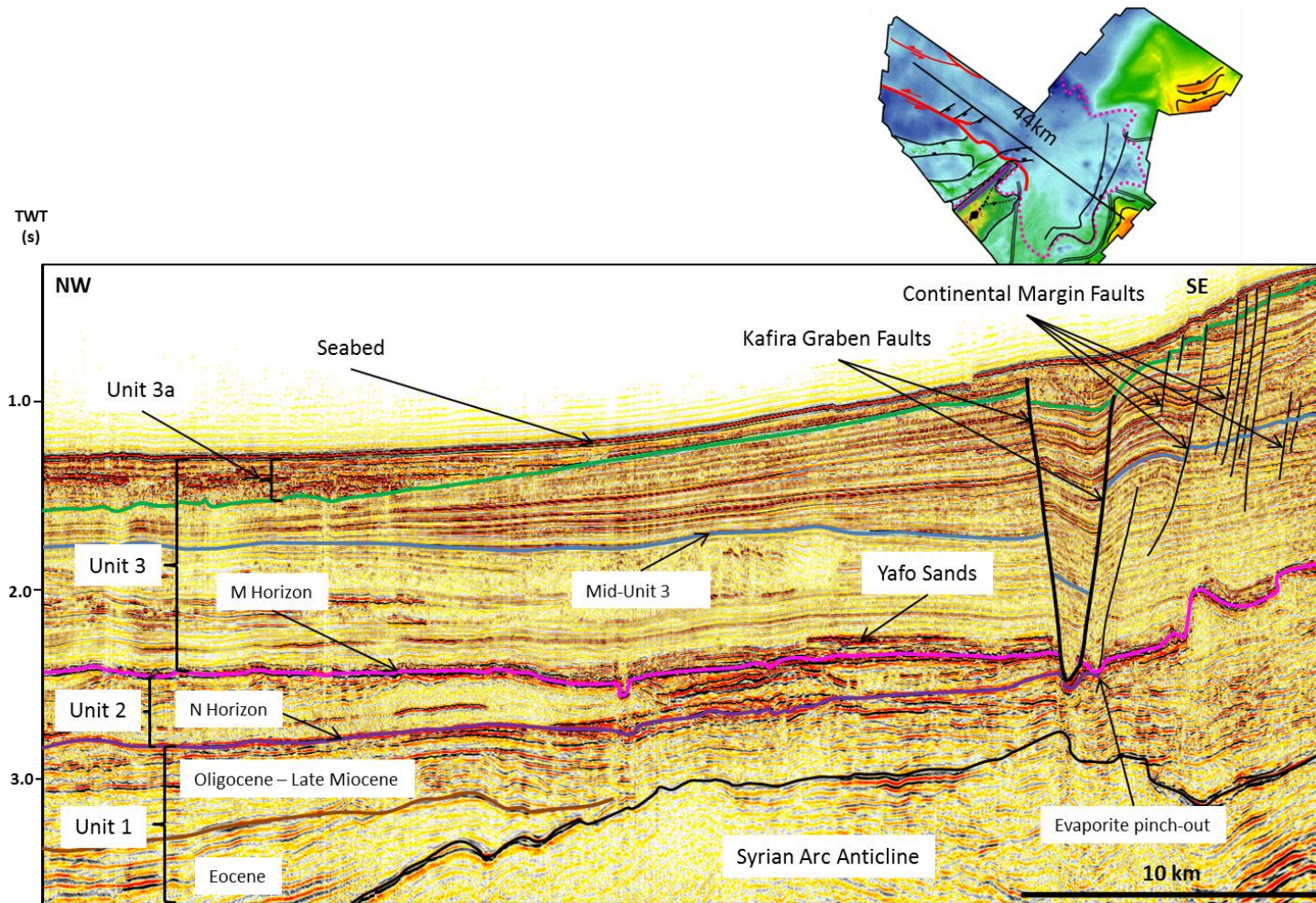
Figure 4.5 - Representative profile section of the Levant A dataset showing extensional faults, the salt pinch-out, an underlying Syrian Arc fold, and the stratigraphy used for this study. Location shown on M horizon, base Unit 3 map (Figure 4.7 for larger figure). Vertical exaggeration approx. 6.3.
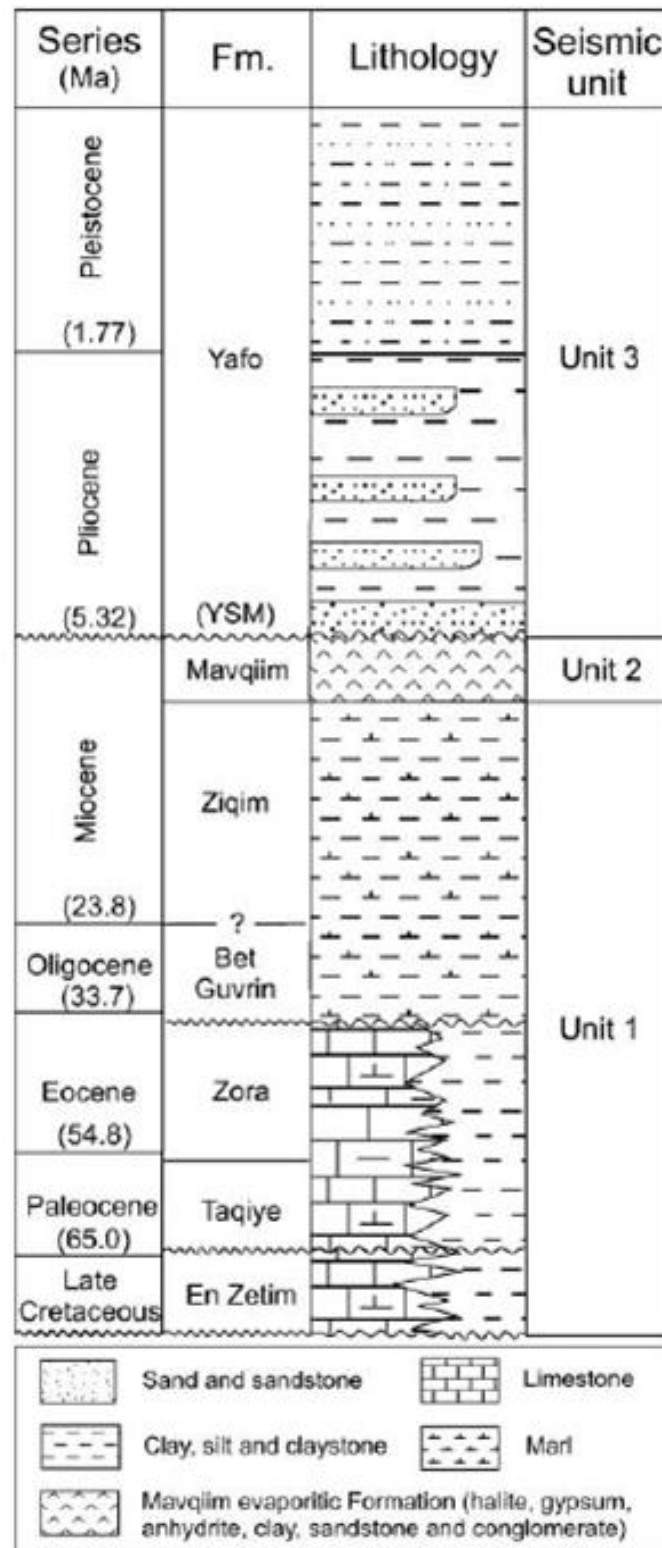
Figure 4.6 - Stratigraphic column showing the main formations observed in the study area using prior studies and an unpublished well report to correlate their age and units.  Fm = Formation; YSM = Yafo Sand Member. Adapted from (Druckman et al, 1995; Gardosh & Druckman 2006; Bertoni & Cartwright, 2006).
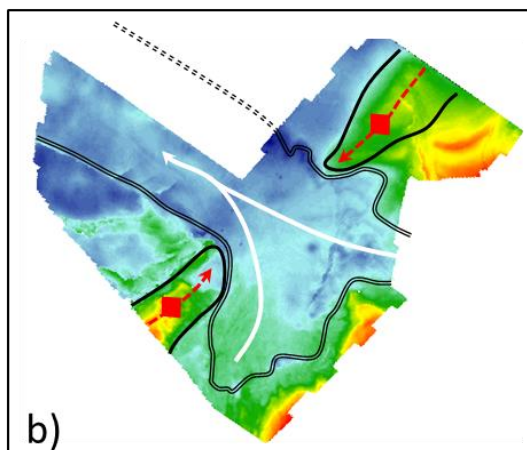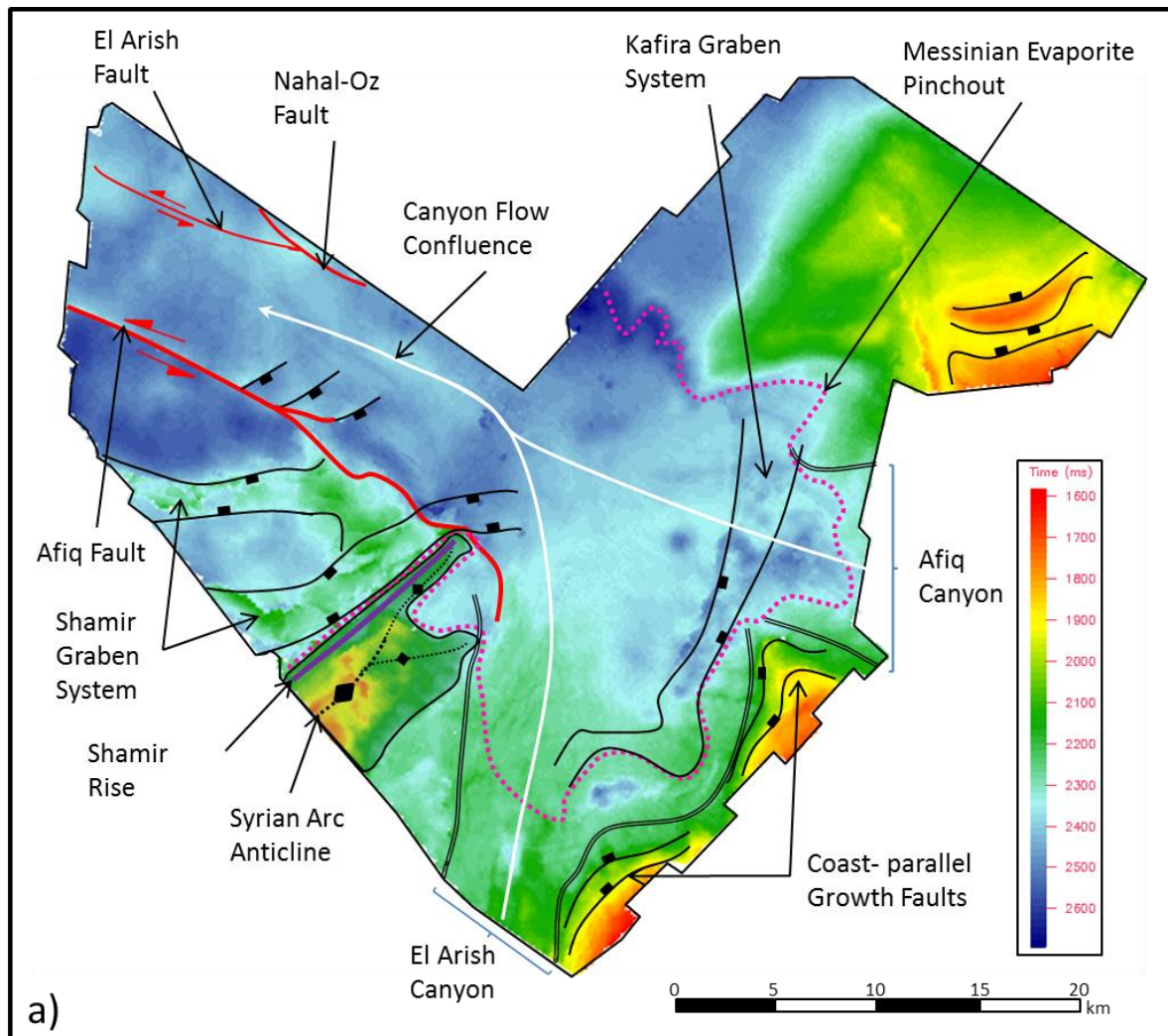
Figure 4.7 - Time map of the M horizon (top of the Messinian Evaporites; however, the horizon continues updip of the pinch-out).  Overlaid onto this figure are the major structural elements of the Levant A dataset as well as showing the evaporite pinch-out and confluence between the El Arish and Afiq Canyons.  b) Shows how canyon confluence is situated between major Syrian Arc folds and where the northeast boundary of the confluence is located (based on 2D seismic lines).

113
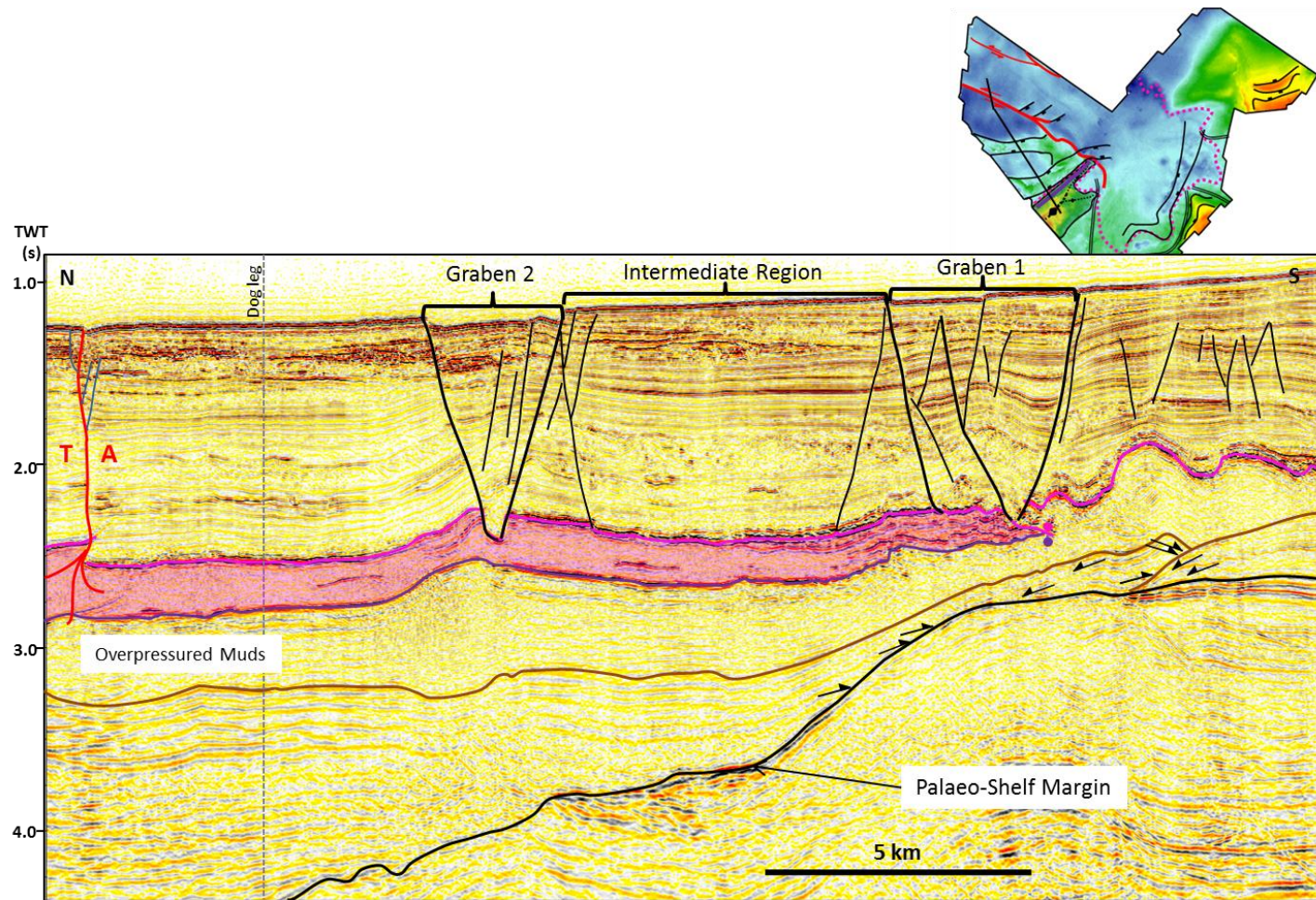
Figure 4.8 - Section showing the deformation that comprises the Shamir Transtension Region, the Shamir Rise, and the variable thickness of the overpressured muds.  Note how Graben 1 forms in a similar location around the salt pinch-out as the Kafira Faults; however, the salt pinchout is located downdip of Figure 4.5.  Also of interest, the palaeo-shelf margin can be delineated here, showing the increased thickness of Unit 1 (located underneath the evaporate layer in pink).
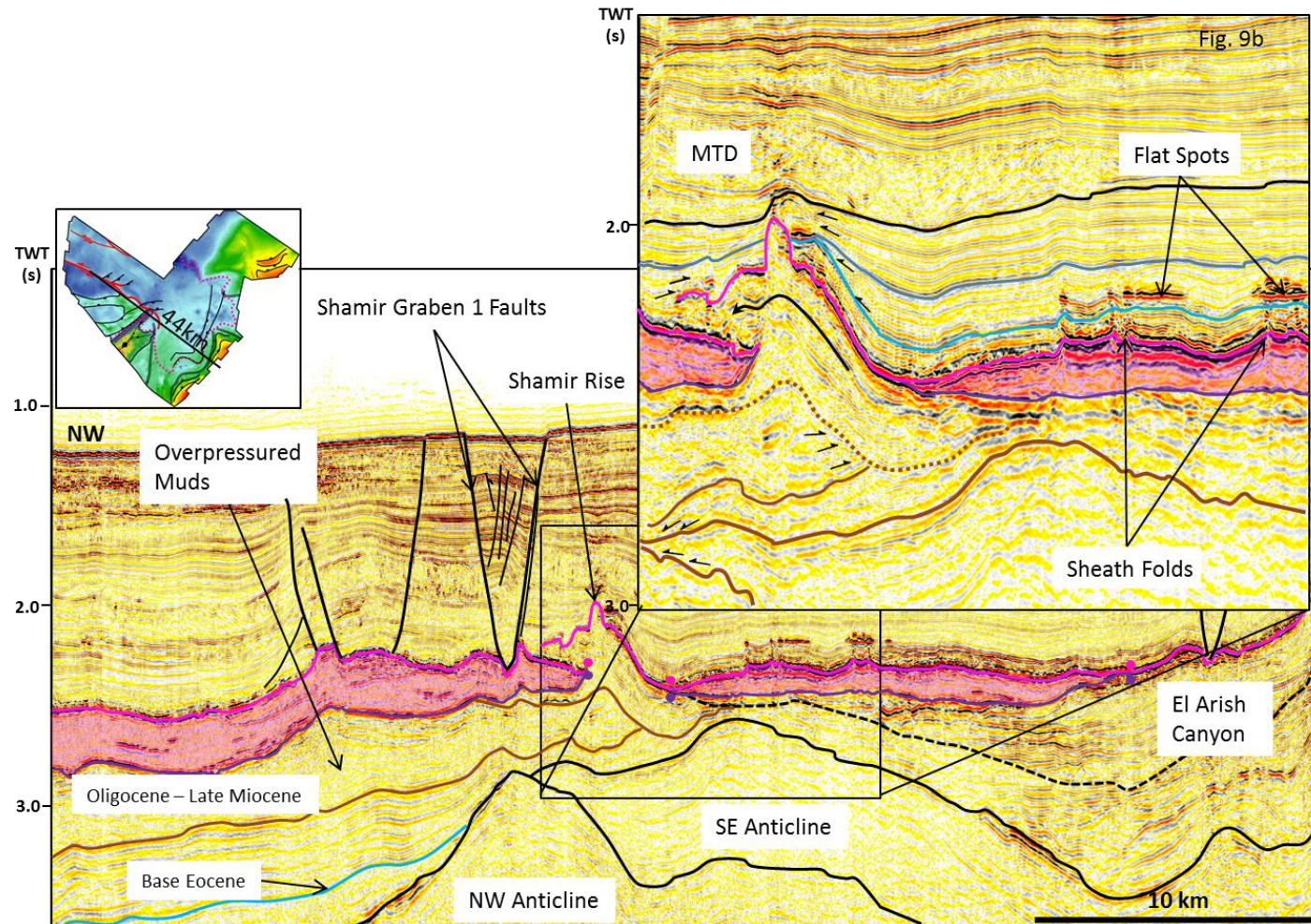
Figure 4.9 - Profile section which shows the structure of the Shamir Rise and the extrusion of the overpressured muds above the salt.

**Fig. 10a:** Top Salt – Base Salt Isopach Map



**Fig. 10b:** Seabed – Top Salt Isopach Map
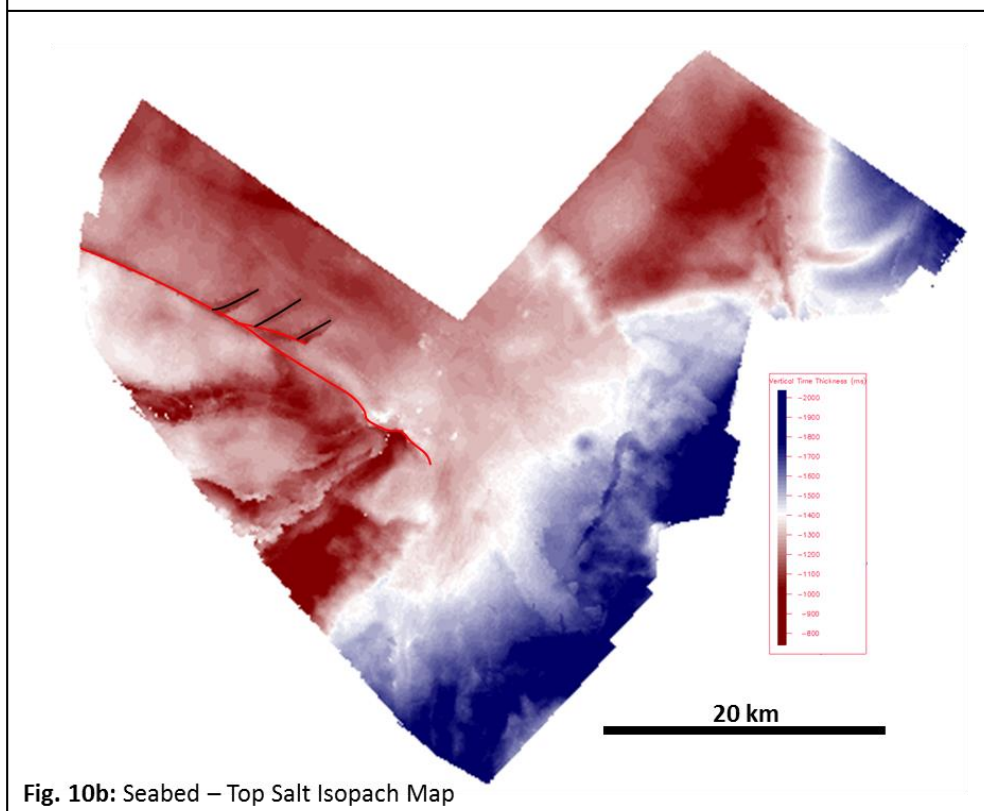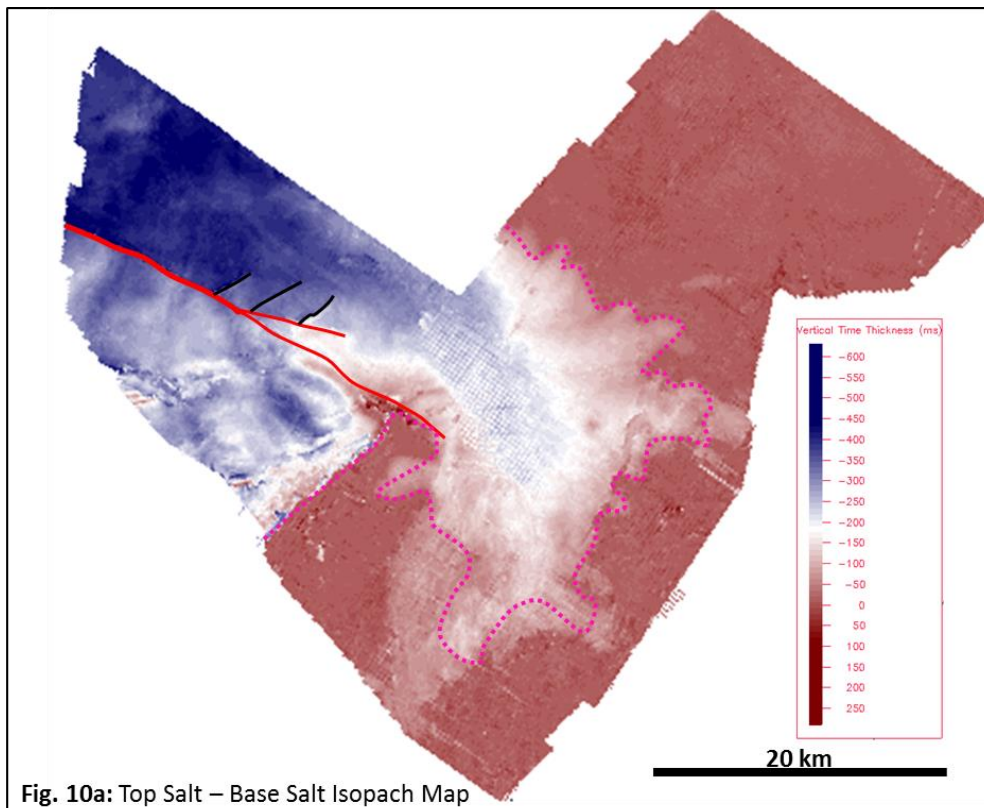
Figure 4.10 - Isopach maps showing the thickness of the (a) the Messinian Evaporites and (b) the Unit 3 overburden.  Note thicker units in blue and thinner in red.  Landwards (southeast) of the Messinian pinch-out line, the map in a) is irrelevant as the N horizon becomes the same as the M horizon.

116

## 4.5      Structural Context

The structures of the Levant slope exhibit deformation similar to other gravity driven fold-thrust belts (e.g. Niger Delta, Gulf of Mexico), including a proximal extensional region dominated by normal faults, a translational zone, and a compressional zone, comprised of thrust faults and corresponding folds(Morley et al., 2011).  However, the Levant differs from other slope margins because many strike-slip faults occur in the translational and compressional domains.  The architecture of these structures is also complicated by interactions related to salt flow and pre-existing structures underlying Unit 1 (the Syrian Arc Foldbelt).  The strike-slip faults at the focus of this study lie in the translational domain and trend in a significantly different direction (NW-SE) from the conjugate set of strike-slip faults that dominate the compressional domain shown in the GalC dataset (See Chapters 3, 5) (Figure 4.1b).

A change in the regional stress fields therefore occurs with progression down-dip, with $\sigma_1$ trending approximately west-southwest in the translational domain and $\sigma_1$ trending towards the northeast in the compressional domain.  The reason for this change is likely due to conflicting salt flow directions from the Levant Margin in the east and the Nile Delta to the south.

The following describes the structures seen in the Levant A dataset to provide a structural context for the strike-slip faults at the core of this study.  This begins with faults populating the extensional coast of the dataset and followed by a description of salt flow evidence in the El Arish and Afiq Canyons (Figure 4.11).  The final two sections focus on deformation above the SAF (termed the Shamir Rise) and a series of transtensional zones forming grabens (termed the Shamir Graben System), before dying out at the major strike-slip Afiq Fault.

### 4.5.1   Extensional Coast Faults

The faults described here comprise two groups: 1) the continental margin faults and 2) the Kafira Graben Faults and are described below.

*Continental Margin Faults-*

The continental margin faults are located up-dip of the Kafira Graben faults (Figure 4.5, Figure 4.12), and dip on average 45° - 50° to the west. They trend parallel to the continental margin (broadly NE-SW) and can be grouped into two sets. Set 1 comprises larger, planar normal faults that reach the seabed (but do not leave a scarp) and propagate downwards below the mid-Unit 3 horizon. Maximum throw values are 50m (50ms TWT) and in plan-view they extend for about 2 km. Set 2 tend to be more landward and are much smaller than set 1, rarely reaching the seabed and usually about a third of the fault length in cross-section (c. 300 m). They are generally present near the mid-Unit 3 horizon; however, some groups are located nearer to the Unit 3a horizon. Maximum throws of set 2 is limited to 10m (10ms TWT).

Although both sets do not detach into the evaporites or at Top-Messinian Unconformity, they are interpreted to have formed in response to sediment loading of the margin following evaporite withdrawal basinwards in agreement with prior studies (e.g. Garfunkel and Almagor, 1984).

*Kafira Graben Faults-*

These faults (Figure 4.5, Figure 4.7) occur near the location of the salt pinch-out with the larger, master faults often forming an antithetic pair that encompasses a major syncline or graben (Figure 4.12). The faults dip on average 45°-50° and trend between 027°-040°, with deformation restricted to Unit 3. Most upper tips of the master faults die out in Unit 3a, although in some regions the tips reach the seabed without forming a fault scarp. The basal tips detach into the Messinian Evaporites. Maximum throw averages 220m (220ms TWT) and corresponds to the mid Unit 3 horizon. Growth strata are observed at multiple levels along these faults, and show that faulting began prior to Mid-Unit C deposition.

The nature of the Kafira faults changes from south to north, with smaller offsets towards the south (east of El Arish canyon) and larger offsets towards the north (near the Afiq canyon). Towards the north, growth strata can be seen in more recent packages, indicating a later stage of faulting. The master faults follow the trend of the syncline, and therefore possess curvilinear traces in plan view (Figure 4.11), following the Messinian pinch-out boundary

(Fig. 4). The syncline and Kafira Faults diverge at the northern edge of the underlying Afiq canyon, with the Kafira fault trending approximately due north (352°-006°). Here, the faults detach into a thicker accumulation of the evaporites rather than at the pinch-out and show greater offsets. Many smaller faults are incorporated into this structure system, and although they possess much lower throws, they tend to follow the same trends and dips as the master faults.

The syncline is defined by concave up reflections (Figure 4.12) and where the Kafira faults and syncline diverges, conjugate normal faults still occur near the syncline edges and cause a steepening of reflections at an inflection point into the syncline. However, these faults are limited to the lower succession of Unit 3 sediments. Towards the south, the east dipping master faults also cross the syncline at the inflection point, indicating faulting initiated in response to the folding of the syncline.

The syncline is interpreted to have formed as a consequence of salt withdrawal, as it is always located above or just up-dip of the salt pinch-out, in agreement with Bertoni and Cartwright (2006) and shows that salt withdrawal began early in Unit 3. The east dipping faults appears to control deformation with greater throw values and by consistently bounding the syncline in the south. The west dipping faults however, do not bound the syncline and become more segmented where the syncline displays high curvature (Figure 4.11).

### 4.5.2   Salt Flow in the Arish Canyon

Further evidence of salt withdrawal can be identified in the El Arish Canyon. The canyon is clearly observed on both base- and top-Messinian time maps (Figure 4.7, Figure 4.13) as located between two structural highs: the continental margin to the southeast and the Shamir Rise to the northwest. The Messinian Evaporites pinch-out towards the south of the canyon (Figure 4.12), whilst a thin accumulation of salt located in the canyon towards the northeast (Figure 4.9). In both sections, reflections below Unit 2 show the approximate shape and location canyon. These show that the structural low occupied by the M horizon overlies the canyon; however, it is not fully concordant (i.e. the thalweg of the canyon is not directly underlying the thalweg of the M horizon). Therefore the pinch-out location of the salt on the southeastern side (and the Kafira Graben faults) approximately coincides with the canyon thalweg. Notably, the pinch-out on the north-western flank does appear to correspond with

edge of the canyon, as the N horizon and canyon scarp reflections terminate against the M horizon.

Small anticlines upright to inclined, open, and mostly symmetrical anticlines are observed on the M horizon (Figure 4.9, Figure 4.12), which deform (and sometimes pierce) the overlying Yafo Sands.  The axial planes of these small folds are not straight and have therefore been refolded into a non-cylindrical geometry (Figure 4.11d).  The folds are more clearly defined at different coherency intervals (Figure 4.11d, insets) and display flow-like textures at deeper intervals, following the canyon basinward. The folds show reflections that warp and lose amplitude directly below the apex of the fold internally, whilst flat spot anomalies are often present above (Figure 4.9).

The anticlines are interpreted as remnant salt anticlines, explaining why they are also present up-dip of the current salt pinch-out.  In regions affected by salt tectonics salt will rise or flow upwards due to differential loading in regions affected by extension due to buoyancy, and form anticlinal structures as a result (Jackson and Talbot, 1986; Jackson and Vendeville, 1994). Thus when salt flows basinward, localised diapirs will likely form in response to heterogeneities or faults in the overlying overburden sediments of Unit 3.  The deformed reflections above the folds suggest that the timing of folding occurred later in the Pliocene. The presence of flat spot anomalies overlying the folds suggest that these remnant structures may have also acted as preferential pathways for fluid flow, causing fractures or subseismic faults to form directly above, and therefore may be indicative of potential hydrocarbon accumulations.

The movement of salt has been attributed to cause ductile shearing along both the roof and floor of salt units that produces folds resembling sheath folding (Talbot and Jackson, 1987, their Figure 12), which may explain the structures seen here.  However, the anticlines from Figure 4.11d are more upright, and neither show evidence of the asymmetries expected in sheath folds nor evidence of full closures, a sheath fold classification may not be pertinent (Carreras et al., 1977; Quinquis et al., 1978; Cobbold and Quinquis, 1980).  However, most of the basinward salt anticlines show evidence of refolding, suggesting that small anticlines may have formed first before moving down-slope basinward.  This effect produces the middle of the salt anticlines to be pushed farther basinward creating a 'V' shape, in a similar mechanism that drives sheath folding in shear zones that have undergone elongation

(Quinquis et al., 1978). The evidence of refolding is therefore indicative of salt movement in a similar method to sheath folding, and the deeper intervals show that the middle of the salt unit has flowed farther basinward than the roof of Unit 2 and show a slight curvature into the El Arish and Afiq Canyon confluence. Importantly, the Afiq Fault lies on the south-western edge of the confluence and would therefore be directly affected by the salt movement.

**Fig. 11a**
**Depth 1200ms TWT**

Kafira Graben Faults

El Arish Fault

Nahal-Oz Fault

Afiq Fault

Syncline

Wing Crack 1

Shamir
Transtension
Zone

Afiq East Tip Damage
Zone

Coast Parallel Faults

N

0      5      10      15      20
                                    km
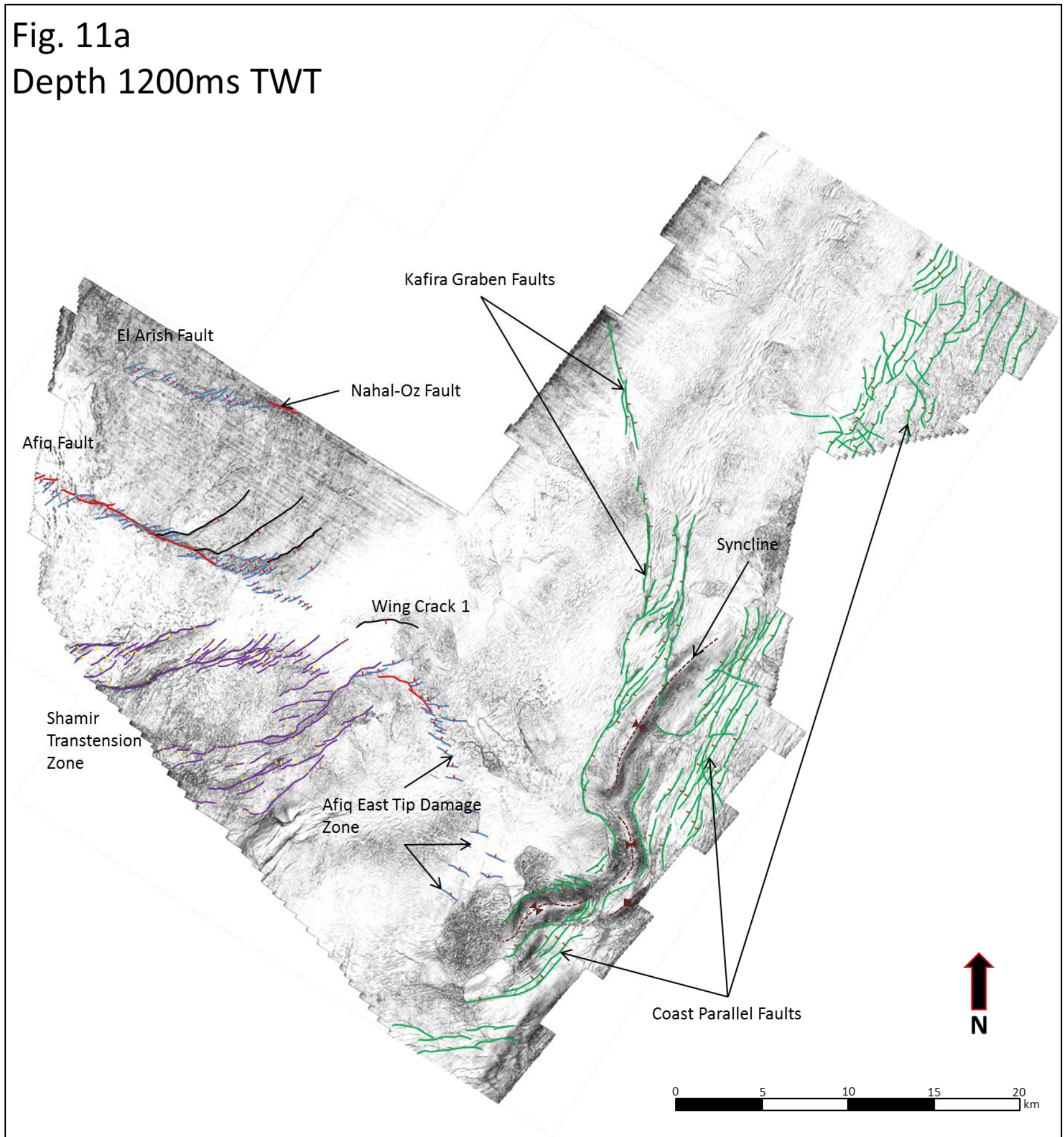
Figure 4.11a - Structural map at 1200ms TWT.  Structures are coloured according to region:  extensional faults (Kafira and Coast Parallel) in green, Shamir Transtension Zone in purple, and the strike-slip faults: El Arish and Afiq Fault are in red and blue.
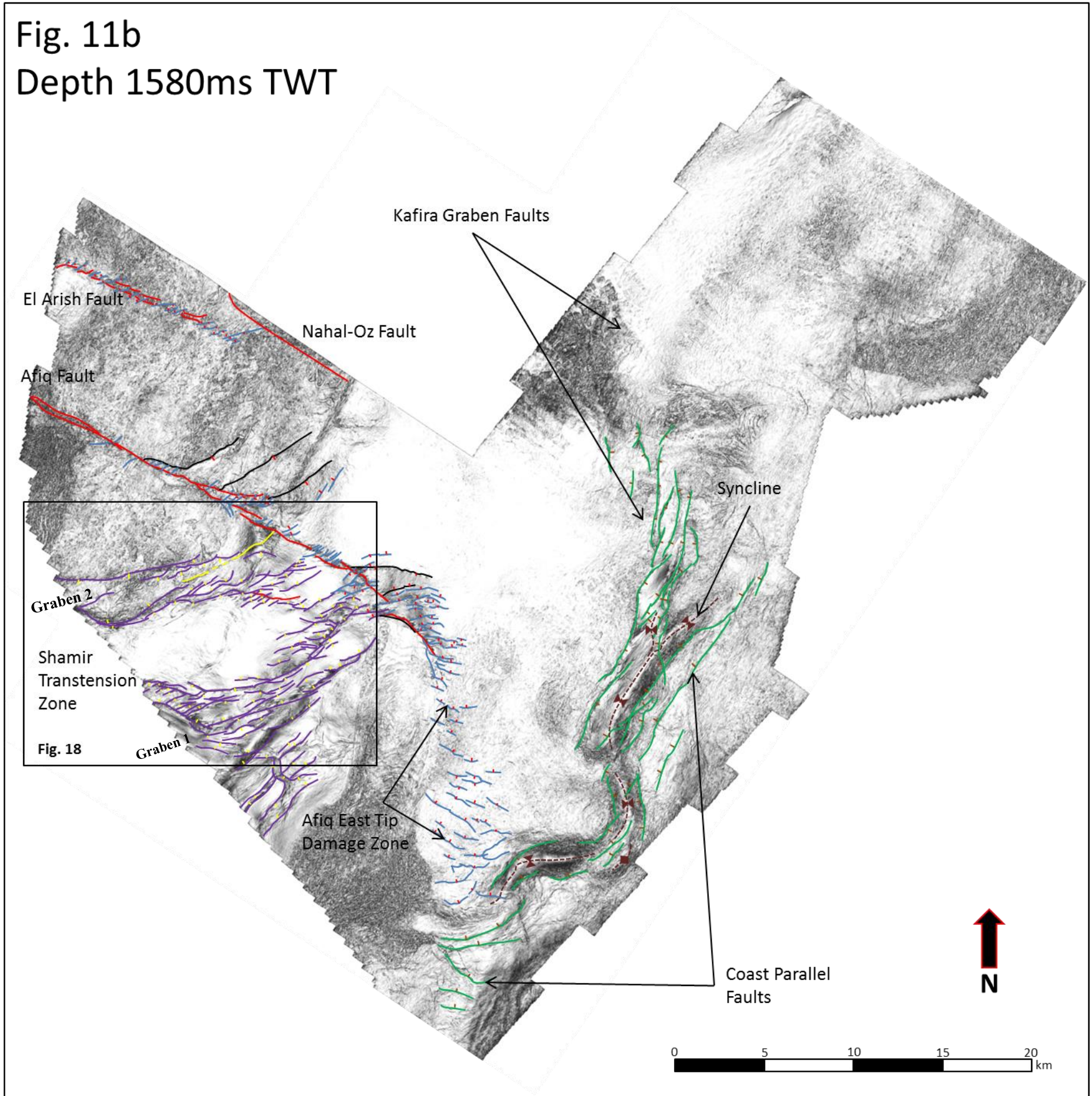
Figure 4.11b - Structural map at 1580ms TWT.  Structures are coloured according to region:  extensional faults (Kafira and Coast Parallel) in green, Shamir Transtension Zone in purple, and the strike-slip faults: El Arish and Afiq Fault are in red and blue.
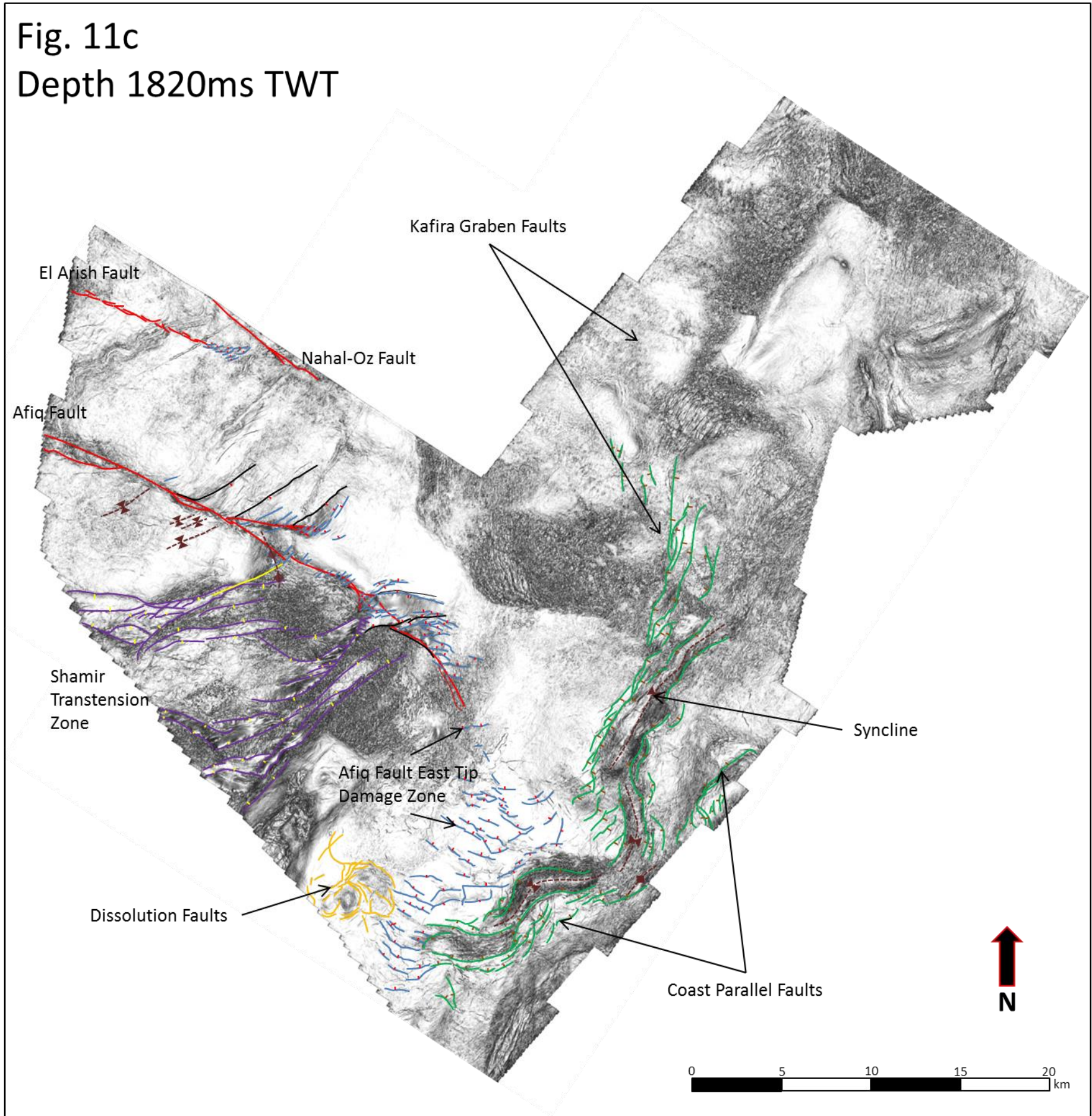
Figure 4.11c - Structural map at 1820ms TWT.  Structures are coloured according to region:  extensional faults (Kafira and Coast Parallel) in green, Shamir Transtension Zone in purple, dissolution faults in orange, and the strike-slip faults: El Arish and Afiq Fault are in red and blue.  Note how the Afiq Fault East Tip Damage Zone is far more prominent than at (a) and (d), whilst the Shamir Transtension Zone is comprised of fewer longer faults than the en echelon arrangement in the shallower sections in (a) and (b).
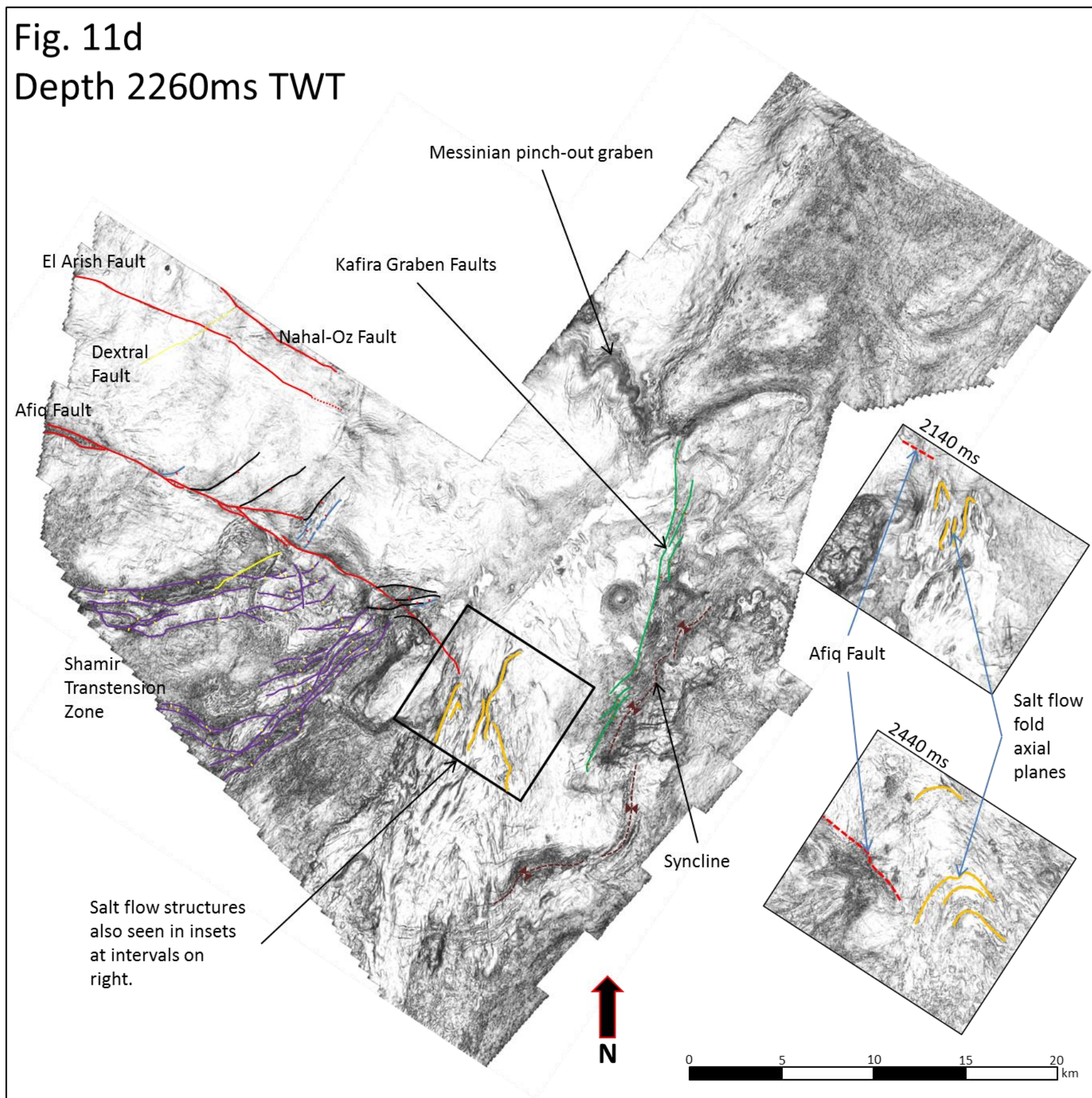
Figure 4.11d - Structural map at 2260ms TWT. Structures are coloured according to region: extensional faults (Kafira and Coast Parallel) in green, Shamir Transtension Zone in purple, salt flow folds in orange, and the strike-slip faults: El Arish and Afiq Fault are in red and blue. There is a large change in structures with depth and the extensional faults are largely absent here. The inserts show more detail of salt flow fold structures at different depths (2140ms, and 2440ms), and how they have been refolded (i.e. 2 phases of folding) with movement down-dip.
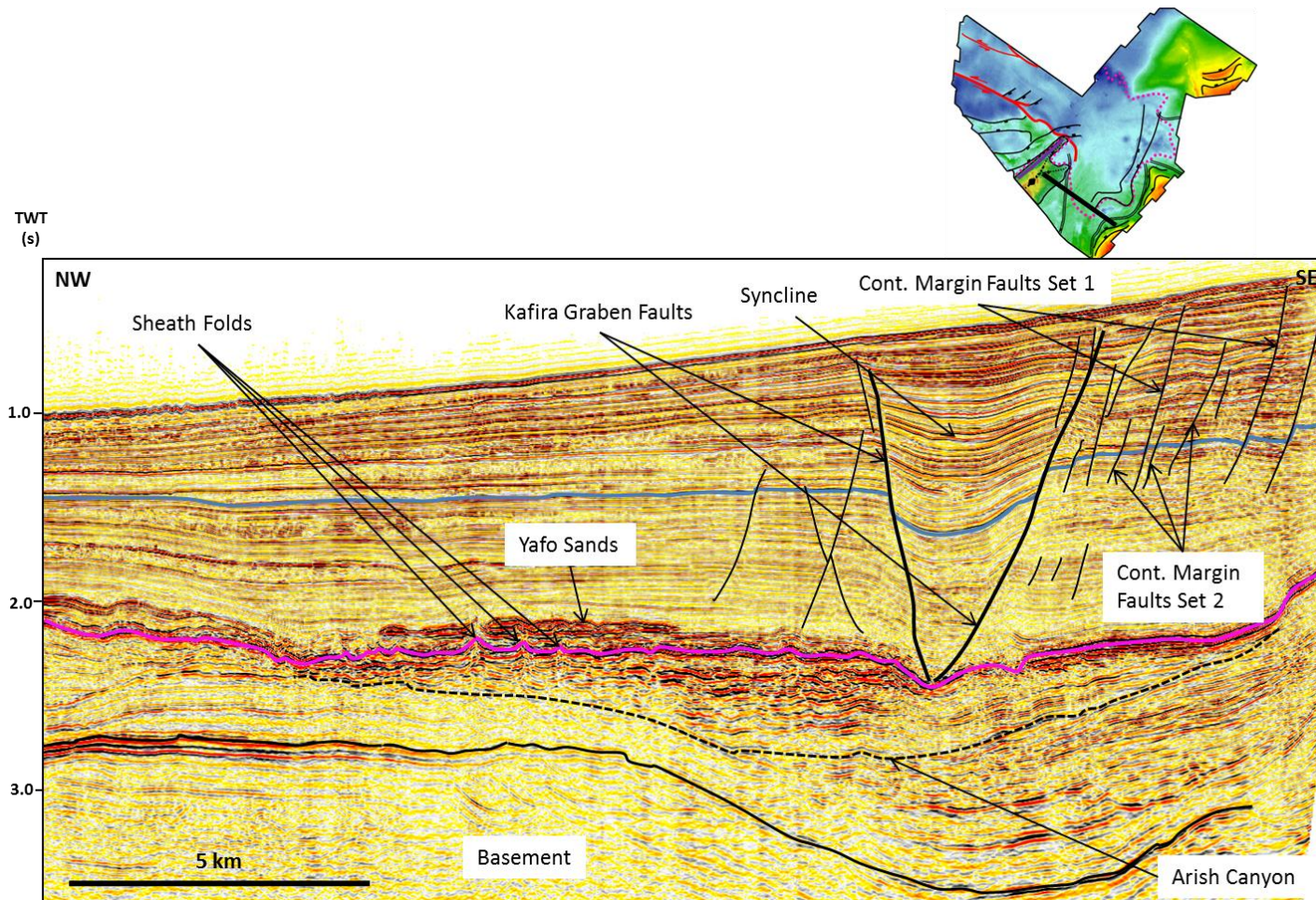
Figure 4.12 - Seismic profile across the El Arish Canyon showing the different faults sets that make up the extensional domain of the gravity slide of the Messinian Evaporites and deform mid-Unit 3 (blue).  Also of note, this line is up-dip of the salt pinch-out, and only the M horizon is observed (pink).  Note the sheath like folds that deform the M horizon and the overlying Yafo sands. Vertical exaggeration, approximately 3.14.

**Fig. 13:** Base salt- time map
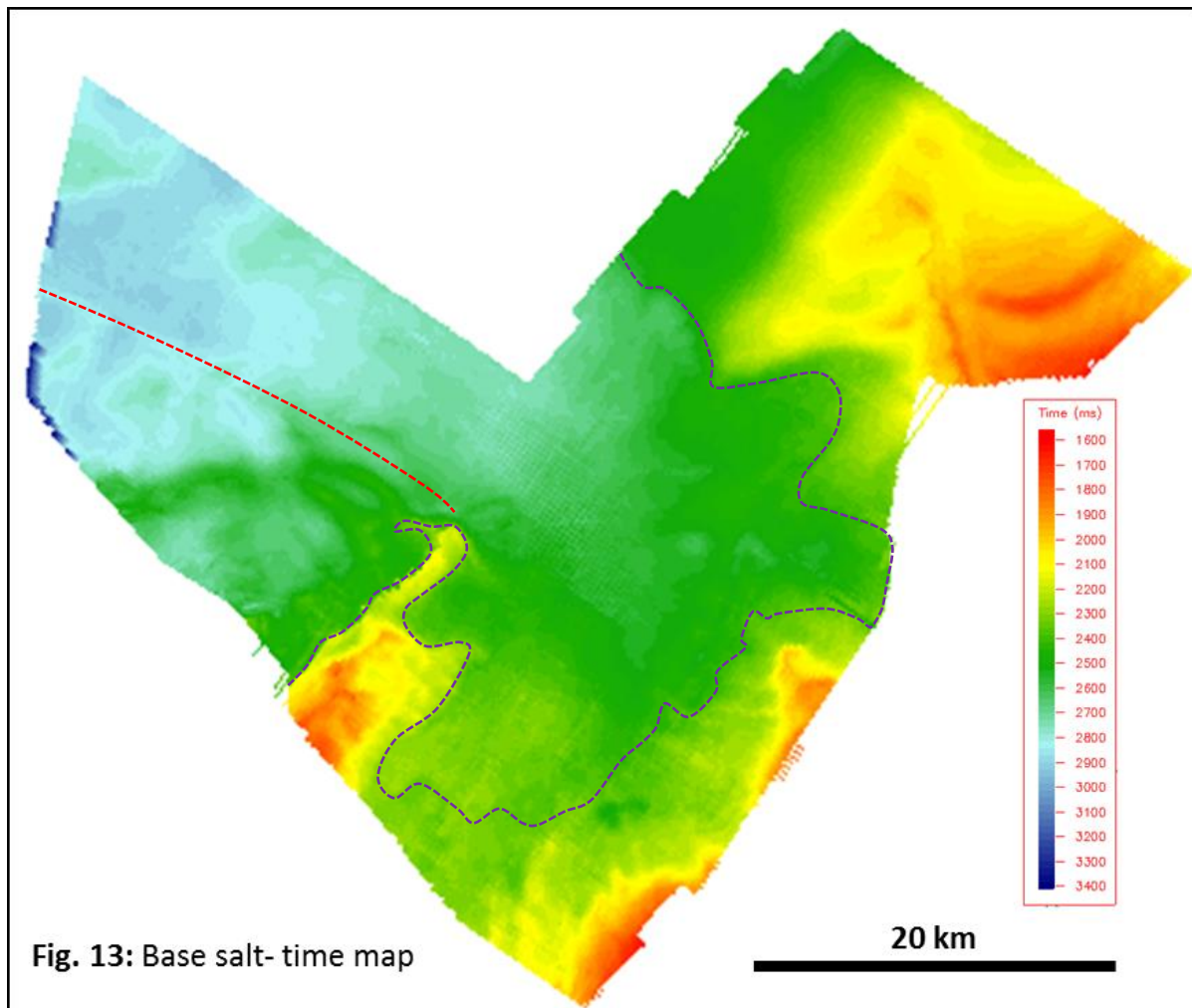
Figure 4.13 – Time map of the base salt (N horizon). Warm colours indicate topographic highs and cool colours topographic lows. There is a clear indication of the canyons in the topographic lows, with the salt pinch-out superimposed in purple and Afiq Fault/SW side of canyon confluence boundary indicated in red (see Figure 4.7 for comparison).

### 4.5.3   The Shamir Rise: Syrian Arc Folds and Overpressured Muds

The M-horizon reaches a structural high above a complex region comprising a Syrian Arc anticline and an overlying dome structure of discordant package of sediments and is herein referred to as the Shamir Rise (Figure 4.7).  The M horizon (in pink on figures) shows considerable topographic variation (Figure 4.8, Figure 4.9), which also extends laterally towards the northeast (Figure 4.14, Figure 4.15).  Importantly, there is no N-horizon in this region i.e. the Messinian Evaporities pinch-out and weld on both sides of the rise.

The underlying Syrian Arc anticline displays significant variability and trends 048°, plunging to the northeast.  Towards the north-western extent, the fold diverges into two smaller anticlines, with amplitudes of 6km and 12km (Figure 4.8, Figure 4.9).  The reflections within the folds are poorly resolved and are therefore difficult to interpret, but it is possible that a deep underlying thrust exists, which has caused the north-western fold to show steeper reflections, with less inclined reflectors of the south-eastern fold truncating against it. Senonian - Eocene sediments both onlap and erosionally truncate against the basement folds to the northwest limb.  The Base Eocene reflections continue above the two anticlines and the El Arish canyon before becoming untraceable likely due to erosion of the canyon.  The reflectors dip 2° to the northwest, and do not change above the anticline except in Figure 4.16, where the reflectors start dipping gently towards the southeast.  The presence of onlap signifies that at least some of the folding occurred during deposition of these units (Gardosh and Druckman, 2006).

The Oligocene – Base Messinian succession is defined by semi-continuous and low amplitude reflections that form a dome shape.  Considerable thickness changes around the Shamir Rise (Figure 4.8, Figure 4.9), and affect the structural high shown by the M horizon. These thickness changes also extend down-dip into the basin (Figure 4.8) and can be observed on isopach maps below the base salt (Figure 4.17).  Notably, the thickness changes when the overlying evaporites experience thickness changes.

This unit is interpreted as an overpressured mud partly because of the opaque seismic facies, but primarily because the thickness change suggests that this unit is reactive to salt movement, and therefore must be a unit that is capable of behaving in a fluid-like manner. This is further supported by a thick accumulation of mud at the Shamir Rise, which resembles

a cored salt dome structure.  The mud dome possesses a basal reflection, suggesting the material originated from down-slope in response to a disequilibrium compaction the overlying Units 2 and 3 causing a lateral transfer of fluids and a state of overpressure (Yardley & Swarbrick, 2000).  In some sections the overpressure has been so great that the mud has erupted over the Messinian Evaporites (Figure 4.9b).  The dome also exhibits parasitic folds, suggesting regions of more localised overpressure.

The timing of mud upwelling and volcanism can be traced using the onlap of overlying Unit 3 sediments (Figure 4.9, Figure 4.16- inset).  The sub-unit immediately overlying the Shamir rise shows conjugate onlap of sediments, whilst the younger sub-unit shows parallel onlap, suggesting that the upwelling began in the Early Pliocene.  The convergent onlap is indicative of a very rapid growth of the mud dome, suggesting the overpressured muds were highly reactive to salt movement and therefore indirectly to Unit 3 loading.  The second sub-unit denotes an onlap that remains mostly convergent.  However, the angle of onlap is not as steep, suggesting an intermediate phase between convergent and parallel onlap, and therefore a slowing of growth.  It is possible that the growth continued into the overlying slump complex, but onlap and growth strata are difficult to identify.  There are growth strata overlying the extruded material from the mud volcano, suggesting that the eruption over the Messinian Evaporites was also early, rather than a subsequent event from greater overburden pressure.  There is sagging of the slump complex above the apex of the mud dome, suggesting that there may have been some relaxation of mud into the middle Pliocene.  Numerous bright spot anomalies appear over the mud dome suggesting fluids have also escaped vertically over the M horizon unconformity and even through the slump complex.

The interpretation of sediment remobilisation as suggested here is consistent with similar sediment remobilisation nearby the Afiq Canyon (Frey-Martnez et al., 2007).  Furthermore, recent studies have identified pockmarks derived from methane release in the region, and attributed the gas to originate from units of the same age (Lazar et al., 2012; Bertoni et al., 2013).  Thus by analogy, this interpretation is strongly supported by other works in the Levant Basin (see also Reiche et al., 2014), and the overpressured muds are likely the result of trapped gas.  The fluid-like properties of this layer may affect the genesis of the Afiq Fault in particular as a detachment layer, and is described further in Section 4.7.7.
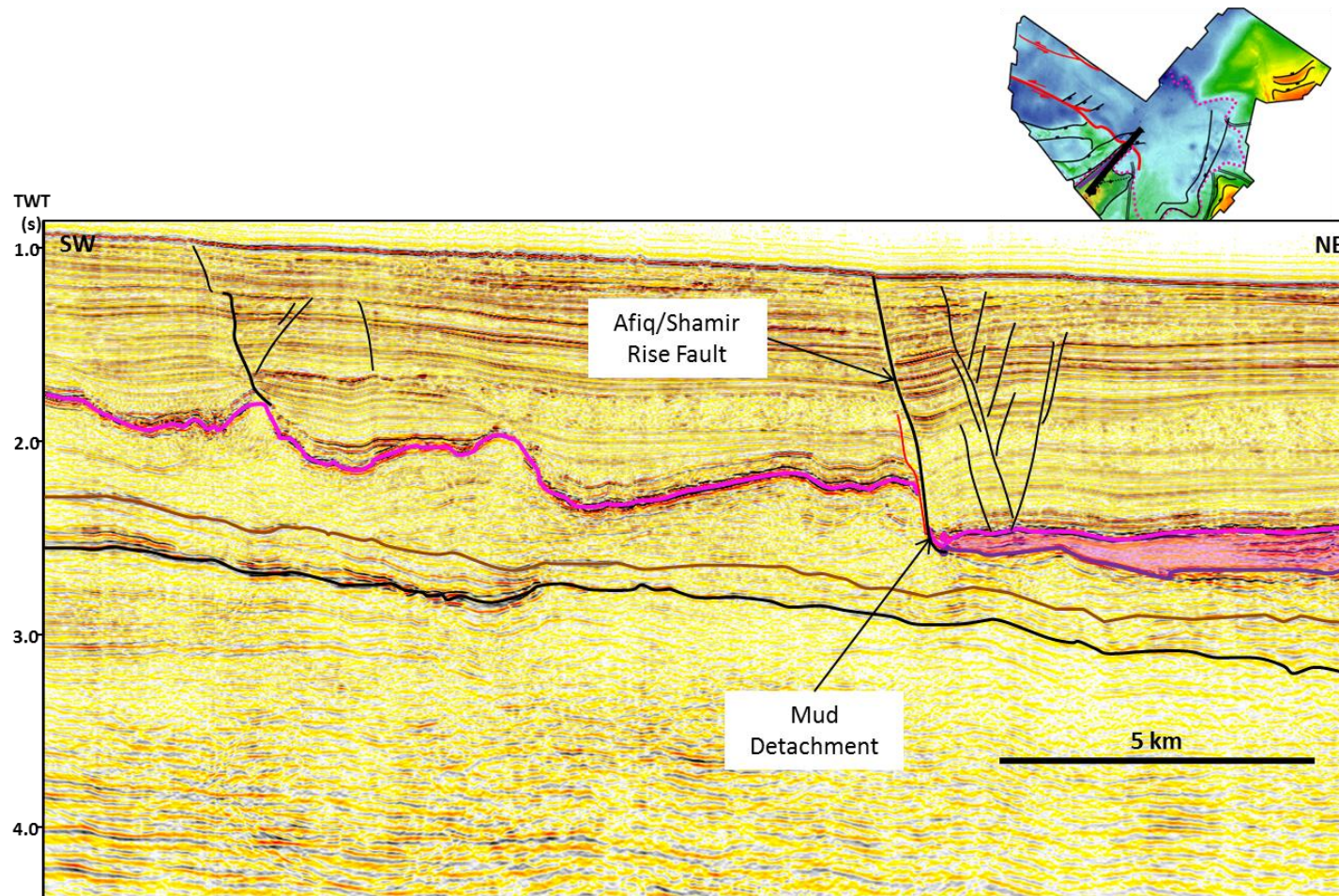
Figure 4.14 - Profile section showing the plunging of the Shamir Rise to the northeast as well as view of the structure along strike.  The Afiq Fault/Shamir Rise Fault detaches directly into the overpressured muds as the evaporites pinch-out here.
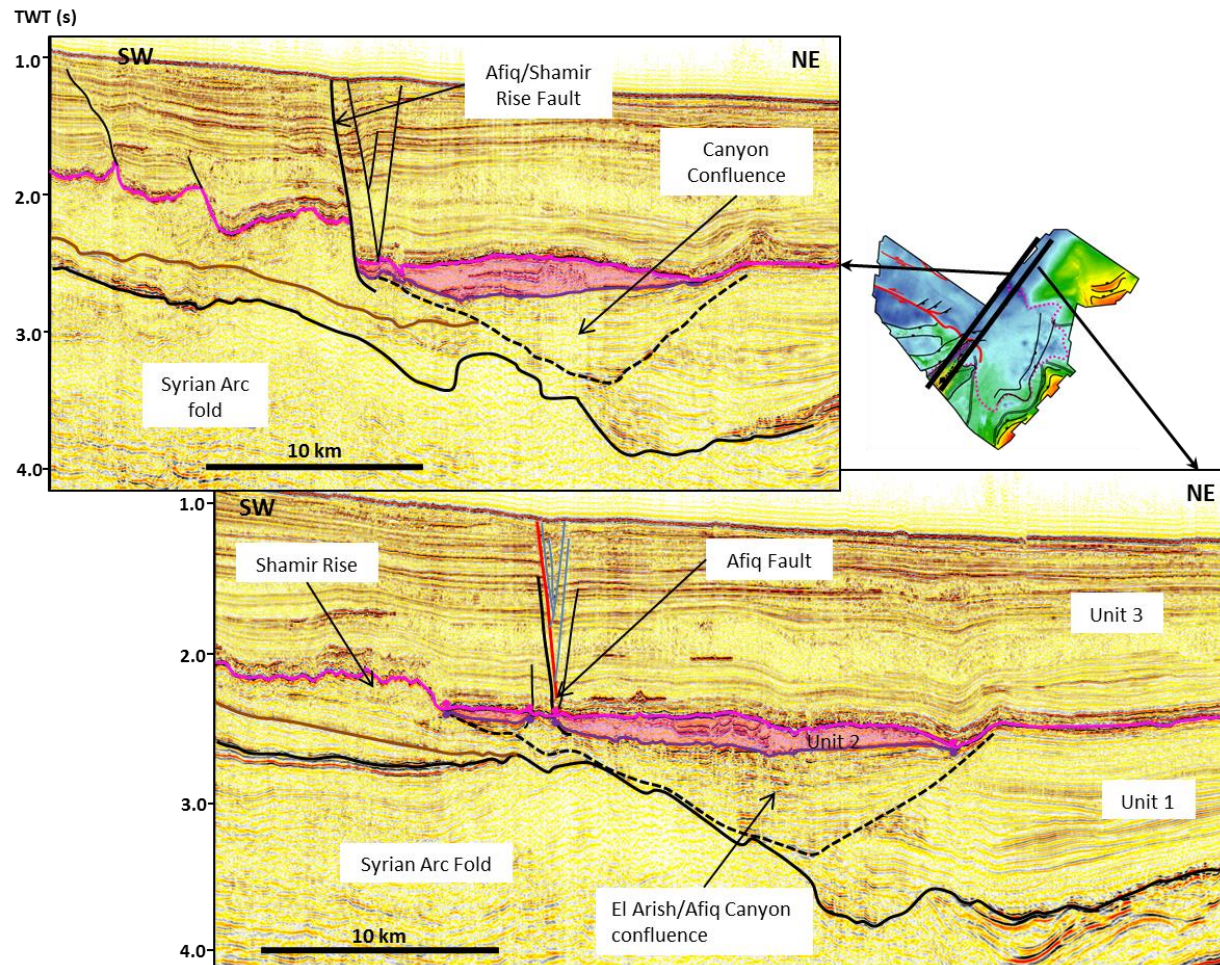
Figure 4.15 - Seismic profiles showing the thickening of the evaporites with progression down-dip as well as the change in geometry as the canyon narrows at the confluence.
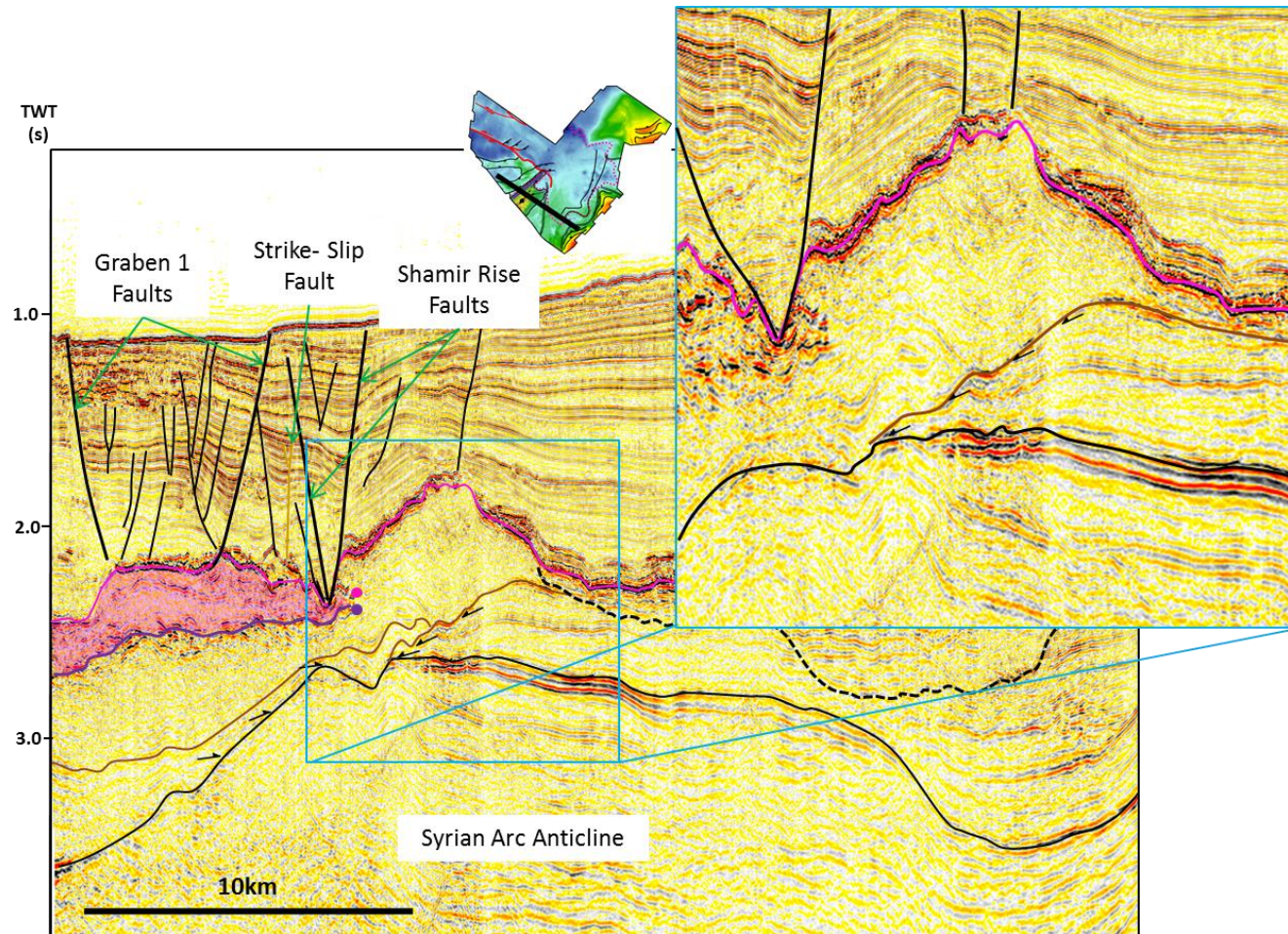
Figure 4.16 - View of the Shamir Rise towards the southwest. The geometry differs significantly from Figure 4.9, with no extrusion of mud over the salt, and a wider base accumulation.

Fig. 17: Base of overpressured muds – base salt isopach
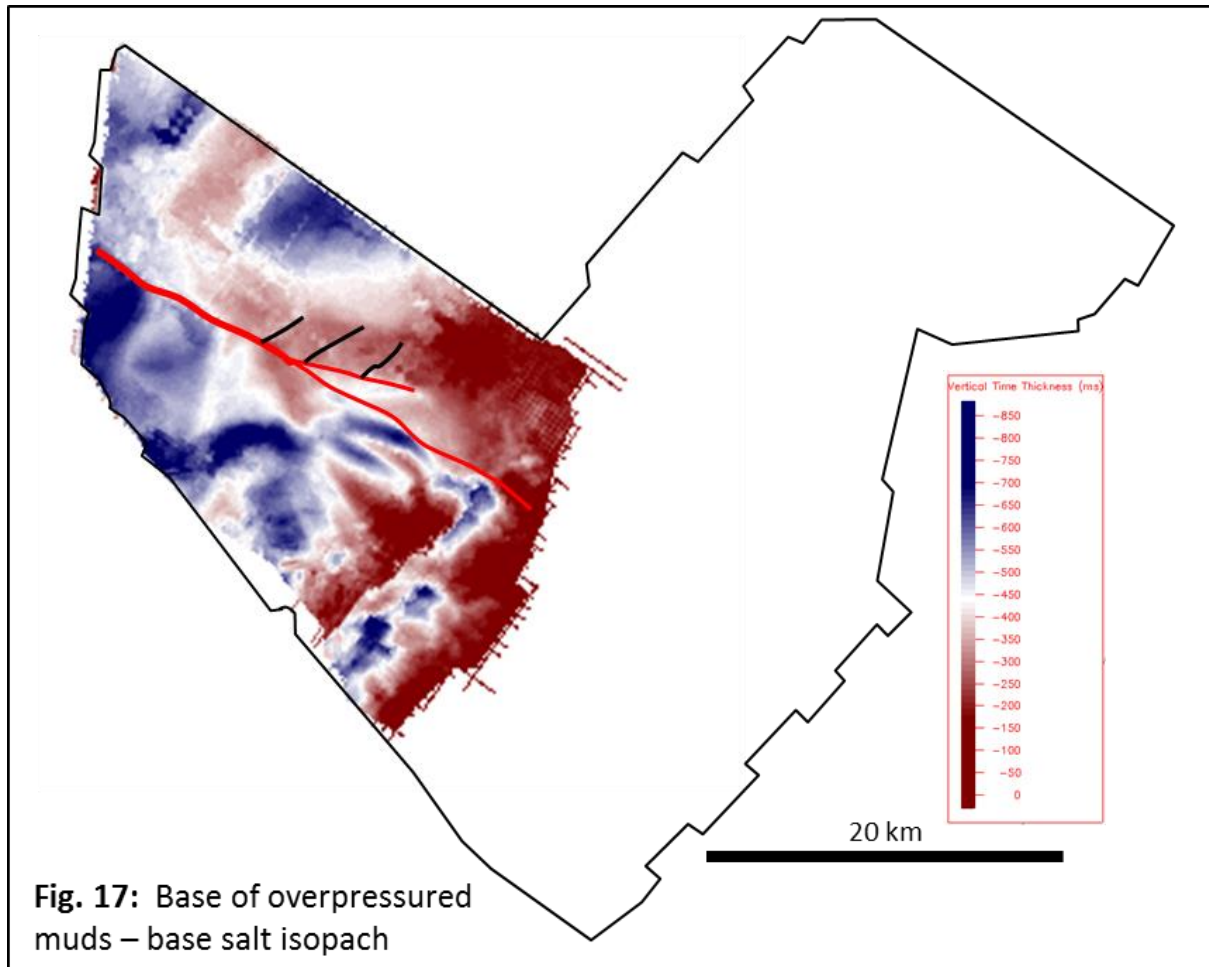
Figure 4.17 – Isopach map between the base of the salt (N horizon) and the base of the overpressured muds. The majority of the length of the Afiq Fault (shown with interpretation) denotes a change in thickness of the muds on either side of the fault. Similarly, significant changes in the thickness of this unit occur at the Shamir Rise and the Shamir Transtension Region faults, indicating the muds likely affect or are affecting by the faulting in this region.

### 4.5.4  The Shamir Transtension Region

The Shamir Transtension Region extends down-dip of the Shamir Rise towards the northwest and is comprised of the following structures: a set of faults overlying the Shamir Rise (henceforth referred to as the Shamir Rise Fault), two major grabens, and an intervening region between the grabens (Figure 4.8). Each graben is comprised of several fault segments, often forming en echelon arrangements in the shallower depths (Figure 4.11).  The intervening region is bounded by the two grabens to the northwest and southeast and by the Afiq strike-slip fault in the northeast.

This region is located near the edges of both the Levant margin and the Nile Delta margin, which causes competing directions of gravitational/transport forces to the northwest and northeast, respectively (Figure 4.1b, Figure 4.18).  As such, the region is dominated by extensional graben structures that also display evidence of transtension.  Below is a description of some of main attributes of the Shamir system starting in the southeast and moving progressively northwest (down-slope).


*The Shamir Rise Faults -*
These faults are characterised by mostly small throws (maximum 20-30ms TWT) that displace sediments in Unit 3 directly above the Shamir Rise (Figure 4.16).  The largest faults in this group (maximum throw 120ms TWT) occur approximately at the salt pinch-out location where the Shamir Rise dies out.  They trend parallel to the Shamir Rise (048°) and with an antithetic pair forming a small graben up-dip of Graben 1 towards the southwest. Towards the north however, the faults dipping to the southeast die out as they interact and link with Graben 1 faults.

The Shamir Rise Fault set likely act as accommodation faults between the structural high of the Shamir Rise and the structural low created by Graben 1 (Figure 4.7, Figure 4.18) in the southern region.  The linkage of these two fault sets towards the north suggests a merging of the two structures with proximity to the dying out of the Shamir Rise and may also be affected by the Afiq Fault.

*Graben 1-*

Graben 1 trends obliquely to the Shamir Rise at 107° towards the southwest (Figure 4.8), and curves to trend parallel to the Shamir Rise at 048° towards the northeast. When Graben 1 becomes parallel with the Shamir Rise, the location of the basal tips of the master faults changes to the location of the salt pinch-out and also detach at the pinch-out, after linking with the Shamir Rise Faults (Figure 4.8).

Both the detachment and deformation in seismic profile resemble the Kafira Faults geometry. However, differences exist as no major syncline in the overburden is present within Graben 1 (with the exception of drag related folding), and the larger, more dominant faults dip basinwards (towards the NW), with a maximum throw of 180ms TWT. The bounding master faults also form seabed scarps indicating the faults are still active; however, growth strata present at the units just below Unit 3a show the majority of growth occurred in the late Pliocene. The faults that interact with the Afiq Fault show different interactions with depth, principally with linkages with different faults (Figure 4.11, Figure 4.18).

Graben 1 faults are interpreted to have faulted in a similar mechanism to the Kafira Graben Faults i.e. due to salt withdrawal, albeit at a later time. The noted differences in morphology may be attributed to influence from both the Shamir Rise structure and Afiq Fault. The amplitude of the former may affect the loading of overburden sediments and location of the salt-pinchout, which in turn affects the amount of displacement and width of the faults. Interactions with the Afiq Fault suggest a degree of contemporaneous growth, and it is therefore logical to expect that these interactions will also affect the geometry of the Afiq Fault.

The distinct segmentation shown on the coherency images occur in left stepping en echelon arrangements (Figure 4.18) indicative of a dextral simple shear deforming the system (Sylvester, 1988). Despite observable kinematic indicators providing a magnitude of horizontal offset, the fact that the faults clearly show dip-slip morphology in profile-section (dipping approximately 60° and forming antithetic pairs), suggests that this region of dextral transtension is dominantly normal with a strike-slip component i.e. the influence of the Nile Delta causes the normal faults to change strike on an oblique slope, forming en echelon

arrangements, but does not generate significant strike-slip movement required to form a strike-slip morphology or 'flower structure'.

*Intermediate Region-*

The region between Grabens 1 and 2 is structurally quiescent towards the southwest; however, towards the northeast (at close proximity to the Afiq Fault) Grabens 1 and 2 converge, creating an intermediate zone comprised of many smaller normal faults with a small sinistral strike-slip fault. The normal faults step right in an en echelon array, consistent with a sinistral region of transtension, and a possible quantifiable kinematic indicator at 1580ms TWT, which may show a 130m left-lateral offset (Figure 4.18b). Overall the fault zone trends about 100°, with the normal faults diverging from the overall trend at high angles (58°).

*Graben 2-*

Graben 2 shows similar characteristics to Graben 1: it is bounded by antithetic master faults, which detach into the Messinian Evaporites, and the faults form an array of right stepping en echelon faults. Furthermore, the basinward dipping faults are larger, with maximum throws of 120m, whilst the landward dipping faults have a maximum throw of 86m (Figure 4.8). The timing of these faults is noticeably later than Graben 1, with larger scarp displacements at the seabed (~30 – 40m) and noticeable growth strata located in Unit 3a.

The similarities with Graben 1 geometry and later timing of faulting are interpreted as an effect of salt movement basinward controlling the deformation. However, the landward dipping faults are larger here, and this difference may be attributed to the thicker accumulation of Messinian evaporites in this region. The M horizon also reaches a structural high due to a gentle doming of underlying overpressured muds, and suggests an interactive relationship between both the mud and evaporites.

*Graben 2 and Strike-Slip Faulting-*

The landward dipping faults of Graben 2 die out towards the Afiq Fault where a small strike-slip fault is observed, which appears to replace the bounding normal faults that dip towards

the margin (Figure 4.19). The strike-slip fault continues to intersect with the Afiq fault whilst the basinward dipping faults of Graben 2 curve into the intermediate zone. The strike-slip fault exhibits similar geometries to the El Arish Fault and therefore will be mentioned later as a means of comparison.

No quantifiable kinematic indicators are observed across the strike-slip fault; however, based on its location within a dextral transtension system, its angle with the Afiq fault (60°), and the left stepping normal faults, it is interpreted as a conjugate dextral strike-slip fault.
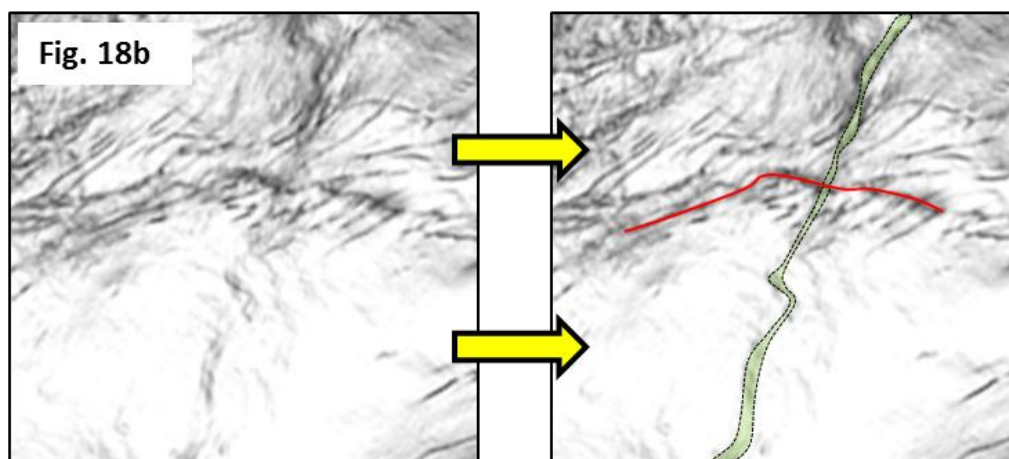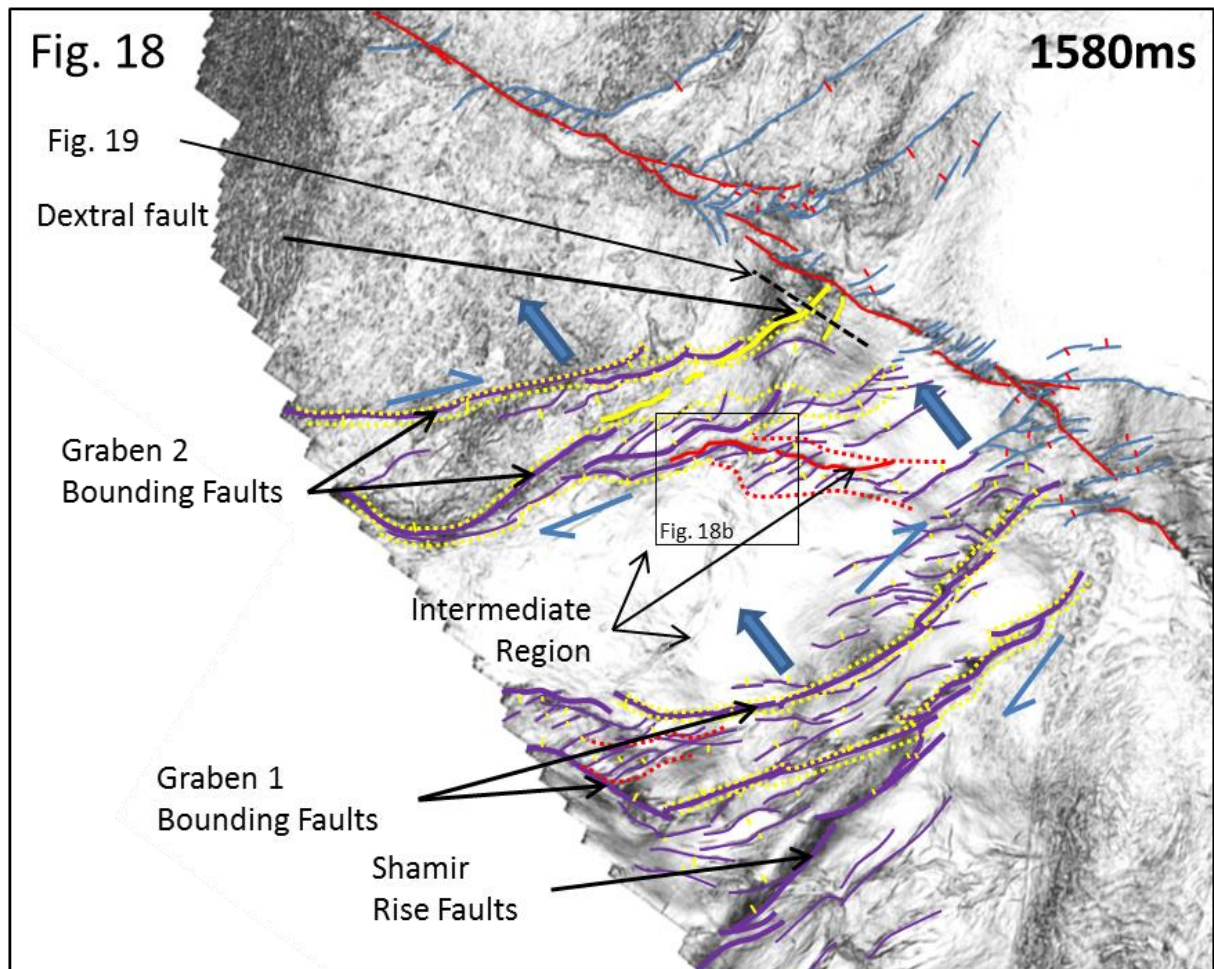
Figure 4.18 - Close-up of the Shamir Transtension Region from Figure 4.11b.  Dotted lines show inferred sense of strike-slip movement on a dominantly dip-slip region: yellow = dextral and red = sinistral.  Solid yellow and red lines denote dominantly strike-slip faults of dextral and sinistral faults, respectively.  Blue arrows shows transport direction based on slope, and therefore the two conflicting directions define a region dominated by transtension.  b) View of a possible kinematic indicator that may show a sinistral slip of up to 130m.
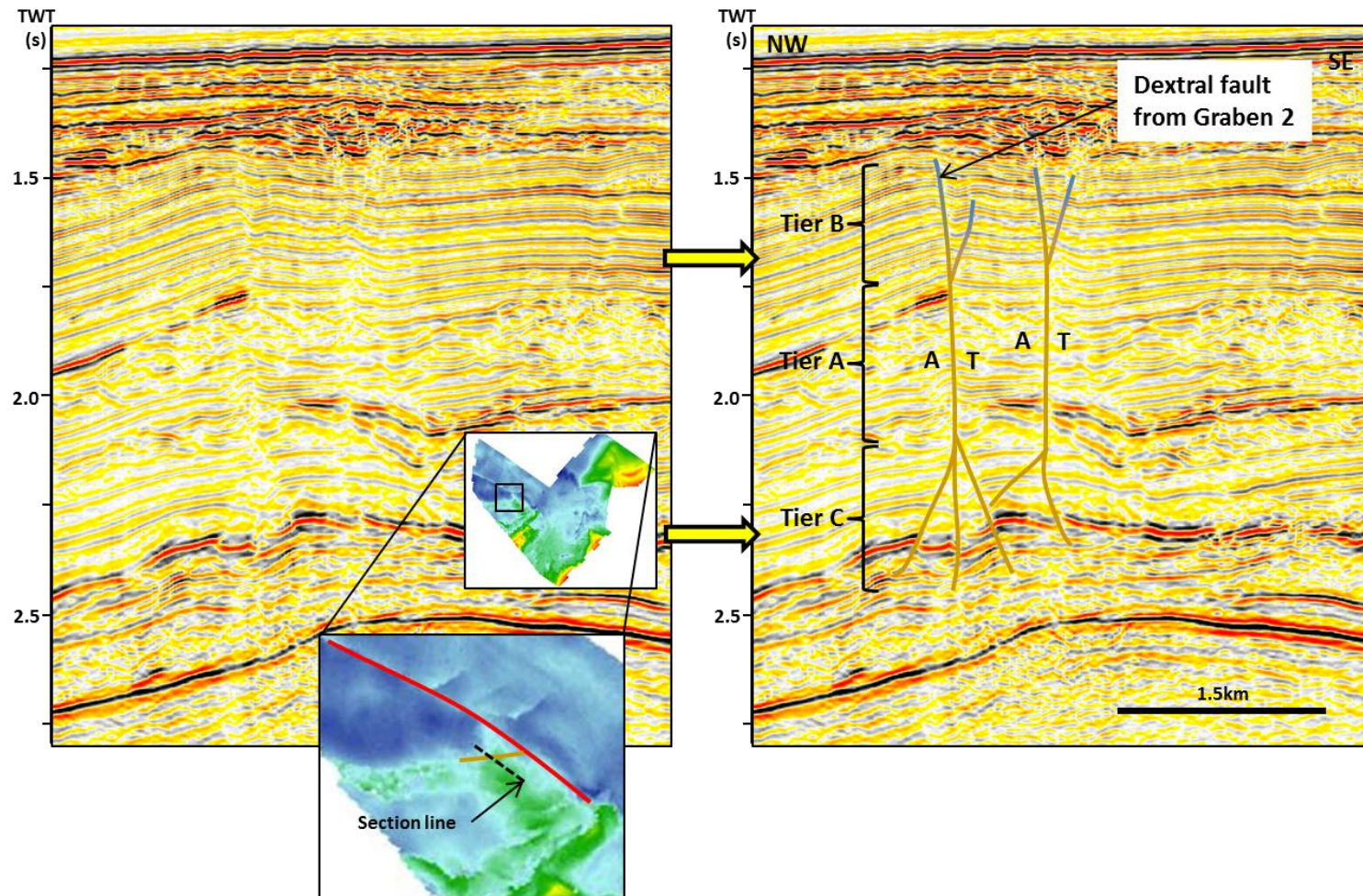
Figure 4.19 - Profile section of a dextral fault that extends from Graben 2 of the Shamir Transtension Region before intersecting with the Afiq Fault. The structure is divided into 'tiers,' which is described in detail in the El Arish Fault and Afiq Fault sections. A second, smaller dextral fault is also located next to it (see Fig. 18 for plan view).

## 4.6      The El Arish Strike-Slip Fault

The El Arish Fault (EAF) is a major strike-slip fault that deforms the Unit 3 sediments, and detaches into the Messinian Evaporites.  It is located above the confluence of the El Arish and Afiq canyons and trends NE-SW at 114° for a minimum length of 16km,with the western lateral tip extending beyond the limits of the Levant A dataset, (Figure 4.1, Figure 4.7).  The total height of the EAF is about 1500m at the fault centre, and decreases with proximity to lateral tips.

The high quality data images the fault zone spectacularly in both profile seismic sections and horizontal coherency slicing, and thus enables a detailed study into the geometry and displacement distribution of a naturally occurring strike-slip fault in three dimensions.  The EAF geometry is simpler than the Afiq Fault and can be clearly categorised, and is therefore a logical fault to begin an investigation into strike-slip fault dynamics.  Furthermore, the EAF has low displacement given its long length, and will serve to contrast the Afiq Fault in the discussion.  This section comprises three sections: a description of its geometry and architecture, a quantitative description based on a displacement distribution plot, and a synthesis to organise the main points.

### 4.6.1   Geometry

The descriptions of fault geometry are divided into profile sections from seismic data to illustrate how the fault zone changes with depth, and is aided by plan views from coherency slices to illustrate changes along strike and build a 3D picture of the fault.  This starts with an overview showing a representative section as well as two coherency images to provide a simple overview.  Subsequent sections provide a more detailed inspection of the EAF geometry, using both profile sections and coherency slices.  This culminates with a short section using the 3D package GeoViz, to illustrate the upper regions of the fault.

#### *4.6.1.1   Overview*

*Profile Section-*

The fundamental observation of EAF geometry comprises three distinct tiers of deformation in profile section (Figure 4.20). The tiers are classified by simplicity, with Tier A being the simplest: defined by a single, sub-vertical, through-going strand and is located at the central region of the fault. Tier B is located above Tier A and shows a fault geometry that comprises multiple faults that dip steeply (normally > 60°) to define the upper tips. There are normally two major strands diverging from the Tier A strand and dipping towards each other, forming a distinct 'Y' shape. The Tier B geometry also encompasses several smaller strands that diverge (splay) from the major two strands upwards and will be described in greater detail later. The Tier A/B boundary is thus defined by the node where all strands meet on the 'Y' and is located in an MTD unit. Tier C defines strands that dip away from each other and diverge from Tier A forming an inverse 'Y' shape. Tier C strands are located below Tier A, mostly in the Messinian Evaporites (Unit 2), with the boundary between Tier A and Tier C geometries often occurring at the M horizon.

*Plan View-*

Two coherency slices illustrate the difference in geometry between Tiers A and B in plan view (note that Tier C is very poorly imaged due to distortion caused by the evaporites). The deepest slice at 2260ms TWT captures the EAF at Tier A (Figure 4.21a) and is defined by a single through-going fault strand, consistent with observations from the profile section. The Tier B fault strands are shown in a slice from 1360ms TWT (located just below the seabed, Figure 4.21b), and depict fault strands forming two right stepping en echelon sets. These sets dip in opposite direction towards each other (Set 1 dips to the south and Set 2 dips to the north), striking at 064°, and forming a 46° angle to the underlying Tier A fault strand, and therefore show a high angle relationship with the through-going fault. Tier B fault lengths are c. 500 - 750m.

A second major observation of the EAF geometry is a change in trend between the deeper Tier A and the seabed geometry at Tier B. At 2260ms TWT, a neighbouring structure is clearly depicted trending roughly parallel to the EAF, with a curvilinear trace. This is a major fault termed the Nahal-Oz Fault (NOF). Both faults are connected by a set of relay fault strands at the deeper interval that trends 098°. The EAF shows a slight change in trend

on either side of the relay faults (114° northwest of the relay zone and 125° southeast of the relay zone), with the eastern showing a curvilinear trace that is parallel to the NOF.  At 1360ms TWT, however, the EAF and NOF are clearly depicted as one fault (albeit comprised of numerous en echelon strands) trending 110°, and the EAF strand southeast of the relay faults is no longer visible.  This is an important observation in the kinematics between the two faults and will be highlighted later.
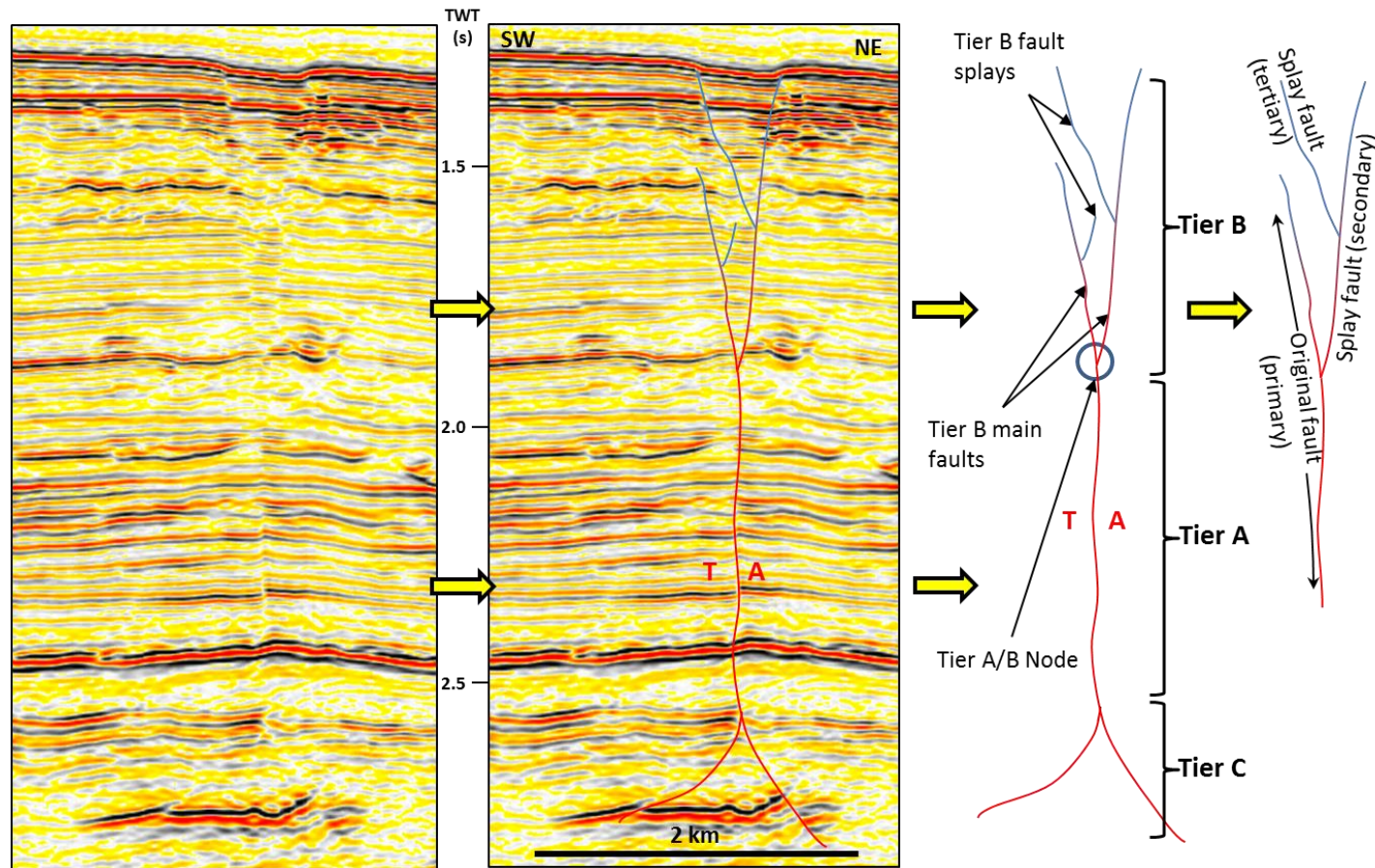
Figure 4.20 - Seismic profile showing the basic structure of the EL Arish Fault (EAF). The fault is comprised of 3 Tiers, with Tier A defining a simple through-going, sub-vertical fault. Tier B is defined by the fault becoming steeply dipping and often forming a splay that produces a 'Y' shape. Subsequent splays can form from both the original fault (in a Tier B geometry) and the main splay fault. Section location shown in Figure 4.21. Tier C is also defined by the splaying of strands and a change in the dip. However, Tier C is often located in Unit 2, and is therefore distorted by the salt, meaning that the structure is sometimes very difficult to interpret. Here, it is interpreted to form an upside down 'Y' shape.

**Fig. 21a: El Arish Fault: Tier A (depth- 2260ms TWT)**
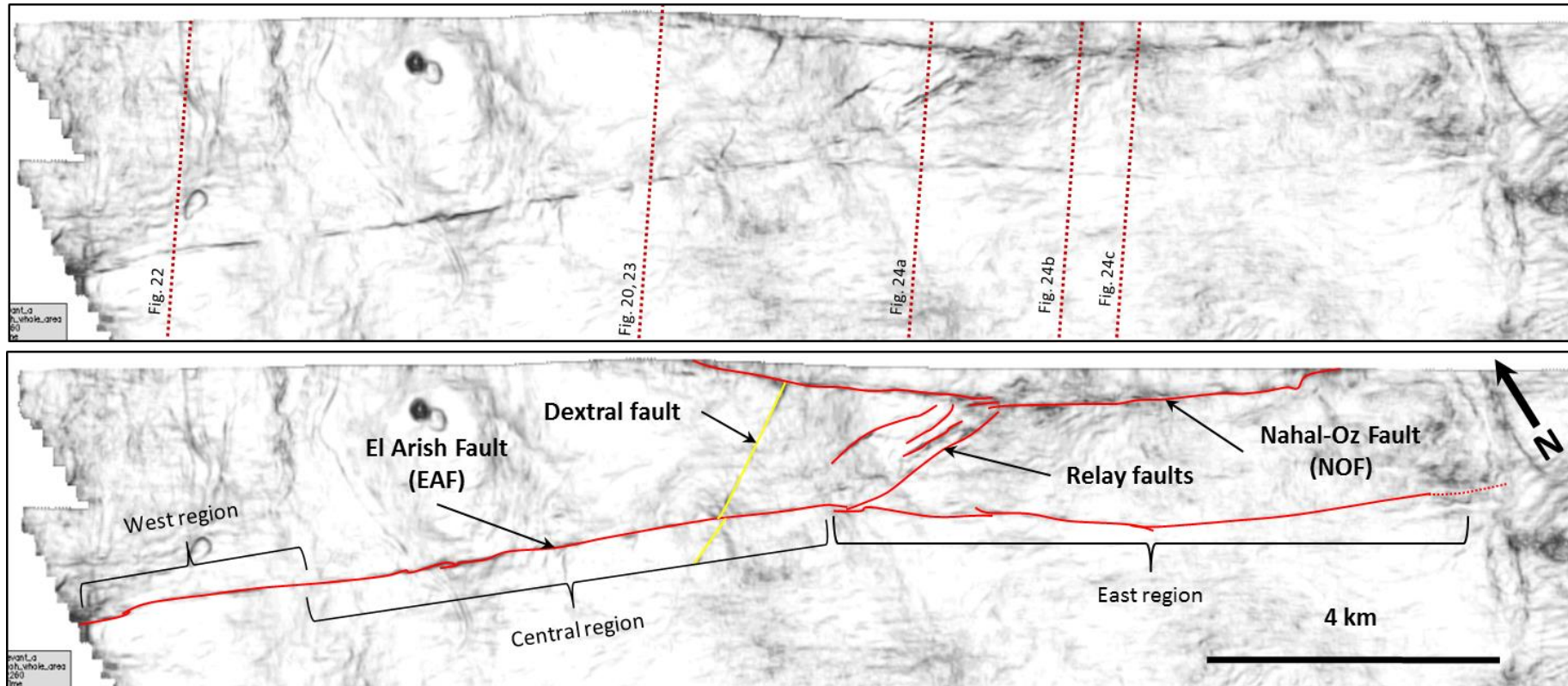


Figure 4.21a - Coherency slices showing the plan view of the El Arish Fault.  a) The EAF at depth shows a single, through-going fault strand, as well as a relay zone with the neighbouring Nahal-Oz Fault.

**Fig. 21b: El Arish Fault: Tier B (depth- 1360ms TWT)**
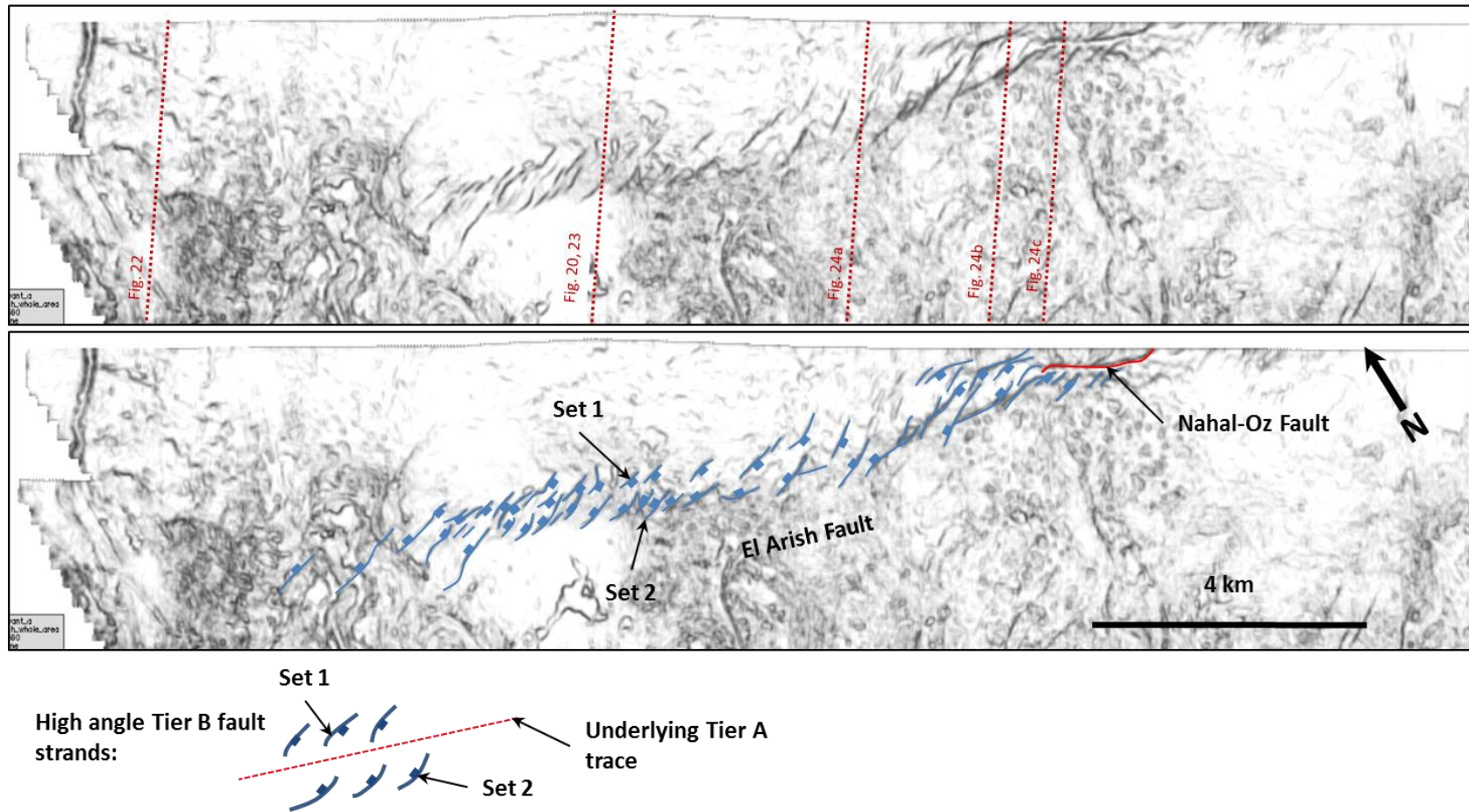


Figure 4.21b - The EAF at the seabed is characterised by two sets of en echelon Tier B fault strands oriented at a high angle to the underlying Tier A trace.  At this level the EAF trends directly into the Nahal-Oz Fault (although the NOF also shows a Tier A strand at the seabed).

145

### *4.6.1.2  Profile Sections in Detail*

The EAF is divided along strike into a central, western, and eastern region to illustrate how the fault changes from West to East (Figure 4.21 for locations).

*Western Region-*

Profile sections along western region (Figure 4.22) display all three deformation tiers, with Tier A maintaining a sub-vertical fault strand.  Tier B faults do no extend up to the seabed and show a simple Y geometry, with only two fault strands splaying up from Tier A.  The splaying into the Y geometry also occurs in an MTD unit.  Reflections in the Messinian Evaporites show little evidence of disruption and therefore the Tier C strands appear shorter (less than 200m).

*Central Region-*

The central section is the most developed with Tier B faults reaching the seabed and the Tier C faults shown more clearly in Unit 2.  Large variation occurs laterally between profile sections with less than 1km between them (Figure 4.23).  Despite the large variation, each section shows the clear Tier A, B, and C hierarchy described in the overview.  Tier A strands often show a curvilinear or undulating trace, forming localised regions where the fault is not sub-vertical, instead dipping steeply.  Tier B strands show the largest variation, with a different number of faults that splay off each other and from the Tier A fault strand in each profile section.  The strands always reach the seabed to form scarps, however, it is not consistent which fault strands reach the seabed, with only splays reaching the seabed in Figure 4.23 whilst the two major strands reach the seabed in Figure 4.20.  Interestingly, all sections show the transition from a Tier A to a Tier B geometry occurring in an MTD unit (in the central region).  The Tier C faults extend further into the Messinian Evaporites in the central region (up to 1km) and also show more than two fault strands in some cases (Figure 4.23).  Interestingly, the location of the Tier A/B node shows little variation across the central and western regions, signifying that height of the Tier A remains the same, despite changing heights of the Tiers B and C fault strands.

Although section 4.6.2. focuses on the displacement distribution, it is important to highlight the apparent dip-slip variation across the EAF.  For example, at Tier A, the reflections show

little apparent dip-slip offset.  However, at Tier B, apparent dip-slip values of up to 20ms TWT are observed, with an increase in offset occurring upwards from Tier A towards the seabed.

*Eastern Region-*

The eastern region is bounded by the relay faults with the Nahal-Oz Fault (NOF) and the lateral tip.  Here, seismic expression of the EAF becomes less developed with progression eastwards.  For example, Tier B fault strands deform the seabed near the relay fault (Figure 4.24a), however towards the east, the upper fault tips plunge down section.  Furthermore, fewer splays form from the reduced size of Tier B strands, producing a more explicit 'Y' geometry (Figure 4.24b).  Disruption of the evaporite layer also reduces eastwards, and the Tier C faults therefore appear to reduce in length eastwards.

The eastern fault tip location is difficult to pinpoint as the discontinuities in seismic reflections that define the fault become less apparent (Figure 4.24c).   For example, the easternmost profile section shows little evidence of the reflection discontinuities; however, small folds in the reflections do occur, allowing the inference that the fault is likely present, and the fault is beneath the limits of seismic resolution.  The significance of this interpretation is that the eastern lateral tip of the fault may continue beyond the interpretation and the actual length is therefore longer than 16km.

*Nahal-Oz Fault*

The NOF (Figure 4.24b, c) displays a considerably different geometry from the EAF.  Most noticeably the Tier A strand is highly sinuous with distinct undulations forming a thicker fault zone, which extends up to the seabed.  This is a critical observation, which will become more apparent with descriptions of the Afiq Fault.  The Tier B faults do not splay as widely from Tier A, forming a thinner, asymmetric 'Y' structure.  The apparent dip-slip movement on the NOF is larger (up to 35ms TWT), and also forms scarps along the seabed, showing that it is currently active.

### *4.6.1.3  Plan View in Detail*

Two additional coherency slices are shown here to elucidate the change in the internal geometry of Tier B.  The bottom slice at 1820ms TWT is located less than 100m (100ms TWT) on average above the Tier A/B boundary and therefore depicts the Tier B strands close to the splay point (Figure 4.25a), whilst the upper slice at 1700ms TWT is located around 120m above the former (and 340m below the seabed shown in the overview) and depicts an intermediate stage of Tier B faulting (Figure 4.25b).

The lower stage of Tier B faulting is characterised by right-stepping, short en echelon segments (c. 500-600m) that form conjugate pairs that dip towards the underlying Tier A strand (Figure 4.25a). They trend on average at N110°, or 4° from the underlying through-going fault trace, and therefore form a low angle relationship.  Interestingly, a small conjugate, dextral fault that is offset by the EAF also shows Tier B fault strands at a low angle to its underlying fault Trace of Tier A, whilst the NOF shows a dominantly Tier A geometry.

The intermediate view of Tier B faults shows both low angle and high angle Tier B fault strands (Figure 4.25b).  The high angle faults trend on average N064° in the central region, N086° in the western region, and N072° in the eastern region, and corresponds to angles of 46°, 28°, and 53° with the main fault trace, respectively.  Notably, there is a significant difference in divergence angle at the central region here from the seabed.  The low angle Tier B faults (especially noticeable in the central and western regions) trend N106° on average, with an average angle of 8° to the main fault trace, which is a larger angle than at 1820ms TWT.

When the low angle Tier B strands are concentrated towards one side of the underlying fault, it coincides with Tier B strands that are oriented at a high angle to the underlying Tier A trace (Figure 4.25b).  This phenomenon switches sides along strike of the Central Region of the EAF, and the side of the fault with the low angle strands is termed the 'dominant side of the fault'.  This geometry combined with the 3D views in the subsequent section provides integral clues to the upward propagation of the EAF, which is explained in section 4.6.3.

The high angle faults shown here are interpreted as the same faults from the seabed, whilst the low angle faults are interpreted as the same fault strands as the 1820ms TWT slice based on their similar geometries. This signifies that an increase in divergence angle occurs upwards on a Tier B fault and suggests that a rotation upwards occurs in an anti-clockwise motion on the low angle faults. The noticeably lower angle of the high angle Tier B faults in the central region is attributed to the strands being imaged in mid-rotation from the underlying low angle Tier B geometry.

*The NOF-*

The NOF does not show the well-defined Tier B geometry as observed in the EAF (Figure 4.21, Figure 4.25b). Although it could be argued that the NOF transitions to the EAF at the seabed, this occurs northwest of the relay zone. A small segment of a Tier A fault can be observed at the very edge of the dataset, suggesting that it continues for several kilometres beyond. Therefore it is interpreted that southeast of the relay zone, the NOF acts as a separate fault that has formed a considerably different geometry, and suggests a different growth history.

### 4.6.1.4   3D Geometry of Tier B Faults

The geometry that links the Tier B fault geometry described above is elucidated using 3D visualisation software GeoViz (Figure 4.26). Several Tier B faults were mapped and show that a single fault can exhibit both low and high angle relationships with the through-going fault, depending on distance upwards from the Tier A strand. Each fault strand maintains a similar length at the basal and upper tips; however, it is unclear if the fault strands are separate at the point of divergence from the Tier A geometry, or if they diverge as one long fault along strike before quickly splaying into shorter segments.

In Figure 4.26, the faults were mapped individually downwards to Tier A, because the interpretation was conducted from the seabed, where the faults are clearly separated. However, this produces a bias in the interpretation because at the base of the Tier B geometry, there is no coherency image to confirm that each fault is separate until the Tier A geometry. However, given that the EAF propagates upwards (this is discussed in 4.6.3.), the

Tier A strand must have been deflected from vertical before splaying into the individual Tier B strands (in a progressive manner), therefore forming a geometry summarised in Figure 4.26d.

For simplicity, only fault strand 5 is shown dipping in the opposite direction (northwards); however, it does allow an interpretation to be made as to how the two sides of the Tier B geometry interact. Fault 5 forms a low angle orientation at its basal tip before rotating upwards to form a high angle orientation at the upper tip. Fault strands 1 – 4, however, are the 'dominant side of the fault', showing a similar rotation over a greater height. Therefore the side that splays from the original fault must undergo the same amount of rotation in a shorter vertical distance.
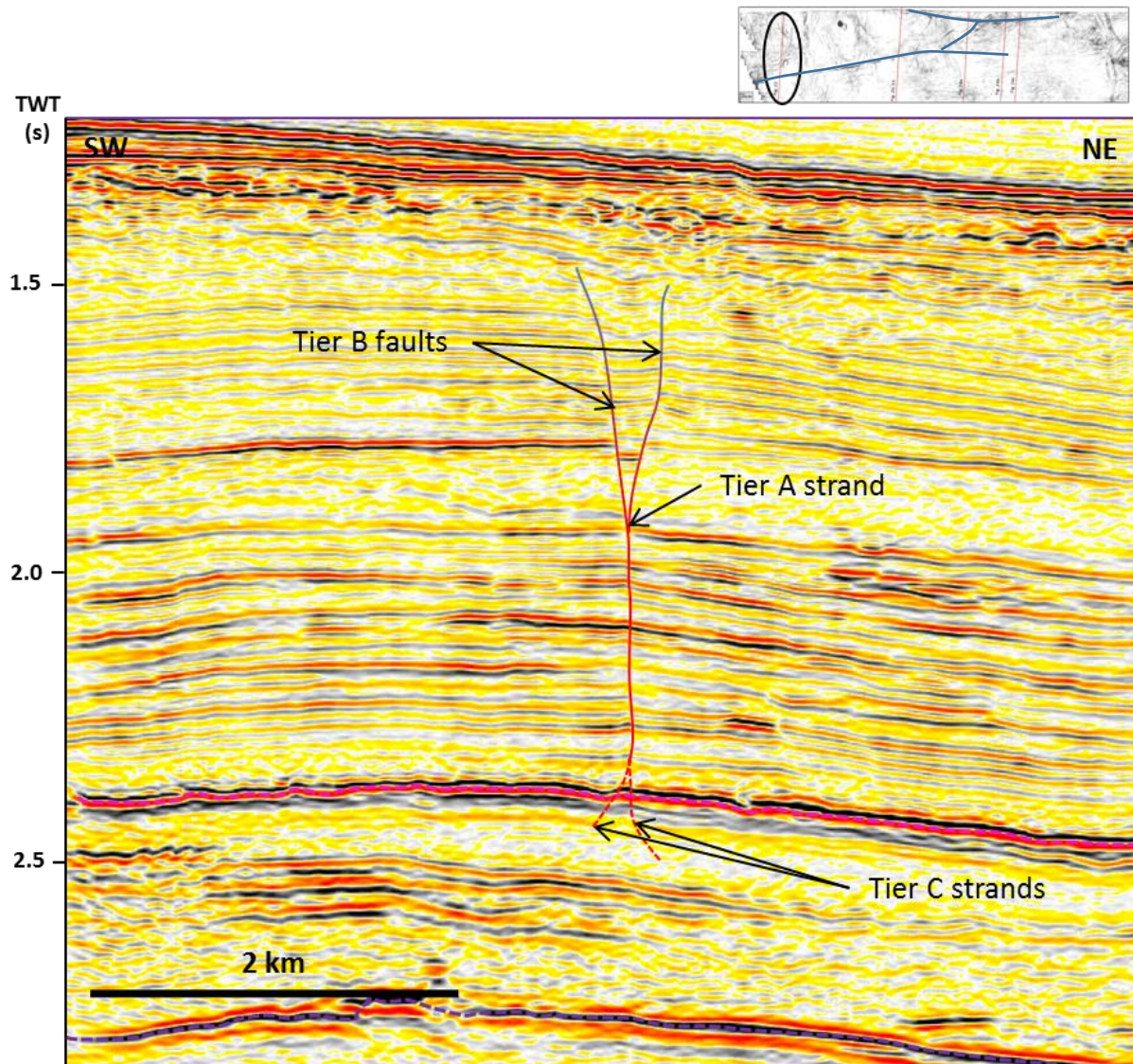
Figure 4.22 - View towards the western region of the EAF.  The structure is simpler, with fewer splays in the Tier B geometry and shorter Tier C strands.  The upper tip of the EAF has therefore plunged below the seabed in this region.  Note the splay between the Tier A and Tier B strands occurs at an MTD.
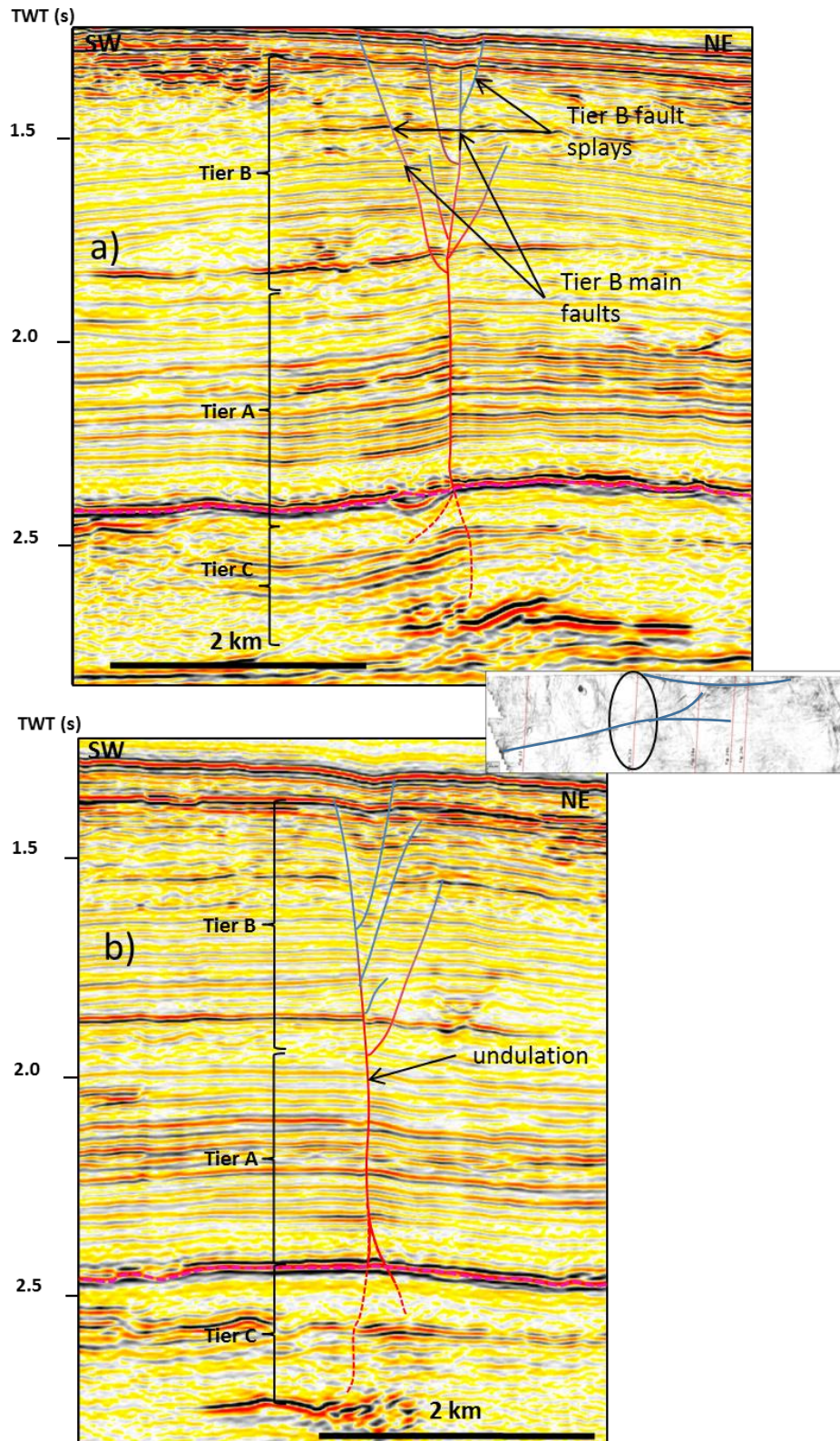
Figure 4.23 - Two profile sections located less than 1km either side of Figure 4.20 highlight the large variation that occurs in a short lateral distance. Although the basic Tier structure is consistent, the amount of Tier B and C splays is highly variable. Note the transition from Tier A to Tier B occurs at an MTD.
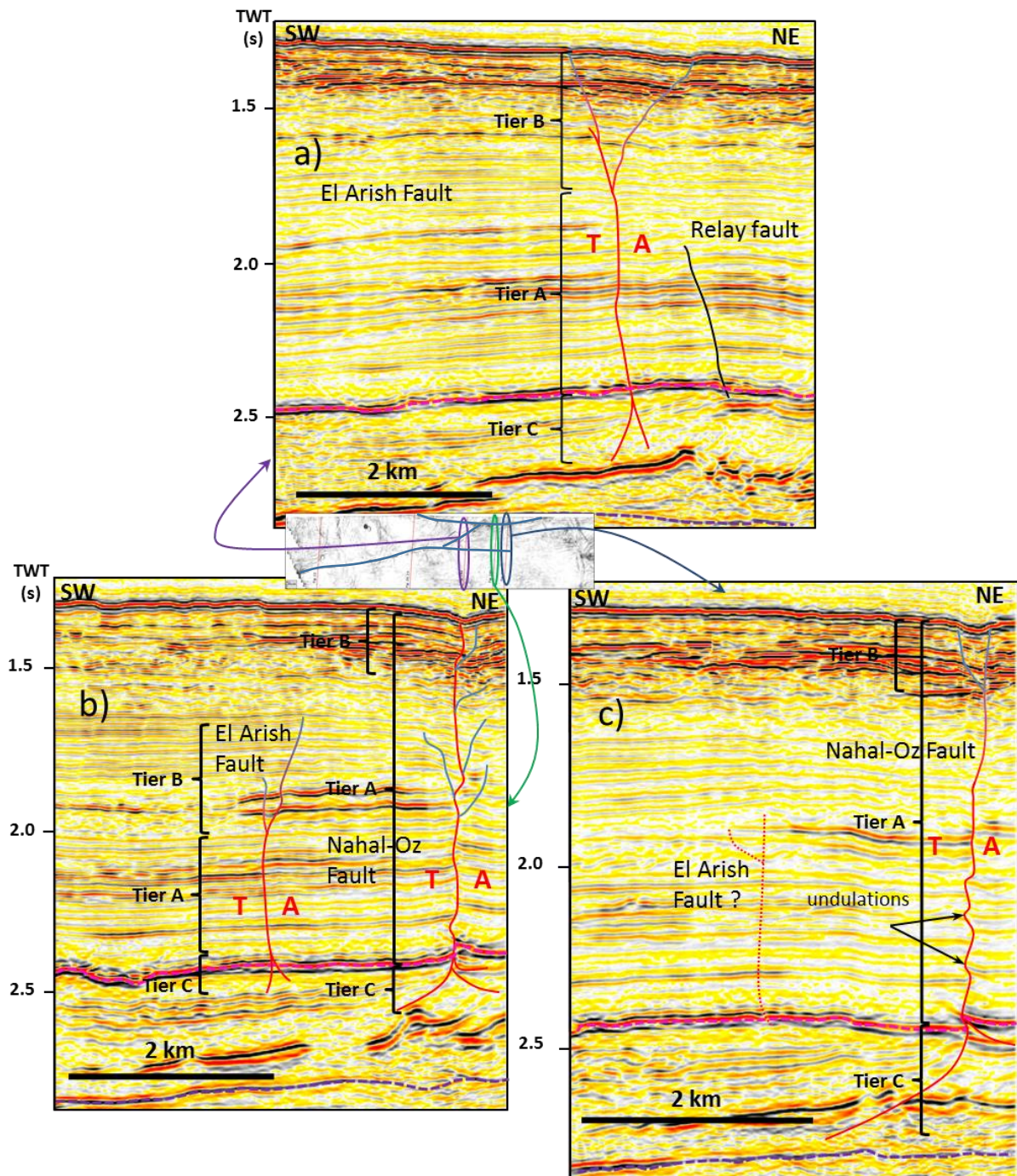
Figure 4.24 - Profile sections of the EAF from the eastern region. With further distance east, the EAF plunges below the seabed and by (c), the fault cannot be confirmed with a high degree of confidence as it falls below seismic resolution. In (b) and (c), the Nahal-Oz Fault (NOZ) is also observed to show a very different structure, with Tier A extending to the seabed in addition to the Tier B fault strands. The importance of this change in Tier morphology will be explored further with the Afiq Fault.

153
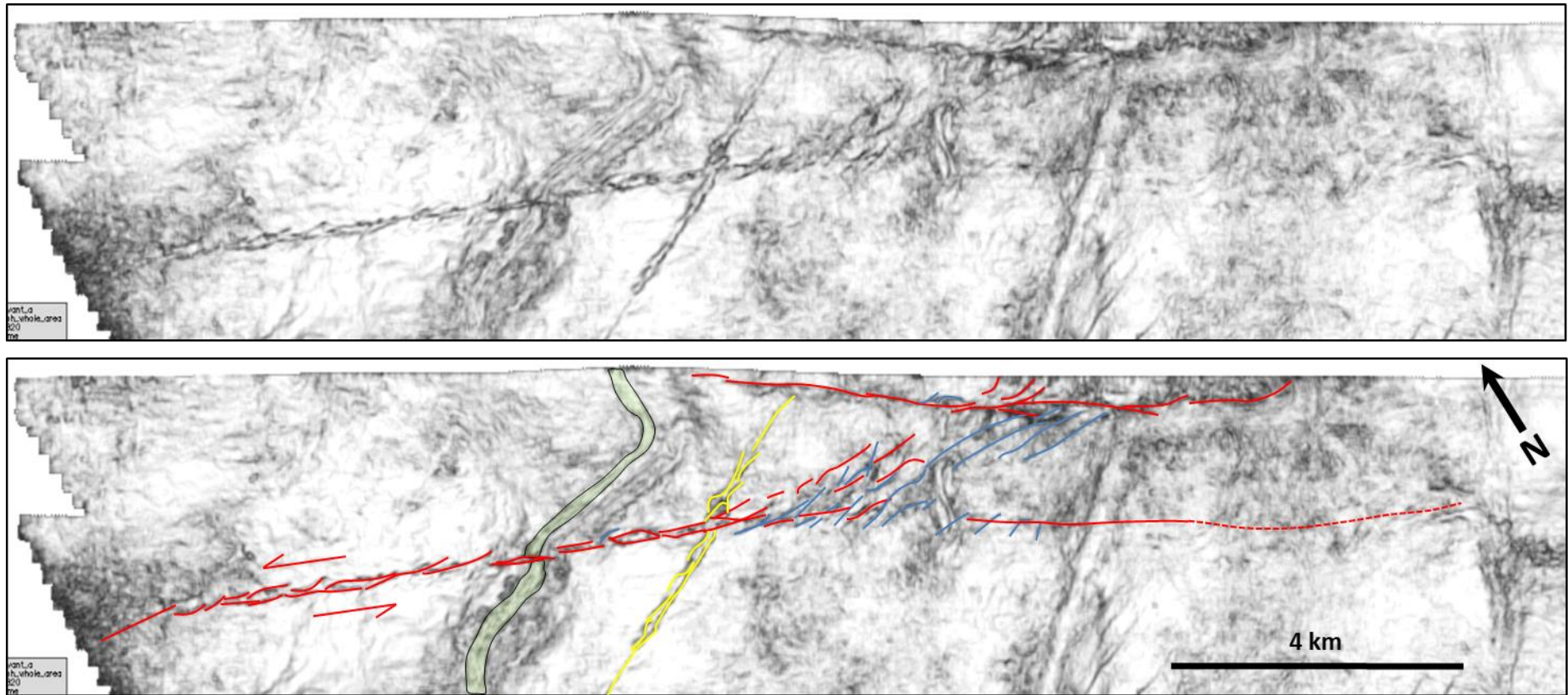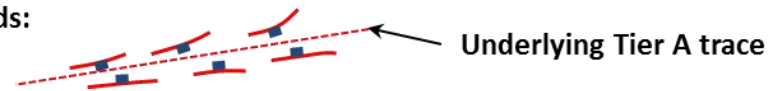
Figure 4.25a - El Arish Fault (*depth- 1820ms TWT*).  Tier B faults are oriented at low angles to the underlying Tier A trace.  Also observed is a channel that shows a clear offset of 140m, and a dextral fault also displaying into a Tier B geometry.
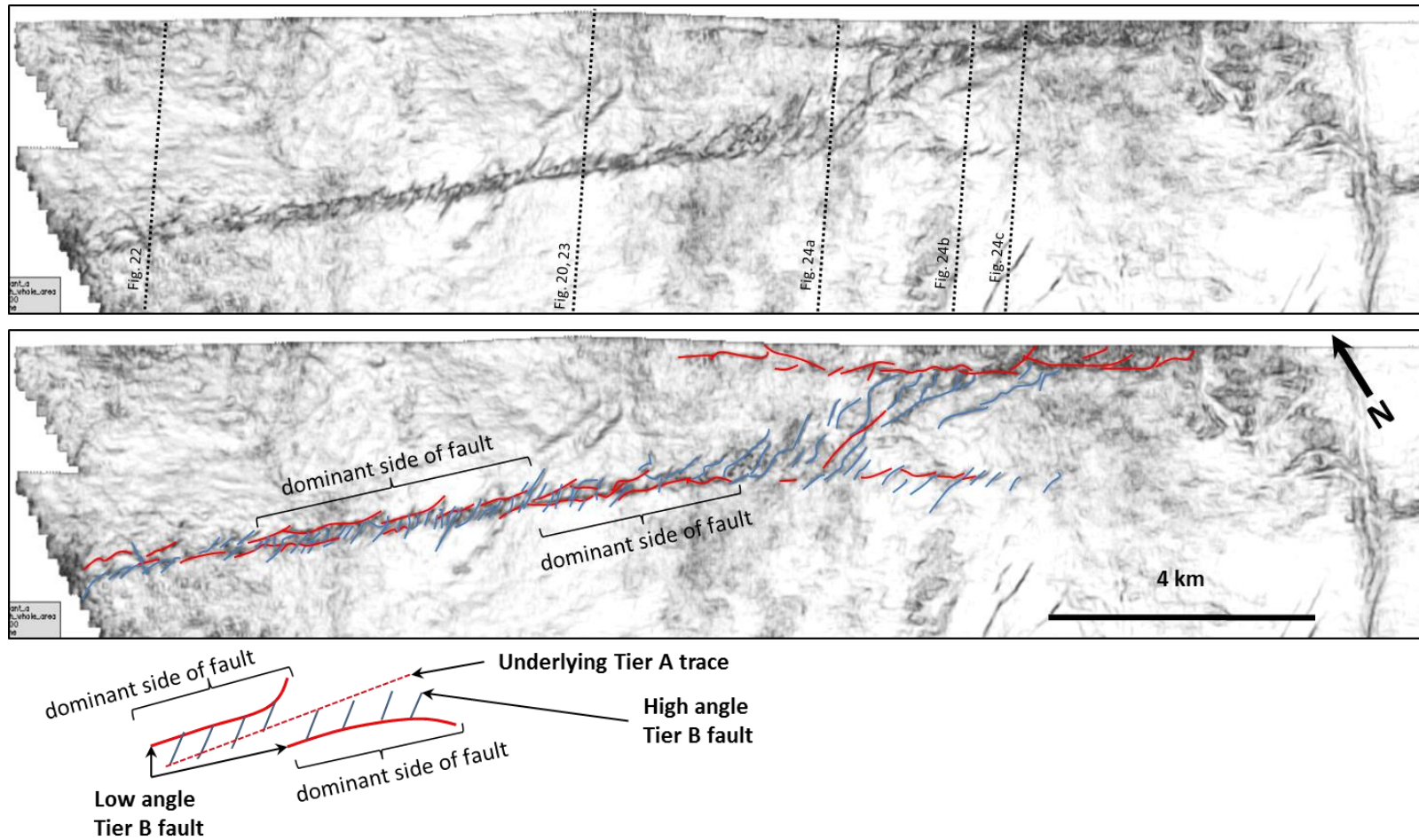
Figure 4.25b - El Arish Fault (*depth- 1700ms TWT*).  Tier B faults are oriented at both low and high angles; with one side showing a low angle Tier B and the other side showing a high angle Tier B fault.  This phenomenon switches sides along strike and is termed the 'dominant side of the fault' for the side with low angle Tier B geometry.
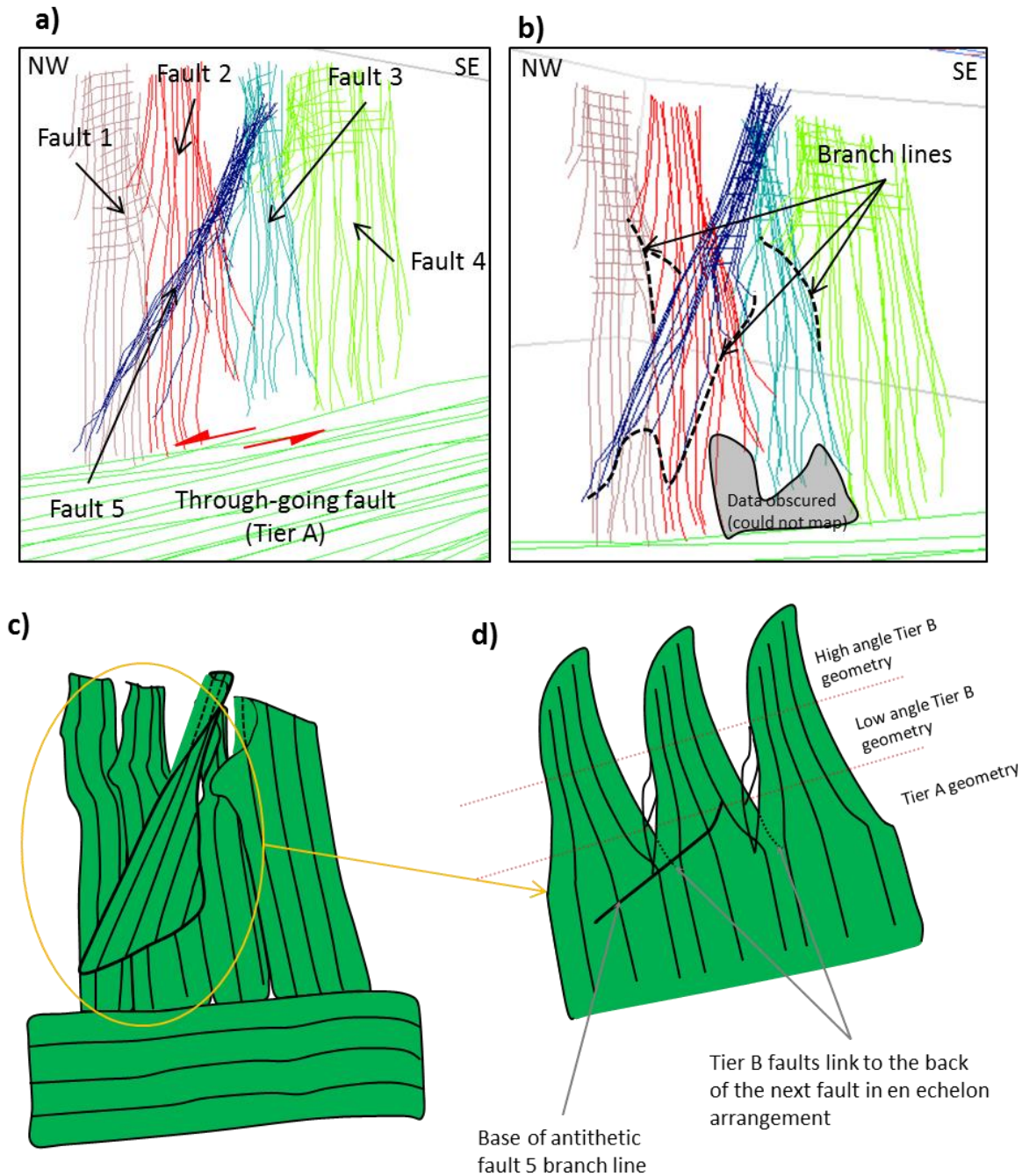
Figure 4.26 - View of Tier B faults using GeoViz. Although the fault sticks show individual, thin faults that branch from the Tier A fault, this may be an artefact of interpretation as faults were mapped downwards from the seabed to meet the Tier A strand. Therefore the interpretation fails to account for a single Tier A strand branching upwards into the Tier B geometry as observed in profile section. Therefore the cartoon in d) depicts a more likely geometry based on all observations, where Tier A branches into separate Tier B segments upwards.

### *4.6.1.5  Geometry Synthesis*

Combining the observations from coherency slices, profile sections, and GeoViz there is a clear change in Tier B morphology from low angle fault strands near the Tier A/B boundary to high angle fault strands at the seabed (Figure 4.26c, d).  Observations derived from profile sections do not document this rotation; however, they do show that both the main Tier B faults and subsequent splays reach the seabed.  However, not all of the Tier B main strands reach the seabed, signifying that the striking pattern formed by the two en echelon sets is a combination of both main strands and splay faults, with each type rotating away from the trend of the underlying Tier A fault with increased height upwards.

The upper tips of the El Arish Fault clearly changes along strike by plunging below the seabed in the western and eastern region suggesting the fault height decreases at the tips.  This is further corroborated by the reduced length of Tier C detachment faults, suggesting a plunging upwards of the basal tips.  Importantly, the plunging vertical tip in the Western Region suggests that the lateral tip should occur within a few kilometres outside of the dataset limits.  Despite the reduction in fault height of both the Tier B and C strands towards the lateral tips, the height of Tier A actually maintains a roughly uniform height across the entire fault.  Conventional faults reduce in size towards the tips (Walsh and Watterson, 1988), and a constant height in Tier A may suggest that the lateral tips may extend well beyond what can be visualised in the seismic data.  Given that vertical features are poorly imaged in seismic data, a threshold fault zone width would be required to be actually imaged, and this may explain why the eastern tip was difficult to constrain.

The basal tip geometry of a strike-slip fault has never been reported in any previous study and it can be summarised that the length (in profile section) of the extension of the Tier C strands appear to penetrate deeper into the evaporites towards the EAF centre (laterally) and very little penetration towards the lateral tips.  This suggests that the fault has developed a stronger 'root' system underneath Tier A and therefore it is expected that larger offsets across Tier A would correspond to longer and more defined Tier C strands.  Although the 3D geometry cannot be imaged, it is envisaged that they may also splay and grow in a rotational manner, similar to the Tier B fault geometry.  This would explain why there is large variation in the number of fault splays in each profile section beyond the main two detachment faults (Naylor et al., 1986).  Given that the Tier C strands are propagating into a more ductile medium than

157

Tier B strands, the strands likely diffuse at the mechanical contrast and thus probably develop into a more ductile shear zone within the evaporite sequence rather than a discrete fault.

### 4.6.2   Strike-Slip Displacement Distribution

This section begins by highlighting some of the observed kinematic indicators and their importance towards the understanding of strike-slip fault kinematics before presenting the displacement distribution plot and corresponding analysis.

#### 4.6.2.1   Kinematic Indicators

The maximum  measured offset across the EAF was 185m, a very low value considering the long length of the fault (at least 16km).  However, it is important to note that there was a large source of error on a kinematic indicator preserved into the Top Messinian Unconformity (the M reflection) which was recorded as 150m but may be up to 200m, due to a large degree of uncertainty (Figure 4.27).

The error is important as it signifies that the largest offset across the EAF is potentially located at the M reflection instead of in Unit 3 at 2040ms TWT (Figure 4.28).  This would shift the maximum offset downwards to near the detachment level, and would suggest a considerably different growth history.  However, given that the Afiq Fault also shows a lower offset at the M horizon (described later), it is interpreted that the offset recorded here is lower than the displacement maximum of 185m.

A variety of kinematic indicators from Tier A at the 2040ms TWT slice (Figure 4.28) include MTD grooves which cross the El Arish Fault, two relay fault splays, and a dextral fault (also represented by a Tier A fault strand) as well as meandering channel scarps.  The largest offset was recorded by the MTD grooves at 130m; however the splays show offsets of 120m and 90m, which is high considering their short length (approx. 2km from separation with the EAF).  The dextral fault shows offsets of 70m, which is relatively high given its short length (less than 5km compared to the minimum 16km length of the EAF).

Kinematic indicators at the lower region of Tier B (1820ms TWT) show offset channels of up to 140m across the EAF (Figure 4.25a). This provides a critical insight into the kinematics of the Tier B fault strands as the strike-slip offsets are not significantly less than across the underlying Tier A strand (Figure 4.28). However, up-section kinematic indicators (Figure 4.29) show no resolvable strike-slip movement (where the Tier B faults are oriented at high angles to the through-going fault). Interestingly, if no horizontal offset across the upper tips of the Tier B strands, the dip-slip movement recorded in profile section is not an apparent value, as observed across the rest of the fault.

Given the observation of increasing dip-slip displacement in Tier B strands coupled with decreasing strike-slip displacement, Tier B faults are therefore interpreted to change sense of movement with distance from upwards from the Tier A fault strand. To summarise: Tier A faults are dominantly strike-slip movement across the entire strand, whilst Tier B faults are dominantly strike-slip at low angle to the through-going fault, and become dominantly normal faults at high angles to the through-going fault (Figure 4.30).

Kinematic indicators also cross the NOF fault show a clear sinistral slip, however, the magnitude of offset cannot by accurately determined as the channel levees are poorly imaged. Nevertheless, the kinematic indicators constrain offset to between 300 - 600m, signifying that the NOF exhibits considerably larger offsets than the EAF (Figure 4.28).
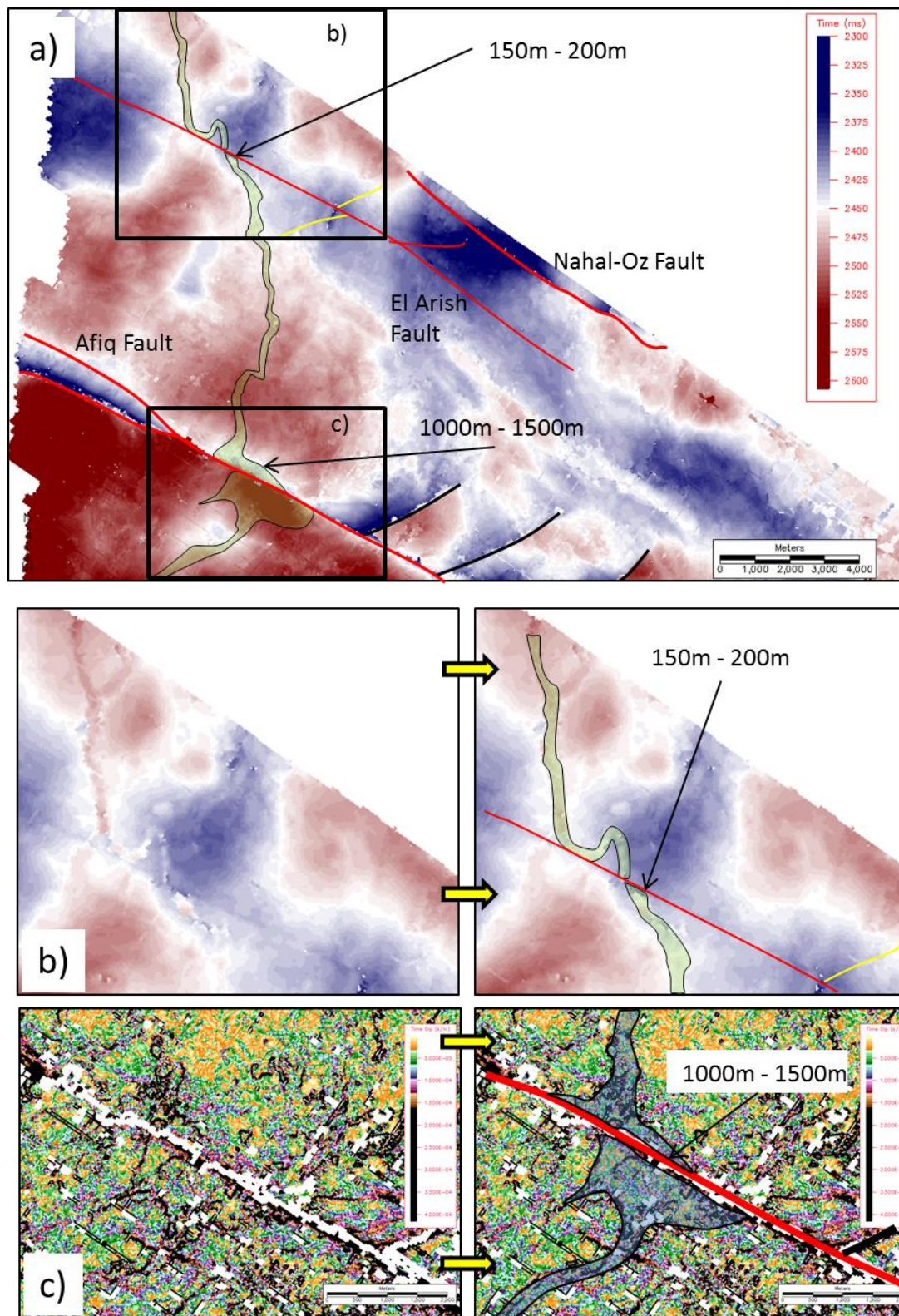
Figure 4.27 - View of a kinematic indicator (a submarine channel) that is offset across both the EAF and the Afiq Fault, but cannot be very accurately constrained.  Given that the offset across the Afiq Fault is considerably less than its maximum offsets (1000m – 1500m measured in c, whilst the Afiq fault $D_{max}$ = 2900m, see Figure 4.49), the EAF is interpreted to show a lower offset of 150m.

160
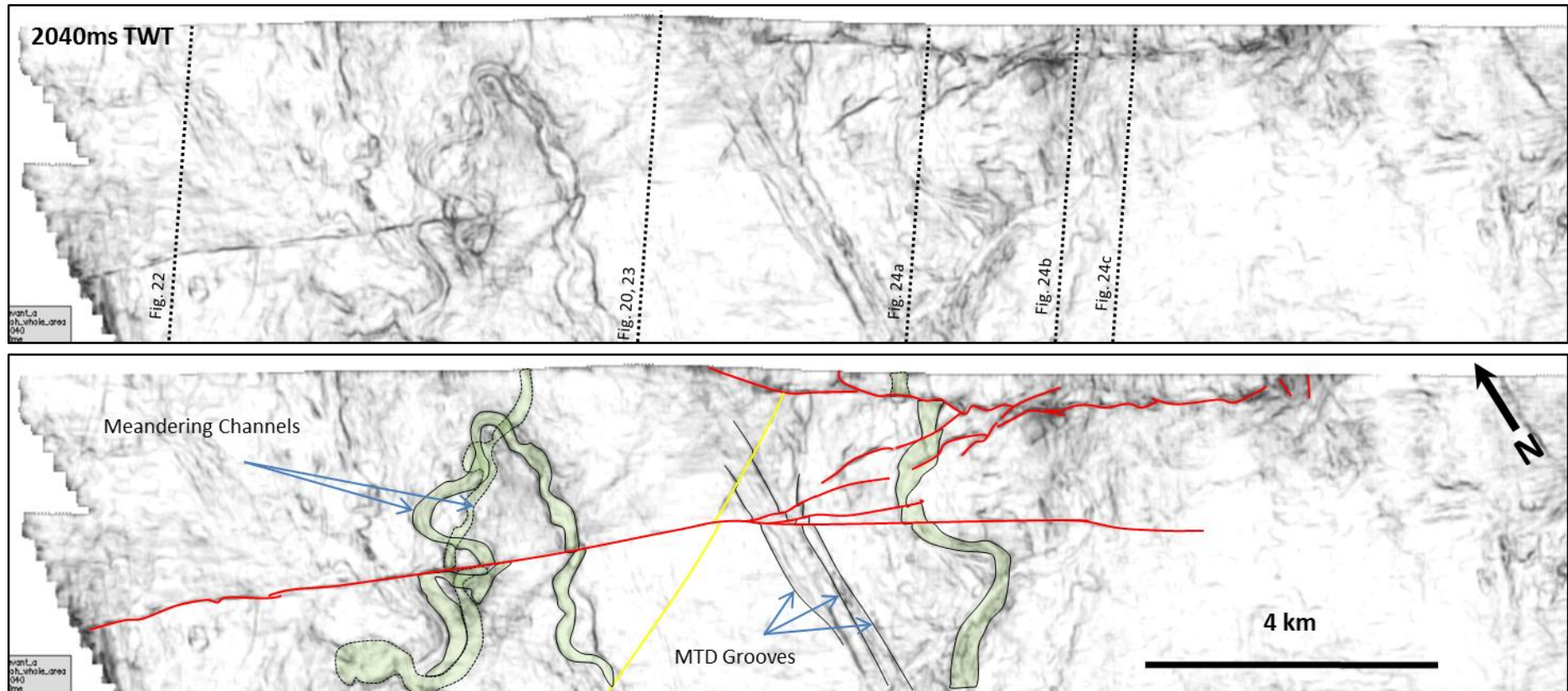
Figure 4.28 - (*depth- 2040ms TWT*). View of the EAF in a Tier A geometry with various kinematic indicators offset across it.  These include submarine channels, MTD grooves, and a dextral fault (in a Tier A strand).
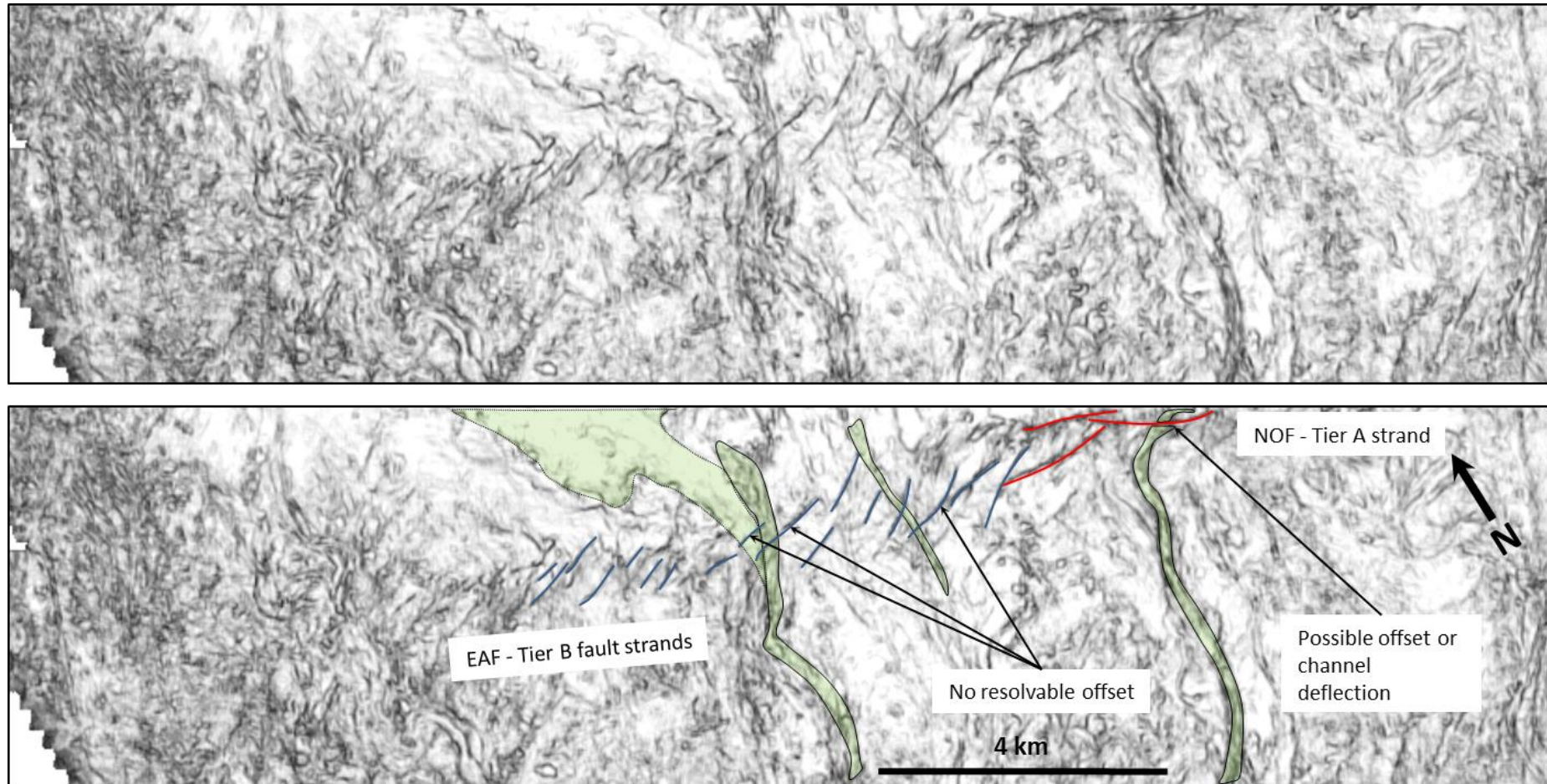
Figure 4.29 - Kinematic Indicators across the EAF and NOF (depth- 1400ms TWT) show 0m offset across Tier B stands oriented at a high angle to the underlying Tier A trace.
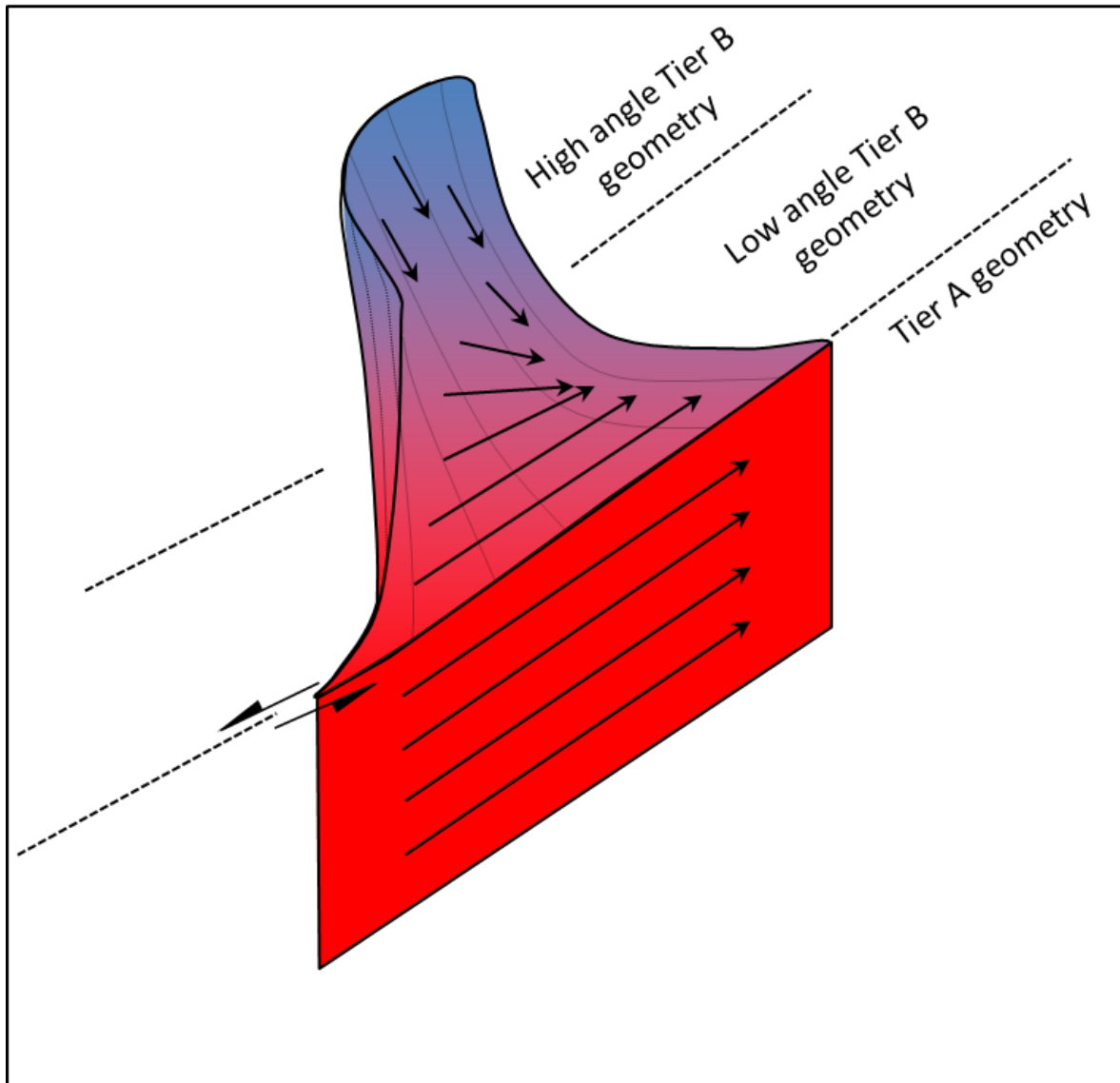
Figure 4.30 - Schematic of El Arish Fault slip vectors, showing the relative orientation (direction of arrow) and magnitude (length of arrow) for the different fault geometry.  At the Tier A strand, slip is almost entirely strike-slip as well as showing the largest offsets.  As the fault transfers to a Tier B geometry, there is a gradual reduction in strike-slip slip magnitude, whilst the dip-slip remains about constant. This corresponds to a change in the slip vector orientation, and by the upper tip of the Tier B fault, slip vector becomes vertical, denoting entirely dip-slip (normal) movement.  Note the colours reflect a change from sinistral strike-slip (red) movement to dip-slip (blue) movement.

#### *4.6.2.2   Displacement Distribution Plot*

The contoured distribution plots are presented in both two-way time (Figure 4.31) and in depth to more accurately show fault shape in the evaporites (Figure 4.32).  Both plots show a crudely elliptical fault plane, in agreement with the geometric descriptions.  It is important to note that the data is sparse at the basal tips and relies almost entirely on profile observations to approximate the tip line loop.  The plot is also limited by the fault continuing outside of the dataset limits towards the northwest, and as such, the plot forms a "three-quarter" ellipse with the presumed remaining "quarter" outside of the dataset limits.

The most intriguing feature is the occurrence of two displacement maxima depicting regions of displacement greater than 150m.  The maximum towards the northwest is much larger and extends downwards towards to the M horizon, and appears to be located deeper than the southeast maximum.  However, this may be due to a lack of kinematic indicators at the M horizon underneath the southeast maximum.  A third, smaller offset maximum (100m) occurs towards the southeast tip and beyond the relay faults with the NOF and splay faults.

The two maxima could be attributed to measurement errors due to resolution in the intervening piercing points, or that the EAF started as two major segments that have linked together to form one major fault.  Given that there are three points showing less offset at two different intervals, with a minimum of 35m between the nearest points, it seems unlikely that this is a seismic artefact, and are therefore interpreted to have formed by fault linkage.  Interestingly, they are closely spaced, suggesting that the two segments would have interacted early on whilst lateral propagation continued radially for several kilometres along the free tips.

The slight depth difference between the two maxima may suggest an element of dip linkage occurred concurrently with lateral linkage, and therefore the two segments may have initiated at slightly different locations, however, this would be no more than 40ms (40m), which is small considering the overall height of the fault.  Furthermore, it cannot be constrained that the southeast displacement maximum does not extend deeper and therefore the displacement maxima are interpreted to have developed in the same stratigraphic package.

The small maximum towards the southeast may suggest that the EAF is comprised of another fault segment. However, this is difficult to constrain as there are no kinematic indicators located directly between points to confirm an offset minimum, and is therefore not interpreted as such.

Importantly, the displacement distribution plot projects all offsets onto a single fault plane in order to maintain simplicity. For example, the kinematic indicator crossing two low angle Tier B faults (Figure 4.25a) is the total offset across two faults and it is unknown how displacement is shared between the two faults. Thus this plot incorporates total offset measurements from both Tier A and Tier B faults. This results in the 0m contour line of strike-slip (horizontal) offset that does not correspond to the tip line loop shown in normal faults (Watterson, 1986). The area between the two lines represents where Tier B faults comprise entirely dip-slip movement and are oriented at a high angle to the underlying Tier A fault.

Finally, no significant change in displacement occurs where the Tier A/B boundary line crosses the plot, confirming that a fault splaying from a Tier A to a Tier B geometry undergoes a gradual reduction in strike-slip movement rather than undergoing a sudden decrease.

*Displacement Gradients and Aspect Ratios-*

Both the shape of the EAF and its displacement gradients show significant differences from normal faults and therefore a 1:1 scale is presented along with both horizontal and vertical displacement distance (d-x) plots (Figure 4.33). The horizontal d-x plot shows a rough cone shape (C-type) profile across the majority of the EAF length, with very distinctive C-types occurring around the two displacement maxima (based on the classification by Muraoka and Kamata, 1983). The horizontal gradient averages 0.02, although this value increases between the two maxima. The vertical plot exhibits a C-type profile across the fault with much higher gradients: the centre to upper tip gradient is 0.31 and a centre to basal tip gradient is 0.28, and therefore the vertical gradient averages c. 15 times greater than the average horizontal gradient.

Visualising the fault at a true scale also shows that the aspect ratio is very high when compared to field scale normal faults, which averages 2:1 (Nicol et al., 1996).  When the maximum height of 1200m and the measured length of 16km are applied, a minimum aspect ratio of 13.3:1 is calculated.  However, the EAF likely extends to over 20km when including the region of the fault that lies outside of the dataset limits, and thus a more reasonable aspect ratio when considering this fact is c. 17:1.

The large difference in gradients between the lateral and vertical axes suggests a high degree of vertical restriction on the fault.  At the basal tip, restricted growth is conceivable due to the Messinian Evaporites, whilst the upper tip is liklely restricted by propagation directly to the free surface.  Given the higher gradient for the upper tip, it is interpreted that upward propagation has been restricted at least for some parts of its growth history and therefore the EAF has undergone some element of syn-sedimentation propagation.  However, determining the extent of syn-sedimentation versus blind propagation with this level of data proves problematic and is discussed in section 4.8.
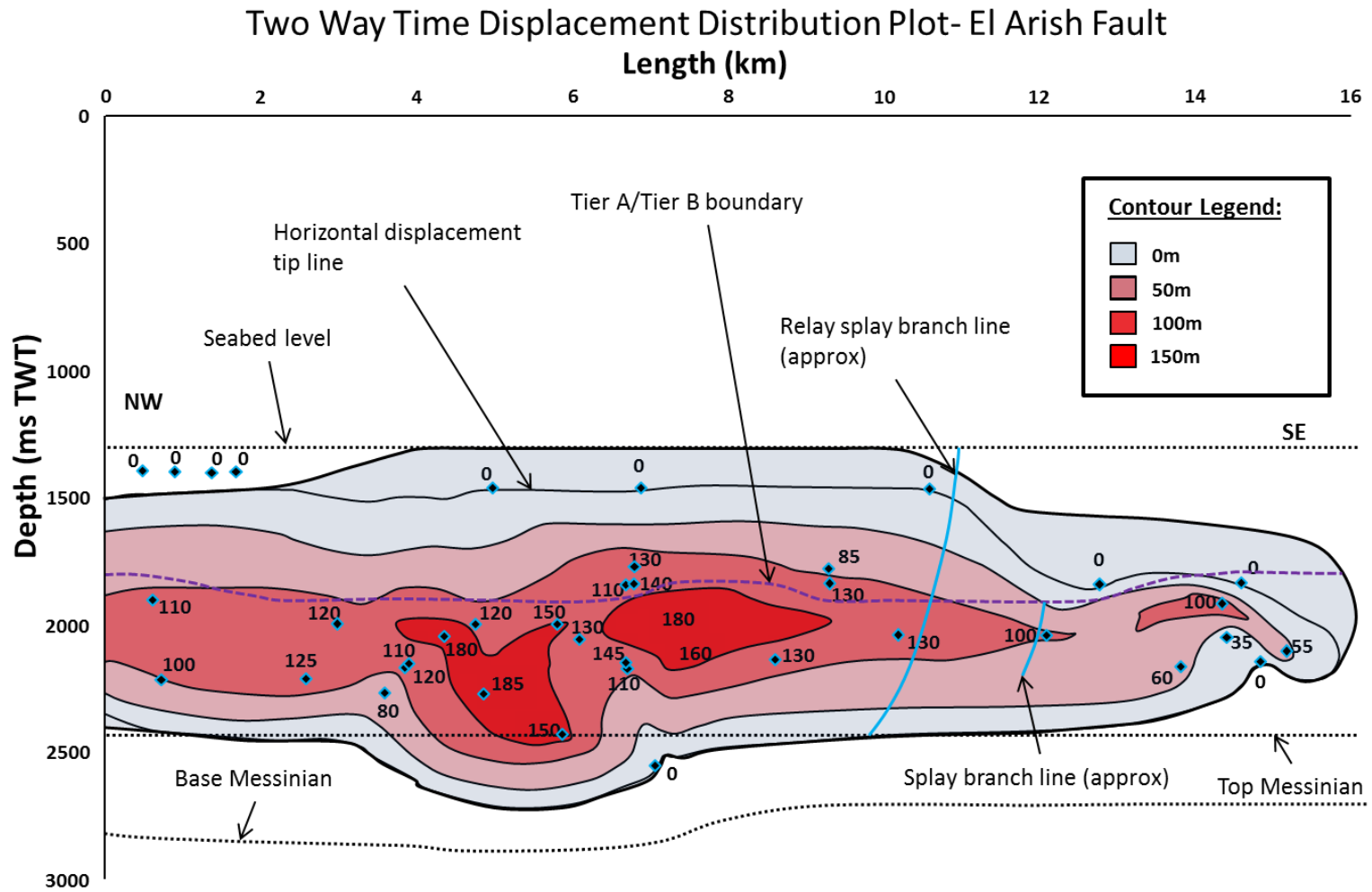
Figure 4.31 - Displacement distribution plot of the EAF with the vertical axis in two-way time (TWT) and the horizontal axis.  The contours are in 50m intervals.

# Depth Converted Displacement Distribution Plot- El Arish Fault
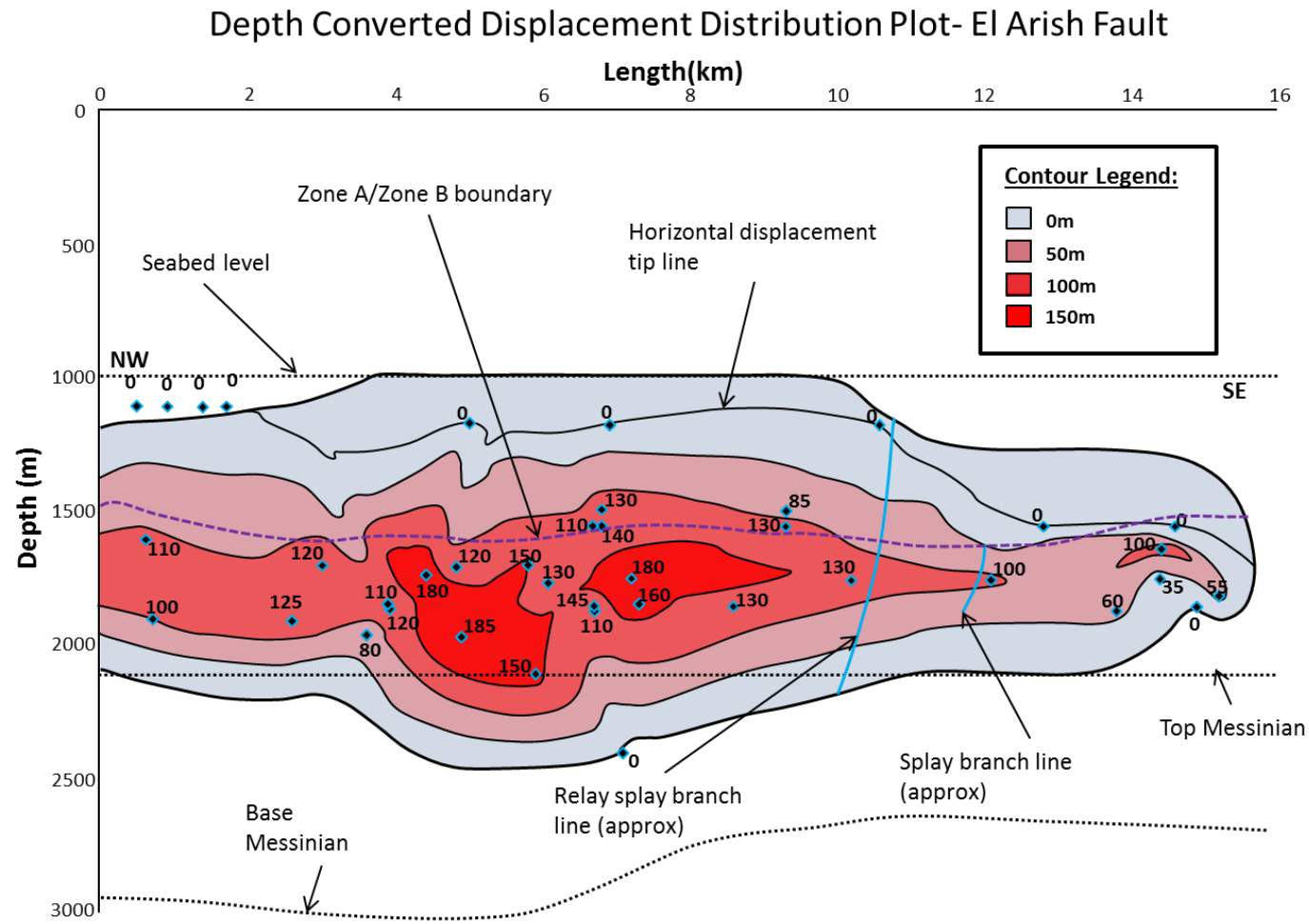


Figure 4.32 - Displacement distribution plot of the EAF.  The vertical axis was converted to depth in order to show a more accurate thickness through the Messinian Evaporites.
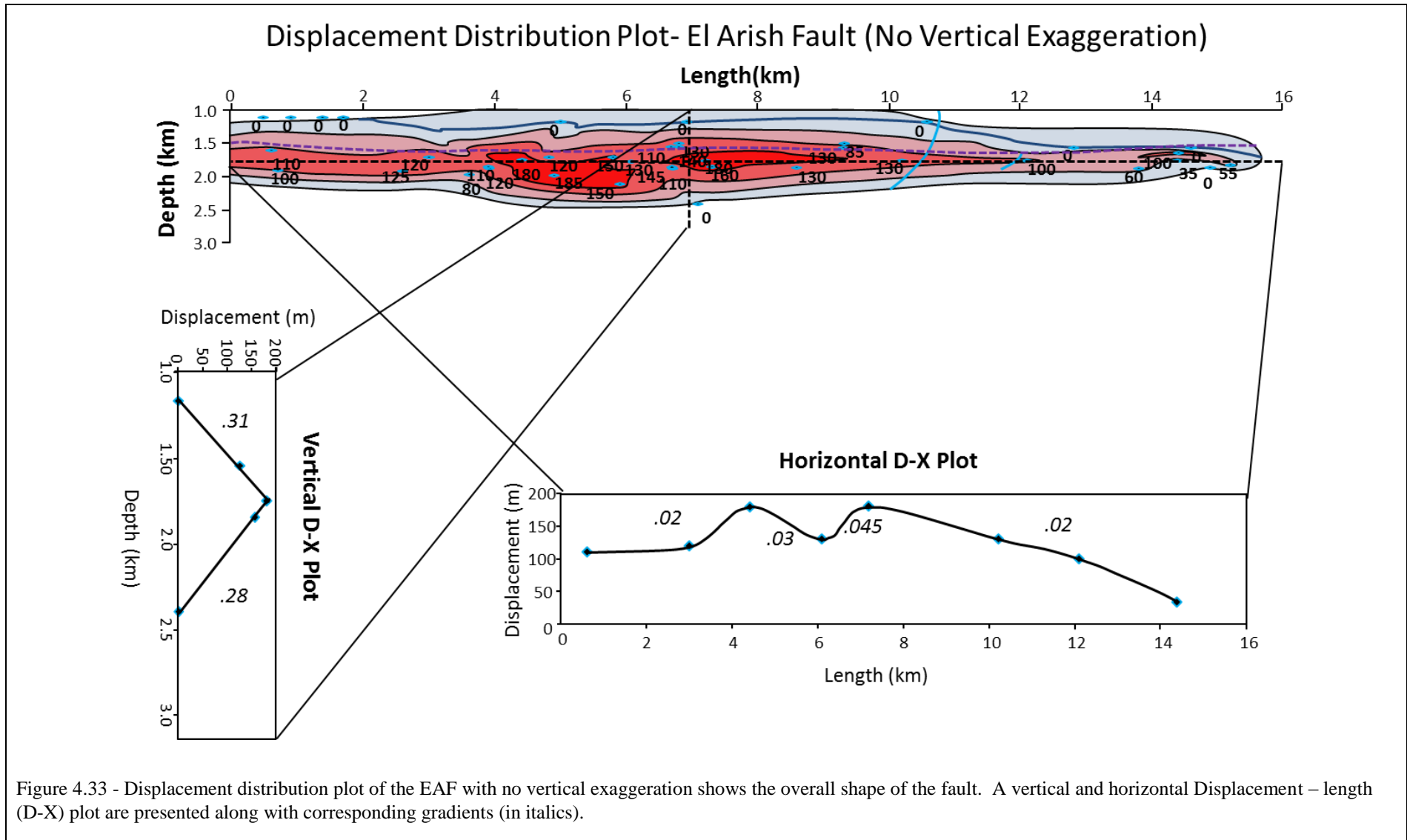
Figure 4.33 - Displacement distribution plot of the EAF with no vertical exaggeration shows the overall shape of the fault. A vertical and horizontal Displacement – length (D-X) plot are presented along with corresponding gradients (in italics).

### 4.6.3   El Arish Fault Discussion

The primary objective of this section is to propose a model for upward propagation of the EAF using the observations based on both geometry and displacement distribution analysis. In order to derive a clearer understanding of the Tier A to Tier B transition, observations from coherency slices, profile sections, and GeoViz were collated (Figure 4.34). This section also includes preliminary suggestions for the evolution of the EAF.

The gradual reduction in strike-slip offset upwards suggests that the splaying upwards is a continuous process instead of a discrete change in evolution.  Therefore, it is suggested that the Tier A strand does not splay into two Tier B faults, but is instead deflected away from vertical when propagating upwards (Figure 4.35).  This is also corroborated by the 'dominant side of the fault' geometry, which suggests a seamless transition from the Tier A to a Tier B (rather than the alternative in which Tier A arrests growth and splays to form a Tier B geometry).  This new geometry, however, requires accommodation, and forces a secondary strand to splay, producing the 'Y' shape observed in profile section.  The latter stage of upward propagation could also result in abandonment of the original fault, and a splay growing off of the secondary Tier B fault, resulting in a tertiary structure.

Extrapolating this evolutionary model into 3D, the growth of the secondary fault is most likely related to the beginning of anticlockwise rotational growth of the original fault, as it changes from a Tier A fault to a Tier B fault (Figure 4.36).  Continued fault growth results in a fault dip decrease with its strike changing to form a higher angle with the through-going fault, with distance upwards (Figure 4.36).  It is possible that the change in orientation makes strike-slip movement mechanically unfavourable, explaining why fault slip changes to normal in the Tier B geometry.

*Relative slip of Tier B faults-*

When the secondary Tier B faults splay from the original fault (i.e when the fault first forms a Y shape, Figure 4.20), it is also possible that strike-slip movement does not occur on the new splay, and it therefore acts entirely as a normal fault.  The strike-slip offset measured across low angle Tier B faults only shows a total displacement between the two strands, and therefore the relative offsets of each strand cannot be determined.  Analogue studies on pull-

apart basins show that strike-slip movement is commonly concentrated on a single fault, whilst the other fault shows dominantly normal movement, producing an asymmetric depression (McClay and Dooley, 1995; Dooley and McClay, 1997).  It is reasonable to infer that the same process occurs here; however, it also cannot be ruled out that the two fault strands share horizontal displacement equally.

*Lateral propagation model-*

The majority of the EAF propagation can be summarised as the linkage of two major segments (with a potential third segment), which have since propagated radially, and this evolution is summarised in Figure 4.37.  Notably, this evolutionary model assumes that the fault segments initiated in the same manner as classic examples of isolated, blind normal faults: the region of maximum displacement (Rippon, 1984; Watterson, 1986; Barnett, 1987). However, are these models pertinent assumptions for the EAF?  Given the regional setting within the confluence between the El Arish and Afiq Canyons, a possible mechanism for faulting is the basinward flow of salt, which may in turn affect nucleation location.  This idea will be developed further in Section 4.8 and in Chapter 6.

*Aspect Ratios compared to tectonic scale faults-*

The large aspect ratio is of interest since it differs from normal faults.  But how does this compare to other large strike-slip faults in nature?  It is possible that large strike-slip faults grow preferentially laterally than vertically, producing more highly exaggerated aspect ratios. For instance the maximum depth of the San Andreas Fault (c. 30-40km depending on crustal depth) compared to its length (c. 1300km) produces a minimum aspect ratio of c. 33:1, and is therefore more vertically restricted than the faults presented here.

### 4.6.4   El Arish Fault Summary

- Low displacement, quasi-elliptical strike-slip fault, which is defined by a single, sub-vertical fault strand (Tier A) before splaying both upwards (Tier B) and downwards (Tier C), towards the upper and basal tips, respectively.

- A major relay zone occurs towards the eastern region, linking with the NOF (a higher displacement strike-slip fault), and a southern splay that gradually dies out towards the southeast.

- The fault is composed of a minimum of two major segments which linked early in its history. Subsequent fault propagation occurred radially from the lower region of Unit 3 (where the $D_{max}$ is located).

- Tier B faults rotate upwards in an anticlockwise motion away from the Tier A strand. When oriented at low angles to the Tier A strand (in plan view), they exhibit large horizontal offsets, but when oriented at a high angle to the Tier A strand, they exhibit no resolvable horizontal offset and up to 20ms TWT dip-slip movement.

- A fault exhibiting the classical form of a Tier A geometry does not necessarily splay upwards into two Tier B faults. Instead the Tier A fault may deflect from vertical and become a Tier B fault, before a second Tier B fault splays off of it. This occurs consistently on one side of the fault for c. 3km before switching sides and defines a 'dominant side of the fault'.

- The EAF can be regarded as highly vertically restricted, with an aspect ratio (length/height) of minimum of 13.3:1.
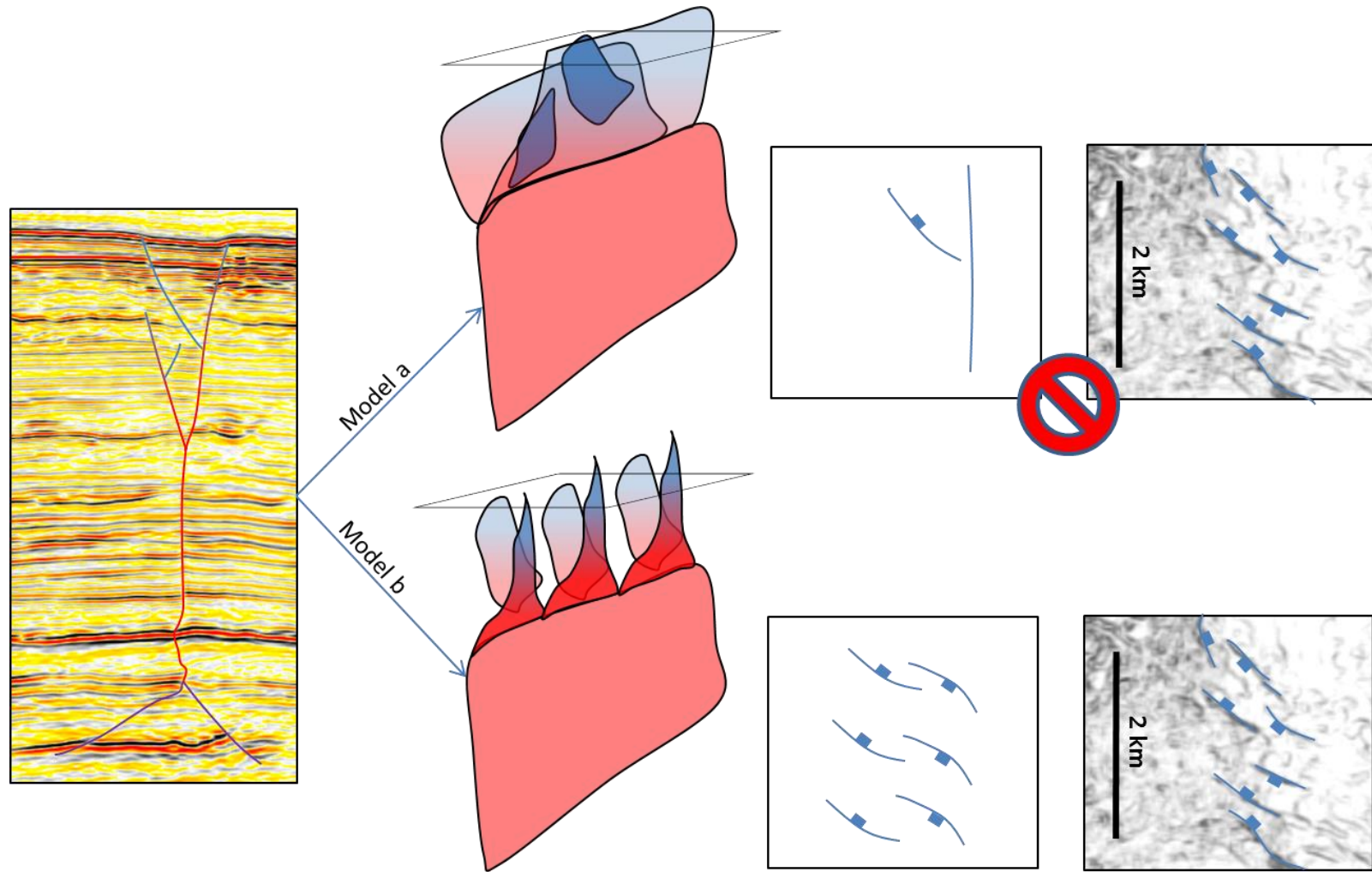
Figure 4.34 - Figure showing how a 3D model was derived using seismic profile and the geometry of coherency slices.
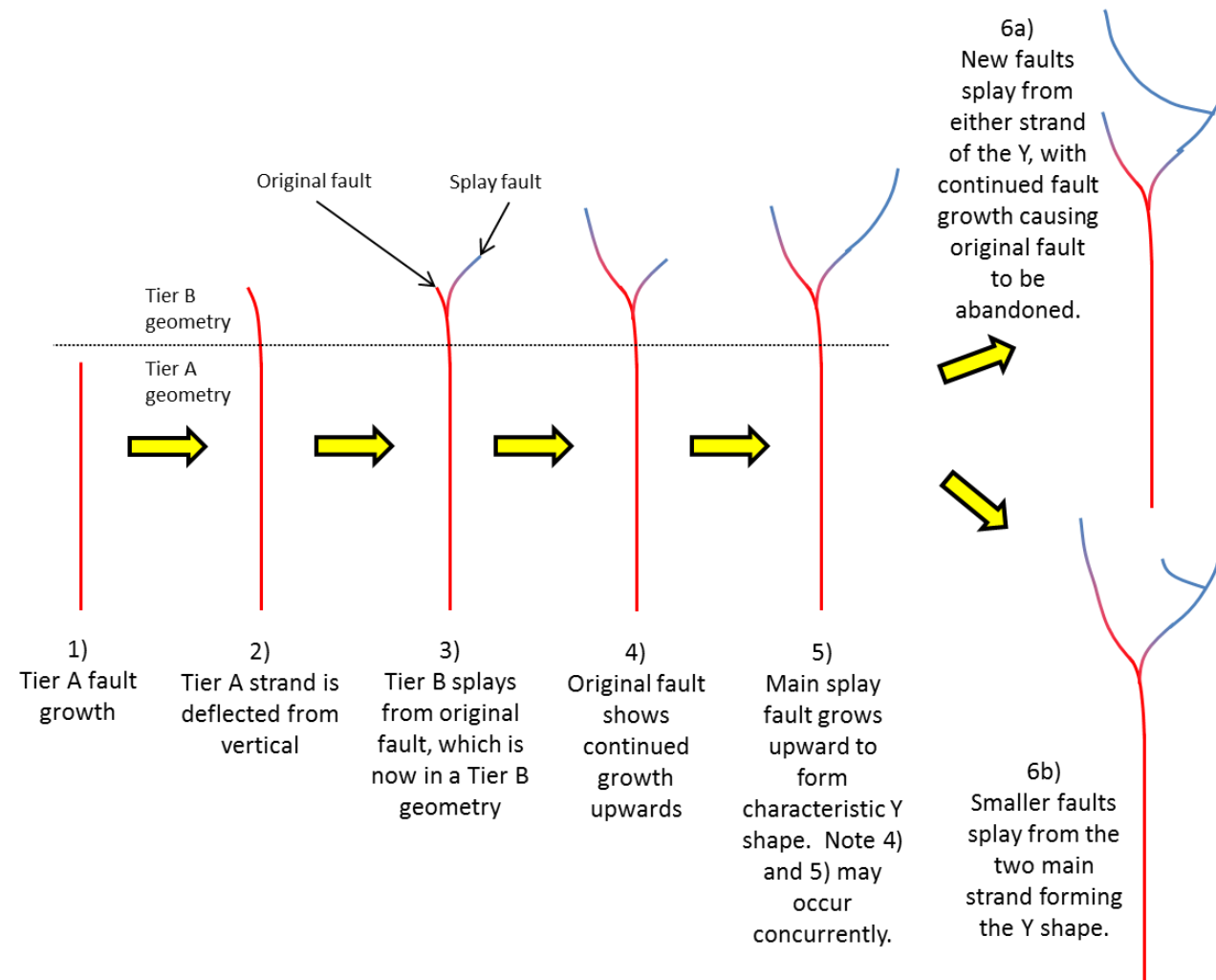
Figure 4.35 - Model showing how the upward propagation of the EAF occurred in 2D (profile view).

1. Blind Tier A propagation.

2. Original fault deflects from vertical into Tier B geometry. Splays initiate.

3. Original fault branches with increased growth upwards.

4. Propagation continues upwards on both Tier B faults.

5. Tier B splays rotate upwards.

6. Tier B splays rotate upwards on the original fault and strike-slip faults become entirely dip-slip.
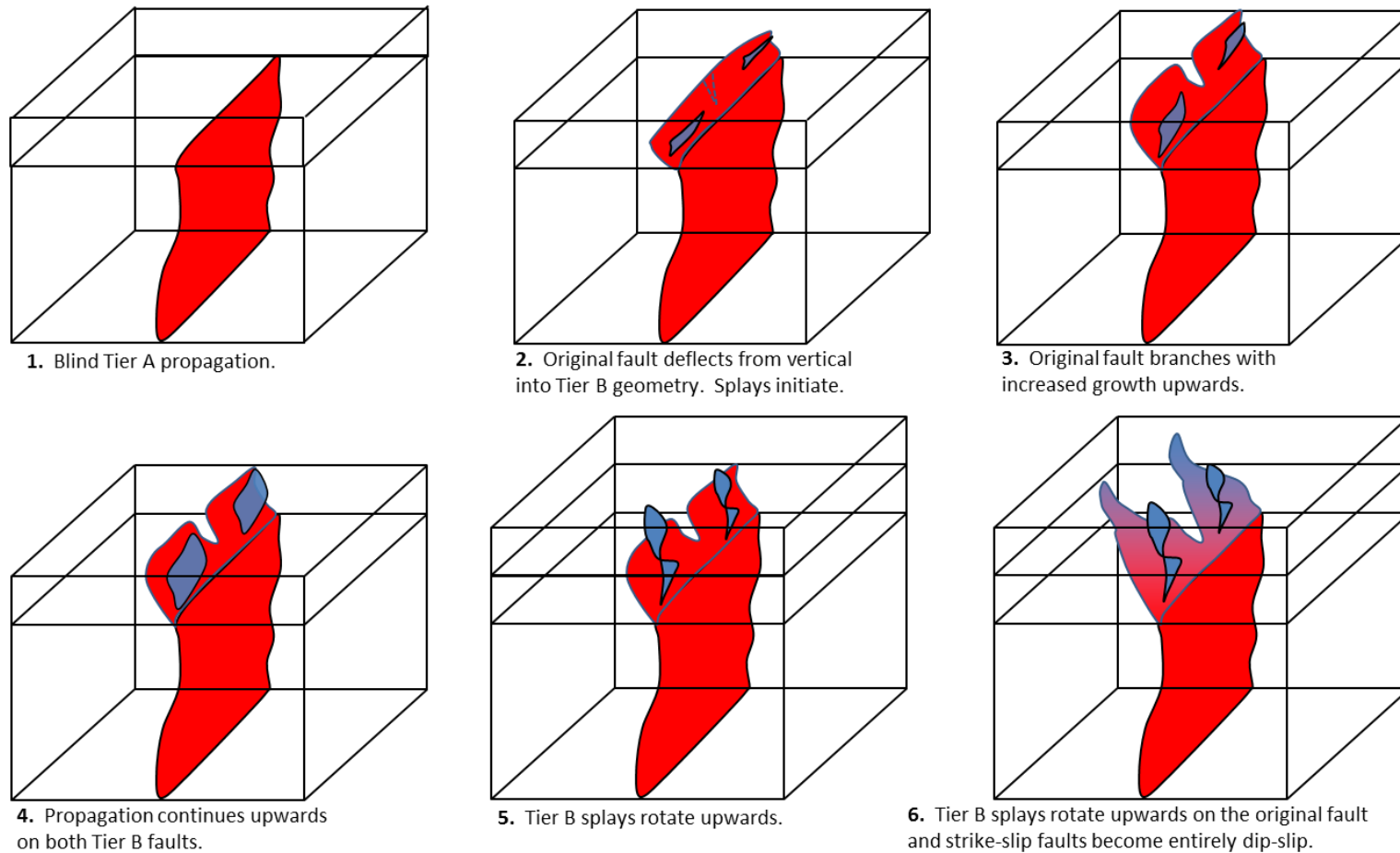
Figure 4.36 - The upward propagation model from Fig. 35 is extrapolated into 3D to show the progressive anti-clockwise rotation. Note that steps 5 and 6 may occur concurrently or in the opposite order. Although this model includes added sedimentation, it does not take into account pre-kinematic growth and syn-kinematic growth (discussed in section 4.8), and is therefore used as a guide for the relative heights of Tier B growth.
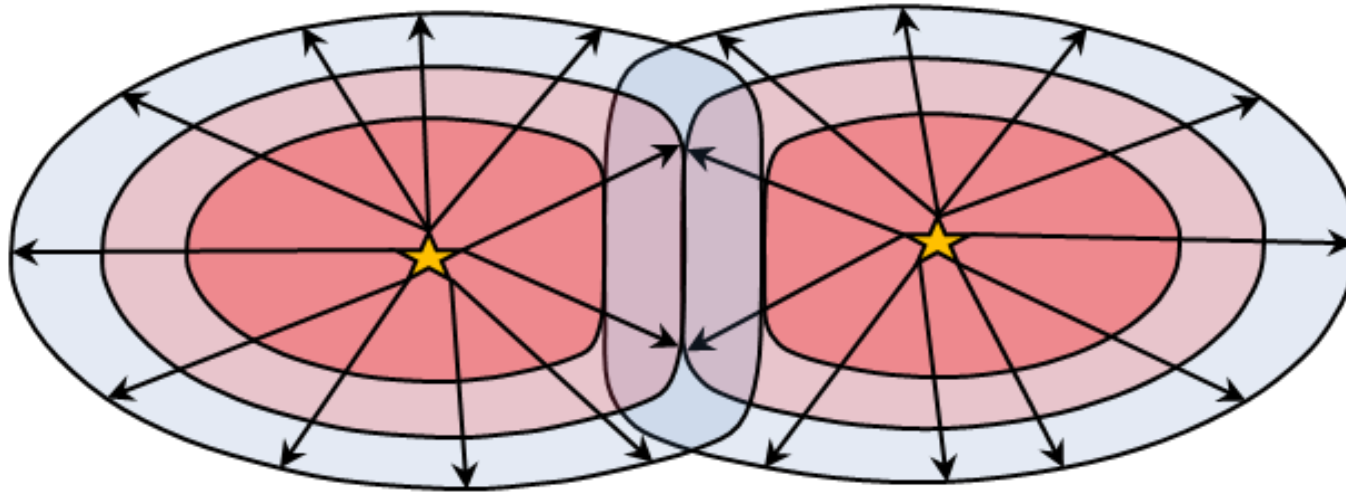
Figure 4.37 - Schematic of El Arish Fault propagation and evolution. Two segments propagated radially, with linkage of the two segments occurring early in the evolution.

## 4.7     The Afiq Strike-Slip Fault

The Afiq Fault (AF) lies on the south-western side of the confluence between El Arish and Afiq Canyons and represents a major divide that separates the structural expressions of the canyons from the Shamir Transtensional Zone towards the southwest (Figure 4.7, Figure 4.11).  It is 33km long when measured on the dataset; however, it extends beyond the limits of the dataset towards the northwest (corroborated by 2D seismic profiles) for a minimum c. 20 kilometres.  The AF is much larger in terms of both fault length and displacement than the EAF, and as such, the fault geometry differs considerably.  The AF therefore provides a more evolved, higher displacement example of strike-slip fault propagation and evolution, and serves as a useful comparison with the more juvenile EAF.  This section is structured similarly to 4.3 by describing the fault geometry in detail before describing the displacement distribution.  There is also a section on the extensional lateral tip features along the AF, a separate section on fault morphology in the Messinian Evaporites, before finishing with a discussion of the results.

### 4.7.1   Geometry Overview

The AF is a highly complex structure and is divided into several divisions for ease of explanation based on natural changes in the geometry (Figure 4.38).  Broadly it can be grouped into three major structural domains: the Afiq Fault West (AFW), the Afiq Fault North (AFN), and the Afiq Fault East (AFE).  The AFW shows larger displacements and a profile structure that resembles the NOF, whilst the AFE shows much smaller displacements and in general has a structure that more closely resembles the EAF.  The AFN is a splay from the AFW, and shows an intermediate structure that more closely resembles the EAF.  It is described in section 4.7.3.  Importantly, the AFW changes to the AFE at the splay with the AFN.

#### 4.7.1.1   Profile Section

*Afiq Fault West-*

The AFW can be described using the Tier A, B, C approach/nomenclature presented in Section 4.6.  It exhibits an obvious change in the height and structure of the three tiers

(Figure 4.39). In particular, the AFW has a taller height and more well defined Tier A fault strand measuring c. 1900m in height (compared to c. 600m at the EAF), that extends both to the seabed and into the Messinian Evaporites and may even extend into Unit 1. The Tier B fault height is significantly reduced (c. 430m) here, mostly occupying the Unit 3a strata, whilst the Tier C detachment faults extend through the top interval of Unit 2 (c. 250m).

The Tier A structure features greater complexity in comparison to the EAF as it comprises several fault strands dipping c. 55° on the south-western side (termed Tier A1 faults), and the undulations form a more substantial curvilinear trace (Figure 4.39). The AFW Tier A/B boundary is less defined as the through-going fault strand propagates to the seabed, resembling the NOF. The characteristic 'Y' shape defined by the EAF therefore becomes thinner and asymmetric. Tier B faults are thus defined by fault strands that splay from the through-going fault and show an element of rotation (in plan view). Tier C is also more complex, with the detachment shear zones appearing to flatten outwards away from the fault zone, resembling a thrust geometry (shallow dip of 40° that decreases to 16° with distance from the fault, forming a listric fault plane), whilst the Tier A strand actually propagates into the evaporite layer and remains sub-vertical.

*Afiq Fault East-*

The Afiq Fault East by contrast has a structure that more closely resembles the EAF: the three tiers having similar heights (Tier A c. 500m, Tier B c. 600m, and Tier C c. 500m) and a simpler structure (Figure 4.40). Tier A does not show fault strands splaying off the through-going fault, whilst Tiers B and C form a more characteristic wide 'Y' shape (and inverse 'Y') shape. Importantly, the Tier A strand dies out and splays into Tiers B and C, in contrast to the AFW. Interestingly, most of the main Tier B fault strands die out before the seabed, with only splays deforming the seabed.

### 4.7.1.2  Plan View

The Afiq Fault is imaged in plan view using a slice at 2280ms TWT to highlight the fault at depth and a slice located just under seabed at 1280ms TWT to show how the fault transitions from a Tier A through-going fault strands to a more complex combination of Tier A and B

faults strands (Figure 4.38).  There are noticeable changes that occur between these slices and are described in detail during sections 4.7.2 through 4.7.4.

*Afiq Fault West-*

The AFW shows a similar geometry to the El Arish Fault at depth (2280ms TWT): a fault zone comprised of a single Tier A fault strand that trends N118° (Figure 4.38a).  However, several features are noticeable that contrast with the EAF geometry:  On the south-western side of the Tier A fault strand, Tier A1 faults trend parallel to the Tier A strand, whilst on the north-eastern side of the fault zone, three large normal faults strike on average at 060°, or c. 58° from the through-going fault (termed Horsetail Faults 1, 2, and 3 and described in section 4.7.6.1.).  Despite no linkage occurring with another major strike-slip fault (e.g. the EAF and NOF), the geometry of the AFW also becomes more complex with the presence of two major splays.  One is located at the north-western edge of the dataset and forms a complex transfer zone, whilst the second splay diverges from the AFW, and is the Afiq Fault North (AFN) and extends towards the east-southeast with a trend of N100°.  Southeast of the latter splay point, the AFW changes to the Afiq Fault East (AFE).

At the seabed (1280ms TWT), the geometry of the AFW shows a combination of Tier A fault segments and en echelon Tier B faults (Figure 4.38b, c).  This is a crucial observation as it signifies that the through-going fault reaches the seabed in addition to the Tier B fault strands. The AFN, however, exhibits a fault geometry that more closely resembles the EAF, with only Tier B faults (oriented at a high angle to the underlying fault trace) observed.

*Afiq Fault East-*

At depth the AFE appears as a relatively continuous Tier A fault, with one noticeable overlapping segment (Figure 4.38a).  However, at the seabed, there is a clear change in morphology that can be further subdivided into two domains: Domain 1 towards the northwest and Domain 2 towards the southeast (Figure 4.38b, d).  Domain 1 shows a geometry that resembles the EAF with en echelon arranged Tier B faults at a high angle to the underlying Tier A fault (and was shown in profile section).  Domain 2 is a very complex region that shows fault interactions with several large, extension dominated structures. Domain 2a comprises high angle Tier A faults that interact with the Wing Crack Faults

(WCF) 1 and 2 and Domain 2b shows high angle Tier B faults that interact with the Shamir Rise Fault towards the southeast.  The Tier B faults show en echelon arrangements in Domain 2; however, they differ from Domain 1 and the other strike-slip faults described in this chapter.  This discrepancy is described in greater detail in Section 4.7.4.
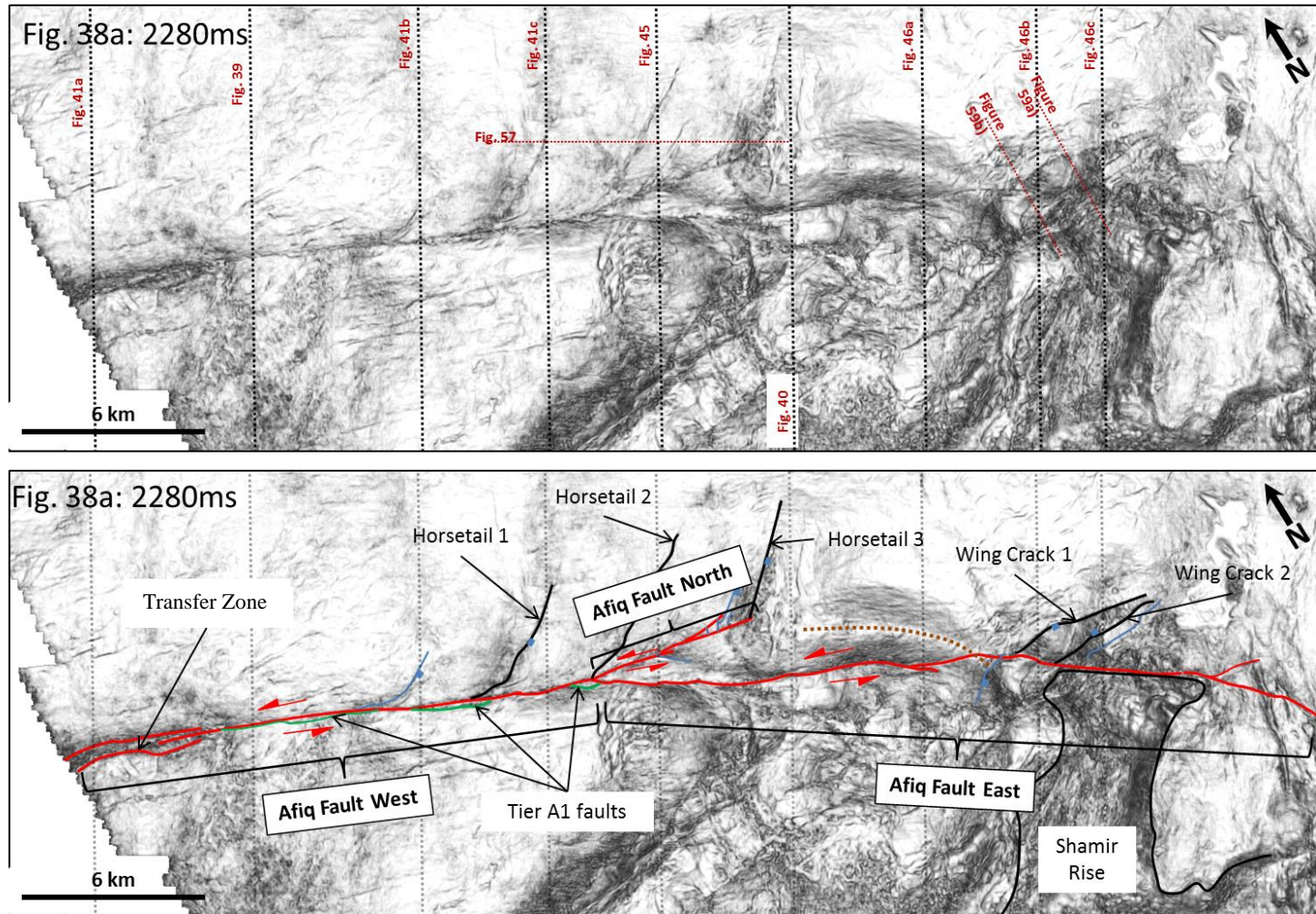
Figure 4.38a - Coherency slice of the AF at a depth of 2280ms TWT.   Profile sections are shown on the uninterpreted slice.  The fault is entirely in a Tier A geometry.
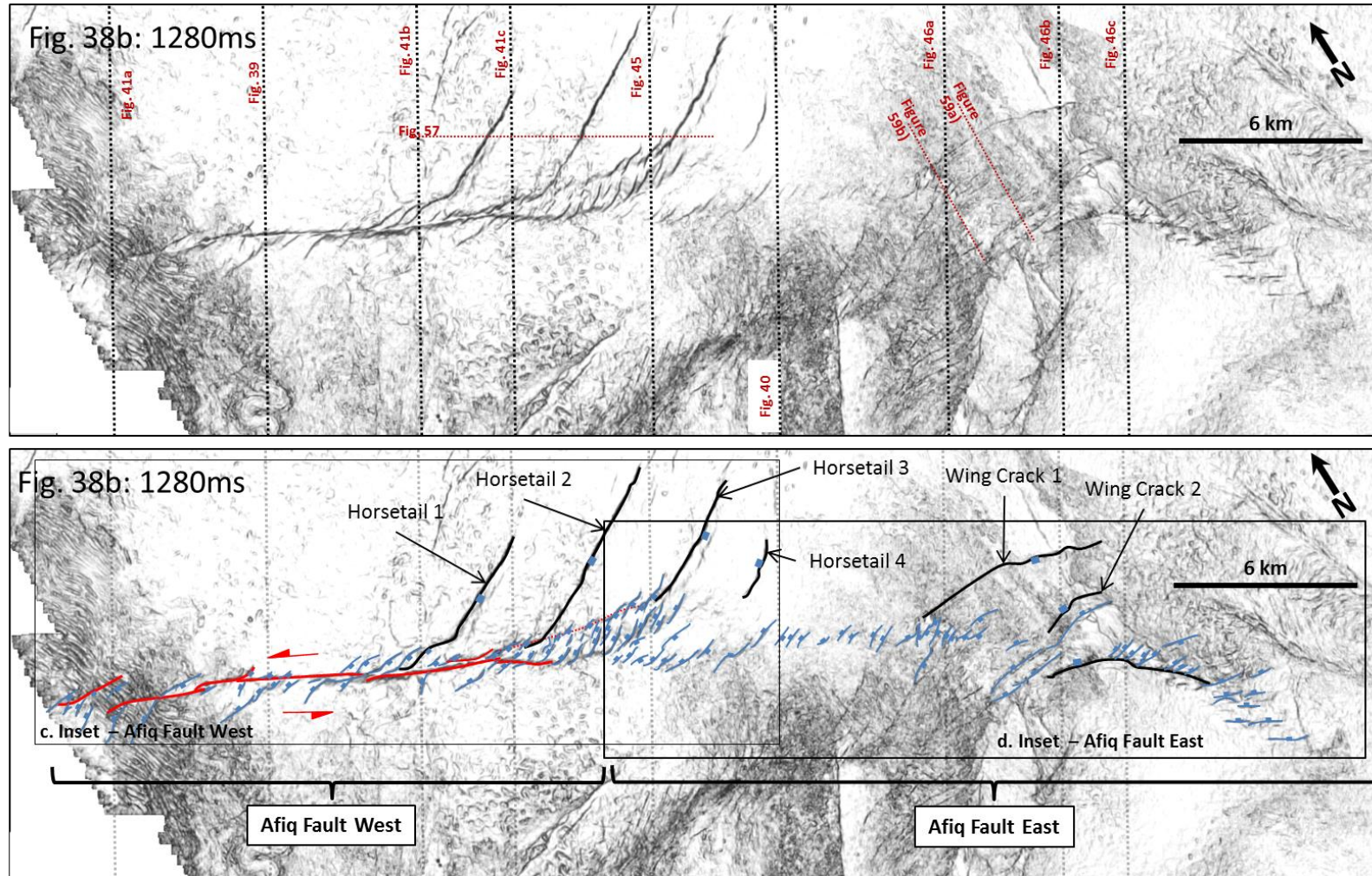
Figure 4.38b - Coherency slice of the AF at a depth of 1280ms TWT, located just below the seabed. The fault is a combination of Tier A and B geometries.
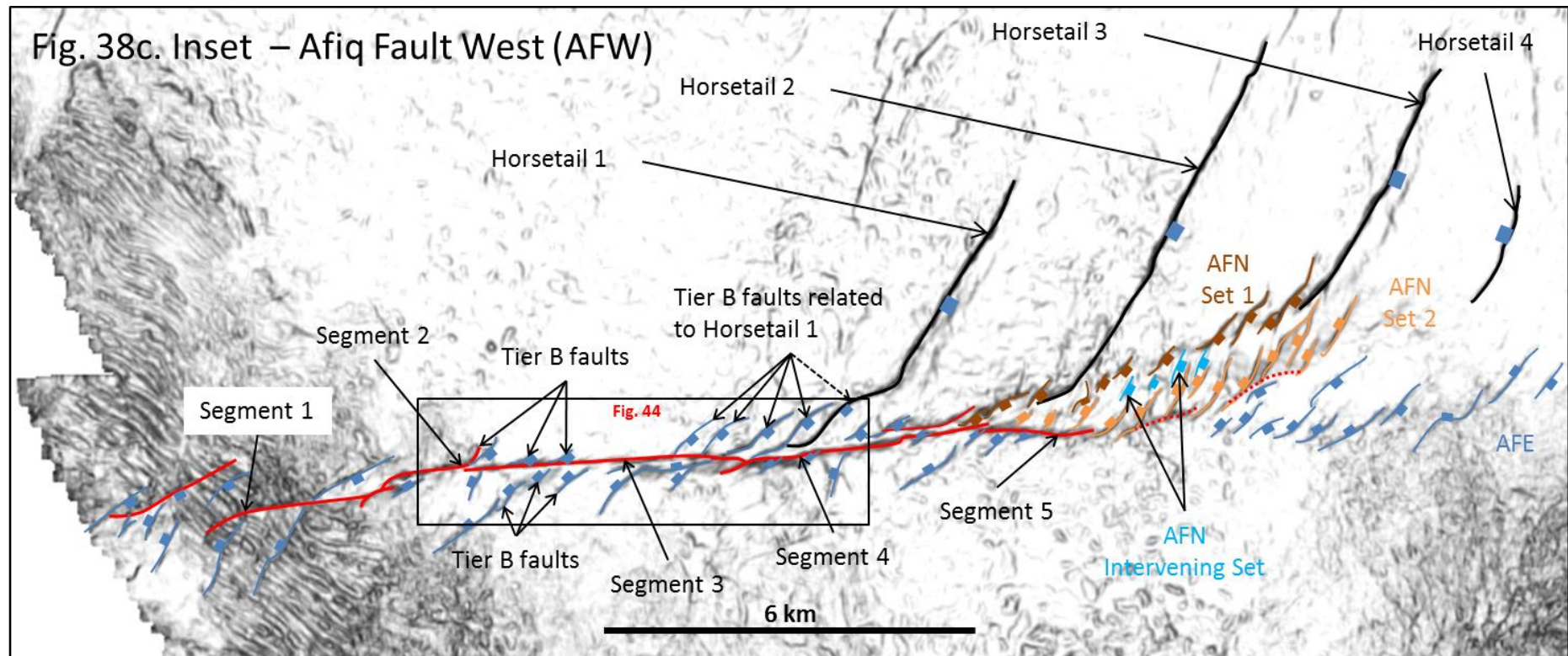
Figure 4.38c - Close-up of the AFW and AFN structure at the seabed (1280ms).  The AFW is comprised of segmented Tier A strands and high angle Tier B strands.  The AFN is comprised of three sets of high angle Tier B strands.  Its structure is very similar to the EAF, with the exception of the additional intervening set.
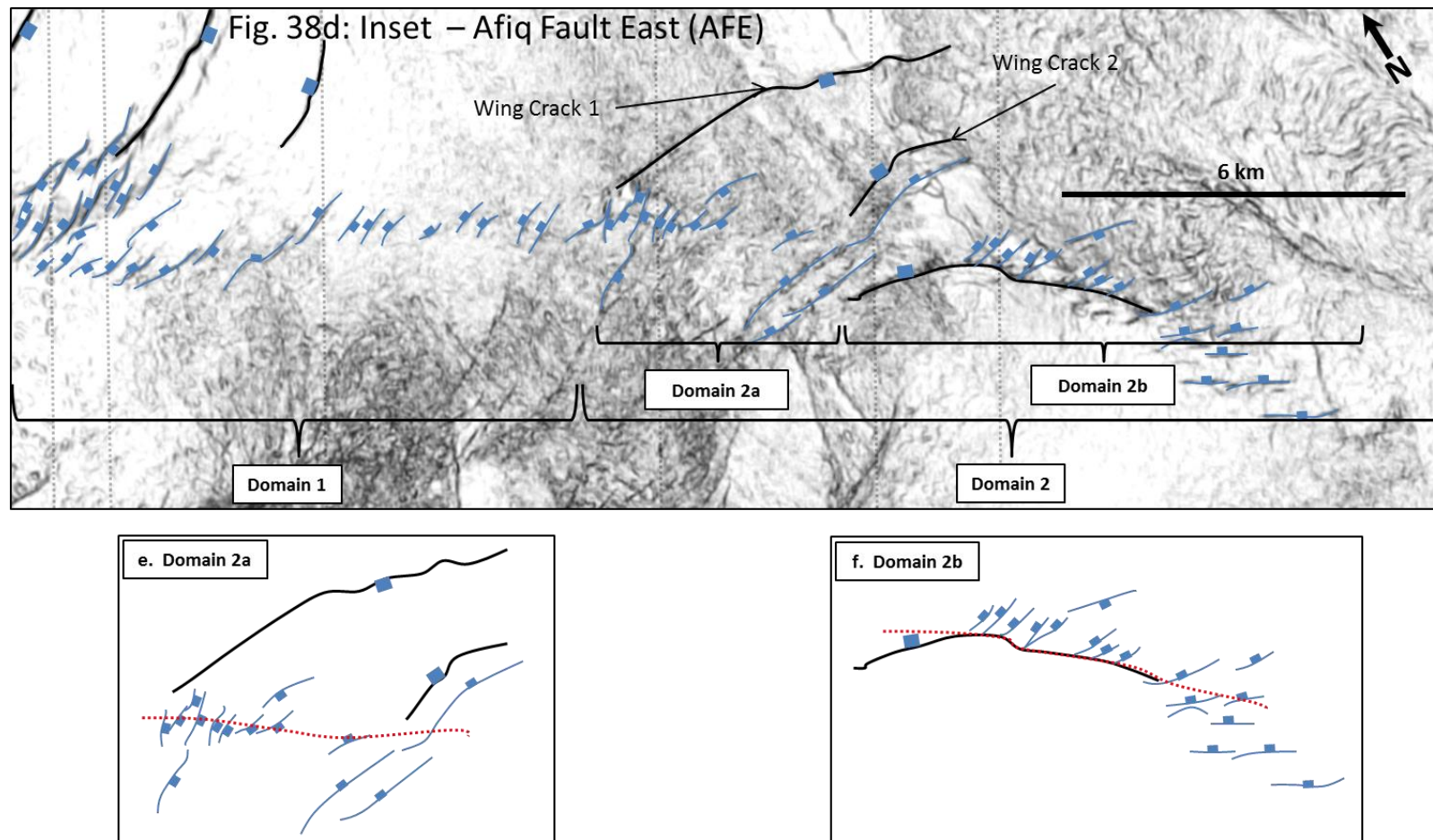
Figure 4.38d - Close-up of the AFE at 1280ms.  Domain 1 is comprised of a set of high angle Tier B strands dipping almost entirely to the northwest.  Domain 2 is highly complex showing en echelon high angle Tier B strands which are mostly antithetic to Domain 1 in Domain 2a (dipping to the southeast) and then antithetic again in Domain 2b (dipping to the northwest).  e) and f) show the underlying Tier A trace as a guideline.
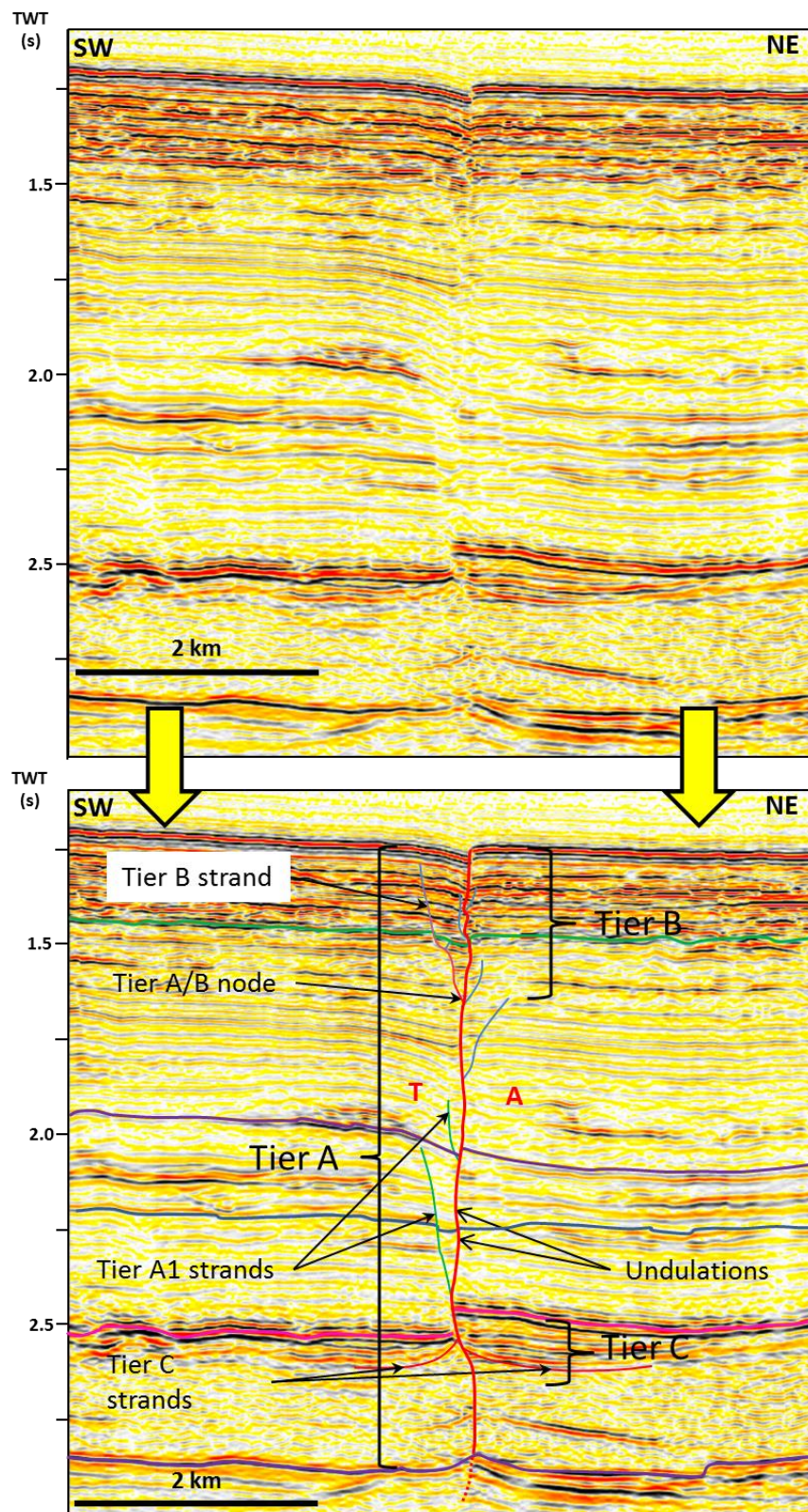
Figure 4.39 - Overview profile section of the Afiq Fault West (AFW).  Note how the Afiq Fault shows an overlapping of Tiers, and thus Tiers B and C can occur concurrently with Tier A.  Notice how Unit 3 shows significant sediment growth packages alternating on either side of the fault.  Vertical Exaggeration approx. 3.1.
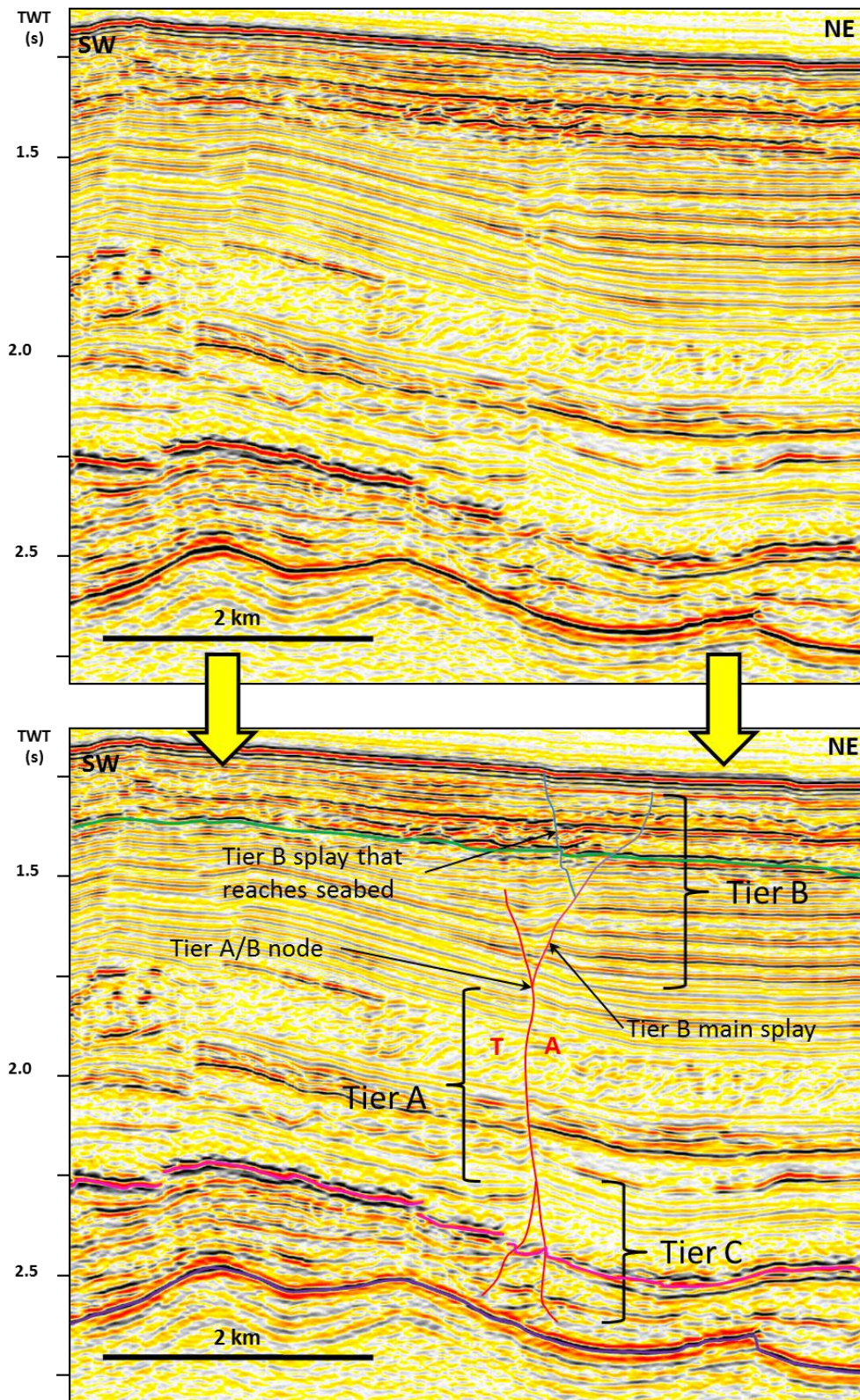
Figure 4.40 - Overview profile section of the Afiq Fault East.  Note how the Tiers do not overlap here, and thus more closely resemble the El Arish Fault geometry.  Vertical Exaggeration approx. 2.9.

## 4.7.2    Afiq Fault West (AFW)

### *4.7.2.1    Geometry - Profile Section*

The AFW basic structure depicted in the overview becomes more complex with proximity to other structures and splays.  This section describes how the profile structure changes starting in the northwest and moving progressively towards the southeast (approaching the splay with the AFN).  Importantly, all sections show scarps at the seabed, signifying that this region of the fault is currently active.

Towards the northwest edge of the dataset the AFW shows two through-going faults with several faults splaying upwards towards the seabed (Figure 4.41a).  The uppermost of these forms high angle Tier B faults that are identified on slice 1280ms TWT (Figure 4.38a).  Importantly, both Tier A strands extend into Unit 2 and do not appear to link at any point at depth.  The strata between the two Tier A strands show concave up reflections forming a small syncline (just below the green horizon, Figure 4.41a); however, towards the base of Unit 3, the reflections become convex upwards, thus both push-up and pull-down occurs in the structure.  A localised push-up structure is also formed between one of the Tier A fault strands and a Tier B strand, which contrasts the concave up reflections at that depth between the Tier A strands.

The profile is interpreted to show a complex transfer zone between two major segments based on the presence of the two Tier A strands that separately extend into the evaporites.   The presence of both contractionally and extensionally deformed strata between the two strands presents an interesting situation as the presence of either would suggest a pull-apart basin or a push-up structure.  However, the fact that both appear may suggest multiple phases of movement, with early movement occurring in transpression, whilst later movement occurs in a transtensional setting.  Another possibility is the stress field between the two strands changes with how close each strand is to each other.  For example, towards the base of Unit 3, the strands are located c. 250m away from each other; whilst upwards, where the concave reflections occur, the distance doubles to 500m.  Thus, there is no clear interpretation for this region and it will be referred to herein simply as a transfer zone.  The small push-up structure between the Tier A and B faults suggest that complex strains and block rotation occur in the

transfer zones, with elements of transpression in the splays, despite showing more transtension at that depth.

The interactions between the AFW and a major splay normal fault, Horsetail 1 (H1), are very complex and are illustrated with two section lines (Figure 4.41b, c). H1 shows a relatively short height c. 850m, diverging from the AF at the Tier A strand (Figure 4.41b), and highlights how H1 could be misinterpreted as a Tier B or Tier A1 fault and therefore emphasises the importance of a combined interpretation approach using seismic sections and coherency slices. Whilst towards the southeast, Figure 4.41c shows that with distance from the splay point, H1 extends downwards into Unit 2 where it also detaches and may intersect with the AFW. H1 therefore intersects differently with the AFW at depth then at shallow levels, which is summarised in Figure 4.42.

Fig. 41a)



Fig. 41b)
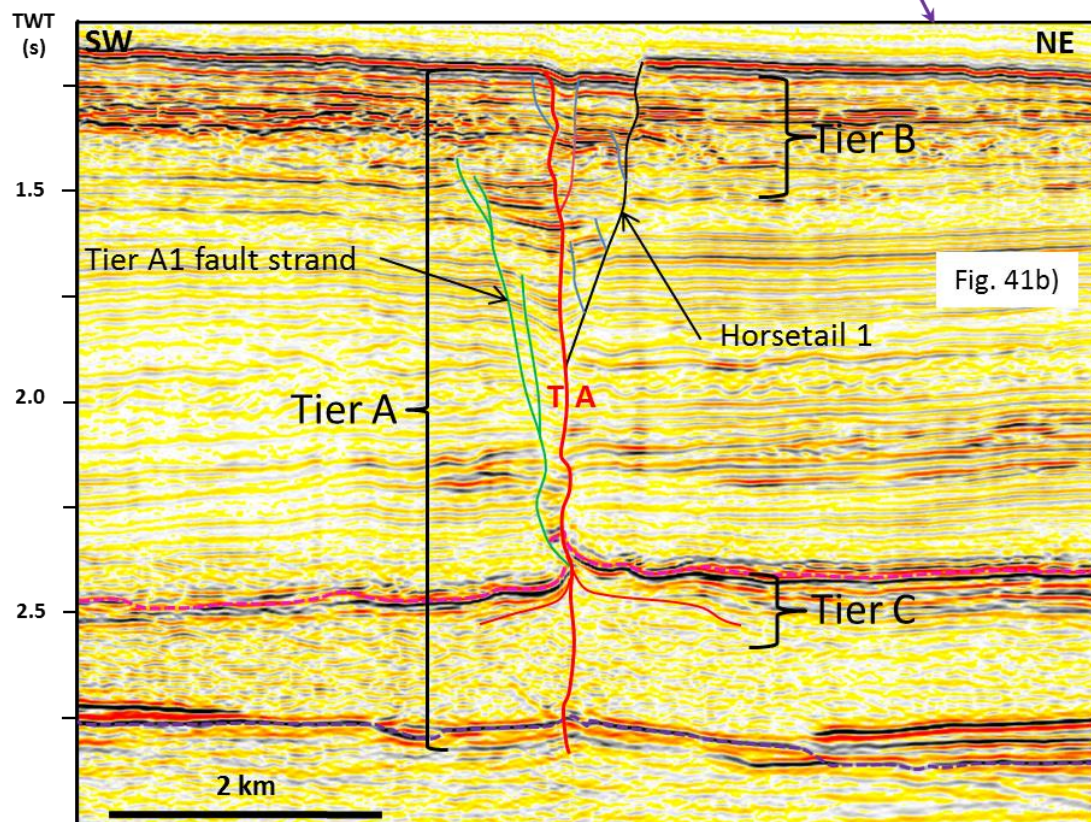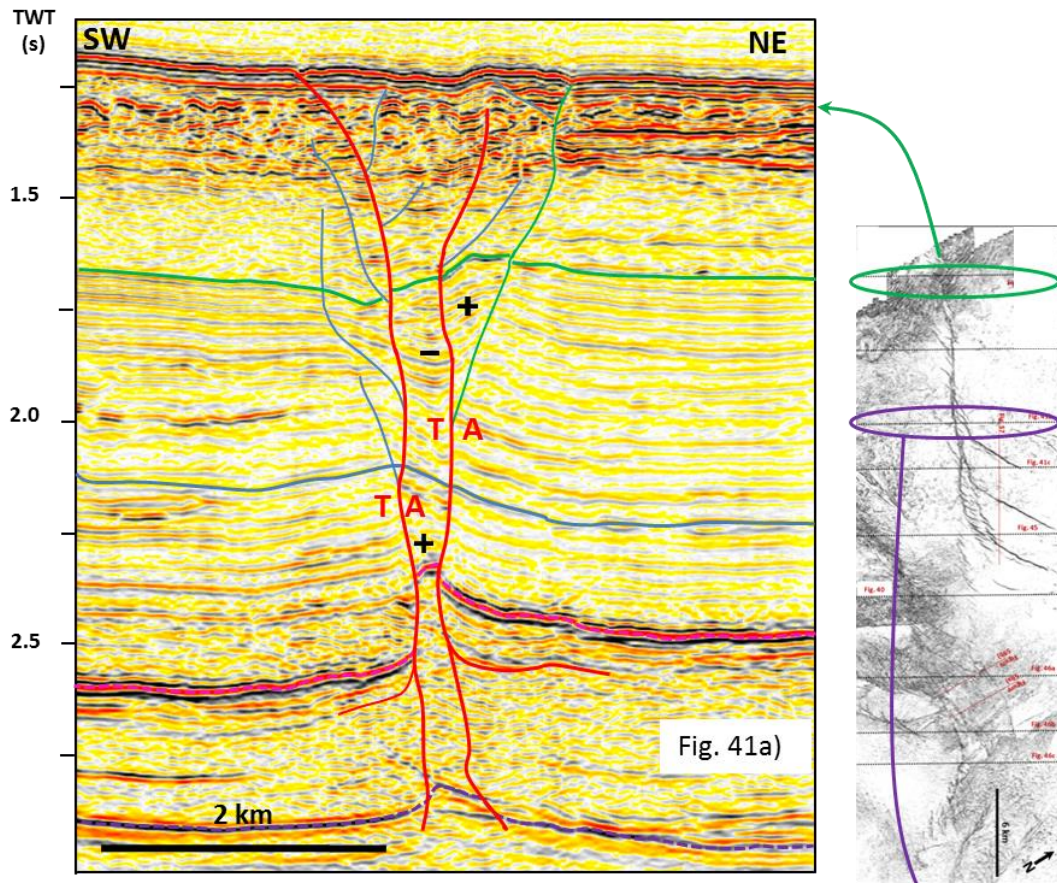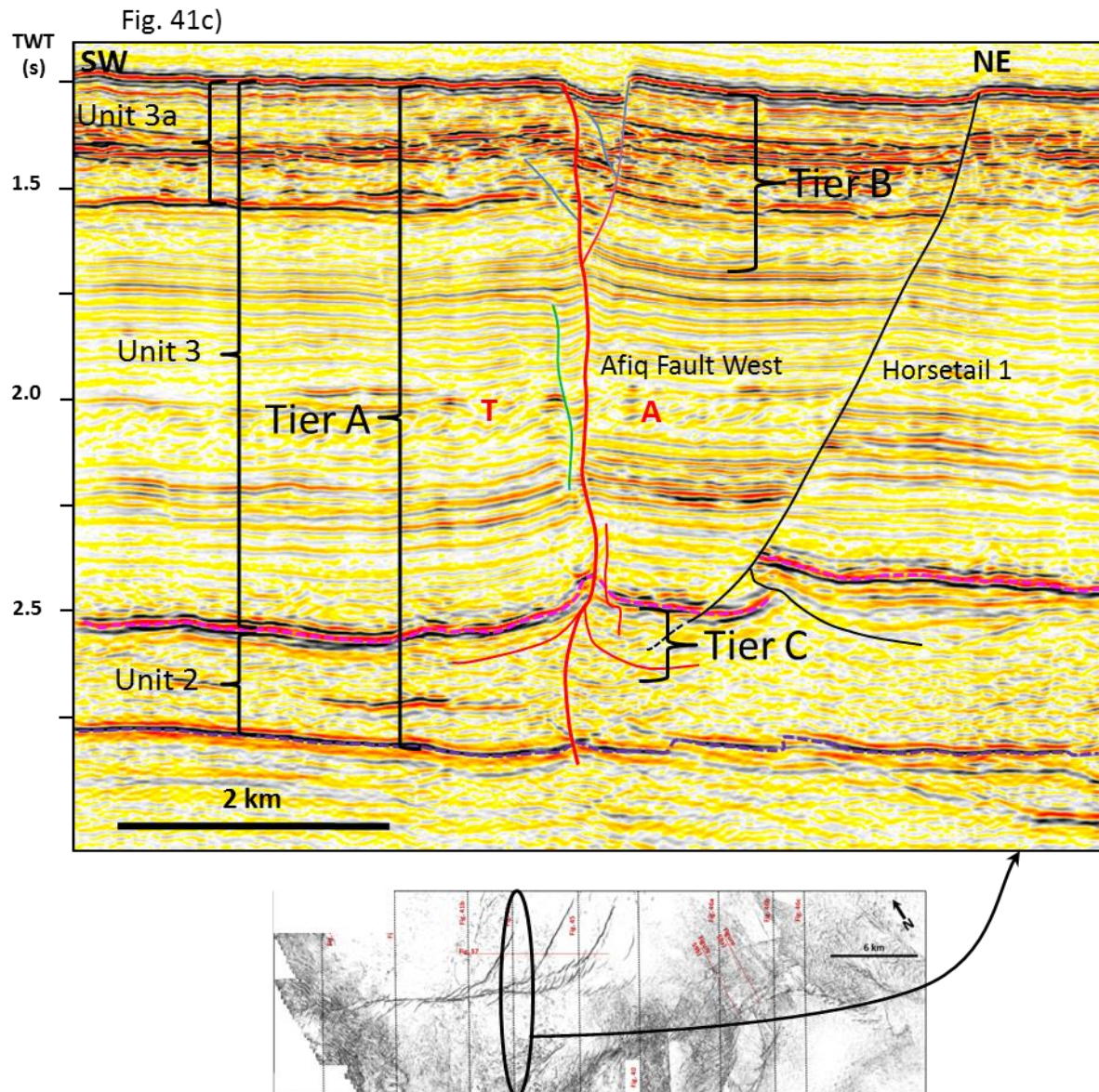
Figure 4.41 - Profile sections detailing changes along strike of the AFW. Towards the northwest a) shows the transfer zone, which is defined by two separate Tier A strands, whilst b) and c) detail the structural interaction with Horsetail 1.
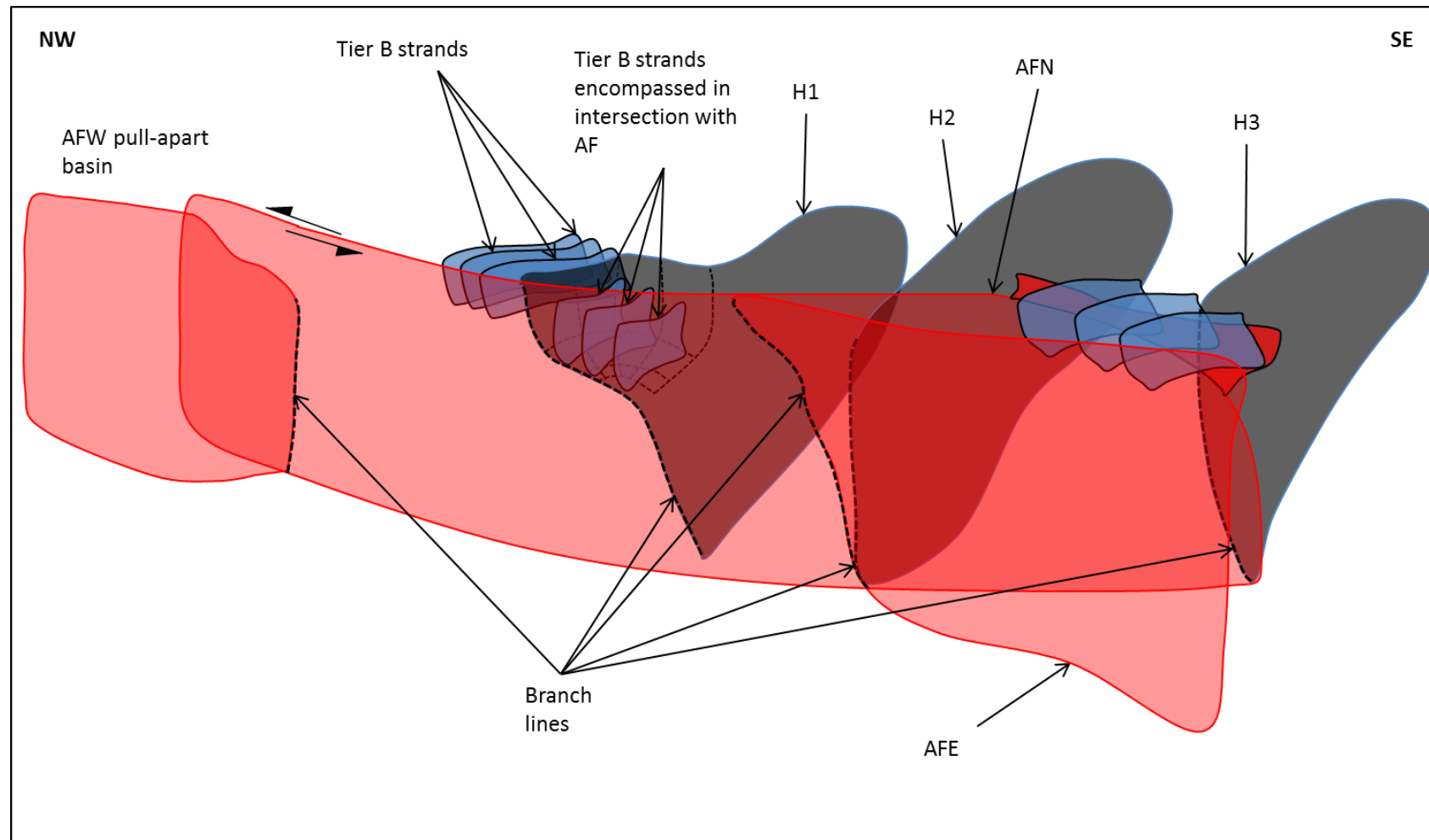
Figure 4.42 - Schematic cartoon of the intersection relationships between major splays and extensional faults along the Afiq Fault. These were drawn based on collating the profile and coherency slices.

### *4.7.2.2   Geometry - Plan View*

The Afiq Fault geometry changes upwards from the simple Tier A strands at the fault centre to the more complex interactions of Tier A and B faults at the upper tips, and therefore it is important to highlight these changes in order to complete the 3D picture.  Note, slices from 1280ms TWT and 2280ms TWT were shown in section 4.7.1.2; however, they are used again here to describe some of the features in greater detail.

The deepest slice (2280ms TWT) shows that a through-going Tier A fault strand and 3 shorter sub-parallel trending Tier A1 faults dominate the deformation (Figure 4.38a).  The Tier A1 faults range between 3.8km - 4.5km in length and are located about 250m away from the south-western side of the AFW.  Interestingly, these faults intersect the AFW at both of their lateral tips, and therefore do not overlap each other nor form en echelon arrays.

The Tier A1 faults are interpreted as significantly different from the Tier B faults due to these changes in geometry and therefore have formed from different mechanics.  Their geometry resembles smaller extensional features that formed due to sidewall rip-outs described in the field by Swanson (1989; 2005), and therefore are interpreted as larger scale equivalents of these.  Furthermore, these are only observed where displacement is high along the AFW (section 4.4.5.), and may explain why this fault type was not observed along the EAF.

A gradual change upwards in fault geometry is depicted by slices at 1800ms, 1700ms, and 1580ms (Figure 4.43).  Specifically, a decrease occurs in Tier A geometry, whilst Tier B strands becomes more prominent.  These changes are especially noticeable at the transfer zone, where three fault strands are present at 1800ms.  The two Tier A strands at depth (2280ms TWT, Figure 4.38a) are still present, however an addition of a Tier A1 fault (labelled I, Figure 4.43a) marks a widening of the fault zone.  This trend continues in the 1700ms slice as a low angle Tier B fault appears (labelled iv, Figure 4.43b), and by the 1580ms slice, high angle Tier B strands are observed in the transfer zone between the two Tier A strands (ii and iii, Figure 4.43c).

The rest of the AFW shows a similar transition, with the 1700ms and 1580ms slices showing that Tier A1 faults gradually disappear whilst high angle Tier B faults gradually become observed.  Interestingly the Tier A1 fault remaining at 1580ms becomes very round and

encompasses a set of high angle Tier B faults.  Also of note, no low angle Tier B faults can be identified and the observed high angle faults are shorter in length relative to the seabed.

The AFW geometry at the seabed is comprised of Tier A strands and Tier B strands oriented at a high angle to the through-going trace (Figure 4.38c).  The Tier B strands dip antithetically on either side of the underlying fault zone at an average trend of 076° (42° away from the underlying Tier A fault).  Interestingly, the EAF high angle Tier B faults diverged at 46°, indicating that a similar orientation to the underlying fault trace occurs between the two faults.  The Tier A fault strands comprise 5 segments, with each segment curving towards the SW side of the fault zone towards the north-western end of the segment, and curving towards the NE side of the fault zone at the south-eastern end of the segment. The Tier A strands therefore show a subtle en echelon arrangement.  The fault zone is also wider at the seabed than at depth, which is attributed to the presence of small splays encapsulated by the larger high angle Tier B fault strands (Figure 4.44).

The absence of low angle Tier B faults does not mean that this stage of rotation does not occur on the AFW.  The lack of low angle Tier B faulting can be explained by: 1) MTDs are present that have distorted the coherency and 2) width of the through-going fault zone.  In the case of the latter, the fault zone in profile section is considerably wider than the EAF, and therefore the distance between the low angle Tier B faults would be very low, and the constraints of seismic resolution may not image the smaller faults.  Stated alternatively: the low angle Tier B faults and the Tier A fault are imaged as one fault on the coherency, explaining why the fault zone is wider at the seabed (Figure 4.44).

The Tier A faults forming an en echelon arrangement at the seabed suggests that the through-going fault is beginning to splay upwards in addition to the splays that formed the Tier B faults.  It seems reasonable to suggest that with further slip and sedimentation, these small splays would start forming a more mature Tier A and B relationship.  In essence this could form a second set of faults that occur within the older Tier B faults or a second 'Y' within the original 'Y', or the current set of Tier B faults may be abandoned with continued growth occurring on the later set.  The fact that this is not observed on the EAF may reflect the nature of the upward propagation of strike-slip faults, which will be explored in Section 4.8 and Chapter 6.
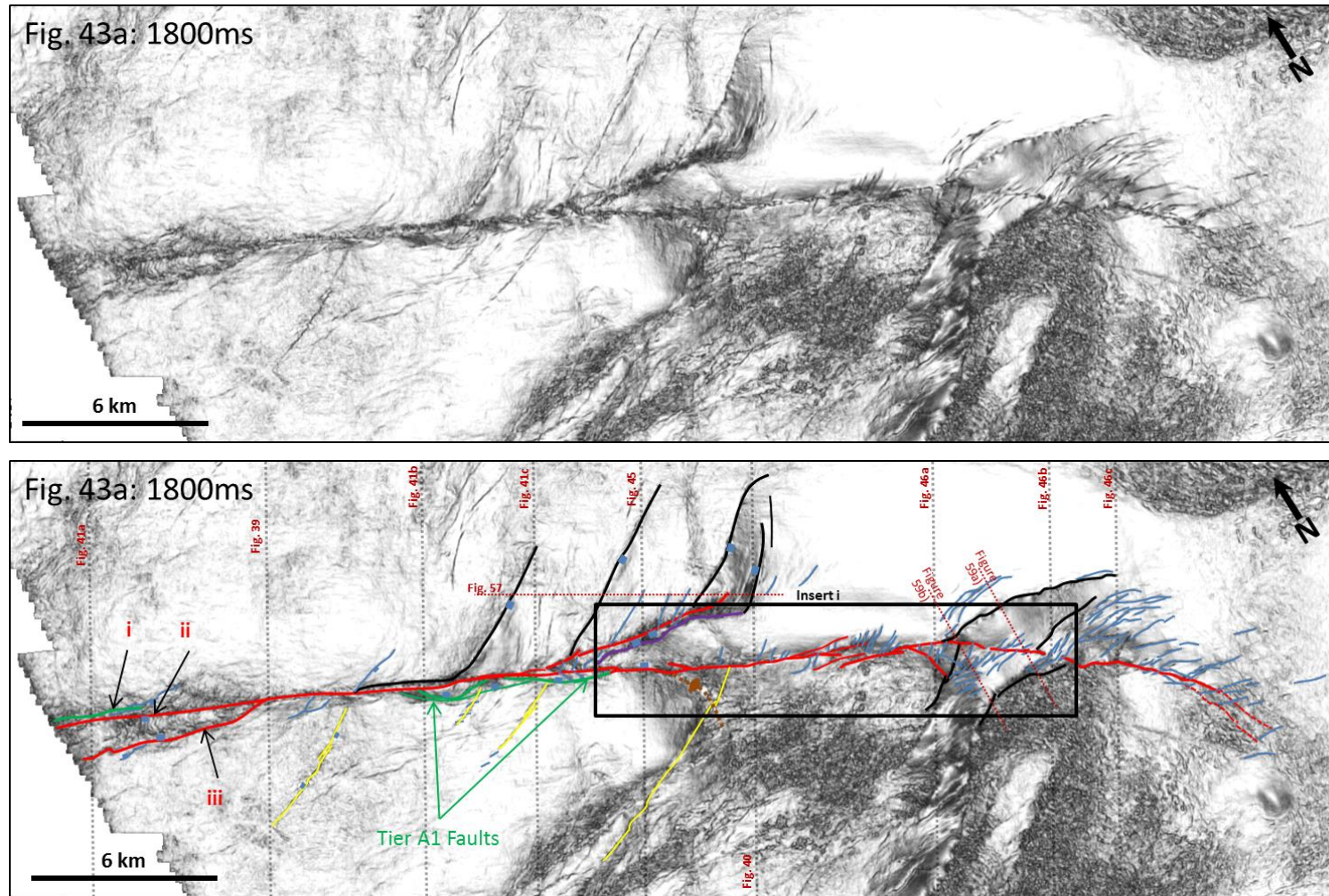
Figure 4.43a - Coherency slice of the AF at a depth of 1800ms TWT. Tier A = red, Tier A1 = Green, Tier B = blue, and Tier B1 = purple. Normal faults are shown in black.
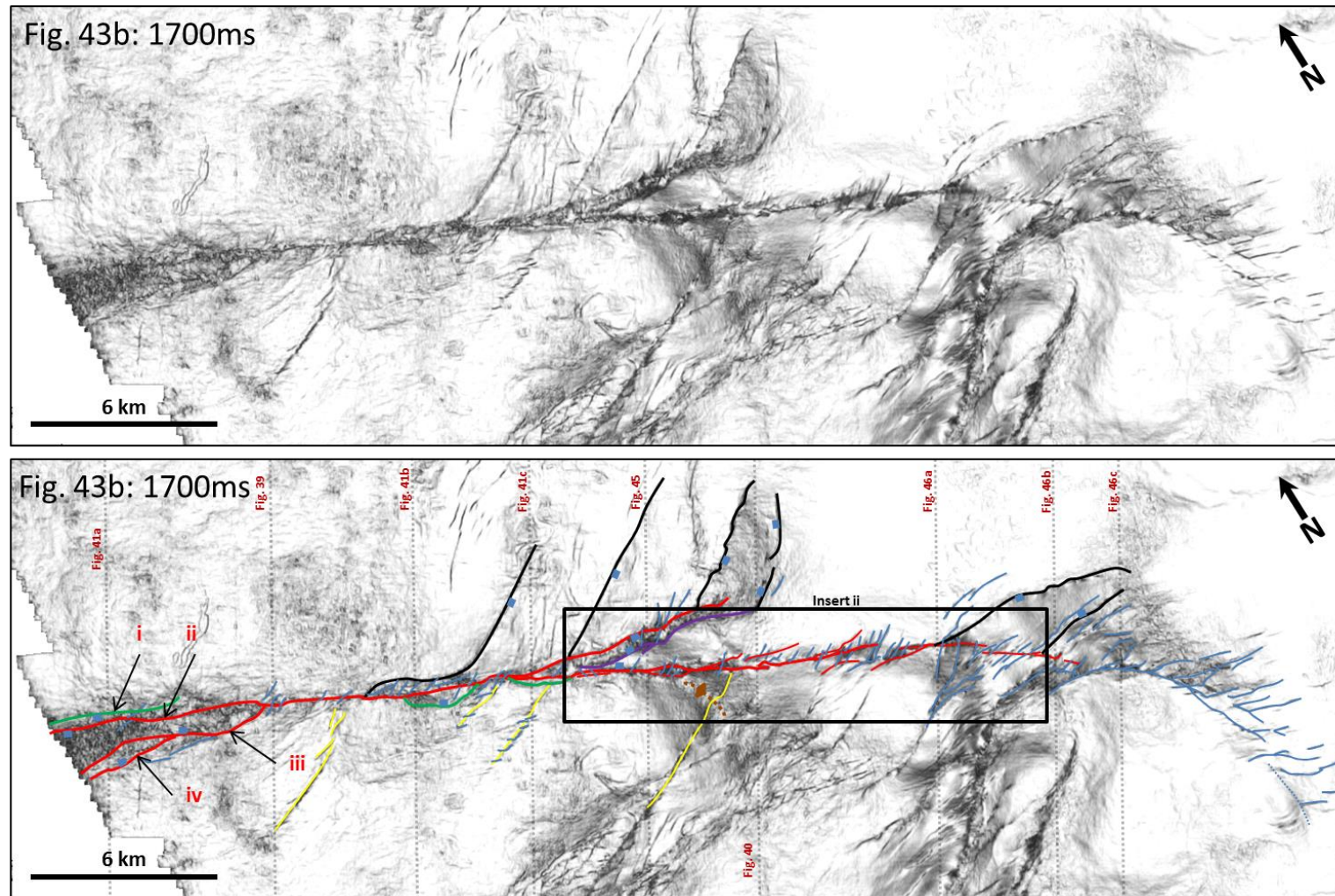
Figure 4.43b - Coherency slice of the AF at 1700ms TWT.   Tier A = red, Tier A1 = Green, Tier B = blue, Tier B1 = purple, normal faults = black, dextral faults = yellow.
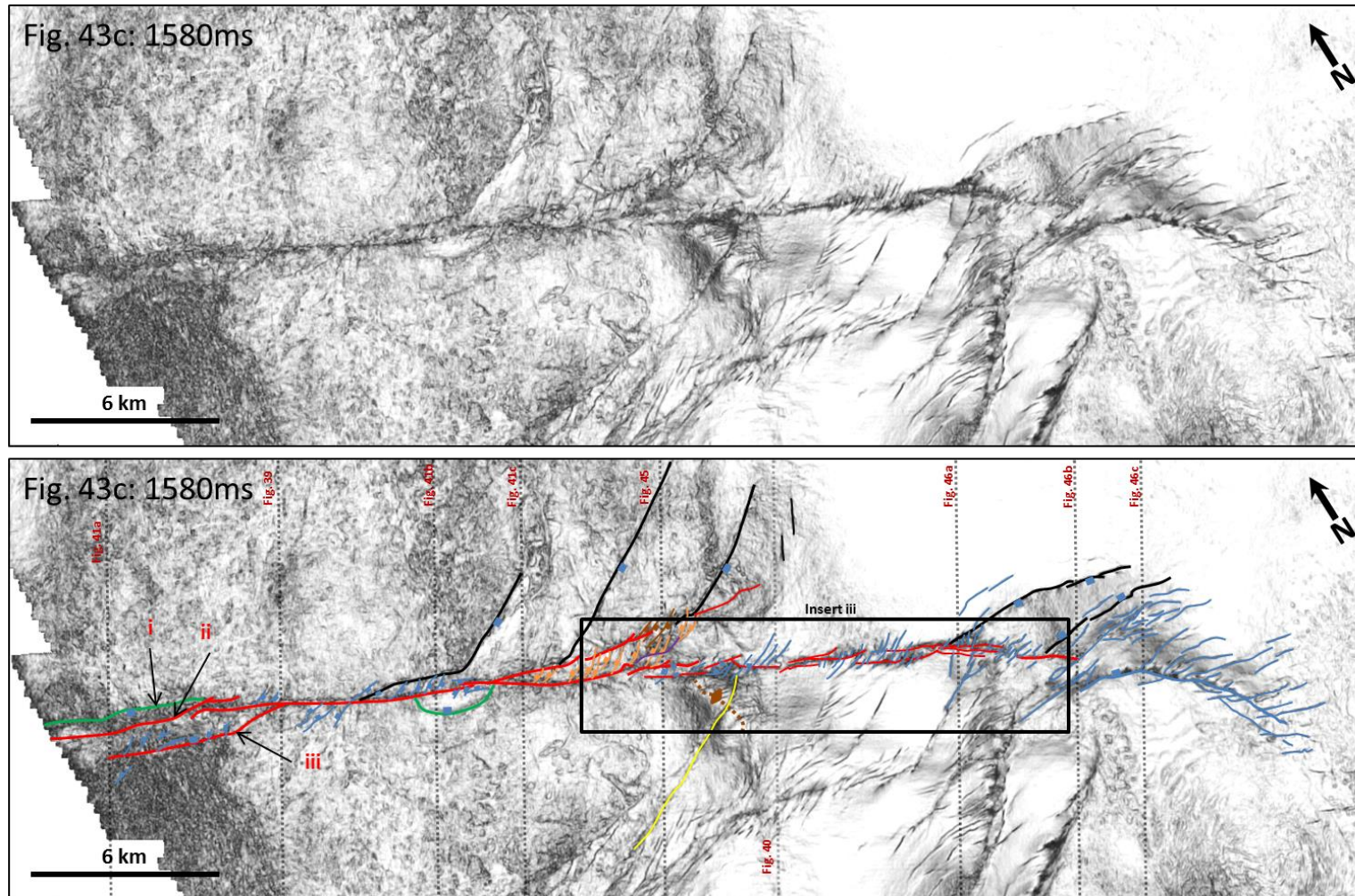
Figure 4.43c - Coherency slice of the AF at 1580ms TWT.   Tier A = red, Tier A1 = Green, Tier B = blue, and AFN Tier B = brown and orange.  Normal faults = black.
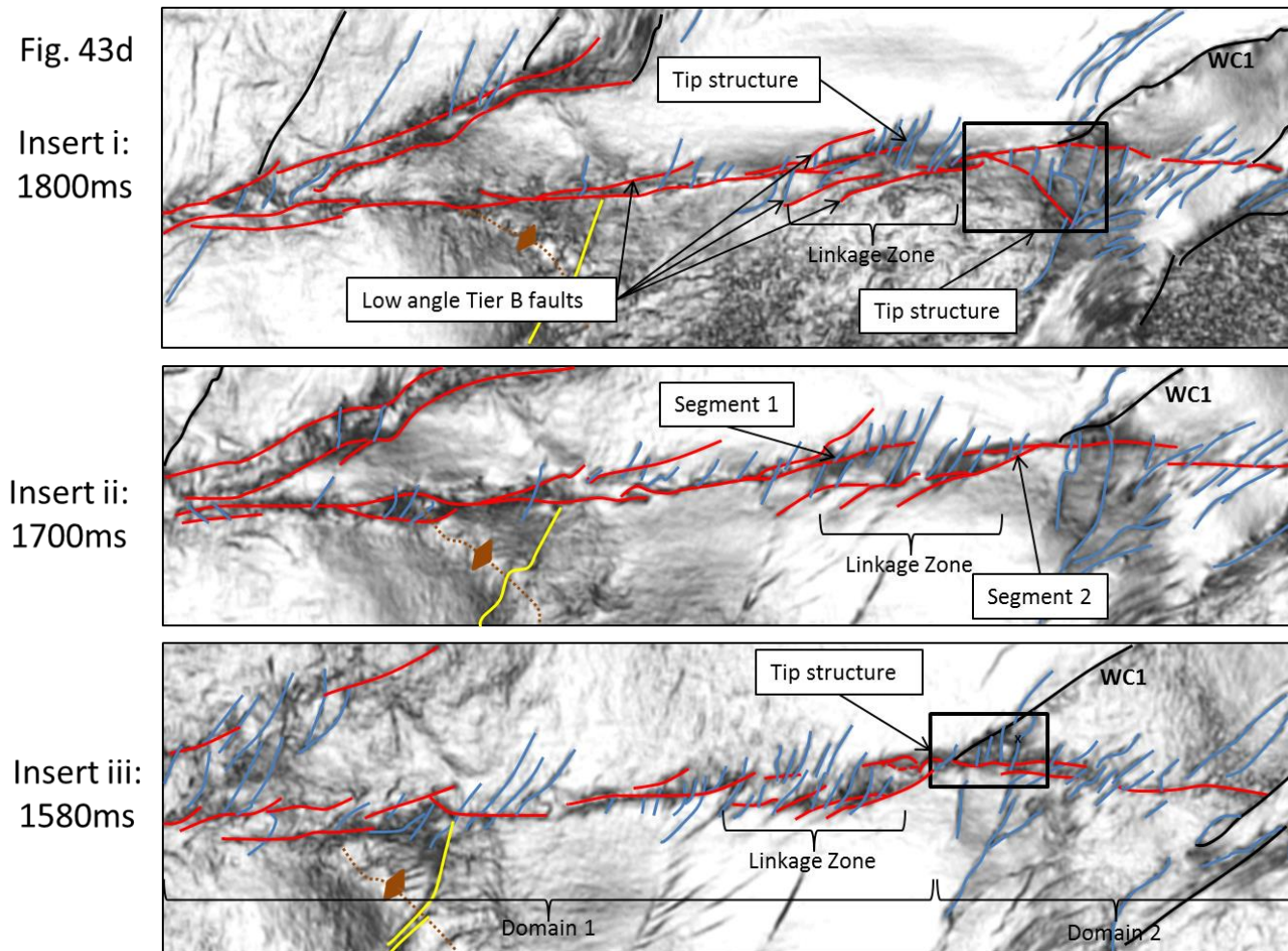
Figure 4.43d - Close-up of the region near the Domain 1 and 2 boundary, which show structures that resemble the 'tail damage zones' described by Kim and Sanderson (2003, 2004).
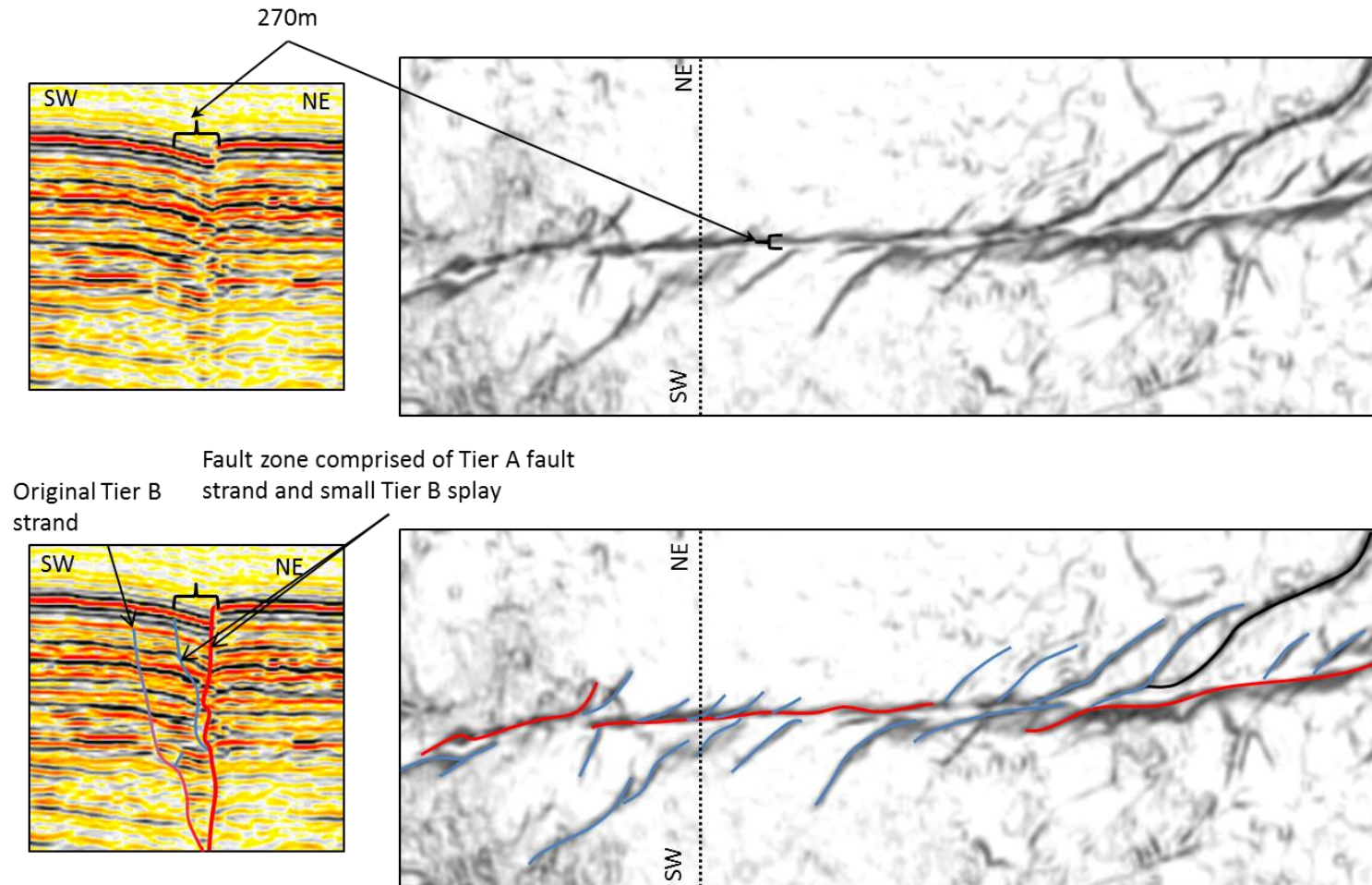
Figure 4.44 - The width of the AFW fault zone at the seabed is considerably thicker (c. 270m) at the seabed than other fault strands.  This is attributed to the coherency picking up the zone of deformation between the Tier A strand and a Tier B splay that likely postdates the original Tier B strand.

### 4.7.3   Afiq Fault North (AFN)

*Profile Section-*

The structure of the AFN resembles the EAF and AFE with a distinct transition between Tier A and B fault strands and symmetric 'Y' shape (Figure 4.45).  However, the Tier A strand extends through Unit 2, which more closely resembles the structure of the AFW.  A new fault strand type is also identified at the AFN: Tier B1a.  Despite showing a similar geometry to both Tier A1 and Tier B faults, it shows both reverse movement and normal movement (inset, Figure 4.45) and is classified as a different fault (further differences and interpretations will be presented in plan view).

Interestingly, this section line also shows the AFE shortly in proximity to the AFN splay point showing the Tier A extending into Unit 2; with the rest of the structure resembling the AFE shown in the overview Section 4.7.1.1.  Noticeably, neither Tier A fault strand extends to the seabed, signifying the upper tip line of the Tier A faults plunge downwards southeast of the splay point.   However, the AFN Tier A strand shows a greater height (c. 1300m compared to c. 950m).  The Tier B faults of both shows an intriguing geometry as the south-western side of the AFN propagates above the Tier B faults on the north-eastern side of the AFW, and therefore the only representation of the AFE at the seabed is a single Tier B strand.

The Tier A strands of both faults extend into the Messinian Evaporites are interpreted to be related to the proximity to the splay point.  Given that the geometries of the upper tips changes considerably here (the Tier A faults no longer propagate upwards to the seabed, and Tier B faults dominate the deformation), it is likely that the basal tip follows suite (as it plunges upward to the M horizon between the section line here and the one presented in the overview, Figure 4.39).  However, there is a clear disconnect in the change of geometry between the upper and basal tips.  Due to the short length of the AFN, this plunging upward of the Tier A strand is not observed before the fault dies out.

*Plan View-*

The AFN, like the AFW, shows a single Tier A strand at 2280ms TWT (Figure 4.38a), however the Tier A1 faults are notably absent.  There is a small splay that occurs on the north-eastern side of the fault zone (opposite to the Tier A1 strands) but the geometry does

not match the Tier A1 faults and is therefore classified as a simple splay approaching the AFN lateral tip.

The intermediate depths from 1800ms TWT to 1580ms TWT show a gradual transition to a geometry that resembles the EAF (Figure 4.43).  At both 1800ms and 1700ms, there are two notable strands that trend sub-parallel to each other.  The strand to the northeast is the Tier A strand, whilst the south-western strand is a Tier B1 fault strand.  At 1700ms, the Tier B1 fault is clearly composed of two segments (each c. 3km long, with some overlap), which is important as it may explain the normal and reverse movement shown in Figure 4.45.  Also at 1700ms, high angle Tier B faults begin to be observed and they are bounded by the Tier A and Tier B1a strands.

The Tier B1 fault reduces to a single, shorter segment at 1580ms depth (Figure 4.43c), with high angle Tier B faults (dipping to the north) replacing the Tier B1 fault and dominating the deformation at this interval.  The Tier A fault is still present on the northeast side of the fault zone, except for small area near Horsetail 3, where the geometry changes to high angle Tier B faults that dip to the south (these are defined in greater details in the next paragraph).  Importantly, the high angle Tier B faults have splayed from the Tier A fault and not the Tier B1 fault.

The seabed deformation (300m above the 1580ms slice) shows a change to almost entirely high angle Tier B faulting (Figure 4.38b, c).  The AFN geometry resembles the EAF with two major well-developed sets of en echelon faults: Set 1 trending on the eastern side (above the Tier A strand) at 078° on average (22° to the fault trace) and dipping to the south, and Set 2 faults on the western side of the fault that trend 064° on average (39° to fault trace) and dip to the north.  There are a few smaller high angle Tier B faults that form an intervening set, with lengths averaging less than 1km and dipping in the same direction as Set 1 (south).  The distance between the two sets increases with distance from the central zone from overlapping each other to a spacing of over .5km to the east.  Similarly, the lengths of the faults in both sets also increase from less than 300m near the splay point to over 1.5km towards the southeast.  The geometry of the AFN is complicated by intersections with two major normal Faults (Horsetails 2 and 3), which will be described later. It should be noted that the entire intersection region between the AFN and AFW has moved towards the northwest about 3km upwards from the 2280ms slice to the seabed (c. 1000m).

The lower angle between Set 1 and the underlying fault trace suggests that the Tier A strand has splayed at a shallower depth from the faults in Set 2. This is in agreement with the observations with the 1580ms slice, where Set 2 faults are established, whilst the Tier A strand is yet to splay. It remains unclear how the intervening set relates to the first two sets: they could be segments separated from Set 1 or they may have grown in response the upward propagation of Set 2 faults. Although there is little evidence in favour of either interpetation, the difference in morphology suggests that the two sets diverged from the through-going fault at different times and have rotated at different stages, with the smaller, juvenile faults of the intervening set forming last.

The presence of the Tier B1 faults on the AFN, suggest a slightly different upwards fault propagation history from the EAF. Specifically, it suggests two sets of splays have occurred, with the Tier B1 fault splaying early from the Tier A strand. Later this fault is abandoned whilst the Tier A fault splays into Tier B faults. The absence of low angle Tier B faults above the Tier A strand is interpreted to be caused by distortion the coherency in intervening slices by MTDs. This interpretation assumes that the low angle state of Tier B faulting occurs only in a short interval before rotating quickly upwards to form high angles. This may be an attribute common to the 'dominant side' of the fault as mentioned on the EAF: when splaying upwards of the dominant side of the fault occurs, rotation occurs in a short vertical distance, whilst the other side is reactive and rotates over a greater distance.
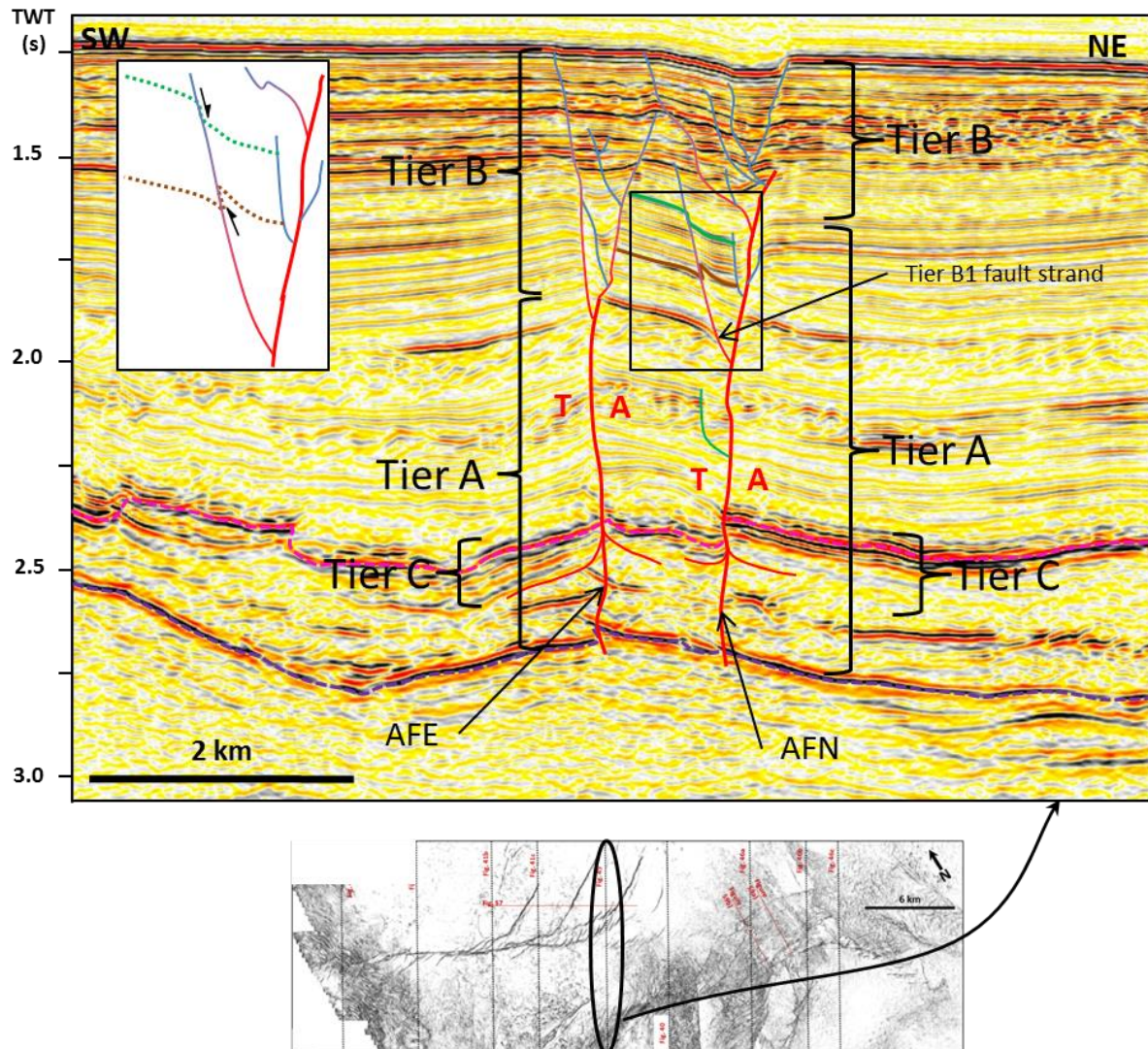
Figure 4.45 – Profile line showing the juxtaposition of the AFE and AFN. They show similar geometries, however, the Tier A strand is taller in the AFN. Furthermore, the Tier B strands of the AFN propagate over one set of the AFE Tier B strands, explaining why the AFE is difficult to identify at the seabed. Interestingly, both show Tier A extending into Unit 2, which is not observed in the rest of the AFE.

### 4.7.4   Afiq Fault East (AFE)

The AFE continues another 17km beyond the AFW and shows a considerably different geometry both in profile section and plan view.  Internally, the AFE also shows considerable difference in geometry between the two domains and is therefore subdivided into Domains 1 and 2 for clarity.

#### 4.7.4.1   Geometry – Profile Section

*Domain 1-*

Little variation occurs in profile sections in Domain 1 of the AFE, with exception of the Tier A strand plunging upwards to the M horizon towards the southeast shown in Fig. 45, and is not described further.

*Domain 2-*

Domain 2 shows a large variation in profile structure between the subdomains: Domain 2a maintains a similar geometry to Domain 1, whilst the profile structure departs from the characteristic 'Y' shape in Domain 2b.  The AFE is encapsulated by normal faults from the Shamir Transtension Zone and Wing Crack Fault 1 (WCF1) at Domain 2a (Figure 4.46a).  However, there are subtle changes in morphology with Tier A lengthening and showing a notable lensoidal geometry.  Main Tier B fault strands are relatively short; however, secondary splays can extend to the seabed.  Importantly, the Messinian Evaporties are absent here, meaning that the Tier C faults detach into the presumed overpressured muds of Unit 1. The Tier C strands are short here, which may reflect the change in lithology of the detachment unit.

Towards the southeast, the structure of Domain 2b of the AFE changes to link with the Shamir Rise Fault (Figure 4.46b, c).  The typical 'Y' structure therefore becomes shorter and changes from a Tier A sub-vertical fault, to become a fault that dips towards the north at 58° on average.  This occurs because the AFE merges with the Shamir Rise Fault that curves around the Shamir Rise structure.  The AFE appears to utilise the passage of the pre-existing Shamir Rise Fault for the majority of Domain 2b; however, it occasionally breaks out of the plane to show a 'Y' shape (e.g. Fig. Figure 4.46c).
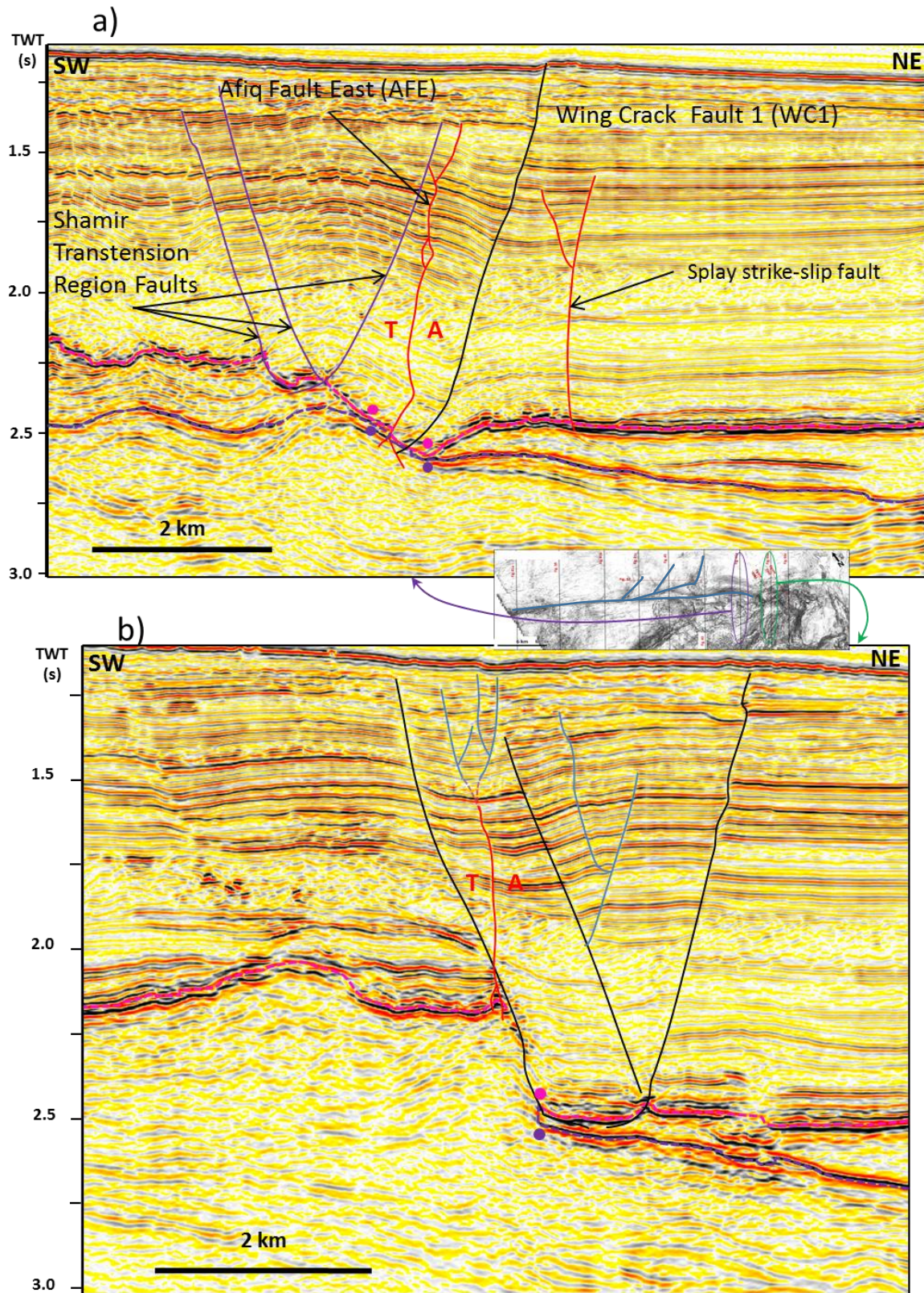
Figure 4.46 – Profile sections from Domain 2 of the AFE. a) Shows the structure of Domain 2a and b) shows the structure of Domain 2b.
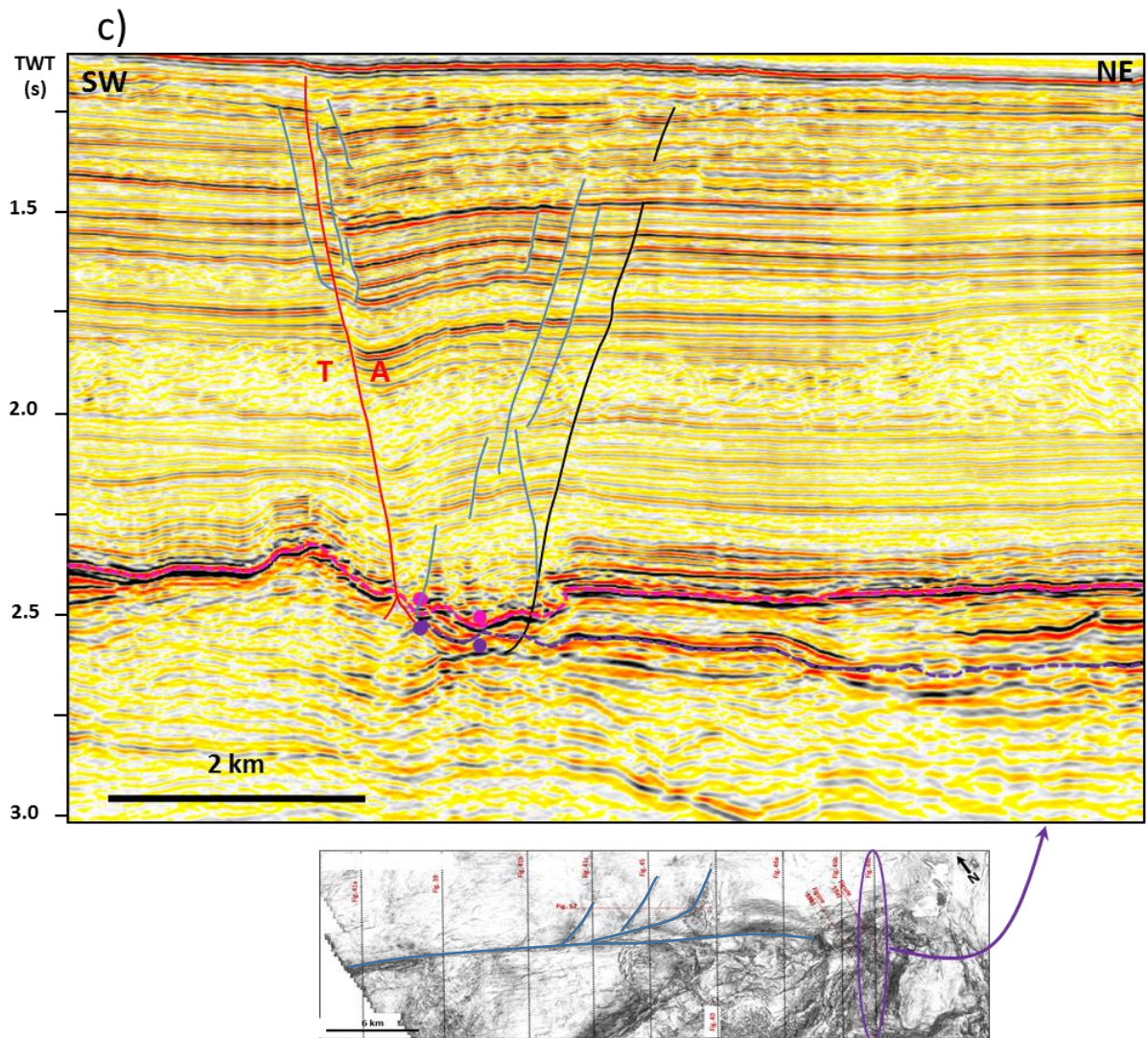
Figure 4.46 - Profile sections from Domain 2 of the AFE. b) and c) illustrate the variability of Domain 2b.

### 4.7.4.2   Geometry – Plan View

Like the previously described strike-slip faults in this chapter, there is a change in fault geometry upwards.  The structures show complex geometries in the intermediate and shallow depths, which is especially noticeable in Domain 2 due to interactions with surrounding structures.

*Domain 1-*

The deeper slices do not show any features different from the AFW and are not described further.  The rest of this section focuses on the evidence of two segments overlapping towards the southeast (near the transition with Domain 2), and features that resemble tip structures at intermediate depths as well as structure of Tier B strands at the seabed.

Images of the fault at intermediate intervals (1800ms, 1700ms, and 1580ms TWT, Figure 4.43) show a progressive change from the Tier A fault strand and lower angle Tier B faults to the high angle Tier B faults.  For instance at 1800ms, the Tier A strand becomes segmented, with low angle Tier B faults (trending on average 075°, with a divergence of 11° from the main trace) located mostly near the linkage zone described in the 2280ms slice (Figure 4.38a).  A few high angle Tier B faults are present near the tips of the low angle Tier B faults where the linkage occurs.  At 1700ms and 1580ms TWT, there is an increase of high angle Tier B faults upward.  It should be noted that most of the high angle Tier B faults are concentrated above the linkage zone, with distance of each fault lengthening away from the Tier A and low angle Tier B faults.

The high angle Tier B faults in this region are interpreted as tip structures based on a resemblance to tail damage zones described by (Kim et al., 2004; Kim and Sanderson, 2006) and are located above the segment overlap observed at 2280ms TWT.  This geometry suggests that two segments propagated towards each other and linked at depth.  However, in more shallow positions, the segments do not overlap and instead show tip structures in close proximity to each other.  This reflects a quasi-elliptical shape as the upper tip of both segments must plunge downwards towards the lateral tips.  The segment overlap and tip structures are therefore interpreted to represent a linkage between the south-eastward

propagating AFE (which is a continuation from the AFW) and a second segment that formed in a region affected by the Shamir Transtension Region.

Two similar structures of interest in the intermediate intervals are located towards the south-eastern extent of Domain 1.  At 1580ms TWT, WCF1 and a low angle Tier B fault of the AFE diverge at an angle of 35° where four smaller faults, each dipping to the southeast, bisect them (Figure 4.43d, inset iii).  Noticeably, both the distance between the bisecting faults and their lengths increase with distance from the splay point.  The second structure at 1800ms TWT, shows a fault splaying from the AFE trace towards the Shamir Transtension Region and bounds a set of bisecting faults, which increase in length with distance from the splay point (Figure 4.43d, inset i).

These structures resemble tail damage zones described by Kim et al (2003; 2004), and are interpreted as such.  However, these structures were argued to represent a mode II tip, which theoretically represents a location of maximum lateral propagation of a fault (Kim et al., 2003).  If this were to be the case here, the fact that they occur at different depths suggests that the lateral extent of propagation along an AFE segment has altered in a relatively short vertical distance, and also switched structures with which it interacts.  Therefore WCF1 and the Shamir Transtension Region may have alternated in activity (slip episodes), and affected the AFE at different times, to form more complex structural interactions.

At the seabed the high angle Tier B faults resemble the EAF and AFN; however, only one full set of fault strands is observed (Figure 4.38b, d).  The majority of the faults dip in the same direction (towards the north), whilst only three faults dip antithetically (towards the south).  The latter of which occur on the other side of the underlying through-going fault zone.  They trend 061° on average, an angle of 58° with the underlying Tier A fault (and a 16° greater angle than with Tier B faults on the AFW).

The low numbers of south dipping Tier B faults are interpreted as a second set of faults has begun to form in the same way as the EAF and AFN.  However, as this second set is less developed, the AFE thus shows a more juvenile status of faulting.  It is therefore possible that the displacement 'shared' with the AFN may hinder displacement along the AFE and therefore impede the development of the Tier B sets.  Furthermore, the small magnitude of strike-slip offset across the EAF (especially at the eastern tip) produces a simple 'Y' shape

structure in cross-section with minimal splays and a similar structure here suggests that the offset is also low across the AFE at boundary between Domains 1 and 2.  Therefore regions where a simple 'Y' geometry is observed may indicate regions of low offset or the presence of a strike-slip fault tip.

*Domain 2-*

The geometry of the AFE along Domain 2 at the seabed shows a very complex relationship with surrounding faults (e.g. the Wing Crack faults and the Shamir Rise Fault).  Domain 2 can therefore be divided into two regions based on the relationship of these faults: Domain 2a, a region comprising a set of high angle Tier B faults bounded to the north and south by two major normal faults that form an intervening graben (the Wing Crack Faults) and Domain 2b, a region dominated by high angle Tier B faults that splay off the Shamir Rise Fault (Figure 4.38d).

Focussing on Domain 2a, the 1280ms slice (Figure 4.38b) depicts a set of high angle Tier B faults that form an en echelon arrangement.  However, the arrangement differs from the other faults presented in this chapter by directly overlying the through-going Tier A strand as opposed to dipping towards the underlying fault.  Furthermore, faults located nearer to WCF1 dip only towards the southeast, whilst faults located near to WCF2 dip to the northwest.  The Tier B faults do not display an obvious change in trend between the two sets of dipping faults; however, both show a lot of variation, trending on average 074° (55° from the underlying fault trace trending at 129°).  These faults are bounded by the Wing Crack faults, which do not link at this interval (in contrast to slices at depth, Figure 4.38a).

Domain 2b shows another very complex zone of deformation that follows the boundary of the Shamir Rise Fault.  The AFE in this region is comprised of several en echelon Tier B faults that are located on the northeast side of the Shamir Rise Fault and dip mostly to the northwest at the seabed (Figure 4.38d).  Some antithetic dipping faults occur, but do not intersect the AFE.  Towards the northwest end of this region, the main fault curves to trend almost east-west and approaches the Shamir Graben 1 faults.  Towards the southeast the AFE curves around the northern extent of the Shamir Rise, with a trend of 145° and the main fault strand

becomes replaced by a series of faults that extend into the El Arish Canyon. The majority dip to the northeast and trend 100°, (c. 45° to the fault zone) with trends of the faults rotating with distance from the Afiq to become almost orthogonal. Their lengths tend to increase with distance from the fault. These faults extend deep into the El Arish canyon and are the blind normal faults described by Baudon & Cartwright (2008b), (Figure 4.11).

The normal faults that extend beyond the south-eastern tip of the AFE are interpreted as a large scale tail damage because of the striking similarity of this fault array configuration to tail damage zones described by Kim et al (2003; 2004). These normal faults are interpreted as antithetic faults or fractures that propagate ahead of the main fault zone in an approximately orthogonal orientation with length increasing with distance from the fault. Although the faults here do not reach an orthogonal orientation, they spread from the Afiq in a similar manner, and instead of being antithetic strike-slip faults or fractures, they are normal faults. The different orientation may be a result of the fault 'wrapping' around the Shamir Rise and locally perturbing the regional stress field as a consequence (e.g. Kim and Sanderson, 2006).

### 4.7.5  Strike-Slip Displacement Distribution of the Afiq Fault

The displacement distribution established for the Afiq Fault is based on kinematic indicators that were measured mostly along the AFW; however, a few data points were obtained that were located along Domain 1 of the AFE, producing a total length of coverage over 19km. 29 points were used to contour the displacement distribution, with depths ranging from 1400ms TWT (a little over 100ms below the seabed) to a kinematic indicator located on the N horizon at the base of Unit 2 (approximately 2860ms TWT), corresponding to a total fault height of 1910m. Most kinematic indicators are derived from three stratigraphic layers where submarine channels occurred in high frequency and allow for greater lateral gradient extrapolation. Some of the kinematic indicators are described below to highlight displacement relationships between various fault splays and also highlight areas of uncertainty. Finally, the contoured displacement distribution of the AF is presented with analysis of the aspect ratio and displacement/distance (d-x) gradients.

*From depths 1420 -1540ms TWT (Figure 4.47) -*

Kinematic indicators across the AFW show low offsets between 100m – 200m at the depth of 1420ms TWT (Figure 4.47), signifying that strike-slip offset occurs near the seabed.  The horizontals offsets are in contrast to the El Arish Fault, which showed dominantly normal fault movement near the seabed.  Interestingly, channels crossing H1 and H2 show 0m resolvable horizontal offset, confirming their movement as dominantly normal faults.

A set of kinematic indicators offers insight into the lateral tip of the AFN as well as how displacement compares between the AFN and AFE (Figure 4.48).  No offset is recorded across the AFE; however, the same channel also crosses the AFN in multiple locations and shows zero offset towards the southeast, and increases to 70m and 100m towards the northwest.  Given that the AFE continues for a significantly greater distance towards the southeast, it is logical to expect that the AFE would show larger offsets, which is not the case.  Both the AFE and AFN (south-western splay) show zero offset across shorter segments indicating these segments are also Tier B geometries and therefore the absence of horizontal slip due may be attributed to proximity to both lateral and upper tips.

*From 2140 ms TWT –*

Offsets recorded at this depth are the highest, and therefore this surface represents the position of the $D_{max}$ (Figure 4.49).  Specifically, the largest offset is located across the transfer zone towards the northwest (Figure 4.49, VII).  This contrasts the theoretical drop in displacement, which often occurs at transfer zones at minimal segment overlap (reflecting fault tip interactions) (Walsh and Watterson, 1990).   However, when considerable segment overlap occurs, the total shared displacement can match or exceed the $D_{max}$ of one of the segments (Walsh and Watterson, 1990; Cartwright et al., 1995).  The channel location southeast of the transfer zone on one side suggests that considerable segment overlap is not relevant here.  Therefore the larger displacement may be explained by linkage occurring early in the growth history, and therefore the fault has become a single, coherent fault to overcome the initial displacement deficit near the segment tips.

Interestingly 220m up-section, the indicator at V (1920ms TWT, Figure 4.50) does not show the $D_{max}$ at the transfer zone, which is instead located just to the southeast at IV. This may suggest a slight change in the kinematics between the fault segments up section from the interval of $D_{max}$. However, the difference in offset is only 150m, which is small relative to displacements of over 2500m and may suggest that the AF comprises a large area of $D_{max}$, with localised variation within.

The 2140ms depth also reveals an interesting observation in how displacement is shared between the AFE and AFN. A total displacement of 1630m (IV, Figure 4.49) is shared across both splays, but individually the AFN shows an offset of 770m whilst the AFE has as offset of 860m. Importantly, the offset across the AFE is located farther to the southeast than the offset across than the AFN. It therefore lies at a greater distance from the $D_{max}$ value mentioned above (the kinematic indicator at VII, Figure 4.49), than offset across the AFN, which given that displacement is decreasing towards the southeast, is contrary to what might be expected.

Thus, a smaller offset across the AFN is interpreted to reflect that less strike-slip offset occurs along the AFN compared to the AFE. This may be due to the presence of the extensional tip structures (Horsetail Faults), which accommodate large offsets from the AFW, and form in the extensional quadrant of the AF (Kim et al., 2003). However, it may also reflect that the AFN is a splay from the original fault strand, defined by the AFW and AFE. Ultimately, branching fault geometry and displacement relationships are poorly understood and will be explored further in Chapter 5.

*M Reflection –*

One kinematic indicator can be located at the M horizon across the AFW (Figure 4.27). Unfortunately, it is poorly resolved due to the Messinian Evaporites and the amount of offset can only be measured to a range between 1000m and 1500m. The time-dip maps outline a channel that approaches the fault zone where it appears to widen sharply into a broader feature before narrowing back into a channel northeast of the fault and meandering towards the EAF.

Despite the lack of constraint on this kinematic indicator, a clear displacement decrease occurs vertically between the offsets from 2140ms TWT and the M horizon at 2560ms (about 420m below); suggesting the fault offset reduces towards the basal tip as it penetrates the salt. Critically, the decrease noted both here and in the EAF have implications to the nucleation and growth history of strike-slip faults and are discussed in Section 6.

*N Reflection –*

At the base of the Unit 2 evaporites the clastic bodies described in detail in (Bertoni and Cartwright, 2007a) are identified as potential kinematic indicators. These were interpreted as clastic remnants left by two palaeo-submarine channels that cross the Afiq Fault as they travel down-slope into the canyon and pool to form an alluvial fan by high positive acoustic impedance responses (Figure 4.51). Unfortunately, the clastic material cannot be located around the fault zone. This is partly attributed to the distortion caused by sharp velocity contrast of the evaporite succession and Unit 1 but may also be due to activity on the AFW in the evaporites causing a large damage zone and destroying the remaining clastics. Therefore these kinematic indicators cannot be interpreted with a high degree of confidence. For example, the easternmost channel may possess a natural meander at the fault zone shown in case 2 (inset, Figure 4.51). However, if the channel is offset (case 1), then 210m occurs at the N horizon and the basal tip therefore propagates into Unit 1.

There is insufficient data to confidently interpret in favour of either case. However, a zero offset is used for the displacement distribution plots shown below in order to constrain the tip line of the basal tip. Furthermore, if there is a small offset at the N horizon, the basal tip of horizontal displacement would be expected to occur within c. 100m – 200m below (using the gradients shown below), and would not significantly alter the displacement distribution plot.
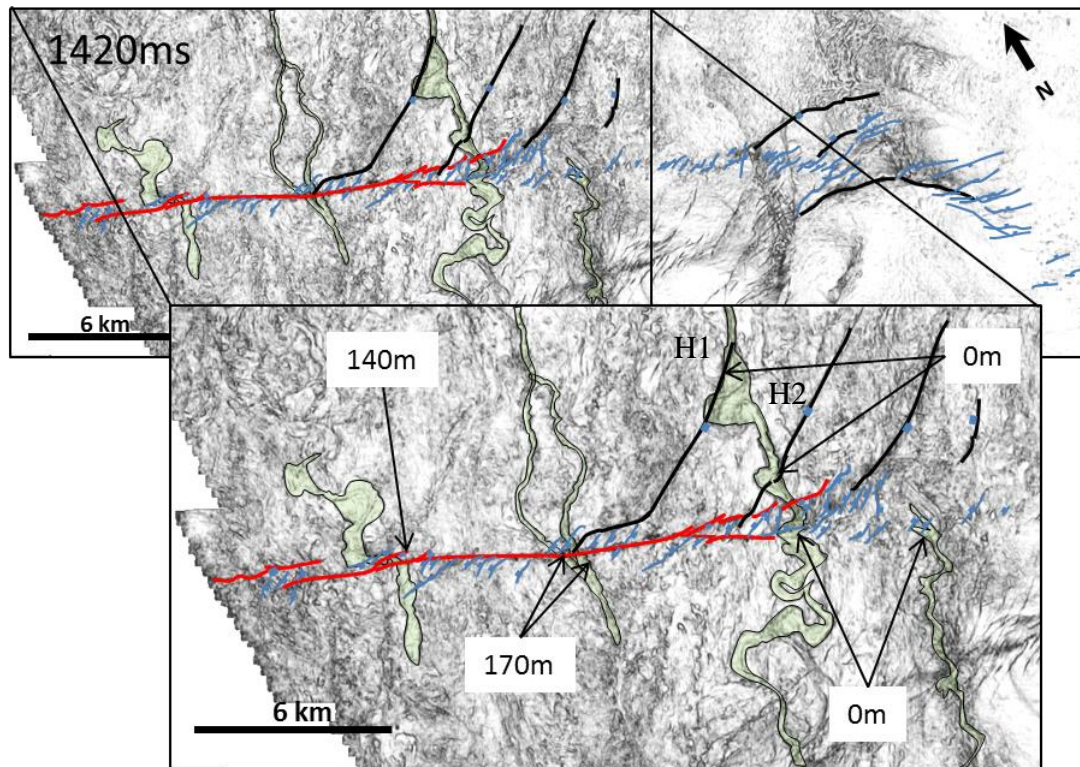
Figure 4.47 - Kinematic indicators from approximately 120m below the seabed show offsets across the AFW, but 0m offset across the AFE and H1 and H2.
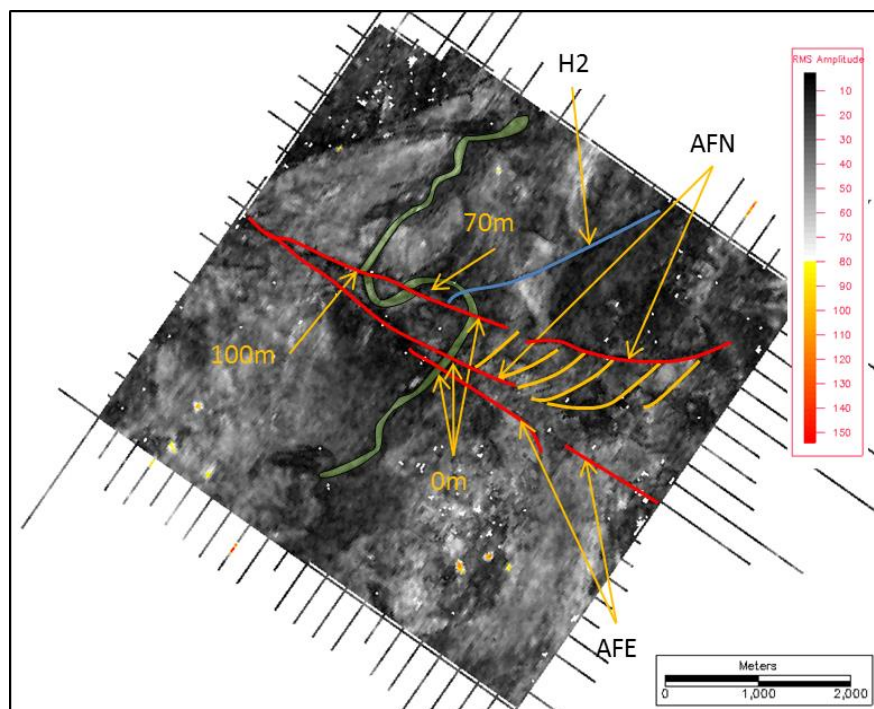


Figure 4.48 - Kinematic indicators from 1540ms TWT show how offset along the AFN reduces to 0m towards the southeast.  This offers insight into how displacement changes with proximity to a low angle Tier B segment.

213
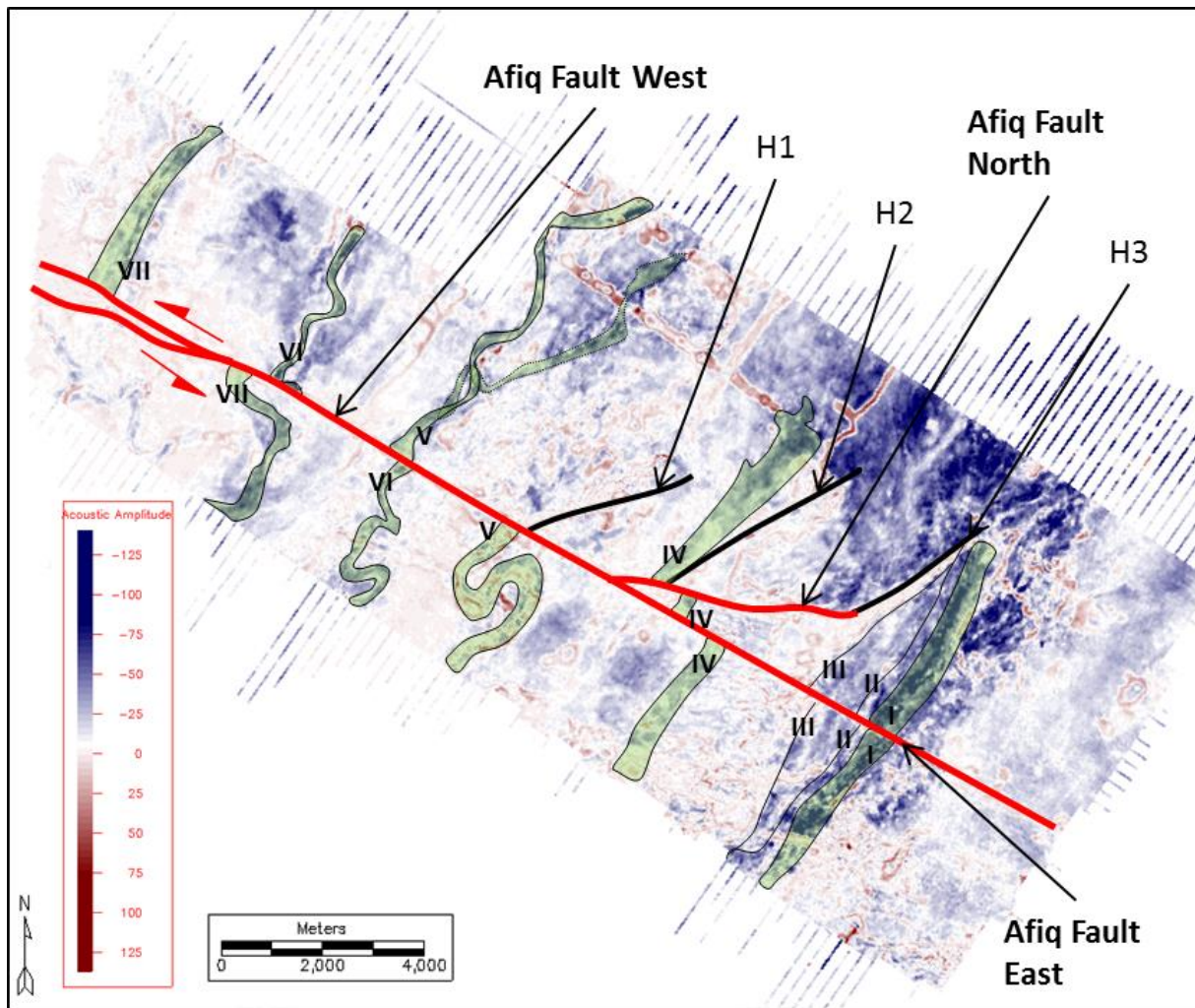
Figure 4.49 - Offsets across the AF from the stratigraphic interval that displays $D_{max.}$ Representative offsets:  I = 350m, II = 280m, III = 510m, IV = 1630 m (860m across AFE and 770m across the AFN), V = 2530m, VI = 2650m, and VII = 2900m.
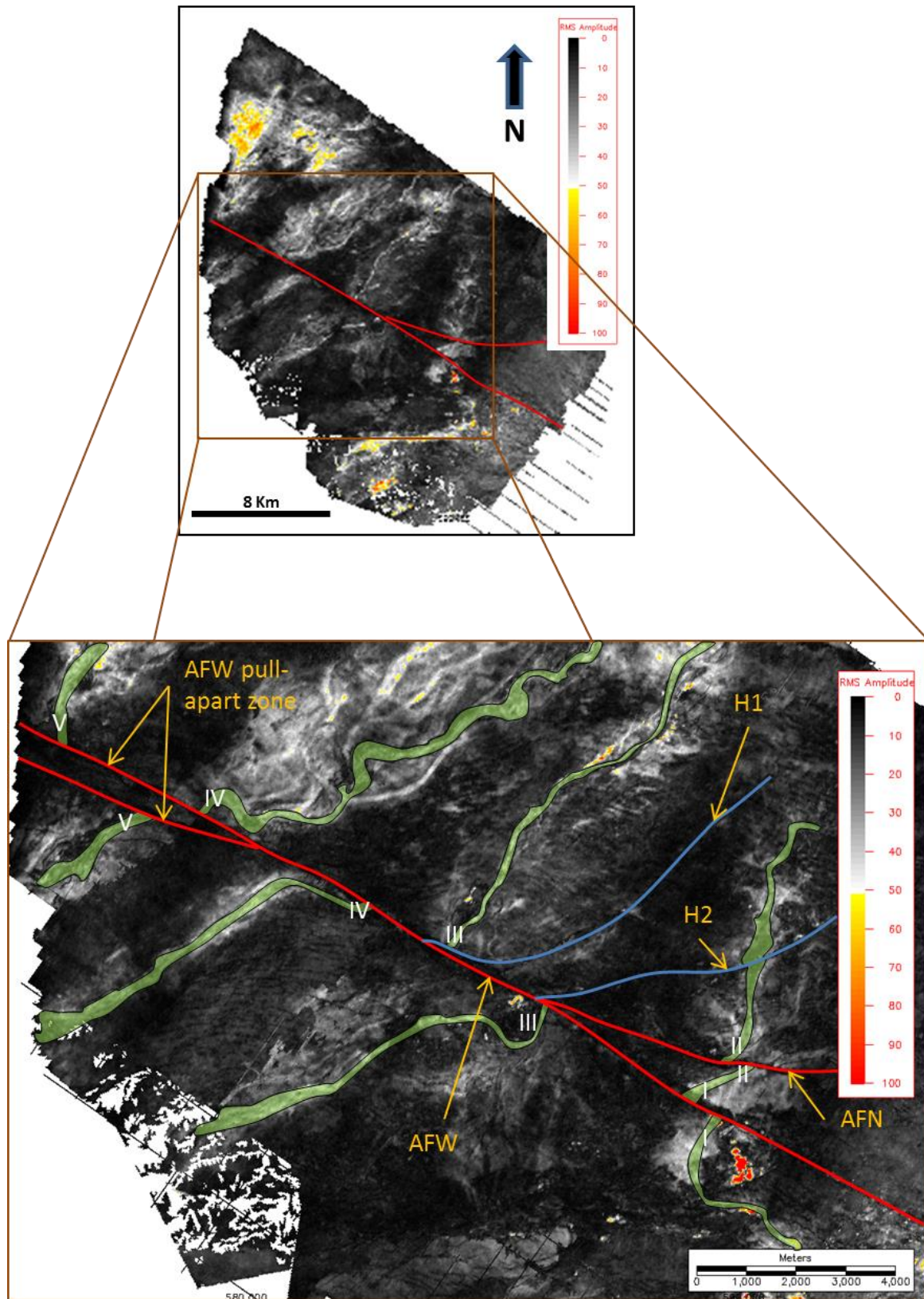
Figure 4.50 - View of kinematic indicators at a depth of 1920ms TWT.  Offsets: I = 550m, II = 380m, III = 2150m, IV = 2750m, and V = 2600m.  Note that $D_{max}$ is located just southeast of the transfer zone.
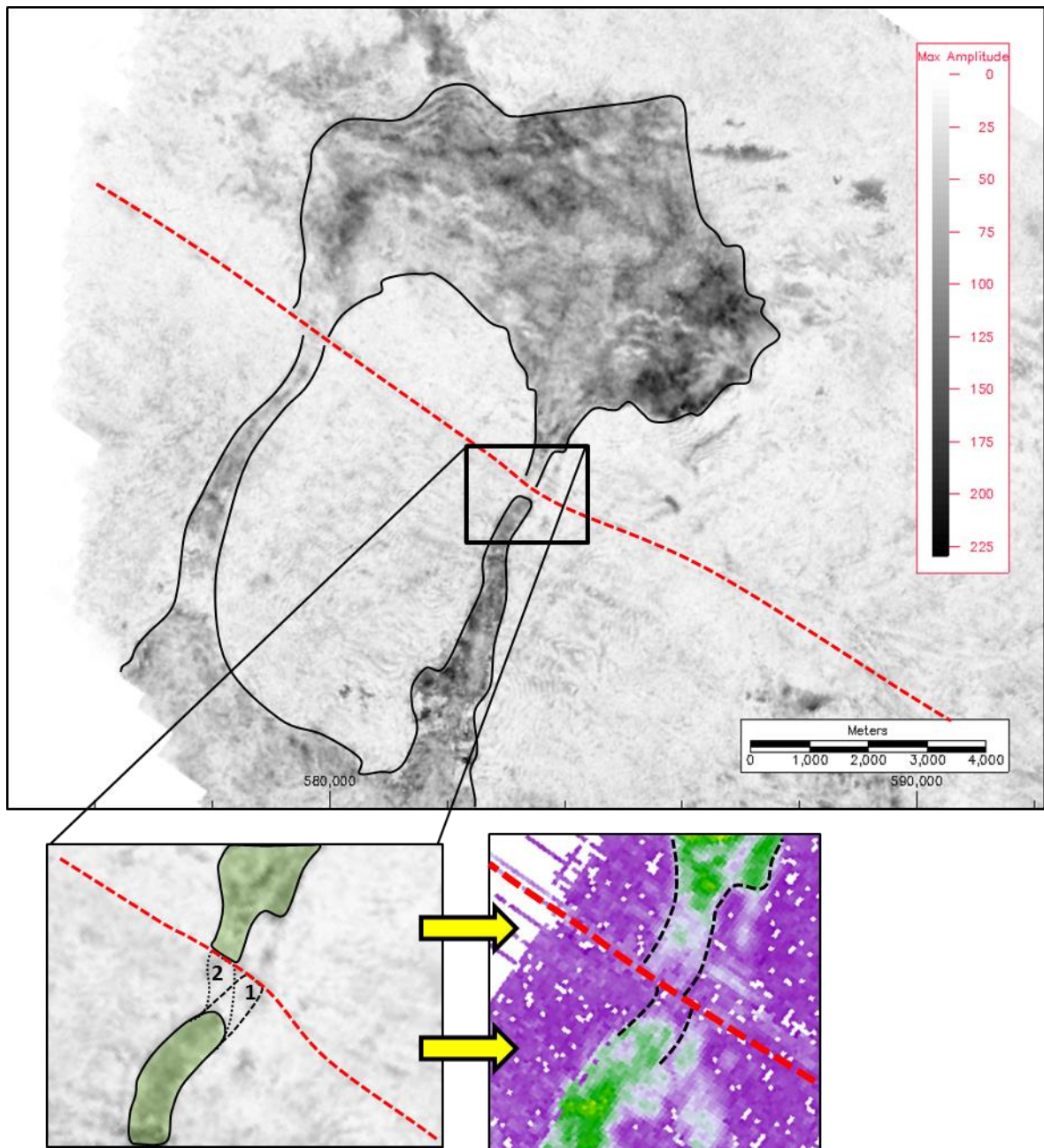
Figure 4.51 - Potential kinematic indicators located as the base of Unit 2.   These could show an offset of 210m if an offset occurs in case 1, or if the channel meanders, then this kinematic indicator is a 0m value.

### *4.7.5.1   Displacement Distribution Plots*

Two displacement distribution plots are presented:  the first shows Two Way Time (TWT) on the Y axis, whilst the second is a depth converted plot to provide a better visualisation of the fault shape through the Messinian Evaporites (Figure 4.52, Figure 4.53).  The AF shape is rectangular, in contrast to the more elliptically shaped EAF.  Interestingly, strike-slip movement reduces to zero at the seabed c. 1km southeast of the splay line with the AFN (shown in red).  This is depicted by a zero contour for the strike-slip displacement plunging downwards from the seabed and tapering at depth towards the southeast side of the plots.

The plunging strike-slip zero contour reflects the change in geometry between the AFW and AFE.  Thus the Tier A fault strand plunges downwards from the seabed near the splay line; however, the fault still reaches the seabed southwest of the splay line in the form of Tier B faults (resembling the Central Region of the EAF, Figure 4.32).  Importantly, the plots do not provide coverage of the entire AF, because kinematic indicators are only observed along the AFW and the north-western half of Domain 1 of the AFE.  Therefore the linkage zone and the complex structural interactions of Domain 2 that were described in Section 4.74. are not shown.

The AF fault plane is characterised by a single large displacement maximum region over 2500m, which decreases radially towards the vertical and south-eastern tips.  No linkage zones are observed from displacement maxima, in contrast to the EAF.

*Aspect Ratio and Displacement/Length Gradients-*

A true scale displacement distribution plot is presented to convey fault shape, aspect ratio and d-x gradients (Figure 4.54).  The aspect ratio was measured using twice the length of the fault, as the fault reaches a displacement maximum at the edge of the dataset, and therefore the fault is expected to be much longer, estimated at greater than 40km in total length.  In addition, this value excludes the length of Domain 2, where the fault continues with a different structure, and potentially increases the total length to over 50km.  An aspect ratio range of c. 28:1 is therefore calculated using a height of 1910m.

The vertical d-x plot shows a C-type profile with a difference in distribution between the centre to top-tip and centre and to basal tip (Figure 4.54).  The displacement/length gradients

217

show very high value 3.33 from the centre to upper-tip and 2.83 from centre to basal-tip. Interestingly, each gradient is almost exactly ten times as high as the gradients across the EAF.

The extremely high vertical gradients and aspect ratio suggest an even higher degree of growth restriction than the EAF. This is not surprising as the height of the AF is only c. 700m taller, yet accommodates offsets up to 16 times the EAF. Both faults show a higher gradient towards the upper tip, which suggests upwards propagation has been more highly restricted by the seabed than downwards propagation into the Messininan Evaporites.

Further inspection of the vertical gradients reveals interesting observations. For instance, the upper gradient is defined by two clusters, with two points located near the centre (offsets of 2550m and 2370m) showing a gradient change of 0.82 whilst the two points located near the seabed (150m and 160m offsets) show a very low gradient change of 0.10 (Figure 4.55). The intervening gradient between the two sets of kinematic indicators shows an extremely high gradient of 4.42. The kinematic indicators from centre to basal-tip do not show the same clustering as the top half of the fault. If a 210m offset does occur at the N horizon, the basal tip of strike-slip movement could extend downwards to a depth of 2950ms (c. 100m below Unit 2).

The sudden changes in gradients are interpreted to indicate a change from pre-kinematic to syn-kinematic propagation. The fact that an already high gradient of 0.82 must increase to 4.42 seems an unlikely phenomenon if the kinematic indicators near the seabed were also pre-kinematic. Furthermore, if the low value kinematic indicators (both of which are channels) were active contemporaneously with slip on the AF, then it is possible that they may show considerably lower values (Childs et al., 2003), which would in turn would cause the intervening gradient to increase, as observed here. The fact that the Tier A fault strands (which show dominantly strike-slip motion) also reach the seabed here, suggests that strike-slip motion is actively occurring at present day, and corroborates the interpretation of these channels as syn-kinematic indicators.

The maximum lateral gradient is plotted for the kinematic indicators located at 2140ms TWT. The lateral gradient averages 0.16, and shows a quasi half C-type profile. A notable increase in gradient from 0.056 to 0.33 occurs northwest of the splay with the AFN, indicating that

offset reduces at a faster rate in proximity to a major splay.  Southeast of the splay, the gradient drops to 0.12, indicating that offset reduction reduces at a slower rate after splaying occurs.  A rough prediction of where the zero contour (tip line) should occur is 21.3km; which coincides with the boundary between Domain 1 and 2.   Interestingly, if this is compared to a plot that includes the offsets of the AFN collated in to one fault plane, there is a clear change in the gradients, which also affects the distribution of displacement contours (Figure 4.56).

Given that the AFE continues for many kilometres (with clear evidence of Tier A strands) to the southeast suggests that the gradient calculated above to estimate the tip location is incorrect.  Despite no kinematic indicator constraints along the AFE, it is unlikely that there is no strike-slip movement.  Therefore it is interpreted that the AFE must experience a further reduction in displacement gradient towards the southeast.  This reduction may still be derived by the splaying of the AFN, which has inhibited further slip along the AFE, with the effects compounding with distance from the splay point.  Furthermore, interactions with the Wing Crack Faults and Shamir Transtension Region may also affect the displacement distribution, with some of the slip transferred into these neighbouring structures.
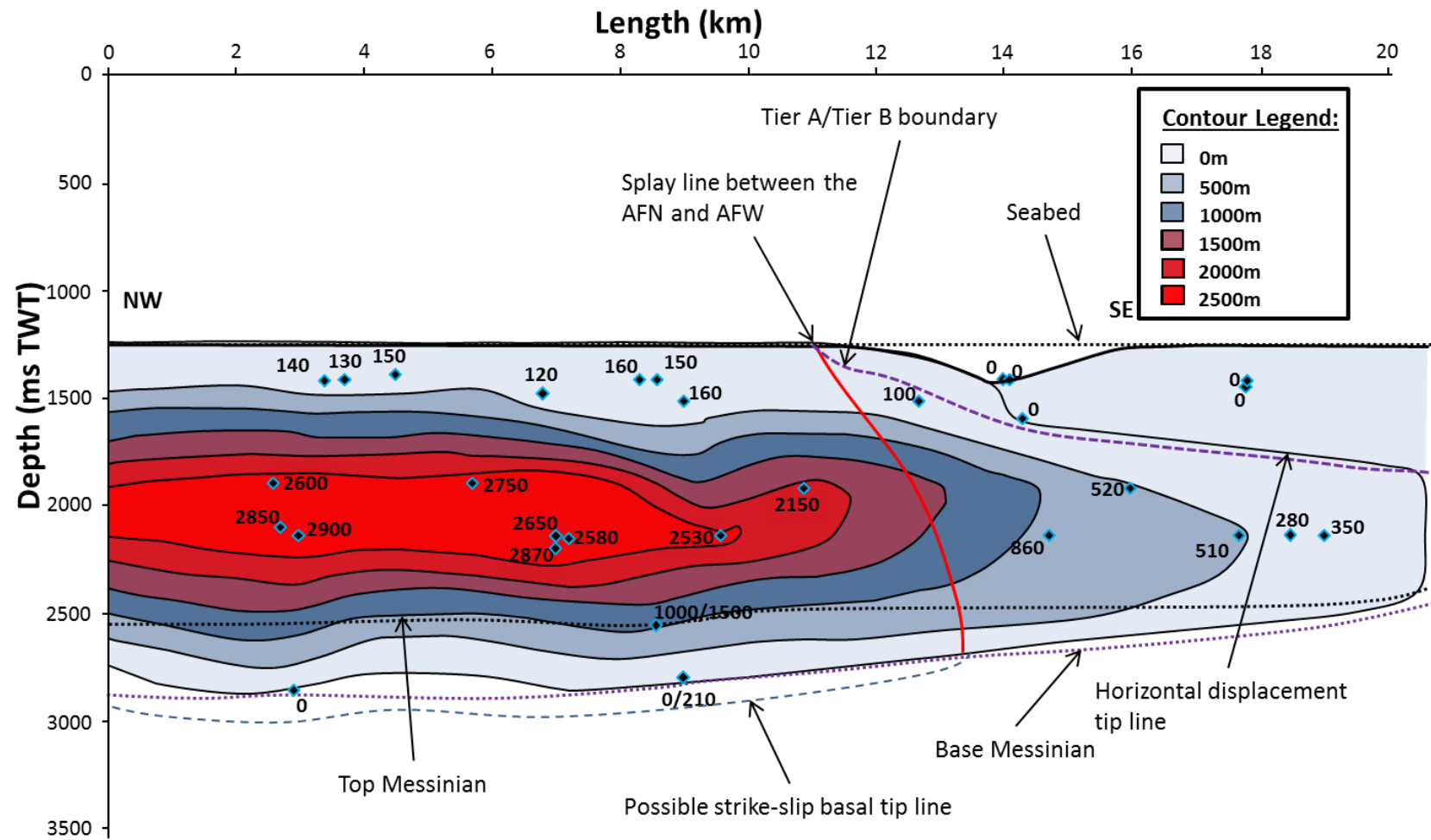
Figure 4.52 - Displacement distribution plot of the AF in ms TWT.  Most of the offsets are derived from the AFW.  Southeast of the red line, the fault changes to the AFE.
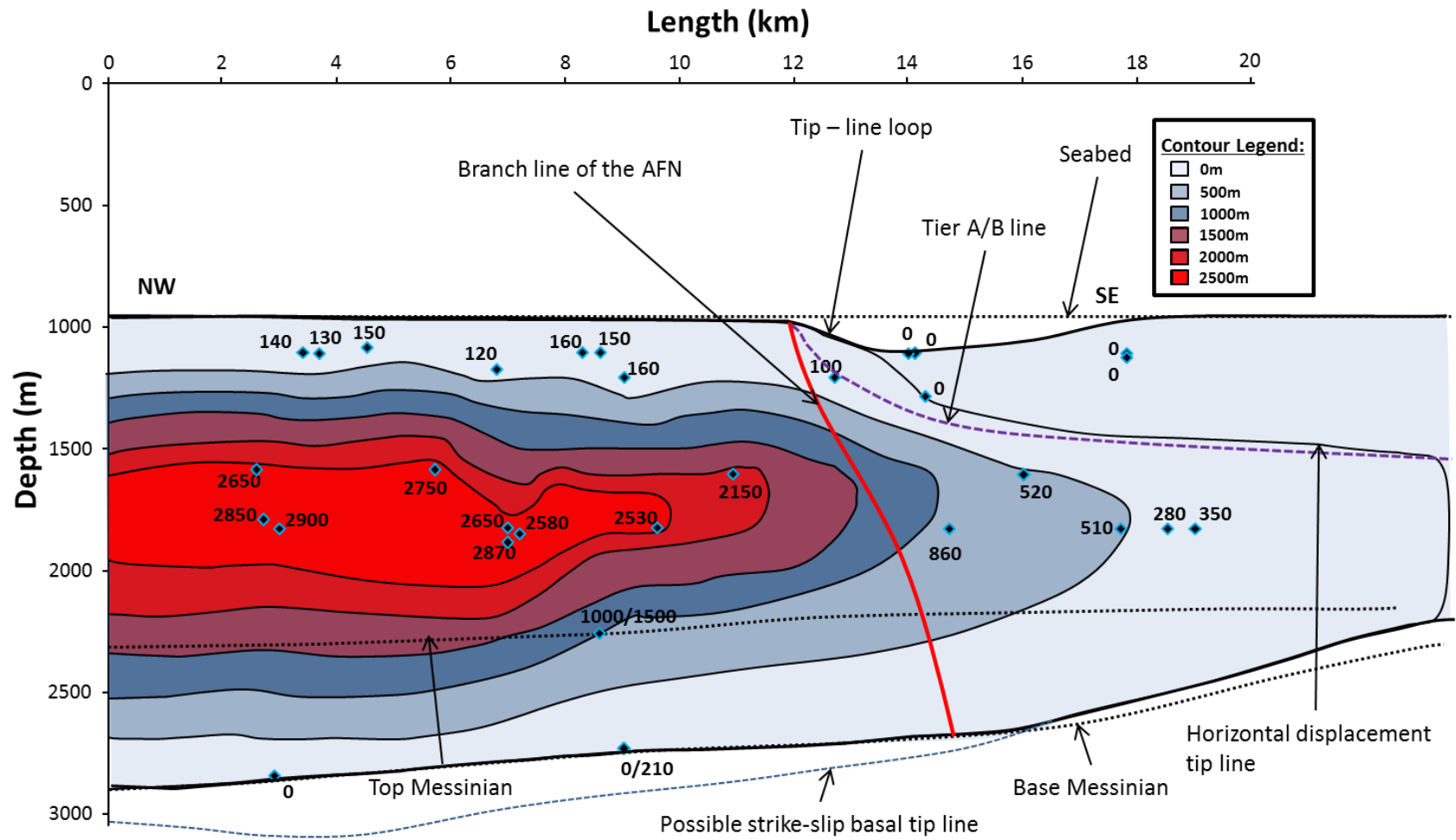
Figure 4.53 - Depth converted displacement distribution plot of the AF to better account for the shape through the Messinian Evaporites.
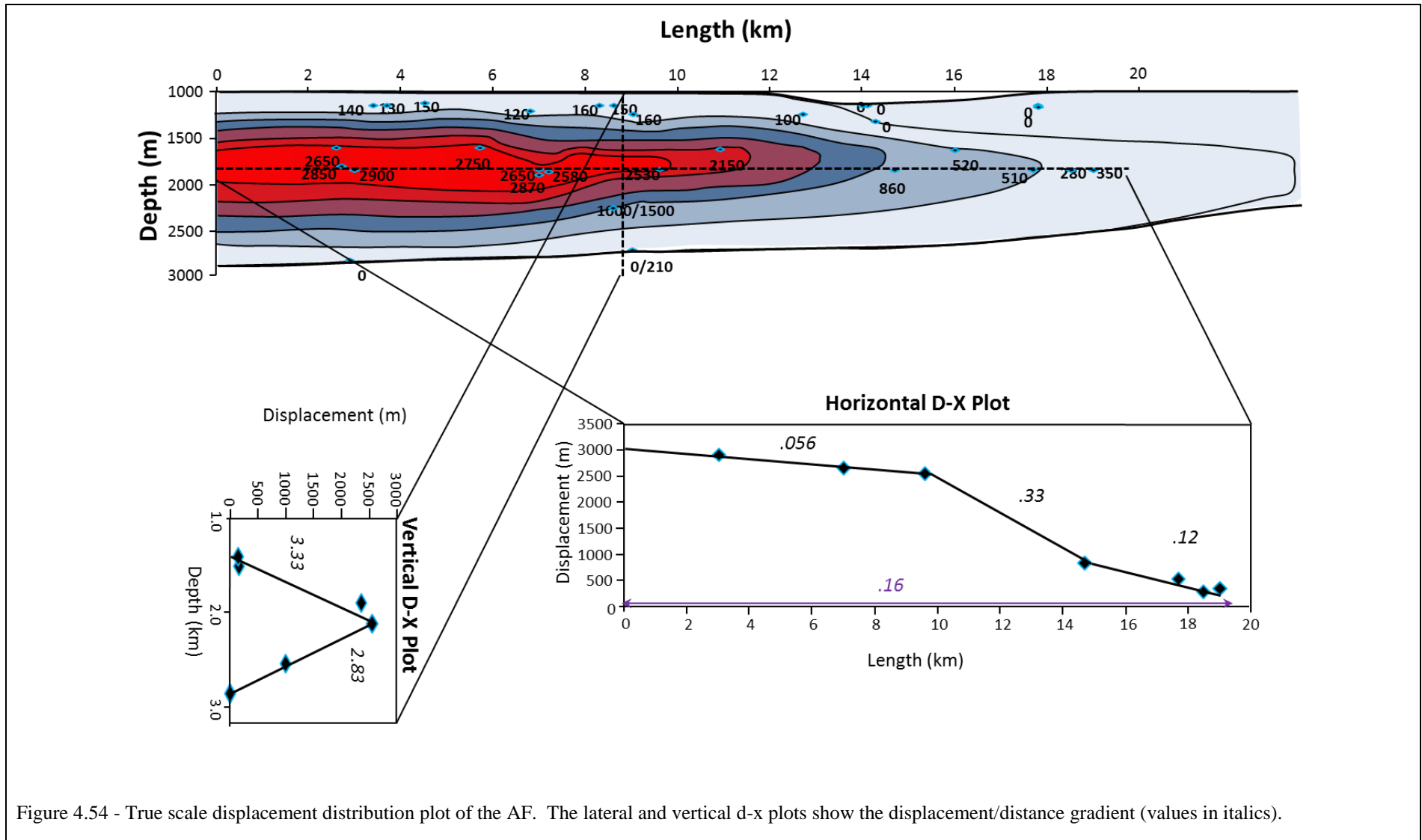
Figure 4.54 - True scale displacement distribution plot of the AF.  The lateral and vertical d-x plots show the displacement/distance gradient (values in italics).
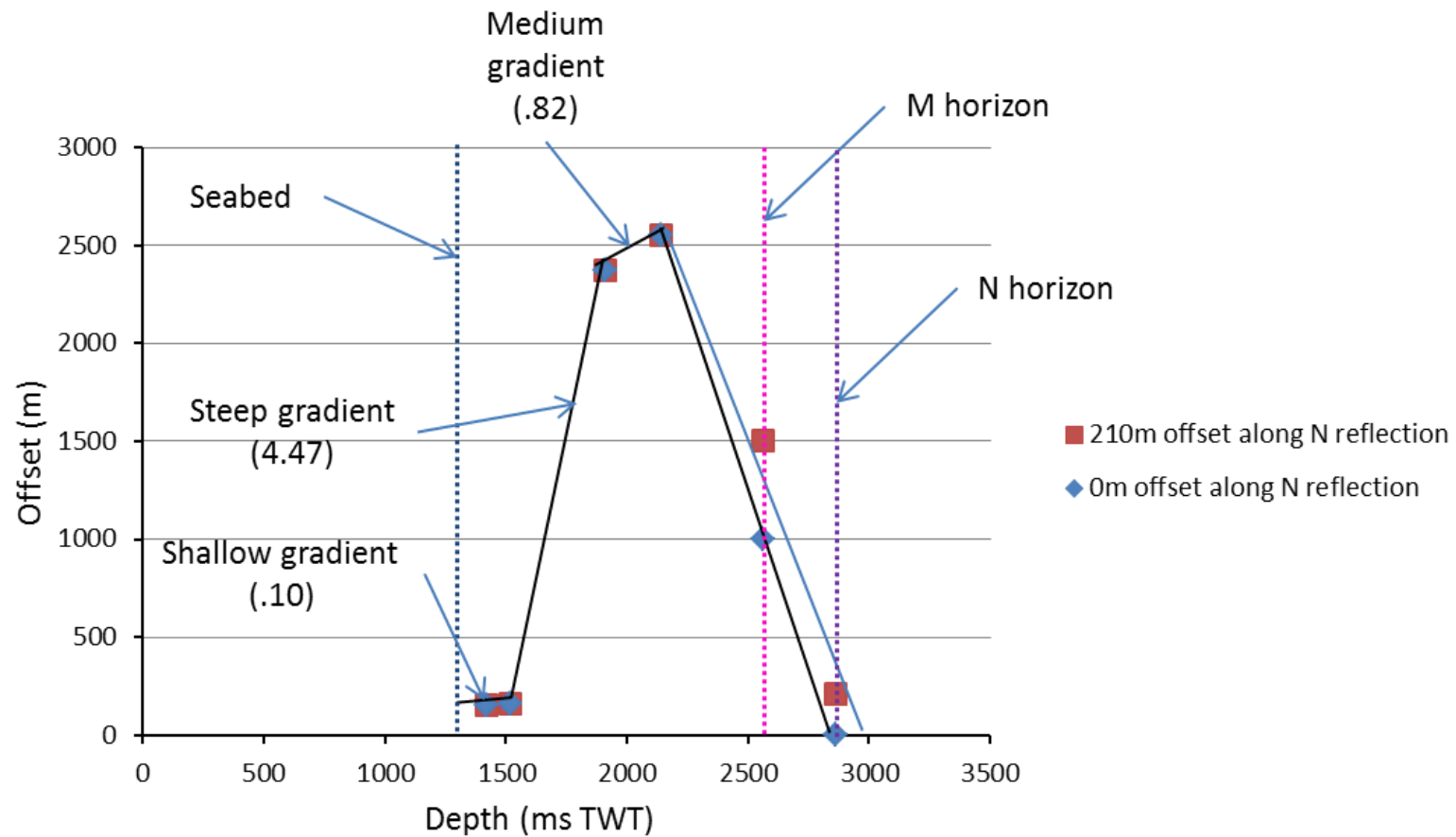
Figure 4.55 - The same vertical d-x plot from Figure 54 is shown in greater detail, with two end-member situations.  The first assumes 0m displacement at the N reflection and a smaller 1000m offset at the M reflection, whilst the second assumes the higher possibilities of 210m at the N reflection and 1500m at the M reflection.  This allows for a crude prediction of the basal depth of the AF.  Noticeably there are several distinct changes in gradients of the upper indicators.  The extreme gradient change between .82 and 4.47 may suggest that the shallowest indicators are affected by syn-kinematic conditions.
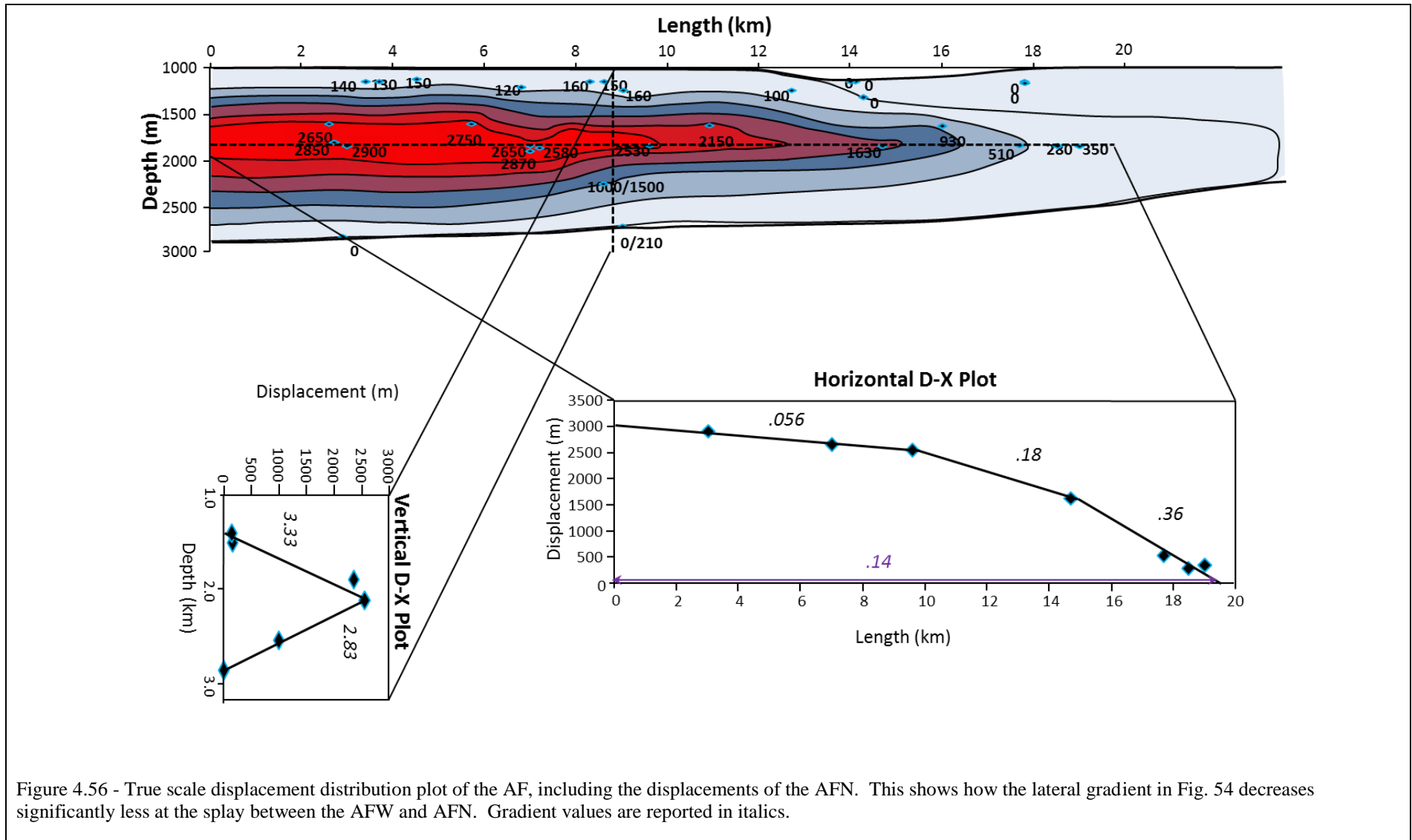
Figure 4.56 - True scale displacement distribution plot of the AF, including the displacements of the AFN.  This shows how the lateral gradient in Fig. 54 decreases significantly less at the splay between the AFW and AFN.  Gradient values are reported in italics.

### 4.7.6   Extensional Tip Faults of the Afiq Fault

Tip structures or damage zones of strike-slip faults have been studied in detail in several studies (e.g. Kim et al, 2003; 2004) and can provide useful information into understanding the timing of faulting.  The primary objective of this section is to present profile sections that show the timing of the faulting and relate these to the timing and growth of the Afiq Fault. The tip structures are divided into two sets: the Horsetail Faults and the Wing Crack Faults, with the former splaying from the AFW and AFN, whilst the latter structures splay from the AFE.  Together they allow a comparison into timing of deformation between the two regions of the AF.

#### 4.7.6.1   Afiq Fault West/North – The Horsetail Faults

Three large normal faults intersect the AFW and AFN, and are denoted Horsetails 1, 2, and 3 (H1, H2, and H3).  They are interpreted as extensional features that formed in response to the sinistral motion on the AF and have been studied in detail by Nelson (2007).  Although this study focuses on the propagation of strike-slip faults, the timing of growth on extensional features provides insight into the timing of strike-slip movement along the AF, and is therefore described here.

The horsetail faults are best shown in profile section to describe their geometry and displacement (Figure 4.57). All three are planar faults that dip between 62°- 66° towards the southeast, with basal tips detaching into the Messinian Evaporites and the upper tips reaching the seabed, and forming fault scarps.  Maximum throw values on H1 and H3 is 150ms TWT, whilst the throw of H2 is lower at 90ms TWT.  Interestingly, the upper reflections in Unit 3a show no thickening in the hanging wall.  Growth packages are clearly seen in the succession just below Unit 3a (labelled units b and c) on H1 and H3 in particular; however, H2 shows minimal or no hanging wall thickening.  A fourth antithetically dipping fault, H4, links at depth with H3 and shows smaller throws of 20ms (shown on coherency slices Figure 4.38).

The horsetail faults show a similar linear trace in plan view that trend between 059° - 062° (Figure 4.38).  However, H2 is significantly longer (7km) than H1 and H3, (3.9km and 4.6km, respectively).  Each fault shows variable intersections geometries at different depths with the AF.  This is particularly noticeable at H1, which curves to link with en echelon Tier B faults at the seabed; however, it links with the Tier A strand at depth.  This signifies that

H1 has grown to accommodate the changing AF geometry, and highlights how complex fault interactions can be in 3D (discussed more in Chapter 5).

These faults were interpreted as horsetails faults by Nelson (2007) and this classification is adopted here in accordance to the classification of smaller extensional tip structures by (Kim et al., 2004; 2006), where horsetails are defined as small extensional fractures that open in the extensional quadrant of a strike-slip fault at an angle of c. 30°. Although the features observed here are faults and oriented at a slightly higher angle, they show a geometry that resembles horsetails in the field (Figure 1.18). Fault H4 is interpreted as a small accommodation fault that accommodates the dip-slip deformation from H3.

The timing of movement along these tip structures provides insight into the timing of movement on the AF. The growth strata on H1 and H3, in particular, show that movement mostly occurred in the Plio-Pleistocene and that that the growth was likely episodic. However, the lack of growth strata on H2, suggests that it propagated later as a blind fault (following the criteria proposed by Baudon and Cartwright, 2008b). Displacement distribution by Nelson (2007) show that H1 and H3 have displacement maxima located near the branch lines with the AF (Figure 4.58), which suggest that the faults initiated as extensional structures in the tip region of the AF, which subsequently propagated radially away. H2 by contrast shows a displacement maximum at the centre of faults, suggesting that it initiated at a distance from AF, and has grown to accommodate the extensional deformation from H1 and H3 at a later stage.

### 4.7.6.2   Afiq Fault East – The Wing Crack Faults

The Wing Crack Faults (WCF) are large normal faults that show differing interactions with the AFE at different depths. This section focuses on WCF1, as it links directly to the AFE at most depths. Importantly, these interactions allude to the timing of deformation at the AFE and provide insight into the growth history and geometry of the AFE (similar to the Horsetail faults along the AFW).

Throw variation across WCF1 allows insight into the timing of normal sense offset that has occurred as well as its distribution near the divergence with the Afiq. Two section lines (Figure 4.59a, b) are oriented approximately orthogonal to strike (location on Figure 4.38).

From plan view perspective, the first line is taken at the centre of the WCF1 to ascertain the maximum throw values, whilst the second line is situated close to the intersection point with the Afiq fault.  The former (Figure 4.59a) shows a maximum throw of 198ms TWT.  Importantly, there are two packages of sediments that show thickening in the graben, signifying that deposition occurred syn-kinematically with fault movement (Thorsen, 1963; Edwards, 1995).  This shows that fault growth occurred in two separate periods, with the first occurring in the late Pliocene.  The second occurs on Unit 3a (in green), and shows that faulting is currently active.  It should be noted that there is thickening of the intervening sediments between the green and blue packages; however, due to the presence of MTDs it is difficult to discern if this is actually a syn-kinematic package.  Importantly, intervening reflections between the MTD units do not show thickening and therefore indicate a period of quiescence in fault activity (Edwards, 1995).

The second section line crosses WCF1 near the lateral tip that intersects the Afiq fault (Figure 4.59b).  Throw values are significantly less on WCF1, with a maximum throw of 116ms TWT at the top of the MTD (brown horizon), with the two syn-kinematic packages showing a reduced thickening into the graben.  Importantly, despite WCF1 having a reduced offset in this section, the throw does not reduce to below seismic resolution as expected for a free tip (Nicol et al., 1996).

*Interpretation-*

A throw of 116ms TWT (about 116m), suggests that WCF1 does not die out at the AFE, and is instead kinematically linked with it. However, as the larger offsets occur deeper in the Unit 3 sediments, it is interpreted that WC1 formed before the AFE, probably as a result of accommodation of collapsing sediments uplifted by the Shamir Rise structure.  The timing of this would have been early in Unit 3 (late Pliocene), the AFE would have then propagated through the wing crack region and linked with WCF1 at a later time, likely coinciding with the second of the syn-kinematic packages.  It is important to note that the second set of growth strata near the seabed suggests that movement has occurred on these faults more continuously than the Horsetail Faults, and also appears to be later.  This is explained by both proximity to the lateral tip of the AF towards the southeast, and the added movement derived from the neighbouring structures.

The kinematics governing these faults is highly complex and their genesis is probably the result of conflicting deformation zones from the Shamir Transtension Region and the sinistral AF movement.  For example, faults WCF1 and WCF2 could have formed as extensional faults responding to the sinistral movement of the AFE (in a similar mechanism to the Horsetail faults from the AFW) or they could be a continuation of the Shamir transtension zone as the graben formed by WCF1 and W2 follows a similar trend to Graben 1, or a combination of both.
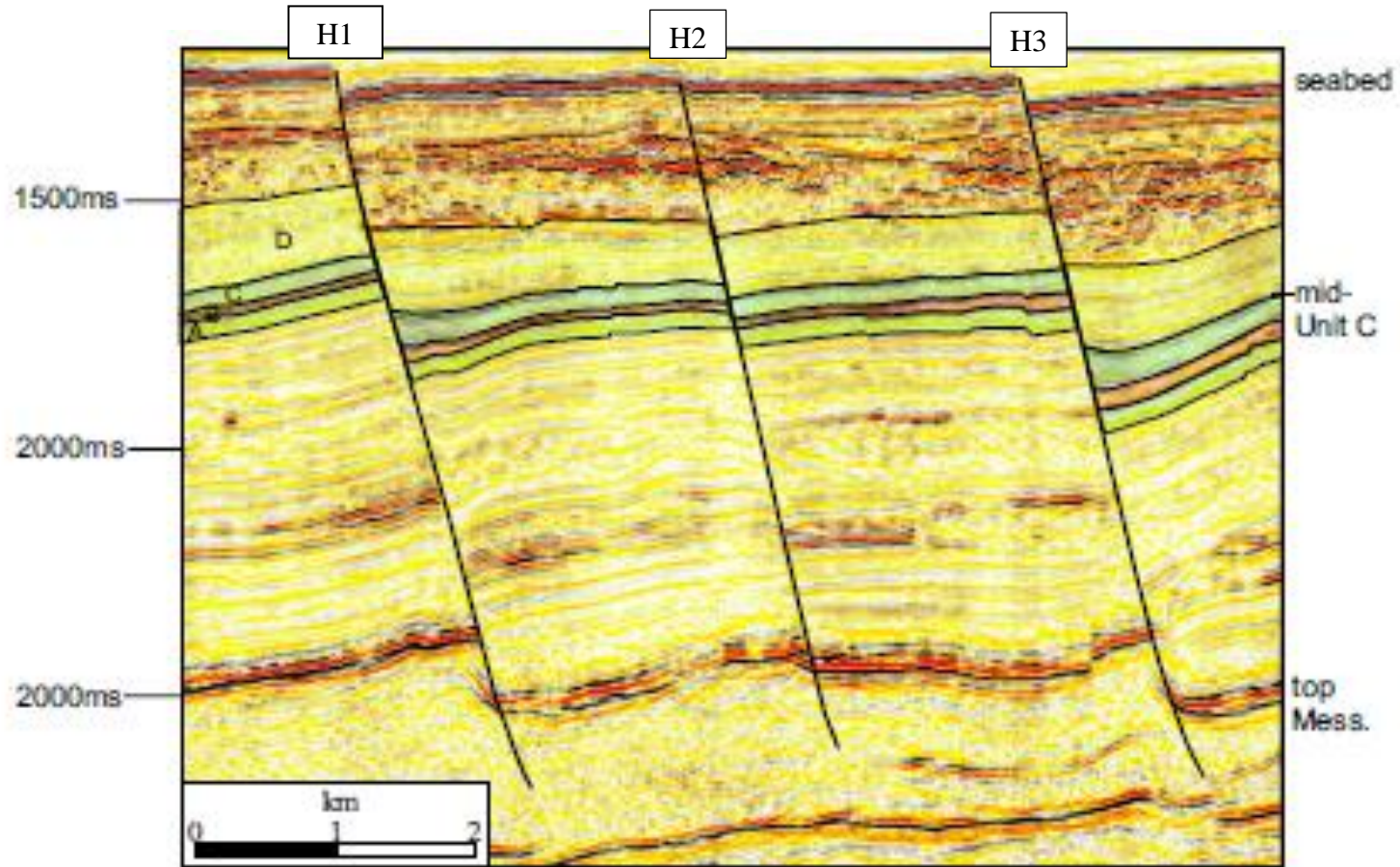
Figure 4.57 - Profile-section showing the structure and displacement on the horsetail faults. Note that growth strata are observed at the units labelled b and c on H1 and H3. However, little growth is observed in Unit 3a. Adapted from Nelson (2007).
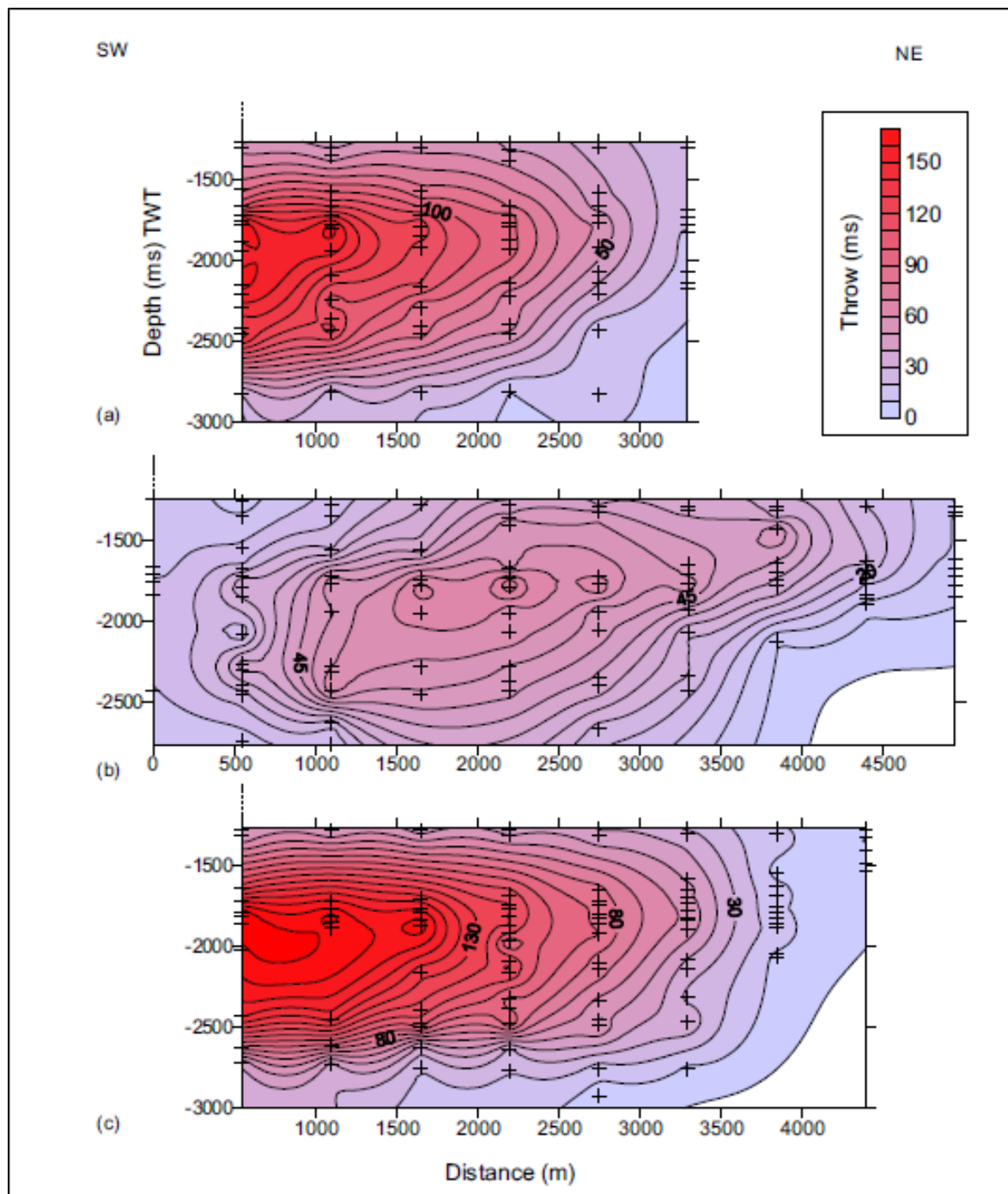
Figure 4.58 - Shows the displacement distribution of the three horsetail faults.  a) H1 shows displacement maximum occur at the intersection with the AF, b) H2 shows less total offset with the maximum occurring at the fault centre, and c) H3 shows a similar relationship to H1, with maximum displacement occurring at the AF and reducing with distance away from the fault. Adapted from Nelson (2007).
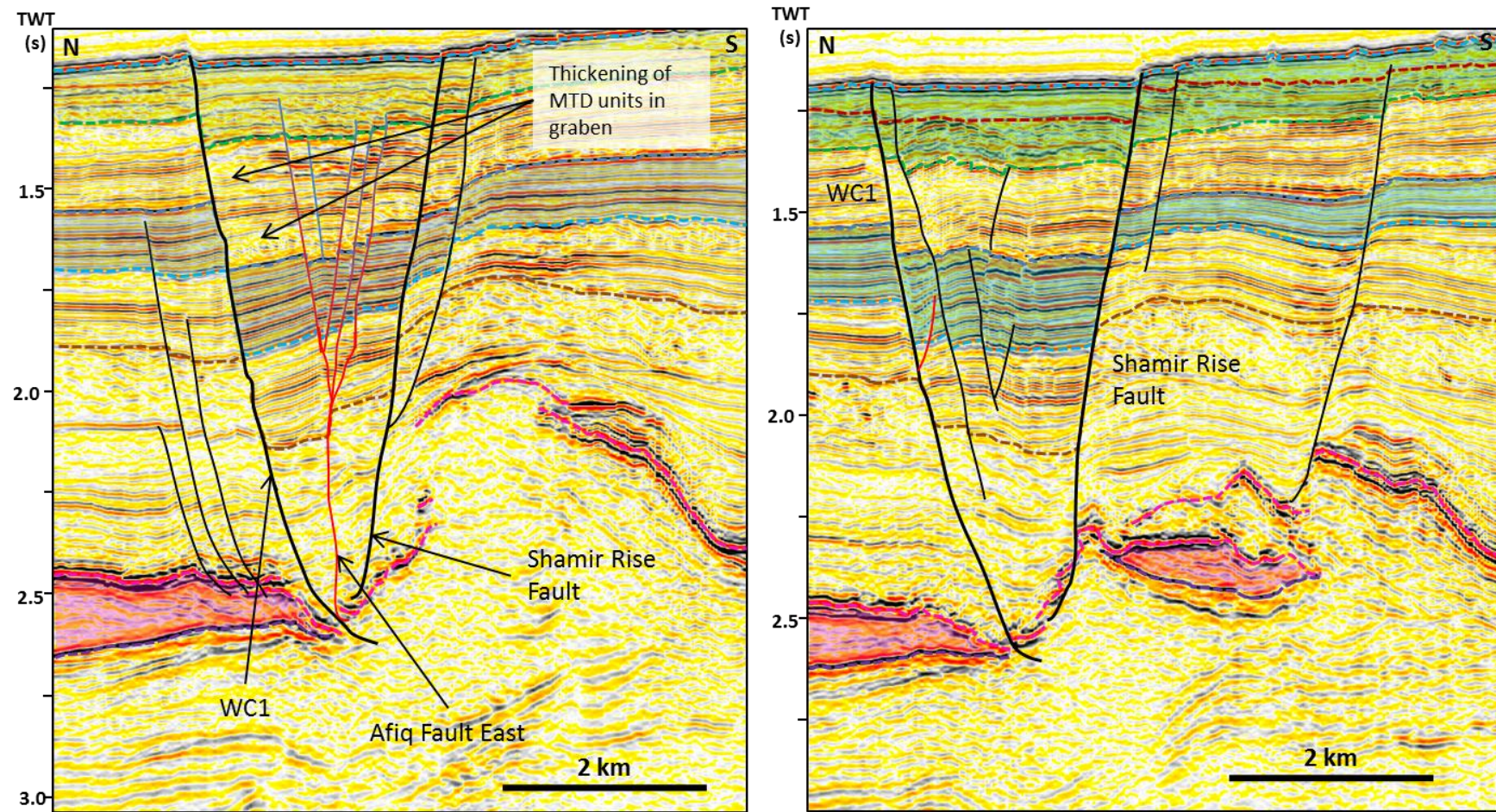
Figure 4.59 - a) The first profile shows a maximum throw of 198ms TWT on WCF1 and 134ms TWT on the Shamir Rise fault.  This is taken from the brown horizon at the top of an MTD.  Growth strata are identified in the blue and green packages, suggesting at least two phases of syn-kinematic growth.  Profile b) shows reduced displacements at the brown horizon (116ms); however, this is still significant given its proximity to the intersection with the AFE.

### 4.7.7 The Afiq Fault Geometry in the Messinian Evaporites

Due to the poor imaging of the AF in the Messinian Evaporites, the geometric descriptions were only briefly stated in the overview.  However, the basal tips of strike-slip faults are rarely studied.  It is important to present some observations here that allude to the structure of the faults at this level.  The aim of this section therefore is to highlight questions that observations from profile section and displacement distribution induce.

*Afiq Fault West Geometry-*

The AFW consistently shows two faults diverging from the Tier A at the M horizon and propagating into the evaporites for about 1km on the south-western side and 1.5km on the north-eastern side (Figure 4.39).  Both fault strand exhibit a geometry that resembles thrust faults with the north-eastern fault propagating under a package of continuous, medium amplitude reflections (Figure 4.60).  The thickness of this package increases towards the AFW and decreasing to zero away from the fault.

The package is interpreted as a more stratified evaporite layer within Unit 2, and suggests a relationship with the fault geometry.  Either this subunit was uplifted at an early stage, causing the notable change in seismic response, or it may have acted as a plane of weakness, which was utilised by the detachment fault.  The thrust like geometries are interesting as it may suggest that when a gravity driven fault initiates at the salt, the Tier C strands act as thrust shear zones before becoming dominantly strike-slip and forming the characteristic Tier A geometry.

*Afiq Fault East Geometry-*

The structural style of faulting changes in the AFE to resemble geometries exhibited by the EAF.   Principally, the Tier A fault is not observed within Unit 2, (with the exception of proximity to the splay point with the AFN, Figure 4.45).  Instead faulting is composed of two or more Tier C fault strands that are shorter and dip more steeply than at the AFW.  Importantly, no apparent dip-slip offset of the M horizon is observed and may also account for the lack of distortions below Unit 2.  Finally, in Domain 2 the AFE tips out directly into Unit 1, where the evaporites are absent (Figure 4.46a).

The structure of the AFE may be affected by the folding of a thinner evaporite unit above the upwelling of overpressured muds. A fault extending into the evaporites on a slope may suggest a more mobile unit and therefore fault propagation may be disrupted, and splaying into detachment faults is preferential to maintaining a Tier A fault geometry. However, this idea is not supported at the EAF, where the salt is sub-horizontal. Therefore fault geometry is likely affected by other factors, such as displacement amount and other factors (described in Section 4.8.).

The fact that the AFE does not always detach into the evaporites may suggest multiple detachment layers (into the Eocene overpressured muds), which have also been described in normal faults (Maloney et al., 2012). Importantly, despite the AF origin being attributed to salt movement, it implies that the fault can continue to propagate laterally and downwards in the absence of salt, which supports the argument of a Tier A strand propagating into the underlying Unit 1.

*Tier A Propagation Discussion-*

How far the Tier A strand propagates downwards is a very intriguing question and directly impacts our understanding of strike-slip propagation of basal tips as well as how we understand faulting through a salt layer. Firstly and foremost, can a fault propagate through the evaporites and into Unit 1? This is a difficult interpretation to make, however, as the dip-slip component across the M horizon causes artefacts due to the extreme velocity contrast, which induces pull-up effects and thus distorting the reflections surrounding the fault, which continues downwards to below 4s TWT (Figure 4.61). Intriguingly, there are noticeable thickness changes in both the evaporites and overpressured muds (Unit 1) across the fault, showing a thickening towards the northeast and southwest, respectively.

It is considered unlikely that the fault propagates as deep as 4s TWT given the little to no offset shown by kinematic indicators found at the bottom along the N reflection. However, the thickness changes of this degree cannot be explained exclusively by velocity anomalies and are interpreted as real features. This change may illustrate a pre-existing fault or discontinuity that the AF was able to utilise and allow propagation beyond the detachment levels in the evaporites and into Unit 1. Given the AF location on the boundary of the canyon confluence, it is logical that a fault/discontinuity would form here, and may allow for

233

preferential propagation downwards.  If the AF has reactivated a fossil basement fracture/fault, the basal tip line of strike-slip movement would still occur near the N horizon despite the fracture potentially propagating deeper into Unit 1 (and not alter the displacement distribution plots).
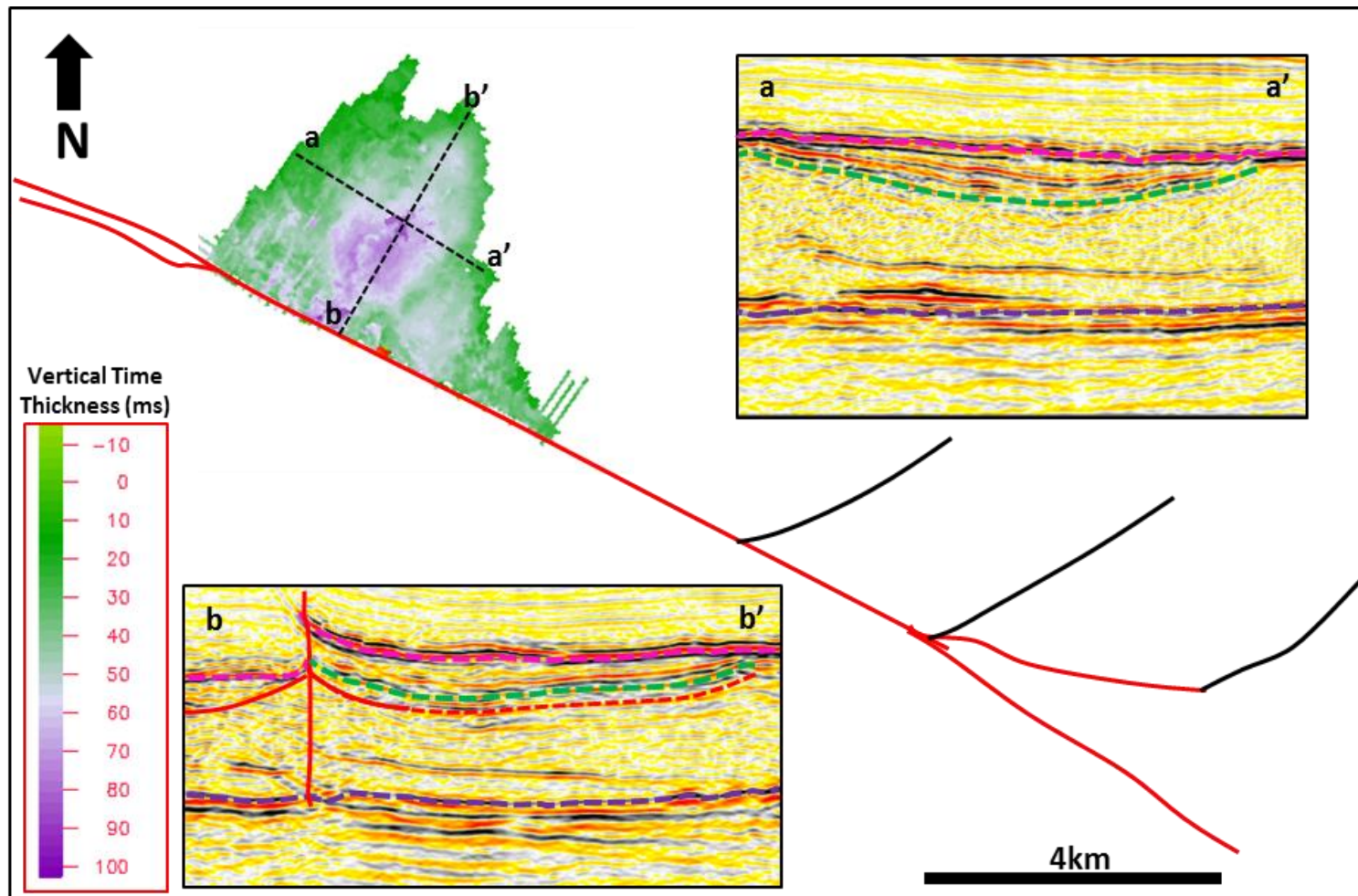
Figure 4.60 - Figure showing thickness of the stratified sub-unit at the top of the evaporite layer (Unit 2) in an isopach map.  Two profile sections are also provided to show the structure.
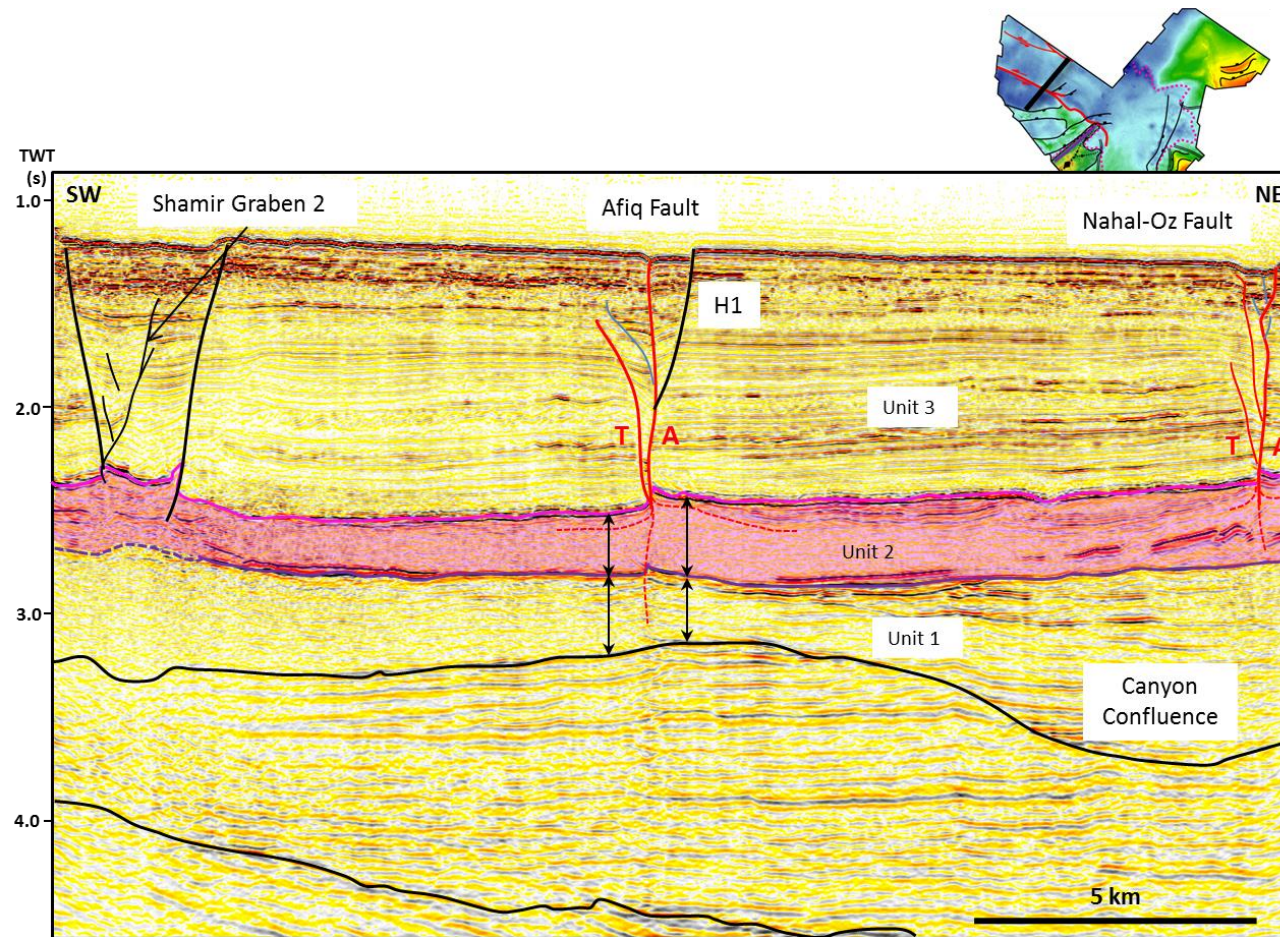
Figure 4.61 - Regional view of the Afiq Fault and its location at the boundary of the confluence between the El Arish and Afiq Canyons.  Interestingly there is a large change in thickness of the Messinan Evaporites across the Afiq Fault, which is also mirrored by the overpressured muds from Unit 1.  This large contrast in thickness may suggest that the Afiq Fault has exploited a pre-existing fracture located at the canyon boundary.

### 4.7.8   Afiq Fault Discussion

The primary aim of the discussion here is to propose models of lateral and upward propagation along the Afiq Fault, since there are distinct differences between different sections as well as the EAF.  Note downward propagation is not examined here due to the tentative nature of the interpretation and is explored further in Section 4.10 and Chapter 6.

#### *4.7.8.1   Upward Propagation*

The models of upward propagation can be distinguished by division of geometry. Principally, the AFW, AFN, and AFE all show slightly different geometries and therefore have different upward propagation models.

- *The AFW*- dominated by Tier A strands, the AFW only shows Tier B strands near the seabed whilst maintaining the Tier A strand.  Therefore, the Tier A fault likely propagates to the seabed, before Tier B faults grow off of it, with new sedimentation. This results in potential abandonment of Tier B structures as well as healing of the Tier A strand (Figure 4.62).

- *The AFN*- Similar to the EAF, the Tier A strand propagates upwards and is deflected from vertical and splaying, forming a Tier B geometry.  A Tier B1 splays from it in response to the rotational movement.  Renewed strike-slip movement occurs on the fault, causing the original fault strand to continue growing and the Tier B1 splay is abandoned.  New Tier B strands splay off of the original strand forming the two sets of en echelon faults at the seabed.  Finally, the intervening set forms (Figure 4.63).

- *The AFE*- Also similar to the EAF, growth occurs to form the characteristic Y shape. However, the strike-slip movement is likely very low in this area, and only Tier B splays make it to the seabed.  Occasionally a secondary splay forms to form the antithetic secondary set at the seabed (Figure 4.64).

#### *4.7.8.2   Lateral Propagation*

The lateral propagation was derived from the displacement distribution plots in addition to the analysis of the geometry of both the AF and its extensional features (the Horsetail Faults in the AFW/AFN and the Wing Crack Faults at the AFE).  For simplicity this model is

derived using a 2D view and is therefore representative of the propagation at the level of maximum displacement (Figure 4.65).

Stages 1 and 2 depict that the AF grew radially and then linked to form the transfer zone at the edge of the dataset towards the northwest.   This follows the interpretation made in Section 4.7.5, that in order to exhibit a displacement maximum, the segments must have linked early in fault genesis (Figure 4.49).  Stage 3, shows the radial propagation of the AF towards the southeast, and how the AFN and AFE formed.  WCF1 and WCF2 formed up-dip of the fault in response to deformation from the Shamir Transtension Region and Shamir Rise.  Stage 4 shows how the extensional faults H1 and H3 began to propagate away from the AF, in order to accommodate the large strike-slip movement downslope.  Domain 2a began to form as a set of smaller segments between WCF Faults.

In stage 5, H1 and H3 continued to grow, accommodating further horizontal offset whilst H2 nucleates at a distance from the AF to accommodate the deformation between H1 and H3. The AFE became more developed with hard linkage occurring between Domains 1 and 2, with the south-eastern tip propagating around the Shamir Rise Fault and into the El Arish Canyon, forming the faults in the El Arish Canyon described by Baudon & Cartwright (2008). The WCF Faults also link with the AFE at this stage.  Finally in stage 6, H2 propagated towards the AF and links with it.  The AFE became more connected with segments linking and forming a more defined trace.
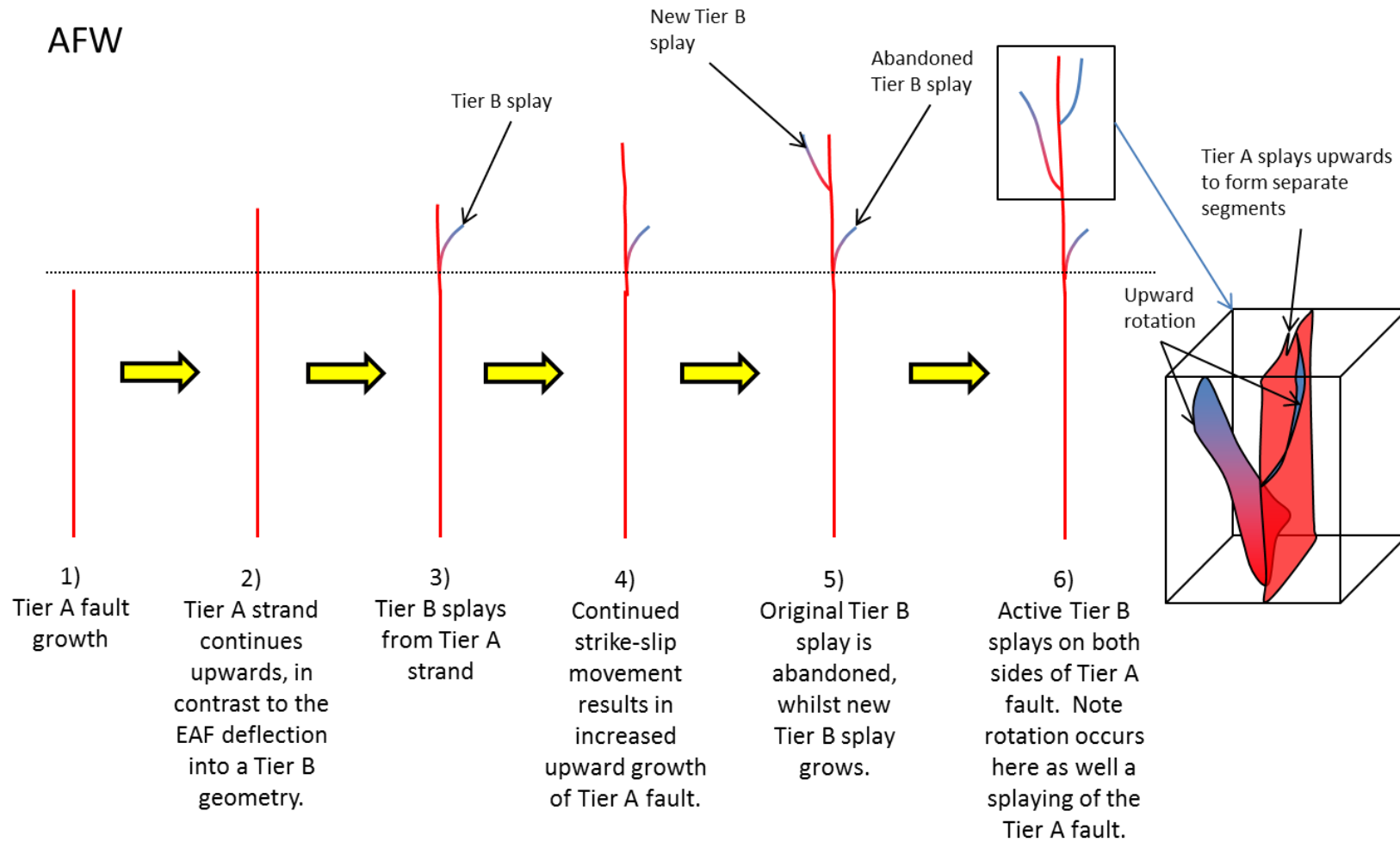
Figure 4.62 - 2D upward propagation model of the AFW.  Also included is a 3D model of the structure AFW structure near the seabed.
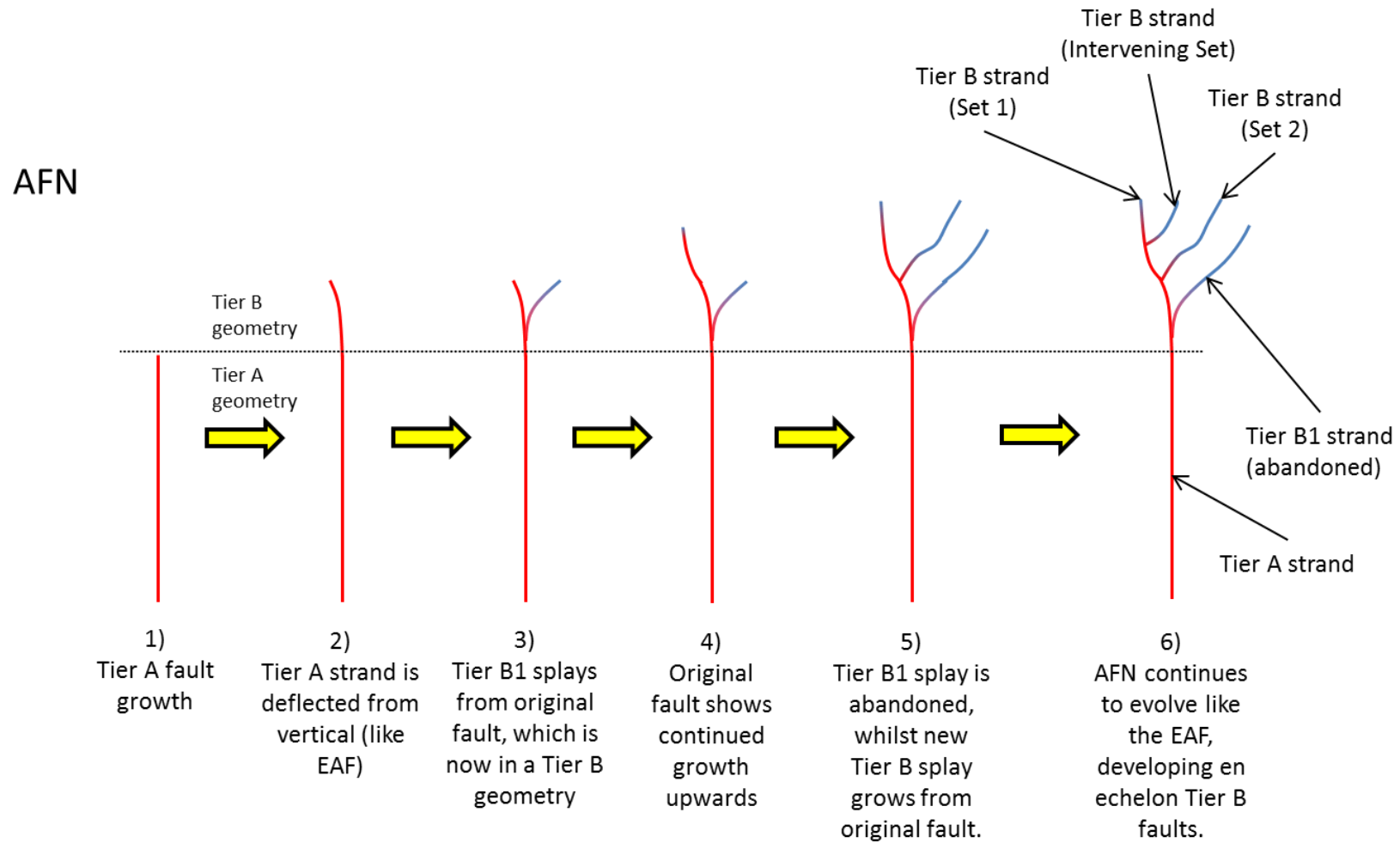
Figure 4.63 - 2D upward propagation model of the AFN.  The model is similar to the EAF, with the addition of extra Tier B strands.
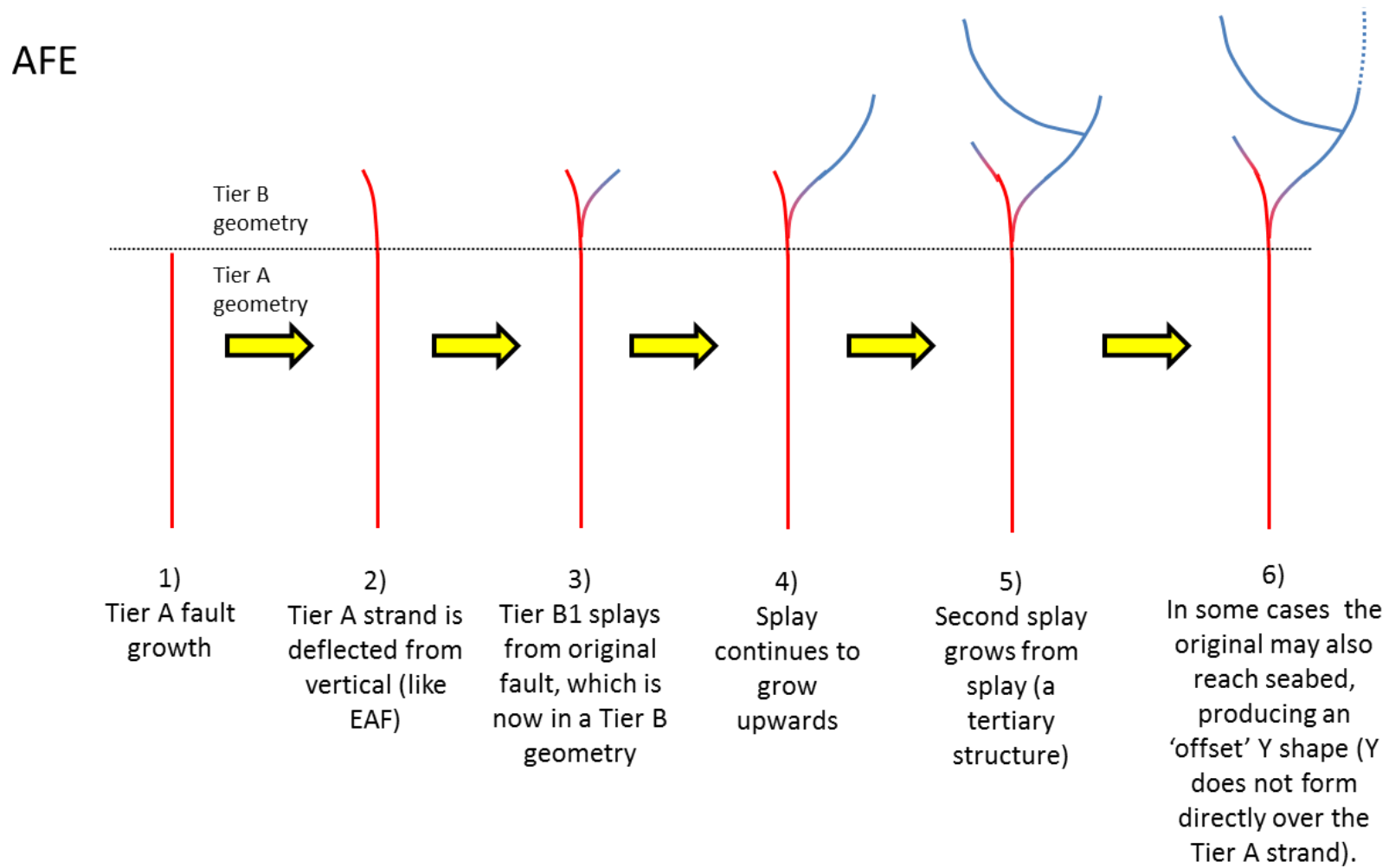
Figure 4.64 - 2D upward propagation model of the AFE.  The model also resembles the EAF, but with a simpler structure due to less Tier B splays.
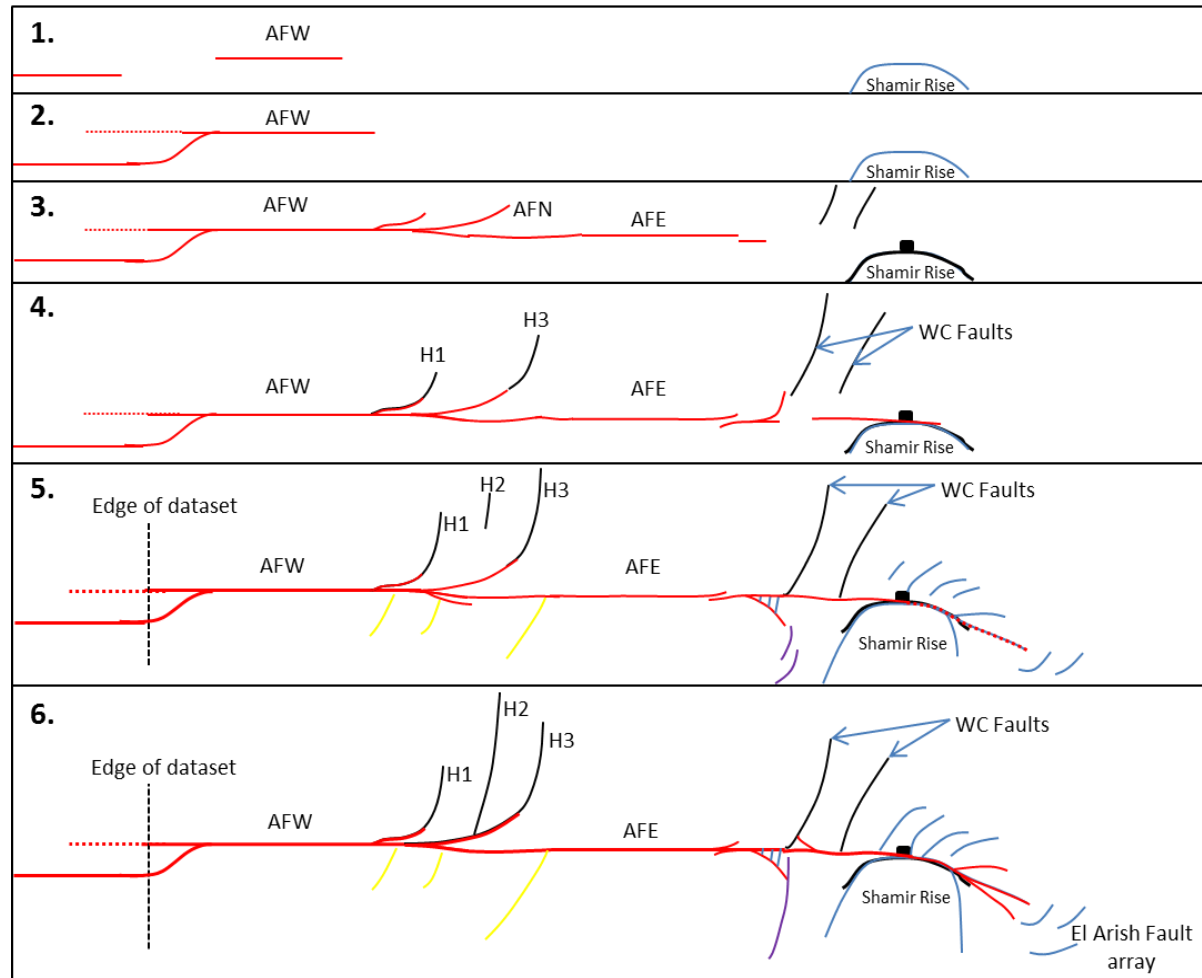
Figure 4.65 - 2D plan view model of the lateral propagation of the Afiq Fault towards the southeast. Propagation is mostly radial; however, this changes to linkage of smaller segments in Domain 2 of the AFE.

### 4.7.9   Synthesis of the Afiq Fault

- The AF is divided into three sections: the AFW, the AFN, and the AFE, based on changes in geometry.

- The AFW shows high displacements and a significantly different geometry from the EAF, with a Tier A fault that extending upward to the seabed and downward through Unit 2, whilst occurring in conjunction with both Tiers B and C.

- The AFE and AFN more closely resemble the EAF structure with Tier A changing into a Tier B geometry.  The AFE likely has low offsets to match the EAF whilst AFN shows higher offsets, despite a similar geometry.

- The AFW has likely undergone a significant component of syn-kinematic upward propagation.

- Extensional tip structures of the AFW and AFE allow for insight into the timing of lateral propagation.

- The AF has likely exploited a pre-existing fault/discontinuity allowing for propagation into Unit 1 by the Tier A strand.  The fault may have caused the large thickness changes in the overpressured muds.

## 4.8     Analysis of Displacement Distribution and Strike-Slip Fault Geometry

Following the detailed description of fault displacement and geometry, it is important to consider if there are any patterns that link the two.  To summarise: the EAF shows low displacement with a corresponding geometry comprised of a short (in height) Tier A strand and longer Tier B faults that splayed widely, to form a distinct 'Y' shape.  In contrast, the AFW shows high displacement with a much taller Tier A strand that extends through Unit 3 to the seabed and extends downwards into Unit 2 (and possibly even Unit 1).  The Tier B faults, are much shorter and do not splay as widely from the Tier A fault, creating a much thinner 'Y' shape.

Two structural styles are therefore observed:  Type I (low displacement and wide, symmetric Y shape, Figure 4.66) and Type II (high displacement and narrow, asymmetric Y shape,

Figure 4.67).  These models are supported by the AFE and NOF, with the former representing a more juvenile Type I structure and the latter representing a Type II structure.  The structure of the AFN also shows similarities to a Type I structure, despite showing some differences in the Tier B geometries.

The application of relating displacement to geometry in strike-slip faults is important since not all strike-slip faults identified in a 3D seismic dataset will show measurable kinematic indicators to quantify how much offset has occurred across the fault.  Therefore if an interpreter observes strike-slip fault showing a similar structure to either model, then they will have a better inclination as to whether the fault has accommodated larger displacement (hundreds of metres or greater) or low displacement (less than 200m).  However, the reasons for changes in structural style are likely more complex than simply the displacement magnitude, for instance the AFN has a maximum offset of 770m, which is considerably larger than the EAF, and yet exhibits a Type I structure. Therefore the following factors are explored into affecting the geometry and displacement relationship: timing of faulting, strain rate, and lithology and sedimentation.

### 4.8.1   Timing of Faulting

An important question concerning the timing of faulting: did the faults initiate at the same time (with the AF accruing displacement at a faster rate) or did the initiation of the AF predate the EAF?  To answer this question, it is pertinent to first place the evolution of the EAF and AF into the regional setting.  Most of the structures in this dataset have formed due to the gravity driven salt movement down-slope, and it is reasonable that the same driving mechanism applies here.  For instance, the EAF and AF are located in the El Arish and Afiq Canyon confluence, where salt was interpreted to have flowed down-slope in Section 4.5.2. If a lateral change occurred in the rate of salt movement down-slope between two areas, shearing will occur, which could lead to faulting (Figure 4.68).  It has been shown that the salt movement in the Levant Basin flows down-dip in an asymmetric Poiseuille model, meaning that in a vertical section, the middle region flows faster than at the edges and the overburden (Cartwright et al., 2012).  It is therefore conceivable, salt will flow faster in the canyons for three reasons: 1) the asymmetric Poiseuille model also works in a similar form laterally, with salt flowing faster towards the centre of the canyon, 2) the slope of the canyon

is steeper than in the Shamir Transtension Region, and 3) the evaporite layer is thicker in the canyon than the Shamir Transtension Region, which means that the effect of the vertical Poiseuille flow will be greater.  Although it is beyond the scope of this chapter to confirm the first two points, the third point is based on a considerable thickness increase of the salt in the canyon (Figure 4.10a, Figure 4.61).  The first two may also work in conjunction with the third to increase the flow differential.

Given that the AF is situated on the canyon slope margin, a large offset is expected from the large salt flow differential (Figure 4.68).  The EAF, however, lies in the canyon itself, and may represent a region where salt movement was hindered slightly (possibly due to palaeo-topography of the M horizon).  Therefore, the salt movement velocity differential on both sides of the fault is low; with the north-eastern side flowing slightly faster, and deforming the overburden as a result.

Given that both faults likely formed in this way, it is therefore logical that they nucleated contemporaneously.  Furthermore, both faults show a $D_{max}$ towards the lower succession of Unit 3 (between 2000ms TWT and 2140ms TWT), and it is interpreted that both faults slip preferentially in this interval.  If a traditional growth model is assumed then the nucleation location is at the $D_{max}$ region (Rippon, 1984), which also suggests that the timing of nucleation is relatively contemporaneous.
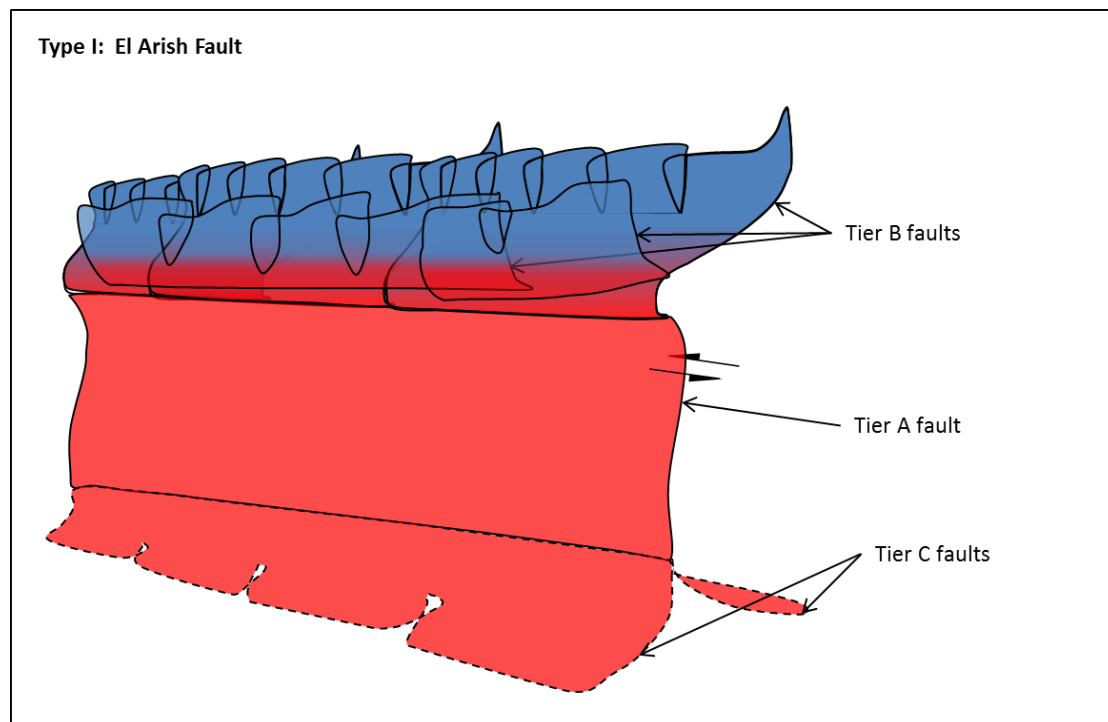
Figure 4.66 - 3D model showing the El Arish Fault, a Type I structure. The model shows a Y shape between Tiers A and B, whilst Tier A and C form an upside down Y. The colours show dominant strike-slip motion in red and dominantly dip-slip motion in blue. Note it is unknown how displacement is distributed across the Tier C faults and is left as red for simplicity.
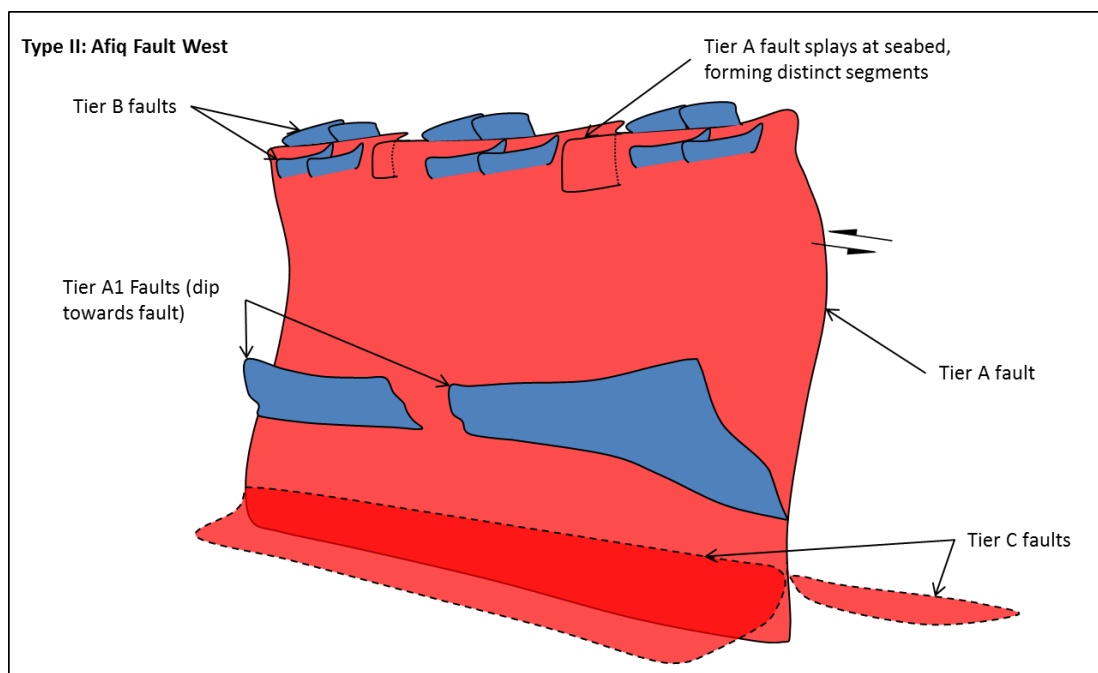


Figure 4.67 - 3D model showing the Afiq Fault West, a Type II structure. The Y shape between Tiers A and B is less defined than the Type I structure, given that the Tier B faults are smaller and form on either side of the Tier A strand, which extends to the seabed. Tier A and C form an upside down Y, with the Tier A strand extending downward between the stalks of the Y.
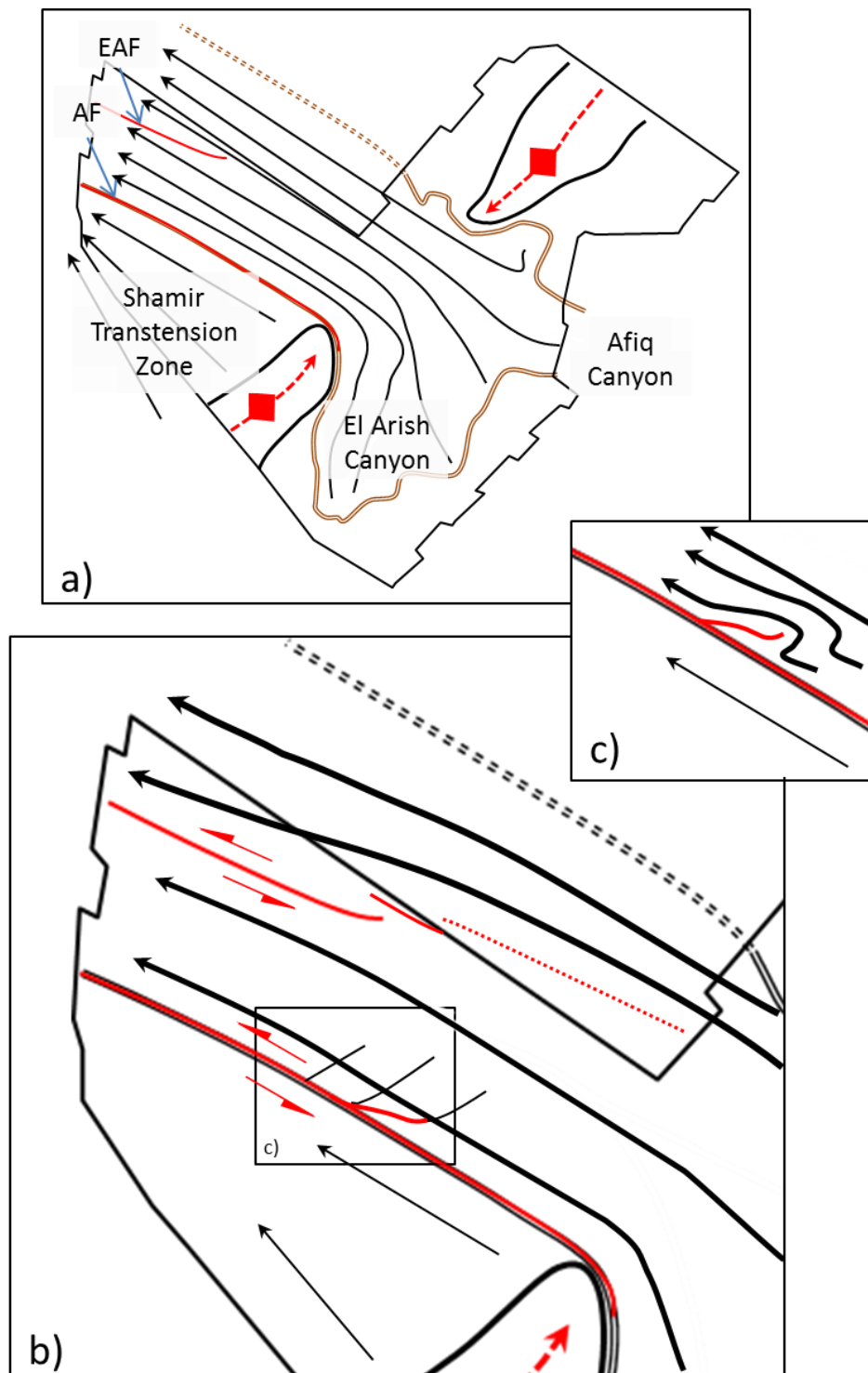
Figure 4.68 - a) Schematic showing the salt flow as vectors into the confluence between the El Arish and Afiq Canyons (arrow widths indicate relative velocities of salt flow). b) Close-up showing salt flow vectors, which cause the sinistral strike-slip faults to form. More salt loading allows for greater (and faster) salt movement down the canyon over the Shamir Transtensional Zone. The greatest disparity occurs at the canyon margin. However, salt movement from the Afiq Canyon can flow straight into the confluence, whilst salt from the El Arish Canyon must flow around the Shamir Rise, accounting for greater flow towards the northeast and the El Arish Fault and Nahal-Oz Fault. c) Close-up of salt flow vectors around the AFN.

### 4.8.2  Strain Rate

If the faults have maintained roughly the same lifespan, then the AF has accrued a relatively high displacement whilst the EAF has accrued relatively low displacement. It therefore follows that the AF has been subject to high strain rates, whilst the EAF has been subject to comparatively low strain rates.

It is proposed that an increased strain rate may allow for a preferential propagation both upwards and downwards of the Tier A through-going strand in a fault. In contrast, the lower strain rate results in a slower radial vertical propagation of the Tier A strand, which means the forces necessary for upward propagation are lowered (Figure 4.69). Once the forces drop below a certain threshold, the fault can no longer continue propagating upwards vertically and the dip reduces to a steep angle, thus initiating the change into a Tier B geometry. When this change occurs, the fault will continue to evolve into a Type I structure. In the case of high strain, then the Type II structure will form as there is always enough force for the fault to propagate vertically to the seabed.

In variable strain rates, more intermediate structures may be observed. For example, in the case of the AFN, the strain rate was likely quite high at the splay point; however given its oblique orientation to salt flow and with little difference of salt flow velocities on either side of the fault, the strain rate would be very low (Figure 4.68c). Therefore a structure closer to Type II would be observed near the splay, whilst a Type I structure would be observed at a distal section across the fault (Figure 4.45). Similarly if a Type I structure undergoing lower strain rates, suddenly underwent high strain rate conditions, the Tier A strand may reactivate and continue vertical propagation, abandoning the Tier B geometry in the process.

### 4.8.3  Lithology and Sedimentation

Lithology and sedimentation likely exerts a control on fault geometry in three major categories: 1) lithologic boundaries, 2) influx of sedimentation, and 3) syn-kinematic growth. In case 1) if a fault propagates through units of different cohesive strengths, the propagation may be hindered, the direction of propagation may be deflected (i.e. changing in dip), and splaying may become preferential (Richard et al., 1995; Carne and Little, 2012). In case 2), analogue experiments show that increased sedimentation during fault growth can alter the

fault dip, geometry, and amount of R shear rotation from the underlying fault (Atmaoui, 2006; Ghosh and Chattopadhyay, 2008).   In case 3) analogue experiments show a change from blind to syn-kinematic propagation significantly alters the geometry when the upper tip reaches the free surface, and the fault continues to slip concurrently with sedimentation by forming splays at the base of the syn-sedimentary layer (Richard et al., 1995).

Both the EAF and AF mostly deform Unit 3, which is a relatively uniform layer, and therefore the change in fault geometry is expected to be low as a result.  However, the EAF changes from a Tier A to a Tier B geometry in an MTD (e.g. Figure 4.20, Figure 4.22), which likely has higher anisotropy and cohesive strength than the surrounding Unit 3 sediments (Frey-Martínez et al., 2006), and thus may promote the change (Figure 4.70a).  The AFW, in contrast, shows a Tier A strand the reaches the seabed whilst the Tier B strands splay in Unit 3a (Figure 4.71a).  It is expected that Unit 3a would also have greater anisotropy and cohesive strength based on the chaotic reflections, which are indicative of a large number of slump deposits, and thus may explain why the Tier B geometry splays are formed here. However, it does not explain why the Tier A fault continues to propagate through this unit, and suggests that lithologic boundaries alone cannot determine the reason for the Type I and II structures.

Cases 2 and 3 are considered together as case 2 alone would likely only result in a subtle change in fault dips fault rather than a cause for splaying or a change in fault geometry of a pre-kinematic unit (Le Guerroué and Cobbold, 2006).  However, if a fault propagated blindly to the free surface, and then continued evolution with an influx of sedimentation, then the fault geometry is likely to change considerably (Richard et al., 1995; Le Guerroué and Cobbold, 2006).   Although the AF Tier B strands may have splayed because of a lithologic boundary, it is also possible that the splays occurred contemporaneously with sedimentation (Figure 4.71b). Given that the variable upper tip gradient of the AF suggests that it has reached the free surface and is presently growing as a syn-kinematic fault (Figure 4.55), it is therefore considered more likely that case 3) has caused the splays to form; however, it may be that case 1) affects the geometry of these Tier B strands to a lesser degree.

Determining if the EAF has propagated under dominantly blind or syn-kinematic conditions proves more problematic.  Although the average upper tip gradient is larger than the basal tip gradient like the AF, there is not the same clustering of data to suggest that the gradient

changes significantly with depth. Furthermore, the relatively high offsets across the low angle Tier B strands (Figure 4.25a) do not indicate any reduction or loss of displacement due to syn-kinematic conditions (Childs et al., 2003). Therefore it is considered more likely that most of the upward propagation has occurred blindly, with the Tier B geometry forming due to the weaker cohesive strength of the MTD (Figure 4.70a). Given that the EAF establishes scarps at the seabed, it is possible that propagation became syn-kinematic above where the horizontal slip had reduced to zero, and therefore only affects the normal slip component of the fault.

### 4.8.4  Strain Rate and Sedimentation

The different models of upward propagation for Type I and Type II structures are clearly affected by both strain rate and sedimentation conditions. If a low strain results in slower upward propagation of the Tier A strand, then it is more difficult for the fault to emerge at the seabed and propagate as a syn-kinematic fault. Similarly, if it is under lower strain rates it will be more prone to forming the Tier B geometry, which may only require a weaker lithology to initiate this change. A Type II structure in contrast will more likely propagate upwards faster under higher strain rates, and therefore be more prone to syn-kinematic conditions. To summarise: Type I and Type II structures are not necessarily controlled by displacement alone, but a combination of strain rate and lithologic/sedimentation factors, which may aid future interpreters when kinematic indicators are sparse or absent.
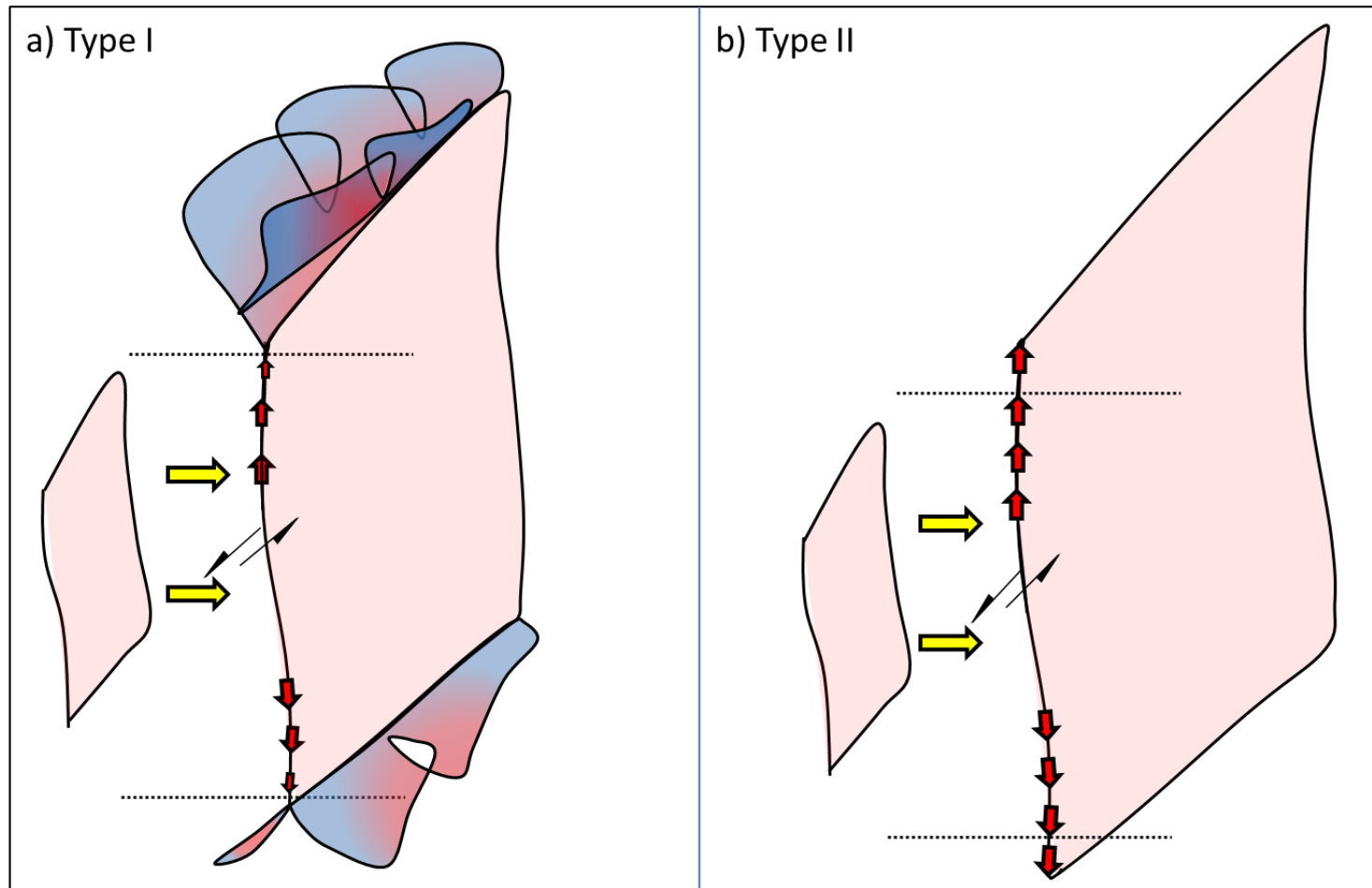
Figure 4.69 - Cartoon model showing how as the fault propagates radially, in a low strain rate condition the force applied to the fault becomes much smaller at the vertical tips, which causes the splaying into a Tier B geometry. Type II however, experiences high strain rate and the forces are higher at the tips allowing for the Tier A strand to continue propagating.
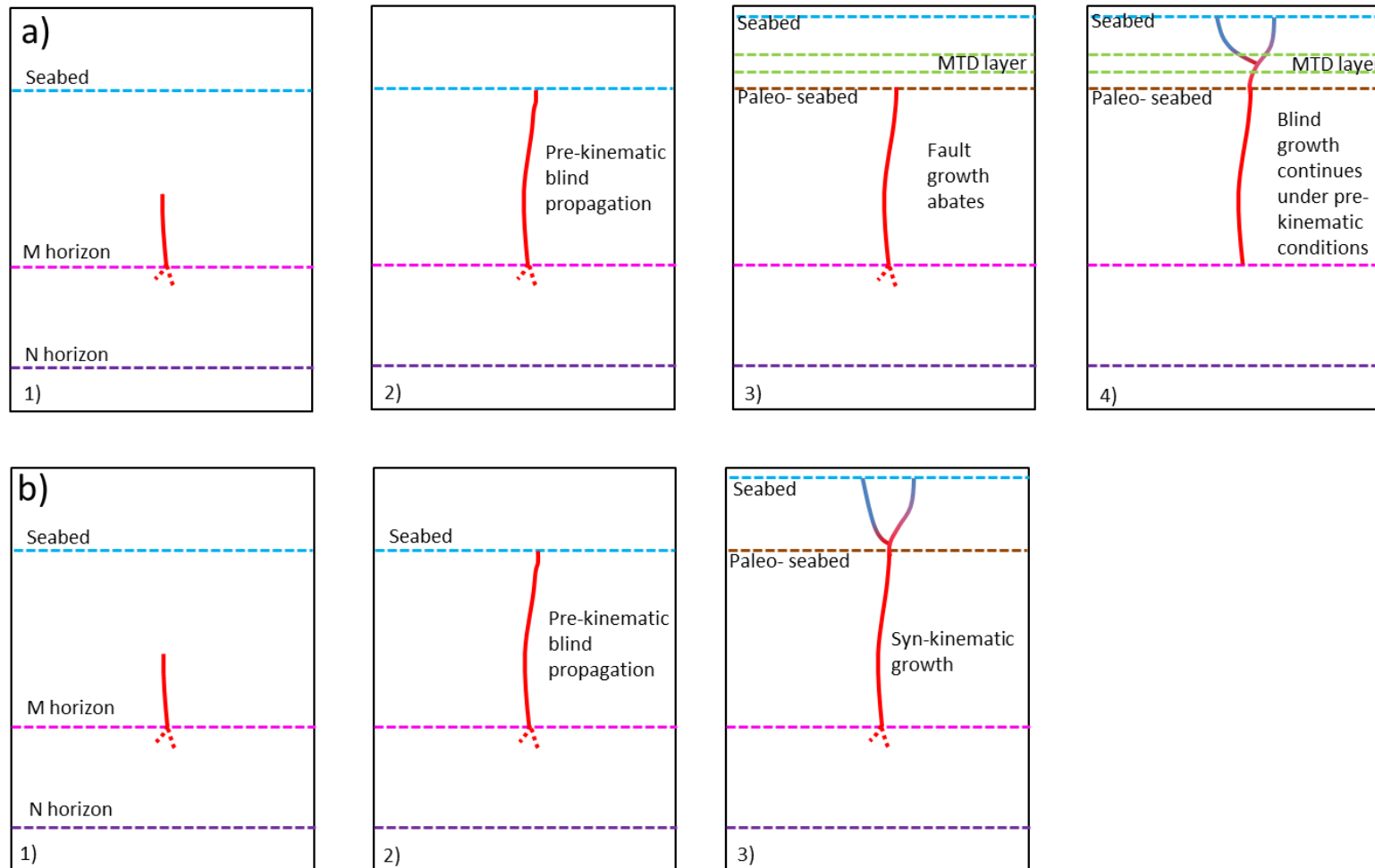
Figure 4.70 - Upward propagation models of the El Arish Fault.  a) The Tier A strand propagates upwards as a blind fault, until it hits an MTD layer and splays into the Tier B geometry.  Model b) begins with the same Tier A propagation, however, it transitions to a Tier B geometry when the fault emerges at the seabed.
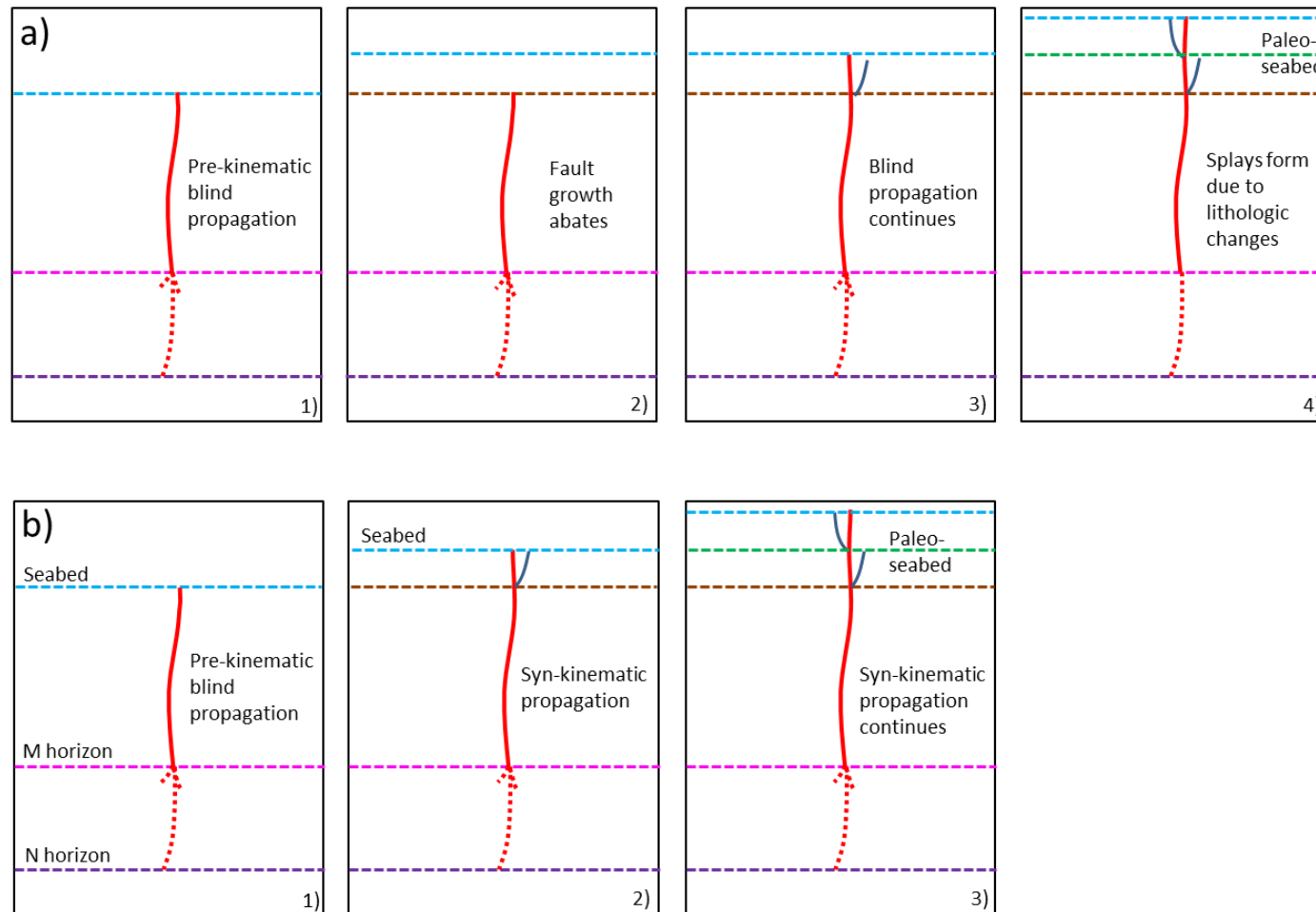
Figure 4.71 - Upward propagation models of the Afiq Fault West.  a) the Tier A strand propagates upwards as a blind fault, and upon encountering less cohesive units, forms Tier B  splays.  Model b) begins with the same Tier A propagation, however, the Tier B splays form when the fault emerges at the seabed and propagates syn-kinematically.

## 4.9     Why is the Tier A Trace Curvilinear?

One possibility is the presence of fault corrugations, defined as show sinuous profiles of ridges and grooves parallel to slip direction at a range of scales from several metres to kilometres (Hancock and Barka, 1987; Ferrill et al., 1999).  These have been attributed to form from the overlapping of en echelon fault arrays by two breakthrough mechanisms: lateral propagation of curved fault tips and linkage of connecting faults (Ferrill et al., 1999).  It is logical that corrugations will also form in strike-slip faults under the same mechanisms, with the exception that corrugations would be observed along the fault trace in cross-section (Figure 4.39, Figure 4.72).  However, the appearances of these undulations in 3D are not well defined and may suggest an alternate mechanism for their formation.

The standard formation of corrugations in a strike-slip fault assumes that dip linkage (i.e. fault segments that link vertically) has occurred (Figure 4.73), which has not been observed in the strike-slip faults here.  Although little evidence of dip linkage is generally observed in seismic data (Mansfield and Cartwright, 1996), studies identifying dip linkage are on dip-slip faults whose location is orthogonal to slip, which maintains a low preservation potential (Mansfield and Cartwright).  In strike-slip faults, dip linkage is parallel to slip and may explain the observed undulations.  However, the displacement distribution of both faults do no show the stacking of displacement maxima characteristic of dip linkage (Figure 4.73), and it is therefore considered unlikely to have occurred here. Furthermore, these faults would require greater aspect ratio exaggeration on each linking segment, which, given the already large aspect ratios of each fault, seems an unlikely geometry.

An alternative model to fault corrugation formation involves pure lateral propagation.  If different levels of the fault encountered different regions of pre-existing weakness in the overburden, then it is logical that the tips of the fault may be deflected in different directions at different depths with continued lateral propagation.  This results in the fault splaying in slightly different directions forming 'tears' or bifurcations in the fault plane (Figure 4.74). Further propagation would cause the bifurcations to grow and link, forming a curvilinear trace in profile section.  This is considered a likely form of propagation as it uses the radial model suggested by the displacement distribution, and linkage is limited to a localised

secondary process at the tip. This would produce far more small scaled corrugations than a dip linkage model and may explain why they are not well defined along the AF (Figure 4.72).

These bifurcations of the fault plane may serve as preferential nucleation points for the mode II tips structures observed along the AFE (Section 4.7.4.2). Given that neighbouring structures are also slipping contemporaneously, the bifurcations may preferentially interact with the neighbouring structures, thus abandoning the proposed model of linking back together and instead continue to propagate as separate fault tips that eventually form the intervening faults (Figure 4.43d).

*Corrugations influence on net-slip sense?*

Fault surfaces are also known to be rougher in the direction perpendicular to slip (Sagy et al., 2007; Resor and Meer, 2009) indicating that an undulations observed here may 'roughen' the fault zone, therefore creating preferential movement along strike and may explain why strike-slip fault segments tend to be straight in plan-view. Furthermore, large scale corrugations on the through-going fault would likely act as natural barriers to any dip-slip movement by locking each block in place (Figure 4.75). Finally, corrugations are known to act as a source of geometric asperities and barriers that are known nucleation and termination sites for rupture inducing earthquakes (Wesnousky, 2006; Wesnousky, 1988; Resor and Meer, 2009) and represent an important feature for future strike-slip fault hazard mitigation studies.

**Corrugation Model**

Fault shows small changes in the undulations along strike
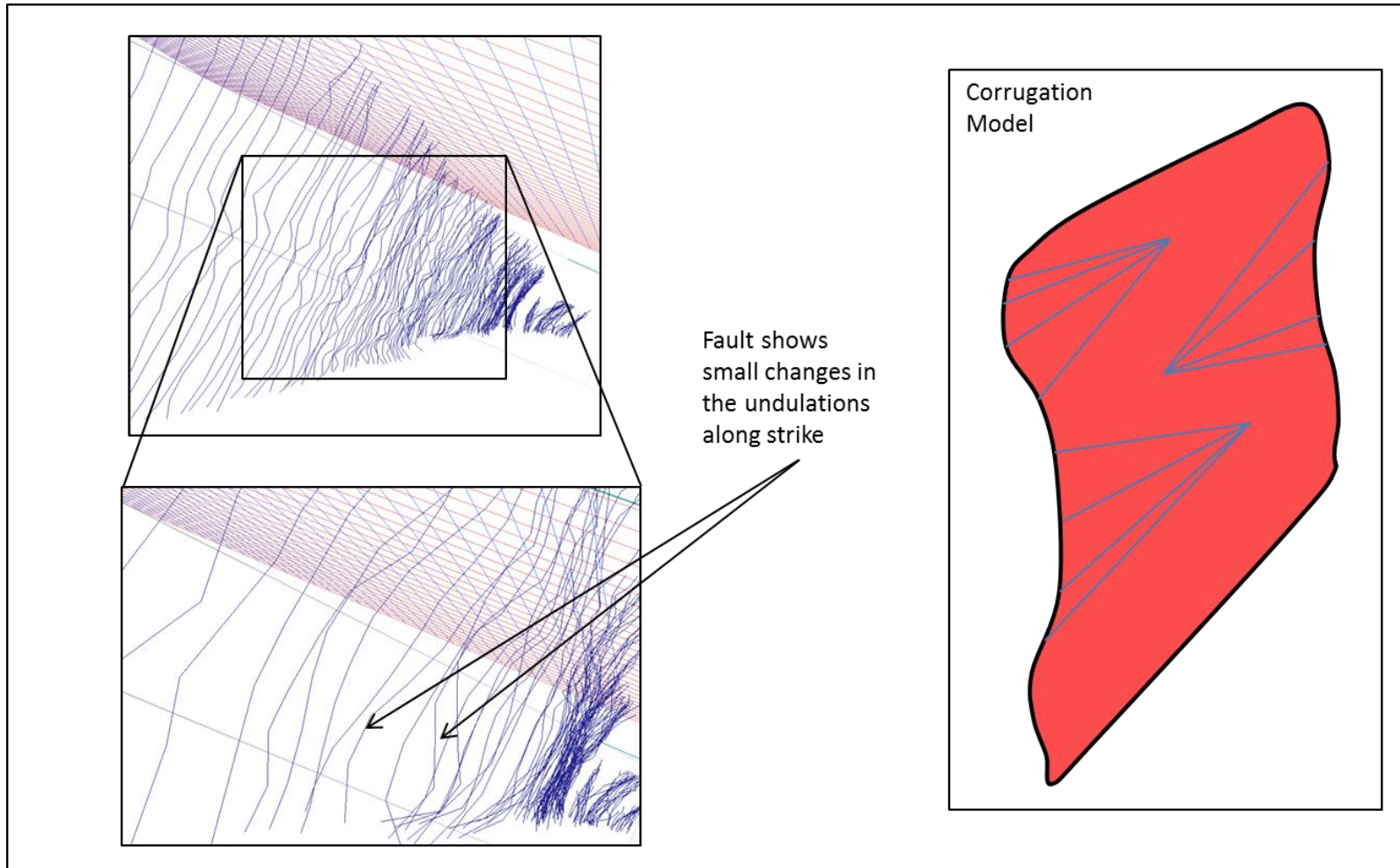
Figure 4.72 - Figure showing 3D view of the undulations that define each fault stick in profile section.  The model to the right shows a cartoon model of the fault corrugations.
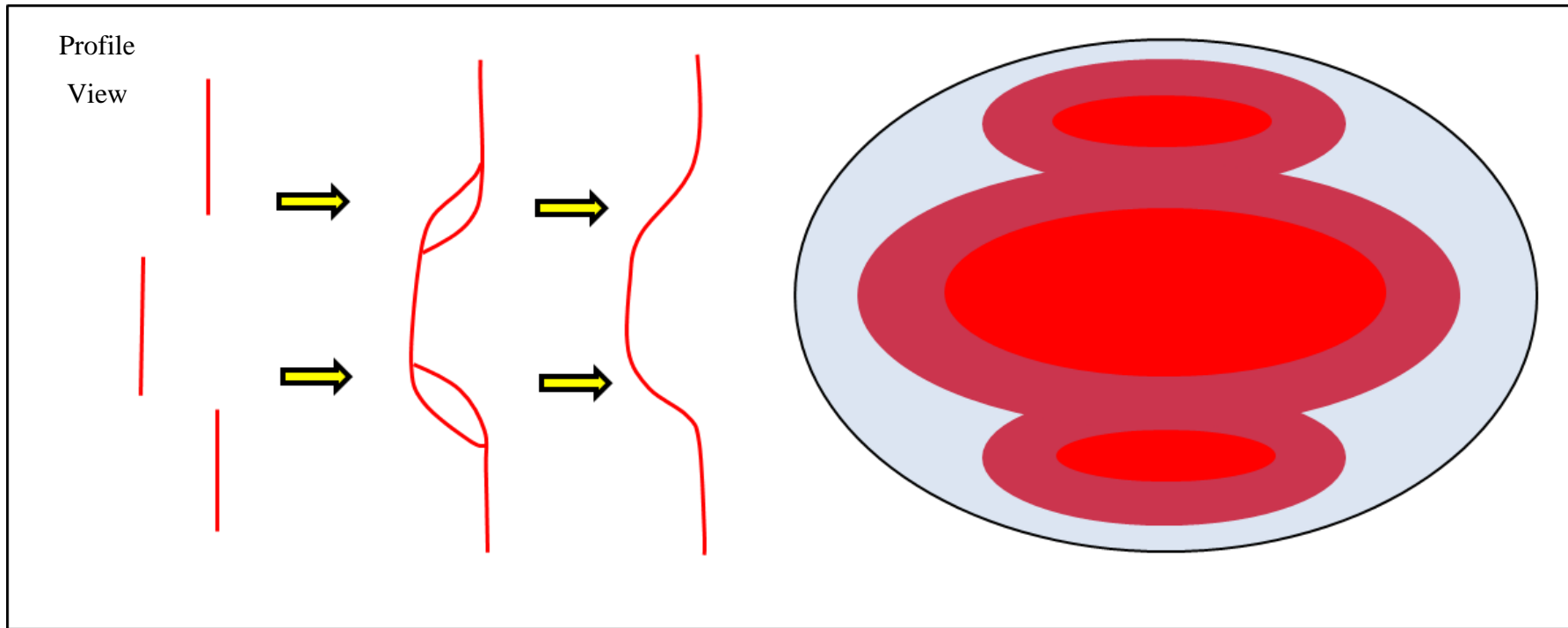
Figure 4.73 – In profile view, three Tier A segments propagate upwards and downwards towards each other to form relay structures and by the final step, have formed a corrugation in profile section.  A corresponding displacement distribution is also presented showing how the faults would show dip linkage using a displacement distribution plot.
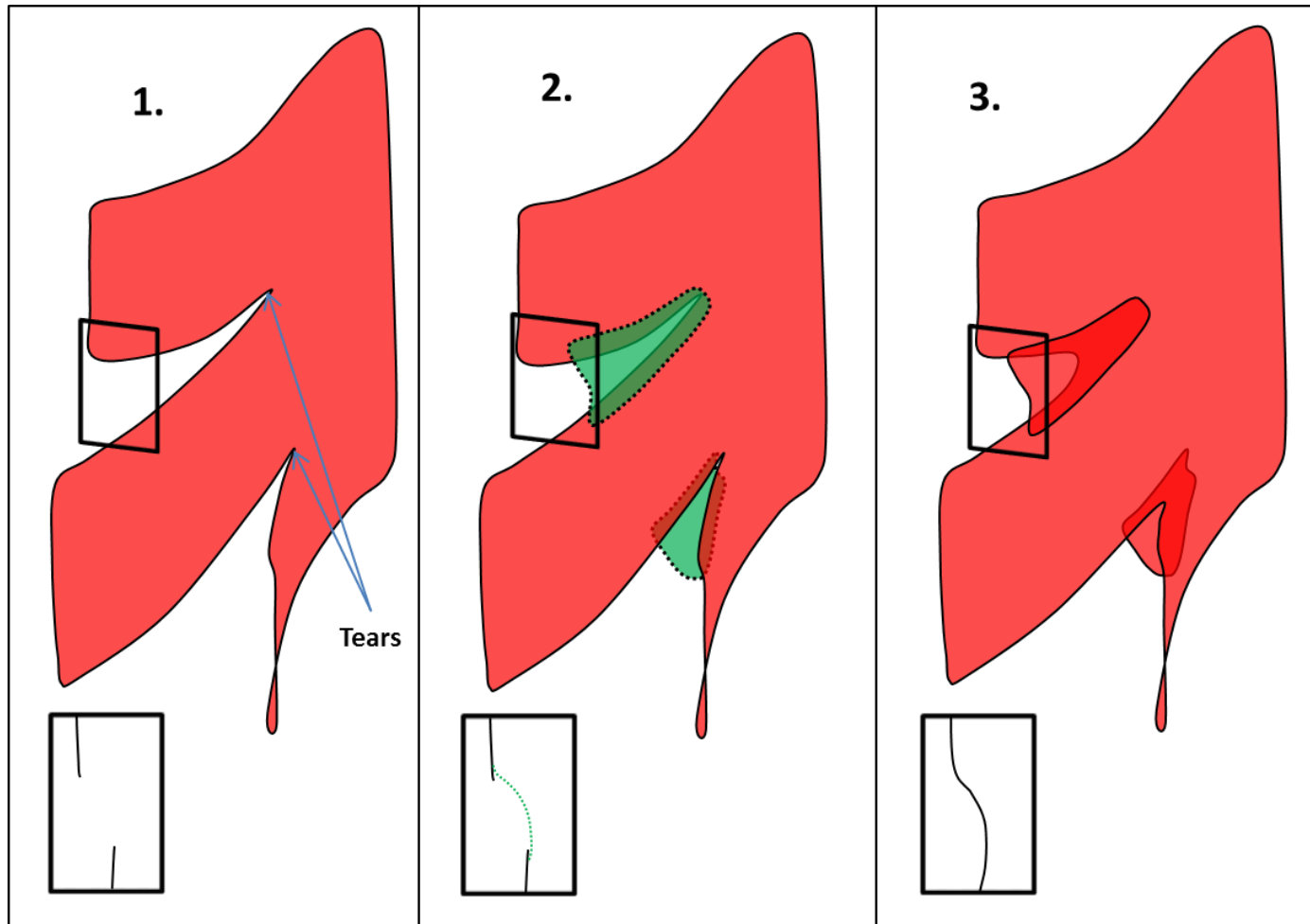
Figure 4.74 - Model of lateral tip propagation that forms undulations in profile section.  This occurs by the fault plane 'tearing' or bifurcating with lateral propagation and eventually healing by growth of each segment (in green) and forming small undulations in the fault plane.
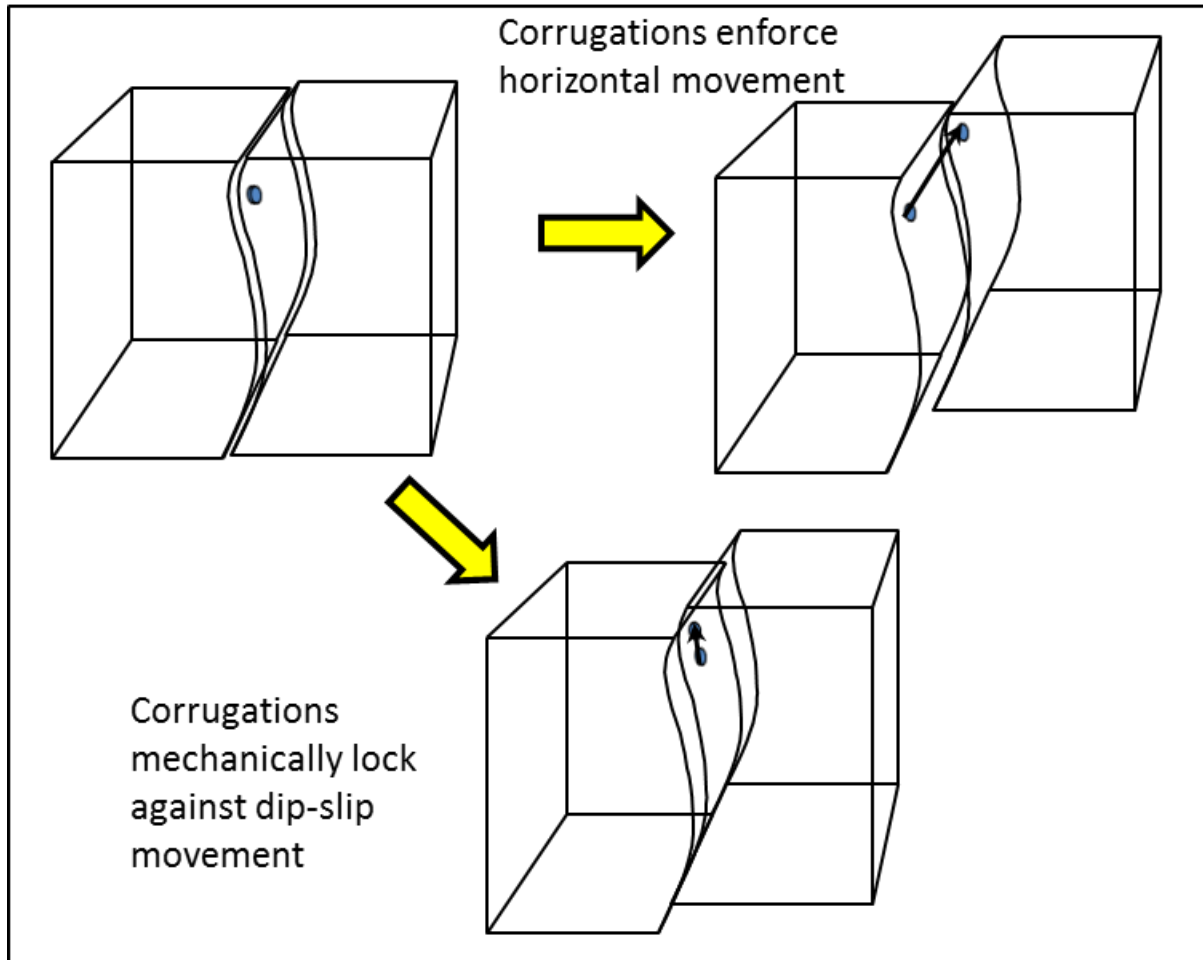
Figure 4.75 - Model of how presence of fault corrugation may increase the strike-slip component in an oblique-slip fault, which is the case for both the EAF and AF.

## 4.10    Faulting in the Messinian Evaporites

Faulting in the Messinian Evaporites has remained largely speculative due to the limits in visualisation; however, it is pertinent to compare the Tier C geometries in order to better understand how a fault propagates through the evaporites and the control it exerts on geometry.  To summarise what has been established thus far: the EAF shows multiple Tier C strands that detach into the evaporites whilst the AFW comprises a Tier A strand that extends through the evaporites and two Tier C strands that detach into the salt, whilst resembling thrust faults.  This section briefly examines the Tier C geometries observed (the Tier A fault in the evaporites is described in Section 4.7.7).

The Tier C faults of the EAF and other Type I structures show a similar structure at first glance, but is highly variable where splaying into the Tier C geometry occurs (Figure 4.76). Principally, the splays occur either at or very near the M horizon (Figure 4.23a, b), but sometimes the splays occur below (Figure 4.20), whilst occur above (Figure 4.19, Figure 4.23b).  The latter is especially curious as the salt represents an obvious change in lithology that could alter the geometry given the reduction in the forces driving propagation has occurred (Figure 4.69).

Both examples splay into the Tier C geometry in an MTD in a similar style to the Tier B strands of the EAF.   This suggests that MTDs are a difficult unit to propagate through and therefore when the strain rate is low during downwards propagation; a fault may change geometry before propagating into the evaporites.  This has a large implication for fault nucleation, which will be described in Chapter 6.  Interestingly, where the Tier A strand extends into the evaporites (Figure 4.20), it suggests that lithology alone was not enough to change the geometry and may suggest a region of higher strain rate occurred here.

The difference between the Tier C strands in Type I and Type II structures shows a decrease in dip of the strands as well as a lengthening of the strands (Figure 4.24, Figure 4.39, Figure 4.76).  This is an interesting feature, which may suggest higher strain rates require larger faults at the base.  In this respect, it may resemble a tree, which requires larger roots for stability as the fault grows upwards.
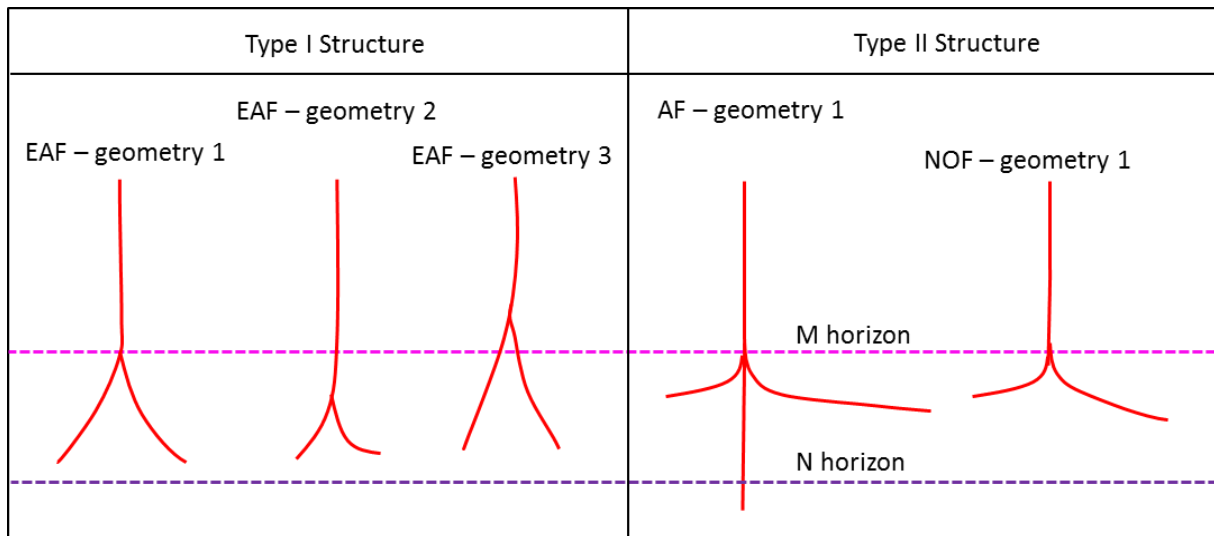
Figure 4.76 - Tier C example geometries. The Type I structures show an interesting change in splaying geometry, where all detach into the evaporites, however, the splaying node changes from some overlying the salt and some within the salt. The Type II structure are flatter (shallowly dipping), but do not always show the Tier A structure.

## 4.11    Conclusion

This chapter has explored the geometry, displacement, and growth of two large strike-slip faults located in the confluence between the El Arish and Afiq Canyons using high resolution 3D seismic data to improve upon prior models of fault geometry as well as document the distribution of displacement using the technique presented in Chapter 3.  The El Arish Fault shows low displacement and a characteristic 'Y' shape structure in cross-section (Type I) whilst the Afiq Fault shows large displacement with a much thinner 'Y' in cross-section (Type II).  Both faults are comprised of strands which show three different geometries, and are classified by Tiers:

- Tier A – the through-going fault which contains the majority of the strike-slip displacement.

- Tier B – faults strands that dip steeply towards the Tier A strand and show a progressive decrease in strike-slip motion from the base to become a dominantly normal fault at the upper tip.  They also show an anti-clockwise rotation that increase upwards from the base.

- Tier C – strands underlie the Tier A strand and diverge from the fault in a similar means to the Tier B strands, producing an upside down Y structure.  The faults mostly occur in the Messinian Evaporites and poorly imaged; however, it is likely they form in a similar manner to the Tier B faults.

The upward propagation of the faults is controlled by strain rate and lithologic/sedimentation properties, which considerably alters the geometry and propagation history of each fault. Laterally, the EAF propagated by the linkage of two major segments, which grew radially thereafter.  The AF propagated radially towards the southeast until Domain 2, where it changes to the linkage of several small segments.

The curvilinear trace may be attributed to fault corrugations, which have formed from lateral propagation producing small 'tears' or bifurcations at the tips that subsequently re-link back together.

# Chapter 5

# A Preliminary Analysis of Strike-Slip Fault Propagation at Fault Intersections and Fault Tips in 3D

# 5   A Preliminary Analysis of Strike-Slip Fault Propagation at Fault Intersections and Fault Tips in 3D

## 5.1   Introduction

Faults are rarely isolated in nature and understanding how they interact and affect network connectivity directly impacts our ability to predict precious resource recovery and hazardous earthquakes.  Most of our understanding of strike-slip fault propagation is based on field studies (e.g. Segall and Pollard, 1983; Peacock, 1991; Kim et al., 2003) at small scales.  However, fault interactions are rarely simple, especially at seismic scale, and 3D seismic data offers a unique opportunity to visualize these at several stratagraphic intervals, allowing for a true 3D analysis beyond most field studies.  This study aims to investigate several themes of faulting at intersections, including: 1) Conjugate relationships, 2) fault branching, and 3) Tip Structures.  The strike-slip faults that dominate the deformation in the GalC dataset (introduced in Chapter 3) are immensely complex, and to fully understand how they interact and have evolved is beyond the scope of this thesis.  This study therefore serves as a preliminary insight into complex fault interactions in 3D that should direct future research.  The chapter will begin with an analysis of regional patterns in the strike-slip faults, with a focus on orientation, displacement and length, and timing in order to provide context for the examples provided.

## 5.2   Regional Structural Elements

The aim of this section is to provide a brief summary of the structures of the GalC dataset, before exploring the relationships between strike-slip faults on a regional scale.  The regional history and stratigraphy is described in Chapter 3.

Three structure classes deform the GalC dataset: blind normal faults, segmented thrust faults, (and associated folds), and a conjugate set of strike-slip faults (Figure 5.1).  The latter two have

formed due to salt withdrawal into the basin (Cartwright and Jackson, 2008; Cartwright et al., 2012), and represent the compressional toe domain of a system deformed by gravity driven salt tectonics, whilst the blind normal origin is unknown. However, it is likely that they pre-date most of the structures here as they are cross-cut and offset by the strike-slip faults (see Chapter 3). Previous work on this dataset has shown that the thrust and strike-slip faults formed coevally within the same tectonic regime, with the strike-slip faults even compartmentalizing and acting as barriers to thrust propagation (Nwosu, 2014).

Examples of thrust faults affecting strike-slip fault propagation are less obvious, as plan view maps cannot show this aspect of deformation. However, this does not necessarily imply that the strike-slip faults are unaffected by thrust fault deformation. Indeed, profiles lines show evidence of thrust faults cross-cutting strike-slip faults (Figure 5.2); however, this phenomenon is rare and only occurs across small strike-slip faults. More often, thrust faults affect the structure of the Tier A (see Chapter 4 for definition) strand to form a highly curvilinear structure (Figure 5.3), but do not alter the fault strike. A final example of thrust fault and strike-slip fault interaction includes a strike-slip fault tipping out at a thrust fold (Figure 5.4). Here, it is not clear if the strike-slip fault tips out because of the presence of a thrust fault or if directly transfers displacement into the thrust fault. Ultimately, evidence of direct hindrance or obstruction of propagation of strike-slip faults are rare, and examples shown below were deliberately selected on the basis that they display minimal interaction with thrust faults in order to focus on interactions that are an integral part of the strike-slip fault system.

### 5.2.1   Strike-Slip Fault Overview

Two distinct sets of strike-slip faults with contrasting strikes deform GalC (Figure 5.1, Figure 5.5). The first set comprises sinistral faults, which trend E-W and average 094°, whilst the second set comprises dextral faults that trend NE – SW and average 030°. A clear change in structural style occurs across the dataset and is therefore divided into three regions: North, Central, and South.

*The Northern Region*– is dominated by the dextral set of faults, with the sinistral faults appearing mostly as smaller faults bisecting dextral faults or splaying from them.  These sinistral faults are therefore considered as secondary structures.  In general there is less strike-slip deformation within this region and increased thrust faulting as well.

*The Central Region*- shows a relatively equal distribution of dextral and sinistral faults and contains the majority of the conjugate intersections.  Despite the equal distribution overall, there is a change in style from west to east.  Towards the west, major sinistral faults S1, S2, and S3 dominate the deformation (with the exception of D1).  Towards the centre, several conjugate intersections occur, with dextral faults appearing more deformed by the sinistral set, and often abutting against them.  Towards the east, dextral faults are more dominant, with sinistral faults abutting against larger faults D5, D6, D7, and D45.

*The Southern Region*– is dominated by sinistral faults, specifically S4, S5, and S6.  A significant change in strike occurs here to trend on average ESE – WNW, or 104˚.  However, the largest faults (e.g. S4, S6, and S7) actually show a strong NW – SE trend, which interestingly share roughly the same strike as the El Arish Fault and Afiq Fault from Chapter 4.  The dextral faults also show a change in trend as they appear to bisect the major sinistral faults in this region.  Thrust folds are absent in this region, with the notable exception of one example (Figure 5.4).

### 5.2.2   Fault Characteristics

A notable characteristic in GalC is a lack of isolated faults; with almost every fault interacting with at least two other faults; free lateral fault-tips are almost entirely absent.  Furthermore, fault intersections often occur at multiple locations along a fault, meaning that faults are highly segmented. It is therefore difficult to interpret whether a fault is continuous (i.e. the same fault) across an intersection.  For example, it is possible that S2, S9, S10 are all segments of the same fault; however, given that each segment may have evolved differently, they are assigned different names (Figure 5.1).

Fault displacements range widely from smaller faults at the threshold of seismic resolution (c. 40m) to regional scales over 2600m.  Broadly, they can be organised into 3 orders: 1st order

greater than 700m, $2^{nd}$ order between 700m and 200m, and $3^{rd}$ order less than 200m.  The first order faults are defined by the major faults that dominate the structural maps (e.g. S1 − S7, D1, and D5 − D7; Figure 5.1, Figure 5.5).  However, some faults are relatively shorter in length (e.g. S13 and S14).  The second order faults mostly comprise the faults in the Central Region that produce conjugate intersections (e.g. D23, D27, and D28) or faults that splay from first order faults (e.g. S9, S10).  Third order faults mostly comprise the splay faults noted in the Northern Region; however, smaller faults such as S16, S17, and D35 are included within the order.

The distribution of fault displacement is notable because many of faults measured have shown displacement values close to $D_{max}$ at the Top Messinian Unconformity.  This is significant as the $D_{max}$ region occurs immediately above the evaporites, where the faults detach.  The segmented nature of the GalC faults means that fault lengths are too short to form a distribution plot due to a lack of available kinematic indicators.  However, extrapolating displacement information from both Fault S1a and S1b enables a schematic to be drawn showing a crude displacement distribution of the upper and basal tips (Figure 5.6).  The $D_{max}$ region contains a significant part of the fault height and shows a uniform displacement distribution. Furthermore, the $D_{max}$ location encompassing the M horizon suggests that the GalC faults have propagated and possibly initiated under differing conditions from the El Arish and Afiq Faults and will be discussed in the subsequent chapter.

### 5.2.3   Fault Displacement and Length

Faults in nature commonly show a positive correlation between displacement and length (e.g. Ranalli, 1977; Watterson, 1986), and the strike-slip faults of GalC are no exception.  However, questions such as how a conjugate system affects length versus displacement relationships are rarely addressed at seismic scale, and GalC represents an excellent opportunity to explore this regional relationship.  It should be noted that fault lengths were measured as individual segments and therefore the results may be over-represented by faults with shorter lengths.  Similarly, some faults extend outside of the dataset and will also be represented by shorter lengths due to spatial truncation.

Maximum displacement values were compiled for 98 faults (69 sinistral, 29 dextral) that showed a kinematic indicator, and are compared to segment length (Figure 5.7).  A weak correlation is shown, with $R^2$ = .64, signifying that displacement amount is not strongly dependent on length. Sinistral faults show a stronger correlation over dextral faults with $R^2$ values of .70 and .60, respectively.  Categorising the data by displacement order shows a large overlap in lengths between fault orders (Figure 5.8).  Dextral faults tend to have longer lengths relative to displacement values in comparison to sinistral faults (Figure 5.8b).

The large overlaps in lengths suggest that fault displacement can accrue without a simultaneous growth in length.  This is not a surprising result given that most faults intersect with other faults, meaning that the fault lengths are locked, likely at an early stage.  The variable lengths per order may also suggest variable growth rates, as shorter faults with high displacements would likely accrue displacement quickly to accommodate the growth of the larger and longer first order faults.  Interestingly, the first order faults could also be subdivided into a group with displacements larger than 1800m, these faults include S1 (a and b), S4, S7, and D1.  These faults may represent master faults that initiated earlier, whilst many of the remaining faults grow as accommodation structures.

### 5.2.4   Fault Intersections at the Regional Scale

Most intersection examples presented in this chapter will focus on individual cases; however it is important to highlight some regional changes between strike-slip fault intersections with changes in depth.  Time-dip maps from three stratigraphic levels (the seabed, the base of PM3, and the M horizon) yield several important observations (Figure 5.5): 1) there is a reduction in faults upwards; 2) most dextral faults are not visible at the seabed; and 3) some first order sinistral faults show differing branching relationships with depth.

The observations imply a highly complex growth history of faults in GalC.  For example, if the number of faults reduces upwards then it suggests that some faults die out, whilst others continue to accrue slip and remain active.  This point is exemplified by the burial of most dextral faults without expression at the seabed, and suggests they are currently inactive, whilst activity across

sinistral faults is evidenced by syn-kinematic channels at the seabed (Figure 3.7, Figure 3.8). It can be concluded, therefore, that fault activity does not occur simultaneously, and instead occurs episodically. The importance of this point will be explored in Section 5.3.

The changing branching relationships also imply complex growth histories. For example, at the M horizon, S5 branches from S4, before S4 branches again with S6. Interestingly, S6 appears to be the more dominant fault (based on the fault width and strong signal). However, at the base of PM3, S6 is mostly buried, and S4 and S5 are clearly the dominant faults. At the seabed, S4 becomes mostly buried and only S5 remains active. Faults segments are therefore clearly active at different stratigraphic levels and therefore at different times.

### 5.2.5  Fault Timing

Timing the onset of faulting is problematic without the aid of growth strata that are commonly found associated with normal and thrust faults. Although some kinematic indicators show syn-kinematic elements (see Chapter 3), these are only located near the seabed and can only help differentiate which faults are currently active. However, small pull-apart basins show evidence of growth strata and allow a crude estimation of faulting onset once the fault has propagated to the free surface; these are located on faults S1, S15, and S94.

Comparing profile lines from the western edge of GalC and the centre shows a considerable change in the distribution of growth strata (Figure 5.9). Towards the west, there are notable growth strata present in Units PM2c and PM3, indicating that both faults S1 and S15 were active from the late Pliocene. By contrast, growth strata from a profile line towards the east are only observed in PM3. This suggests that fault activity breached the free surface earlier towards the west and therefore, assuming a similar rate of upward growth, a lateral propagation direction to the east for sinistral faults. Extrapolating this idea to the regional map (Figure 4.1), it suggests that the sinistral faults formed due to increased influence from the gravity induced salt tectonics of the Nile Delta and propagated towards the basin. A notable exception is the sinistral faults in the Southern Region, which display a similar trend to the El Arish and Afiq Faults (Chapter 4).

These faults may have formed either as down-dip equivalents or potentially as relay faults between the two systems.
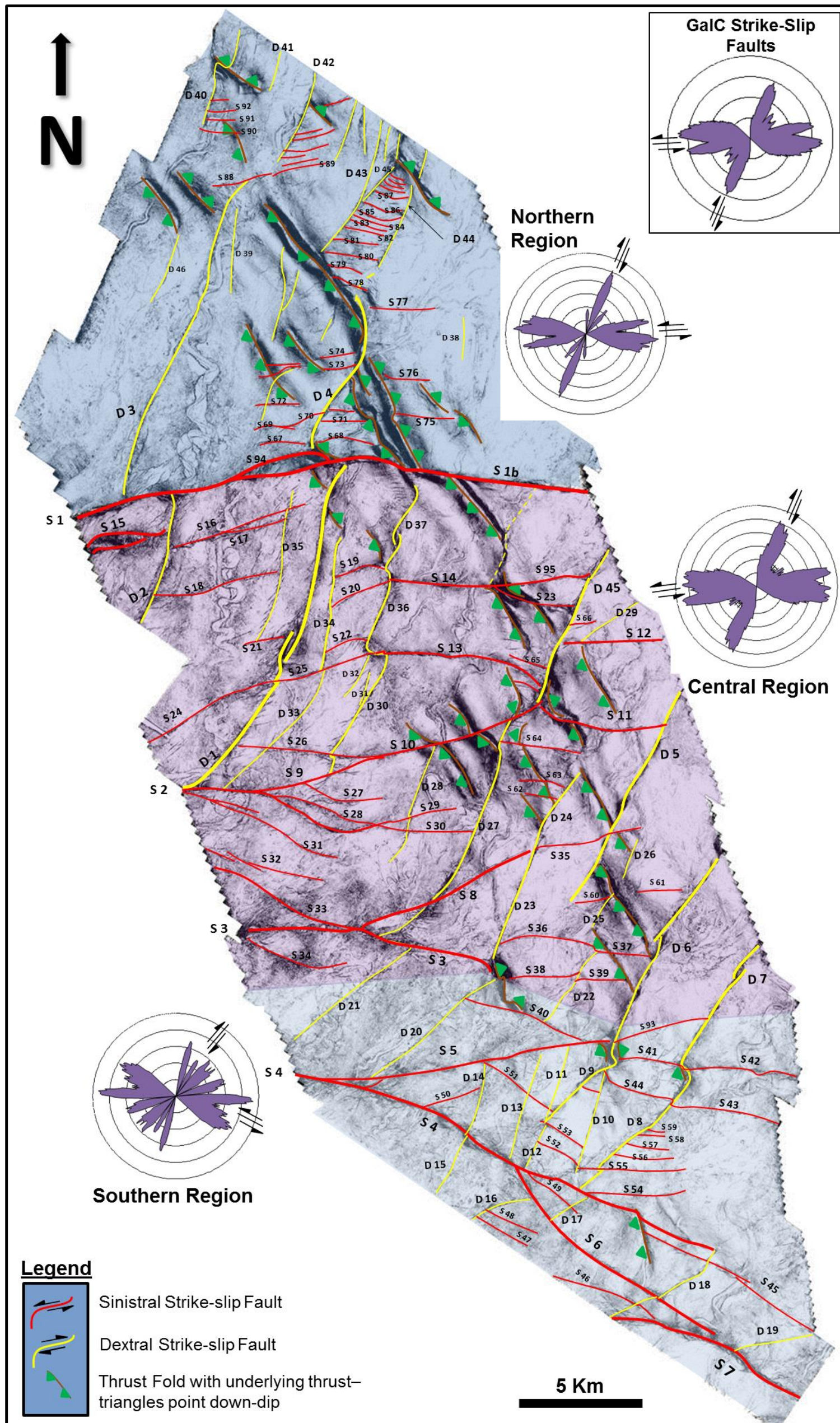
Figure 5.1 - Coherency slice of the GaIC dataset showing the structural framework of thrust related folds and a conjugate set of strike-slip faults.  There are notable changes in trend and structural expression of the strike-slip faults, and the dataset is subdivided into three regions.  Equal area rose diagrams are presented to show the trends in each region as well as overall (latter at top right).  These were computed using MARD 1.0 with an aperture of 9 and a weighting factor of 0.9 (Munro and Blenkinsop, 2012).
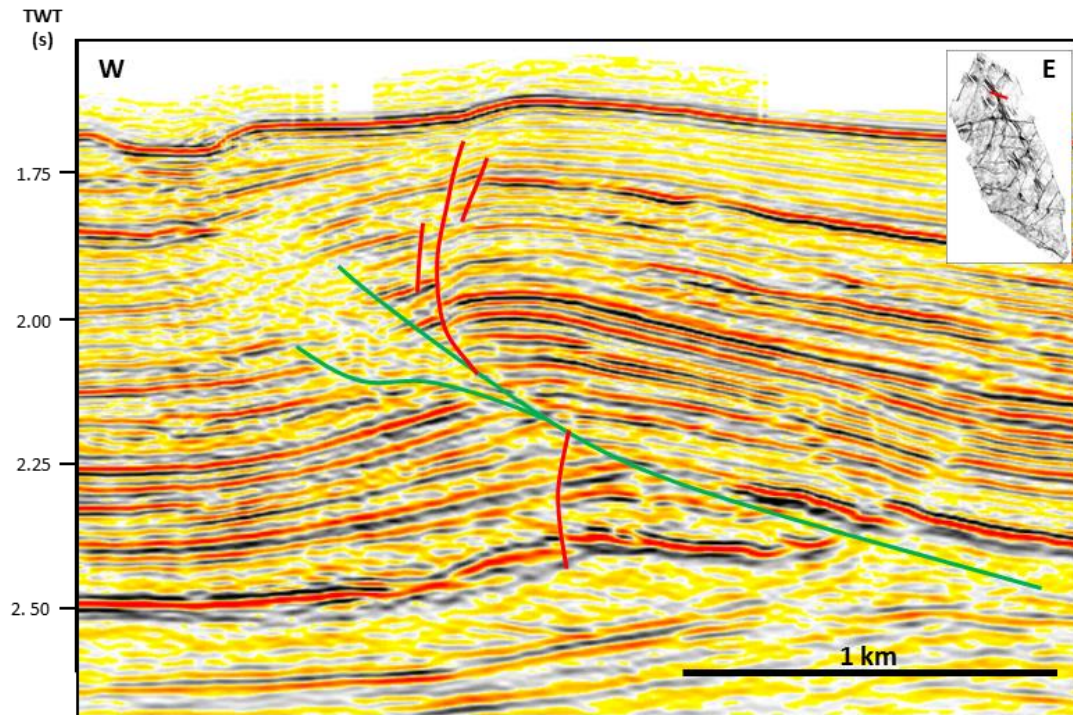
Figure 5.2 - Profile section showing evidence of thrust fault with tri-shear (in green) cutting a sinistral strike-slip fault (in red).
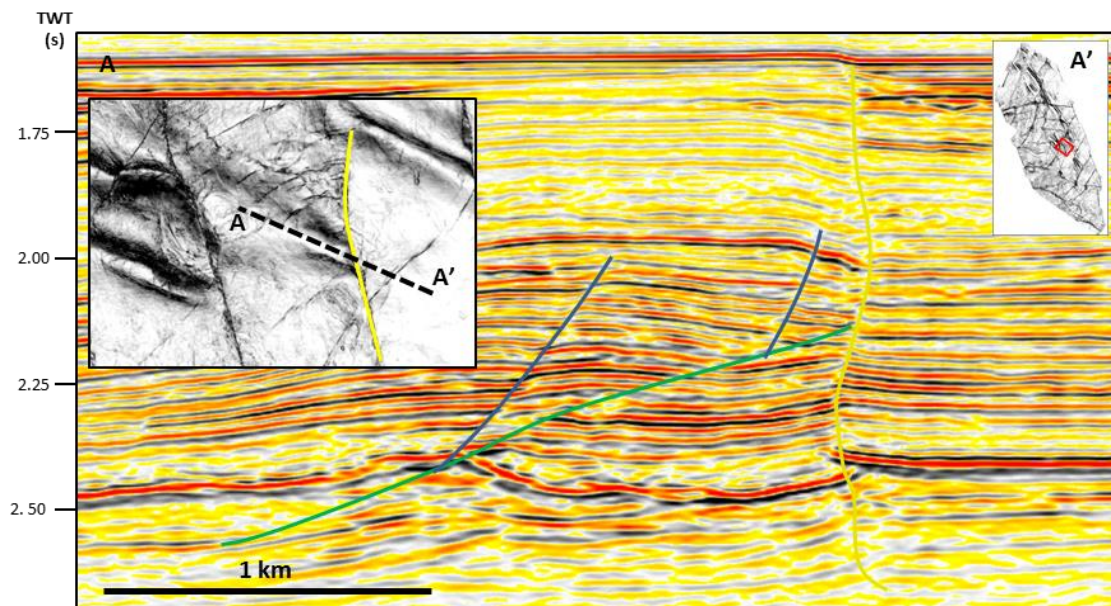


Figure 5.3 - Profile section showing evidence of thrust fault (in green) abutting against a dextral strike-slip fault (in yellow).  Note how the trace of the strike-slip fault is deformed around the thrust fault, suggesting that both structures may have interacted at the same time.
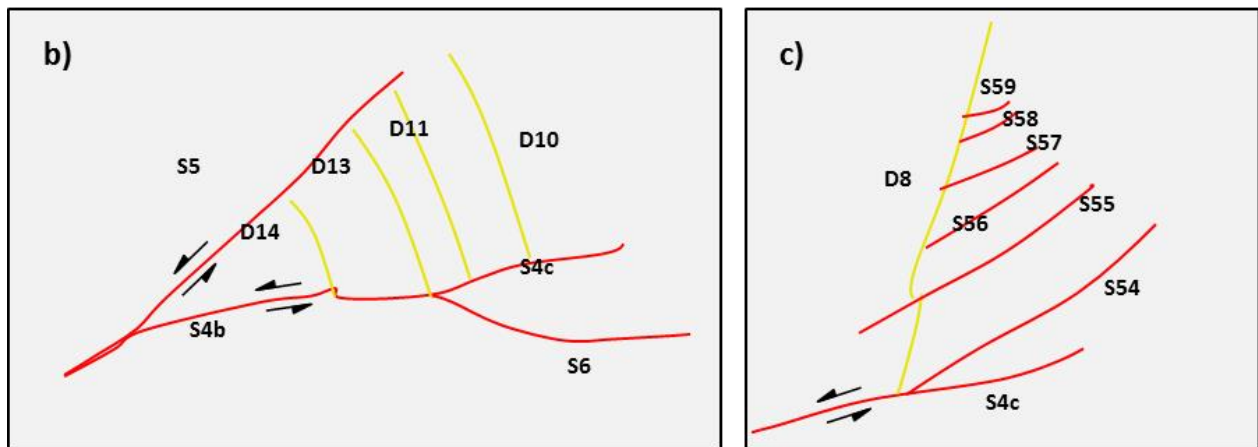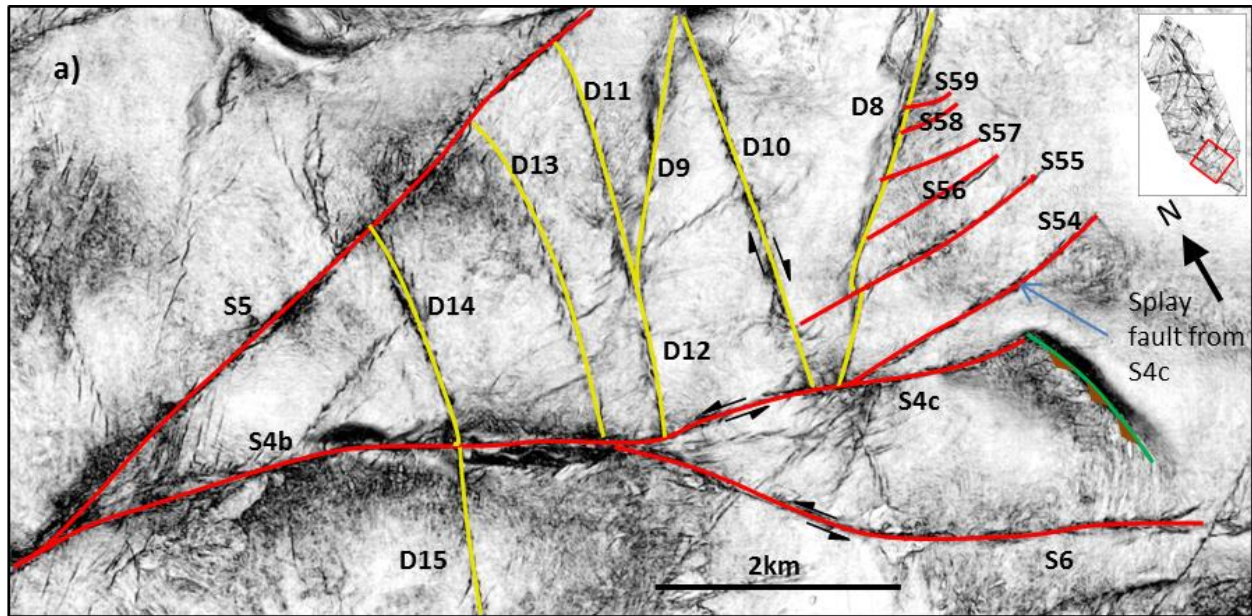
Figure 5.4 - a)  Coherency slice showing a sinistral strike-slip fault (in red) tipping out laterally into a thrust fold with an underlying thrust fault (in green).  Note that this fold is in the compressive quadrant of the strike-slip fault, and a compressional derived structure would be expected here. b) Simplified interpretation of branching faults encasing antithetic dextral faults.  c) Antithetic splay faults that may represent a tip structure of D8.
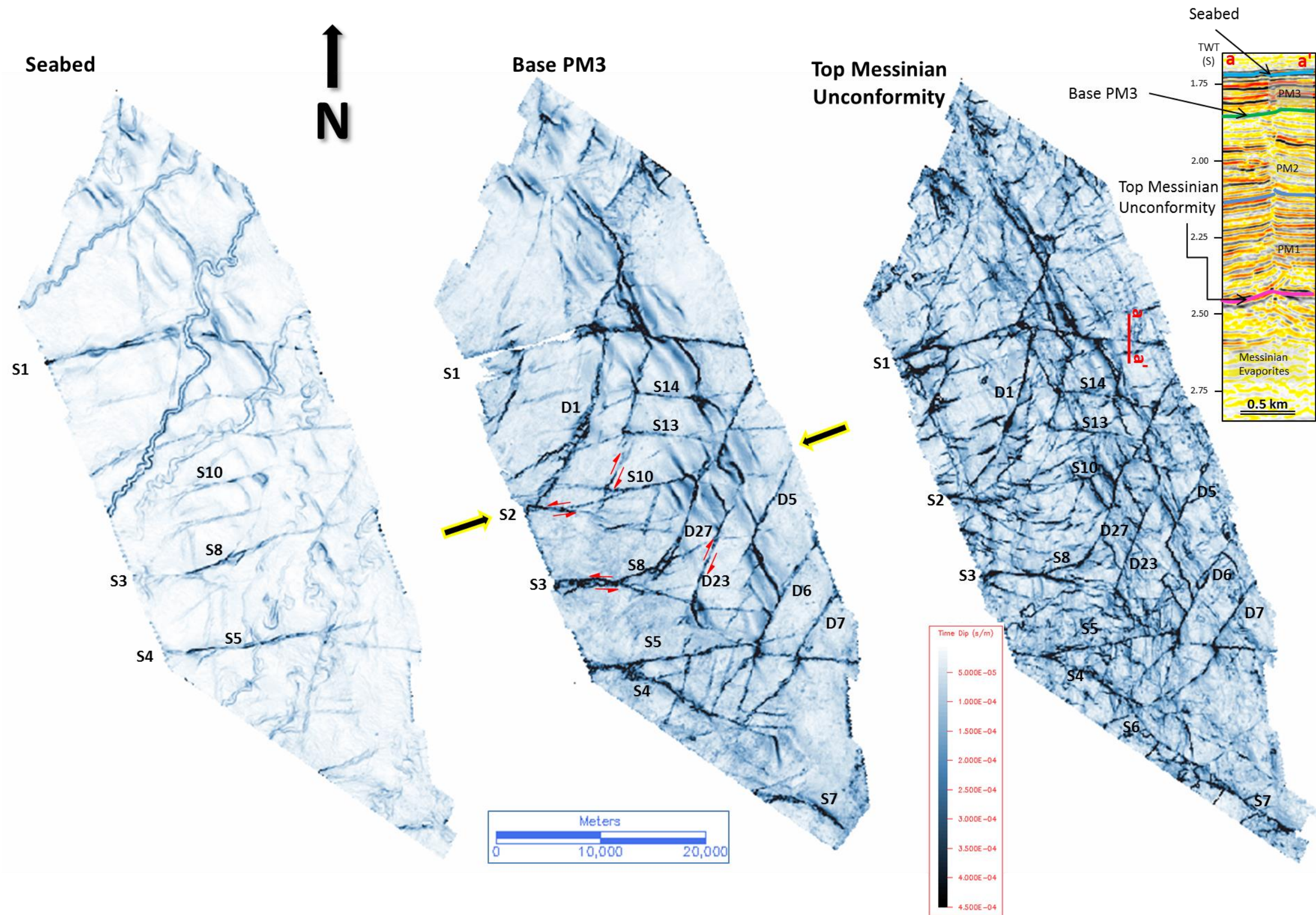
Figure 5.5 - Time-dip maps of three levels of the GalC dataset. Note the changes in regional relationships as the maps move upwards from the Top Messinian Unconformity (M horizon). There is a significant decrease in faulting upwards, with most dextral faults oriented NE-SW buried at the seabed. The base PM3 horizon shows some wider faults zones, indicating the presence of Tier B geometries.
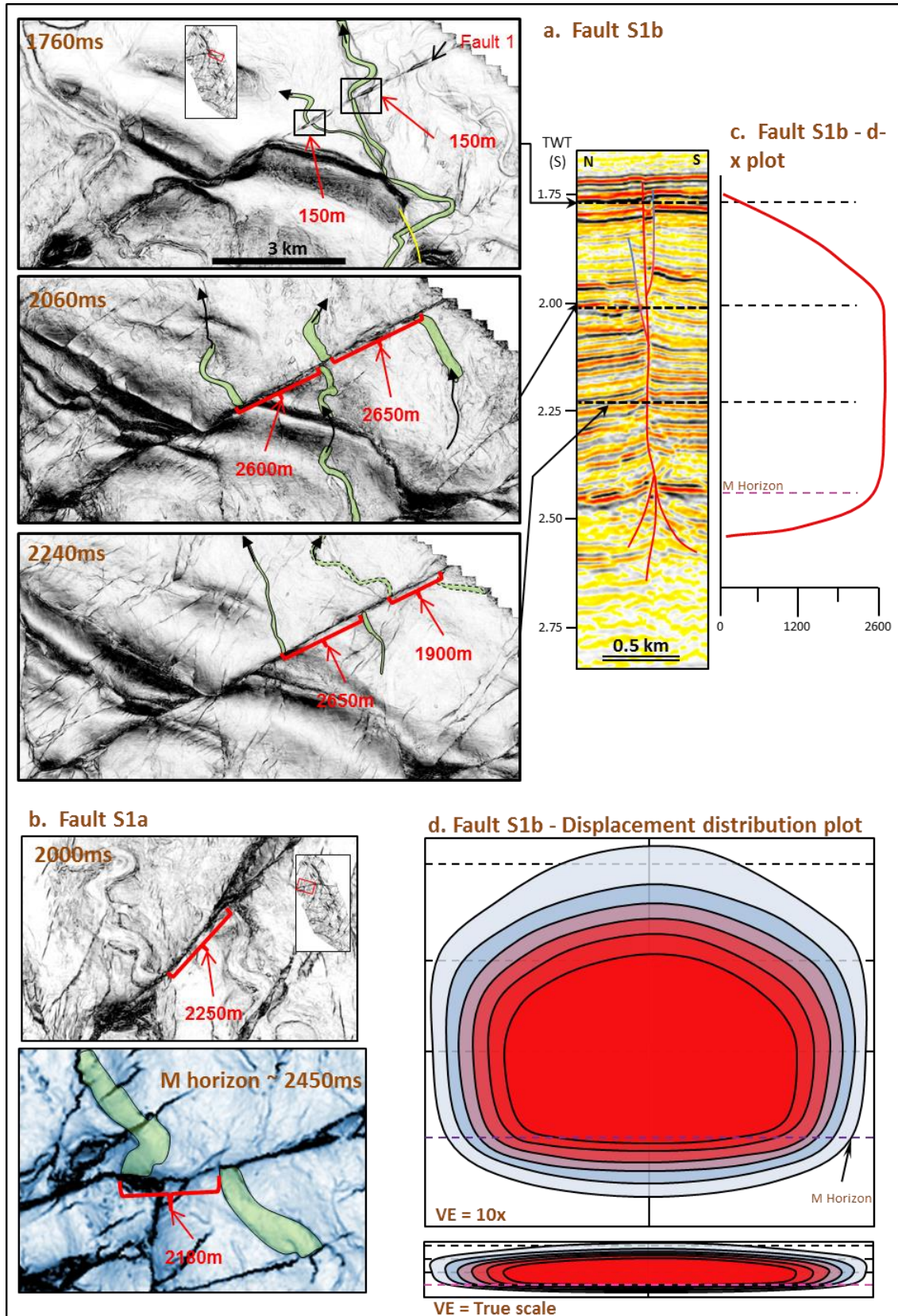
**Figure 5.6** - Crude analysis of the displacement distribution of GalC Fault S1b using minimal data. a) Three slices show how displacement changes with depth, with displacement decreasing quickly upwards. b) Two

kinematic indicators from Fault S1a show that an offset decrease is small from the overburden unit to the M horizon at the top of the evaporite succession. The information suggests that large offsets are prevalent in Units PM1 and PM2, and this is reflected in the d-x plot (c), which uses the displacement information from (a) and the information concerning displacement amounts at the M horizon from (b). d) Using the d-x plot, a cartoon distribution is formed to illustrate the large area of maximum displacement. It is important to note that the lateral tips are likely incorrect as the fault extends eastwards beyond the dataset limits, and therefore do not reduce to zero in the length measured (12.25km). Similarly at the western tip, there is a linkage with Fault 1a, suggesting that although the offset may reduce, it would not reduce to zero. However, with a lack of valid kinematic indicators in this region this cannot be verified. What can be extrapolated from this plot is the asymmetric displacement distribution, with tighter contours in the Messinian Evaporites. The upper tip contours have been drawn to include displacement data from just below the seabed, which is likely affected by syn-kinematic movement and therefore may be lower than measured. Despite the true length of the fault remaining unknown, a minimum aspect ratio can be calculated as 12:1, suggesting that the larger strike-slip faults undergo heavy restriction to vertical propagation. Note that the kinematic indicators shown in (a) are only the submarine channels. Although the thrust folds are apparently offset, it is hard to determine if they record a true offset or just exhibit an apparent offset from different two independent thrust folds. Further work on this matter was conducted by Nwosu (2014), and showed conflicting results depending on the thrust folds and strike-slip faults.
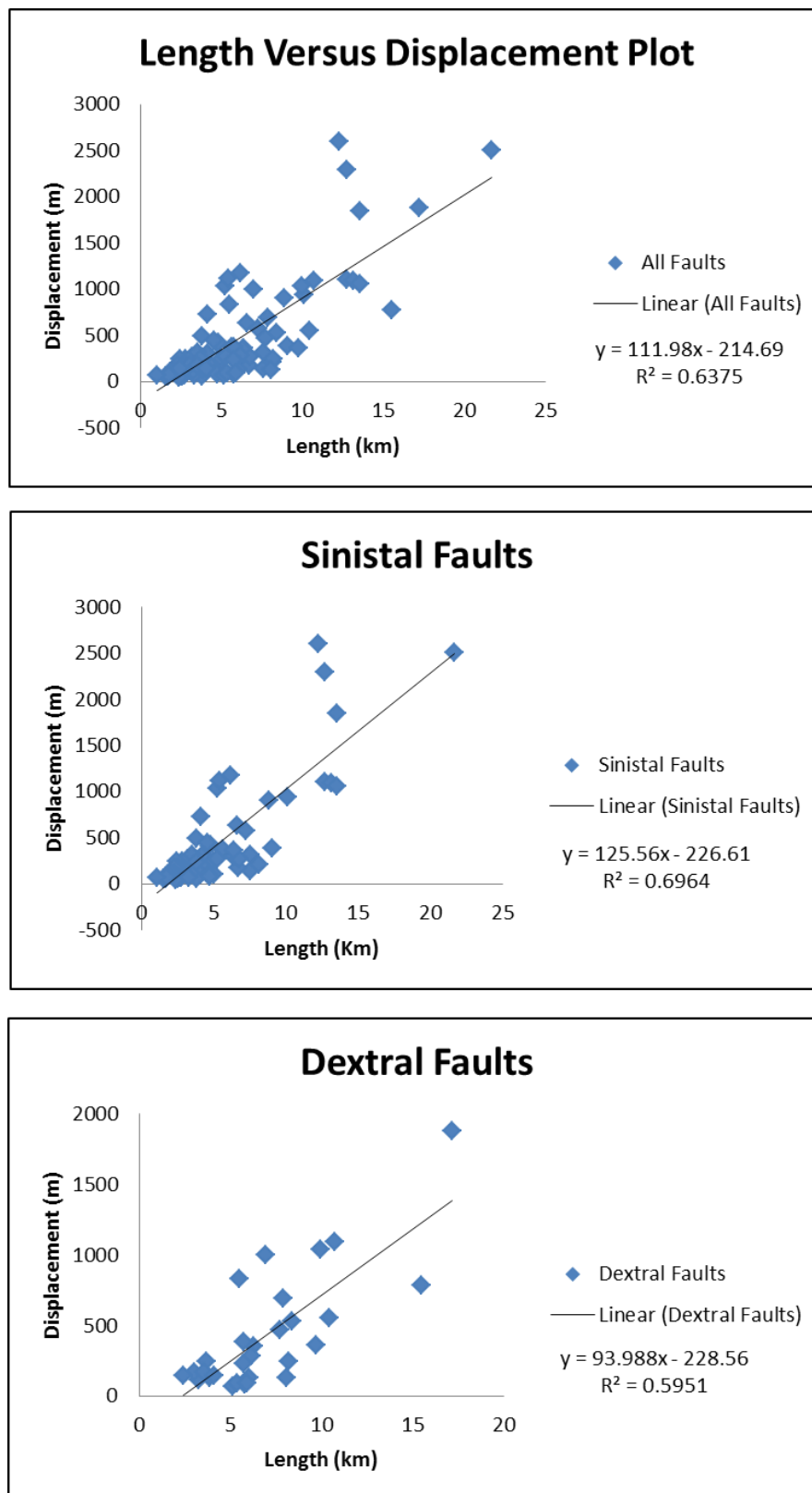
Figure 5.7 - Length versus displacement plots (d-x) for all GalC faults, only sinistral faults, and only dextral faults. Note the correlation is not very strong, indicating that a wide variety of lengths can accommodate different amounts of displacement.
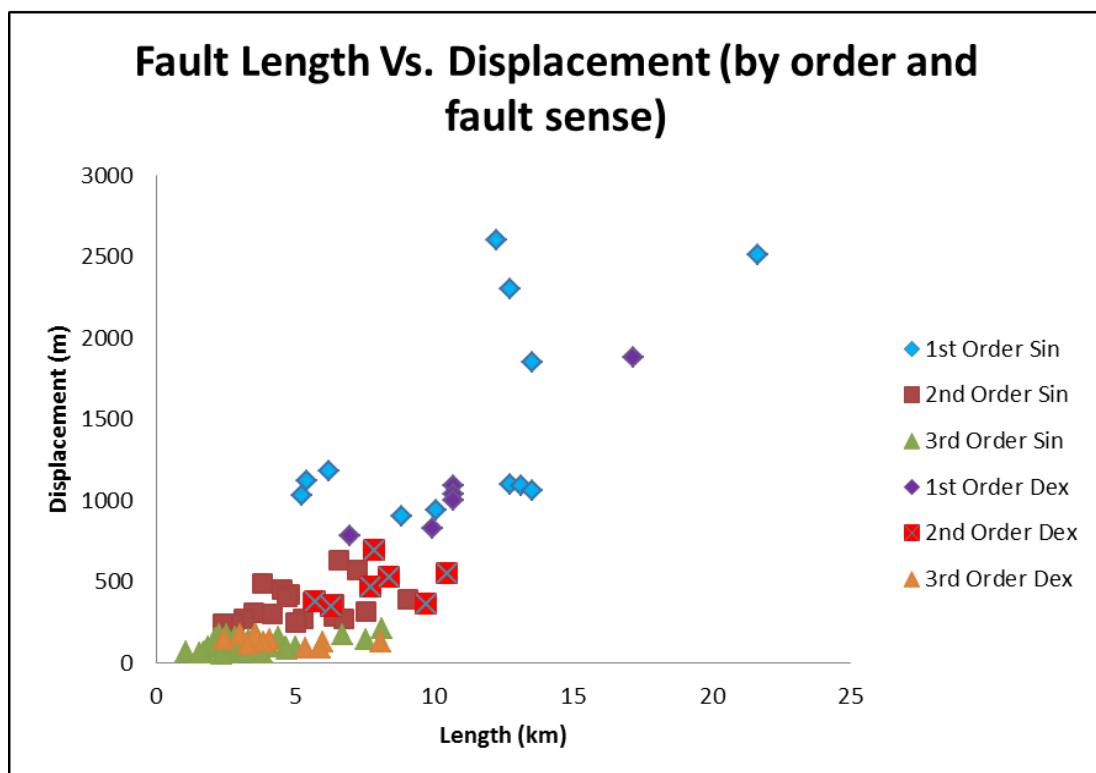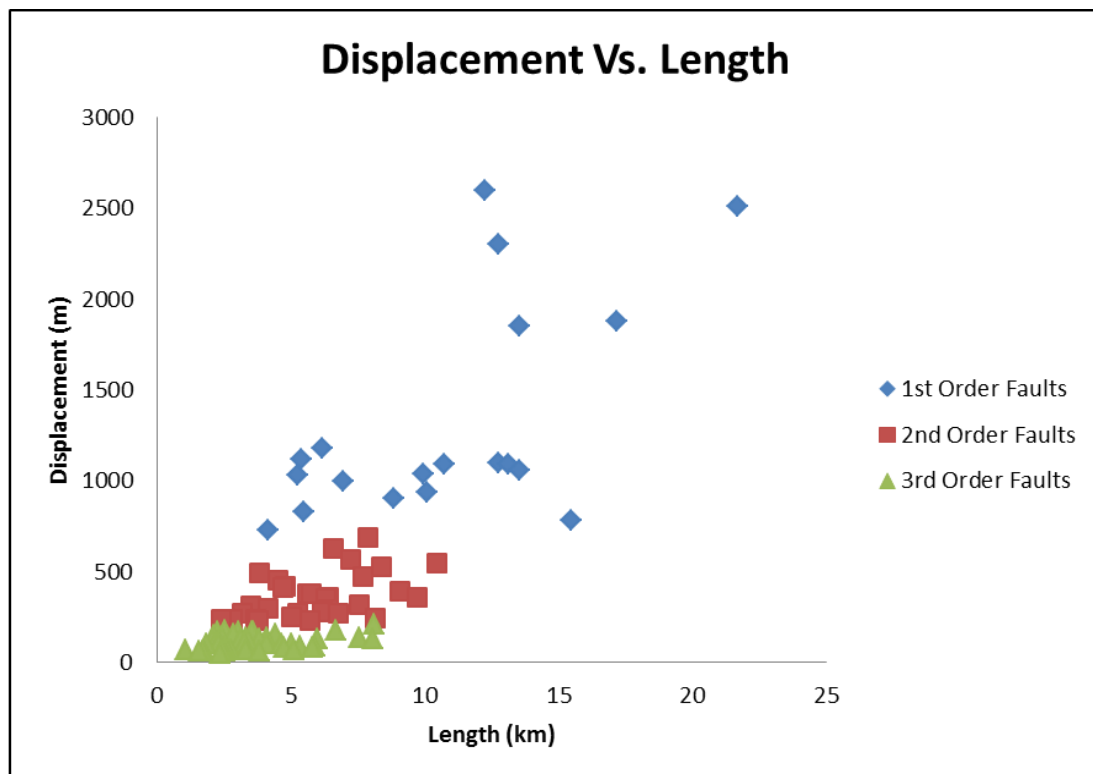
Figure 5.8 - a) Length versus displacement plots (d-x) for GalC faults by orders of displacement magnitude. Note that each order has a large amount of overlap in length.  b) Same plot, further subdivided into sinistral and dextral.  This shows a slight tendency of dextral faults to have longer lengths for the same amount of displacement at the $3^{rd}$ and $2^{nd}$ orders, but this not case at the $1^{st}$ order.
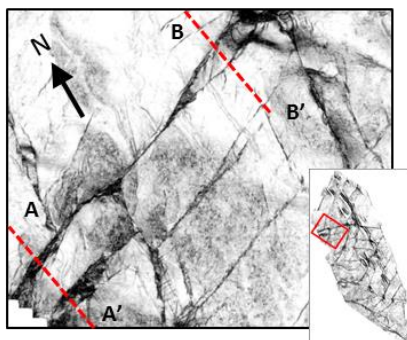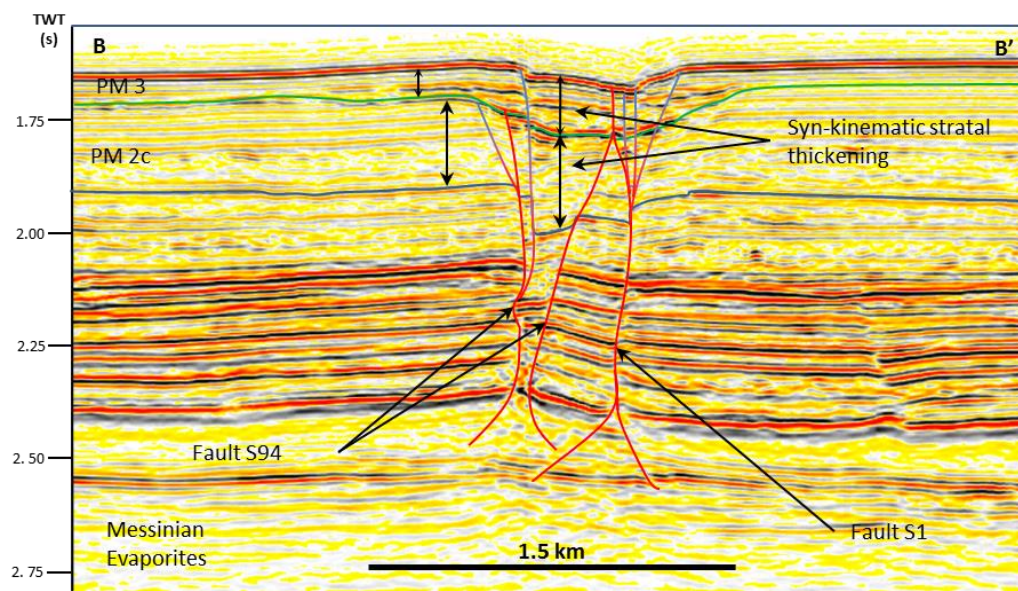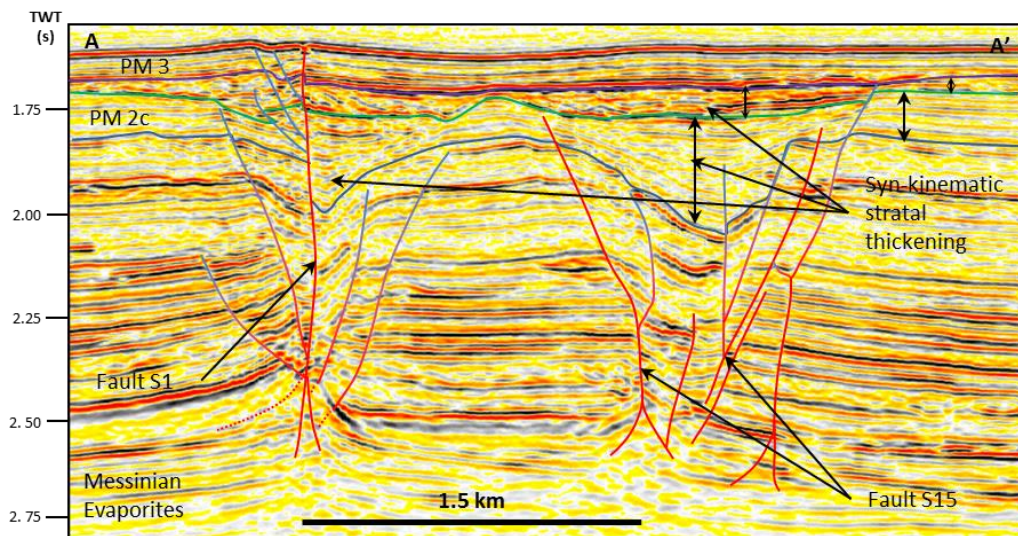
Figure 5.9 - Profile sections from west to east showing growth strata in sinistral faults S1, S15, and S94.  Note that in the west, growth strata are observed in both Unit PM2 and PM3.  Whilst towards the east, growth strata are observed to reduce in PM2 and increase in PM3.  This suggests that faults were active earlier towards the west and therefore suggests an eastern propagation direction of the sinistral faults.

279

## 5.3   Conjugate Fault Intersections

Conjugate fault propagation and timing from studies on normal faults and analogue experiments have greatly expanded our knowledge since the pioneering works of Anderson (1951).  For example, Horsfield (1980) showed that all four fault segments in a crossing conjugate array show a displacement decrease towards the intersection, and allow for true simultaneous slip on all four faults as originally suggested by Anderson (1951).   However, field studies suggest that although a conjugate pair may propagate coevally (under the same stress field); the actual slip movements occur episodically (Ferrill et al., 2000; 2009). Although studies have addressed the kinematics at conjugate intersections (An, 1998; Schwarz and Kilfitt, 2008), few have focused on how an intersection varies in three dimensions, especially with strike-slip faults.  This section will first analyse the angles of fault intersections, before using several coherency slices at different depths to provide a three-dimensional analysis of the intersections.

### 5.3.1   Conjugate Intersection Angles

Inspecting the angle of intersections is pertinent to elucidate how fault intersections in GalC compare to the 'Anderson' model of conjugate faulting (Anderson, 1951).  That is, do conjugate fault pairs in GalC deform under a pure shear conditions at the expected angle of around 60˚, with $\sigma_1$ bisecting the faults (Ferrill et al., 2000)?

Angles were measured between all conjugate intersections across GalC at two depths: 1700ms TWT, which lies roughly 100 – 200m below the seabed; and at 2200ms TWT located roughly near the PM1 and PM2 boundary (Figure 5.10).  Overall, both depths show a similar distribution with peaks close to 60˚; however, there are subtle differences as the peak at 2200ms is between 56˚- 60˚, whilst the peak is 61˚- 65˚ at 1700ms.  Separating the intersections by region (at both depths) yields an interesting observation: the Northern and Central Regions show peaks between 56˚- 65˚, whilst the Southern Region shows a more scattered distribution.

The latter observation is interpreted to be caused by the notable change in fault trends that occur in the Southern Region (Figure 5.1), and suggests the sinistral and dextral faults have not changed trends uniformly.  Furthermore, some of the smaller, third order sinistral faults

show a splay-like geometry from a second order dextral fault, and therefore may not strictly form a conjugate intersection (Figure 5.4c). Although several of these splay fault intersections are also identified in the Northern Region, the angles were often close to 60˚, and therefore do not permit differentiation between intersection types.

The intersections mostly form angles close to the expected 60˚, and are interpreted to show a true conjugate relationship (with the exception of the third order splay faults). The increase in intersection angle from 2200ms to 1700ms is curious as it may suggest an overall rotation of faults upwards to form a wider intersection angle. However, it is also possible that intersections that formed more acute angles were buried by 1700ms, thus skewing the data. Smaller deviations from 60˚ are attributed to the heterogeneities within the strata of GalC as well as the presence of the thrust faults and folds. Finally, intersections commonly showed the faults curving towards the intersection (explained in the next section) and therefore measuring the angle became arbitrary. Here the angle was measured before the curvature where possible; however, some fault traces curve for many kilometres before the intersection, which resulted in several intersections forming angles significantly higher and lower than 60˚.

### 5.3.2   Fault intersections in 2D

Simple fault intersections can be summarised with the following geometries based on observations from this study:  1) a dextral fault offset by a sinistral fault, 2) a sinistral fault offset by a dextral fault, 3) both faults offset each other (mutually coeval), 4) neither faults offsets, and 5) and 6) form opposite abutment relationships (Figure 5.11). These examples define the simplest interaction zones one might expect to see in nature; however, field examples often show that fault zones are often more complex with the inclusion of either splay faults, neighbouring faults, or both (Figure 5.12). The Arches National Park example illustrates how a fault can be offset then form a later splay that is not offset, thereby forming a more complex intersection that can lead to erroneous interpretations. Furthermore, analogue studies show that faults under conjugate conditions, will form a 'confluence bow' as a propagating fault approaches its conjugate pair (Schwarz and Kilfitt, 2008). The confluence bow forms from a fault approaching the intersection and curving towards the direction of slip, where a later splay will then propagate to the intersection with the same

281

trend as the fault (Figure 5.13).  Thus intersections may show several segments, splays, and tip curvature towards an intersection, which will produce a more complex morphology.

Most complex intersections can be simplified into the models listed above (Figure 5.11), allowing for an interpretation of the intersection kinematics.  For example models 1 and 2 imply that one fault was older and then cross-cut and offset by the younger.  Model 3 implies that both faults were active at the same time and mutually offset each other, producing the curvature expected at a fault intersection from both faults forming confluence bows (Schwarz and Kilfitt, 2008).  Model 4 suggests that displacement around both faults has reduced to 0, leaving an X shape with no notable offset, although a slight confluence bow of the fault zone may occur.  The abutment models (5 and 6) suggest that the abutting fault is the younger fault because as in the case of model 5, continued lateral propagation of fault b is prohibited by the presence of fault a.  To clarify this point: the abutment models allows for a prediction for the timing of faulting at the intersection.  It is possible that the both faults initiated contemporaneously, but preferential propagation of fault a (in model 5) means that it reaches the intersection region before fault b, and therefore the propagation of the latter is inhibited by fault a.
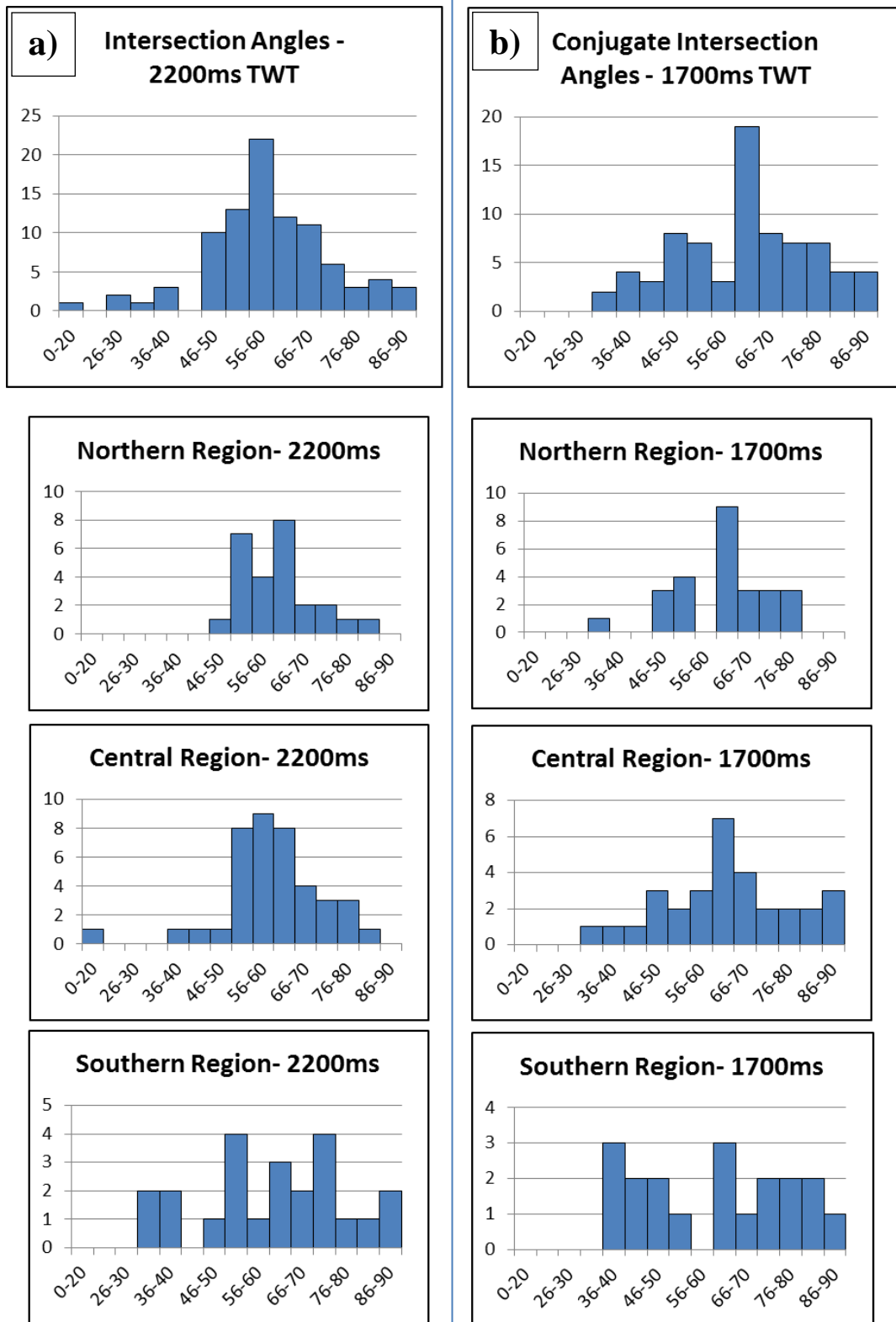
Figure 5.10 – a) Histograms showing the intersection angle distribution for the entire GalC dataset, and for individual regions at depth 2200ms TWT.  b) Histograms showing the intersection angle distribution near the seabed (1700ms) for the same regions. It should be noted that some parts of the seabed in the Northern Region were located below 1700ms TWT, and measurements were taken up to 100m below.
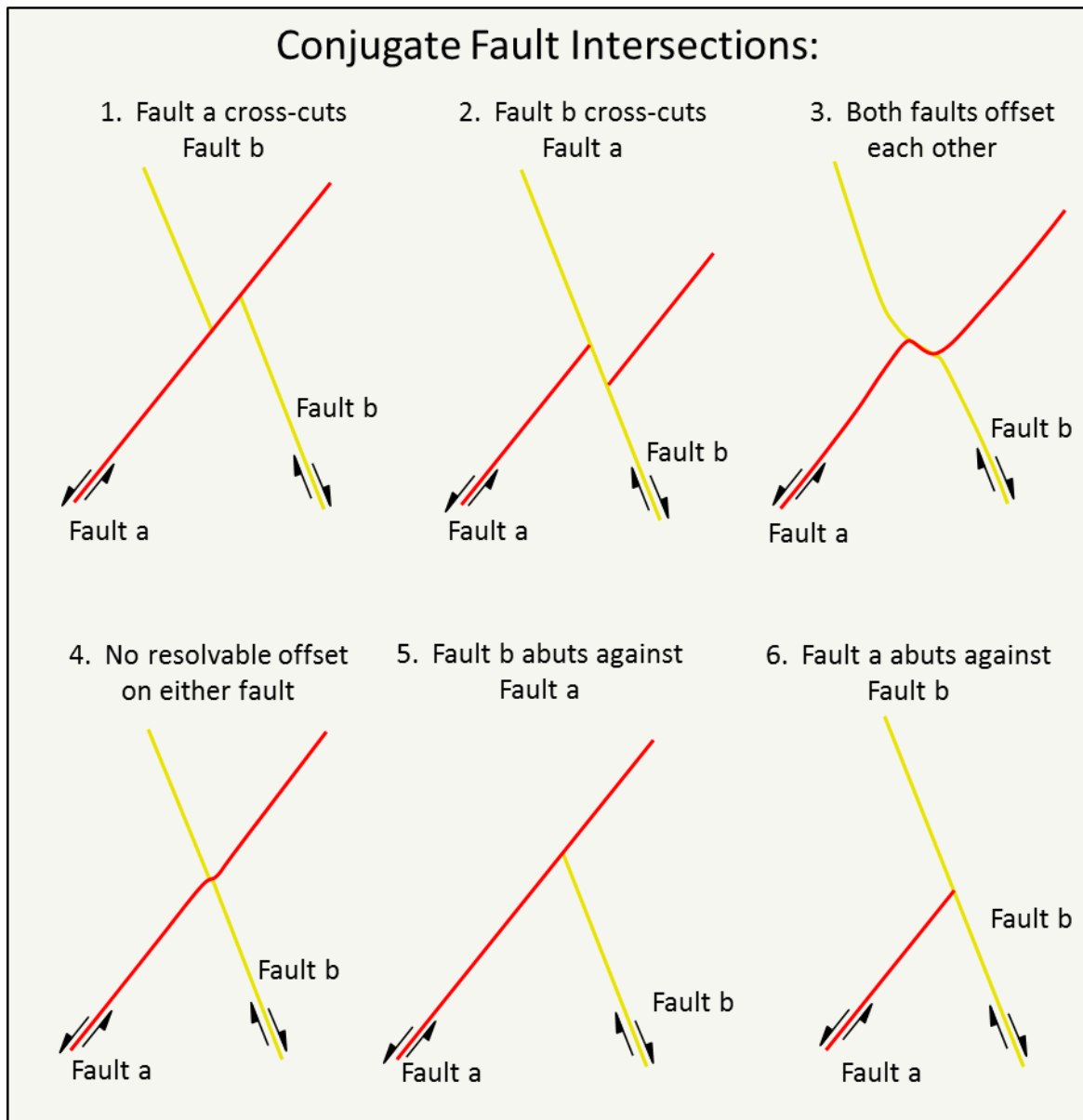
Figure 5.11 - Conventional models of conjugate fault intersections. Models 1 – 4 show crossing faults, whilst 5 & 6 show abutment relationships. Notably in model 4, the faults may show some curvilinear features at the intersection; however, no offset is observed.
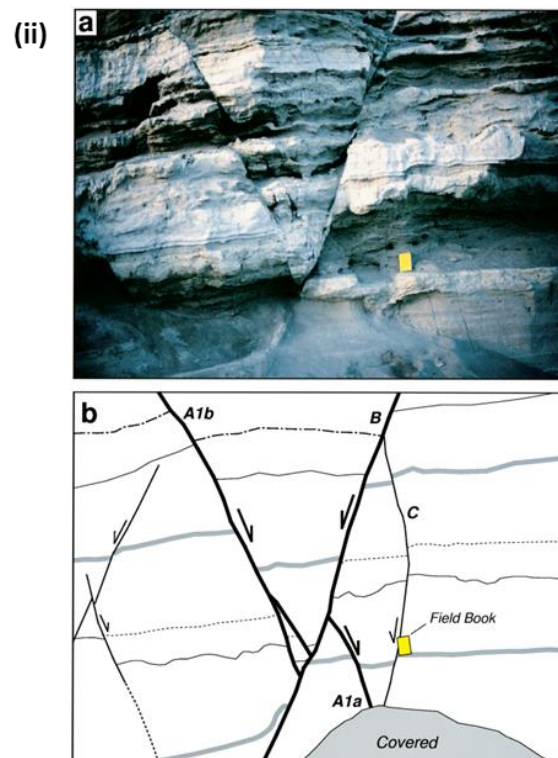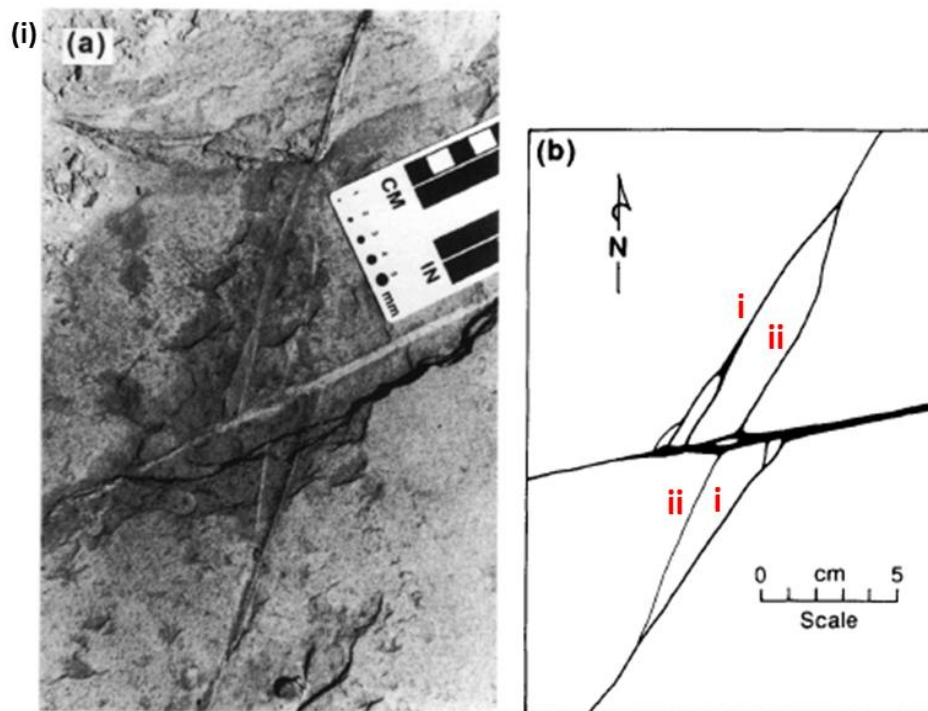
Figure 5.12 - Examples of conjugate fault intersections from the field. The first (i), from Arches National Park, Utah, is a sinistral strike-slip fault offsets a dextral fault, where a second splay later grows and crosses the sinistral fault with no offset (adapted from Zhao & Johnson, 1991). The second example (ii) shows normal faults that splay towards the intersection from Owens Valley, California (adapted from Ferrill et al, 2000).
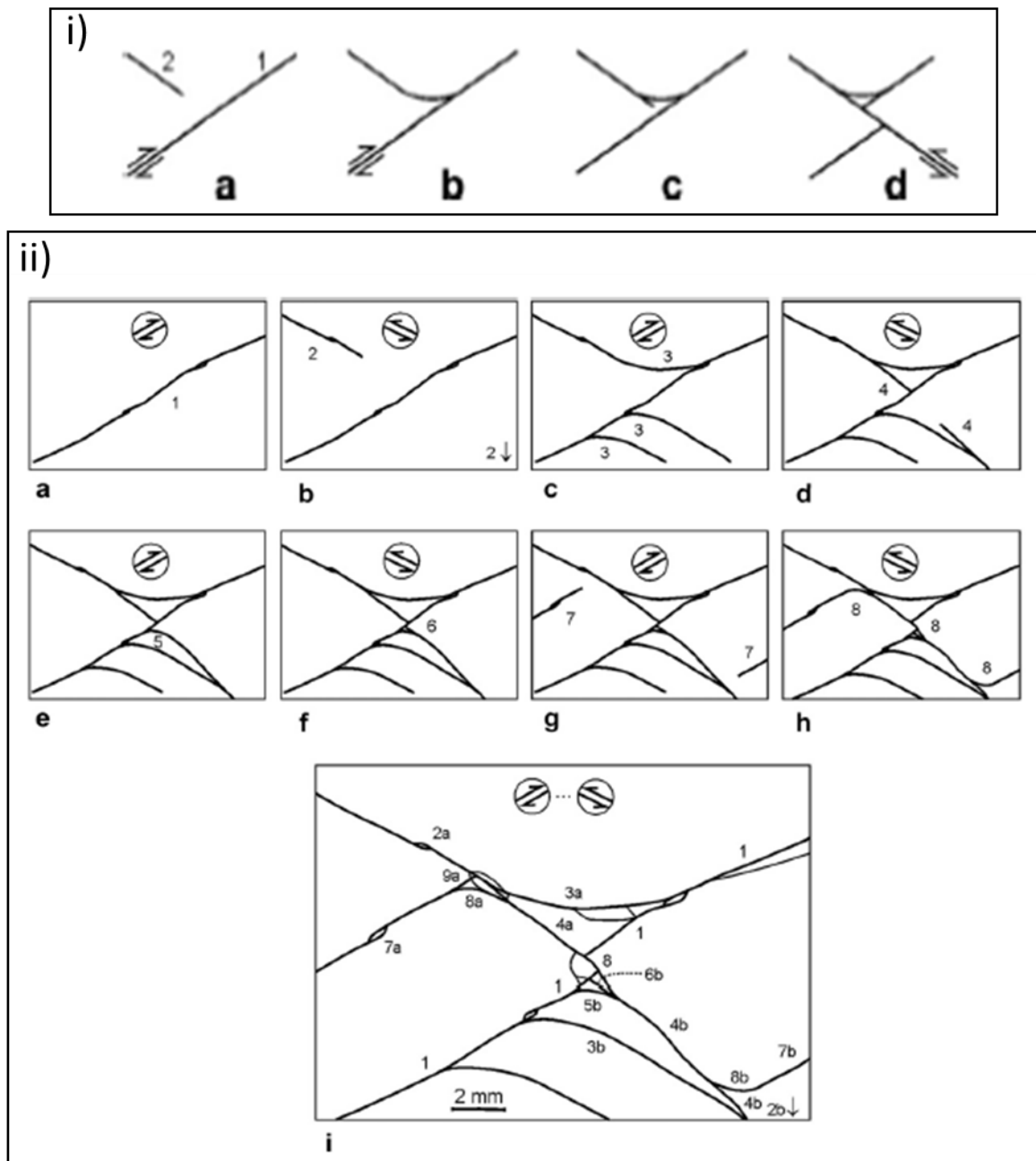
Figure 5.13 - Examples of conjugate fault intersections from an analogue study.  i) depicts the theoretical evolution of a conjugate intersection starting with: (a) Simple system consisting of a dextral fault 1 and a sinistral fault 2 growing towards fault 1, (b) Curved linkage of both faults called the ''confluence bow'', (c) Fault 2 branch propagating in a straight direction, and (d) Intersection of fault 1 by fault 2.  ii) example of an experiment, which shows how confluence bows form on either side of fault 1, before several fault segments link together (e.g. faults 2, 4 , and 8) to cross-cut and offset original fault 1. (adapted from Schwartz and Kilfitt, 2008).

### 5.3.3   Fault intersections in 3D

Coherency slices provide a snapshot of the intersection zone, which allows for the interpretation of its kinematics. However, if faults grow episodically, is it reasonable to expect that an intersection zone is homogenous in depth? Preliminary results from this study suggest that this is not the case, and three examples are presented to elucidate the true complexities of a fault intersection zone in three dimensions.

*Example 1-*

The first example, located in the northwestern part of the Central Region, focusses on the intersection zone between S16 and D35. S16 is a 2$^{nd}$ order fault with maximum offset of 210m, whilst D35 is a 3$^{rd}$ order fault with 130m offset. At the seabed, both faults are buried and therefore do not intersect, whilst at 1800ms TWT, they appear to form a Type 5 abutment (Figure 5.14). However, closer inspection reveals that the intersection is actually more complex due to the presence of Tier B fault strands (see Chapter 4 for definition) on the northern side of S16. It is also not possible to identify if an offset occurs across S16 due to the change in structural style. This geometry remains the same at the 2000ms TWT slice, although the length of the Tier B fault strands decreases and also change strike.

A significant change in intersection geometry occurs at 2100ms TWT, where S16 and D35 both show a curving towards the intersection zone (in a Tier A geometry), and both show an offset by the other fault, thereby forming a Type 3 intersection. 300m below at 2400ms TWT, the intersection zone shows a further change to Type 4, with no clear offset defined by either fault.

The geometries are summarized by simple line drawings (Figure 5.14c) to illustrate how variable the intersection zone is through a 600m change in depth. The shallower levels (1800ms, 2000ms) suggest that both faults show a level of kinematic interaction, otherwise a Tier A geometry would occur on both sides of S16. This signifies that both faults were active at this time, with the intersection compartmentalizing fault D35 and causes a transfer to the Tier B geometry. It is likely that activity on S16 also continued after D35 was buried, which would explain the apparent Type 5 geometry and the change in strike of the Tier B strands.

The Type 3 intersection further suggests that both faults were active at the same time; however, given the assumption above that S16 was also active after D35, then it would be expected that the mutual offset geometry would be obliterated into a Type 1 intersection. The Type 4 intersection at depth is particularly curious as the 2400ms slice is still a minimum 100m above the basal fault tips in the Messinian Evaporites, and therefore cannot be attributed to displacement decrease with proximity to the basal tip.

To summarize, there is a juxtaposition of three conflicting intersection types, with each suggesting different kinematics of the fault zone. In order to truly understand how the faults in this intersection slipped, more analysis is required. Likely, a more precise timing of growth with displacement data would be required to surmise a legitimate interpretation as well as careful interpretation and modelling of the faults in 3D.

*Example 2 –*

This example highlights the problem of defining whether a fault is comprised of separate segments or simply two separate faults (Figure 5.15). In this case, S38 and S39 may be the same fault or two separate faults that have propagated into D22. Offsets were measured on all three faults: S38 = 170m, S39 = 120m, and D22 = 140m. Although the offset of S38 is 42% higher than S39, each measurement was taken either side of D22 and separated by several kilometres, and thus the magnitude of offset alone is not sufficient to determine if the faults are separate. At first inspection, the intersection of an intermediate depth (2000ms TWT, Figure 5.15) shows a simple Type 2 intersection with D22 offsetting S38 from S39 by 240m in a dextral sense. However, given that the maximum offset of D22 is 140m, this is likely a false kinematic indicator. Instead, a closer inspection reveals that S38 and S39 show separate interactions across D22 at different depths.

Starting with the shallowest slice, D22 is buried and S38 and S39 form two overlapping segments of what appears to be the same fault. However, 120m deeper at 1820ms TWT, D22 cross-cuts and offsets both S38 and S39 in a Type 2 intersection. Interestingly, the intersection between D22 and S39 shows a sinistral offset, and is therefore a modified Type 2 intersection. Also of note, both sinistral faults show a small segment on the other side of D22 at this level, which is not consistently observed at all depths. The three deeper slices show differing geometries at each depth, mostly characterized by Type 2, Type 4, and Type 6

intersections. Interestingly, the deepest slice (2320ms TWT) shows a Type 2 intersection between S38 and D22, with an additional segment across the fault.

Both sinistral faults show a different intersection geometry at a different depth and therefore form a complex geometry in 3D. However, D22 does not appear deformed and it has clearly offset segments of S38 and S39, suggesting that it is a younger fault. The incorrect sense of offset at 2000ms, may be attributed to the presence of a small, separate, pre-existing fracture or fault discontinuity that was exploited or due to a seismic artefact. Unfortunately, there is not sufficient evidence in either case to make an interpretation with a reasonable amount of confidence.

Given that S38 and S39 appear as one fault with overlapping segments near the seabed, they are interpreted to have undergone soft linkage. This suggests that after activity ceased on D22, the two faults continued to grow towards each other and begin to form a single fault, meaning that two initially separate faults can link to become one at a shallow depth, despite being kinematically separated by a third fault at a different depth. This could significantly change the outcome of a fluid flow model through these faults and further highlights the importance of analysing these intersections in 3D. It should also be noted that this interpretation fails to explain why the smaller segments of S38 and S39 were absent at some depths. This discrepancy suggests that the kinematics are even more complex than the simple interpretation provided here, and warrants future investigation.

*Example 3 –*

The final example examines how different fault splays at depth can form an intersection that shows how different fault sets can dominate the deformation at different levels (Figure 5.16). Third order fault S8 shows a maximum offset of 140m and splays from S3; it intersects with D27, which shows maximum offset of 550m. Near the seabed at 1580ms, the smaller S8 dominates the deformation as D27 abuts against it in a Type 5 intersection. However, at 1700ms (120m below), D27 outcrops on both sides of S8 and is clearly offset in a Type 1 intersection. Two splays of S8 are observed at this level, with splay 2 showing a curvilinear trace. 300m deeper (2000ms) and the intersection remains relatively unchanged; however, S8 appears to be segmented and splay 2 shows a much straighter trace. At 2140ms, the intersection dynamics change considerably with D27 clearly cross-cutting and offsetting S8

by almost 500m to form S8a and S8b; interestingly however, this 'offset' shows a sinistral sense. Critically, only splay 2 of S8 is observed at this slice. This relationship is maintained through to 2340ms and below into the Messinian Evaporites.

The splaying geometry of S8 is interpreted to cause the large apparent displacement shown by D27 at depth. Importantly, it suggests that D27 has not been reactivated to become a sinistral fault, instead showing a false kinematic indicator. Because S8 is not offset by D27, S8a actually forms a Type 6 abutment geometry. Similarly, the segment of S8 east of D27 maintains the same position at all depths, meaning that at depth it abuts against D27 in a Type 6 geometry as well, providing the overall view of a modified Type 2 intersection. This suggests that S8a and S8b are separate faults at depth, which link upwards due to the growth of Splay 1, and likely a reduction of activity along D27.

The fact that an intersection can switch from separate faults at depth to continuous fault at the seafloor provides insight into how complex this intersection is in 3D, despite apparently simple intersections in 2D (Figure 5.16). This change in kinematics with depth is similar to Example 2, and therefore suggests that conjugate fault pairs often change kinematics with depth, likely based on the episodic movement from one fault in the pair to the other. Furthermore, it directly impacts the connectivity of this region, which could provide potential leakage points in a hydrocarbon setting.

### 5.3.4  Conjugate Discussion

To summarise, most intersections form angles close to 60˚, and can therefore be classified as conjugate. Experiments from 2D analogue studies show that the cross-cutting process is both episodic and highly complex (Schwarz and Kilfitt, 2008); however, these intersections can be simplified into the six basic types shown in Figure 5.11 to determine the kinematics and age. The three examples each show different intersection types at different depths, which leads to conflicting interpretations of their propagation history.

Interestingly, these examples are not unusual because almost every conjugate intersection in the dataset displays conflicting geometries of varying degrees. Therefore it can be concluded that fault intersections are rarely simple in nature, and this effect is magnified in 3D. The reason for these complexities has already been attributed to episodic movement, which likely

causes several stages of fault reactivation, segmentation, and linkage. Other reasons for the complexity could be the confluence bow and associated deformation, which forms complex intersections in 2D (Schwarz and Kilfitt, 2008) (Figure 5.13). Extrapolating these segments into 3D builds an even more complex problem; for instance are the multiple fault segments (Figure 5.13ii) all splays from the main fault or small isolated faults that have grown to accommodate deformation or a combination of both? Furthermore, when factoring in multiple stages of movement and reactivation, it is conceivable that several confluence bows could form at one intersection at different depths (Figure 5.18).

Given the variable evolution of fault segments, it is reasonable to expect that conjugate intersections can induce compartmentalization of fault propagation. This means that parts of a fault may be inhibited from further propagation at some depths (due to interaction with intersecting fault), whilst propagation continues at other depths, so that only certain regions of the fault are active at a given slip episode. This may explain why the intersections are incredibly variable; for instance, if a fault in the intersection dies out (such as the dextral fault in Example 2), and slip continues on the sinistral faults, it would be expected that earlier intersection geometry types at depth would be obliterated to become a Type 1 intersection if propagation occurred uniformly across the sinistral fault. However, if propagation of the lower region of the fault were locked, then the original intersection geometries will be preserved. Thus, complex 3D intersections may reveal snapshots into how the faults interacted at different times. This would have significant implications to fluid flow in these regions, which is illustrated theoretically in Figure 5.18 by fluid flow vectors that now move laterally in a system where the faults originally acted as barriers.

Although S18 is the only fault present at this level, notice how the geometry transfers from Tier A dominated to exclusively Tier B strands where a small underlying dextral fault is located (location shown in the 1800ms slice).

Combination of Type 5 intersection (abutment) and fault D35 segmentation into Tier B geometry.

Type 3 intersection

Type 4 intersection
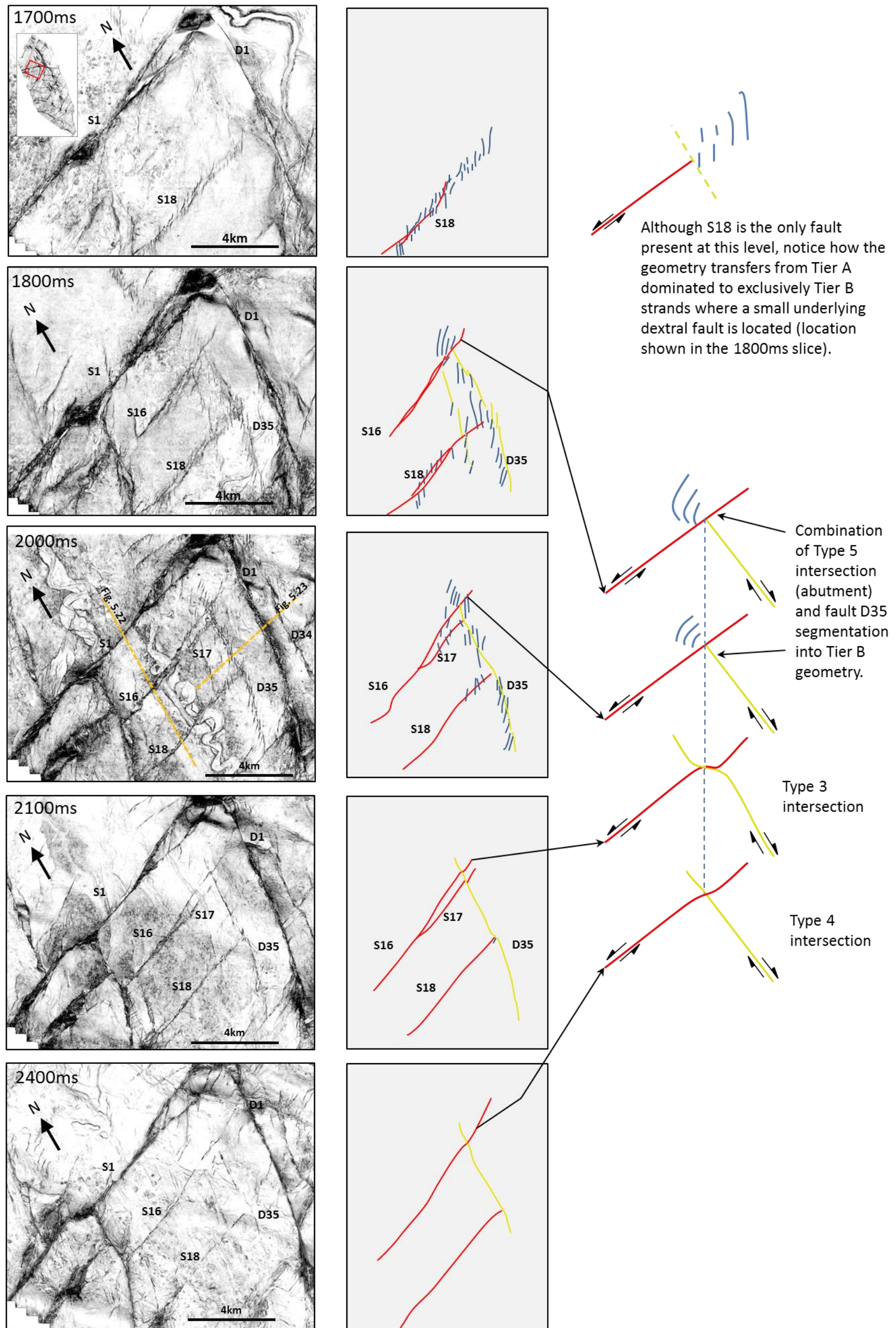
Figure 5.14 – Five coherency slices showing faults intersecting at different depths. Particular attention is drawn to the intersection between S16 and D35, which are shown in simplified line drawings on the right. These chronicle three different intersection types, which are explained in text. Note the locations for seismic lines of Figures 22 and 23 are shown in the 2000ms slice.

Figure 5.14b – Close-up of the 1800ms slice, showing how faults S1 and D1 comprise mostly Tier A strands, whilst S16, S18, and D35 show dominantly en echelon Tier B strands.  However, as illustrated in the inset, D35 shows a dominant side of the fault geometry to the northeast with Tier B strands comprising the northwest side of the underlying fault and a combination of Tier A and B strands on the northeast side.

*1700ms-* no intersection. D22 is buried and S38 and S39 appear as a single fault with overlapping segments.

*1820ms-* Type 2 intersection S38/D22. A modified Type 2 intersection for S39/D22, with sinistral offset.

*2000ms-* Type 6 intersection for S38/D22 and Type 2 intersection for S39/D22.

*2200ms-* Type 2 intersection for S38/D22 and Type 4 intersection for S39/D22.

*2320ms-* Type 2 intersection for S38/D22 with additional splay and Type 6 intersection for S39/D22.

Figure 5.15 – Five coherency slices depicting the changing intersection geometry with depth between faults S38, S39, and D22. See text for details.
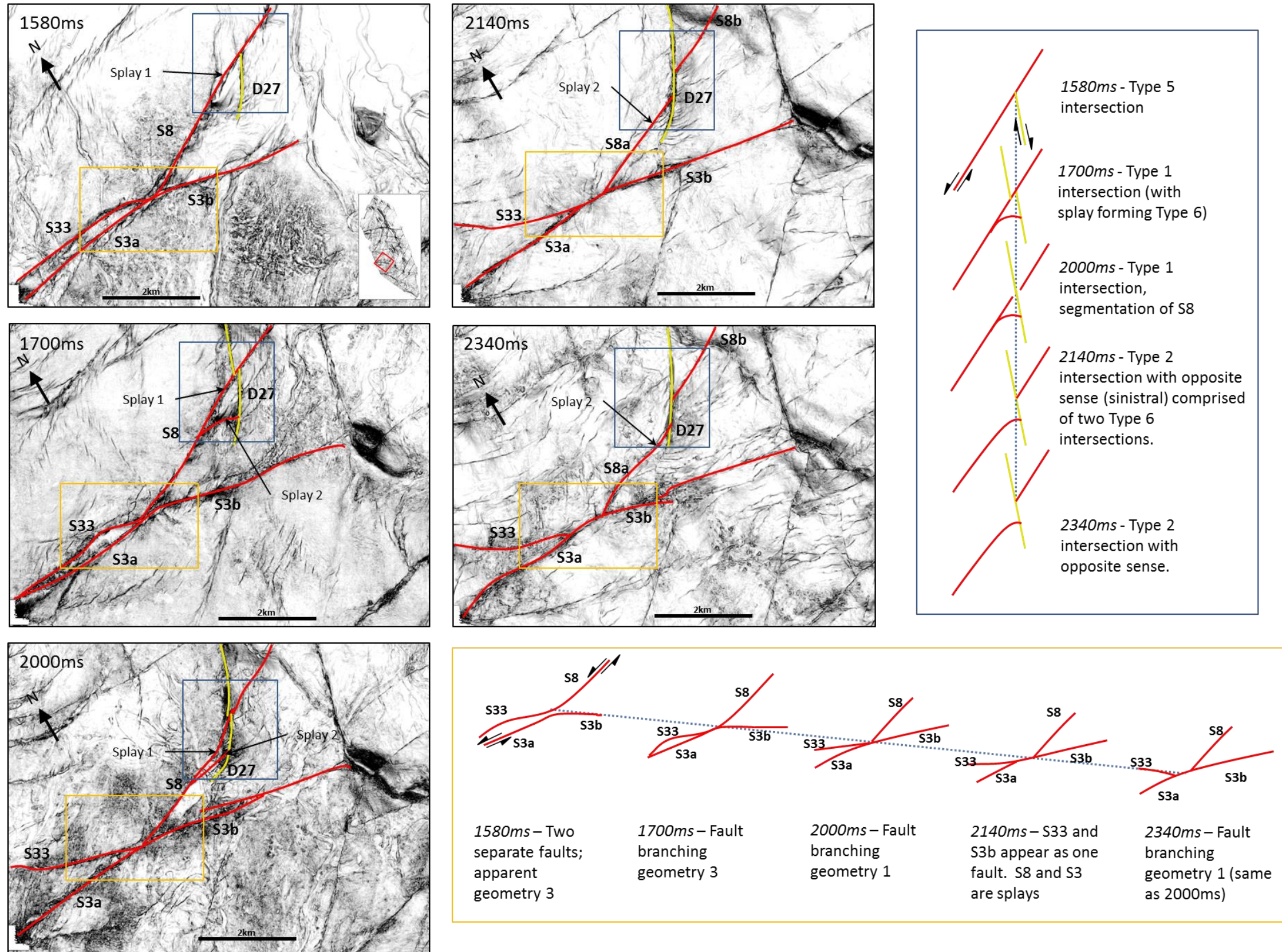
Figure 5.16 – Coherency slices depicting a conjugate intersection between S8 and D27, with line drawings shown in blue rectangle. The slices also show a branching intersection between S3, S33, and S8 with line drawing shown in orange. See text for details.
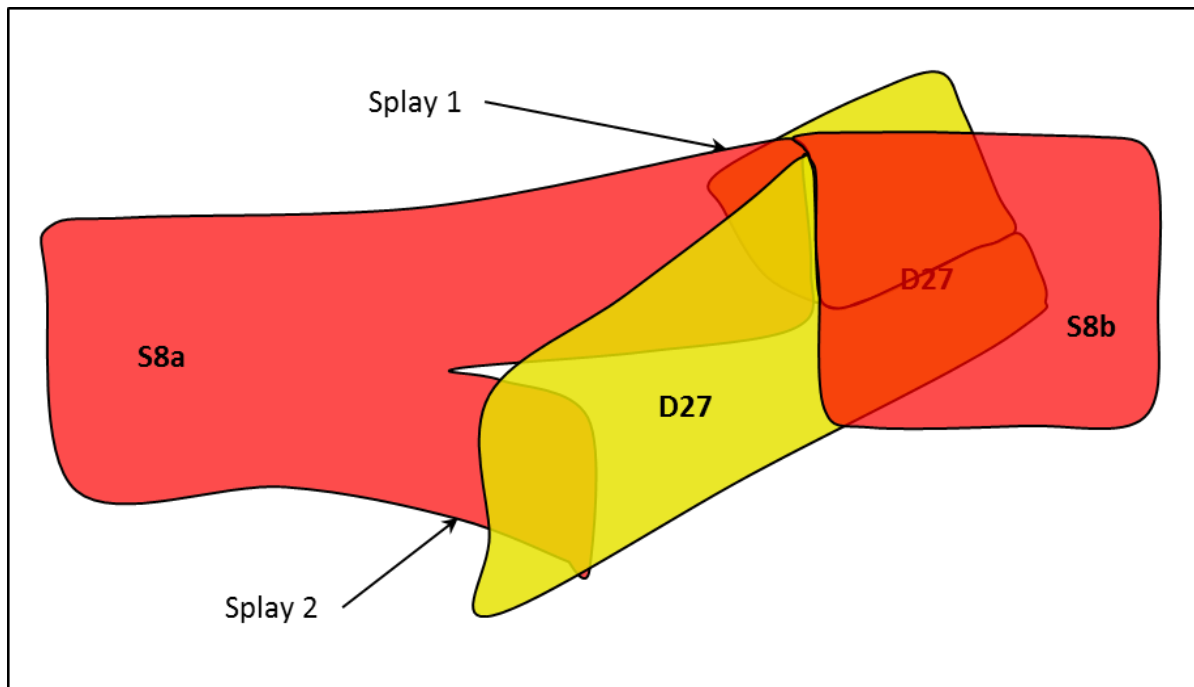
Figure 5.17 - Cartoon interpretation of the intersection between D27 and S8.
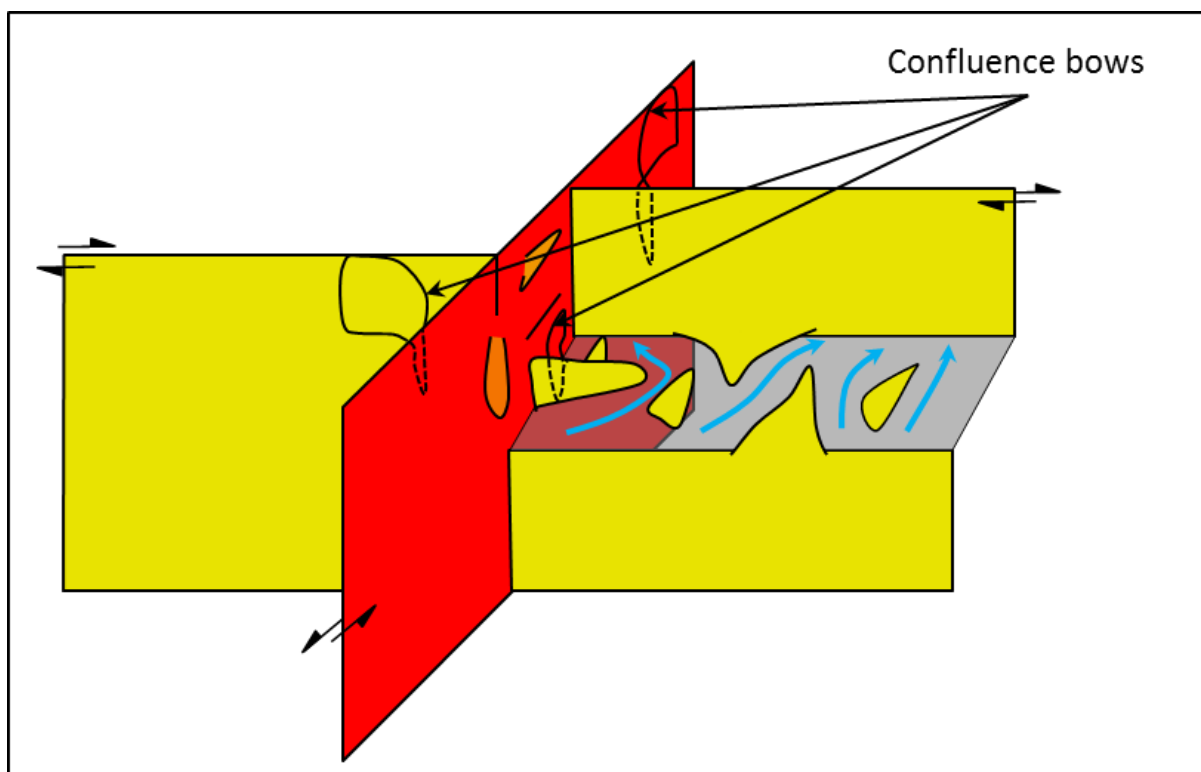


Figure 5.18 - Cartoon schematic of a complex intersection in 3D showing multiple confluence bows as well as regions where the fault plan of the dextral fault (in yellow) has been offset by the sinistral fault (red).  Blue arrows represent potential fluid flow pathways opened up by preferential movement on the upper half of the sinsistral fault. Note bottom half of faults shows a Type 4 intersection (no offset).

## 5.4   Branching Faults

Fault branching is a common phenomenon in fault propagation (e.g.McGrath and Davison, 1995; Kim et al., 2003; 2004) and seismic scale faulting is no exception.  Building upon the regional observations from section 5.2.4, there are clear changes in branching geometry, especially on the first order faults.  Based on the observed geometries, it is possible to make a preliminary interpretation over which fault segment is the original, and which is the splay (Figure 5.19).  The original fault shows a straight trace, whilst the splay fault diverges from the straight trace at angle.  This geometry has been documented in seismogenic based studies (e.g. Fliss et al., 2005; their figure 1).  However, is this geometry necessarily indicative of a splaying process?  This geometry could also be formed by another fault that has propagated in the opposite direction to intersect with the original fault (Figure 5.19, propagation model ii). The answer to this question could be answered with d-x plot analysis; however, when kinematic indicators are absent near the fault tips, this is not a viable solution.  Here, two examples of branching fault geometries are explored in 3D to investigate what information can be extracted from the intersection geometry.

*Example 1-*

The first example shows how the geometry of Fault S3 changes with depth as it branches with Fault S8 at an angle between 35° - 40°.  The time-dip map of the seabed (Figure 5.5) shows that S3 branches and its southern splay (S3b) dies out quickly with depth, whilst S8 extends for another c. 15km.  S3 and S8 therefore define a continuous fault, whilst S3b splays from it in a Type 2 geometry (Figure 5.19).  By contrast, a coherency slice c. 90m below the seabed (at 1580ms), shows a more symmetric branching and therefore resembles a Type 3 geometry (Figure 5.16).  Furthermore, the faults appear as two separate faults, with S33 and S8 as one connected fault and S3a and S3b as one fault.  This geometry continues at 1700ms; however, there is a decrease in the width between S33 and S3a.  Also at this level, S3b extends further eastwards into a complex intersection zone of strike-slip faults and thrust folds.  300m below at 200ms, there is a change to a Type 1 geometry, with S3a and S3b showing a continuous fault.  Intriguingly, both S8 and S33 clearly splay from S3.  Deeper at 2100ms, the geometry continues to change with S33 and S3b appearing as one fault, with S3a

and S33 appearing as splays.  Finally at 2340ms, the geometry returns to the Type 1 geometry observed at 2000ms.

The changing branching geometries with depth are interpreted as an expression of how the four fault segments are interconnected, and likely show which faults were more active at a particular depth.  For instance at 2000ms, the Type 1 geometry suggests that Fault S3 is a single fault and therefore slip was concentrated on these two faults, whilst 100m below at 2100ms, S33 and S3b are the single fault and therefore more slip may have occurred on these segments, obliterating the original intersection geometry.  However, this interpretation raises further questions such as what causes fault segments to switch in activity and why does this result in such a large variation at different depths?

The observations do not provide much evidence leading to the deduction of the correct propagation model, and the identification of which fault segment is the splay and which fault segment is the master, changes with depth (Figure 5.19).  However, given that Fault S1 propagates eastward, it suggests that the faults would splay from the main fault (presumably Fault S3), and propagate towards the east as well.  Furthermore, splay propagation towards the west would conflict with the regional propagation direction, and therefore seems unlikely.

*Example 2-*

The second example shows conflicting branching geometries that resemble the first example; however, the maximum displacements are larger, with both splays belonging to the 1st order (Figure 5.20).  Fault S4 branches into S5 and S4b at an angle of 20°, with S5 trending in the same direction as most of the major sinistral faults in the dataset, whilst S4b trends roughly parallel to the El Arish and Afiq Faults.  At the seabed (slice 1520ms) S4 and S5 are defined by a continuous trace that appears connected.  S4b branches off from S4, showing a Type 2 geometry (Figure 5.19).  By 1580ms (40m below) this geometry has shifted to show mutual branching or a Type 3 geometry, signifying a change in the splay kinematics in a short depth.  At 1740ms the geometry changes subtly to a combination of Type 1 and Type 3.  That is both faults seem to curve off each other, but fault S4b shows a straighter trace.  240m deeper at the 1980ms slice, the system has transitioned fully into a Type 1 geometry, and therefore has the opposite geometry at depth than at the seabed with S5 appearing to splay from S4b.  The

deepest slice (2140ms) maintains this geometry, but has the added complexity of a small splay fault connecting S5 to S4b.

The differing branching geometries of S4b and S5 are interpreted to show a changing in the dominance of one fault segment over the other with time.  The deeper geometries show S4b as the more dominant geometry with S5 splaying from it, which suggests that more slip was concentrated along S4b at depth.  Given that the larger offsets occur at depth, it is logical to expect that this was the dominant geometry earlier in the growth history.  Upwards in the stratigraphy, the geometry changes from Type 1 to Type 3, suggesting that S4b and S5 become mutually active before S5 becomes the dominant fault in a Type 2 geometry.  At the seabed S4 and S5 may act as a single coherent fault, with only limited slip on S4b as it now acts as a splay fault.  The fact that S4b is half buried at the seabed suggests that activity is only concentrated closer to the branching intersection and therefore displacement is largest here, before dying out to the southeast.  By extrapolation to the deeper levels, it may suggest that the lateral propagation direction of S4b was to the southeast; however, given the extremely variable fault kinematics observed in prior examples, this interpretation is proposed tentatively.

The branching geometries of S4b and S5 also fit into the regional setting.  If S4b was active earlier, it could be a down-dip extension or relay of a nearby fault to El Arish or Nahal-Oz fault (Figure 4.1).  The dominance of S5 at the seabed is in accordance with the majority of sinistral East – West trending faults at the seabed, suggesting that slip on these faults is still active due to salt movement towards the west from the Nile Delta.  Therefore, the uplift that triggered the salt flow down-slope in the Levant Margin likely predates the uplift in the Nile Delta.

The faulting in this area is increasingly complex as fault S4b also re-branches into S4c and S6 (Figure 5.20).  Kinematic indicators have shown that offsets across S6 are 1060m (1st order) whilst S4c is only 300m (second order) (Figure 3.4).  However, the kinematic indicator crosses S4c nearby another splay (S54, Figure 5.4), which has an offset of 450m, and may represent displacement share between both faults.  Intriguingly, despite S6 having a larger offset, it is buried at the seabed (1520ms).  At the deeper levels, the branching geometry observed is a Type 3.

The fact that S4c and S6 always maintains a Type 3 geometry, suggests that S4b branched into S4c and S6 at roughly the same time, with neither fault branch dominating the deformation. If the combined offsets S4c and S54 are factored together, then the offset of S6 is 310m greater than S4c, which although significant, means that both faults are first order, and may explain why this branch shares a far more uniform geometry through the depths. The only exception is nearer the seabed where S6 is buried; suggesting that all slip became concentrated on S4c. However, this fails to explain why the geometry does not switch to Type 2, and suggests added complexity to the region.

### 5.4.1  Branching Discussion

To summarise, branching is a notable phenomenon in this dataset, especially amongst the first order faults and are fundamentally different from the conjugate intersections for two reasons: 1) both faults show the same sense of movement, and 2) they branch at angles of 40° or less. These intersections therefore offer insight into the regional evolution as well as fault behaviour, which is discussed below.

Without the aid of kinematic indicators located near the tips of these branching faults, it is impossible to measure the displacement/length gradient and infer the direction of propagation in order to determine if the faults splayed or propagated towards each other and linked (e.g. Type 1i or 1ii, Figure 5.19). However, based on the geometries observed here, it appears more likely that these are splay faults that have branched away (bifurcated) from the intersection. Although both examples display a change from a Type 2 geometry at the seabed to a Type 1 geometry at depth, the effect is more pronounced in Example 2. This suggests that the changing stress fields from the Levant Margin to the Nile Delta affect the Central Region to a lesser extent than the Southern Region, but is still enough to trigger the branching fault geometry.

The deformation derived from the younger stress field therefore changes the fault geometry at shallow depths from deeper depths, which may suggest that fault propagation at branching intersections operates in a similar mechanism to the conjugate intersections. Thus geometries preserved at depth reflect the kinematics of upper tip propagation between segments at an earlier time, which suggests that propagation geometry at an intersection is not overprinted by a later deformation event. Ultimately, this change in geometry can significantly alter the

understanding of faulting in the area without a 3D perspective to investigate the relationships at depth.  Given that Type 1 geometries are dominant for most depth of the fault intersection in both examples, an observation from the seabed would exclude most of the fault intersection growth history, and also affect the understanding of network connectivity as a result.
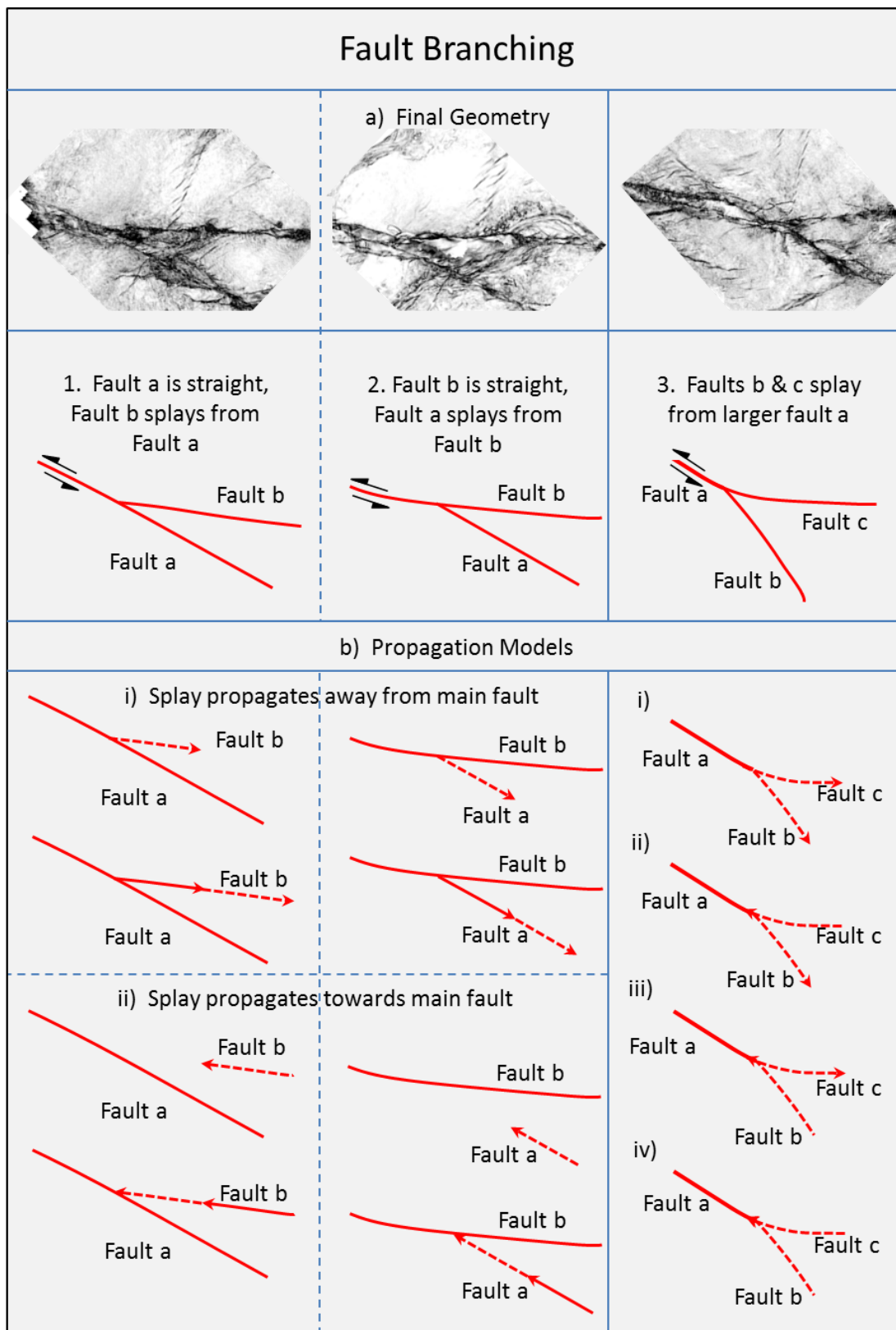
Figure 5.19 - Schematic examples of fault branching. The top 3 show examples of final geometries in the Gal C dataset, whilst the lower figures show possible propagation models to explain the final geometry. Note that

geometry 3 suggests the splays occur at the same time and hence form a more symmetric 'Y' shape.
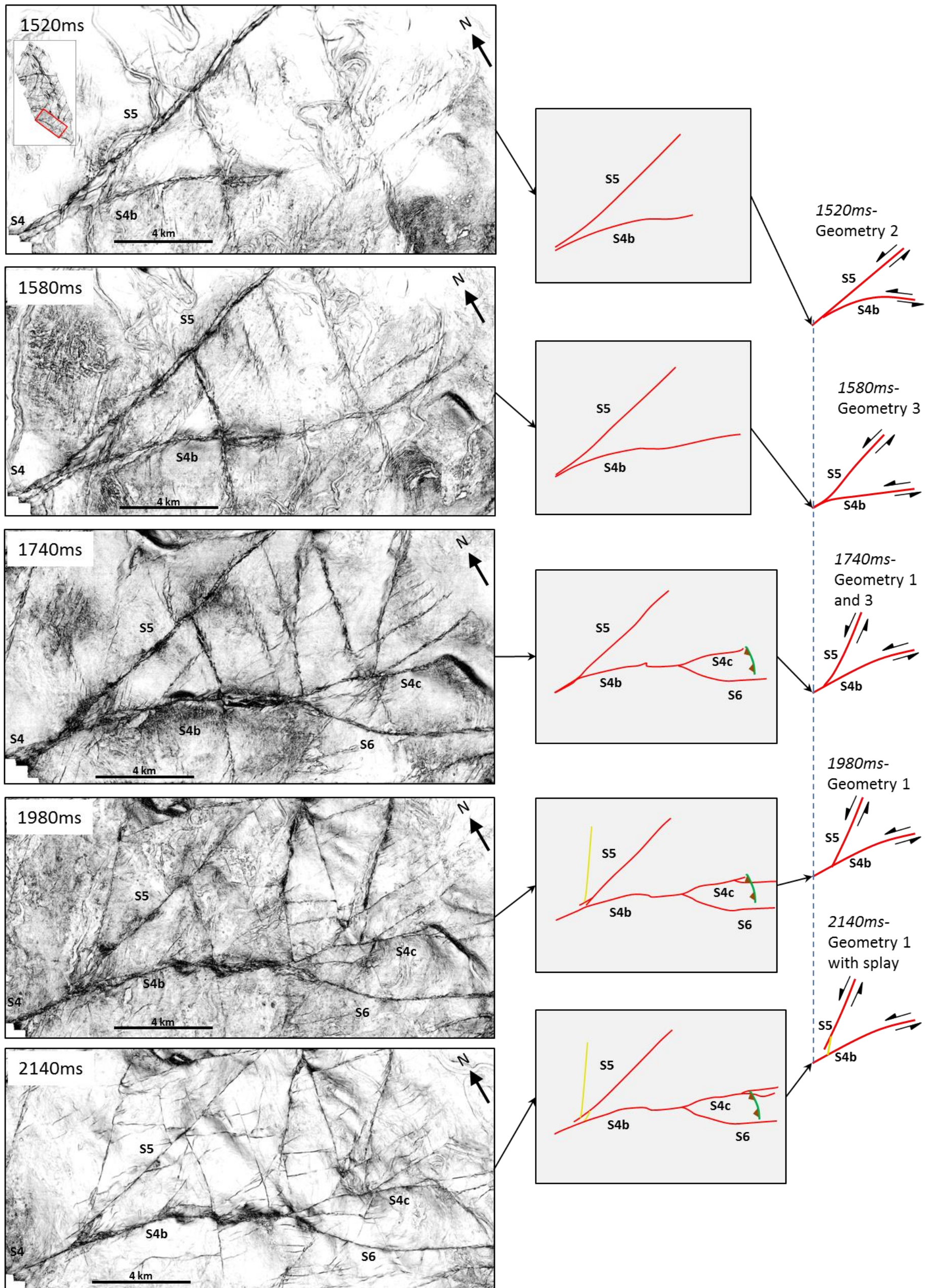
Figure 5.20 – Coherency slices detail multiple branching relationships.  The primary branch occurs between faults S5 and S4b, which are shown in simplified line drawings. The secondary branch is between S4c and S6.  Note that S4c details a potential contractional tip structure described in section 5.5.1.

## 5.5   Fault Tips

The final subject that this chapter explores is the geometry of fault tips and what propagation information can be extracted from them.  This section is divided into two parts: lateral tips and vertical tips.

### 5.5.1   Lateral Tips

Several field studies have shown how fault tip geometries can be used to determine fault sense and conditions at which a fault grew (McGrath and Davison, 1995; Kim et al., 2003; Kim et al., 2004).  Although some studies have also applied the findings to large scale faulting, they do not inspect the tips at different stratigraphic levels.  A model produced by Kim et al (2003) suggested that lateral tips were the product of mode II fractures whilst upper and lower tips were mode III fractures, with intermediate tips showing a combination of mode II and III (Chapter 1; Fig. 19).  However, it is unknown in how the geometry changes from a mode II to a mode II + III structure or a mode III to a mode II + III.  A preliminary investigation here shows that what might be interpreted as a lateral tip structure at one depth, might be interpreted differently at another depth.

*Example 1- Horsetail Faults*

Fault S13 is a first order sinistral fault with a displacement of 900m, which at 1800ms depth shows a clear horsetail geometry at its extensional quadrant (Figure 5.21).  The three faults that splay from S13 resemble geometries observed in the Afiq Fault (Chapter 4) and documented examples from the field (Kim et al, 2003; 2004).  However 200m below at 2000ms, the clear horsetail geometry is no longer observed, with faults still splaying from S13 but also intersecting with fault D45, and therefore resembling smaller third order faults that branch between S13 and D45.  Also of note, S13 intersects with D45 at this level, but does not cross it.  Interestingly, the kinematic indicator showing a 900m offset is located in close proximity with the splay faults.

The change in planform geometry between slices taken at different depths raises questions concerning the origin of splay faults.  For instance, they could have formed originally as a horsetail set of that propagated towards D45 and happen to intersect with it at depth, or they

could have formed as accommodation structures between large sinistral and dextral faults.  In the latter case, the faults might not branch with D45 due to reduced activity upwards (D45 is buried at the seabed), and activity only continued on S13 (Figure 5.5).  The large offset in close proximity to the splay faults is interesting as reduced offsets would be expected near a fault tip.  This may suggest that displacement/length gradients are very high in the GalC dataset, given that the faults must accommodate large amounts of shortening (i.e. high displacements) on relatively short lengths.  Unfortunately, kinematic indicators do not occur in both locations to test this theory on any fault.  Given the discrepancy between depths, classifying this example as a true tip structure may not be correct, and therefore it is important to consider how faults may interact at depth before classifying structures as a fault tip.

*Example 2- Contractional Tip Structures*

If Fault S4c was observed terminating abruptly at a thrust fold in coherency slice 1580ms and 1740ms (Figure 5.20) in the field, it would likely be interpreted as a tip structure forming in the contractional quadrant of the fault.  However, this geometry is not maintained at all depths.  At 1980ms, S4c branches at the location of the thrust fold, with one of the splays continuing beyond the fold for several kilometres towards the southeast.  This trend also continues at 2140ms, except both splays extend beyond the thrust fold. An interpretation of a tip structure at the shallower depths may therefore prove to be an oversimplification.

Determining what has driven the deformation in this region is not possible without dedicating a large effort aimed at analysing both the geometry and displacement distribution of the strike-slip faults and thrust folds.  However, it is worth nothing that this thrust fold is the only one observed in the Southern Region, and it naturally raises the question: why is it located here?  The answer may lie in the episodic nature of fault evolution; the thrust fold initially formed as a contractional tip structure before further slip caused Fault S4c to propagate beyond the fold.  The splay observed at deeper intervals may also represent a tip structure, since branching faults have also been documented (Kim et al., 2004; Kim and Sanderson, 2006).  However, this raises the question of why does the tip structure change with depth? Multiple reasons could explain this change in geometry: a change between mode II and mode III dominated propagation as predicted in the model by Kim et al., (2003); or a change in the regional and local stress fields with evolution.  Ultimately, it is beyond the scope of this

chapter to determine the origin of the thrust fold, and the reason for the change in tip structure; however, it is pertinent to highlight that a lateral tip structure in three dimensions may not be consistent across the height of the fault.

*Example 3- Antithetic Splay Faults*

The aim of this example is to present a set of structures that resemble the antithetic faults geometries described by Kim et al. (2003; 2004) rather than focus on three dimensional discrepancies. However, due to conflicting fault trends and geometries it is again difficult to assign a lateral tip classification. The branching of S4 into S4b and S5 shows four bisecting antithetic (dextral) faults (D10, D11/12, D13, and D14; Figure 5.1, Figure 5.4b), which deform the intervening region, and resemble a set of antithetic faults in a tip structure. Interestingly, there are actually more faults than shown in Figure 5.4b; however, these are either dextral faults with different trends (D8 and D9) or smaller sinistral faults that are bounded by the dextral faults and are not characteristic of the tip structure. Notably, D9 and D8 share the same trend as D6 and D7, respectively to the north (Figure 5.1).

A problem with classifying the damage zone between S4 and S5 as a tip structure is that it is unknown if Fault S4 continues westward beyond the dataset limits for a significant distance. Given the size of the fault, and the offsets recorded across it (2510m), it is expected that the fault would continue on the order of 10s of kilometres to form a tip damage zone of this magnitude. Unfortunately, it cannot be checked if this is the case, and given that the faults branching history likely reflects conflicting stress fields, these faults may accommodate block rotation between the two segments, even if S4 dies out in a short distance (towards the west) beyond the dataset limits. Thus classifying it as large scale tip structure may lead to incorrect assumptions over the length of S4.

The presence of other faults in this damage zone is also curious and may suggest two generations of faulting. For instance faults D9 and D8 are likely continuations faults D6 and D7 (first order faults that extend beyond dataset limits), respectively. This interpretation is based on the fact that they share the same trends as D6 and D7, despite extending through the deformed region controlled by S4 and S5. Interestingly, there are small thrust faults with associated folds that separate D9 from D6 and D7 from D8, which likely represent compressional jogs or push-up structures. Therefore D9 and D8 differ in trend from the other

dextral faults in the S4/S5 damage zone because they belong to a different fault system. Interestingly, D9 in Figure 5.4a resembles a relay fault between D10 and D11/12, and would be interpreted as such without the aid of a larger map. This relay geometry may suggest that the faults can only propagate into this region because their trend is mechanically feasible to double as a relay fault.

Fault D8 noticeably shows several sinistral, antithetic faults splaying from it (S55 – S59), which could also be interpreted as a tip structure. However, this classification is again difficult to assign when the splay faults cover most of the length of D8. If D7 and D8 are a continuous fault, then a tip structure classification is far more feasible. However, problems arise from faults S54 and S55. Firstly, S54 does not actually splay from D8, and instead splays from S4c; despite showing the same geometry as the other splay faults. Secondly, S55 crosscuts and appears to offset D8, which seems an unusual characteristic of a splay fault or tip structure. Ultimately, it is difficult to make an interpretation in favour of a tip classification or not.

*Lateral Tips Summary-*

Simple geometries in this dataset are difficult to classify without ignoring the fact the region is extremely complex. The outcome of the investigation therefore warrants future study into how tip structures evolve in complex systems. Many of the geometries observed in this dataset bear a striking resemblance to previously documented cases; however, when inspected in three dimensions or near neighbouring structures, these relationships become less clear. Which begs the question, are these features truly mode II structures and if so, why are they not observed consistently at all depths? One reason may be due to different episodes of movement, which correspond to differing interactions with neighbouring structures. These changes in interactions will alter the surrounding stress field, and may thus cause the original structures to be reactivated or abandoned.
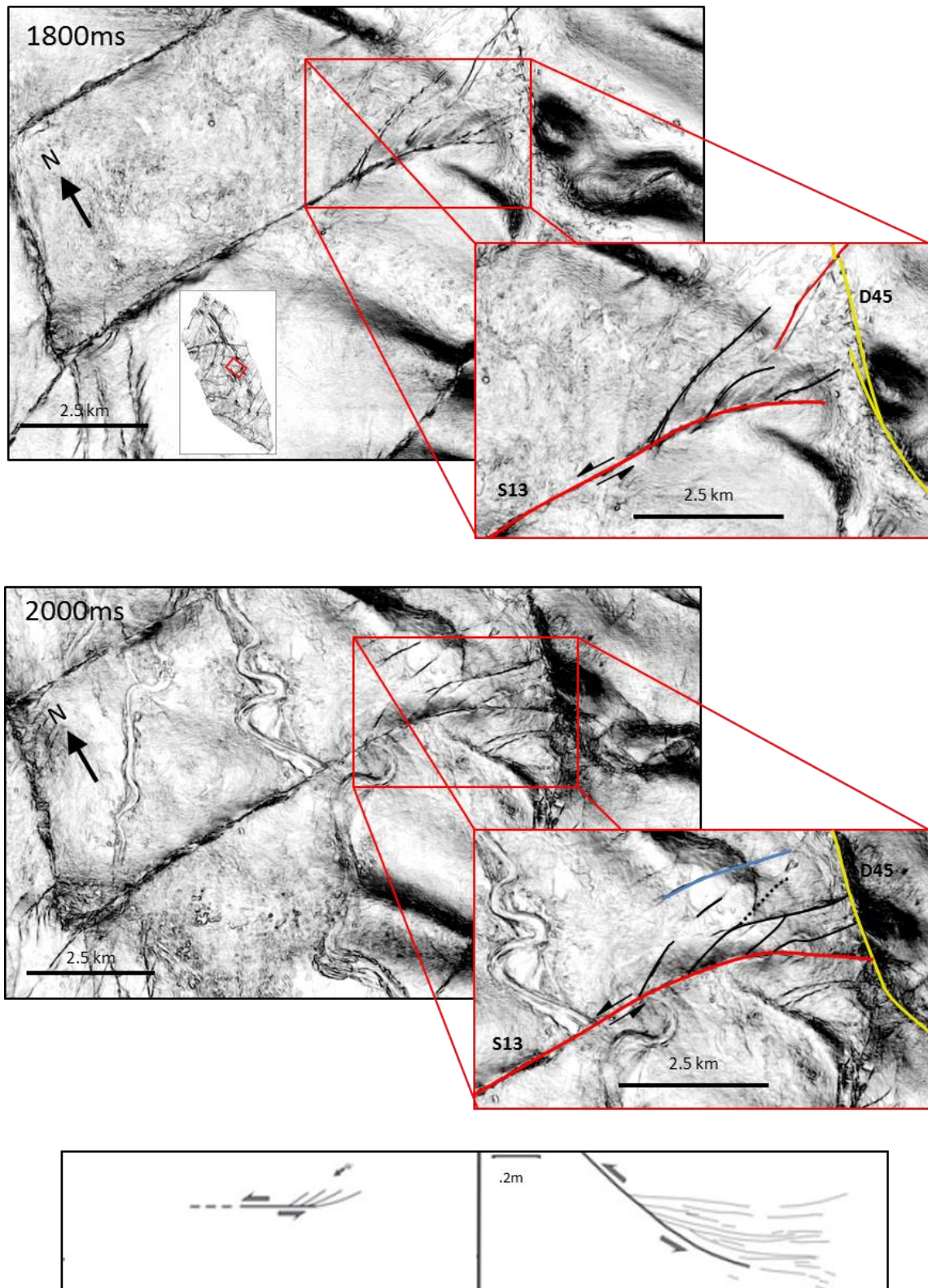
Figure 5.21 - Two slices showing deformation at the lateral tip of Fault S13. Faults in black are faults that splay directly from S13, whilst the fault in blue represents a small isolated fault. Below is a schematic example of previously documented horsetail faults from Kim & Sanderson (2006) for comparison. Note this figure has been inverted to show a sinistral fault instead of a dextral fault.

### 5.5.2 Vertical Tips

The aim of this section is to show profile sections that examine the structure of the upper and basal tips. Like the previous chapter, the basal tips in are largely speculative due to the loss of resolution in the Messinian Evaporites, and will therefore focus dominantly on the upper tips and the relationship between Tier A and Tier B geometries.

*Sinistral Faults -*

Three sinistral faults are presented to provide an overview of how the strike-slip geometry varies between faults (Figure 5.22). The basic structure (described in chapter 4) comprises the Tier A, B, and C geometries. Beginning with first order fault S1a, there is a clear Tier A strand that extends through the PM units to the seabed (height c. 850m). The Tier B geometry also outcrops at the seabed and overlaps with the Tier A strand, showing a short height (c. 250m), and forming a thin zone of deformation with the Tier A fault strand (width c. 190m). The Tier C faults show striking detachment geometries that resemble the El Arish Fault, with a height of c. 500m; however, it differs from the Afiq Fault, with the Tier A strand not extending into the evaporites.

Third order Fault S16 by contrast shows a shorter Tier A Geometry (c. 250m), which does not overlap with Tier B. The height of Tier B is also much larger (c. 450m) and splays into a much wider fault zone (c. 410m). Interestingly, the transfer from a Tier A to a Tier B geometry occurs at the boundary between units PM1 and PM2. The fault dies out early and the upper tips are buried by unit PM3. Fault S18 (also third order) shows a similar geometry to S16, with separate Tier A and Tier B strands and a wider fault zone. However, S18 extends to the seabed and shows a longer Tier A strand and shorter Tier B strands. Interestingly, the transfer in geometry occurs at an MTD, instead of the PM1/PM2 boundary. Both faults show multiple splay detachments that comprise the Tier C geometry; however, S16 appears to penetrate deeper into the evaporites (similar to S1a), whilst S18 only extends c. 200m into the evaporites. The Tier A/C transfer location differs, with S16 occurring in the salt and S18 occurring in an MTD, directly overlying the salt.

The geometries observed here share many similarities with the geometries observed in the faults from Chapter 4. Fault S1a resembles the Afiq Fault West and Nahal-Oz Fault (a Type

II fault), whilst S16 and S18 share similarities with the El Arish Fault and Afiq Fault East (a Type I fault). This is furthered in coherency slices at the seabed, which show that Fault S1a is comprised of longer Tier A segments, with occasional shorter Tier B segments, whilst S16 and S18 are comprised dominantly of en echelon sets of Tier B strands (Figure 5.14b, slices 1800ms and 2000ms). This is particularly interesting as it suggests there is a common trait between the faults of both datasets that causes two notable geometry types.

*Dextral Faults -*

Three dextral faults are also presented to serve as comparison to the sinistral faults (Figure 5.23). First order fault D1 resembles S1, and shows a Type II structure with a Tier A strand that extends to the seabed and overlaps with Tier B strands. Interestingly, the Tier B strands are poorly developed with short heights (c. 100m), and do not reach the seabed. There is also a large Tier A1 fault that splays from it; however, the sense of slip is reverse. Importantly, the Tier C strands also resemble S1, and the Tier A strand does not extend into the evaporites. Third order faults D34 and D35 by contrast show Tier A strands that branch upwards into a Tier B geometry, in a similar manner to the sinistral third order faults, and therefore show a Type I structure. Both faults change geometries at the PM1/PM2 boundary, resembling fault S16. The structure of Fault D35 is more complex due the presence of a small thrust fault originating at the same area.

The reverse movement on the Tier A1 strands is opposite to the Tier A1 strands in Chapter 4, which is likely due to the proximity of thrust folds in the region. This suggests that these fault strands may not have formed by the same sidewall rip-out mechanisms, and therefore form fundamentally different structures. The kinematics of these strands may offer insights into the effect of thrust faulting on strike-slip faults and therefore warrants future study.

*Vertical Tip Summary-*

There is a clear similarity in geometry shared by both sets of strike-slip fault that is separated by order, and by analogy, fault structure type. Due to the rotational nature of the Tier B fault strands, two profile sections taken very close to each other will show considerably different geometries (shown in Chapter 4), therefore it is expected for the faults shown here to appear differently, especially with the amount of Tier B strands present. However, this does not

account for changes in Tier A lengths and therefore the reasons for the difference between Type I and Type II faults in GalC faults is discussed in Chapter 6.
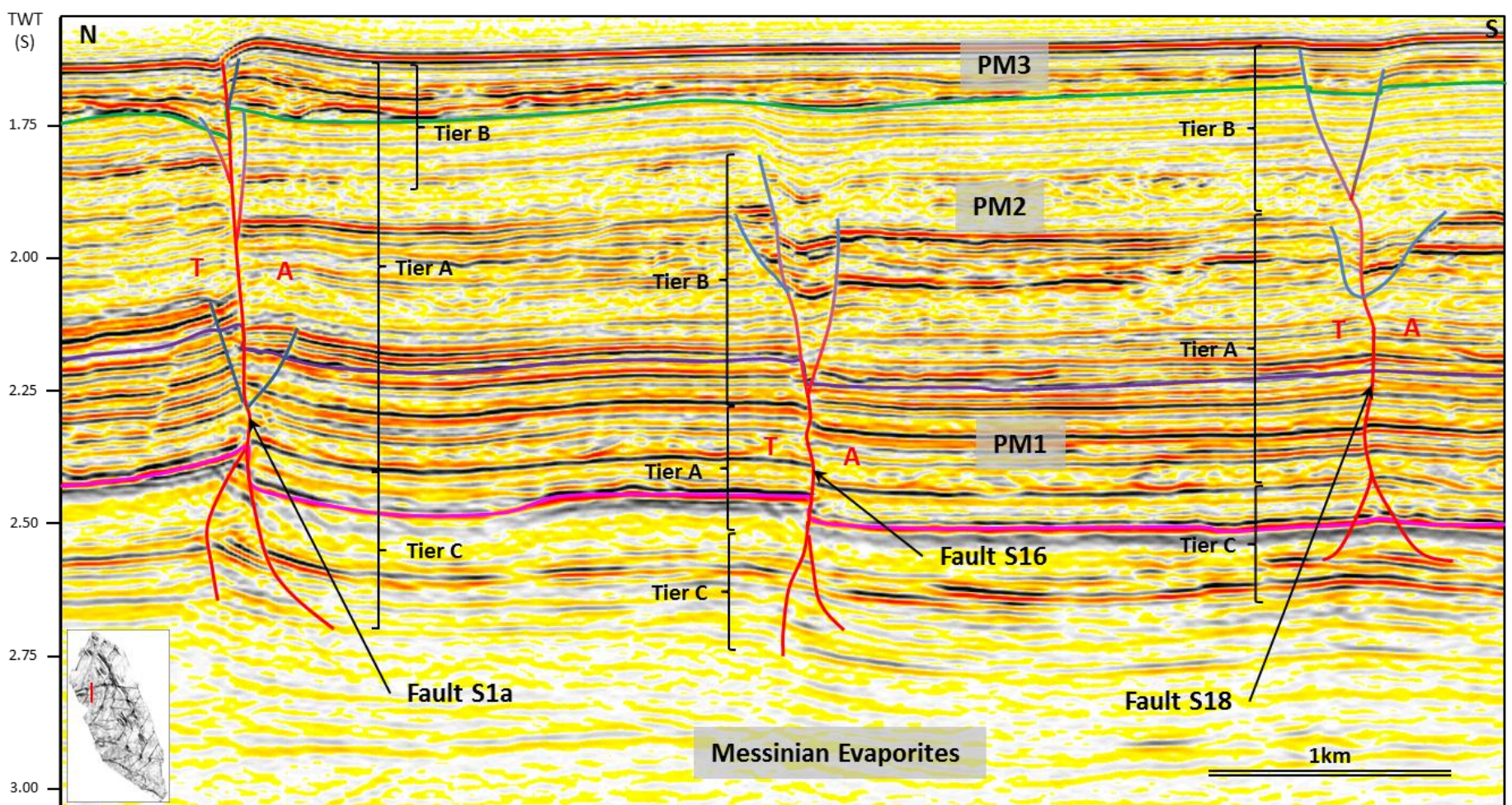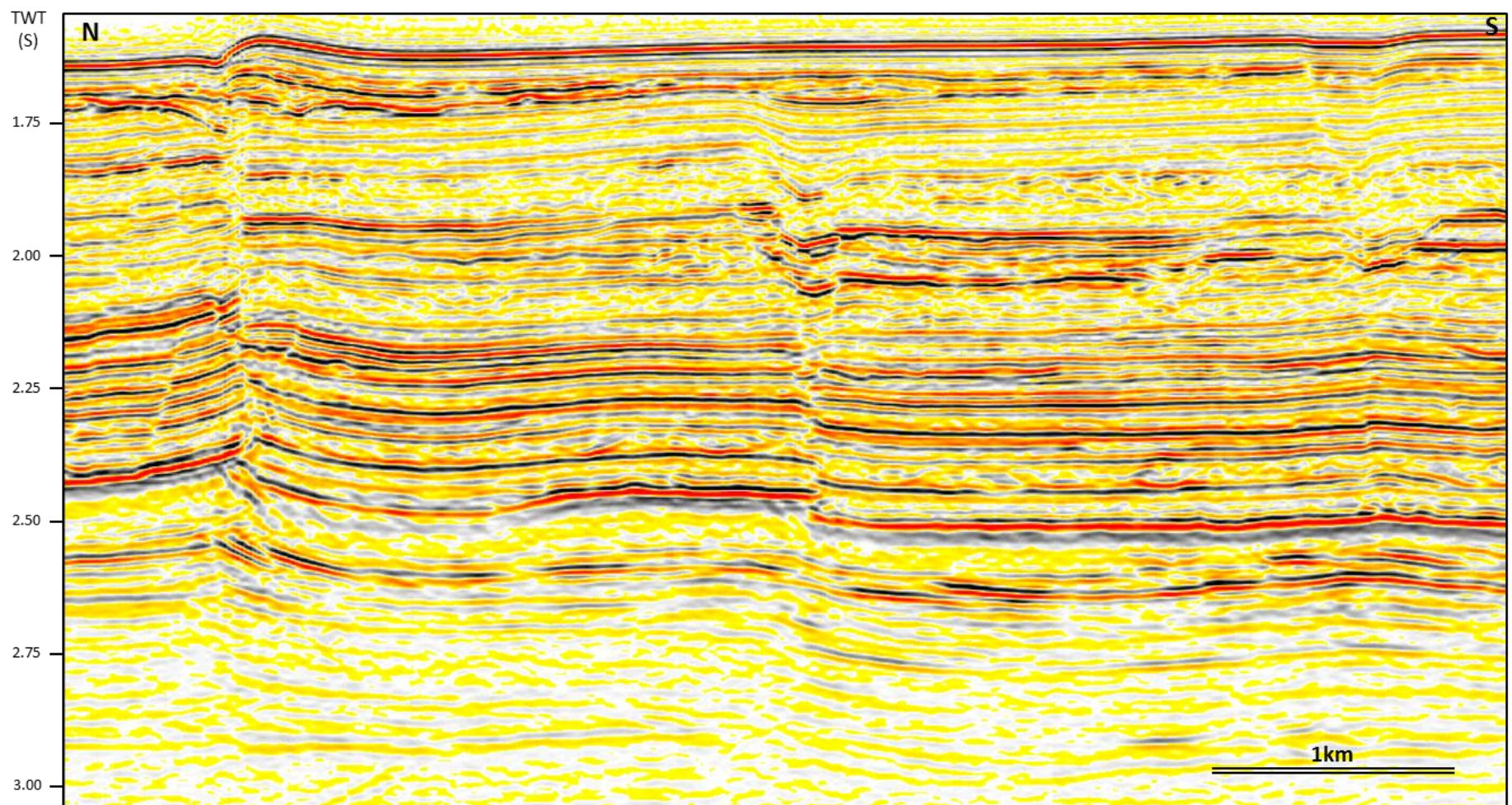
Figure 5.22 - North – South section line showing three sinistral faults of differing offset magnitude.  Fault S1a = 1st order fault (Dmax: 2250m), S16 and S18 = 3rd order faults (Dmax: 210m, 175m, respectively).  Note the difference in Tier A/B relationships between the 1st order fault and the 3rd order faults.
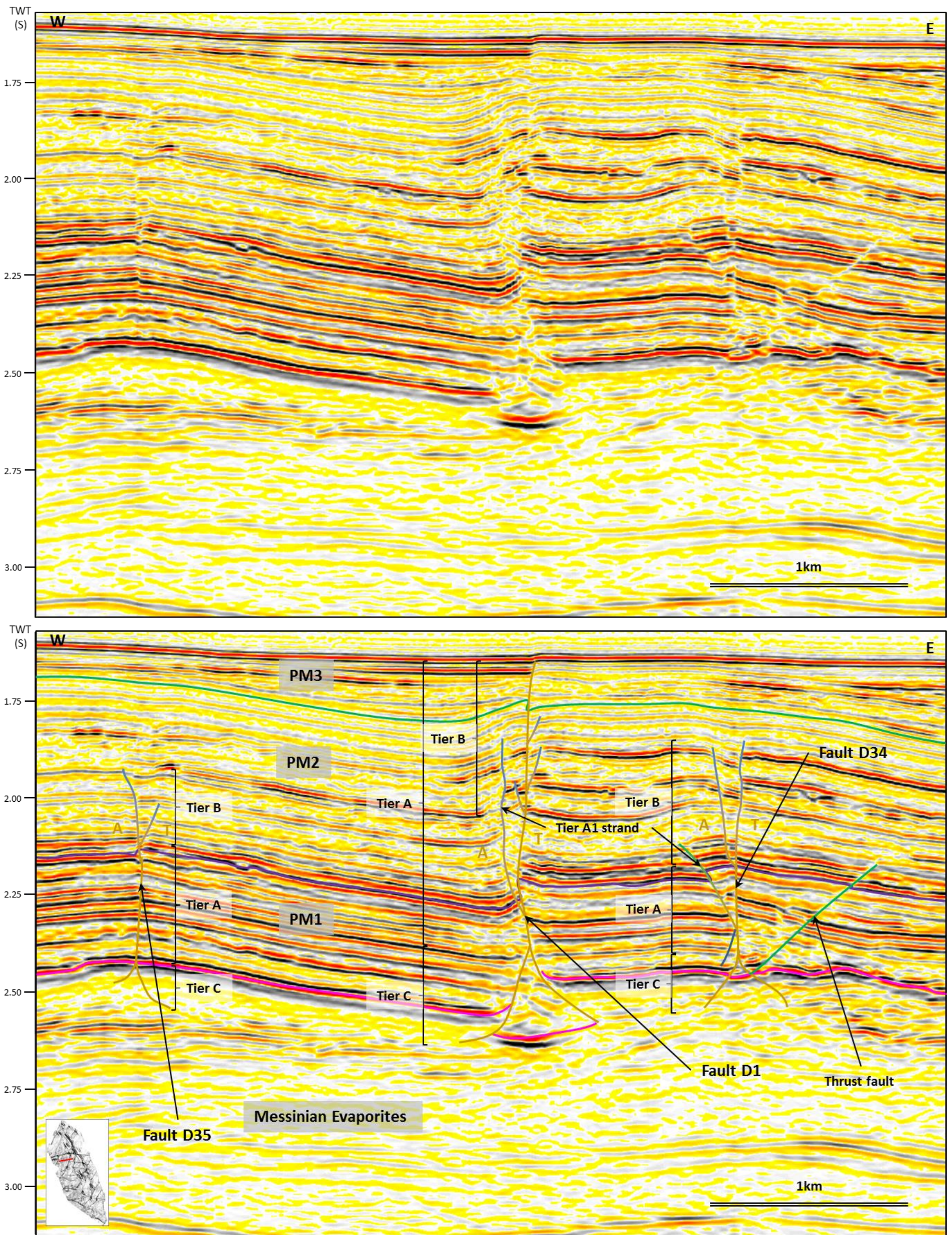
Figure 5.23 - West – East section line showing three dextral faults of differing offset magnitude (location also shown on Fig. 13). Fault D1 = 1st order fault (Dmax: 1880m), D35 = 3rd order Fault (Dmax: 130m). Fault D34 offset unknown, likely a 2nd or 3rd order fault based on geometry.

## 5.6   Summary

This chapter has explored several aspects of strike-slip faults that have never been reported before using seismic data (to our knowledge).  In particular, intersections in 3D have shown immensely complex geometries that lead to conflicting interpretations of fault growth and activity at different depths.  These complexities in intersections have never been presented before and highlight the risk associated with resource extraction and earthquakes due to the changing connectivity that likely occurs between these depths.

The same is true with intersections formed by branching faults.  The variable geometries between depths lead to conflicting interpretations over which fault was the original and which was the splay.  It is possible that when propagation concentrates on the second fault branch, the geometry of the intersection changes at the depth this occurs, which leads to different geometries as the faults propagates upwards.  However, without the aid of kinematic indicators, determining the propagation direction and timing of the branches remains largely speculative and could thus be the focus of future research.

Lateral fault tips in 3D also highlight unexpected complexities.  Even classifying a tip structure proves difficult when faults act so variably at different depths as shown in the first two examples.  The final example showed structures that resemble tip structures, but without a larger dataset and more information about the growth history, might prove an erroneous interpretation.  An erroneous interpretation can again lead to misleading information about the connectivity of a system.  For instance, in Example 1; fluid may flow from S13 into D45 through the 'horsetail faults' of S13 at depth, but without observing this geometry, an interpreter would consider S13 an isolated fault.

Vertical tips resemble the geometries observed in Chapter 4, which suggest a relationship in the mechanics driving the fault propagation upwards and downwards.  This will be explored in greater detail in the discussion (Chapter 6).

# Chapter 6

# Discussion

# 6  Discussion

## 6.1  Introduction

The principal aim of this chapter is to summarise and explore the results from the three core chapters (3, 4, and 5) in greater detail.  Principally, this chapter will investigate relationships and discrepancies between the strike-slip faults of the Levant A and GalC datasets, in geometry, displacement distribution, and nucleation.  The second part of the discussion will compare these geometries to established models from analogue studies and explore the differences that exist.  Finally the discussion concludes with a short section detailing where future work on strike-slip faults can be directed, in order to better develop our understanding of strike-slip fault propagation and evolution.

## 6.2  Chapter Summaries

The thesis began with a brief review that encompasses the work completed on strike-slip faults thus far.  This was separated into studies comprising field work and analogue studies as well as included a section on normal faults, which details where work on strike-slip fault is lacking.  It was concluded that 3D visualisation of strike-slip faults was notably lacking on naturally occurring examples, and our knowledge is therefore derived from the analogue studies.  The same is true for displacement distribution.  Several studies have investigated how displacement gradient changes along strike in field studies (e.g. Peacock, 1991; Nixon et al., 2011), but none have been able to apply this information apply into a contoured 3D displacement distribution plot, in order to understand the vertical propagation of a strike-slip fault.  The core chapters were therefore established to target these deficiencies in the understanding of strike-slip faults.

### 6.2.1  Chapter 3

Chapter 3 introduced a technique using seismic attributes to produce plan view images of strike-slip faults at several stratigraphic levels in the GalC datatset.  This was completed

using horizon based attributes (such as time-dip, amplitude, and RMS amplitude) and horizontal attributes (such as coherency). Together, these attributes revealed two classes of kinematic indicators: stratigraphic and structural. Stratigraphic indicators encompassed offset submarine channels and Mass Transport Deposits (MTDs) whilst structural indicators included the systematic offset of older, pre-existing structures such as older strike-slip faults and normal faults. This chapter also explored the potential to use kinematic indicators to better evaluate how fault networks interacted and how offset varied along strike. The same methodology was also applied at different depths to produce a 3D understanding of displacement distribution on strike-slip faults. Finally, the chapter explored how kinematic indicators, may also show indications of being a syn-kinematic feature, which would allow the timing of faulting to be identified.

### 6.2.2  Chapter 4

Chapter 4 used the Levant A dataset to study two faults of contrasting displacements: The El Arish Fault (low displacement) and the Afiq Fault (high displacement). A detailed geometric description of each was produced in conjunction with a 3D displacement distribution plot to examine how these faults propagated vertically and laterally. The upward propagation of a naturally occurring strike-slip fault has never before been inspected holistically and the faults were thusly divided by geometry of the fault in cross-section into 3 Tiers: A, B and C, in order to better examine this propagation. Particular attention was directed towards the upwards propagation, which characterised the transition from Tier A, defined by a discrete, simple, and vertical through-going strand, to Tier B, which changed to steeply dipping strands that splayed upwards. Tier B strands were oriented at a low angle to the underlying Tier A strand at the base and rotated upwards in an anti-clockwise motion to be oriented at a high angle at to the Tier A strand at the upper tips. It was determined that slip changed from being dominantly strike-slip at the Tier A strand to become dominantly dip-slip at the upper tip of Tier B. A similar transition has been tentatively interpreted downwards from Tier A to Tier C, which showed a splaying of fault strands into the Messinian Evaporites; however, this is purely speculative due to the low seismic resolution and the 3D nature and displacement could not be inspected further.

There was a distinct difference in geometry between the two faults with low displacement El Arish Fault showing a discrete change between the Tier A strands and the Tier B and C strands, which displayed a wide Y shape at the upper half of the fault (in profile section) and an upside down Y shape at the lower half of the fault. This was classified as a Type I structure. The high displacement Afiq Fault showed a Tier A strand that extended the entire height of the fault, with Tiers B and C, splaying from it at the upper and basal tips, respectively. These formed a Y shape at the upper half that was much thinner and asymmetric, and was classified as a Type II structure. The Afiq Fault was especially complex as its geometry changed beyond a splay point, with each splay forming a Type I structure. It was determined that a Type I structure resulted from low strain rates, and mostly blind propagation; whilst Type II structures resulted from high strain rates, and likely underwent an early stage of blind propagation before propagating as a syn-kinematic fault.

### 6.2.3   Chapter 5

Chapter 5 returned to the GalC dataset to examine fault intersections in 3D and first examined the general characteristics, displacement and length relationships, regional relationships, and timing of strike-slip faults. The collated data was primarily used to investigate 1) conjugate relationships, 2) fault branching, and 3) tip structures. It was determined that both 1) and 2) formed very complex intersections in 3D that could not be truly interpreted without more time and displacement information. Similarly lateral tip structures were revealed to often be products of upward splaying, and therefore imaged vertical tips instead. This chapter thus alludes to how complex structures are in nature and in 3D, and therefore serves as a warning that an oversimplification could lead to errors in interpretation of the connectivity between faults, which could affect both earthquake models and precious resource extraction.

## 6.3   Type I and Type II structures in GalC

Chapter 5 established that the same basic strike-slip fault Tier structure applies to both GalC and Levant A datasets; however, it was worth inspecting if the same factors that controlled propagation and geometry type in Chapter 4 also apply to the GalC faults. The faults can be similarly grouped into Type I and Type II structures (defined in section 4.8) (Table 1) based on the amount of displacement: $3^{rd}$ order faults (displacement less than 200m) show a Type I

structure whilst 1$^{st}$ order faults (displacement greater than 700m)  show Type II structures. 2$^{nd}$ order faults (displacement between 200m and 700m) showed a more variable geometry and could be either Type I or Type II structures.  In Chapter 4, it was asserted that displacement magnitude alone does not determine the fault geometry but instead a combination of strain rate and propagation condition (i.e blind or syn-kinematic).  It is proposed here that the geometry Type I and II structures in GalC are also controlled by the same factors (although individual factors may have affected the faults differently).

It was suggested in Chapter 5 that some of the largest 1$^{st}$ order faults (with displacements greater than 1800m) may pre-date the rest as master faults, whilst the remaining GalC faults act as accommodation structures.  If this is the case, then it is difficult to determine if 1$^{st}$ order faults have been undergone high strain rates whilst 3$^{rd}$ order faults propagated under low strain rate conditions.  However, given that salt movement down-dip is argued to have occurred later in the Nile Delta than the Levant Margin (see Chapter 5), then the faults in GalC have likely evolved in a relatively shorter timeframe than those from Chapter 4, which are still active.  Therefore it is conceivable that despite a later initiation, the 1$^{st}$ order GalC faults may have been subjected to similar high strain rates as the Afiq Fault.   Given that the larger faults in GalC control most of the deformation, they must accommodate the majority of the salt driven shortening, and therefore smaller displacement, 3$^{rd}$ order faults are likely to undergo low strain rates as accommodation structure, thus forming Type I structures as observed in Chapter 4.

The effect of lithology and sedimentation on fault geometry is less clear in GalC than in Chapter 4, with the transfer from a Tier A to Tier B geometry not always occurring in an MTD in the case of a Type I fault.  Interestingly, this transfer occurs on several of the faults at PM1/PM2 boundary (e.g. S16, D34, and D35), whilst only S18 changes geometry at an MTD (Figure 5.22 and Figure 5.23).  The reflections at the top of PM1 and base of PM2 do not show any obvious or significant change in impedance response, suggesting that the units have a similar lithology and are thus unlikely to cause the splaying.  Another possibility is that the top of PM1 represents a palaeo-seabed and therefore the change occurs due to a change from blind to syn-kinematic propagation (representing a pause in fault growth). However, the fact that growth strata from S1 is largely located in PM2 and PM3, suggests that these faults did not become emergent until after sedimentation of PM2 had begun.  Thus

it is unclear what drives the splaying outside of strain rate, unless the unconformity between the two units is enough of a mechanical boundary to drive the change in geometry, without being thick enough to produce a notable change in seismic response.

A final point on lithologic control is that it may also be attributed to the nature of the sediment consolidation.   Towards the seabed, it is expected that the sediments will be less consolidated, and thus would represent a change in the cohesive nature, which could induce splaying effects (Le Gourroue and Cobbold, 2006).  However, this would likely only occur towards the top of the overburden (such as Unit 3a in the Levant A dataset), which is situated above the transition from Tier A to Tier B geometry.  Thus it may cause more Tier B splaying but is unlikely to be a control on the Tier A/B change in geometry.

Type II structures offer less insight into upward propagation controls due to the Tier A strand extending to the seabed.  However, there are noticeable splays that occur on the faults before overlapping with the Tier B splays (Figure 5.22, Figure 5.23).  The presence of these splays is unknown as they are not well imaged on the coherency, which therefore prohibits any form of 3D visualisation.  One possibility is that they are the smaller Tier A1 strands and represents small, localised sidewall rip-outs (Swanson, 1989); however, multiple splays occur above each other on the same fault side, which seems an unlikely feature of a rip-out structure.  This is because the original rip-out could simply continue to propagate instead of forming multiple strands up-section, forming the large strands observed on the Afiq Fault.  Another possibility is that they are abandoned Tier B strands, which initially grew during syn-kinematic propagation, before continued strike-slip offset under high strain rate condition made it unfavourable for the Tier B strand to propagate.  Unfortunately, without more evidence, neither of these theories can be argued with much credence, and thus represents an interesting line of future work on the upward propagation of strike-slip faults.

*Summary-*

Ultimately, it is interpreted that strain rate likely plays the most important factor in the final fault geometry in GalC in the same way as the Levant A faults.  Whilst the transition from blind to syn-kinematic propagation likely plays an important role as well, the GalC faults do not offer an immediate insight without conducting a thorough inspection on an individual fault basis in this dataset, which is beyond the scope of this thesis.  Similarly, whilst Type I

faults often splay at MTDs, it is not always the case, and there are clearly other lithologic controls that should be explored in future studies.

Table 1 - Outline of the differences in fault characteristics between Type I and Type II faults.

| Fault Characteristics Table | | |
|---|---|---|
| Fault | Type I | Type II |
| Displacement | Low | High |
| Structure | Discrete Tiers | Overlapping Tiers |
| Upper Tip Expression | High angle Tier B strands | Tier A strand and high angle Tier B strands |
| Cross-section Geometry | Y | Y |
| Examples | El Arish Fault, Afiq Fault North and East, 3rd order GalC faults | Afiq Fault West, Nahal-Oz Fault, 1st order GalC faults |
| Strain Rate | Low | High |

## 6.4   Tier C Faults

Tier C faults have already been examined extensively in Chapter 4, and therefore this section aims to briefly draw comparisons between the Tier C fault geometries in the Levant A and GalC and also question how the  slip sense and displacement of the Tier C faults is distributed.

*A comparison between Levant A and GalC-*

A comparison between the geometry of Tier C strands in Type I and Type II faults was previously conducted in Section 4.10.  However, in the Levant A and GalC areas, none of the 1$^{st}$ order faults (Type II structures) show a Tier A fault strand extending into the evaporites. This is in contrast to the Afiq Fault, which suggests a fundamental difference in its evolution. It was previously suggested that due to its location at the canyon confluence margin, it was possible that the Afiq Fault has re-activated a fossil fracture or fault, which may have provided a preferential weakness for the fault to propagate straight through the evaporites (where it would normally be inhibited or deflected from vertical in the case of Tier C strands).  Given that no other fault shows this geometry nor is located at a canyon margin, it is considered likely that the Afiq Fault has exploited a pre-existing discontinuity.

*Slip Sense-*

Chapter 4 established that the geometry of Tier C strands resembles thrust faulting, which by analogy, applies to the faults from GalC.  However, is it possible that slip sense also resembles thrust faults towards the basal tips of the Tier C strand?  The effect appears more pronounced in Type II faults, where the evaporites more often show a vertical separation, and it may be reasonable to expect that at least part of the vertical separation is due to a dip-slip component.  Given that the slip sense of Tier B strands transfers from dominantly strike-slip at the Tier A/B node to normal-slip at the upper tips, it is conceivable a similar change in strike-slip to dip-slip occurs on the Tier C strands.  However, the mechanism that causes this is likely quite different.  For instance, it may be driven by slip or movement of the overburden creating a small accommodation space at the fault plane that may allow for a passive diapiring of the salt (Figure 6.1).  Here salt preferentially flows up towards the fault plane and may also form zones of weakness for the fault to propagate downwards.  The final

geometry and sense of movement on Tier C strands therefore becomes thrusting at the basal tips, which becomes gradually re-oriented to strike-slip motion as it gets closer to the Tier A strand (where the majority of strike-slip motion occurs, Figure 6.1c).  Given the flow-like properties of salt (Jackson and Talbot, 1986; Jackson and Vendeville, 1994), the fault zone may change to a thicker, more ductile shear zone as well; however, this is difficult to surmise with the given data (Figure 6.2).

The degree of strike-slip displacement in the evaporites poses an interesting question.  For instance, it was shown in the Chapter 4 that the displacement decreases from $D_{max}$ to the M horizon, and eventually decreases to zero either within the evaporites or deeper; however, does the reduction of strike-slip displacement follow the same gradient as in the overburden? It is possible that the displacement may also be hindered in the evaporites and therefore reduces at the M horizon (case 2, Figure 6.2b).
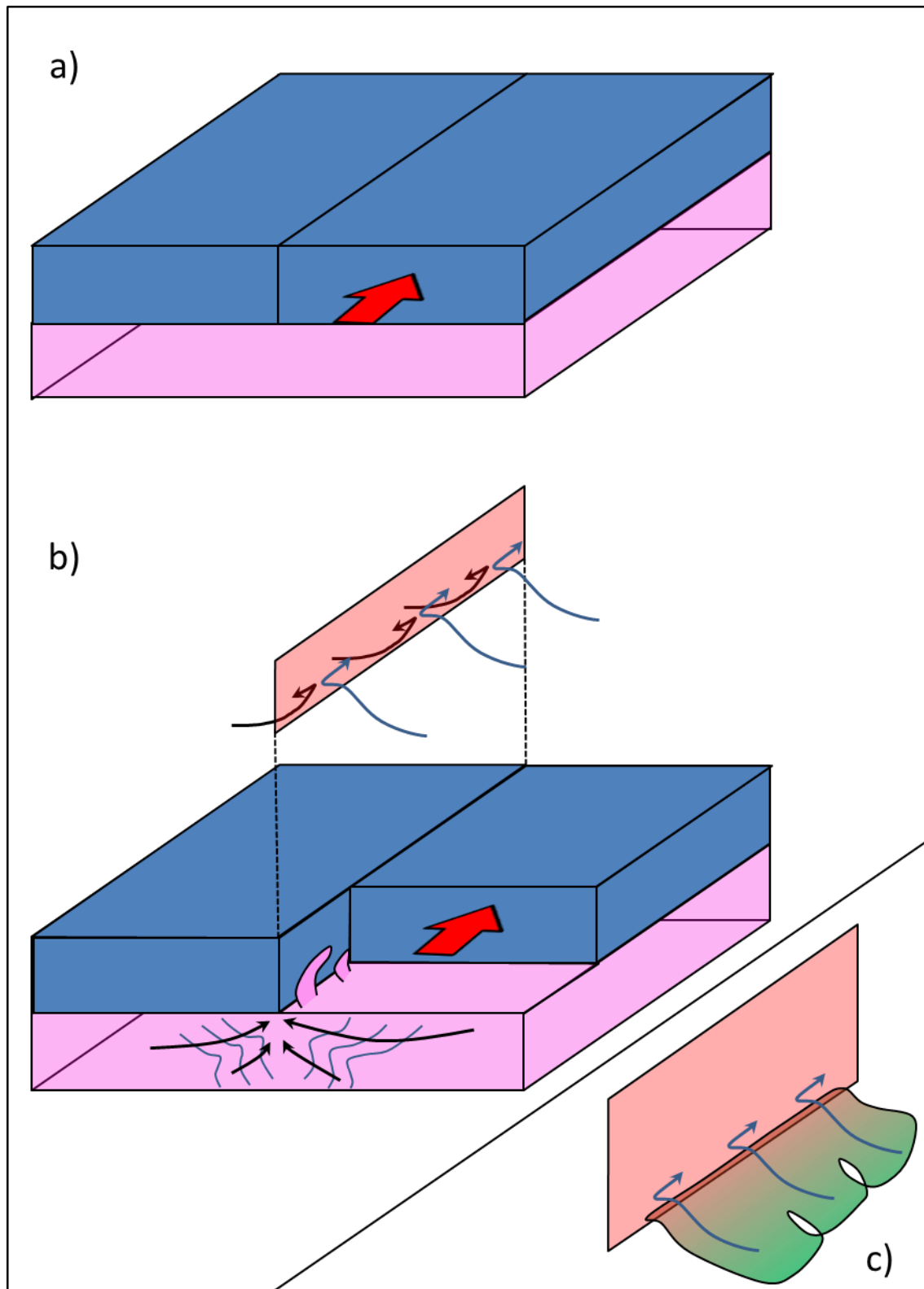
Figure 6.1 - Theoretical model showing how the offset of the overburden allow salt to rise upwards towards the fault zone, and form zones for Tier C shear zones.   This model predicts that the basal tips of the Tier C would be dominantly reverse-slip, and would gradually re-orient to strike-slip motion with proximity to the Tier A strand.
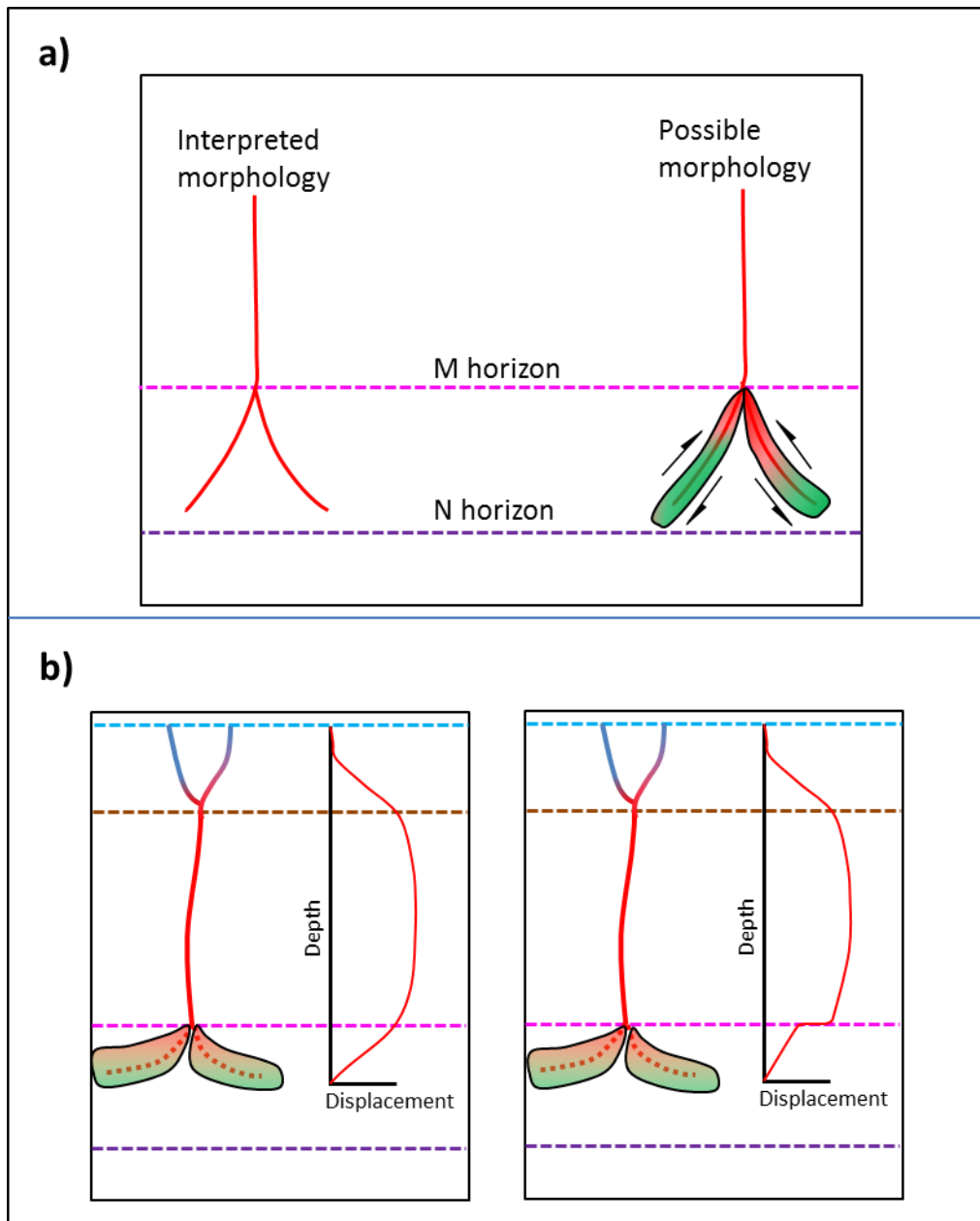
Figure 6.2 – A) A proposed morphology of the Tier C shear zones shows a Tier A fault strand changes to a more ductile style of deformation in response to salt flow upwards. B) This figure asks how displacement is distributed within as the fault changes into a  shear zone within the salt.  For instance, does displacement decrease uniformly or is there a discrete change?

## 6.5   Fault Nucleation

Before considering how a fault nucleates, it is worth contrasting how the vertical displacement distribution of the El Arish and Afiq Faults differ from the GalC faults. The principal difference is the location of the $D_{max}$ region, which in the Chapter 4 faults, is located in the overburden c. 200m – 400 m above the M horizon (Fig. 4.53), and shows a variable displacement within the region. The $D_{max}$ from Chapter 5 faults define a larger region that encompasses the M horizon, PM1, and most of PM2, which spans c. 400m in the case of fault S1 (Figure 5.6, Figure 6.3).

Most faults are thought to initiate in their propagation at the $D_{max}$ position (Rippon, 1984; Barnett, 1987; Walsh and Watterson, 1987); however, is this a logical assumption for the strike-slip faults in this thesis? Given that these faults have deformed by the flow of salt down-slope, a logical location for fault initiation could also be the M horizon because this represents the greatest mechanical contrast in the succession (Figure 6.4). However, given the differences in the $D_{max}$ locations between datasets, three possible situations are reviewed to explore which nucleation point seems most feasible: 1) the faults nucleate at one single location in the overburden (c. 200m above the M horizon), 2) the faults nucleate at the M horizon, and 3) the faults nucleate at different locations (Figure 6.4).

Situation 1 assumes that a fault nucleates at $D_{max}$ and propagates radially outward, in the classical isolated model (Rippon, 1984; Watterson, 1986; Barnett, 1987). Applying this to the faults from Chapter 4 suggests they initiated in the overburden. The large $D_{max}$ region for the GalC faults, however, suggests that the fault could have nucleated anywhere within the region, and therefore could propagate from either the overburden or the M horizon. However, if both faults nucleate in the same manner, then the GalC faults would nucleate in the overburden at a similar depth, before propagating radially outward. If this is the case, the larger $D_{max}$ region of the GalC faults may seem unusual, and could be explained by displacement accruing more uniformly, which in turn may suggest that displacement has accrued more quickly across the GalC faults.

In order for situation 2 to be feasible, it must assume that the Chapter 4 faults accrue displacement in a non-radial fashion between the $D_{max}$ and the nucleation point at the M horizon. However, this does not necessarily imply that displacement does not accrue radially

upwards from the $D_{max}$. The GalC faults, by contrast, could have nucleated at the top of the evaporites before propagating radially away, with the Tier A strand accruing most of the displacement equally to produce the large $D_{max}$ region. Notably, there are large data gaps in the kinematic indicators, and therefore, it is possible that internal variation occurs within the $D_{max}$ region that has not been documented.

Situation 3 suggests that the Chapter 4 and GalC faults have initiated from different nucleation locations. Thus, the GalC faults have nucleated at M horizon (as in situation 2); whilst, the Chapter 4 faults have propagated from the $D_{max}$ location in the overburden (as in situation 1).

The conflicting displacement distributions present a complex problem with little evidence in favour of either situation. However, logic suggests that the overburden must begin being deformed when the salt flows faster on side of the fault relative to the other. Therefore, the faults should form at the M horizon (situation 2), signifying that an element of non-radial propagation has occurred on the El Arish and Afiq Faults. Explaining why or how the non-radial propagation occurs proves problematic. However, it may be linked to a preferential zone of slip in the overburden, such as a more cohesive unit overlying an MTD. Furthermore, at the M horizon, the evaporites may deform in a more ductile manner, leading to folding and increased drag, and decreasing the measurable offset of a kinematic indicator as a result (Figure 6.5).

A caveat in this theory follows: why is the same phenomenon not observed at the GalC faults? One possibility is that there was no preferential slip in the overburden units, or that the increased strain rates on the Type II GalC faults results in less ductile slip at the M horizon, meaning that the theoretical situation from Figure 6.5 does not occur. It is also possible that due to gaps in the GalC kinematic indicators, internal variation within the $D_{max}$ region has not been documented.

A second caveat pertains to the Type I structures that change to the Tier C geometry above the M horizon. It seems unlikely that these faults nucleated in a Tier C geometry, given that most of the strike-slip deformation is represented by the Tier A strand, and as strike-slip faults, their initiation must have been due to horizontal slip. Furthermore, the splaying into a Tier C geometry has been interpreted as a change into a basal tip structure, which therefore

indicates that nucleation of these faults, must have occurred above the M horizon in the M horizon.  However, splaying above the salt has only been observed in some Type I faults, and may suggest that whilst Type II faults (and some Type I faults) have nucleated at the M horizon in response to salt flow down-slope, Type I faults that have nucleated in the overburden to accommodate deformation caused by the salt driven strike-slip faults.

*Summary-*

Evidence for either situation is lacking; however, situation 3 (nucleation at various locations) appears the most logical given that the driving mechanism for faulting is the salt flow down-slope for Type II structures, and some Type I structures, whilst other Type I structures have formed in the overburden as accommodation structures.  It is also possible that the faults from both datasets nucleate at the M horizon and both propagated non-radially upwards into the overburden, before faster displacement increases in GalC faults cause the $D_{max}$ region to distribute more evenly.
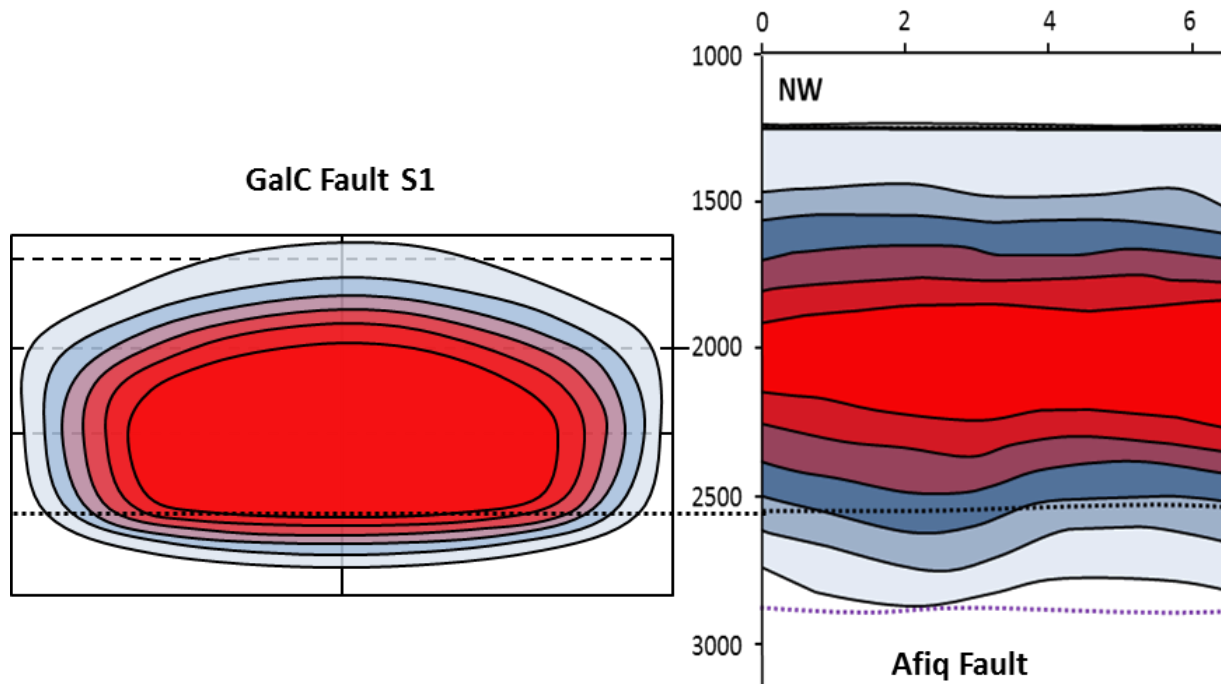
Figure 6.3 - Comparison of the vertical $D_{max}$ region of Fault S1 and the Afiq Fault (centre contour in red). The lateral tips should be ignored for the purpose of this figure, with the comparison showing relative positions and thickness of the $D_{max}$ regions on a Two-Way Time (TWT) vertical scale. S1 shows a much thicker $D_{max}$ region, despite a shorter fault plane, meaning it features a larger displacement/length (d-x) gradient. Black dotted line = M horizon.
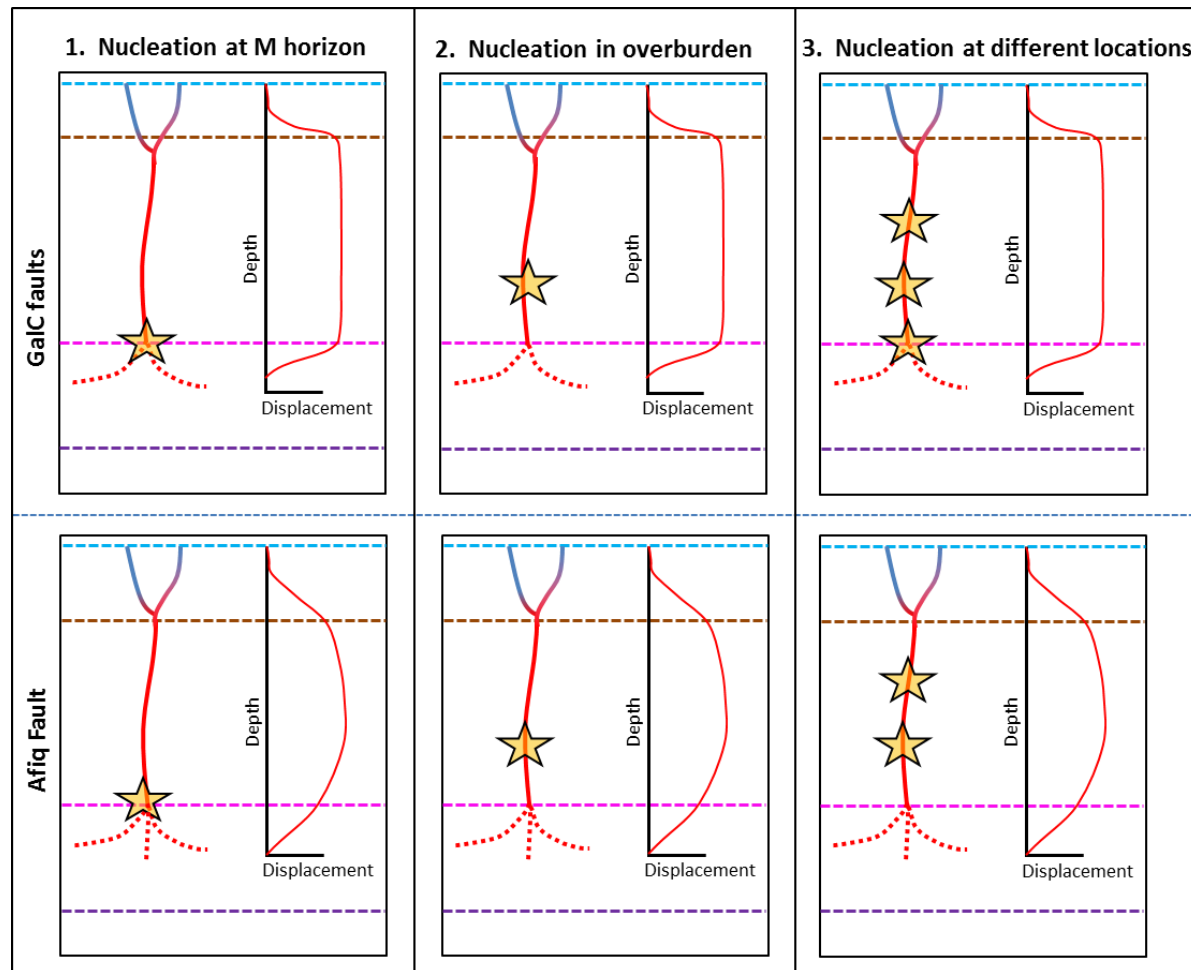
Figure 6.4 - Afiq Fault and GalC faults show a noticeable change in the distribution of $D_{max}$, which leads to different potential interpretation of the nucleation point.  These three situations outline the most likely possible locations for fault nucleation
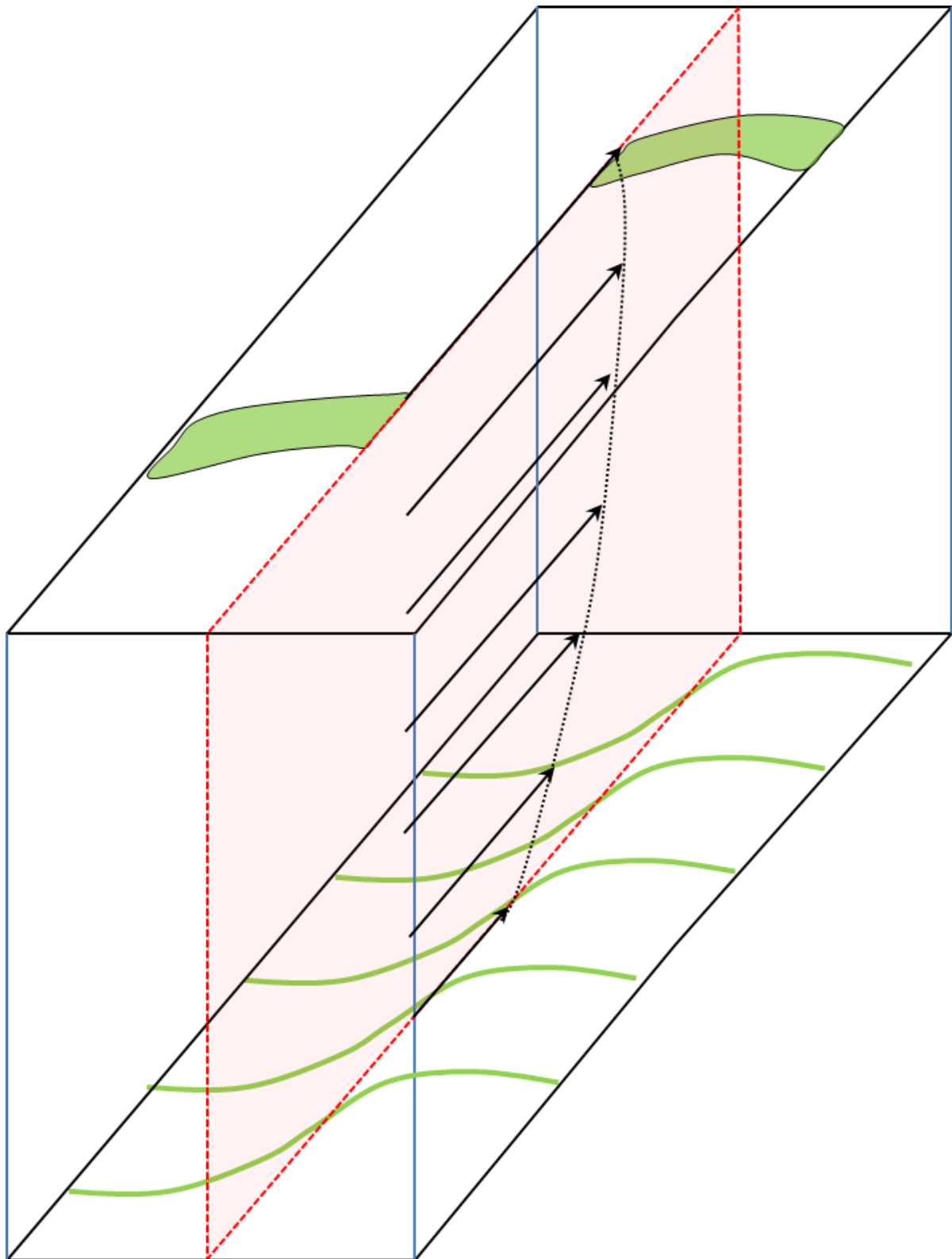
Figure 6.5 - Schematic showing how material might deform in a ductile manner at the top of the evaporites (M horizon). However, up-section, the overburden deforms in a brittle manner, which 1) allows for a preferential region of slip, and 2) kinematic indicators do not show folding or drag, and therefore both reasons suggest a higher offset.

## 6.6   Explaining Conjugate Faulting in GalC

The structural suite found in GalC varies significantly from other fold and thrust belts due to the prevalence of the conjugate set of strike-slip faults (Briggs et al., 2006; Higgins et al., 2007; Morley et al., 2011).  However, the reason for this discrepancy has not been examined. The sinistral GalC faults located in the Southern Region (Fig. 5.1) show a similar trend to those from Chapter 4 and were asserted to have formed from the salt flow down-slope in the Levant Margin (Chapters 4 and 5).  By contrast, the sinistral faults from the Central and Northern Region have formed from salt movement down-slope of the Nile Delta, signifying that contrasting slope directions, naturally forms two contrasting regional stress fields (Figure 6.6).  For the faults formed from the Nile Delta, the southern block has slipped down-slope relative to the northern block, whilst in the Levant Margin the north-eastern block has slipped downwards greater than the south-western block.  Thus overburden sediments located in the basin at the distal ends of these slides are affected by both transport directions, which should invoke a clockwise rotation (Figure 6.6).  This rotation could be accommodated by a dextral fault movement, given brittle conditions, and therefore produce the set of observed dextral faults as a result. Interestingly, given that most of the dextral faults are likely inactive, the block must have rotated until it became locked by the two sets of sinistral faults.  Thus, the continued movement of the sinistral faults from the Nile Delta will continue to slip and may eventually completely overprint evidence of dextral fault deformation at the seabed.  This continued evolution presents interesting questions towards how this will affect the 4D connectivity of these faults across buried intersections in the future (previously mentioned in Chapter 5).
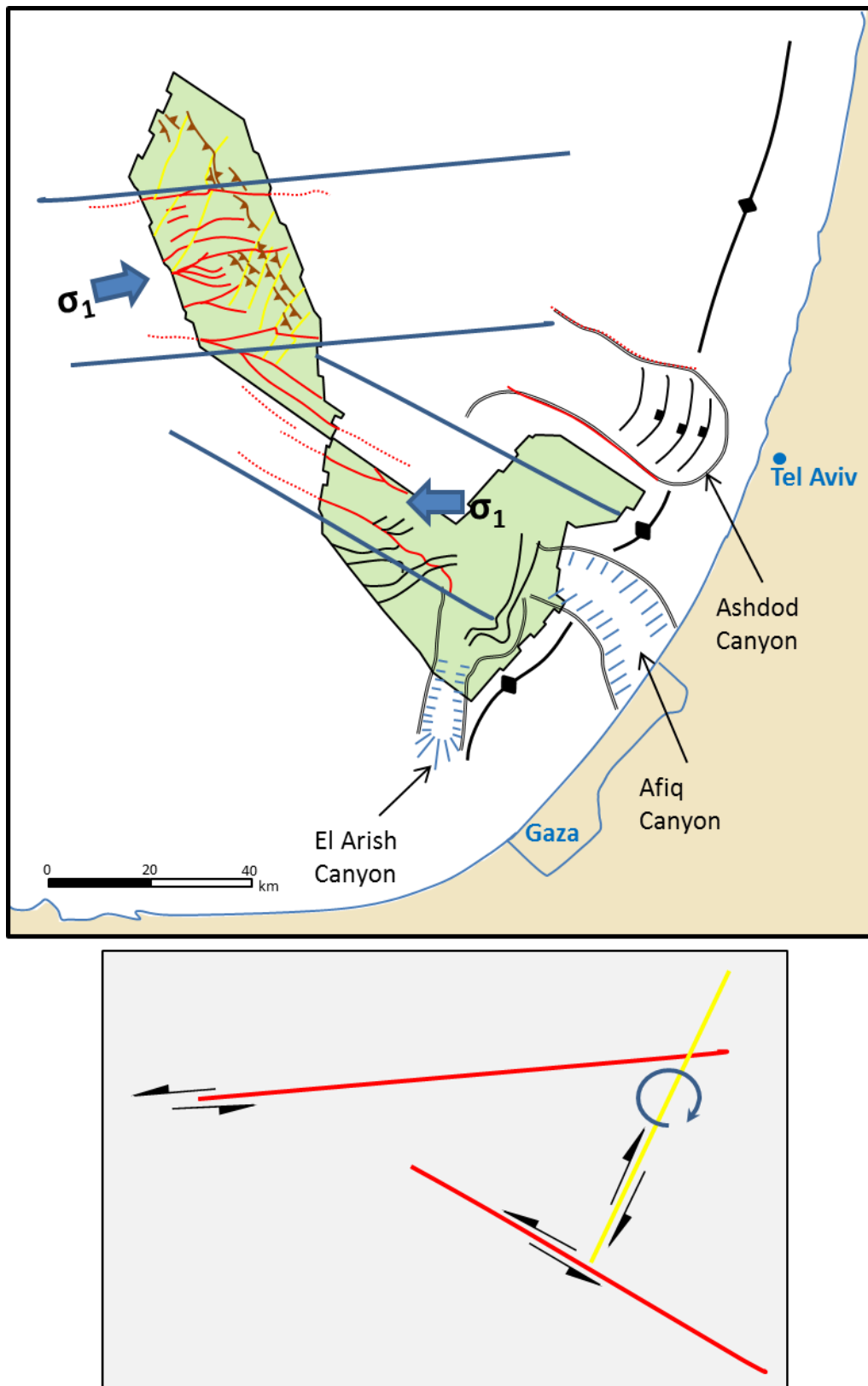
Figure 6.6 - Location map showing how the conflicting slope directions form sinistral faults trending in different directions.  The conflicting movement of blocks results in a clockwise motion, which is accommodated by the inception of a set of dextral faults.

## 6.7   Relating the Tier Structure to the Riedel Shear Model

The objective of this section is to relate the structures presented in this thesis to the structures identified in prior studies.  The focus here is especially on the discrepancies found with the laboratory based analogue models that have followed the Riedel Shear models because these studies have identified the terms and structures that most field studies use to classify structures (e.g. Carne and Little, 2012).

The terminology used to describe the structure of strike-slip faults in this thesis is noticeably different from prior terminology, such as the Tier A strand being used as alternative to 'the through-going fault' used in prior studies (Tchalenko, 1970; Sylvester, 1988).  The reason for this is to separate the structure of Tier B strands from previously used terms, such as the Riedel (R) Shear.  Despite the Tier B strands forming en echelon arrangements, and showing a crude similarity in shape to the helicoidal R shears, they depart from the structure that defines R shears (and other related secondary structures) in three major ways:

1. Location of trace in plan view
2. Orientation to the underlying through-going fault
3. Sense of slip (i.e. additional dip-slip component)

In plan view Tier B faults clearly form on either side of the underlying fault, whilst R-shears cross the underlying through-going fault (Fig. Figure 6.7, Figure 6.8) (e.g. Naylor et al., 1986; Sylvester, 1988; Dooley and Schreurs, 2012).  The orientation differs by the average angle with the through-going fault, most R-shears show an angle of c. 10° - 20° (Naylor et al., 1986; Sylvester, 1988); whilst the low angle Tier B strands show angles of 4°-8° and high angle Tier B strands show angles that average c. 46°.  Finally, analogue models show the sense of slip on R-shears is strike-slip and synthetic with the slip sense of the underlying fault, whilst these faults show variable slips, which becomes dominantly dip-slip at the upper tips (Naylor et al., 1986; Dooley and Schreurs, 2012).

Tier B strands also exhibit a distinctly different structure from the other secondary structures predicted in a Riedel simple shear Model (Tchalenko, 1970; Naylor et al., 1986).  P-shears share the same differences as R-shears, with the difference in angle with the underlying fault even more pronounced, whilst R'-shears also require a different angle and slip sense, with all

structures requiring a crossing of the underlying, through-going fault.  The only Riedel Model structure that fits is the tensional (T) fractures that are predicted to form at 45°, which closely fits with the angles measured in this study.

Interestingly, analogue studies have not explored how normal faults (or T fractures) formed in detail, and it is unclear if the rotational and helicoidal like shape of R-shears was also expected for these structures.  It is suspected that the T fractures documented in prior studies only occurred with the R-shears, and therefore this insight into the 3D nature of their structure has never been explored.  However, if this is the case, why are the R, P, and R'-shears absent from these faults?  This is explored in the subsequent section and is followed by short sections addressing pure shear and simple shear mechanisms as well as usage of the term 'flower structure' to further relate the findings of this study to prior work.

### 6.7.1   Why are the R-Shears Absent?

This section aims to explore the question asked above- why are R shears (and other associated structures) notably absent from the structures observed in both datasets; the section will focus on three potential reasons: transtension, juvenile structures, and scale and seismic resolution.

*Transtension-*

One possibility is that the faults propagate in a transtensional setting.  Analogue experiments conducted with a pre-determined $\sigma_1$ imposed parallel to the through-going fault, form a transtensional environment  in which R-shears rarely occurred, and faulting was mostly made-up of a single through-going fault, occasionally forming en echelon arrangements at the free surface (Naylor et al., 1986).  The results of this experiment share similarities to the Afiq Fault expression at the seabed, which is defined by a through-going Tier A strand, which is segmented at the upper tip to form a crude en echelon arrangement (Figure 4.38c, Figure 6.7).  The Tier A strand deformation may therefore indicate that the Afiq Fault formed in a transtensional setting, which is feasible given its location on the Levant slope and at a canyon margin.  Given that Type II faults in GalC resemble the Afiq Fault, by analogy, it is conceivable that these have also formed under a transtensional setting.

Type I faults do not share the same analogy, given that the Tier A strand does not reach the free surface. The fact that the Tier B strands at the seabed show normal-slip suggest an element of transtension may occur across these faults; however, the normal-slip only occurs at the upper tips. Thus, a change in the stress field of the Tier B strands must occur up-section, with $\sigma_1$ moving from horizontal to vertical (Figure 6.9), and the transtension would only apply towards the upper tips.

There are other problems with assuming transtension occurs across these faults; firstly, given the compressional toe domain location of the GalC strike-slip faults, a transpressional setting would be more structurally reasonable. However, the GalC faults show very little dip-slip displacement components (c. 20-30m on average on a 1$^{st}$ order fault), whilst also sharing the regional deformation with thrust faults (Fig. 5.1). Thus, the strike-slip faults show little evidence of compression, otherwise the reverse-slip component would be significant. This suggests that despite the regional transpression, there is a partitioning of fault motion, and the shortening is almost entirely accommodated by the thrust faults (Tron and Brun, 1991; Richard et al., 1995). Determining if transtension occurs locally on individual faults proves problematic as the only evidence for it are Tier B strands exhibiting normal-slip at upper tips. Interestingly, in a simple shear model, $\sigma_1$ is oriented 45° to the through-going fault (Tchalenko, 1970), whilst in a pure shear model $\sigma_1$ bisects the acute angle between two conjugate faults, and is therefore only oriented 30° on average from each fault (Naylor et al., 1986; Ferrill et al., 1999). An angle of less than 45° suggests that transtension could affect the individual faults (Naylor et al., 1986), and may explain the lack of R-shears.

The second problem is that the dip-slip component that occurs across the Afiq Fault is reverse slip, and therefore also indicative of transpression (Figure 4.4, Figure 6.10). However, the Afiq Fault also shows normal-slip Tier B strands at the free surface; suggesting transtension may also affect the upper tips as in Type I faults (and explain the lack of R shears at the free surface).

Evidence for transtension is therefore not overwhelming in the faults from either dataset; however, it may affect the upper tips of both Type I and II faults enough to inhibit the growth of R-shears. Future work is clearly needed to ascertain the effect of transtension on fault structure. It should be noted; however, that if transtension does occur, it implies that the changing stress fields towards the upper tips is not enough to differentiate whether a fault

propagates into a Type I or Type II fault, which affirms that fault geometry is controlled more by strain rate and blind versus emergent propagation, i.e. syn-sedimentation (Section 6.3).

*Juvenile Faulting-*

A second possible explanation for the lack of R shears assumes the faults in this thesis are relatively juvenile compared to those shown in experiments. It is possible that in a Type I fault, Tier B strands represent precursor structures to the R shears (Figure 6.11). Further strike-slip motion along the fault would make normal-slip not mechanically favourable, and thus the fault responds by changing into strike-slip motion along all parts of the Tier B strand. This forces lateral propagation of the Tier B segments, which interact and link to each other (Figure 6.11). Interestingly, this model signifies that the splays had originally branched upwards to form individual strands, eventually re-link laterally to form R shears. Experiments by Ueta et al (2000) showed that early formation of R shears begins in a similar manner, with splays forming upwards on either side of the underlying through-going fault, and forming the Y shape shown by Type I faults in this study. R shears later formed by the splays propagating laterally and linking to form the helicoidal shape. Thus it is feasible that Type I fault geometry are proto-R shears.

It is less clear how a Type II fault forms R shears, given that in order for Type B strands to link, they would have to cross-cut and inhibit further propagation along the Tier A strand. However, continued strike-slip motion may result in further upward propagation of the segmented Tier A strands (Figure 6.7). These Tier A strands would rotate upwards in a similar manner to the Tier B strands, whilst maintaining strike-slip motion, thereby forming R shears. Interestingly, if linkage occurred similarly to the proposed propagation of Tier B strands above, then it is also possible that Tier A strands propagates upwards by splaying, with former tips undergoing further slip, and re-linking to develop a single Tier A trace at shallower depths (Figure 6.12).

*Scale and Seismic Resolution-*

A final factor to consider is the scale of the structures and the seismic resolution that this thesis deals with. In all cases the Tier A strand was interpreted holistically as a relatively straight line on the coherency slices; however, a closer inspection reveals short perturbations

along the trace (e.g. Figure 6.13).  It is possible that these perturbations are R and P shears that have anastomosed to form the through-going fault zone described in analogue studies.  If this view is extrapolated to a profile section, then the undulations described in Chapters 4 and 5 may also be explained by these structures.  If this is the case, then the R shears are in fact present but operate at a relatively smaller scale.  However, this raises interesting questions, such as why do the normal faults form at the larger scale?  Noticeably, some undulations observed in profile sections (e.g. Figure 4.39) are larger than the small scale fault zone region comprised in the seismic, suggesting that both scale and lateral propagation models presented in Chapter 4 could be at work.

*Summary-*

Ultimately, more work is needed to test these suggested models for fault evolution.  It is conceivable that all three factors influence whether R shears form in strike-slip faults, and the fact that transtension occurs, requires faults to be in a more mature state before the formation of R shears can occur (Naylor et al., 1986).  Notably, the juvenile faulting models do not explain why Type I and Type II faults would form the same end geometries despite showing considerably different geometries at their currently observed states.  Thus, there are clearly more factors that could be tested using analogue models.  It may also be possible that one of the fault types never develops R shears.  For instance, Type II faults have such high strain rates, that it is simply not possible for R-shears to form, and final analogue models have never really shown this structure due to strain rates being too low and high contrast in mechanical strength between the sliding boards and sand or clay.  If the R shears are present at the smaller scale, then the normal faults may suggest that transtension is indeed playing a role at the upper tips; however, transtension must therefore occur in greater amounts where the Type I structures form.  Given the setting of El Arish, Afiq, and Nahal-Oz Faults, it is hard to understand why this would be the case and thus requires further study.
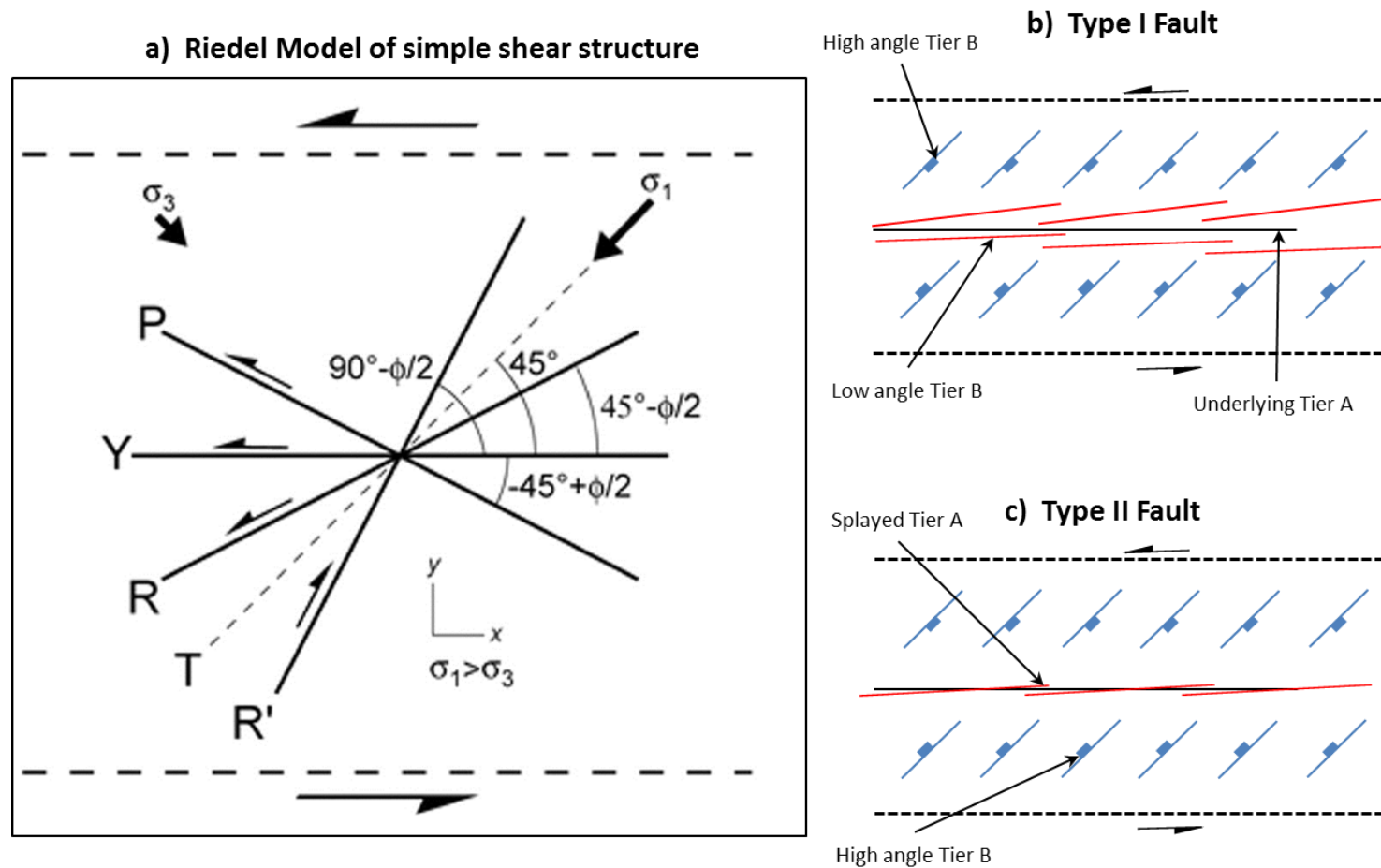
Figure 6.7 - a) Schematic illustration of the Riedel model for simple shear deformation of a strike-slip fault- Adapted from Tchalenko, 1970; Swanson, 1988.  b) Schematic illustrating the relative orientations of components of the Type I fault (e.g. low angle and high angle Tier B strands). c) Schematic illustrating the orientations of Type II fault components (e.g. high angle Tier B strands and splayed Tier A strand).
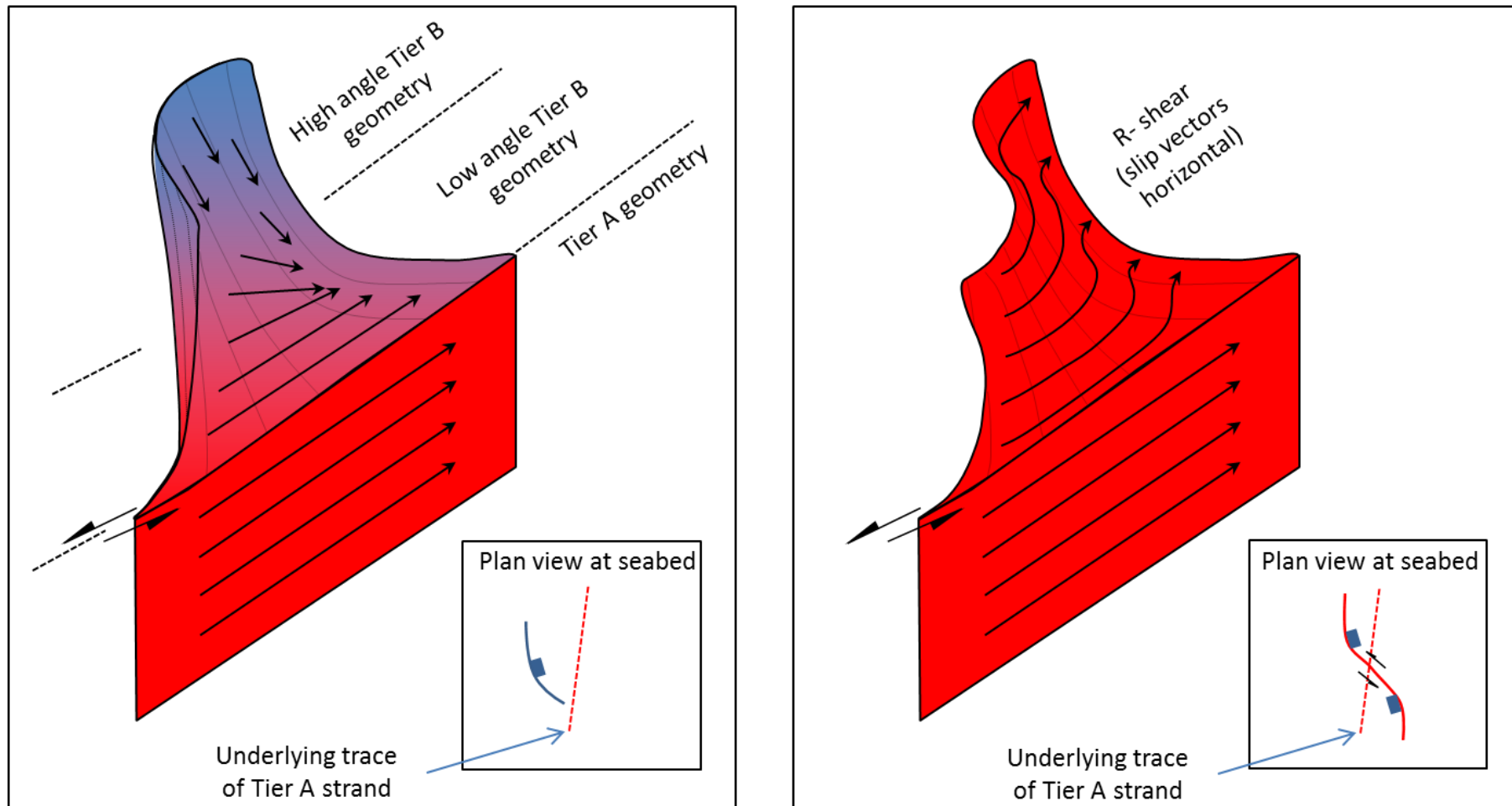
Figure 6.8 - a) Schematic illustrating the difference in geometry between a Tier B strand documented in this thesis and an R-shear, a commonly observed feature in  analogue studies (e.g. Tchalenko, 1970; Naylor et al, 1986) and regional field studies (e.g. Carne and Little, 2012).
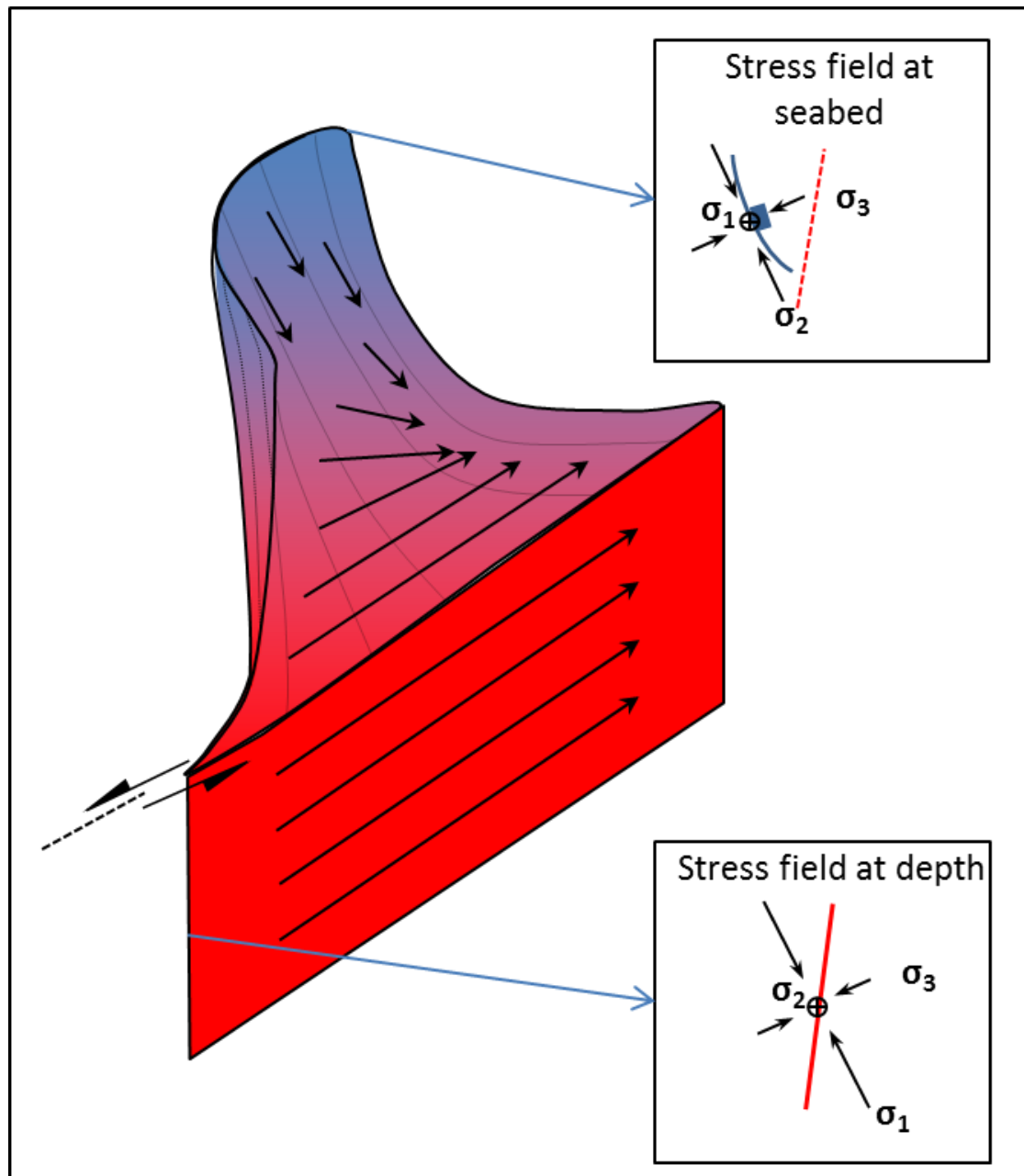
Figure 6.9 - Schematic of the different stress fields at different depths.  At depth along the Tier A strand, the stress field follows a simple shear model with $\sigma_1$ oriented 45° to the fault.  However at the seabed, the fault shows normal-slip and therefore the stress field must have changed upwards into a normal fault arrangement, with $\sigma_1$ oriented vertically.  A stress field at the lower region of a Tier B strand would show $\sigma_1$ at an oblique orientation between horizontal and vertical.
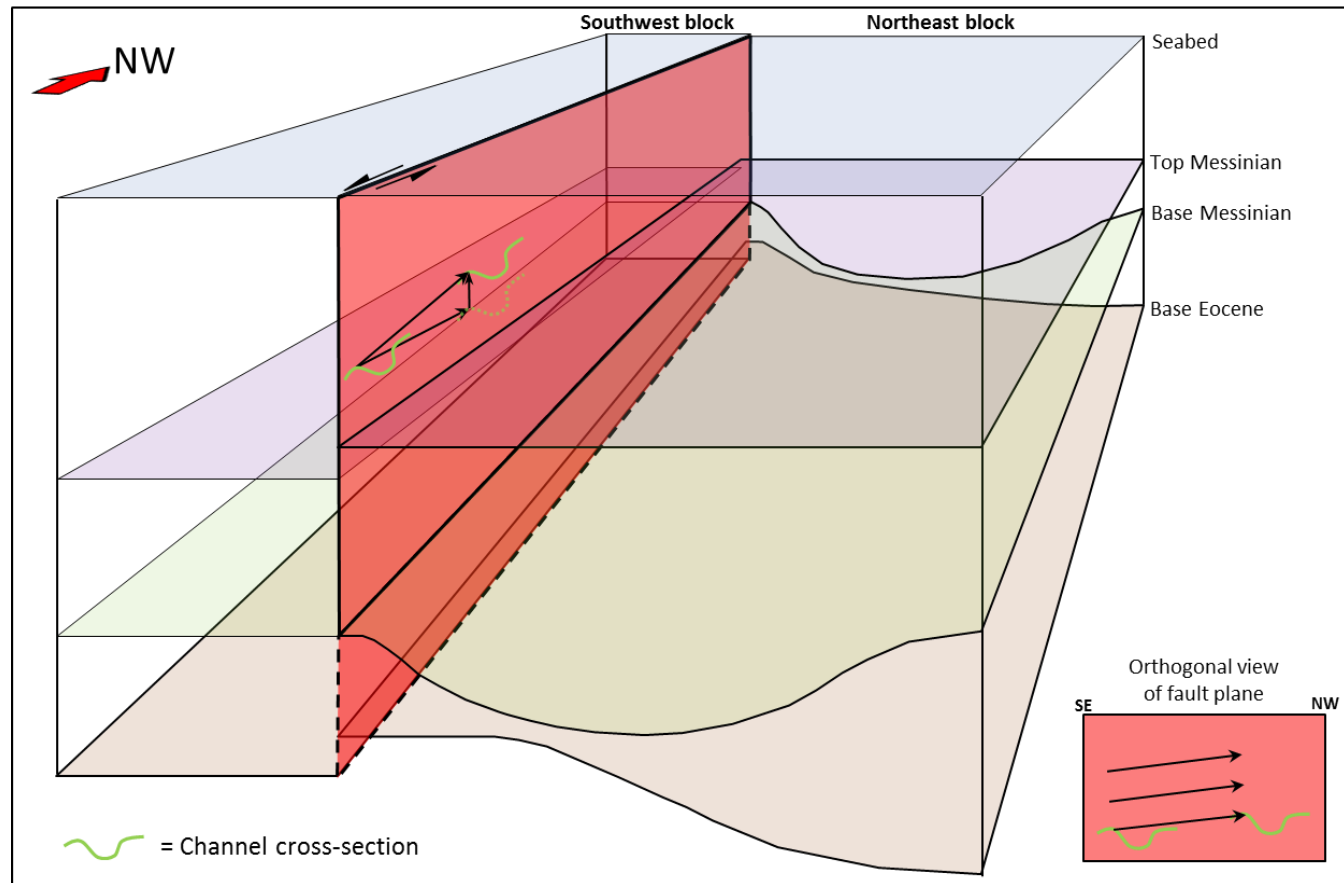
Figure 6.10 - Schematic of the Afiq Fault, showing relative levels of different units across the fault, looking towards the northwest (down-slope). A channel is shown, which shows that the north-eastern side is uplifted relative to the south-western side. Assuming the northeast block has slipped down-slope relative to the southwest block (explained in Chapter 4), the southwest block therefore represents the footwall, and the northeast block represents the hanging wall. The dip-slip motion is thus reverse, implying a slight transpression. This also takes into the account of the regional dip of the overburden, which is noticeably less than the dip-slip component. Note: not drawn to scale.
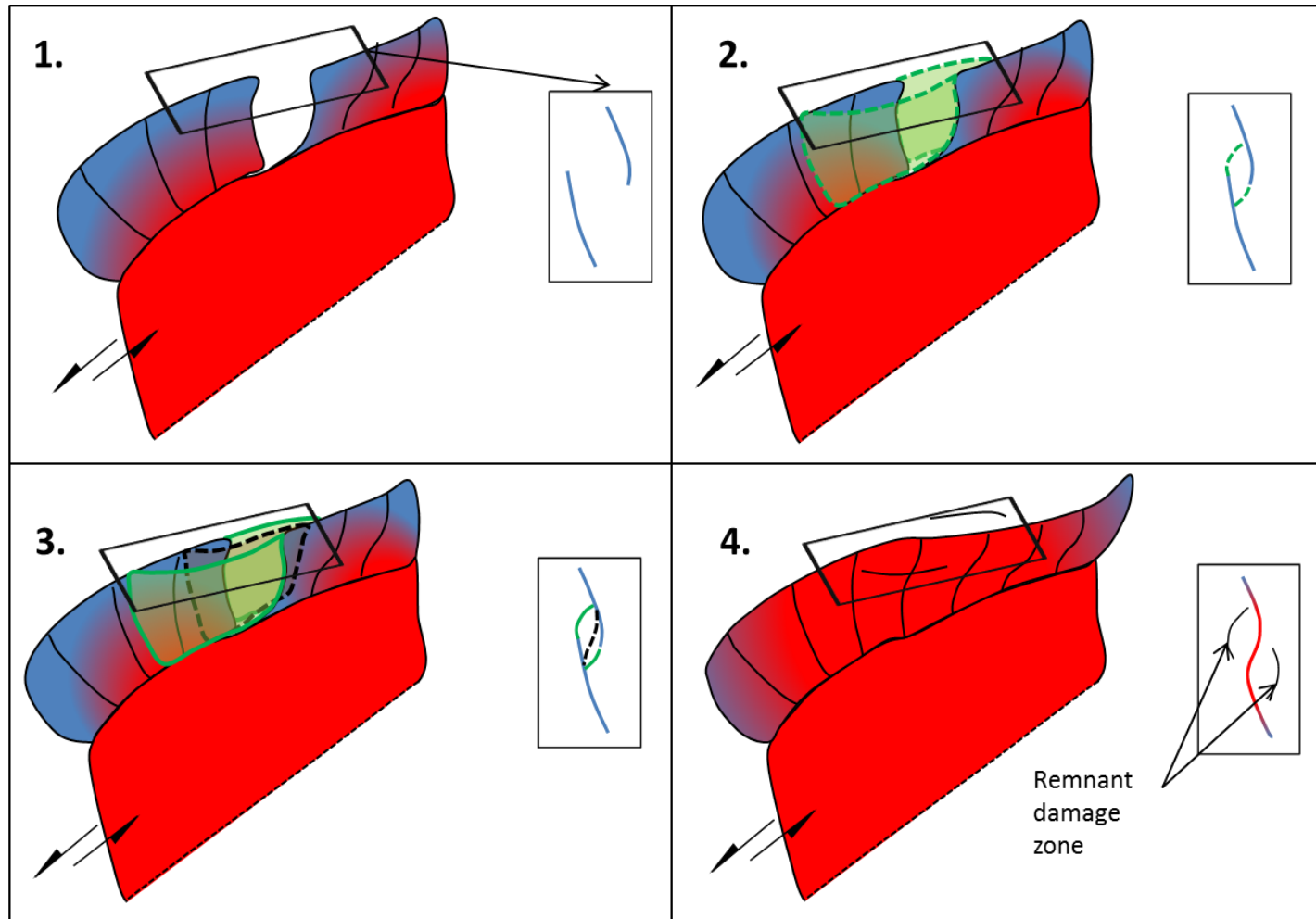
Figure 6.11 - Schematic of how the Tier B structures in this thesis may represent juvenile features of R-shears.  Increased strike-slip motion, results in the lateral linkage of Tier B strands, which connect to form shear faults that cross the trace of the underlying Tier A strand, and slip becomes dominantly strike-slip at the upper tips.

**1. Upward propagation of a Type II structure, results in splaying or branching of Tier A strand**

**2. Tier A splays propagate laterally, and interact with neighbouring splay**

**3. Continued propagation results in splays re-linking and trace becomes a single Tier A strand again**
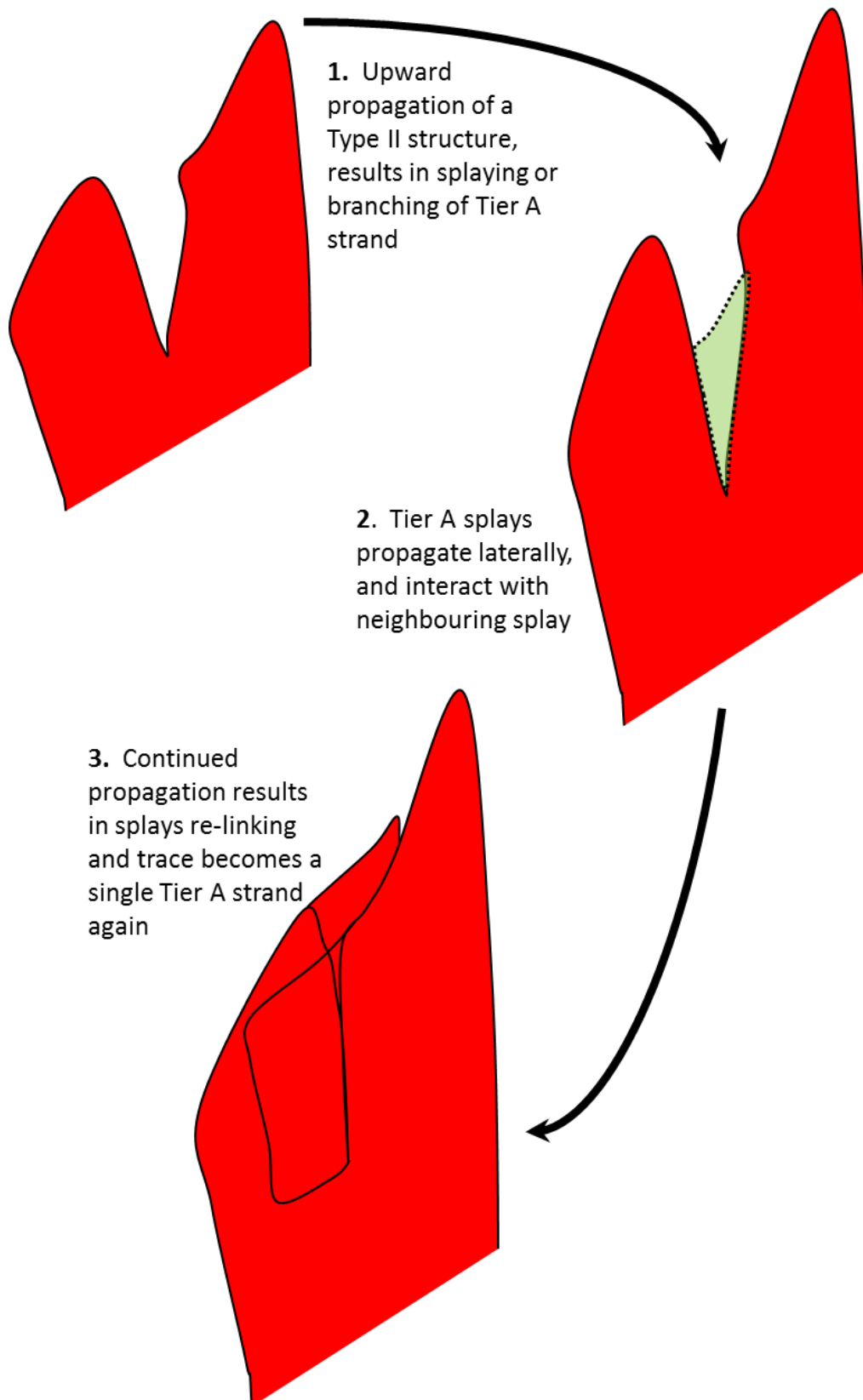
Figure 6.12 - Schematic of upward propagation showing how a Tier A segment that has splayed upward, may re-link laterally with continued strike-slip motion to form a single Tier A strand again.
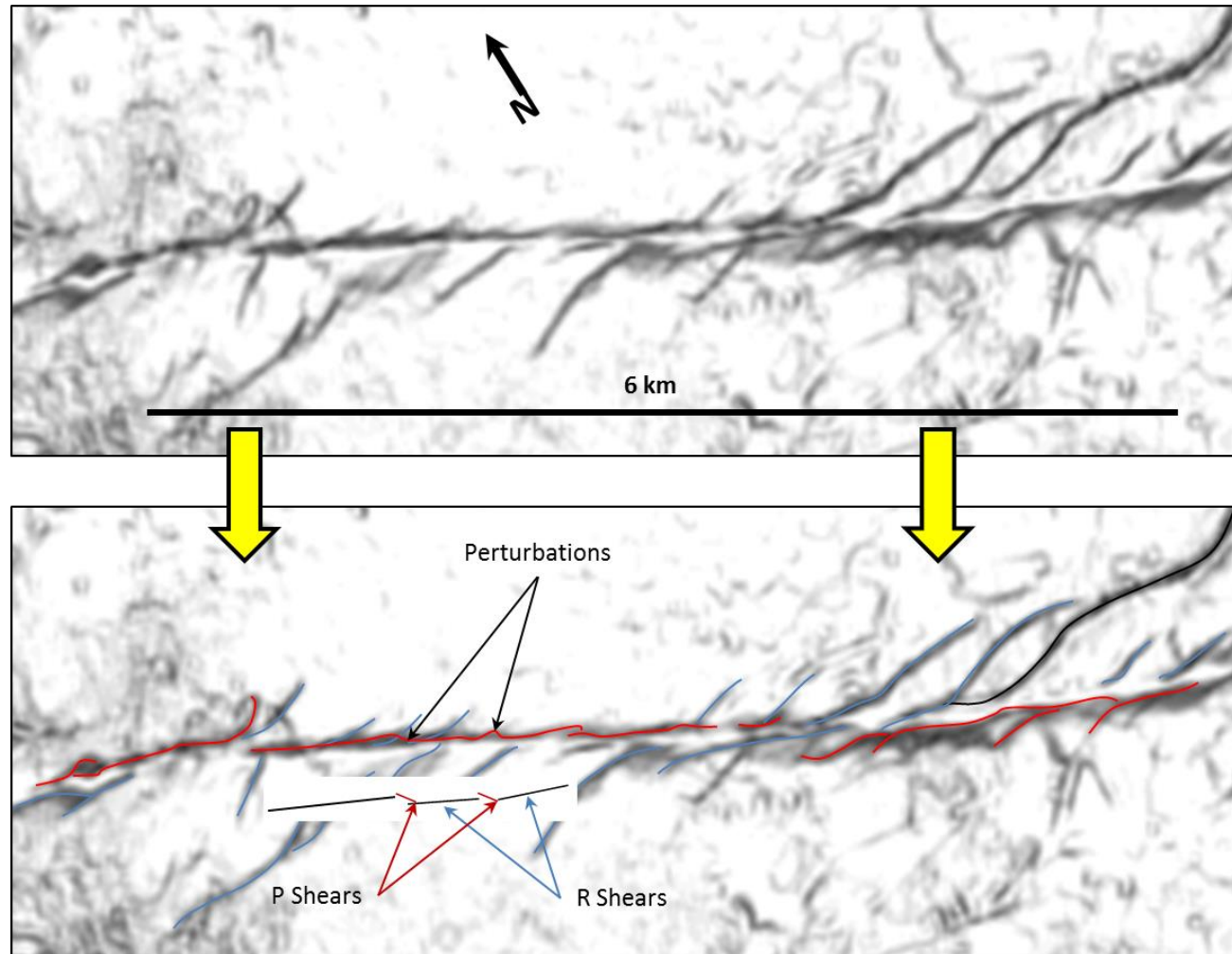
Figure 6.13 – The scale at which faults have been picked have concentrated on the larger scale and show a single fault trace; however, smaller scale shows small perturbations which may be the combination of small R and P shears described in analogue models.

### 6.7.2   Pure shear vs simple shear?

This section briefly aims to question how simple shear and pure shear mechanisms work together.  For instance, the en echelon arrangements and Tier B strands forming at a similar angle with the Riedel model of simple shear, suggests that both Type I and II faults form under a simple shear mechanism.  However, on the larger scale, individual simple shear derived faults form conjugate pairs, thereby deforming under a pure shear mechanism.  Thus both mechanisms can drive deformation in juxtaposition, possibly at different scales.

Interestingly, conjugate relationships extend outside of the GalC dataset with small dextral faults observed forming at conjugate angles to the El Arish and Afiq Faults.  Thus even in a region dominated by sinistral strike-slip motion under a simple shear model, the pure shear mechanism applies to a lesser degree.

The juxtaposition of mechanisms naturally leads to questions, including: are both strain mechanisms always present when there are contrasting stress fields?  Can strike-slip faults propagate purely under a pure shear mechanism, i.e. can they form with no simple shear deformation at the upper and basal tips?  Conversely, can faults exist purely in simple shear, or will smaller conjugate faults always occur to a lesser degree?  Finally, as mentioned in section 6.7.1., does a pure shear condition driving the formation a conjugate pair allow for simple shear at the tips due to localised variations within the stress field?  It is believed here that these two mechanisms are too often considered separately, and not to what degree they apply in conjunction with each other.

### 6.7.3   Is the Flower Structure an Appropriate Term?

In light of the results of this study, it appears the term 'flower structure' can be somewhat misleading.  For instance, flower structures are classified as positive or negative based on their structure, which leads to the interpretation that they are forming in regions of transpression and transtension, respectively.  However, in textbooks, these instances are considered at jogs between segments and do not account for the majority of the fault along the segment (Twiss, 1992).  Analogue studies have refined this by describing cross-sections across segments, with negative flower structures observed in experiments that where strike-slip and transtension occurred, and positive flower structures observed when reverse-slip or

transpression occurred (Naylor et al., 1986).  However, depending on where the cross-section is taken, positive flower structures could be expected between two shears, and therefore a fault could be misinterpreted as a transpressional when it is deformed entirely by strike-slip motion (Figure 6.14).

Following on this idea, the faults in this thesis always show negative flower structures because of the normal-slip on the Tier B faults (with the exception of a few positive flower structures located at restraining bends), which implies that these faults are undergoing regional transtension.  However, it is not entirely clear if this was the case (see Section 6.7.1); and if transtension does occur, it is likely only at the upper tips, and therefore not characteristic of the entire fault height.  It is therefore proposed that future interpreters should apply caution when inspecting a flower structure and classifying it as forming in a transpressional or transtensional setting on its classification of a positive or negative flower structure.
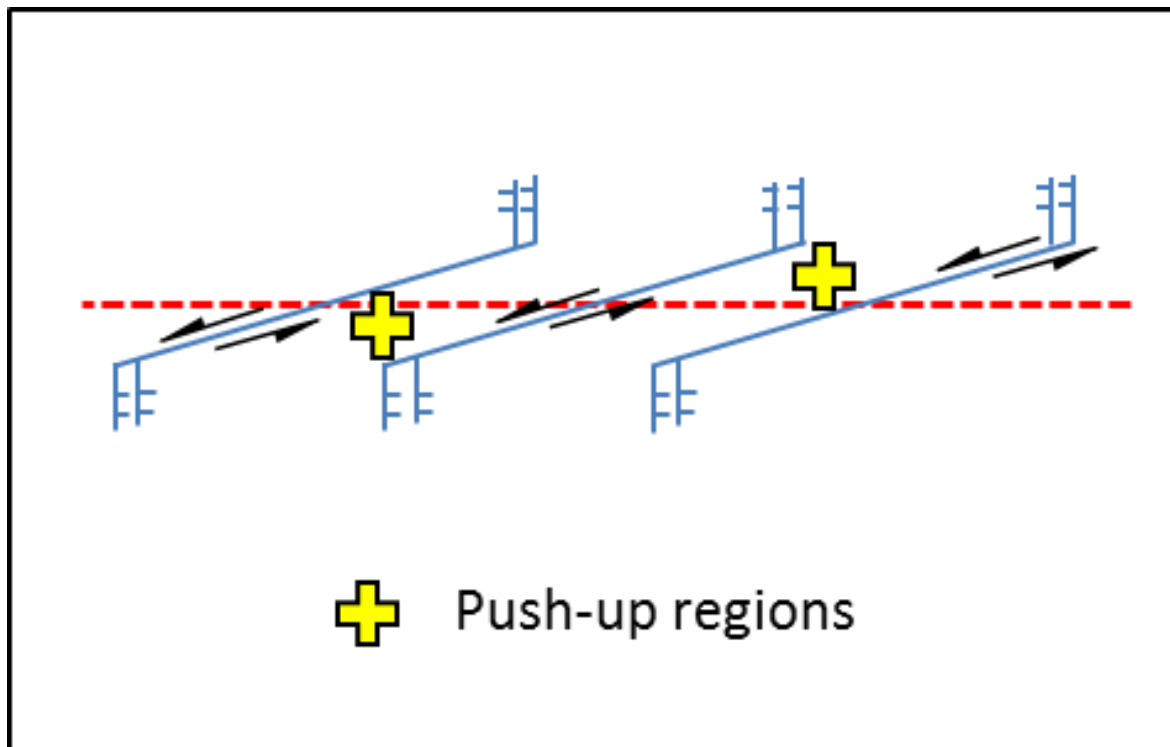
Figure 6.14 - Schematic of how R-shears could produce regions of transpression between each fault strand, in a similar manner to compressional jogs.  However, at the R shear tips, there is also extensional features (e.g. wing cracks or horsetails) and thus depending where a section is taken, it might show a positive or negative flower structure.

## 6.9   Future Work

This thesis has served to further our understanding of strike-slip fault propagation using a relatively understudied medium, 3D seismic data, to quantify displacement and link it to novel structural 3D descriptions.  However, this study has only touched the surface of what can be studied in seismic data, and for every fundamental insight gained, another question is raised.  For instance, how do thin-skinned detachment faults compare to larger, basement controlled faults?  Are the structures observed here and propagation models applicable to faults derived from different driving mechanisms?  Both this chapter and Chapter 5 have already highlighted several lines of future work and this section aims to highlight some of the overriding questions as well as potential ideas to inspect the models and theories in this thesis using analogue models.

*Basal Tips-*

This study has highlighted that a fault does not simply die out as a through-going fault at the basal tip, but splays into a different geometry in the same way as the upper tips; however the 3D structure and displacement distribution on these strands remains a mystery.  Further 3D seismic studies could also focus on the 3D structure and (if possible) the displacement across the Tier C faults to test if thrust faulting becomes dominant at the basal tip.  Future analogue studies could also investigate this subject by placing clay below two moving boards, to inspect how the downward deformation propagates.  Furthermore this experiment could be extended to sand and a salt proxy (e.g. silicon) to compare how the deformation contrasts.  A salt proxy would be especially interesting as it would allow insight into the detachment dynamics speculated upon in this thesis.  X-ray tomography can effectively visualise the deformation in 3D (as shown by Ueta et al., 2000), since visualising the deformation underneath the places would be problematic.

*Regional Evolution-*

Analogue studies could also be used to test how the regional evolution of the GalC conjugate faults formed as well as the Afiq Fault.  For instance, designing a sandbox model with two obliquely trending slopes and an overburden translating upon a salt layer, could provide interesting insights into the structure types formed, and how they interact.  The Afiq Fault

351

could serve as an analogue model itself to test if the same geometries would require a pre-existing fracture. Similarly, another experiment to determine under what conditions Tier B strands formed would be immensely interesting, and help explain why these structures have never been observed in analogue studies before. Finally, tests on how sedimentation and lithology could be more precisely explored, to see which has a greater effect on geometry. Similarly strain rate effect alone, could be quantitatively monitored to explore its effect on structure.

*Fault Nucleation-*

Section 6.6 highlighted that there is little constraint or evidence towards the nucleation point of these strike-slip faults and an analogue experiment designed to target a fault from inception would yield very interesting results. Most analogue experiments slide two boards against each other to monitor the deformation in an overburden, which fails to account for the inception of the through-going fault. However the alternate model used by An and Sammis, (1996) to deform clay from a strike-slip fault at inception could be built upon, especially by adding an underlying salt proxy layer to determine how this may affect fault nucleation, and more importantly where in the succession fault nucleates.

*Relating Analogue Models to Naturally Occurring Faults-*

The deformation observed in experiments differ considerably from both the Riedel based experiments (e.g. Tchalenko, 1970; Wilcox et al., 1973; Naylor et al., 1986; Richard et al., 1995), the alternate model by An and Sammis (1996), and the structures observed in this study. The experiments run by An and Sammis (1996) bear similarities to the regional setting of the strike-slip faults studied in this thesis; however, the structures and their relative orientations are very different from the faults observed here and in their experiments. Thus further work directed to replicating the faults observed here may help explain the discrepancies. Discovering what causes the difference in structures would be intriguing to test if the differences are based on strain rate, lithology, and propagation condition (e.g. blind versus syn-kinematic). Furthermore, this may help bridge between the discrepancies already described by the Riedel experiments in Section 6.7.

*Displacement Distribution at 3D conjugate interactions-*

Although analogue models show that the faults propagate towards the intersection before offsetting the older fault (Schwarz and Kilfitt, 2008) (Figure 5.13), the displacement distribution of these faults could provide interesting insights into how the fault segments interact around an intersection, and therefore question whether the evolution shown by the analogue model is always the case.  For instance, if two faults segments act as separate faults until the intersecting fault dies out (Figure 6.15a), then the analogue model is likely correct. If the fault segments are kinematically linked at an early stage and the intersecting fault offsets them later, then it would suggest that fault 2 was the older fault (Figure 6.15c).  If a combination of the two occurred, then a contemporaneous evolution may be the case with two segments acting separately at first, but link at the intersection, and show a central displacement maximum (Figure 6.15b).  Further work could investigate the displacement distribution of intersecting faults to establish if each case occurs and how often.  Similarly, when fault intersections show such complexity, future work should explore how displacement continues on individual fault segments.  If a region of fault segment becomes offset, does it continue to slip and accrue displacement, at some depths or does the entire segment become exctinct, or remain active?

*Comparison to 3D Seismic Datasets Around the World-*

Most of this section has focussed on future work using analogue models to test the questions and hypotheses raised by this thesis.  However, an important component of this thesis has been to provide a framework to aid future inspection of strike-slip fault propagation in other 3D seismic datasets.  Thus, how will the 3D structure and displacement distribution compare to 3D seismic datasets located in other parts of the world, with different regional settings driving the deformation?  Future work could further constrain the displacement distribution plots shown here and add insight to the propagation of these faults.

### 6.9.1   Applicability to Industry

There are three likely reasons for strike-slip faults being less studied in seismic data 1) complex structures, 2) poor imaging feasibility, and 3) applicability to hydrocarbon extraction.  The latter case is important because it dictates where seismic data is acquired, and given that strike-slip fault systems tend to develop smaller hydrocarbons accumulations (Harding, 1974; Sylvester, 1988), fewer seismic surveys will be shot in strike-slip dominated

regions. Furthermore, datasets that are deformed by strike-slip faults are both poorly imaged and could not quantify slip (prior to this study), thus strike-slip faults have remained understudied. However, as technology improves and reserves decrease, smaller accumulations located in strike-slip dominated areas will become increasingly important. Furthermore, in regions dominated by thrusts or normal faults, strike-slip faults may still intersect and therefore impact the sealing capacity of a trap. Hence this research is currently important to the hydrocarbon industry and may become increasingly so with time.

This research may also have more immediate tangible applications with mineral resource extraction and earthquake mitigation. For instance, strike-slip faults often work as baffles for fluid flow, allowing for the precipitation of precious minerals, and an understanding of how slip accrues on a strike-slip fault will aid future fault models in targeting these accumulations. Similarly, the same fluid that travels through faults to form these minerals, can create fluid overpressure in a 'weak' fault zone, and lower the effective stress, meaning it will become increasingly prone to failure, thereby causing large earthquakes in transform faults (Zoback et al.; Byerlee; Bellot, 2008). Given that large populations of human live in proximity to transform faults in Turkey, California, and several other countries, the process of strike-slip fault propagation and displacement transfer will build upon our understanding of how faults rupture, and thus improve future hazard mitigation.
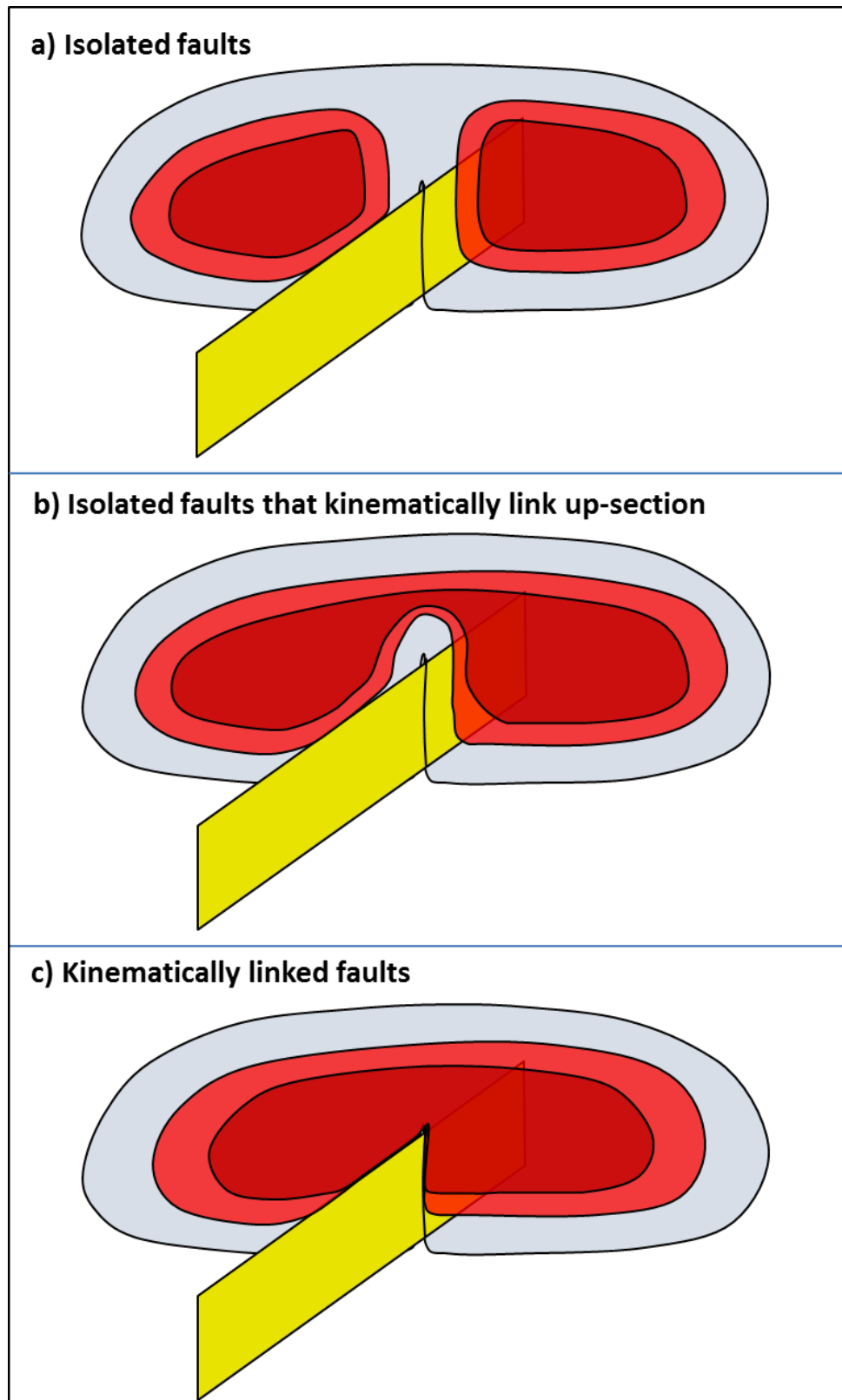
Figure 6.15 - Cartoon schematic of three models of two faults that are intersected by a fault, which dies out midway up-section.  It would be interesting to ascertain the kinematic interaction between the two segments to determine if they act as separate faults (a), a single coherency fault (c), or a combination of the two (b).

# Chapter 7

# Conclusions

# 7   Conclusions

3D seismic data have been used in this thesis to investigate the displacement distribution, geometry, and interactions of strike-slip faults in order to gain a better understanding of how they propagate.  The examples presented here have all derived from the Levant Basin, Eastern Mediterranean, and should be applicable to other strike-slip faults around the world; which will in turn promote better understanding of fluid flow and precious resource extraction as well as improve future earthquake models.  The primary conclusions as well as chapter specific conclusions are presented below to address the key findings outlined in the aims of Chapter 1.

## 7.1   Primary Conclusions

- Strike-slip fault displacement can be constrained and measured in 3D seismic data using kinematic indicators.
- Compiling several kinematic indicators across a single fault yields novel strike-slip fault displacement distribution diagrams, which show how displacement reduces outwards, both vertically and laterally.
- Detailed inspections of fault geometry show that strike-slip fault deformation can be separated into 3 Tiers: A, B, and C; and a high displacement and low displacement faults show distinct differences in the distribution of these tiers.
- Upward propagation of a strike-slip fault can be constrained by strain rate, mode of propagation, and lithology.
- Intersections in 3D are highly complex and often produce conflicting interpretations.

## 7.2   Chapter 3 Conclusions

- Strike-slip fault offset can be measured using kinematic indicators in 3D seismic data using attribute maps.
  - Horizon based attribute maps such as time-dip or amplitude can image features in plan view that show this offset.

- o Horizontal based attributes such as coherency offer the most useful method for identifying kinematic indicators as it does not require a long interpretation time, and can be very effective at imaging offset features.

- Kinematic indicators can be divided into two classes: stratigraphic and structural.
  - o Stratigraphic indicators include submarine channels and MTDs.
  - o Structural indicators include the systematic offset of older strike-slip faults and normal faults.

- Submarine channels are the most abundant and diverse group of kinematic indicators, and are the most important for determining displacement distribution.

- Care must be taken when measuring offsets of channels as they can sometimes show incorrect senses of displacement due to the channel travelling along the trace of the strike-slip fault.

- The application of kinematic indicators can allow D/L plots to inspect displacement variation along strike, but more importantly, these can be created on multiple stratigraphic levels to determine vertical displacement, and create 3D displacement distribution plots.

- Stratigraphic kinematic indicators can be used to determine timing of faulting and constrain if the fault has grown syn-kinematically.

## 7.3   Chapter 4

- Detailed mapping of regional structures confirms that faulting has occurred due to the movement of salt down-slope into the basin.

- Mapping of strike-slip faults can be conducted with the simultaneous use of profile section and coherency slice to track fault strands which show a rotational plane.

- The strike-slip faults in this study show a dominantly strike-slip component of slip, with the exception of upper tips of some faults (Type I).

- 3D displacement distribution plots can be drawn for strike-slip faults.

- Strike-slip fault geometry is comprised of three tiers: A, B, and C.

- o Tier A is defined by a through-going, sub-vertical fault, which shows the largest strike-slip displacements across the fault.

  o Tier B comprises steeply dipping faults that are located at the upper tips, and change from dominantly strike-slip at the base to dominantly normal-slip at the upper tips. These faults rotate upwards to become oriented at high angles to the underlying fault trace and form en echelon arrangements.

  o Tier C comprise strands that resemble thrusted shear zones at the basal tips of the fault. The transition often occurs at the M horizon, and may act as detachments. Due to poor imaging in the salt, the 3D geometry and slip sense is poorly constrained and the interpretations made here are tentative.

- Two types of strike-slip structures are formed: Type I and Type II.

  o Type I show a distinctive Y shape and the tiers do not overlap, and have low displacement.

  o Type II show a thinner and asymmetric Y shape and comprises overlapping Tiers, with high displacements.

- Strain rate, mode of propagation, and lithology control geometry with strain rate likely determining the mode of propagation (Type I = slow, Type II = fast).

- Curvilinear undulations in the Tier A strand may be the product of fault corrugations, which have grown from lateral propagation 'tearing' before re-linking. They may also represent small scale R and P shears that are not resolved within the seismic resolution.

### 7.3.1  El Arish Fault

- A Type I fault with low displacements.

- Defined by multiple displacement maxima, suggesting lateral linkage has occurred in conjunction with radial propagation.

- Likely propagated upwards as a blind fault.

### 7.3.2  Afiq Fault

- A Type II fault with high displacement at the Afiq Fault West before splaying into the Afiq Fault north and Afiq Fault East, which show Type I geometries.
- Defined by a single displacement maximum, suggesting lateral propagation has been mostly radial.
  - Two exceptions are the transfer zone at the AFW and a region of segment overlap near the boundary between Domains 1 and 2 of the AFE.
- The Afiq Fault East can exploit the pre-existing Shamir Rise fault and likely formed the El Arish Normal Fault array in Baudon and Cartwright (2008b) as a tail damage zone.
- Sidewall rip-outs can occur in regions of high displacement, termed Tier A1 strands.
- Large scale tip structures (Horsetail and Wing Crack Faults) constrain the timing of deformation.
- Likely propagated upwards as blind fault early before becoming emergent and thus syn-kinematic.
- Exploited a pre-existing discontinuity to propagate through the evaporites and the overpressured muds.

## 7.4  Chapter 5

- GalC strike-slip faults show 3 orders of displacement, which do not have a strong correlation with fault length due to the large amount of intersections.
- Evolution of the conjugate set of faults likely occurred episodically.
- Strike-slip faults show a tendency towards high aspect ratios (i.e. very long lengths compared to height), especially when the lateral tips are unrestricted.
- 3D geometries of fault intersections are highly complex and produce conflicting interpretations at different depths of observations.

- Conjugate intersections form angles around 60° and can be simplified into simple geometry types at individual depths to attempt a preliminary analysis of propagation history.

- Branching fault intersections occur at an angle of 40° or less and can be simplified into simple geometry types at individual depths to attempt a preliminary analysis of propagation history.

- Both conjugate and branching intersections may inhibit or lock the fault growth so that displacement can only continue to accrue further at different depths (or parts of the fault plane), and thus the geometry at a certain depth may provide insight into the intersection kinematics that occurred at that depth when a fault propagated there as an upper tip.

- Lateral tip structures are not always clearly lateral tip structures with changes in depth, and thus care should be applied when making interpretation of lateral tip deformation in 3D.

- The Type I and Type II structures defined in Chapter 4 applies to the GalC faults.

## 7.5   Chapter 6

- The controls on Type I and Type II geometry (strain rate, propagation mode, and lithology) apply to faults in both datasets.

- Tier C faults may form by evaporites flowing upwards into the overburden, leaving planes of weakness for the fault to exploit, producing geometries that resemble thrust faults.

- Nucleation is poorly constrained; however, larger displacement faults may have nucleated at the M horizon in response to salt flow, whilst some smaller faults may have nucleated in the overburden to accommodate deformation by the larger strike-slip faults.

- The geometry of the faults in this study is distinctly different from prior analogue model studies; principally there are no R shears (and associated structures).

- This may be due to transtension at the tips, a juvenile state of faulting, or a combination of both.

- Understanding of how pure shear and simple shear drive structures appears to be poorly understood and warrants future study, especially into scale dependency.

- Flower structures may be misunderstood if an interpreter has only read about strike-slip faults in textbooks and thus increased awareness of the complexities of the flower structure and its definition may aid future interpreters.

- Several lines of new analogue studies could be conducted to validate the models presented in this thesis.

- The findings of this study may benefit future hydrocarbon extraction with improved 3D visualisation and quantification of strike-slip displacement allowing for improved structural models and fluid flow prediction.

- Earthquake prediction models may also benefit by better understanding of the displacement distribution leading to improved rupture models.

# Chapter 8

# References

# 8   References

AN, L.-J. 1998. Development of fault discontinuities in shear experiments. *Tectonophysics,* 293**,** 45-59.

AN, L. J. & SAMMIS, C. G. 1996. Development of strike-slip faults: shear experiments in granular materials and clay using a new technique. *Journal of Structural Geology,* 18**,** 1061-1077.

ANDERSON, E. 1951. The Dynamics of Faulting and Dyke Formation with Application to Britain (2nd edn) Oliver and Boyd. Edinburgh.

ANDERSON, E. M. 1905. The dynamics of faulting. *Transactions of the Edinburgh Geological Society,* 8**,** 387-402.

ATMAOUI, N. 2006. *DEVELOPMENT OF PULL-APART BASINS AND ASSOCIATED STRUCTURES BY THE RIEDEL SHEAR MECHANISM: INSIGHT FROM SCALED CLAY ANALOGUE MODELS.* PhD, Geowissenschaften der Ruhr-Universität Bochum.

ATMAOUI, N., KUKOWSKI, N., STÖCKHERT, B. & KÖNIG, D. 2006. Initiation and development of pull-apart basins with Riedel shear mechanism: insights from scaled clay experiments. *International Journal of Earth Sciences,* 95**,** 225-238.

BAHORICH, M. S. & FARMER, S. L. 3-D seismic discontinuity for faults and stratigraphic features: The coherence cube. 1995.

BARNETT, J. A. M., MORTIMER, J., RIPPON, J.H., WASLSH, J.J., WATERSON, J. 1987. Displacement Geometry in the Volume Containing a Single Normal Fault. *AAPG Bulletin,* 71**,** 925-937.

BARTLETT, W. L., FRIEDMAN, M. & LOGAN, J. M. 1981. Experimental folding and faulting of rocks under confining pressure Part IX. Wrench faults in limestone layers. *Tectonophysics,* 79**,** 255-277.

BATES, R. L., JACKSON, J. A. 1987. Glossary of Geology (3rd edition): Alexandria, Virginia. *American Geological Institute***,** 788.

BAUDON, C. & CARTWRIGHT, J. 2008a. Early stage evolution of growth faults: 3D seismic insights from the Levant Basin, Eastern Mediterranean. *Journal of Structural Geology,* 30**,** 888-898.

BAUDON, C. & CARTWRIGHT, J. A. 2008b. 3D seismic characterisation of an array of blind normal faults in the Levant Basin, Eastern Mediterranean. *Journal of Structural Geology,* 30**,** 746-760.

BELLOT, J. P. 2008. Hydrothermal fluids assisted crustal-scale strike-slip on the Argentat fault zone. *Tectonophysics,* 450**,** 21-33.

BENEDICTO, A., SCHULTZ, R. A. & SOLIVA, R. 2003. Layer thickness and the shape of faults. *Geophys. Res. Lett.,* 30**,** 2076.

BENESH, N., PLESCH, A. & SHAW, J. 2013. Geometry, Kinematics, and Displacement Characteristics of Tear-Fault Systems: An Example from the Deep-Water Niger Delta. *AAPG Bulletin*.

BERTONI, C. & CARTWRIGHT, J. 2005. 3D seismic analysis of slope-confined canyons from the Plio–Pleistocene of the Ebro Continental Margin (Western Mediterranean). *Basin Research,* 17**,** 43-62.

BERTONI, C., CARTWRIGHT, J. & HERMANRUD, C. 2013. Evidence for large-scale methane venting due to rapid drawdown of sea level during the Messinian Salinity Crisis. *Geology,* 41**,** 371-374.

BERTONI, C. & CARTWRIGHT, J. A. 2006. Controls on the basinwide architecture of late Miocene (Messinian) evaporites on the Levant margin (Eastern Mediterranean). *Sedimentary Geology,* 188-189**,** 93-114.

BERTONI, C. & CARTWRIGHT, J. A. 2007a. Clastic depositional systems at the base of the late Miocene evaporites of the Levant region, Eastern Mediterranean. *Geological Society, London, Special Publications,* 285**,** 37-52.

BERTONI, C. & CARTWRIGHT, J. A. 2007b. Major erosion at the end of the Messinian Salinity Crisis: evidence from the Levant Basin, Eastern Mediterranean. *Basin Research,* 19**,** 1-18.

BOMBOLAKIS, E. & BRACE, W. 1963. A note on brittle crack growth in compression. *J. geophys. Res,* 68**,** 3709-3713.

BRIGGS, S. E., CARTWRIGHT, J. & DAVIES, R. J. 2009. Crustal structure of the deepwater west Niger Delta passive margin from the interpretation of seismic reflection data. *Marine and Petroleum Geology,* 26**,** 936-950.

BRIGGS, S. E., DAVIES, R. J., CARTWRIGHT, J. A. & MORGAN, R. 2006. Multiple detachment levels and their control on fold styles in the compressional domain of the deepwater west Niger Delta. *Basin Research,* 18**,** 435-450.

BROWN, A. 1999. Interpretation of Three-Dimensional Seismic Data. *AAPG Memoir,* 42**,** 514.

BROWN, A. R. 1996. Seismic attributes and their classification. *The leading edge,* 15**,** 1090.

BUCHBINDER, B. & ZILBERMAN, E. 1997. Sequence stratigraphy of Miocene-Pliocene carbonate-siliciclastic shelf deposits in the eastern Mediterranean margin (Israel): effects of eustasy and tectonics. *Sedimentary Geology,* 112**,** 7-32.

BULL, S., CARTWRIGHT, J. & HUUSE, M. 2009. A review of kinematic indicators from mass-transport complexes using 3D seismic data. *Marine and Petroleum Geology,* 26**,** 1132-1151.

BURBANK, D. W. & ANDERSON, R. S. 2001. *Tectonic Geomorphology*, Blackwell Science Ltd.

BYERLEE, J. 1990. Friction, overpressure and fault normal compression. *Geophysical Research Letters,* 17**,** 2109-2112.

CARNE, R. & LITTLE, T. 2012. Geometry and scale of fault segmentation and deformational bulging along an active oblique-slip fault (Wairarapa fault, New Zealand). *Geological Society of America Bulletin,* 124**,** 1365-1381.

CARRERAS, J., ESTRADA, A. & WHITE, S. 1977. The effects of folding on the c-axis fabrics of a quartz mylonite. *Tectonophysics,* 39**,** 3-24.

CARTWRIGHT, J., JACKSON, M., DOOLEY, T. & HIGGINS, S. 2012. Strain partitioning in gravity-driven shortening of a thick, multilayered evaporite sequence. *Geological Society, London, Special Publications,* 363**,** 449-470.

CARTWRIGHT, J. & MANSFIELD, C. 1998. Lateral displacement variation and lateral tip geometry of normal faults in the Canyonlands National Park, Utah. *Journal of Structural Geology,* 20**,** 3-19.

CARTWRIGHT, J. A. & JACKSON, M. P. A. 2008. Initiation of gravitational collapse of an evaporite basin margin: The Messinian saline giant, Levant Basin, eastern Mediterranean. *Geological Society of America Bulletin,* 120**,** 399-413.

CARTWRIGHT, J. A., MANSFIELD, C. & TRUDGILL, B. 1996. The growth of normal faults by segment linkage. *Geological Society, London, Special Publications,* 99**,** 163-177.

CARTWRIGHT, J. A., TRUDGILL, B. D. & MANSFIELD, C. S. 1995. Fault growth by segment linkage: an explanation for scatter in maximum displacement and trace length data from the Canyonlands Grabens of SE Utah. *Journal of Structural Geology,* 17**,** 1319-1326.

CHILDS, C., EASTON, S., VENDEVILLE, B., JACKSON, M., LIN, S., WALSH, J. & WATTERSON, J. 1993. Kinematic analysis of faults in a physical model of growth faulting above a viscous salt analogue. *Tectonophysics,* 228**,** 313-329.

CHILDS, C., NICOL, A., WALSH, J. J. & WATTERSON, J. 1996. Growth of vertically segmented normal faults. *Journal of Structural Geology,* 18**,** 1389-1397.

CHILDS, C., NICOL, A., WALSH, J. J. & WATTERSON, J. 2003. The growth and propagation of synsedimentary faults. *Journal of Structural Geology,* 25**,** 633-648.

CHILDS, C., WATTERSON, J. & WALSH, J. J. 1995. Fault overlap zones within developing normal fault systems. *Journal of the Geological Society,* 152**,** 535-549.

CITA, M. B. 1973. Mediterranean evaporite: paleontological arguments for a deep-basin desiccation model. *Messinian events in the Mediterranean***,** 206-228.

CLARK, I. R. & CARTWRIGHT, J. A. 2009. Interactions between submarine channel systems and deformation in deepwater fold belts: Examples from the Levant Basin, Eastern Mediterranean sea. *Marine and Petroleum Geology,* 26**,** 1465-1482.

CLARK, I. R. & CARTWRIGHT, J. A. 2011. Key controls on submarine channel development in structurally active settings. *Marine and Petroleum Geology*.

CLOOS, H. 1928. Experiments on inner structure(tectonics). *Centralblatt for Mineral. Geol. und Palaontol.,(West Germany)***,** 609-621.

COBBOLD, P. R. & QUINQUIS, H. 1980. Development of sheath folds in shear regimes. *Journal of Structural Geology,* 2**,** 119-126.

CURREN, I. & BIRD, P. 2014. Formation and Suppression of Strike–Slip Fault Systems. *Pure and Applied Geophysics,* 171**,** 2899-2918.

DOOLEY, T. & MCCLAY, K. 1997. Analog modeling of pull-apart basins. *AAPG Bulletin,* 81**,** 1804-1826.

DOOLEY, T., MCCLAY, K. & BONORA, M. 4D evolution of segmented strike-slip fault systems: applications to NW Europe.  Geological Society, London, Petroleum Geology Conference series, 1999. Geological Society of London, 215-225.

DOOLEY, T. P. & SCHREURS, G. 2012. Analogue modelling of intraplate strike-slip tectonics: A review and new experimental results. *Tectonophysics,* 574**,** 1-71.

DRUCKMAN, Y., BUCHBINDER, B., MARTINOTTI, G. M., TOV, R. S. & AHARON, P. 1995. The buried Afiq Canyon (eastern Mediterranean, Israel): a case study of a Tertiary submarine canyon exposed in Late Messinian times. *Marine Geology,* 123**,** 167-185.

DURAND-RIARD, P., SHAW, J. H., PLESCH, A. & LUFADEJU, G. 2013. Enabling 3D geomechanical restoration of strike- and oblique-slip faults using geological constraints, with applications to the deep-water Niger Delta. *Journal of Structural Geology,* 48**,** 33-44.

EDWARDS, M. B. 1995. Differential Subsidence and Preservation Potential of Shallow-Water Tertiary Sequences, Northern Gulf Coast Basin, USA. *Sedimentary Facies Analysis.* Blackwell Publishing Ltd.

ENGELDER, T. & PRICE, N. 1993. *Stress regimes in the lithosphere*, Princeton University Press Princeton, NJ.

EYAL, Y. & RECHES, Z. E. 1983. Tectonic analysis of the Dead Sea Rift Region since the Late-Cretaceous based on mesostructures. *Tectonics,* 2**,** 167-185.

FAULKNER, D. R., MITCHELL, T. M., RUTTER, E. H. & CEMBRANO, J. 2008. On the structure and mechanical properties of large strike-slip faults. *Geological Society, London, Special Publications,* 299**,** 139-150.

FERRILL, D. A., MORRIS, A. P. & MCGINNIS, R. N. 2009. Crossing conjugate normal faults in field exposures and seismic data. *AAPG bulletin,* 93**,** 1471-1488.

FERRILL, D. A., MORRIS, A. P., STAMATAKOS, J. A. & SIMS, D. W. 2000. Crossing conjugate normal faults. *AAPG bulletin,* 84**,** 1543-1559.

FERRILL, D. A., STAMATAKOS, J. A. & SIMS, D. 1999. Normal fault corrugation: implications for growth and seismicity of active normal faults. *Journal of Structural Geology,* 21**,** 1027-1038.

FLISS, S., BHAT, H. S., DMOWSKA, R. & RICE, J. R. 2005. Fault branching and rupture directivity. *Journal of Geophysical Research: Solid Earth,* 110**,** B06312.

FLODIN, E. & AYDIN, A. 2004a. Faults with asymmetric damage zones in sandstone, Valley of Fire State Park, southern Nevada. *Journal of Structural Geology,* 26**,** 983-988.

FLODIN, E. A. & AYDIN, A. 2004b. Evolution of a strike-slip fault network, Valley of Fire State Park, southern Nevada. *Geological Society of America Bulletin,* 116**,** 42-59.

FREUND, R. 1970. Rotation of strike slip faults in Sistan, southeast Iran. *The Journal of Geology***,** 188-200.

FREY-MARTÍNEZ, J., CARTWRIGHT, J. & JAMES, D. 2006. Frontally confined versus frontally emergent submarine landslides: a 3D seismic characterisation. *Marine and Petroleum Geology,* 23**,** 585-604.

FREY-MARTNEZ, J., CARTWRIGHT, J., HALL, B. & HUUSE, M. 2007. Clastic intrusion at the base of deep-water sands: A trap-forming mechanism in the eastern Mediterranean.

FREY MARTINEZ, J., CARTWRIGHT, J. & HALL, B. 2005. 3D seismic interpretation of slump complexes: examples from the continental margin of Israel. *Basin Research,* 17**,** 83-108.

FU, B., AWATA, Y., DU, J. & HE, W. 2005. Late Quaternary systematic stream offsets caused by repeated large seismic events along the Kunlun fault, northern Tibet. *Geomorphology,* 71**,** 278-292.

GARDOSH, M. A. & DRUCKMAN, Y. 2006. Seismic stratigraphy, structure and tectonic evolution of the Levantine Basin, offshore Israel. *Geological Society, London, Special Publications,* 260**,** 201-227.

GARFUNKEL, Z. 1998. Constrains on the origin and history of the Eastern Mediterranean basin. *Tectonophysics,* 298**,** 5-35.

GARFUNKEL, Z. & ALMAGOR, G. 1984. Geology and structure of the continental margin off northern Israel and the adjacent part of the Levantine Basin. *Marine Geology,* 62**,** 105-131.

GAUDEMER, Y., TAPPONNIER, P. & TURCOTTE, D. L. 1989. River offsets across strike-slip faults. *Annales Tectonicae,* 3**,** 55-76.

GEE, M. J. R., GAWTHORPE, R. L. & FRIEDMANN, J. S. 2005. Giant striations at the base of a submarine landslide. *Marine Geology,* 214**,** 287-294.

GHALAYINI, R., DANIEL, J. M., HOMBERG, C., NADER, F. H. & COMSTOCK, J. E. 2014. Impact of Cenozoic strike-slip tectonics on the evolution of the northern Levant Basin (offshore Lebanon). *Tectonics*.

GHOSH, N. & CHATTOPADHYAY, A. 2008. The initiation and linkage of surface fractures above a buried strike-slip fault: An experimental approach. *Journal of Earth System Science,* 117**,** 23-32.

GRADMANN, S., HÜBSCHER, C., BEN-AVRAHAM, Z., GAJEWSKI, D. & NETZEBAND, G. 2005. Salt tectonics off northern Israel. *Marine and Petroleum Geology,* 22**,** 597-611.

HANCOCK, P. L. & BARKA, A. A. 1987. Kinematic indicators on active normal faults in Western Turkey. *Journal of Structural Geology,* 9**,** 573-584.

HARDING, T. P. 1974. Petroleum traps associated with wrench faults. *AAPG Bulletin,* 58**,** 1290-1304.

HARDING, T. P. 1985. Seismic characteristics and identification of negative flower structures, positive flower structures, and positive structural inversion. *American Association of Petroleum Geology, Bulletin,* 69**,** 582-606.

HART, B. S. 1999. Definition of subsurface stratigraphy, structure and rock properties from 3-D seismic data. *Earth-Science Reviews,* 47**,** 189-218.

HEMPTON, M. R. & NEHER, K. 1986. Experimental fracture, strain and subsidence patterns over en échelon strike-slip faults: implications for the structural evolution of pull-apart basins. *Journal of Structural Geology,* 8**,** 597-605.

HIGGINS, S., CLARKE, B., DAVIES, R. J. & CARTWRIGHT, J. 2009. Internal geometry and growth history of a thrust-related anticline in a deep water fold belt. *Journal of Structural Geology,* 31**,** 1597-1611.

HIGGINS, S., DAVIES, R. J. & CLARKE, B. 2007. Antithetic fault linkages in a deep water fold and thrust belt. *Journal of Structural Geology,* 29**,** 1900-1914.

HORSFIELD, W. T. 1980. Contemporaneous movement along crossing conjugate normal faults. *Journal of Structural Geology,* 2**,** 305-310.

HSIAO, L., GRAHAM, S.A., TILANDER, N 2004. Seismic reflection imagin of a major strike-slip fault zone in a rift system: Paleogene structure and evolution of the Tan-Lu fault systym, Liaodong Bay, Bohai, offshore China. *AAPG Bulletin,* 88**,** 71-97.

HSIAO, L. Y., GRAHAM, S. A. & TILANDER, N. 2010. Stratigraphy and sedimentation in a rift basin modified by synchronous strike-slip deformation: southern Xialiao basin, Bohai, offshore China. *Basin Research,* 22**,** 61-78.

HSU, K. J., MONTADERT, L., BERNOULLI, D., CITA, M. B., ERICKSON, A., GARRISON, R. E., KIDD, R. B., MELIERES, F., MULLER, C. & WRIGHT, R. 1977. History of the Mediterranean salinity crisis. *Nature,* 267**,** 399-403.

HUANG, W. 1993. Morphologic patterns of stream channels on the active Yishi Fault, southern Shandong Province, Eastern China: Implications for repeated great earthquakes in the Holocene. *Tectonophysics,* 219**,** 283-304.

JACKSON, M. P. A. & TALBOT, C. J. 1986. External shapes, strain rates, and dynamics of salt structures. *Geological Society of America Bulletin,* 97**,** 305-323.

JACKSON, M. P. A. & VENDEVILLE, B. C. 1994. Regional extension as a geologic trigger for diapirism. *Geological Society of America Bulletin,* 106**,** 57-73.

JIANG, S., WANG, H., CAI, D., XIE, X. & GUO, H. 2011. Characteristics of the Tan-Lu Strike-Slip Fault and Its Controls on Hydrocarbon Accumulation in the Liaodong Bay Sub-Basin, Bohai Bay Basin, China. *Advances in Petroleum Exploration and Development,* 2**,** 1-11.

JONES, O. T. & PUGH, W. J. 1915. The Geology of the District around Machynlleth and the Llyfnant Valley. *Quarterly Journal of the Geological Society,* 71**,** 343-352,NP,353-385.

KATTENHORN, S. A. & POLLARD, D. D. 2001. Integrating 3-D seismic data, field analogs, and mechanical models in the analysis of segmented normal faults in the Wytch Farm oil field, southern England, United Kingdom. *AAPG bulletin,* 85**,** 1183-1210.

KEAREY, P. & BROOKS, M. 2002. An introduction to geophysical exploration. *Blackwell Publishing, ISBN,* 978**,** 632.

KELLER, E. A., BONKOWSKI, M. S., KORSCH, R. J. & SHLEMON, R. J. 1982. Tectonic geomorphology of the San Andreas fault zone in the southern

Indio Hills, Coachella Valley, California. *Geological Society of America Bulletin,* 93**,** 46-56.

KELLER, J. V. A., HALL, S. H. & MCCLAY, K. R. 1997. Shear fracture pattern and microstructural evolution in transpressional fault zones from field and laboratory studies. *Journal of Structural Geology,* 19**,** 1173-1187.

KELLY, P. G., SANDERSON, D. J. & PEACOCK, D. C. P. 1998. Linkage and evolution of conjugate strike-slip fault zones in limestones of Somerset and Northumbria. *Journal of Structural Geology,* 20**,** 1477-1493.

KIM, Y.-S., ANDREWS, J. R. & SANDERSON, D. J. 2001. Reactivated strike-slip faults: examples from north Cornwall, UK. *Tectonophysics,* 340**,** 173-194.

KIM, Y.-S., PEACOCK, D. C. P. & SANDERSON, D. J. 2003. Mesoscale strike-slip faults and damage zones at Marsalforn, Gozo Island, Malta. *Journal of Structural Geology,* 25**,** 793-812.

KIM, Y.-S., PEACOCK, D. C. P. & SANDERSON, D. J. 2004. Fault damage zones. *Journal of Structural Geology,* 26**,** 503-517.

KIM, Y.-S. & SANDERSON, D. J. 2006. Structural similarity and variety at the tips in a wide range of strike–slip faults: a review. *Terra Nova,* 18**,** 330-344.

LAZAR, M., SCHATTNER, U. & RESHEF, M. 2012. The great escape: An intra-Messinian gas system in the eastern Mediterranean. *Geophysical Research Letters,* 39**,** L20309.

LE GUERROUÉ, E. & COBBOLD, P. R. 2006. Influence of erosion and sedimentation on strike-slip fault systems: insights from analogue models. *Journal of Structural Geology,* 28**,** 421-430.

LENSEN, G. J. 1968. Analysis of Progressive Fault Displacement During Downcutting at the Branch River Terraces, South Island, New Zealand. *Geological Society of America Bulletin,* 79**,** 545-556.

LOHR, T., KRAWCZYK, C. M., ONCKEN, O. & TANNER, D. C. 2008. Evolution of a fault surface from 3D attribute analysis and displacement measurements. *Journal of Structural Geology,* 30**,** 690-700.

LONCKE, L., GAULLIER, V., MASCLE, J., VENDEVILLE, B. & CAMERA, L. 2006. The Nile deep-sea fan: An example of interacting sedimentation, salt tectonics, and inherited subsalt paleotopographic features. *Marine and Petroleum Geology,* 23**,** 297-315.

MAHMOUD, S., REILINGER, R., MCCLUSKY, S., VERNANT, P. & TEALEB, A. 2005. GPS evidence for northward motion of the Sinai Block: Implications for E. Mediterranean tectonics. *Earth and Planetary Science Letters,* 238**,** 217-224.

MALONEY, D., DAVIES, R., IMBER, J. & KING, S. 2012. Structure of the footwall of a listric fault system revealed by 3D seismic data from the Niger Delta. *Basin Research,* 24**,** 107-123.

MANDL, G. 1988. Mechanics of tectonic faulting: models and basic concepts.

MANSFIELD, C. S. & CARTWRIGHT, J. A. 1996. High resolution fault displacement mapping from three-dimensional seismic data: evidence for dip linkage during fault growth. *Journal of Structural Geology,* 18**,** 249-263.

MARCHAL, D., GUIRAUD, M. & RIVES, T. 2003. Geometric and morphologic evolution of normal fault planes and traces from 2D to 4D data. *Journal of Structural Geology,* 25**,** 135-158.

MART, Y. & BEN-GAI, Y. 1982. Some depositional patterns at continental margin of southeastern Mediterranean Sea. *AAPG Bull,* 66**,** 460-470.

MART, Y. & RYAN, W. 2007. The Levant Slumps and the Phoenician Structures: collapse features along the continental margin of the southeastern Mediterranean Sea. *Marine Geophysical Research,* 28**,** 297-307.

MARTEL, S. J. 1990. Formation of compound strike-slip fault zones, Mount Abbot quadrangle, California. *Journal of Structural Geology,* 12**,** 869-877, 879-882.

MARTEL, S. J. & POLLARD, D. D. 1989. Mechanics of slip and fracture along small faults and simple strike-slip fault zones in granitic rock. *Journal of Geophysical Research,* 94**,** 9417-9428.

MARTEL, S. J., POLLARD, D. D. & SEGALL, P. 1988. Development of simple strike-slip fault zones, Mount Abbot quadrangle, Sierra Nevada, California. *Geological Society of America Bulletin,* 100**,** 1451-1465.

MASCLE, J., BENKHELIL, J., BELLAICHE, G., ZITTER, T., WOODSIDE, J. & LONCKE, L. 2000. Marine geologic evidence for a Levantine-Sinai plate, a new piece of the Mediterranean puzzle. *Geology,* 28**,** 779.

MCCLAY, K. & DOOLEY, T. 1995. Analogue models of pull-apart basins. *Geology,* 23**,** 711-714.

MCGRATH, A. G. & DAVISON, I. 1995. Damage zone geometry around fault tips. *Journal of Structural Geology,* 17**,** 1011-1024.

MITCHELL, T. M. & FAULKNER, D. R. 2009. The nature and origin of off-fault damage surrounding strike-slip fault zones with a wide range of displacements: A field study from the Atacama fault system, northern Chile. *Journal of Structural Geology,* 31**,** 802-816.

MITRA, S. & PAUL, D. 2011. Structural geometry and evolution of releasing and restraining bends: Insights from laser-scanned experimental models. *AAPG Bulletin,* 95**,** 1147-1180.

MOODY, J. D., HILL, M. J. 1956. Wrench Fault Tectonics. *Geological Society of America Bulletin,* 67**,** 1207-1246.

MORLEY, C. & GUERIN, G. 1996. Comparison of gravity-driven deformation styles and behavior associated with mobile shales and salt. *Tectonics,* 15**,** 1154-1170.

MORLEY, C. K., KING, R., HILLIS, R., TINGAY, M. & BACKE, G. 2011. Deepwater fold and thrust belt classification, tectonics, structure and hydrocarbon prospectivity: A review. *Earth-Science Reviews,* 104**,** 41-91.

MUNRO, M. A. & BLENKINSOP, T. G. 2012. MARD—A moving average rose diagram application for the geosciences. *Computers & Geosciences,* 49**,** 112-120.

MURAOKA, H. & KAMATA, H. 1983. Displacement distribution along minor fault traces. *Journal of Structural Geology,* 5**,** 483-495.

MYERS, R. & AYDIN, A. 2004. The evolution of faults formed by shearing across joint zones in sandstone. *Journal of Structural Geology,* 26**,** 947-966.

NAYLOR, M. A., MANDL, G. & SUPESTEIJN, C. H. K. 1986. Fault geometries in basement-induced wrench faulting under different initial stress states. *Journal of Structural Geology,* 8**,** 737-752.

NEEDHAM, D. T., YIELDING, G. & FREEMAN, B. 1996. Analysis of fault geometry and displacement patterns. *Geological Society, London, Special Publications,* 99**,** 189-199.

NELSON, M. 2007. *3D Geometry and Kinematics of Non-Colinear Fault Intersections.* PhD, Cardiff University.

NICOL, A., WATTERSON, J., WALSH, J. J. & CHILDS, C. 1996. The shapes, major axis orientations and displacement patterns of fault surfaces. *Journal of Structural Geology,* 18**,** 235-248.

NIXON, C. W., SANDERSON, D. J. & BULL, J. M. 2011. Deformation within a strike-slip fault network at Westward Ho!, Devon U.K.: Domino vs conjugate faulting. *Journal of Structural Geology,* 33**,** 833-843.

NURIT HILDEBRAND, M. 1979. Deformation near a fault termination, part I: A fault in a clay experiment. *Tectonophysics,* 57**,** 131-150.

NWOSU, O. 2014. *The Compartmentalisation of the Deep Water Fold and Thrust Belt in the Levant Basin* PhD, Cardiff University.

PEACOCK, D. C. P. 1991. Displacements and segment linkage in strike-slip fault zones. *Journal of Structural Geology,* 13**,** 1025-1035.

PEACOCK, D. C. P. & SANDERSON, D. J. 1995. Strike-slip relay ramps. *Journal of Structural Geology,* 17**,** 1351-1360.

POSAMENTIER, H. W. & KOLLA, V. 2003. Seismic geomorphology and stratigraphy of depositional elements in deep-water settings. *Journal of Sedimentary Research,* 73**,** 367-388.

POSAMENTIER, H. W. & MARTINSEN, O. J. 2011. The character and genesis of submarine mass-transport deposits: insight from outcrop and 3D seismic data. *SEPM, Special Publication,* 96**,** 7-38.

QUINQUIS, H., AUDREN, C. L., BRUN, J. P. & COBBOLD, P. R. 1978. Intense progressive shear in Ile de Groix blueschists and compatibility with subduction or obduction. *Nature,* 273**,** 43-45.

RANALLI, G. 1977. Correlation between length and offset in strike-slip faults. *Tectonophysics,* 37**,** T1-T7.

REICHE, S., HÜBSCHER, C. & BEITZ, M. 2014. Fault-controlled evaporite deformation in the Levant Basin, Eastern Mediterranean. *Marine Geology*.

RESOR, P. G. & MEER, V. E. 2009. Slip heterogeneity on a corrugated fault. *Earth and Planetary Science Letters,* 288**,** 483-491.

RICHARD, P., MOCQUET, B. & COBBOLD, P. R. 1991. Experiments on simultaneous faulting and folding above a basement wrench fault. *Tectonophysics,* 188**,** 133-141.

RICHARD, P. D., NAYLOR, M. A. & KOOPMAN, A. 1995. Experimental models of strike-slip tectonics. *Petroleum Geoscience,* 1**,** 71-80.

RIEDEL, W. 1929. Zur mechanik geologischer Brucherscheinungen. *Zentralblatt für Mineralogy, Geologieund und Paläontologie B,* 1929**,** 354-368.

RIPPON, J. H. 1984. Contoured patterns of the throw and hade of normal faults in the Coal Measures (Westphalian) of north-east Derbyshire. *Proceedings of the Yorkshire Geological and Polytechnic Society,* 45**,** 147-161.

ROBERTSON, A. H. 1998a. Mesozoic-Tertiary tectonic evolution of the easternmost Mediterranean area: integration of marine and land evidence. *Proceedings of the Ocean Drilling Program, Scientific Results, Vol. 160; Chapter 54*.

ROBERTSON, A. H. F. 1998b. Tectonic significance of the Eratosthenes Seamount: a continental fragment in the process of collision with a subduction zone in the eastern Mediterranean (Ocean Drilling Program Leg 160). *Tectonophysics,* 298**,** 63-82.

ROWAN, M. G., PEEL, F. J. & VENDEVILLE, B. C. 2004. Gravity-driven fold belts on passive margins.

RYAN, W. B. F. & CITA, M. B. 1978. The nature and distribution of Messinian erosional surfaces — Indicators of a several-kilometer-deep Mediterranean in the Miocene. *Marine Geology,* 27**,** 193-230.

SAGY, A., BRODSKY, E. E. & AXEN, G. J. 2007. Evolution of fault-surface roughness with slip. *Geology,* 35**,** 283-286.

SALAMON, A., HOFSTETTER, A., GARFUNKEL, Z. & RON, H. 2003. Seismotectonics of the Sinai subplate – the eastern Mediterranean region. *Geophysical Journal International,* 155**,** 149-173.

SCHRANK, C. E. & CRUDEN, A. R. 2010. Compaction control of topography and fault network structure along strike-slip faults in sedimentary basins. *Journal of Structural Geology,* 32**,** 184-191.

SCHWARZ, H. U. & KILFITT, F. W. 2008. Confluence and intersection of interacting conjugate faults: A new concept based on analogue experiments. *Journal of Structural Geology,* 30**,** 1126-1137.

SEGALL, P. & POLLARD, D. D. 1983. Nucleation and growth of strike slip faults in granite. *Journal of Geophysical Research,* 88**,** 555-568.

SIEH, K. E. & JAHNS, R. H. 1984. Holocene activity of the San Andreas fault at Wallace Creek, California. *Geological Society of America Bulletin,* 95**,** 883-896.

SMIT, J., BRUN, J. P., FORT, X., CLOETINGH, S. & BEN-AVRAHAM, Z. 2008. Salt tectonics in pull-apart basins with application to the Dead Sea Basin. *Tectonophysics,* 449**,** 1-16.

SWANSON, M. T. 1989. Sidewall ripouts in strike-slip faults. *Journal of Structural Geology,* 11**,** 933-948.

SWANSON, M. T. 2005. Geometry and kinematics of adhesive wear in brittle strike-slip fault zones. *Journal of Structural Geology,* 27**,** 871-887.

SYLVESTER, A. G. 1988. Strike-slip faults. *Geological Society of America Bulletin,* 100**,** 1666-1703.

SYLVESTER, A. G. & SMITH, R. R. 1976. Tectonic transpression and basement-controlled deformation in San Andreas fault zone, Salton Trough, California. *AAPG Bulletin,* 60**,** 2081-2102.

TALBOT, C. J. & JACKSON, M. P. A. 1987. Internal kinematics of salt diapirs. *AAPG Bulletin,* 71**,** 1068-1093.

TAYMAZ, T., YILMAZ, Y. & DILEK, Y. 2007. The geodynamics of the Aegean and Anatolia: introduction. *Geological Society, London, Special Publications,* 291**,** 1-16.

TCHALENKO, J. S. 1970. Similarities between Shear Zones of Different Magnitudes. *Geological Society of America Bulletin,* 81**,** 1625-1640.

THORSEN, C. E. 1963. Age of growth faulting in southeast Louisiana. *Gulf Coast Association of Geological Societies Transactions,* 13**,** 103-110.

TIBOR, G., BEN-AVRAHAM, Z., STECKLER, M. & FLIGELMAN, H. 1992. Late Tertiary subsidence history of the Southern Levant Margin, Eastern Mediterranean Sea, and its implications to the understanding of the Messinian event. *Journal of Geophysical Research,* 97**,** 17593-17,614.

TRON, V. & BRUN, J.-P. 1991. Experiments on oblique rifting in brittle-ductile systems. *Tectonophysics,* 188**,** 71-84.

TWISS, R., MOORES, E. 1992. *Structural Geology*, W. H. Freeman and Company.

UETA, K., TANI, K. & KATO, T. 2000. Computerized X-ray tomography analysis of three-dimensional fault geometries in basement-induced wrench faulting. *In:* YUJI KANAORI, K. T. & MASAHIRO, C. (eds.) *Developments in Geotechnical Engineering.* Elsevier.

WALLACE, R. E. Notes on stream channels offset by the San Andreas fault, southern Coast Ranges, California. 1968. 6–21.

WALSH, J. J. & WATTERSON, J. 1987. Distributions of cumulative displacement and seismic slip on a single normal fault surface. *Journal of Structural Geology,* 9**,** 1039-1046.

WALSH, J. J. & WATTERSON, J. 1988. Analysis of the relationship between displacements and dimensions of faults. *Journal of Structural Geology,* 10**,** 239-247.

WALSH, J. J. & WATTERSON, J. 1990. New methods of fault projection for coalmine planning. *Proceedings of the Yorkshire Geological and Polytechnic Society,* 48**,** 209-219.

WATTERSON, J. 1986. Fault dimensions, displacements and growth. *Pure and Applied Geophysics,* 124**,** 365-373.

WDOWINSKI, S., BEN-AVRAHAM, Z., ARVIDSSON, R. & EKSTRÖM, G. 2006. Seismotectonics of the Cyprian Arc. *Geophysical Journal International,* 164**,** 176-181.

WESNOUSKY, S. G. 1988. Seismological and structural evolution of strike-slip faults. *Nature,* 335**,** 340-343.

WESNOUSKY, S. G. 2006. Predicting the endpoints of earthquake ruptures. *Nature,* 444**,** 358-360.

WILCOX, R. E., HARDING, T. P. & SEELY, D. R. 1973. Basic Wrench Tectonics. *AAPG Bulletin,* 57**,** 74-96.

WILLEMSE, E. J. M., PEACOCK, D. C. P. & AYDIN, A. 1997. Nucleation and growth of strike-slip faults in limestones from Somerset, U.K. *Journal of Structural Geology,* 19**,** 1461-1477.

WOOD, L. J. & MIZE-SPANSKY, K. L. 2009. Quantitative seismic geomorphology of a Quaternary leveed-channel system, offshore eastern Trinidad and Tobago, northeastern South America. *AAPG Bulletin,* 93**,** 101-125.

WOODCOCK, N. H. & DALY, M. C. 1986. The Role of Strike-Slip Fault Systems at Plate Boundaries [and Discussion]. *Philosophical Transactions of the Royal Society of London. Series A, Mathematical and Physical Sciences,* 317**,** 13-29.

WOODCOCK, N. H. & FISCHER, M. 1986. Strike-slip duplexes. *Journal of Structural Geology,* 8**,** 725-735.

WU, J. E., MCCLAY, K., WHITEHOUSE, P. & DOOLEY, T. 2009. 4D analogue modelling of transtensional pull-apart basins. *Marine and Petroleum Geology,* 26**,** 1608-1623.

WYNN, R. B., CRONIN, B. T. & PEAKALL, J. 2007. Sinuous deep-water channels: Genesis, geometry and architecture. *Marine and Petroleum Geology,* 24**,** 341-387.

ZHANG, K., LIU, K. & YANG, J. 2004. Asymmetrical valleys created by the geomorphic response of rivers to strike-slip fault. *Quaternary Research,* 62**,** 310-315.

ZHAO, G. & JOHNSON, A. M. 1991. Sequential and incremental formation of conjugate sets of faults. *Journal of Structural Geology,* 13**,** 887-895.

ZHU, M., GRAHAM, S. & MCHARGUE, T. 2009. The Red River Fault zone in the Yinggehai Basin, South China Sea. *Tectonophysics,* 476**,** 397-417.

ZOBACK, M. D., ZOBACK, M. L., MOUNT, V. S., SUPPE, J., EATON, J. P., HEALY, J. H., OPPENHEIMER, D., REASENBERG, P., JONES, L. & RALEIGH, C. B. 1987. New evidence on the state of stress of the San Andreas fault system. *Science,* 238**,** 1105-1111.